# THE JOURNAL OF PHYSICAL CHEMISTRY

*Volume 74*

APRIL—JULY 1970

PAGES 1405—3028



AMERICAN CHEMICAL SOCIETY, PUBLICATIONS DIVISION

RICHARD L. KENYON
*Director*

JOSEPH H. KUNEY
*Director of Business Operations*
*Director of Publications Research*

DAVID E. GUSHEE
*Publication Manager, Journals*

THE JOURNAL OF

# PHYSICAL CHEMISTRY

*Volume 74, Number 7 April 2, 1970*

# RADIONUCLIDES IN THE ENVIRONMENT

## ADVANCES IN CHEMISTRY SERIES NO. 93

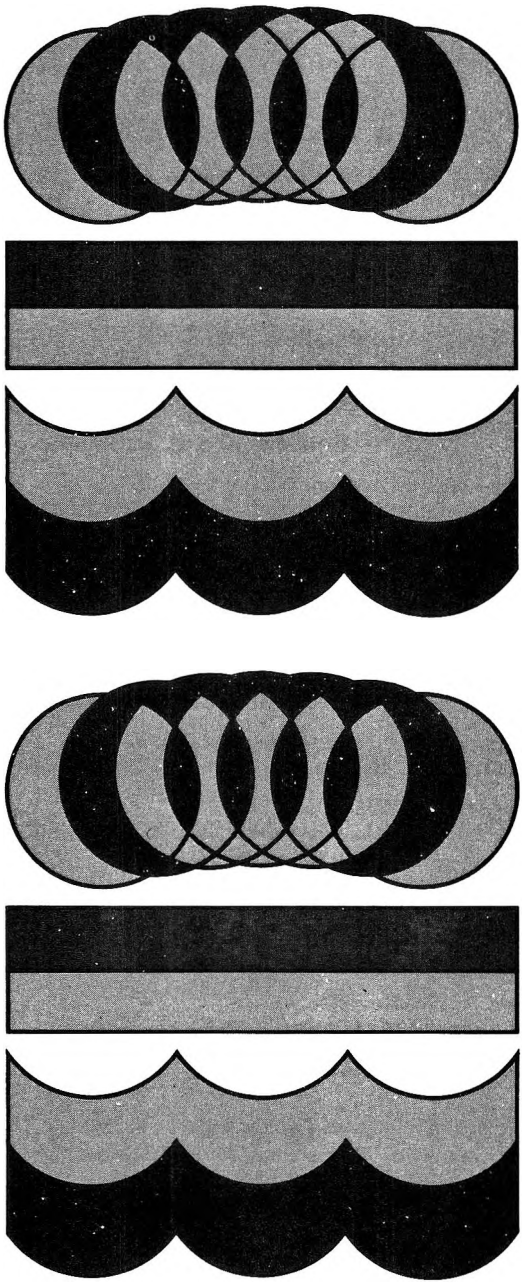

Twenty-eight papers from a symposium sponsored by the Division of Nuclear Chemistry and Technology, chaired by E. C. Freiling.

Pollution . . . a growing concern . . . a concept not generally associated with radionuclides. The successful control of this hazardous waste product of nuclear energy is essential to the continued use and development of nuclear power. Critical to this problem is an understanding of the processes by which radionuclides are produced, dispersed, and retained in the environment.

The papers is this volume discuss and evaluate the properties and problems relating to radionuclides, including

- mechanisms of release, absorption, uptake, transport
- behavior, measurement and characterization, specific weapons tests
- specific activity, public health aspects, fallout
- new methods and equipment

522 pages with index Clothbound (1968) $15.00
Set of L.C. cards with library orders upon request.

Other books in the ADVANCES IN CHEMISTRY SERIES of related interest include:

No. 89 Isotope Effects in Chemical Processes.
278 pages Clothbound (1969) $13.00

No. 82 Radiation Chemistry—II.
558 pages Clothbound (1968) $16.00

No. 81 Radiation Chemistry—I.
616 pages Clothbound (1968) $16.00
No. 81 and No. 82 ordered together $30.00

No. 72 Mass Spectrometry in Inorganic Chemistry.
329 pages Clothbound (1968) $12.00

No. 68 The Mossbauer Effect and Its Application in Chemistry.
178 pages Clothbound (1967) $ 8.00

No. 66 Irradiation of Polymers.
275 pages Clothbound (1967) $10.00

No. 58 Ion-Molecule Reactions in the Gas Phase.
336 pages Clothbound (1966) $10.50

No. 50 Solvated Electron.
304 pages Clothbound (1965) $10.50

No. 40 Mass Spectral Correlations.
117 pages Paperbound (1963) $ 6.00

No. 26 Nonmilitary Defense—Chemical and Biological Defenses in Perspective.
100 pages Paperbound (1960) $ 4.00

No. 18 Thermodynamic Properties of the Elements.
234 pages Clothbound (1956) $ 8.00

No. 15 Physical Properties of Chemical Compounds.
536 pages Colthbound (1955) $10.00

Postpaid in U. S. and Canada; plus 30 cents elsewhere.
Order from:

SPECIAL ISSUES SALES
AMERICAN CHEMICAL SOCIETY
1155 SIXTEENTH ST., N.W.
WASHINGTON, D. C. 20036

## NOTES



## COMMUNICATIONS TO THE EDITOR

## AUTHOR INDEX

THE JOURNAL OF
PHYSICAL CHEMISTRY



VOLUME 74, NUMBER 7 APRIL 2, 1970

# Crystallization of Slightly Soluble Salts from Solution

**by R. H. Doremus**

*General Electric Research and Development Center, Schenectady, New York* *(Received October 20, 1969)*

The rate of crystallization of barium sulfate from aqueous solution was studied simultaneously with two methods, electrical conductivity of the solution and light scattering from the particles. From these measurements the particle size was estimated and the interface growth coefficient was calculated. The results indicated that the particles coagulated in the later stages of precipitation. Results of several authors on crystallization of salts from solution are compared. The order of the crystallization process depends upon the stoichiometry of the salt and its supersaturation. The effect of supersaturation may result from different growth processes on different crystal faces. The interface growth coefficients for different salts, orders of crystallization, and supersaturation are compared. These coefficients are usually not a function of order or supersaturation, but do depend upon the type of salt crystallizing.

## Introduction

Crystals of ionic salts are nearly always prepared and purified by precipitation from solution. Although this process has often been studied, the sequence of events from the mixing of solutions to the final crystals is still debated. The steps of the precipitation process are nucleation of the crystals, their growth by accretion of material from the solution, and possible coagulation and competitive growth (Ostwald ripening).

In the present work the precipitation of barium sulfate from aqueous solution was followed with two techniques simultaneously, electrical conductivity of the solution and light scattering from the crystals. The combination of these two techniques allowed a rough calculation of the particle size and therefore of the interface growth coefficient. Furthermore, these experiments indicated that the particles coagulate in the later stages of precipitation, showing that measurements of nucleation rates from counts of particles are questionable.

The growth of crystals from solution can be studied in several ways. For larger crystals the rate of growth becomes influenced by diffusion of the precipitating ions or molecules in the liquid near the crystal.[1-3] Thus to measure the rate of the interface growth process it is necessary to study small crystals, often submicroscopic. Two methods can be used to measure this growth process. In one, seed crystals are added to a slightly supersaturated solution in which no nucleation can occur. Then growth takes place only on the seed crystals, whose size can be measured in the light or electron microscope. The rate of growth is calculated from the rate at which material disappears from the solution, usually followed with the solution conductance, and the crystal size. In the other method the rate of precipitation of crystals is followed in two different ways so that both the rate of removal of material from solution and the crystal size can be calculated, as was done in the present work. In the precipitation method the supersaturation must be high enough for crystals to nucleate, so that the two methods measure the growth rate at different supersaturations. In this paper, measurements of growth rates at different supersaturations

(1) D. Turnbull, *Acta Met.*, **1**, 764 (1953).

(2) A. E. Nielsen, "Kinetics of Precipitation," Macmillan Co., New York, N.Y., 1964. This book has an extensive bibliography.

(3) R. H. Doremus, *J. Phys. Chem.*, **62**, 1068 (1958).

and for different salts are compared and discussed in terms of various theories.

## Growth Equations

In the present work it is assumed that all particles are nucleated at the time of mixing, so that the number of growing particles $N$ is constant and they are all of the same size. Furthermore it is assumed that the growth rate is controlled by a process at the particle surface (interface control). Turnbull has shown that these conditions are valid for the precipitation of barium sulfate at the concentrations used here.[1] Then the flux of material $J$ per unit area and time that is deposited on the particles is

$$J = \rho\frac{dR}{dt} = \frac{G(C_m - C_0)^n(1 - W)^n}{C_0^n} \quad (1)$$

In this equation $\rho$ is the density of the particles in concentration units, $R$ is their radius, $G$ is an interface growth coefficient, $n$ is the order of the growth process, $C_m$ and $C_0$ are the initial and equilibrium concentration of barium sulfate in the solution, respectively, and $W$ is the fraction of precipitation and is given by

$$W = \frac{4\pi NR^3\rho}{3(C_m - C_0)} \quad (2)$$

Detailed discussions and deviations of these equations are given in a number of publications.[1-3] The factor of $(1 - W)$ in eq 1 accounts for competition between particles for the solute. Nielsen[2] gives a table of values of integrals of eq 1 for different $n$ values, using eq 2 to express $dR/dt$ in terms of $W$.

If $W$, the extent of precipitation, is small, $G$ can be calculated from an integration of eq 1 with $W$ constant and assuming the crystal has negligible radius at the time of mixing. Then

$$G \approx \frac{R\rho}{tS^n(1 - W)^n} \quad (3)$$

where the particle has radius $R$ after growth time $t$. The supersaturation $S$ is

$$S = \frac{C_m - C_0}{C_0} \quad (4)$$

and is the best parameter to use to compare results at different concentrations, with different crystals, and with different $n$ values.

## Experimental Section

Solutions of barium nitrate and potassium sulfate were mixed together with vigorous stirring to give the same final concentration of the two salts. One portion of the mixture was poured into a conductivity cell and the other in a light scattering cell. The resistance and light scattering of the solution was then measured as a function of time. Neither solution was stirred or moved during precipitation.

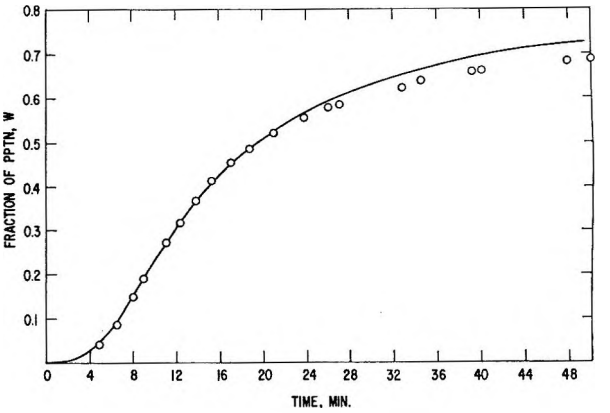


Figure 1. Fraction of barium sulfate precipitation as a function of time. Curve drawn from eq 1 with $n = 3$, points measured from the electrical conductivity of the solution.

The conductivity cell was of standard design and held about 25 ml of solution. The electrodes were shiny platinum, so that they did not nucleate crystals. The resistance of the cell was measured with a Wheatstone bridge of Luder's design.[4] The temperature of the cell was held constant at 25.00 ± 0.02° with a water bath.

The light scattering was measured in an apparatus built by P. D. Zemany and H. T. Hall in this laboratory and having an optical system similar to that of Zimm.[5] The measurements were made at 90° from the incident beam with plane polarized light of 0.546-$\mu$ wavelength. The solutions were filtered through millipore filters just before mixing to ensure that no spurious scattering centers were present. The output of the photomultiplier was recorded continuously.

## Experimental Results

The results of measurements for a solution containing $1.6 \times 10^{-7}$ mol/cm$^3$ of potassium sulfate and barium nitrate are shown in Figures 1 and 2. The fraction of precipitation $W$ was calculated from the conductivity of the solution and the known equivalent conductances of barium, potassium, sulfate, and nitrate ions. No corrections were made for changes in activity coefficients, ion pairing, or equivalent conductances as a function of time, since the solutions were very dilute and the total concentration changed only about 30% in the region of interest. The line in Figure 1 was calculated from eq 1 with $n = 3$. The fit is good up to about 20 min, after which the experimental results drop below the curve. This same deviation was found for other experiments of barium sulfate and strontium sulfate.[3]

The line in Figure 2 is the same as in Figure 1. The raw scattering data were normalized to the line at $W = 0.1$. Since they fit the line fairly well, the scattering

(4) W. F. Luder, *J. Amer. Chem. Soc.*, 62, 89 (1940).
(5) B. H. Zimm, *J. Chem. Phys.*, 16, 1099 (1948).

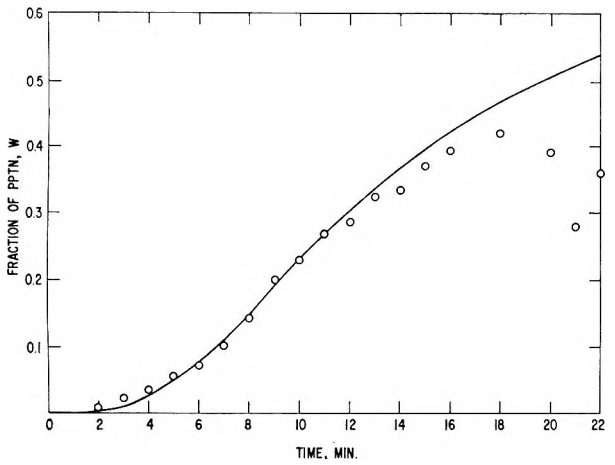


Figure 2. Fraction of barium sulfate precipitation as a function of time. Curve same as for Figure 1; points are intensity of scattered light, normalized with the curve at $W = 0.1$.

is apparently about proportional to the volume of the particles during the growth studied here. The scattering decreased sharply at about 18 min after the start of precipitation, and continued to decrease until it reached nearly background level after about 30 min. Occasional dips, such as the one at 21 min, were observed shortly after the break, and peaks were observed during later stages of the decrease of the scattering.

An estimate of the size of the precipitating particles can be derived from the comparison between scattering and the growth curve in Figure 2. The intensity of 90° scattering calculated for spherical particles for refractive index 1.25 (that of barium sulfate is about 1.22) is plotted against particle size in Figure 3. It is seen that the scattering is proportional to the volume of the particles only over a narrow size range. The scattering results in Figure 2 seem to be slightly less than proportional to the volume of the particles over a size range in which the radius is doubled. If these two size ranges are equated, the radius of the particles is found to be about 1000 Å at $W = 0.05$. Then from eq 4, $G = 2.6 \times 10^{-13}$ mol/cm² sec, and the number density of particles is about $10^8$ per cm³. The following parameters for barium sulfate at 25° were used in this calculation: $\rho = 0.0192$ mol/cm³, $C_0 = 1.06 \times 10^{-8}$ mol/cm³.

## Discussion and Comparison with Previous Results

In an earlier study the deviations from the growth curve shown in Figure 1 were attributed to a change in the mode of growth.[3] In the earlier stages the rate of growth increased proportional to the surface area of the crystals, but after the deviations the rate data behaved as if the area for deposition of material were constant. The light scattering results shown in Figure 2 suggest that coagulation of the crystals formed first is the reason for this change. After about 20 min of growth the crystals begin to coagulate together to form larger crystals

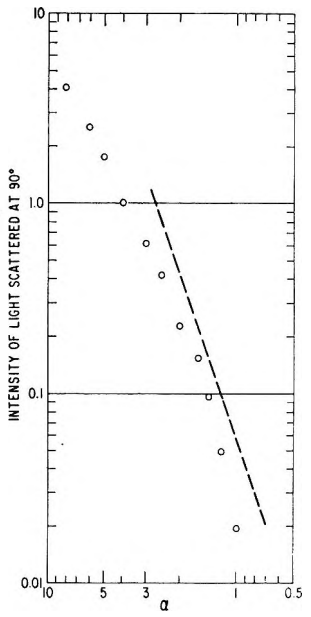


Figure 3. Intensity of light scattered at 90° from incident beam from spherical particles of refractive index 1.25 as a function of $\alpha = 2\pi$(particle radius)/(wavelength of light in solution). Incident light perpendicularly plane polarized. Points are calculated from tables of W. J. Pangonis, W. Heller, and A. Jacobsen, "Light Scattering Functions," Wayne State University Press, Detroit, Mich., 1957, and H. Blumer, *Z. Phys.* **32**, 119 (1925); **38**, 304 (1926); line is drawn with slope 3.

which subsequently sediment to the bottom of the vessel containing them. The larger crystals have a lower scattering cross section per unit volume than do the smaller particles, as shown in Figure 3, so that as coagulation proceeds the scattering actually decreases, as shown in Figure 2. As the particles sediment the scattering also decreases until there are few particles in the scattering volume. After precipitation of slightly soluble salts a deposit often is found in the reaction vessel, consistent with this view. The coagulation of smaller particles into larger ones gives a somewhat smaller effective area for deposition. The area of these larger particles is increased only very slightly with further deposition of material, giving the appearance in the kinetics of a constant growth area. Therefore, the experimental results are consistent with coagulation of the precipitating crystals. Meehan and Miller also concluded that coagulation was occurring in their study of rapid precipitation of silver bromide.[6] Because of the possibility of coagulation, any study of nucleation rates and crystal sizes in precipitation from counts or observation of crystals after a certain time of crystallization is questionable. For example, the original precipitation laws of von Weimarn were deduced from observations of this sort; it seems likely that results were often affected by coagulation.

Various authors have found different values for the

(6) E. J. Meehan and J. K. Miller, *J. Phys. Chem.*, **72**, 2168 (1968).

**Table I:** Order of Growth Laws for the Precipitation of Ionic Crystals

| Salt | Supersatn Low | Supersatn High | Reference |
|---|---|---|---|
| Silver chloride | 2 | | *a, b* |
| Barium sulfate | 2 | 3 (4?) | *c, d* |
| Strontium sulfate | 2 | 3 | *e, f, g, h* |
| Lead sulfate | 2 | | *i* |
| Magnesium oxalate | 2 | | *j* |
| Silver chromate | 3 | 4 | *k, l* |

[a] C. W. Davies and G. H. Nancollas, *Trans. Faraday Soc.*, **53,** 1449 (1957). [b] M. J. Insley and G. D. Parfitt, *ibid.*, **64,** 1945 (1968). [c] See ref 1–3. [d] G. H. Nancollas and N. Purdie, *Trans. Faraday Soc.*, **59,** 735 (1963). [e] See ref 3. [f] J. Salomon, Thesis, New York University, 1964. [g] J. R. Campbell and G. H. Nancollas, *J. Phys. Chem.*, **73,** 1735 (1969). [h] S. Oden and D. Werner, *Ark. Kemi Mineral., Geol.*, **9,** No. 23 and 32 (1926). [i] G. H. Nancollas and N. Purdie, *Quart. Rev.*, **18,** 1 (1964). [j] G. H. Nancollas and N. Purdie, *Trans. Faraday Soc.*, **57,** 2272 (1961). [k] A. Van Hook, *J. Phys. Chem.*, **44,** 751 (1940). [l] J. R. Howard and G. H. Nancollas, *Trans. Faraday Soc.*, **53,** 1449 (1957).

order $n$ of the precipitation process. A summary is given in Table I. From the table one can deduce that $n$ depends on at least two factors, the stoichiometry of the crystallizing salt and its supersaturation, as deduced previously.[3] The results of Salomon[7] are particularly interesting in this regard, since he studied the growth rate of strontium sulfate crystals over a wide range of supersaturation and observed their morphology under the microscope as well. Salomon found that the morphology of the crystals was quite different at high and low supersaturation and that these differences correspond to the change in order from 2 to 3. It seems likely, therefore, that the change of order results from the nucleation of crystals with different crystallographic faces and that the growth mechanism on different faces is different. Further work to clarify and confirm this relation between growth mechanism and morphology should give attractive results.

To calculate the interface growth coefficient $G$ of eq 1 from the rate of precipitation of a suspension of crystals it is necessary to known the size of the crystals. In the seed crystal experiments of Davies and Nancollas and their collaborater the crystals were large enough to observe in the microscope. In the present case the simultaneous measurement of conductivity and light scattering provided information to estimate the particle size and therefore to calculate $G$, as shown in the last section. Calculations of $G$ for various crystal growth experiments are given in Table II. The agreement

**Table II:** Interface Growth Coefficient for Various Crystals

| Salt | Supersatn | Order $N$ | $G$, mol/cm² sec | Ref |
|---|---|---|---|---|
| Barium sulfate | 2 | 2 | $3 \times 10^{-13}$ | *a* |
| | 14 | 3 | $3 \times 10^{-13}$ | *b* |
| Silver chloride | Low | 2 | $3 \times 10^{-11}$ | *c* |
| | Low | 2 | $3 \times 10^{-11}$ | *d* |
| Magnesium oxalate | 0.36 | 2 | $4 \times 10^{-13}$ | *e* |
| | 1.3 | 2 | $10^{-11}$ | *e* |

[a] G. H. Nancollas and N. Purdie, *Trans. Faraday Soc.*, **59,** 735 (1963). [b] Present work. [c] C. W. Davies and G. H. Nancollas, *Trans. Faraday Soc.*, **53,** 1449 (1957). [d] M. J. Insley and G. D. Parfitt, *ibid.*, **64,** 1945 (1968). [e] G. H. Nancollas and N. Purdie, *ibid.*, **57,** 2272 (1961).

between $G$ measured for barium sulfate in the present experiments and those of Nancollas and Purdie on seed crystals, notwithstanding the difference in reaction order, is noteworthy. The agreement between two different sets of experiments on silver chloride, done in quite different ways, also shows the usefulness of comparing $G$ values. The value of $G$ was not a function of supersaturated except in magnesium oxalate. The higher rate at higher supersaturation possibly resulted from the nucleation of new crystals. It would be interesting to obtain more accurate results for $G$ on a wide variety of salts to see if it is related to such factors as ion size, ion polarizability, hydration, and other factors. In any event it appears that $G$, the rate of growth at unit supersaturation, is the correct parameter to compare for different conditions of precipitation.

A number of different theories have been proposed for interface controlled growth from solution.[2,3,8–10] Features such as surface diffusion, surface reactions including dehydration, surface defects such as energent dislocations, surface steps and kinks in the steps, step spacing, surface roughness, impurity adsorption, and others are involved in these theories. To test most of these ideas more detailed study of the crystal surface itself during growth is required. The present results show the importance of stoichiometry of the crystallizing salt, of the orientation of crystal faces, and the possibility of coagulation of crystals during growth from solution.

(7) J. Salomon, Thesis, New York University, 1964.
(8) W. R. Burton, N. Cabrera, and F. C. Frank, *Phil. Trans. Roy. Soc. London*, **243,** 299 (1951).
(9) G. W. Sears, *J. Chem. Phys.*, **29,** 979, 1045 (1958).
(10) J. W. Cahn, *Acta Met.*, **8,** 554 (1960).

# Determination of Diffusion Coefficients for Nitrogen Dioxide in Polystyrene by Chain Scission and Sorption–Desorption

by H. H. G. Jellinek and S. Igarashi

*Department of Chemistry, Clarkson College of Technology, Potsdam, New York 13676* *(Received August 12, 1969)*

Diffusion coefficients for nitrogen dioxide in polystyrene have been determined by using, for the first time, degrees of degradation due to chain scission as indicators for the progress of the diffusion process by penetration; also sorption–desorption experiments were carried out. The experimental data for the calculation of diffusion from degrees of degradation were measured in a specially constructed high-vacuum penetration cell. The coefficients obtained by either method agree satisfactorily. In addition, it has been shown that a substitution reaction, replacing tertiary hydrogen atoms in the polymer by $NO_2$ groups, is negligibly slow compared with the diffusion process and can be neglected for the evaluation of the penetration experiments. Arrhenius parameters are given for the diffusion coefficients, chain scission and substitution rate constants. It was also ascertained that Henry's law holds. The molar heat of solution is negative mainly due to the heat of condensation of the gas.

Reaction of nitrogen dioxide with thin films (*ca.* 20 $\mu$ thick) of polystyrene and butyl rubber has been studied recently.[1,2] Chain scission of main chain links takes place. It was ascertained that in case of such thin films, diffusion of gas into the film does not play a role. An additional reaction, however, takes place with polystyrene. Tertiary hydrogen atoms are replaced along the carbon backbone by $NO_2$ groups. While this latter reaction consumes appreciable quantities of gas, the chain scission uses only negligible amounts of nitrogen dioxide. Thick polymer films give rise to additional complications. Here, chain scission at a certain distance $x$ from the surface cannot take place until the gas has arrived at the distance $x$ by diffusion. The same is true for any other chemical reactions. Thus, diffusion and a simultaneous chemical reaction have to be considered. Once, the gas has diffused to the distance $x$, saturation of the film by the gas is fairly quickly reached, if the chemical reaction is slower than the diffusion process. If this is not the case, saturation may never be achieved and the reaction becomes diffusion controlled.

The present paper deals with the diffusion of nitrogen dioxide into relatively thick polystyrene films or stacks of thin films. Diffusion coefficients are evaluated from penetration and sorption–desorption experiments. The degree of degradation $\alpha$ as a function of $x$, gas pressure, and temperature was utilized as an indicator of the progress of diffusion. This is a novel procedure, which has not been attempted previously. The influence of the chemical substitution reaction has also been evaluated. Solubilities as function of gas pressure and temperature have been determined, and Henry's law is shown to hold. Arrhenius parameters for diffusion coefficients and chemical rate constants have been evaluated. The diffusion coefficients obtained from penetration and sorption–desorption experiments agree satisfactorily.

## Experimental Section

(*a*) *Apparatus.* An all-glass high-vacuum apparatus ($10^{-5}$–$10^{-6}$ mm) as depicted in Figure 1, was used for this work. It had provision for measuring relatively small (Pyrex spoon gauge, modified Fisher McLeod mercury gauge) and large pressures (U-tube manometer), respectively. These pressure gauges were so arranged that mercury comes in contact with the corrosive gas for only short periods of time. In addition, a thermostated glass vessel housing a quartz spring and another one for the penetration-diffusion cell were provided. The diffusion cell was directly connected to the high-vacuum system and had also an attachment, J, for permanent evacuation at the far side of the set of films. This cell is shown in Figure 2. It consists of a large Teflon joint T, which is connected to the high-vacuum apparatus. A set of films, F, is inserted. These films have to be placed loosely into the cell in order to be able to remove all air between them. Once this is achieved, the metal bellows, B, is tightened by means of the screw, K, and the films make a tight seal with the help of a Viton O ring. Thus, the gas has to diffuse through the films in order to pass to the far side of them. The gas pressure is kept constant throughout the experiment. The far side of the film is backed by a Teflon-covered plate, P.

Sorption–desorption experiments were carried out by suspending a film from a quartz spring, which was ther-

(1) H. H. G. Jellinek and F. Flajsman, *J. Polym. Sci., A-1*, **7**, 1153 (1969); H. H. G. Jellinek and Y. Toyoshima, *ibid.*, **5**, 3214 (1967); see also H. H. G. Jellinek, F. Flajsman, and F. J. Kryman, *J. Appl. Polym. Sci.*, **13**, 107 (1969).

(2) H. H. G. Jellinek and F. Flajsman, *J. Polym. Sci., A-1*, in press.

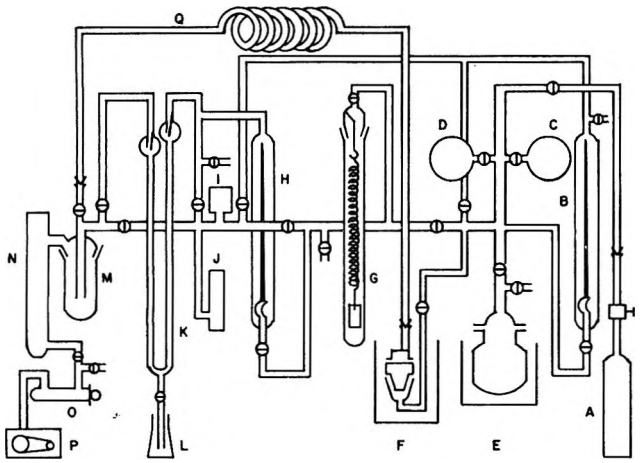


Figure 1. High-vacuum apparatus: A, $NO_2$ tank; B, low-pressure spoon gauge; C, D, storage bulbs; E, flask for drying films; F, diffusion cell; G, quartz spring; H, high-pressure spoon gauge; I, McLeod gauge; J, Nester-Faust (Fisher) pressure gauge, K, U-type Hg manometer; M, cold trap; N, Hg diffusion pump; O, $P_2O_5$ tube; P, rotary pump; Q, special connection between diffusion cell and high-vacuum line.

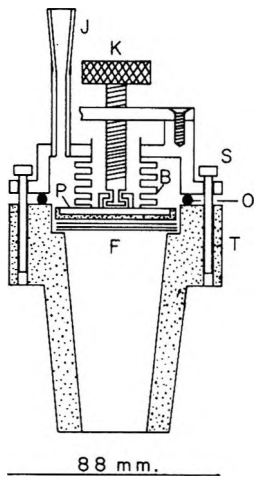


Figure 2. Diffusion cell: B, metal bellows; K, screw for tightening bellows; J, special connection to high vacuum at far side of films; F, set of films (*ca.* 40 $\mu$ each); O, Viton O ring; T, Teflon joint; P, Teflon-covered black-plate; S, screws.

mostated. Intrinsic viscosities were measured in Ubbelohde viscometers in dl/g at 34°.

(*b*) *Materials.* Atactic, isothermal polystyrene was the same as used in previous work[1] and was kindly supplied by the Dow Chemical Co. It was purified by twice precipitating from methyl ethyl ketone (*ca.* 1% w/w) with methanol at room temperature. The polymer was dried, eventually under high vacuum at about 40° for 24 hr. All solvents were of reagent grade quality. The polymer, as received, had a weight-average molecular weight of $\bar{M}_w = 3.72 \times 10^5$ and a ratio of weight- to number-average molecular weights $\bar{M}_w/\bar{M}_n = 2.3$. Thus, the polymer had practically a random molecular size distribution. The intrinsic viscosity–number-average molecular weight relationship for this polymer sample is $[\eta] = 4.85 \times 10^{-5} \bar{M}_n^{0.814}$ dl/g in dioxane solution at 34°; this amounts to a number-average molecular weight of $1.97 \times 10^5$. A random size distribution remains invariant for moderate degrees of degradation. $NO_2$ was obtained from Matheson. It contained negligible amounts of nitrosyl chloride (<20 ppm), a water equivalent of 0.06%, and particulates 1.0 mg/l. It was dried before being introduced into the high-vacuum system. Fluorolube (Gr 544, Hooker Chemical Co.) was used throughout, because of the reactivity of $NO_2$ with other greases.

(*c*) *Film Preparation.* Films were obtained by casting 6% w/v solutions of polystyrene in methyl ethyl ketone onto mercury surfaces and controlling the subsequent evaporation of the solvent. The films were dried under vacuum and eventually in high vacuum (*ca.* $10^{-5}$ mm) at 60° for 70 hr. The film thickness was determined by weighing and measuring the film area (density of polymer 1.06 g/cm³).

(*d*) *Procedure for Penetration Experiments.* A constant total gas pressure was established in the high-vacuum apparatus. The diffusion cell was thermostated and preheated to the desired temperature for at least 1 hr (temperature constancy ±0.2°). The diffusion was then allowed to proceed for a definite length of time (several hours or days). At the end of the diffusion period, the films were degassed for 12 hr, and the intrinsic viscosity of each film of the set was measured. The degrees of degradation $\alpha_x = (1/\overline{DP}_{n,t}) - (1/\overline{DP}_{n,0})$ were derived from these data as a function of $x$, the distance from the film surface (the latter is adjacent to the gas at constant pressure).

(*e*) *Some Preliminary Penetration Experiments (Influence of Solvent).* A number of preliminary experiments were performed in order to ascertain the effectiveness of solvent removal from the films. Benzene was taken as the solvent for these experiments. It is to be expected that degradation increases with decreasing film thickness for relatively short exposure times. Surprisingly, however, the behavior was the exact opposite when benzene was used as solvent. The last stage of drying consisted of 70 hr under high vacuum at 60°. The film thickness ranged from 15 to 425 $\mu$. It appears that benzene clings extremely tenaciously to polystyrene. This was confirmed by determining the benzene content by weighing. Figure 3 shows that traces of benzene left in the film have an appreciable effect on the extent of degradation. Subsequently, only methyl ethyl ketone was used as solvent; this solvent could easily be removed. Films obtained by casting from this solvent gave the correct type of curve as Figure 4 shows. The extent of degradation increases with decreasing film thickness and levels off when a film thickness of about 50 $\mu$ is reached.

(*f*) *Procedure for Sorption–Desorption Experiments.* The quartz spring, from which a polymer film was suspended (*ca.* 50–70 $\mu$ thick, area of film *ca.* 13 cm²),

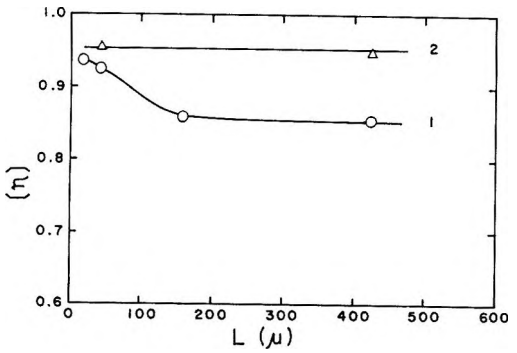


Figure 3. Effect of residual benzene as function of polymer film thickness at 55°, $P_{total}$ = 60 cm, diffusion time 2 hr: (1) exposed, (2) blank.

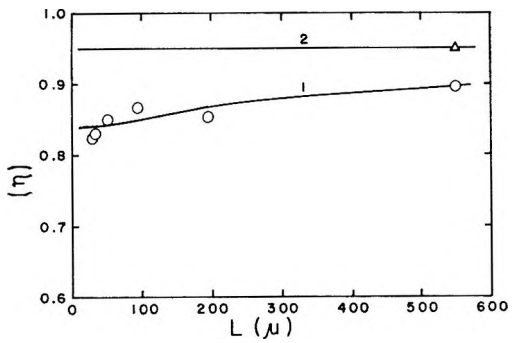


Figure 4. [η] as function of film thickness. Films cast from methyl ethyl ketone solution at 55°, $P_{total}$ = 60 cm, diffusion time 4 hr.

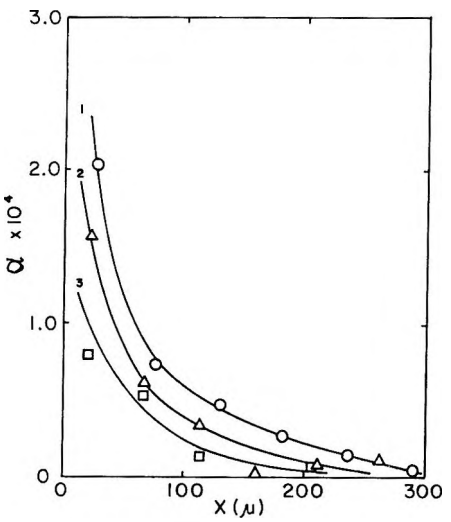


Figure 5. $\alpha_{x,t}$ as function of distance from film surface for various diffusion times at 55°, $P_{total}$ = 60 cm: (1) 8 hr, (2) 6 hr, (3) 4 hr.

was also thermostated to a temperature constancy of ±0.2°. The sensitivity of the spring was 0.0709 cm/mg. The extension was read as a function of time with a cathetometer to 0.05 mm. At the end of each experiment, the film was degassed by fast evacuation, the desorption was then measured as a function of time.

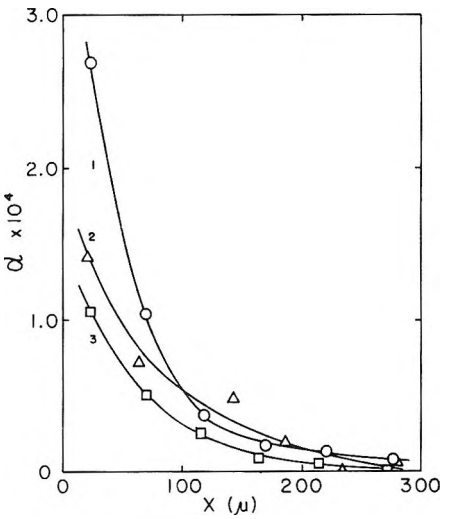


Figure 6. Same as Figure 5 at 45°, diffusion time 14 hr: (1) 60 cm, (2) 30 cm, (3) 21.6 cm.

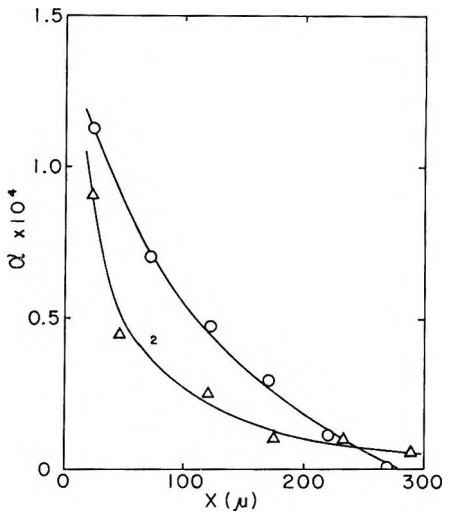


Figure 7. Same as Figure 5: (1) 65°, $P_{total}$ 0.8 cm, 215 hr; (2) 45°, $P_{total}$ = 2 cm, 118 hr.

## Experimental Results

*Penetration and Sorption–Desorption Experiments.* Typical $\alpha_x$ *vs.* $x$ plots are shown in Figures 5–7 as a function of gas pressure, temperature, and diffusion time. $\alpha_x = (1/\overline{DP}_{n,x,t}) - (1/\overline{DP}_{n,0})$ where $\overline{DP}_{n,x,t}$ and $\overline{DP}_{n,0}$ are the number-average chain lengths for diffusion time $t$ at distance $x$ and the initial chain length, respectively; $x = 0$ coincides with the middle of the first film (*ca.* 20 μ from the surface). This is necessitated by the fact that the degree of degradation for each total film of finite thickness is measured; thus $\alpha_x$ is an average value and $x = 0$ should be located rather at the center of the film than at either surface.

Figures 8 and 9 show some typical sorption–desorption curves, where $W_t$ is plotted *vs.* time as function of temperature and gas pressure, respectively. $W_t$ is the weight of gas sorbed in grams by 100 *g of polymer* film.

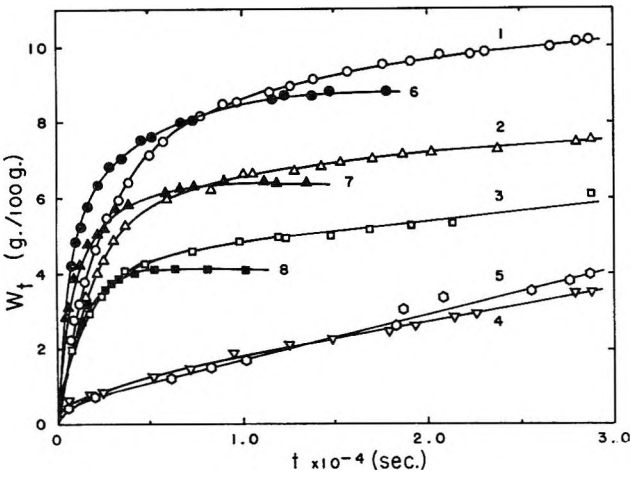


Figure 8. Sorption–desorption curves at $P_{total}$ = 60 cm. Sorption: (1) 35°, 59.5 $\mu$, (film thickness); (2) 45°, 59.5 $\mu$; (3) 55°, 70.4 $\mu$; (4) 85°, 56.1 $\mu$; (5) 95°, 64.3 $\mu$. Desorption: (6) as under (1); (7) as (2); (8) as (3). Desorption corresponding to (4) and (5) is negligible.

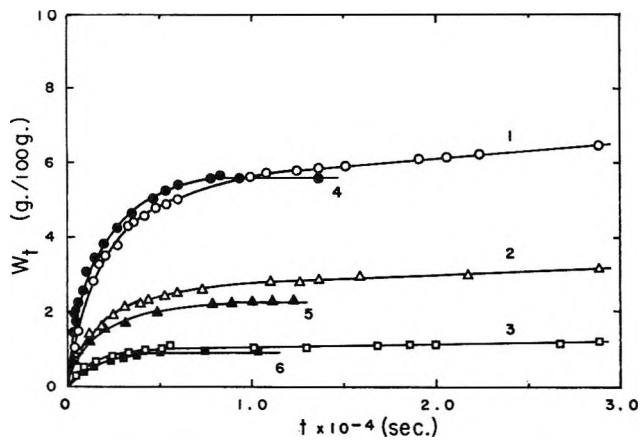


Figure 9. Same as Figure 8 at 45°. Sorption: (1) 60 cm, 69.1 $\mu$; (2) 30 cm, 78.0 $\mu$; (3) 15 cm, 78.0 $\mu$. Desorption: (4) as (1); (5) as (2); (6) as (3).

## Evaluation of Experimental Results

(*a*) *Solubility Coefficients and Rate Constants.* Before diffusion coefficients can be calculated from the experimental data, rate constants for the chain scission and the "$NO_2$-substitution" reaction (tertiary hydrogen atoms are substituted by $NO_2$ groups) have to be known. Also, the solubility coefficients have to be determined, and it is essential to ascertain whether Henry's law holds (*i.e.*, $C_{g,f} = k_H P_{total}$, where $k_H$ is a constant, the solubility coefficient, and $C_{g,f}$ is the gas concentration in the film). The solubility coefficients, $k_H$, were obtained from sorption–desorption data. First, however, it should be pointed out that $NO_2$ is always present in equilibrium with its dimer, $N_2O_4$: $N_2O_4 \rightleftharpoons 2NO_2$.

Below about 2 cm of total gas pressure, this equilibrium lies almost completely on the side of $NO_2$. Some typical values are given below (35°).[3]

| $P_{total}$, cm | 0.1 | 2.0 | 15 | 30 | 60 |
|---|---|---|---|---|---|
| $P_{NO_2}$, cm | 0.099 | 1.85 | 10.4 | 17.1 | 26.4 |
| $K_P$, atm | 0.318 | 0.318 | 0.315 | 0.300 | 0.272 |

The partial pressure of $NO_2$ is given by

$$P_{NO_2} = {}^1/_2[-K_P + (K_P^2 + 4K_P P_{total})^{1/2}] \quad (1)$$

The solubilities (saturation values) of the equilibrium gas mixtures were obtained from desorption curves. These data can, in principle, also be derived from the sorption curves after correction for the "$NO_2$-substitution" reaction. Table I gives the experimental results.

Figure 10 shows $C_{g,f}$ plotted *vs.* $P_{total}$ for 45°. A straight line is obtained, confirming that Henry's law is obeyed by the equilibrium gas mixture. Figure 11 gives the plot of the logarithm of the solubility coefficients *vs.* $1/T$. A satisfactory straight line results, indicating that Henry's law is very likely obeyed, separately, by the monomer and dimer, respectively, as the value for 2 cm pressure fits the plot; the gas for this case consists practically of $NO_2$ only. The equation for the plot in Figure 11 is

$$k_H = (1.41 \pm 0.08) \times 10^{-6} e^{+(7.0 \pm 1.0) \times 10^3/RT} \text{ g/(100 g) (cm)} \quad (2)$$

The heat of solution is $\Delta H_S = -7.0$ kcal/mol.

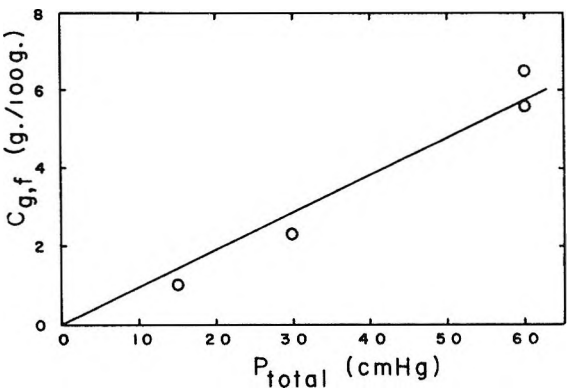


Figure 10. Gas concentration in grams/100 g plotted *vs.* total pressure in centimeters at 45°.

The rate constants for the chain scission reaction, $K_{m,C}$, were obtained as follows. $\alpha$, for experiments at various gas pressures and identical $x$ values at the same temperature, was plotted against the diffusion reaction time. Straight lines result. The relationship, derived from the slopes of these lines, is given by

$$\alpha_{x,t} = K_{m,P} P_{NO_2} t = K_{m,P} C_{NO_2} t / k_H = K_{m,C} C_{NO_2} t \quad (3a)$$

$K_{m,P}$ or $K_{m,C}$, respectively, can then easily be evaluated. In a recent paper,[1] detailed studies of reactions of thin

(3) "Gmelin's Handbuch der anorganischen Chemie, Stickstoff," System No. 4, Leipzig, Berlin, 1936, p N749.

**Table I:** Solubilities of Equilibrium Gas Mixture ($NO_2 + N_2O_4$) in Polystyrene[a]

| | $P_{total}$, cm | | | | | | | |
|---|---|---|---|---|---|---|---|---|
| | 60 | | 30 | | 15 | | 2 | |
| Temp, °C | $C_{total}$ | $k_H$ | $C_{total}$ | $k_H$ | $C_{total}$ | $k_H$ | $C_{total}$ | $k_H$ |
| 35 | 8.5, 10.2 | 0.14, 0.17 | 3.8 | 0.13 | | | | |
| 45 | 5.6, 6.5 | 0.093, 0.11 | 2.3 | 0.077 | 0.95 | 0.063 | | |
| 55 | 4.1 | 0.068 | | | | | | |
| 80 | | | | | | | 0.068 | 0.034 |

[a] $C_{total}$ in grams of gas/100 g of polymer; $k_H$ is the solubility coefficient in grams/(100 g)(cm).

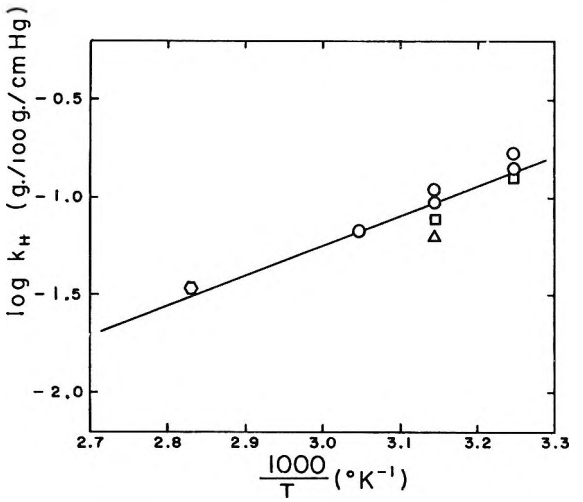


Figure 11. Log of solubility coefficients, $k_H$, plotted *vs.* $1/T$ for $P_{total}$: ○, 60 cm; □, 30 cm; △, 15 cm; ⬡, 2 cm.

**Table II:** Rate Constants for Chain Scission

| Temp, °C | $P_{NO_2}$, cm | $P_{tot}$, cm | $10^{10}K_{m,P}$, $sec^{-1}$ $cm^{-1}$ | $10^8K_{m,C}$, $sec^{-1}$ $(g/100\ g)^{-1}$ | $10^{10}K'_{m,P} \times P_{tot}$, $sec^{-1}$ $cm^{-1}$ ($P_{tot}$ = 30 cm) |
|---|---|---|---|---|---|
| 25 | | | | | 1.70 |
| 35 | 27.4 | 60 | 0.82 | 0.051 | 3.04 |
| 45 | 34.3 | 60 | 1.60 | 0.16 | |
| 45 | 20.7 | 30 | 1.40 | 0.14 | 3.27 |
| 45 | 16.0 | 21.6 | 1.40 | 0.14 | |
| 45 | 6.95 | 8.0 | 1.10 | 0.11 | |
| 45 | 1.92 | 2.0 | 1.21 | 0.12 | |
| 55 | 40.9 | 60.0 | 1.90 | 0.28 | 5.20 |
| 65 | 1.98 | 2.0 | 3.02 | 0.63 | |
| 65 | 0.80 | 0.8 | 1.89 | 0.39 | |
| 75 | 1.49 | 1.5 | 4.58 | 1.39 | |
| 80 | 1.99 | 2.0 | 6.31 | 1.98 | |
| 80 | 1.99 | 2.0 | 5.33 | 2.34 | |
| 85 | 54.10 | 60 | 11.1 | 4.81 | |

polystyrene films with $NO_2$ were presented; the relationship for $\alpha$ was found to be identical with eq 3a

$$\alpha = K'_{m,P}P_{total}P_{NO_2}t \qquad (3b)$$

where $K'_{m,P} = K_{m,P}/P_{total}$. Table II gives the relevant $K_{m,P}$ and $K_{m,C}$ values and also the $K'_{m,P}P_{total}$ of the previous work for comparison.

The Arrhenius plots for $K_{m,P}$, $K_{m,C}$, and $K'_{m,P}P_{total}$ are shown in Figure 12; the relevant equations are as follows (standard deviations are also given)

$$K_{m,C} = (3.1 \pm 0.2) \times 10^3 e^{-(18.0\pm1.0)\times10^3/RT}\ sec^{-1}\ (g/100\ g)^{-1}$$

$$K_{m,P} = (9.4 \pm 0.5) \times 10^{-4} e^{-(10.0\pm0.8)\times10^3/RT}\ sec^{-1}\ cm^{-1}$$

$$K'_{m,P}P_{total} = (1.8 \pm 0.1) \times 10^{-5} e^{-(6.8\pm1.5)\times10^3/RT}\ sec^{-1}\ cm^{-1}$$

The discrepancy in the $K_{m,P}$ and $K'_{m,P}P_{total}$ values is most likely due to the fact that in this work polystyrene films were prepared by casting from methyl ethyl ketone solutions, whereas in the previous work, they were cast from benzene solution. It was shown above and it is well known that it is very difficult to remove traces of benzene from polystyrene.

The rate constant for the substitution of tertiary hydrogen atoms by $NO_2$ groups was derived in the following manner. The sorption curves (see Figures 8 and 9) do not reach a plateau, as expected if only sorption were taking place. The desorption curves, however, finish with a plateau, which represents gas saturation of the films. The sorption curves instead increase linearly. This is due to the "substitution" reaction, whose rate of consumption of $NO_2$, which is the reactive species being an odd electron molecule, is given by

$$-\frac{d[NO_2]}{dt} = k'_C[n]C_{NO_2} \qquad (4)$$

$[n]$ is the concentration of tertiary hydrogen atoms in the system at time $t$. Only a relatively small fraction of hydrogen atoms is replaced by $NO_2$; $[n]$ can therefore be considered with good approximation to remain constant and equal to the initial concentration; hence $[n] \cong [n]_0$. $C_{NO_2}$ represents here the saturation concentration, as the range of the reaction is considered, where desorption shows that saturation has been reached. The saturation value is obtained from the relevant plateau of the desorption curve. The "rate constant" is given by the slope of the straight line of the sorption curve divided by $C_{NO_2}$

$$k_C = k'_C[n]_0 = -(d[NO_2]/dt)/C_{NO_2,sat}\ sec^{-1} \quad (5)$$

These "rate constants" are given in Table III. The Arrhenius plot for $k_C$ is shown in Figure 13; the equation for this plot is

$$k_C = (2.8 \pm 0.2) \times 10^2 e^{-(10,600 \pm 1000)/RT}\ sec^{-1}$$

**Table III:** Rate Constants, $k_C$, for Reactions of $NO_2$ with Tertiary Hydrogen Atoms in Polystyrene

| Temp, °C | $P_{NO_2}$, cm | $P_{total}$, cm | $10^5 k_C$, $sec^{-1}$ |
|---|---|---|---|
| 35 | 27.4 | 60 | 1.28, 0.74 |
| 35 | 17.2 | 30 | 0.99 |
| 45 | 34.3 | 60 | 1.02 |
| 45 | 34.3 | 60 | 0.97 |
| 55 | 40.9 | 60 | 2.13 |
| 85 | 54.1 | 60 | 9.91 |
| 95 | 56.2 | 60 | 14.5 |
| 45 | 20.7 | 30 | 1.92 |
| 45 | 11.9 | 15 | 1.25 |

(*b*) *Diffusion Coefficients.* The penetration experiments were evaluated on the basis of Fick's laws. The expression for diffusion in one dimension, with a simultaneous chemical reaction taking place, is given by[4]

$$\frac{\partial C_{NO_2,x}}{\partial t} = \frac{D\partial^2 C_{NO_2,x}}{\partial x^2} - k_C C_{NO_2,x} \quad (6)$$

Here $C_{NO_2,x}$ is the concentration of the diffusing gas at time $t$ at a distance $x$ from the surface. It is assumed that the equilibrium $N_2O_4 \rightleftharpoons 2NO_2$ is always quickly readjusted.

Initial and boundary conditions for the present case are as follows: $C_{NO_2} = 0$, $t = 0$, and any $x$; and $C_{NO_2} = C_{NO_2,x=0}$ = constant, $t > 0$, at $x = 0$. The solution of eq 6 for a semiinfinite medium is[4]

$$\frac{C_{NO_2,x,t}}{C_{NO_2,x=0}} = \frac{1}{2}\exp\{-x(k_C/D_P)^{1/2}\} \times \operatorname{erfc}\left\{\frac{x}{2(D_P t)^{1/2}} - (k_C t)^{1/2}\right\} + \frac{1}{2}\exp\{x(k_C/D_P)^{1/2}\} \times \operatorname{erfc}\left\{\frac{x}{2(D_P t)^{1/2}} + (k_C t)^{1/2}\right\} = F(D_P, k_C, x, t) \quad (7)$$

$D_P$ is the diffusion coefficient and $t$ the diffusion time. $F$ is the function given by eq 7. $C_{NO_2,x,t}$ and $C_{NO_2,x=0}$ are the concentrations of diffusing species at distance $x$ and $x = 0$ for diffusion time $t$. If $k_C t$ is very small compared with the diffusion process, the flux $J$ is

$$J = -D\frac{\partial C_{NO_2,x}}{\partial_x} = C_{NO_2,x=0}(1 + k_C t)\{D_P/(\pi t)\}^{1/2} \quad (8)$$

If $k_C t$ becomes negligible ($\simeq 0$) compared with the diffusion process, the simple expression for diffusion without chemical reaction can be used[4]

$$\frac{C_{NO_2,x}}{C_{NO_2,x=0}} = \operatorname{erfc}\left(\frac{x}{2(D_P t)^{1/2}}\right) = F(D_P, x, t) \quad (9)$$

The rate constants $k_C$ are known from the evaluation given above. The relationship of $\alpha_x$ as a function of time and constant gas pressure is also known (see above). For thin films one has

$$\alpha = K_{m,P} P_{NO_2} t \quad (10)$$

or in terms of concentrations

$$\alpha = \frac{K_{m,P}}{k_H} C_{NO_2} t = K_{m,C} C_{NO_2} t \quad (11)$$

For thick or a set of films, an equation is valid at an instant of time $t$, at a distance $x$ from the surface, and at constant temperature, as follows

$$d(\alpha_{x,t}) = K_{m,P} P_{NO_2,x,t}\, dt = K_{m,C} C_{NO_2,x,t} dt \quad (12)$$

$P_{NO_2,x,t}$ and $C_{NO_2,x,t}$ are the instantaneous $NO_2$ pressure and concentration and $t$ and $x$, respectively; hence

$$\alpha_{x,t_f} = K_{m,P}\int_0^{t_f} P_{NO_2,x,t}\, dt = K_{m,C}\int_0^{t_f} C_{NO_2,x,t} dt \quad (13)$$

$t_f$ is the total diffusion time. $C_{NO_2,x,t}$ can be replaced by its expression given in eq 7; hence

$$\alpha_{x,t_f} = K_{m,C} C_{NO_2,x=0}\int_0^{t_f} F(D_P, k_C, x, t) dt \quad (14)$$

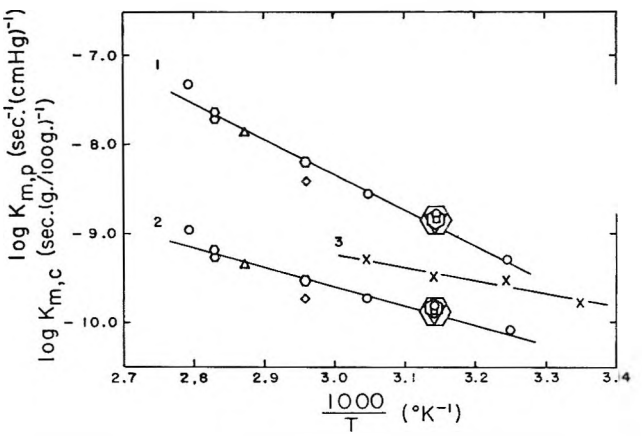


Figure 12. Arrhenius plots for the chain scission reaction: (1) $K_{m,C}'$ (2) $K_{m,P}'$ (3) $K'_{m,P}P_{total}$.

**Table IV:** Comparison of Diffusion Coefficients, $D_P$, Obtained from Penetration Experiments According to Eq 16a and 16b, Respectively

| Temp, °C | $t$, sec | $P_{NO_2}$, cm | $P_{total}$, cm | $10^5 D_P$, $cm^2/sec$ Eq 16a | $10^5 D_P$, $cm^2/sec$ Eq 16b |
|---|---|---|---|---|---|
| 35 | $1.8 \times 10^4$ | 27.4 | 60 | 2.6 | 2.4 |
| 85 | $3.6 \times 10^3$ | 54.1 | 60 | 1.3 | 1.1 |

(4) J. Crank, "The Mathematics of Diffusion," Oxford at the Clarendon Press, 1967.

**Table V:** Diffusion Coefficients $D_P$ from Eq 16b

| Temp, °C | $10^{-4}t$, sec | $P_{NO_2}$, cm | $P_{total}$, cm | $10^4x$, cm: 45 | 70 | 120 | 170 | $10^5D_P$ (av), cm²/sec |
|---|---|---|---|---|---|---|---|---|
| | | | | $10^5D_P$, cm²/sec | | | | |
| 35 | 1.8 | 27.4 | 60 | 2.6 | 2.5 | 2.2 | ... | 2.4 |
| 35 | 4.7 | 27.4 | 60 | 1.1 | 1.0 | 0.8 | ... | 1.0 |
| 45 | 5.05 | 34.3 | 60 | 0.9 | 0.8 | 0.9 | 1.3 | 1.0 |
| 45 | 5.05 | 20.7 | 30 | 1.8 | 1.9 | 2.2 | 2.3 | 2.1 |
| 45 | 5.05 | 16.0 | 21.6 | 1.2 | 1.3 | 1.5 | 1.4 | 1.4 |
| 45 | 10.3 | 6.95 | 8.0 | 1.3 | 1.3 | 1.3 | 1.4 | 1.3 |
| 45 | 42.5 | 1.92 | 2.0 | 0.1 | 0.1 | 0.2 | 0.2 | 0.15 |
| 55 | 1.44 | 40.9 | 60 | 2.8 | 3.1 | 4.2 | ... | 3.4 |
| 55 | 2.16 | 40.9 | 60 | 2.6 | 2.5 | 2.8 | ... | 2.6 |
| 55 | 2.88 | 40.9 | 60 | 2.0 | 2.12 | 2.5 | 3.6 | 2.6 |
| 65 | 14.4 | 1.98 | 2 | 1.2 | 1.2 | 1.0 | 0.9 | 1.1 |
| 65 | 77.5 | 0.80 | 0.8 | 0.20 | 0.21 | 0.23 | 0.23 | 0.22 |
| 75 | 1.51 | 1.49 | 1.5 | 0.25 | 0.26 | 0.28 | 0.40 | 0.30 |
| 80 | 7.2 | 1.99 | 2.0 | 0.95 | 0.96 | 0.98 | 1.1 | 1.0 |
| 80 | 7.2 | 1.99 | 2.0 | 0.70 | 0.80 | 0.74 | 0.65 | 0.72 |
| 85 | 0.36 | 54.1 | 60 | 14.0 | 11.0 | 9.4 | 10.0 | 11.0 |

For $\alpha_{x=0}$, an expression holds as follows (here, the concentration, $C_{NO_2,x=0}$, remains constant throughout the whole diffusion time $t_f$)

$$\alpha_{x=0} = K_{m,C}C_{NO_2,x=0}t_f \tag{15}$$

Combination of eq 14 and 15 gives

$$\frac{\alpha_{x,t_f}}{\alpha_{x=0}} = \frac{1}{t_f}\int_0^{t_f} F(D_P, k_C, x, t)\,dt \tag{16a}$$

or similarly, if the chemical reaction is negligible

$$\frac{\alpha_{x,t_f}}{\alpha_{x=0}} = \frac{1}{t_f}\int_0^{t_f} F(D_P, x, t)\,dt \tag{16b}$$

Equations 16a and 16b are evaluated by calculating $F$ for a number of $D_P$ values. Integration is performed by plotting $F$ *vs.* $t$ and weighing the area under the curve. The correct $D_P$ value has been chosen, when the integrated value multiplied by $1/t_f$ satisfies the experimental ratio $\alpha_{x,t}/\alpha_{x=0}$. The values derived from either eq 16a or 16b are identical within experimental error. Thus, the rate of the "substitution" reaction is negligible compared with the diffusion rate. The diffusion coefficients obtained by eq 16a and 16b, respectively, are collected in Table IV.

Subsequently all data were evaluated only from eq 16b. The results are compiled in Table V.

The logarithms of the diffusion coefficients, $D_P$, are plotted *vs.* the total gas pressure, $P_{total}$, in Figure 14 (45°). Diffusion coefficients from sorption–desorption data are also included. The diffusion coefficients are independent of gas pressure or concentration above 10 cm; below this value they decrease rapidly with pressure or concentration, respectively. (See Table V, with six values below 10 cm.)

The sorption curves were corrected by eliminating the chemical "substitution" reaction. This was

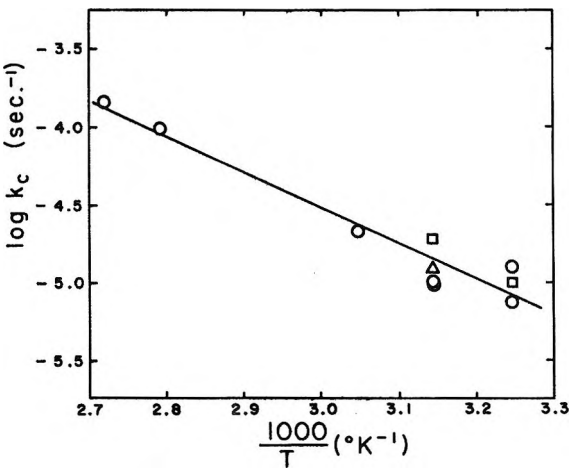


Figure 13. Arrhenius plot for the "substitution" reaction for $P_{total}$: ○, 60 cm; □, 30 cm; △, 15 cm.

achieved by subtracting the difference between the straight line part of the sorption curve and the saturation value of the corresponding desorption curve. The correction for sorption prior to saturation is too small to be applied; it is of no significance and lies certainly within the experimental error of the diffusion coefficients (*ca.* 10% error).

The equation for the calculation of diffusion coefficients from sorption–desorption data is as follows[4] ($2a$ is the film thickness)

$$W_t/W_\infty = 1 - \frac{8}{\pi^2}\sum_{n=0}^{\infty}\frac{1}{(2n+1)^2} \times \exp\left\{-\left(\frac{(2n+1)\pi}{2a}\right)^2 D_{S,D}t\right\} \tag{17}$$

$W_t$ is the weight sorbed or desorbed, respectively, at time $t$ and $W_\infty$ that at saturation. $D_S$ and $D_D$ are the

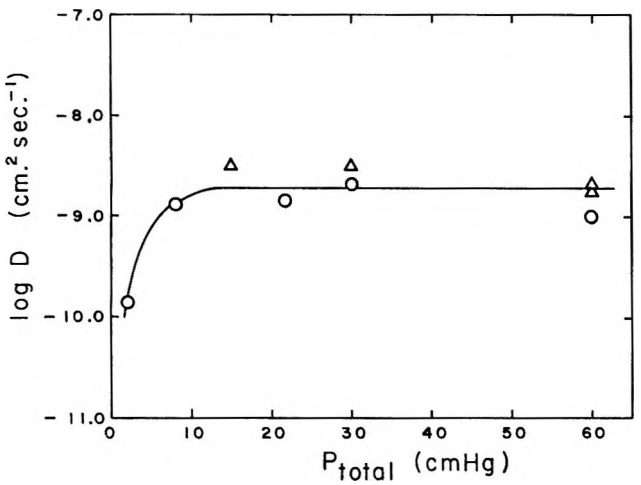


Figure 14. Log of diffusion coefficients, $D$, *vs.* total gas pressure: ○, penetration; △, sorption–desorption (45°).

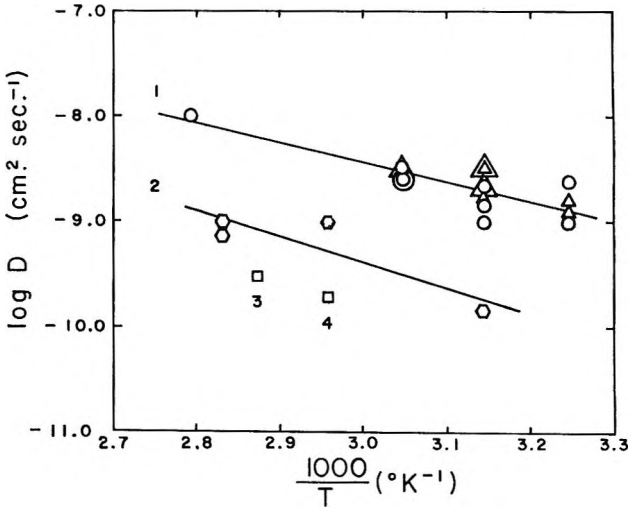


Figure 15. Arrhenius plot for diffusion coefficients from penetration (○, ○, □) and sorption–desorption (△) for $P_{total}$: (1) >10 cm, (2) 2 cm, (3) 1.5 cm, (4) 0.8 cm.

diffusion coefficients for sorption and desorption, respectively. Usually, the average value of the two coefficients is taken

$$D_{SD,av.} = (D_S + D_D)/2 \qquad (18)$$

The diffusion coefficients obtained in this way are given in Table VI. The average values of the diffusion coefficients, $D_P$, obtained from penetration experiments are also given for comparison. Data derived by either method agree quite satisfactorily.

**Table VI:** Diffusion Coefficients from Sorption, $D_S$, and Desorption, $D_D$, Experiments and Their Averages, $D_{SD}$. Average Diffusion Coefficients, $D_P$, from Penetration Experiments Are Also Included

| Temp, °C | $P_{NO_2}$, cm | $P_{total}$, cm | $10^6 D_S$, cm²/sec | $10^6 D_D$, cm²/sec | $10^6 D_{SD,av.}$, cm²/sec | $10^6 D_{P,av.}$, cm²/sec |
|---|---|---|---|---|---|---|
| 35 | 27.4 | 60 | 0.9 | 1.7 | 1.3 | 1.7 |
| 35 | 27.4 | 60 | 1.1 | 2.1 | 1.6 | 1.7 |
| 35 | 17.2 | 30 | 0.8 | 1.7 | 1.3 | ... |
| 45 | 34.3 | 60 | 1.3 | 2.3 | 1.8 | 1.0 |
| 45 | 34.3 | 60 | 1.6 | 2.3 | 2.0 | 1.0 |
| 45 | 20.7 | 30 | 3.6 | 2.6 | 3.1 | 2.1 |
| 45 | 11.9 | 15 | 3.8 | 2.5 | 3.2 | ... |
| 55 | 40.9 | 60 | 2.8 | 3.4 | 3.1 | 2.9 |

An Arrhenius plot for all diffusion coefficients obtained at total pressures larger than 10 cm is shown in Figure 15. In addition a similar plot for experiments at lower pressures is also given in Figure 15. The respective Arrhenius equations are as follows (including standard deviations): for $P_{total} > 10$ cm

$$D_{av} = (1.5 \pm 0.2) \times 10^{-3} e^{-(8.6 \pm 1.8) \times 10^3/RT} \text{ cm}^2 \text{ sec}^{-1}$$

and for $P_{total} = 2$ cm

$$D_{av} = (5.4 \pm 1.6) \times 10^{-3} e^{-(9.4 \pm 5.3) \times 10^3/RT} \text{ cm}^2 \text{ sec}^{-1}$$

## Discussion

It is shown here for the first time, that a chain scission reaction can be used as indicator for the progress of diffusion of a reactive gas in polymer films. Diffusion coefficients are obtained which agree satisfactorily with values calculated from sorption–desorption data. They are not too much different from the diffusion coefficients for relatively large molecules such as $CO_2$ in polystyrene. The coefficients for nitrogen dioxide are about ten times smaller than those for carbon dioxide.

It is also shown here, that the reaction, which consists of replacing tertiary hydrogen atoms in polystyrene by nitrate or nitrite groups, is slow compared with the diffusion process. This is quite apparent from Table IV. Thus, the chemical reaction does not need to be considered at all; results are obtained, which are identical within experimental error, whether or not the chemical reaction is included in the evaluation of experimental data.

It should be pointed out, that an approximation has been made for the expression of the chain scission rate constant $K_m$. There are slight curvatures almost within experimental error, in the $\alpha$ *vs.* time curves.[1] The best straight line through the experimental points, obtained in the present work, has been taken instead. These slight curvatures are due to the decrease in viscosity of the polymer film as chain scission proceeds.[1] However, this correction is so small that it cannot be detected by its effect on the values of the diffusion coefficients. The experimental errors in these coefficients are certainly larger than any effect due to this slight curvature.

A heat of solution of the gas in polystyrene $\Delta H_S = -7.0$ kcal/mol is obtained from solubility data. This heat of solution consists of two terms

$$\Delta H_S = \Delta \bar{H}_{cond} + \Delta \bar{H}_1 \qquad (19)$$

where $\Delta\bar{H}_{cond}$ is the molar heat of condensation of the diffusate and $\Delta\bar{H}_1$ is the partial molal heat of mixing. The latter is generally positive[6] and represents the energy expended by the diffusing molecules while penetrating the polymer. The heat of solution, $\Delta H_S$, for easily condensable gases is usually negative.

The chain scission reaction is controlled by the diffusion of polymer–radical encounter pairs from medium cages. This was discussed in the previous paper.[1] The relatively small energy of activation (18.3 kcal/mol) supports this contention.

The rate constants, $k_C$, belong to the substitution reaction of tertiary atoms by nitrate or nitrite groups. The energy of activation (10.6 kcal/mol) for this process is of the right order of magnitude. High-pressure polyethylene, which has branches and hence tertiary hydrogen atoms, gives for such a substitution reaction an energy of activation of (14 ± 2) kcal/mol.[6]

The diffusion coefficients become concentration dependent below about 10 cm total gas pressure (see Figure 14 and Table V). It is frequently found[5] that the concentration dependence can be expressed by

$$D = D_{C=0}e^{AC} \tag{20}$$

where $A$ is a constant and $C$ the concentration of the diffusing species. If one tentatively assumes, in the present case, that for pressures <10 cm, a straight line is followed for the log $D$ *vs.* $P_{total}$ plot, one obtains (Table V)

$$\log D = 0.37P_{total} - 10.6$$

for $P_{total} > 10$ cm, $A = 0$, and $\log D = -8.7$. The energy of activation and preexponential factor increase with decreasing total pressure below 10 cm. The initial plasticizing action of the gas at low concentrations, loosening the polymer structure, may require more energy than for later stages or higher pressures.

The diffusion coefficients can also be expressed by relations based on the theory of absolute reaction rates or the transition-state theory[7]

$$D = e\lambda^2\frac{kT}{h}e^{\Delta S^*/R}e^{-E/RT}\ \text{cm}^2/\text{sec} \tag{21}$$

Here $E = \Delta H^*$, where $\Delta H^*$ is the enthalpy of activation; volume changes are quite small. $\lambda$ is the average jump distance of the penetrating molecule. This distance is often taken quite arbitrarily equal to the diameter of the diffusing gas molecule. This diameter amounts to *ca.* 3.0 Å for $NO_2$. For $D = 2.18 \times 10^{-9}$ cm²/sec at 45° and 60 cm total pressure, the entropy of activation is $\Delta S^* = -5.0$ eu and the free energy of activation, $\Delta F^* = 10$ kcal/mol. For a coefficient $D = 1.48 \times 10^{-10}$ cm²/sec at 45° and 2 cm total pressure, the corresponding quantities are $\Delta S^* = -2.5$ eu and $\Delta F^* = 11.7$ kcal/mol. One can, of course, interpret entropy values in the usual way, that the transition-state complex at 60 cm pressure has a more ordered structure than the one at 2 cm pressure. It may be pointed out that the Arrhenius parameters ($P_{total} >$ 10 cm, $1.2 \times 10^{-5}$ cm²/sec, 8.4 kcal/mol) are not too different from those for $CO_2$ diffusing in polystyrene ($1.3 \times 10^{-1}$ cm²/sec, 8.7 kcal/mol).[5]

*Acknowledgment.* S. I. wishes to thank Toyo Rayon Co., Ltd., for a generous leave of absence. This work was made possible by a grant from PHS, NAPCA (No. R01-AP00486).

(5) P. Meares, "Polymers: Structure and Bulk Properties," D. Van Nostrand Co., Ltd., London, 1965, Chapter 12; V. Stannett in "Diffusion in Polymers," J. Crank and G. S. Park, Ed., Academic Press, Inc., New York, N. Y., 1968, Chapter 2; C. E. Rogers in "Physics and Chemistry of the Organic Solid State," D. Fox, M. M. Labes, and A. Weissberger, Ed., Interscience Publishers, New York, N. Y., 1965, Chapter 6.

(6) T. Ogihara, S. Tsuchiya, and K. Kurantani, *Bull. Chem. Soc. Jap.*, **38**, 978 (1965).

(7) S. Glasstone, K. J. Laidler, and H. Eyring, "The Theory of Rate Processes," McGraw-Hill Publications, New York, N. Y., 1941.

# Positive Ions of γ-Irradiated Hydrocarbons at 77°K

by Pieter W. F. Louwrier[1] and William H. Hamill

*Department of Chemistry and the Radiation Laboratory,[2] University of Notre Dame, Notre Dame, Indiana 46556*
*(Received August 25, 1969)*

Radical positive ions $RH^+$ have been prepared by γ irradiation of several alkanes (~0.5 mol %) in 3-methylpentane (3MP) and carbon tetrachloride matrices at 77°K, and their optical absorption spectra have been measured. These ions are not observed in matrices of alkanes higher than $C_6H_{14}$, nor in one-component systems (with $CO_2$ as electron trap). The yield of $RH^+$ is much less in 2-methylpentane than in 3MP, which has the lower viscosity and depends also on the ionization potential of the scavenger for a series of alkyl chlorides. The rate of dark decay of $RH^+$ increases with concentration of RH and with temperature in the range 62–77°K. The quantum yield of bleaching increases with frequency and diminishes with progressive bleaching. The yield of $C_6H_6^+$ in 3MP attains a pronounced maximum at 2 vol %, similar to several $RH^+$ in 3MP, and attributed to charge recombination *via* positive hole tunneling.

## Introduction

Alkanes have become quite useful for matrix isolation studies in radiation chemistry because of their relative chemical inertness and their ability to conduct electric charge.[3] It has been found recently that lower alkanes, *e.g.*, 3-methylpentane (3MP), provide satisfactory matrices for higher alkane (RH) radical positive ions,[4] $RH^+$. These ions have intense optical absorption bands, the $\lambda_{max}$ depending somewhat on carbon number and structure. These color centers are easily bleached by optical excitation. Their yields do not vary monotonically with concentration of RH, and this effect has been attributed to hole migration by electron tunneling between $RH^+$ and RH leading to recombination.[4] Because these ions are still rather novel, and the phenomena associated with them are not well understood, it is desirable to study them further. The migration and trapping of positive charge (holes) in these systems is of greatest interest and will be examined with reference to molecular structure, concentration, temperature, and optical excitation.

## Experimental Section

The procedures have been described previously.[4]

3-Methylpentane and 2-methylpentane (2MP), both Phillips pure grade, were passed through a column of activated silica gel. Squalane (Baker) was treated with concentrated $H_2SO_4$, washed, and dried, then passed through a column of activated silica gel. All other alkanes (Aldrich) were used as received. Toluene (Fisher spectroscopic grade), $C_6H_6$ (Fisher Certified grade), and $C_6H_5CCl_3$ (Eastman) were distilled on a spinning band column. Tetramethyl-*p*-phenylenediamine (TMPD) was prepared from the dihydrochloride and sublimed in the dark. 2-Methylpentene-1 (2MP-1, Phillips research grade), $CCl_4$ and $CH_2Cl_2$ (Fisher Certified grade), $C_2H_5Cl$ and $CH_3Cl$ (Matheson), $CH_2ClCH_2Cl$, 1-$C_3H_2Cl$, and 2-$C_3H_7Cl$ (Eastman) were used as received.

## Results

The spectra of the alkane positive ions $RH^+$ depend on the number of C atoms, the molecular structure, and the matrix. The half-widths $\Delta\lambda_{1/2}$ of the $RH^+$ bands in $CCl_4$ are greater and the $\lambda_{max}$ are blue-shifted relative to 3MP. The results for several alkanes are summarized in Table I. The spectra are structureless and bear a general resemblance to those already reported,[4] even for the case of squalane. The large $\Delta\lambda_{1/2}$ in polycrystalline $CCl_4$ is not unique for $RH^+$, since $TMPD^+$ showed the same effect relative to glassy 3MP. The $\Delta\lambda_{1/2}$ was more than twice as great in $CCl_4$, but there was no shift of $\lambda_{max}$.

The absence of $RH^+$ absorption bands for 2-methyltetradecane and 2-methylpentadecane in the 3MP matrix is unexpected because 2-methyloctane, 2-methylnonane, 2-methyldecane (2MD), and 2-methylundecane in 3MP all showed $RH^+$ bands. Since $RH^+$ bands were observed for both of these higher alkanes in $CCl_4$, the effect must be attributed to lack of positive charge trapping. Other glassy alkanes matrices have been tested with higher alkane additives. For matrix molecules with more than six C atoms (3-methylhexane, 3-methylheptane, 2-methyloctane, and squalane) neither the matrix alone nor any alkane additive produced an $RH^+$ band, even though the same additives produced such bands in 3MP.

(1) This work was performed during a leave of absence from the Instituut Voor Kernphysisch Onderzoek, Amsterdam, The Netherlands.

(2) The Radiation Laboratory of the University of Notre Dame is operated under contract with the U. S. Atomic Energy Commission. This is AEC document No. COO-38-689.

(3) (a) W. H. Hamill, "Ionic Processes in γ-Irradiated Organic Solids at −196°," a chapter in "Radical Ions," E. T. Kaiser and L. Kevan, Ed., John Wiley & Sons, New York, N. Y., 1968; (b) J. E. Willard, "Radiation Chemistry of Organic Solids," a chapter in "Fundamentals of Radiation Chemistry," P. Ausloos, Ed., John Wiley & Sons, New York, N. Y., 1969.

(4) P. W. F. Louwrier and W. H. Hamill, *J. Phys. Chem.*, 72, 3878 (1968).

**Table I:** Alkane Positive Ions in 3-Methylpentane and in Carbon Tetrachloride Matrices at 77°K[a]

| Alkane | Vol % | 3-Methylpentane matrix $\lambda_{max}$ | 3-Methylpentane matrix $\lambda_{onset}$ | 3-Methylpentane matrix $\Delta\lambda_{1/2}$ | OD($RH^+$) | Carbon tetrachloride matrix $\lambda_{max}$ | Carbon tetrachloride matrix $\lambda_{onset}$ | Carbon tetrachloride matrix $\Delta\lambda_{1/2}$ |
|---|---|---|---|---|---|---|---|---|
| 2-Methyltetradecane | 0.2 | No band | | | | 930 | 1550 | 850 |
| 3-Methyltetradecane | 0.35 | 1075 | 1530 | 560 | 0.3 | 860 | 1500 | 850 |
| 4-Methyltetradecane | 0.5 | 1050 | 1530 | 540 | 0.8 | 800 | 1500 | 800 |
| 5-Methyltetradecane | 0.8 | 1000 | 1500 | 500 | 1.4 | 875 | 1500 | 800 |
| 2-Methylpentadeeane | 0.2 | No band | | | | 1000 | 1800 | 850 |
| 6-Methylpentadecane | 0.8 | 1010 | 1560 | 520 | 1.2 | 900 | 1800 | 850 |
| Squalane | 0.5 | 1200 | >2000 | 900 | 1.0 | | | |

[a] Samples were saturated with $CO_2$; the dose was $1.2 \times 10^{19}$ eV/g.

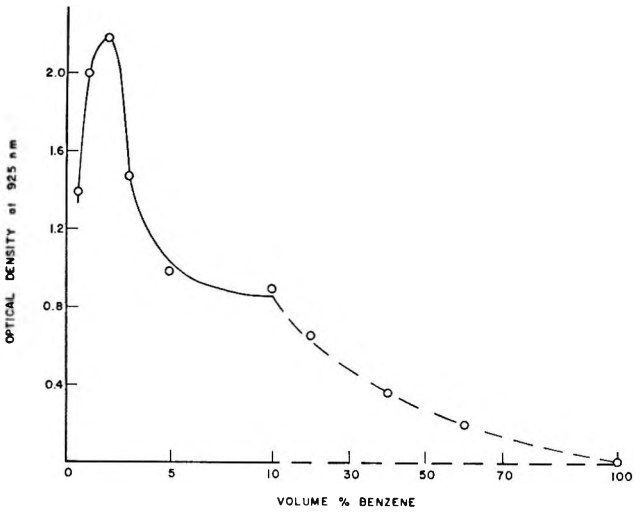


Figure 1. Optical absorption at 925 nm of irradiated benzene–3MP mixtures at 77°K, with 1 vol % $CCl_4$ present as electron trap. Dose $1.2 \times 10^{19}$ eV/g.

Polycrystalline cyclohexane, either alone or with an added electron trap, did not exhibit radiation color centers. This matrix conducts positive charge since addition of TMPD yielded $TMPD^+$ with $\lambda_{max}$ at 637 nm, but the band was much wider than the corresponding band in a 3MP matrix. The cyclohexane matrix also conducts electrons since addition of benzotrichloride yielded $C_6H_5CCl_2\cdot$, with $\lambda_{max}$ at 318 nm. The reaction has been shown to proceed by dissociative electron attachment.[5]

Pure polycrystalline benzene exhibited no radiation color centers, nor did TMPD trap positive charge in benzene when $CCl_4$ was also present to trap electrons. Benzotrichloride in benzene showed an absorption band at 318 nm, attributed to $C_6H_5CCl_2\cdot$ and formed by dissociative electron attachment. Benzene mixtures with 3MP and 1 vol % $CCl_4$ did yield $C_6H_6^+$ with $\lambda_{max}$ at 925 nm. The samples were glassy for concentrations less than 3 vol % $C_6H_6$. In polycrystalline mixtures the effective length of the light path was estimated from the vibrational overtone band of 3-MP at 1140 nm. The prominent maximum in the plot of OD($C_6H_6^+$) *vs.* % $C_6H_6$ shown in Figure 1 is strikingly similar to plots of OD($RH^+$) *vs.* % RH for higher alkanes which have been reported previously.[4] An apparently related effect is the increased rate of thermal decay of the positive ion of 2-methyldecane (2MD) in 3MP at 77°K with increase in concentration of 2MD.[4]

The relative yields of $2MD^+$ for 0.67 mol % 2MD in 3MP with 0.6 mol % alkyl chloride depended considerably on the alkyl chloride being used. These differences may involve both the relative electron scavenging efficiencies of the chlorides and also competition with 2MD for positive charge scavenging. The relevant data have been summarized in Table II.

**Table II:** The Relative Yields of 2-Methyldecane Positive Ion ($2MD^+$) in 3-Methylpentane at 77°K with Varied Electron Scavengers[a]

| Electron scavenger | OD($2MD^+$) | Ionization potential[b] | Relative $e^-$ scavenging efficiency[c] |
|---|---|---|---|
| $CCl_4$ | 0.83 | 11.47 | 1.0 |
| $CH_2Cl_2$ | 0.76 | 11.35 | 0.5 |
| $CH_3Cl$ | 0.54 | 11.28 | 0.15 |
| $CH_2ClCH_2Cl$ | 0.74 | 11.12 | |
| $C_2H_5Cl$ | 0.28 | 10.98 | |
| $C_2H_5CH_2Cl$ | 0.24 | 10.82 | |
| $(CH_3)_2CHCl$ | 0.18 | 10.78 | |

[a] Alkyl chloride concentration was 0.6 mol % in all samples and the dose was $5.8 \times 10^{18}$ eV/g. [b] See ref 8. [c] M. Shirom and J. E. Willard, *J. Phys. Chem.*, **72**, 1701 (1968); E. P. Bertin and W. H. Hamill, *J. Amer. Chem. Soc.*, **86**, 1301 (1964).

In a matrix of 2-methylpentane, the initial OD($2MD^+$) from 0.5 mol % 2MD and 0.1 mol % $CCl_4$ was only 25% as great as that for a similar experiment using a matrix of 3MP. The matrix also affects the rate of dark decay of $2MD^+$ which was much greater in 2MP than in 3MP, although the viscosities are $10^{13}$ and $10^{12}$ P, respectively.[6]

(5) J. B. Gallivan and W. H. Hamill, *Trans. Faraday Soc.*, **61**, 1960 (1965).

(6) A. C. Ling and J. E. Willard, *J. Phys. Chem.*, **72**, 1918 (1968).

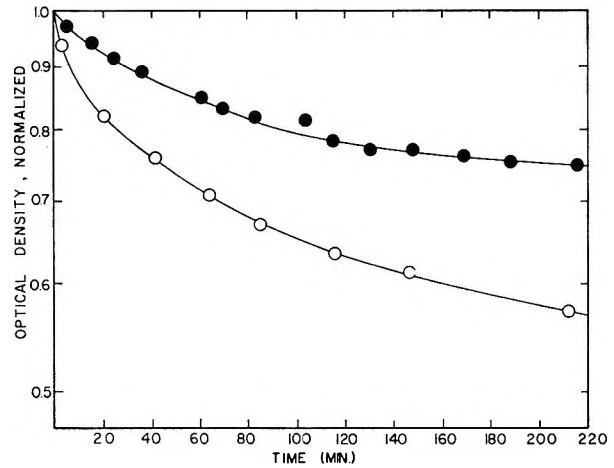


Figure 2. Decay of the $2MD^+$ absorption at 77°K (O) and 72°K (●). Irradiated at 77°K; dose $1.2 \times 10^{19}$ eV/g; concentration 0.75 mol % 2MD; $CO_2$ was used as an electron trap.

The effect of temperature on the rate of dark decay of $2MD^+$ in 3MP saturated with $CO_2$, $\gamma$-irradiated at 77°K, and measured at 77 and 72°K appears in Figure 2. If an Arrhenius dependence applied, the activation energy for thermal decay would be 0.14 eV. At 62°K there was no measurable decay during 3 hr.

Partial optical bleaching of the $2MD^+$ band with polarized light formed two populations of ions. The one, which was observed with the polarizer rotated 90° after bleaching, decayed. The other, which was observed with the polarizer at 0° to its direction for bleaching, grew in at first, then began to decay after ~1 hr (depending on the extent of bleaching). This is a much shorter relaxation time than $2.2 \times 10^4$ sec required for rotation of $TMPD^+$ in 3MP at 77°K.[7]

Optical bleaching with unpolarized light for 0.5 mol % 2MD in $CO_2$-saturated 3MP at 77°K showed that the relative quantum yield of bleaching $2MD^+$ depends on the wavelength and on the previous extent of bleaching. These results appear in Figure 3. If $\epsilon(2MD^+) = 8.2 \times 10^3\ M^{-1}\ cm^{-1}$, based on earlier work,[3] then the initial quantum yield for 675-nm irradiation is about 0.1.

## Discussion

The formation of radical positive ions from 2-methyltetradecane and 2-methylpentadecane in a matrix of $CCl_4$, but not in a matrix of 3MP, suggests inadequate trap depth. The ionization potentials of the higher alkanes are not known, but for *n*-hexane, 2-methylpentane, and 3-methylpentane they are 10.18, 10.12, and 10.06 eV.[8] This indicates that the two molecules being considered have higher ionization potentials than the other alkanes in Table I. The difficulty with attributing the anomalous behavior to trap depth is the fact that four other 2-methylalkanes in 3MP have produced radical ions. Neither does this hypothesis

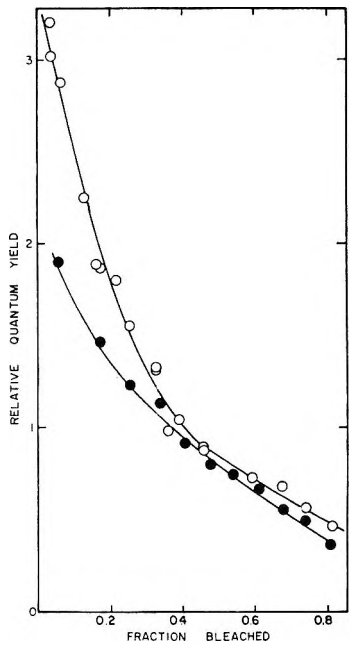


Figure 3. Bleaching of the $2MD^+$ absorption band at 820 nm with light of 675 nm (O) and 983 nm (●) after irradiation of a 0.5 mol % solution of 2MD in 3MP at 77°. Dose $1.4 \times 10^{19}$ eV/g.

account for the small yield and fast decay of $2MD^+$ in 2MP compared with 3MP since one expects the former matrix to provide the deeper trap. Limiting consideration of positive charge trapping to ground-state ionization potentials is probably an oversimplification because there is new evidence that even $CCl_4$, with a nominal ionization potential of 11.47 eV,[8] is able to trap positive charge in a matrix of 3MP[9] and this requires hole conduction by excited states of $RH^+$.

Trapped electrons have not been observed in polycrystalline hydrocarbons by optical absorption, but they have been measured by epr in yields comparable with those in glassy hydrocarbons.[10] The observations of positive hole and electron trapping reported here extend the qualitative similarities of glassy and polycrystalline alkanes as matrices.

The dependence of the yield of $C_6H_6^+$ on the concentration of benzene in Figure 1 resembles the effect of 2-methyl-1-pentene (2MP-1) on the yield of trapped electrons in 3MP.[11] It is also quite similar to the dependence of the yield of $RH^+$ on the concentration of RH.[4] The effect can be attributed to positive

(7) J. R. Lombardi, J. W. Raymonda, and A. C. Albrecht, *J. Chem. Phys.*, **40**, 1148 (1964).

(8) K. Watanabe, T. Nakayama, and J. Mottl, *J. Quant. Spectrosc. Radiat. Transfer*, **2**, 369 (1962).

(9) P. W. F. Louwrier and W. H. Hamill, *J. Phys. Chem.*, **73**, 1702 (1969).

(10) M. Iwasaki, K. Toriyama, and T. Ohmori, *ibid.*, **72**, 4347 (1968).

(11) J. B. Gallivan and W. H. Hamill, *J. Chem. Phys.*, **44**, 2378 (1966).

charge migration by electron tunneling between $M^+$ and M (with M = 2MP-1, RH, or $C_6H_6$) over distances of a few molecular diameters.[4,11] If the process is fast, one or more vertical transitions could occur before self-trapping by intramolecular relaxation of $M^+$. The tunneling process is assisted by the coulombic field, and each transfer lowers the barrier for the next jump as the field increases. The charge pair radial distribution can be assumed to have a cutoff at some lower critical radius, $R_c$, and even an average of one or two charge transfers should produce a measurable depletion of the number of trapped charges. To illustrate, according to one distribution[12] (applicable to a liquid alkane) the probability of charge separation in the range $R \gtrsim R_c$ was found to be $P(R) = (R/R_c)^{-2.7}$ with $R_c = 10^2$ Å. Consequently ~13% of the charge pairs lie between $R = 100$ Å and $R = 110$ Å.

The probability of tunneling within unit time depends exponentially on (barrier height)$^{1/2}$ times (distance), and these parameters can be expressed in terms of ionization potentials and concentrations. The ionization potentials of interest are $I$(2MP-1) ≅ 9.1 eV, $I(C_6H_6)$ = 9.245 eV, $I$(3MP) = 10.08 eV,[8] and one estimates $I$(RH) ≅ 10.0 eV for higher RH. The maximal yields of 2MP-1$^+$ and $C_6H_6^+$ both occur at 2% of additive in 3MP, with barrier heights 1.0 and 0.83 eV, in order. The maxima of OD($RH^+$) lie at ~0.4 mol % and the barrier is ~0.1 eV. These dependences are roughly what one expects for tunneling.

Fast tunneling of the positive hole may be terminated by intramolecular relaxation, to be followed by slow, activated (phonon assisted) tunneling. $2MD^+$ in 3MP at 77 and 72°K provides an example (Figure 2). If the electron vacancy in $2MD^+$ is delocalized among the C–C σ bonds, the internuclear configuration may not differ greatly from that of 2MD, but the adiabatic ionization potential would be somewhat less than the vertical value. This difference may account for the activation energy of 0.14 eV for dark decay.

Positive hole transfer between relaxed $RH^+$ and additive RH (or a second additive, such as TMPD) can also be induced by optical excitation of $RH^+$. Although the extinction coefficient of $2MD^+$ is not accurately known, the quantum yield of bleaching $2MD^+$ (Figure 3) is probably less than unity initially and diminishes thereafter. There are many lower electronically excited states of alkane positive ions,[13,14] and that is consistent with the wide absorption bands of $RH^+$. Failure to observe various $RH^+$ in pure RH matrices indicates that there is no self-trapping of holes by the 3MP matrix, and it must be assumed that carbonium ions account for the survival of matrix-trapped electrons. The progressive decrease in the optical bleaching efficiency of $2MD^+$ in 3MP implies retrapping by 2MD. The higher quantum yield of bleaching (*i.e.*, recombination) at higher frequency may be attributed to longer vibronic relaxation times and higher levels and to a higher density of states. The gradual decrease in quantum yield with progressive bleaching is most readily attributed to efficient removal of charge pairs at small $R$, the center of the distribution being shifted to larger $R$ with partial bleaching by removal of the high-field group.

(12) J. A. Leone and W. H. Hamill, *J. Chem. Phys.*, **49**, 5304 (1968).
(13) C. E. Melton and W. H. Hamill, *ibid.*, **41**, 546 (1964).
(14) K. Fueki, *J. Phys. Chem.*, **68**, 2656 (1964).

# The Radiolysis of Liquid Trifluoroiodomethane

by I. McAlpine and H. Sutcliffe

*Chemistry Department, University of Salford, Salford 5, Lancashire, England* *(Received July 21, 1969)*

The radiolysis of trifluoroiodomethane in the liquid phase at room temperature has been examined. The products and 100-eV yields are tetrafluoromethane (0.37), hexafluoroethane (1.03), and iodine (1.36). Experiments in the presence of oxygen and nitric oxide as radical scavengers indicate that the reaction proceeds mainly by a radical process.

The radiolysis of trifluoroiodomethane in the gas phase has been studied and shown to give the following products and 100-eV yields: tetrafluoromethane (1.08), iodine (0.13), and difluorodiiodomethane (0.82).[1] Surprisingly, hexafluoroethane was absent in this gas phase work. This work was interpreted mainly in terms of radical abstraction of fluorine and radical combination reactions. It is of interest therefore to study the reaction in the liquid phase where spur reactions may be expected to give an increase in those products arising from radical–radical recombination reactions.

We report here the results on the liquid phase radiolysis of trifluoroiodomethane, both alone and in the presence of the radical scavengers oxygen and nitric oxide.

## Experimental Section

The preparation of trifluoroiodomethane and the analysis of products was carried out as described previously.[1,2] Samples for irradiation were sealed in Pyrex tubes 20 cm long × 5-mm i.d., having a wall thickness of 3 mm for all experiments except those involving oxygen. When oxygen was used, the tube was closed with a Hoke needle valve which was fastened to the glass by means of Araldite. The tubes were heated to 400° and evacuated before any reactants were introduced. Irradiations were carried out on a 10,000-Ci cobalt-60 source. The dose was measured using a modified Fricke dosimeter[3] ($G(Fe^{3+}) = 0.66$), and the usual corrections were made for electron density. The density of liquid trifluoroiodomethane at 25° was determined by sealing a known amount of the compound in a glass tube and measuring the volume occupied by the liquid at 25°. A correction was made for the amount of trifluoroiodomethane in the gas phase. In this way a value of 2.115 g/ml was obtained.

All sample volumes were in the range 2.3 ± 0.1 ml in tubes of total volume 4 ml. The amount of sample in the gas phase was thus maintained at <2%.

*Irradiation of Liquid Trifluoroiodomethane.* In a typical experiment 25.102 mmol of trifluoroiodomethane was irradiated for 15.5 hr. The products were fractionated *in vacuo* through traps cooled to −63, −131, and −196°. The fraction condensed at −63° contained iodine together with a trace of trifluoroiodomethane. The iodine was determined by titration with sodium thiosulfate solution. The fraction condensed at −131° contained trifluoroiodomethane. The fraction condensed at −196° contained trifluoroiodomethane, hexafluoroethane, and tetrafluoromethane. The percentage composition was determined by gas chromatography.

The results for several such irradiations are shown graphically in Figure 1. The 100-eV yields for iodine, hexafluoroethane, and tetrafluoromethane were determined from the slope of the graphs.

In one experiment (not plotted on Figure 1) 24.914 mmol of trifluoroiodomethane was irradiated for 150 hr, to a total dose of $24.06 \times 10^{21}$ eV to ascertain if difluorodiiodomethane was being formed in very small amounts. After this time 0.00286 mmol of difluorodiiodomethane was isolated.

*Irradiation of Liquid Trifluoroiodomethane and Oxygen.* A mixture of trifluoroiodomethane (25.446 mmol) and oxygen (0.0327 mmol) was irradiated for 5 hr; the dose received was $0.9517 \times 10^{21}$ eV. The products were fractionated *in vacuo* to yield iodine, trifluoroiodomethane, hexafluoroethane, tetrafluoromethane, and carbonyl fluoride. Some oxygen remained after irradiation, but this was not measured. A small amount of an involatile white solid remained in the reaction tube which liberated iodine from potassium iodide solution. The results are given in Table I.

*Irradiation of Liquid Trifluoroiodomethane and Nitric Oxide.* A mixture of trifluoroiodomethane (25.09 mmol) and nitric oxide (0.472 mmol) was irradiated for 5 hr; the dose received was $0.8695 \times 10^{21}$ eV. After irradiation the nitrogen was transferred by means of an automatic Toepler pump into a vessel of known volume and measured. The purity of the nitrogen was checked by gas chromatographic analysis and found to contain only a slight trace of nitric oxide. The condensable gases were fractionated *in vacuo* through traps cooled to −63, −96, −131, and −196°. The fraction

(1) I. McAlpine and H. Sutcliffe, *J. Phys. Chem.*, **73**, 3215 (1969).
(2) I. McAlpine and H. Sutcliffe, *ibid.*, in press.
(3) E. J. Hart and P. D. Walsh, *Radiat. Res.*, **1**, 342 (1954).

**Table I:** Products and 100-eV Yields for the Products from the Radiolysis of Trifluoroiodomethane

| | G | | | | | | | | |
|---|---|---|---|---|---|---|---|---|---|
| | $I_2$ | $CF_4$ | $C_2F_6$ | $CF_2I_2$ | $N_2$ | $CF_3NO$ | $NO_2$ | $-NO$ | Comments |
| Liquid $CF_3I$ | 1.36 | 0.37 | 1.03 | *a* | | | | | |
| Liquid $CF_3I$ + 0.1% $O_2$ | 4.27 | 0.06 | 5.72 | | | | | | Trace of $COF_2$ and white solid. Oxygen present after irradiation |
| Liquid $CF_3I$ + 2% NO | 4.47 | 0.18 | 1.86 | | 6.93 | 0.36 | *c* | 32.7 | Trace of $COF_2$ and $CF_3NO_2$ |
| Liquid $CF_3I$ + 4% NO | 4.53 | 0.20 | 0.97 | | 17.87 | 1.24 | 26.74 | 71 | Trace of $COF_2$ and $CF_3NO_2$ |
| Gaseous $CF_3I$[b] | 0.13 | 1.08 | 0.0 | 0.82 | | | | | |

[a] A small amount of $CF_2I_2$ is formed at high dose. [b] See ref 1. [c] Not measured.

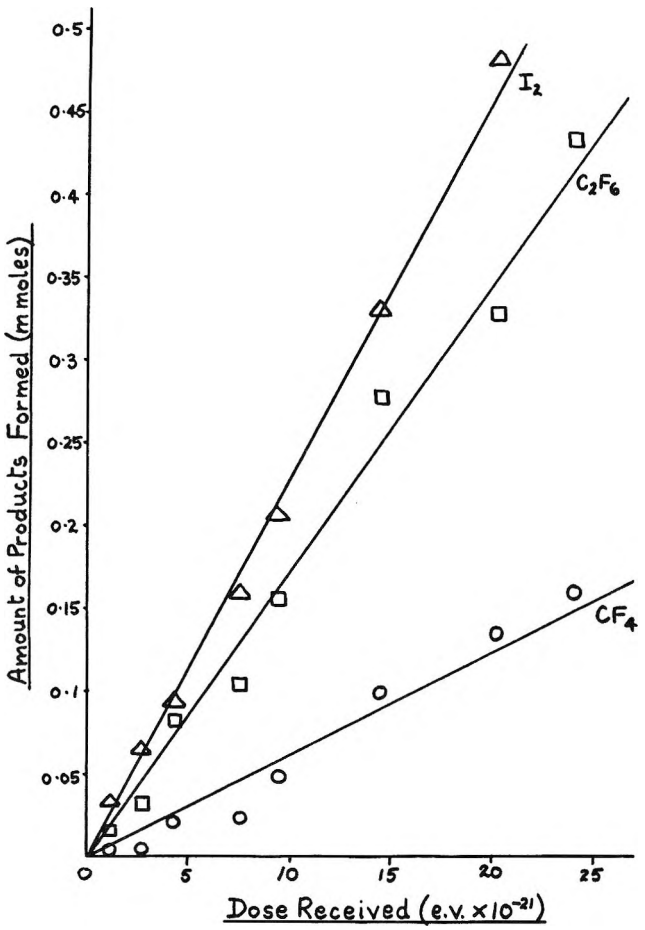


Figure 1. Liquid phase radiolysis of trifluoroiodomethane.

condensed at −63° contained iodine which was determined by titration. The fraction condensed at −96° contained nitrogen dioxide together with a small amount of trifluoroiodomethane; the nitrogen dioxide was determined by titration. The fraction condensed at −131° contained mainly trifluoroiodomethane together with a trace of trifluoronitromethane. The fraction condensed at −196° contained trifluoroiodomethane, hexafluoroethane, tetrafluoromethane, trifluoronitrosomethane, and a trace of carbonyl fluoride. The percentage composition of the mixture was determined by gas chromatography.

The experiment was repeated using 4% nitric oxide; the results from both experiments are shown in Table I.

## Results and Discussion

The products isolated from the radiolysis of liquid trifluoroiodomethane and the 100-eV yields are tetrafluoromethane (0.37), hexafluoroethane (1.03), and iodine (1.36). The yields are linear over the dose range $1.4 \times 10^{21}$–$20.22 \times 10^{21}$ eV., as is shown in Figure 1. These results differ from those obtained in the gas phase in that the yield of tetrafluoromethane is lower, by a factor of 3, whereas the yields of iodine and hexafluoroethane are much higher; see Table I. No difluorodiiodomethane was detected in the liquid phase radiolysis up to a dose of $20.2 \times 10^{21}$ eV. At a dose of $24.06 \times 10^{21}$ eV some difluorodiiodomethane was detected.

This comparison of results in the liquid and gas phase lends support to the idea that in the liquid phase reaction occurs mainly in spurs where a high concentration of reactive species exists.

The initial absorption of energy may be expected to give rise to the reactions

$$CF_3I \rightsquigarrow CF_3I^+ + e^- \quad (1)$$

$$\rightsquigarrow CF_3\cdot + I^+ + e^- \quad (2)$$

$$\rightsquigarrow CF_3^+ + I\cdot + e^- \quad (3)$$

$$\rightsquigarrow CF_3I^* \text{ (excited molecule)} \quad (4)$$

In the liquid phase the chances of deactivation by collision are higher than in the gas phase; thus less reaction of excited radicals is expected and hence the amounts of products arising from excited radicals will be lower than in the gas phase. It has been suggested that tetrafluoromethane is formed in the gas phase radiolysis by an excited trifluoromethyl radical abstracting a fluorine atom from a molecule of trifluoroiodomethane[1]

$$CF_3\cdot^* + CF_3I \longrightarrow CF_4 + \cdot CF_2I \quad (5)$$

Such a process would also be expected to operate in the liquid phase but to a reduced extent owing to the greater probability of deactivation of the excited radicals by collision. A lower yield of tetrafluoromethane is in

fact observed in the liquid phase than in the gas phase; see Table I. Thus, deactivation of excited radicals is playing an important part in this reaction and hence the thermal radicals so produced will also play an important part in this reaction. In the high localized concentration of radicals that exist within a spur dimerization to hexafluoroethane is expected, and a value of $G(C_2F_6) = 1.03$ is observed. Thermal trifluoromethyl radicals will also be expected to recombine with iodine. Doubtless both processes take place

$$CF_3\cdot + I_2 \longrightarrow CF_3I + I \quad (6)$$

$$CF_3\cdot + I + M \longrightarrow CF_3I \quad (7)$$

$$CF_3\cdot + CF_3\cdot + M \longrightarrow C_2F_6 + M \quad (8)$$

with a possibility of the reaction

$$CF_3\cdot{}^* + CF_3\cdot + M \longrightarrow C_2F_6 + M \quad (9)$$

also occurring. Since the yield of iodine and hexafluoroethane are not particularly high, reactions 6 and 7 must predominate over (8) and (9) which in turn predominate over (5).

In the gas phase hexafluoroethane is not formed since there is less chance of deactivation of excited radicals and no localized concentration of thermal radicals.

*Irradiation of Liquid Trifluoroiodomethane in the Presence of Oxygen.* In the presence of *ca.* 0.1% oxygen the tetrafluoromethane yield is reduced to $G(CF_4) < 0.06$, and iodine and hexafluoroethane yields were increased to $G(I_2) = 4.27$ and $G(C_2F_6) = 5.27$; in addition carbonyl fluoride and an unidentified white solid were also present. The white solid appears to be similar to the one produced in the gas phase, in that it liberates iodine from potassium iodide solution. The presence of peroxy or fluoroxy groups is therefore suspected.

No data are available for the solubility of oxygen in trifluoroiodomethane, but the concentration must be <0.1% *M*. It is surprising that at such low concentrations there is almost complete scavenging of tetrafluoromethane. Equally surprising, although consistent with the gas phase work,[1] is the increased yield of hexafluoroethane.

These results are interpreted in terms of the scavenging of excited trifluoromethyl radicals by oxygen, followed by secondary reactions of the peroxy radical to give hexafluoroethane

$$CF_3\cdot{}^* + O_2 \longrightarrow CF_3\cdot O\cdot O\cdot \quad (10)$$

$$2CF_3\cdot O\cdot O\cdot \longrightarrow C_2F_6 + O_2 \quad (11)$$

Reaction 11 may occur directly or *via* free thermalized trifluoromethyl radicals which subsequently dimerize to hexafluoroethane. Thus, once a molecule of oxygen enters a spur and scavenges a radical it is regenerated and is then available for further scavenging. Scavenging followed by regeneration of oxygen explains why such a low concentration of oxygen is effective in almost eliminating tetrafluoromethane as a product. Such a process could proceed until the oxygen diffuses out of the spur.

Other reactions involving the trifluoromethoxy radical are also possible, *e.g.*

$$CF_3\cdot O\cdot O\cdot + CF_3\cdot{}^* \longrightarrow C_2F_6 + O_2 \quad (12)$$

and also result in the formation of hexafluoroethane.

*Irradiation of Trifluoroiodomethane in the Presence of Nitric Oxide.* The radiolysis of liquid trifluoroiodomethane in the presence of 2 and 4% nitric oxide yields iodine, hexafluoroethane, tetrafluoromethane, trifluoronitrosomethane, nitrogen, nitrogen dioxide, trifluoronitromethane, and carbonyl fluoride. See Table I for *G* values. In both experiments only a trace of nitric oxide remained after 5 hr of irradiation. The $G(-NO)$ values are therefore limited by the availability of nitric oxide.

A particularly interesting feature of this reaction is the increased yield of hexafluoroethane in the presence of 2% nitric oxide and a slightly decreased yield of hexafluoroethane in the presence of 4% nitric oxide. Since nitric oxide is a radical scavenger, a reduction in the yield of hexafluoroethane would be expected. This unexpected result is interpreted in terms of secondary reactions of the initially formed trifluoronitrosomethane. The reaction is considered to proceed in two overlapping stages: (a) when nitric oxide is present in sufficient quantities to scavenge the radicals and (b) when the nitric oxide is depleted and trifluoronitrosomethane is acting as a radical scavenger. Trifluoronitrosomethane is known to be susceptible to radical attack, initially on the nitrogen atom.[4]

In the presence of nitric oxide the mechanism is similar to that described for the gas phase work

$$CF_3I \longrightarrow CF_3{}^* + I \quad (13)$$

$$CF_3\cdot{}^* + NO \longrightarrow CF_3\cdot NO \quad (14)$$

$$CF_3\cdot NO + 2NO \longrightarrow CF_3\cdot N_2\cdot NO_3 \longrightarrow CF_3\cdot + N_2 + NO_3\cdot \quad (15)$$

$$\cdot NO_3 + NO \longrightarrow 2NO_2 \quad (16)$$

$$CF_3\cdot + NO_2 \longrightarrow CF_3\cdot NO_2 \quad (17)$$

The overall effect of reactions 14 to 16 is the disproportionation of nitric oxide into nitrogen and nitrogen dioxide

$$4NO \longrightarrow N_2 + 2NO_2$$

and the ratio $G(-NO):G(NO_2):G(N_2)$ should be 4:2:1. The observed ratio 4:1.5:1 in the experiment with 4% nitric oxide is of this order. As the nitric oxide becomes depleted, reaction 15 slows down and there is a buildup of trifluoronitrosomethane.

(4) R. N. Haszeldine and B. J. H. Mattinson, *J. Chem. Soc.*, 1741 (1957).

The difference in the $G(CF_3 \cdot NO)$ values for the two reactions, 0.88, is almost the same as the difference in the $G(C_2F_6)$ values, 0.87. This indicates that a molecule of trifluoronitrosomethane reacts to give a molecule of hexafluoroethane. This is thought to occur by attack of an excited trifluoromethyl radical on the nitrogen of trifluoronitrosomethane followed by decomposition of the nitroxide radical so formed to hexafluoroethane and nitric oxide

$$CF_3 \cdot^* + CF_3 \cdot NO \longrightarrow (CF_3)_2NO \cdot^* \longrightarrow C_2F_6 + NO$$

Bis(trifluoromethyl) nitroxide is a stable compound[5] but as formed from an excited trifluoromethyl radical is expected to decompose as indicated. If the attacking radical is not excited, the nitroxide would presumably be stable until attacked by a second thermal radical to give tris(trifluoromethyl)hydroxylamine

$$CF_3 \cdot + CF_3 \cdot NO \longrightarrow (CF_3)_2NO \cdot \xrightarrow{CF_3 \cdot} (CF_3)_2NOCF_3$$

No tris(trifluoromethyl)hydroxylamine was detected in the present work.

*Acknowledgment.* I. M. wishes to thank the Science Research Council, London, England, for a maintenance award, during the tenure of which this work was carried out.

(5) W. D. Blackley and R. R. Reinhard, *J. Amer. Chem. Soc.*, **87**, 802 (1965).

# The Radiolysis of Liquid Nitromethane[1]

**by James L. Corey and Richard F. Firestone**

*Department of Chemistry, The Ohio State University, Columbus, Ohio 43210* *(Received July 30, 1969)*

Initial 100-eV yields and effects of dose on the rates of formation of 12 products of the $^{60}Co$ $\gamma$-ray-induced decomposition of pure, air-free, liquid nitromethane have been measured at constant dose rate ($9 \times 10^{17}$ eV/g min) at 0° and at room temperature. The *cis* dimer of nitrosomethane, methyl nitrite, and formaldehyde are major initial products at both temperatures. Initial yields of formaldehyde and methyl nitrite exhibit pronounced positive temperature coefficients. Neither the *trans* dimer of nitrosomethane nor nitrogen dioxide is found among the final products. A relatively slow, thermal, dark reaction converts nitrosomethane to methyl nitrite at room temperature, but not at 0°. Effects of increasing dose at room temperature are similar to those of the dark reaction. A mechanism invoking the existence of the intermediate $CH_3(NO)_3$ is proposed to account for effects of dose.

## Introduction

Very few investigations of direct effects of ionizing radiation on the nitroalkanes have been reported. Paszyc[2] has reported relative concentrations of some of the products of the radiolysis of liquid nitromethane and nitroethane at room temperature at a single high dose. Cundall, Locke, and Street have published a preliminary report of an investigation of the steady and pulsed radiolysis of nitromethane[3] and a more complete and detailed report of a comparative study of the photolysis and radiolysis at room temperature.[4] The latter has established the identities and average 100-eV yields of each of an abundant variety of products at two fixed doses and dose rates and has demonstrated occurrence of a thermal dark reaction at room temperature which does not occur in the photolysis.

The present article reports effects of dose on the yields of products of the $^{60}Co$ $\alpha$-ray-induced decomposition of pure, air-free nitromethane at 0° and at room temperature. A set of reaction steps consistent with observed effects of dose, temperature, the initial presence of several products, and apparent effects of dose rate is presented and discussed.

## Experimental Section

Matheson Coleman and Bell Spectroquality reagent nitromethane was purified by fractional distillation at atmospheric pressure and stored under dry nitrogen in total darkness. A portion of the middle half of the distillate was further purified immediately prior

(1) Based upon a dissertation submitted in partial fulfillment of requirements for the Ph.D. degree at The Ohio State University by J. L. C., 1965.

(2) S. Paszyc, *Photochem. Photobiol.*, **4**, 841 (1965).

(3) R. B. Cundall, A. W. Locke, and G. C. Street, *Nature*, **210**, 1354 (1966).

(4) R. B. Cundall, A. W. Locke, and G. C. Street, "The Chemistry of Ionization and Excitation," G. R. A. Johnson and G. Scholes, Ed., Taylor and Francis Ltd., London, 1967, pp 131–140.

to use by passage through a 25 × 1 cm column of basic aluminum oxide (Woelm), and the first half of the effluent was collected. Purified material contained the following quantities (mol %) of detectable impurities: acetonitrile (0.02), propionitrile (0.4), acetone (0.004), nitroethane (0.007), 2-nitropropane (0.03), and less than 0.01 mol % of water. Methyl nitrite was prepared by action of sulfuric acid on a solution of methanol, water, and sodium nitrite. The product was dried over anhydrous calcium chloride and phosphoric anhydride and was purified by bulb-to-bulb distillation on a high-vacuum apparatus.

Measured portions of purified nitromethane were outgassed by freeze–pump–thaw cycles and transferred into Pyrex-glass irradiation vessels which had been previously outgassed by simultaneous pumping and prolonged baking at temperatures near the softening point. Filled vessels were sealed and removed from the vacuum apparatus by fusing the filling arms with a gas–oxygen torch while maintaining the vessel contents at −196°. Irradiations were performed with a nominally 150 Ci $^{60}Co$ $\alpha$-ray source. Dosimetry measurements were made with Fricke dosimeter solution, assuming $G(Fe^{3+}) = 15.6$ ions/100 eV. Analyses for ferric ion were performed spectrophotometrically at 304 nm and 25°, assuming a molar absorptivity equal to 2196 l./mol cm. Dose rates in nitromethane samples have been assumed to be equal to the product of the measured dose rate in the Fricke solution and the ratio of electron densities of the former to the latter solution. All samples were irradiated at dose rates in the range 9.4 to 9.7 × $10^{17}$ eV/g min.

All samples irradiated at 25° and for which data are reported were cooled to 0° immediately after irradiation and subjected to analysis within 20 min. Under these conditions contributions of the dark, postirradiation reaction which proceeds readily at 25° were negligible. Samples irradiated for 6 hr at 25°, for example, and maintained afterward at 0° failed to exhibit detectable changes in the total yield of gaseous products within 2 hr. Gaseous products were separated into two fractions by transfer through cold traps maintained at −196 and −78°, respectively. The −196° fraction consisted predominantly of $H_2$, $N_2$, $CH_4$, and CO. The remaining volatile products (NO, $N_2O$, $CO_2$, $CH_3ONO$, $C_2H_6$, and HCHO) as well as traces of those collected predominantly at −196° were collected at −78° in the presence of nitromethane vapor. The outgassed liquid fraction was separated from a nonvolatile residue by vacuum distillation, and the nonvolatile residue was separated into a water-soluble fraction and a nonvolatile insoluble fraction. Components of the gaseous fractions and of the volatile liquid fraction were determined quantitatively by gas chromatographic analyses using thermal conductivity detection and a 10-ft, 9-mm i.d. Pyrex column packed with 80–100 mesh silica gel operated with He carrier gas (30 $cm^3$/min) at 25° and using flame ionization detection and a 6-ft, 0.125-in. copper column packed with 5 wt % Apiezon L grease on 60–80 mesh Chromasorb P operated with $N_2$ carrier gas (150 $cm^3$/min) at 25° and a 6-ft, 0.25-in copper column packed with 25 wt % Carbowax 20M on 45–60 mesh Chromasorb P operated with $N_2$ carrier gas (300 $cm^3$/min) and a linear temperature program of 3.3°/min commencing at 60°. Analyses for formaldehyde were performed with the latter column and program on aliquots of whole samples prior to separation of gaseous fractions. Methyl nitrite was determined in whole samples by spectrophotometric measurements at 300 to 410 nm. The water-soluble fraction of the nonvolatile residue contained the *cis* dimer of nitrosomethane, which was determined quantitatively by spectrophotometric measurements at 265 nm. Samples of the water-insoluble nonvolatile residue were subjected to wet chemical spot tests which indicated the presence of undetermined small quantities of formaldoxime trimer and traces of formaldehyde polymer in this residue. Qualitative identifications of all products were made by infrared and ultraviolet spectrophotometry, chemical spot tests, and comparisons of retention volumes of gas chromatographic signal peaks with those of known substances.

## Results

The most abundant initial radiolysis products at 0° and at room temperature (25–28°) are, as indicated in Figures 1 and 2, formaldehyde, methyl nitrite, and the *cis* dimer of nitrosomethane. The presence of traces of polymeric formaldehyde and of small un-

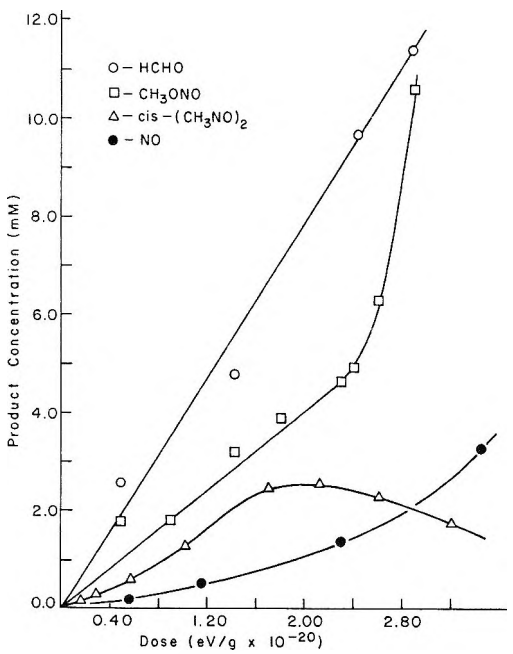


Figure 1. Concentrations of major products as functions of dose at room temperature.

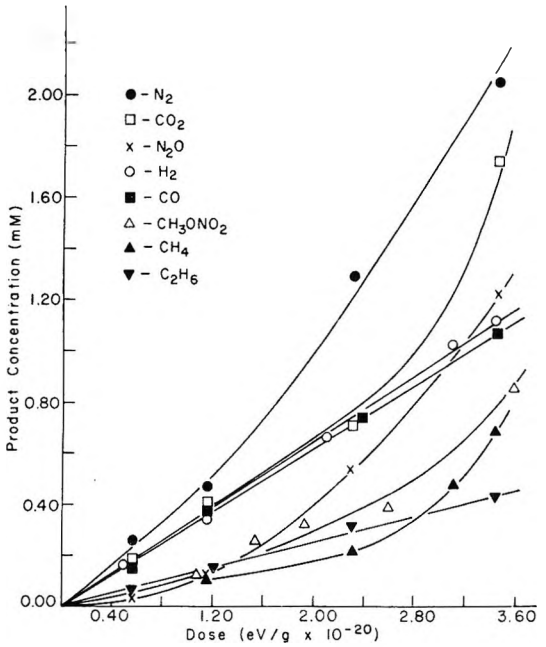


Figure 2. Concentrations of major products as functions of dose at 0°.

determined quantities of formaldoxime has been detected in the water-insoluble residue of nonvolatile fractions of several irradiated samples of nitromethane. Unestimated quantities of products bearing carbonyl groups were also detected by infrared analyses of whole irradiated samples. The absence of nitrogen dioxide and of the *trans* dimer of nitrosomethane in whole samples of irradiated nitromethane in the dose range investigated has also been established. Table I presents instantaneous initial 100-eV yields (columns 2 and 4) of products which have been determined quantitatively.

A postirradiation dark reaction which proceeds readily at room temperature has been observed to form methyl nitrite, methyl nitrate, nitrogen, nitrous oxide, carbon dioxide, methane, and formaldoxime and to consume the *cis* dimer of nitrosomethane. Postirradiation effects were not observed in samples which were maintained at 0° after irradiation. Figures 1 and 2 demonstrate that the instantaneous 100-eV yields of most of these products are functions of dose at room temperature.

The initial 100-eV yields of formaldehyde, methyl nitrite, carbon dioxide, and ethane at room temperature are roughly twice their respective values at 0°. All other products are formed at the same respective rates at both temperatures.

Addition of millimolar quantities of $NO_2$ prior to irradiation of nitromethane at room temperature has been observed to increase the initial 100-eV yield of formaldehyde by a factor of approximately 20, to decrease the rate of formation of methyl nitrite, and to completely inhibit formation of the *cis* dimer of nitrosomethane while inducing no change in the rate of formation of methyl nitrate.

Irradiation of nearly saturated solutions of water in nitromethane at 25° formed methyl nitrite at a 100-eV initial yield half that in the absence of water. At higher doses $G(CH_2ONO)$ approached the value characteristic of zero dose in water-free nitromethane. Nitrous acid seems on the basis of appearance and growth of a characteristic absorption peak at 384 nm to have been formed at a relatively rapid initial rate in the presence of water and to have been consumed at higher doses.

It has also been observed that solutions of NO, $NO_2$, and the *cis* dimer of nitrosomethane react slowly in the absence of radiation at 25° to form methyl nitrite and other products and that methyl nitrite is not formed in the absence of *cis*-$(CH_3NO)_2$ under otherwise identical conditions.

**Table I:** Initial ($G°$) and Integrated Average ($\bar{G}$)° 100-eV Yields from Nitromethane at 0° and Room Temperature

| | This work | | | | Cundall, *et al.*[c] |
|---|---|---|---|---|---|
| | 0° | | Room temp[b] | | Room temp, |
| | $G°$ | $\bar{G}$ | $G°$ | $\bar{G}$ | $\bar{G}$ |
| *cis*-$(CH_2NO)_2$ | 0.53 | 0.66 | 0.53 | 0.36 | 0.52 |
| HCHO | 0.84 | 0.84 | 2.0 | 2.0 | 0.20 |
| $CH_3ONO$ | 0.50 | 0.83 | 1.1 | 1.9 | 1.5 |
| NO | 0.16 | 0.16 | 0.16 | 0.43 | 0.35 |
| $CO_2$ | 0.07 | 0.07 | 0.16 | 0.20 | 0.00 |
| CO | 0.18 | 0.18 | 0.18 | 0.18 | 0.31 |
| $H_2$ | 0.17 | 0.17 | 0.17 | 0.17 | 0.22 |
| $N_2$ | 0.20 | 0.20 | 0.20 | 0.30 | 0.14 |
| $N_2O$ | 0.02 | 0.04 | 0.00 | 0.16 | 0.28 |
| $CH_3ONO_2$ | 0.09 | 0.09 | 0.09 | 0.09 | ... |
| $CH_4$ | 0.07 | 0.09 | 0.07 | 0.09 | 0.06 |
| $C_2H_6$ | 0.03 | 0.03 | 0.06 | 0.06 | 0.09 |
| $-CH_3NO_2$[d] | 3.0 | 3.5 | 4.8 | 5.3 | 3.2 |

[a] Integrated average yield values ($\bar{G}$) are reported at $3.0 \times 10^{20}$ eV/g. [b] Dose rate 9.4 to 9.7 $\times 10^{17}$ eV/g min for 17–400 min and quenched at 0°. [c] Reference 4; dose rate $6.6 \times 10^{18}$ eV/g min for 5.0 min and quenched at −196°. [d] $G(-CH_3NO_2)$ based on sum over carbon atoms among products.

## Discussion

Nitromethane is a difficult substance to study, because identification and quantitative determination of its radiolysis products require extraordinary care with analytical techniques exhibiting a wide range of sensitivity and precision and because of the occurrence at room temperature of a thermally activated dark reaction among the radiolysis products. The identities of fifteen products at moderately low conversions seem to have been firmly established by this work and that of Cundall, *et al.* Neither we nor they, however, have been able to obtain an acceptable material balance among products. Among our yield data there is a marked deficiency at all conversions of N, O, and H relative to C atoms among the products, which may

indicate formation of substantial quantities of undetermined inorganic products, such as water, nitric acid, and nitrous acid. The data of Cundall, *et al.*, reflect deficiencies of O and H and a surplus of N relative to C atoms. Product yields reported by the latter authors differ specifically from ours in two significant respects. Formaldehyde yields reported by Cundall, *et al.*, are consistently an order of magnitude lower, and Cundall, *et al.*, observed no significant dose dependence of the 100-eV yields of any products in the same dose range but at a fivefold lower dose rate than that of the present work.[4] The discrepancy among formaldehyde yields is probably an analytical discrepancy reflecting the tendency of formaldehyde to polymerize, which renders its determination especially sensitive to the history of the sample, including freezing and thawing, and means employed, if any, to separate products prior to analysis. The discrepancy concerning dose dependence may be mechanistically significant, because of the differences in dose rates.

The postirradiation dark reaction does not proceed detectably among photolysis products, which are distinguished from those of radiolysis by lower proportions of nitrosomethane, formaldehyde, and the oxides of nitrogen.[4] Radiolysis products affected by the dark reaction and the extent of its effects depend critically upon the distribution of products when irradiation is terminated. Cundall, *et al.*, have observed that following absorption of $3 \times 10^{20}$ eV/g in a 5-min period the postirradiation reaction at room temperature consumes *cis*-$(CH_3NO)_2$ and that only $N_2$, $CO_2$, and $CH_3ONO$ are clearly products of the dark reaction under these conditions. The present authors have observed that the postirradiation reaction also forms $CH_3ONO_2$, $N_2O$, $CH_4$, and formaldoxime following similar absorbed doses at a dose rate two orders of magnitude lower. Thus, changes effected by steps in the dark-reaction mechanism during irradiation at room temperature may be determined by irradiation time and extent of conversion irrespective of an effect of dose rate or of dose *per se* upon the radiolysis mechanism.

Yield values reported in columns 4 and 5 of Table I are initial and integrated average 100-eV yields ($3 \times 10^{20}$ eV/g), respectively, for samples which have been irradiated at $10^{18}$ eV/g min at room temperature and quenched at 0° immediately after irradiation. Values of column 6 are those of Cundall, *et al.*,[4] from samples irradiated for only 5 min at nearly $10^{20}$ eV/g min and quenched at −196° immediately after delivery of an equal absorbed dose. Initial 100-eV yields and integrated average 100-eV yields at the same dose and the lower dose rate from samples irradiated at 0° appear in columns 2 and 3. Comparisons among the five sets of yield values so tabulated afford several distinctly tentative conclusions concerning effects of dose, dose rate, and reaction time.

The dose effect appears to be absent at high dose rate

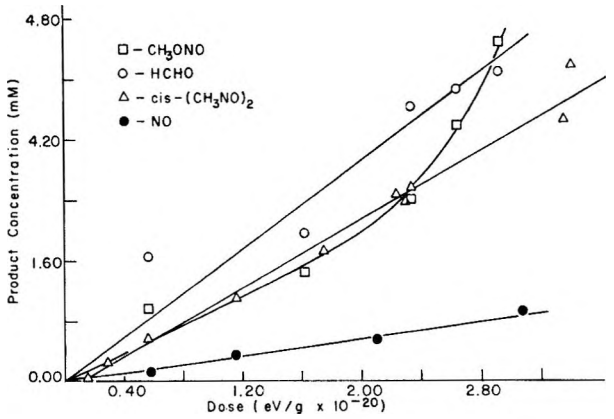


Figure 3. Concentrations of major products as functions of dose at room temperature.

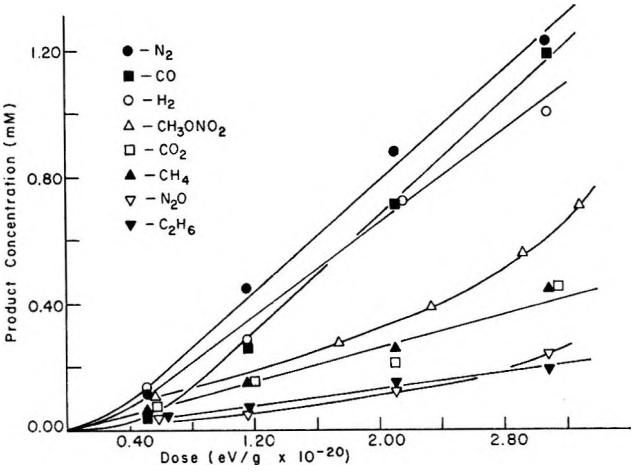


Figure 4. Concentrations of minor products as functions of dose at 0°.

and room temperature as of $3 \times 10^{20}$ eV/g (*cf.* columns 4, 5, 6) for *cis*-$(CH_3NO)_2$, $N_2$, and $CH_4$, all of which are affected by the postirradiation reaction at room temperature. Thus, variations in yields of these products with respect to dose appear to be attributable wholly or in large part to slow thermal reactions among radiolysis products. Dose rate dependence appears to be exhibited by the 100-eV yields of CO, $N_2O$, and $C_2H_6$, each of which is formed in higher yield per unit dose at the higher dose rate. It is also reasonable to suppose that discrepancies between values for the methyl nitrite and nitric oxide yields in columns 4 and 6 are attributable to the dose rate difference. All comparisons between our 100-eV yields and those of Cundall, *et al.*, must, however, be made with caution, because of the different irradiation conditions and the different means employed to quench samples after irradiation. Thus, in discussion to follow principal emphasis is placed upon rationalization of data presented in Figures 1–4 and columns 2–5 of Table I.

Rebbert and Slagg,[5] McGarvey and McGrath,[6] and Cundall, *et al.*,[4] have shown that results of the photoly-

sis of gaseous and liquid nitromethane are consistent with the proposal that the predominant primary step at 253.7 nm is rupture of the C–N bond, *i.e.*

$$CH_3NO_2^* \longrightarrow CH_3\cdot + NO_2 \quad (1)$$

Consistently, Bielski and Timmons[7] and Chachaty[8] have observed esr signals attributable to $CH_3$ radicals and $NO_2$ in nitromethane photolyzed[7] and radiolyzed[8] at 77°K. Chachaty[8] has also observed disappearance of $CH_3$ radicals and appearance of signals attributable to $CH_2NO_2$ radicals upon warming of samples radiolyzed at 77°K, suggesting occurrence of reaction 2 and/or reaction 3. At higher photon energies and in ra-

$$CH_3\cdot + CH_3NO_2 \longrightarrow CH_4 + \cdot CH_2NO_2 \quad (2)$$

$$NO_2 + CH_3NO_2 \longrightarrow HNO_2 + CH_2NO_2 \quad (3)$$

diolysis excited nitromethane may, as suggested by Hirschlaff and Norrish,[9] decompose *via* reaction 4 or *via*

$$CH_3NO_2^* \longrightarrow HCHO + NOH \quad (4)$$

reaction 5 as suggested by Rebbert and Slagg[5] and undergo rearrangement *via* reaction 6, as proposed by

$$CH_3NO_2^* \longrightarrow CH_3O + NO \quad (5)$$

Brown and Pimentel,[10] and later qualified by Pimentel

$$CH_3NO_2^* \longrightarrow CH_3ONO \quad (6)$$

and Rollefson.[11] Among possible ionic steps, Kandel[12] has obtained mass spectrometric evidence which suggests occurrence of the sequence of reactions

$$CH_3NO_2 + e \longrightarrow CH_3NO_2^+ + 2e \quad (7)$$

$$CH_3NO_2^+ \begin{cases} \longrightarrow CH_3\cdot + NO_2^+ & (8) \\ \longrightarrow CH_3O\cdot + NO^+ & (9) \end{cases}$$

$$NO_2^+ \longrightarrow NO^+ + O \quad (10)$$

Henglein and Muccini[13] have reported that the most abundant negative ions in the high pressure mass spectrum of nitromethane are $CH_3NO_2^-$, $O^-$, and $CH_2NO_2^-$, suggesting[14] that the latter two species are probably formed by dissociative electron capture and reaction 12, respectively. The preceding set of reactions does

$$CH_3NO_2 + e \longrightarrow CH_3NO + O^- \quad (11)$$

$$O^- + CH_3NO_2 \longrightarrow OH + CH_2NO_2^- \quad (12)$$

not, of course, include all possible primary and fast secondary steps but appears to include the more probable ones. Discussion of slower secondary reactions may take into consideration the following reactive intermediates species and several reactive products: $CH_3 \rightsquigarrow CH_3\cdot$, $\cdot CH_2NO_2$, $CH_3O\cdot$, $\cdot OH$, $\cdot NOH$, $CH_3NO_2^+$, $NO_2^+$, $CH_2NO_2^-$, $CH_3NO_2^-$.

Two transient species which absorb light in the visible region, one of which is much longer lived than the other, have been observed in the pulse radiolysis of liquid nitromethane.[3] The shorter lived transient species is tentatively believed to be the $CH_2NO_2^-$ anion,[3] and, if so, is probably removed by neutralization (acid–base) steps. The more stable species is assigned the probable identity of monomeric nitrosomethane, $CH_3NO$. Burrell[15] reports light absorption by the nitrosocyclohexane monomer at 700 nm following pulse radiolysis of liquid solutions of NO in cyclohexane.

Formaldehyde, the most abundant initial product in our experiments, is probably formed in part by fast primary reactions, but, because its initial yield is three times as great at room temperature as at 0°, slower secondary steps are of major significance at room temperature. Among previously proposed or known reactions of this kind the reaction of nitrogen dioxide with nitromethyl radicals[16] is a likely possibility

$$NO_2(N_2O_4) + \cdot CH_2NO_2 \longrightarrow NO + NO_2(N_2O_3) + HCHO \quad (13)$$

Contributions from methyl and methoxyl radicals *via* reactions 14 and 15 must be much less important, be-

$$2CH_3O\cdot \longrightarrow HCHO + CH_3OH \quad (14)$$

$$CH_3\cdot + CH_3O\cdot \longrightarrow HCHO + CH_4 \quad (15)$$

cause of the low initial rate of formation of methane and the near absence of methanol. Methanol may, however, be removed by nitrogen dioxide[17]

$$2NO_2(N_2O_4) + CH_3OH \longrightarrow CH_3ONO + HNO_3 \quad (16)$$

This is doubtful, because it is unlikely that methanol would in such case remain a minor product at 0° and because the initial presence of $NO_2$ accelerates formation of HCHO and NO as required by reaction 13 and inhibits formation of methyl nitrite contrary to reaction 16.

(5) R. E. Rebbert and N. Slagg, *Bull. Soc. Chim. Belges*, **71**, 709 (1962).

(6) J. J. McGarvey and W. D. McGrath, *Trans. Faraday Soc.*, **60**, 2196 (1964).

(7) B. H. J. Bielski and R. B. Timmons, *J. Phys. Chem.*, **68**, 347 (1964).

(8) C. Chachaty, *J. Chim. Phys.*, **62**, 728 (1965).

(9) E. Hirschlaff and R. G. W. Norrish, *J. Chem. Soc.*, 1580 (1936).

(10) H. W. Brown and G. C. Pimentel, *J. Chem. Phys.*, **29**, 883 (1958).

(11) G. C. Pimentel and G. Rollefson, unpublished work referenced in "Formation and Trapping of Free-Radicals," A. M. Bass and H. P. Broida, Ed., Academic Press, Inc., New York, N. Y., 1960, p 97.

(12) R. J. Kandel, *J. Chem. Phys.*, **23**, 84 (1955).

(13) A. Henglein and G. A. Muccini, "Chemical Effects of Nuclear Transformations," International Atomic Energy Agency, Vienna, 1961, p 89 ff.

(14) See, also, the discussion of negative ion forming mechanisms in ref 4, for additional possibilities in the liquid phase.

(15) E. J. Burrell, Jr., *J. Phys. Chem.*, **66**, 401 (1962).

(16) T. L. Cottrell, T. E. Graham, and T. J. Reid, *Trans. Faraday Soc.*, **47**, 584 (1951).

(17) A. D. Yoffe and P. Gray, *J. Chem. Soc.*, 1412 (1951).

Methyl nitrite, the second most abundant initial product, is probably formed only to a minor extent by steps which appear to prevail in the photolysis,[4,5] *i.e.*, for example, *via* reaction 17 which ought to be favored

$$CH_3\cdot + NO_2 \longrightarrow CH_3ONO \qquad (17)$$

by solvent cage effects[11] in the liquid phase. The sign and magnitude of the temperature coefficient of the initial 100-eV yield of this product (Table I) indicate that other reactions are of much greater importance at room temperature. The observed depression of the methyl nitrite yield by nitrogen dioxide contradicts the hypothesis that reaction 17 occurs very frequently among homogeneously distributed radicals and suggests that homogeneous $CH_3$ radicals are not important precursors of methyl nitrite. Unimolecular rearrangement of excited nitromethane[18] would appear to be a likely source of methyl nitrite, but this possibility is not clearly relevant to the problem of rationalizing the temperature coefficient. Observation that the presence of nitrosomethane dimer is necessary for appearance of methyl nitrite in the thermal dark reaction suggests

$$CH_3NO + CH_3O\cdot \longrightarrow CH_3ONO + CH_3\cdot \qquad (18)$$

that the monomer, $CH_3NO$, is probably also an important precursor of methyl nitrite in the radiolytic mechanism as, for example, *via* reaction 18 with methoxyl radicals and reactions 20–23 proposed below. Reaction 19 is also a possibility.[5]

$$NO + CH_3O\cdot \longrightarrow CH_3ONO \qquad (19)$$

The 100-eV yield of nitrosomethane dimer exhibits no apparent dose rate dependence and no temperature coefficient, indicating that its immediate precursor, $CH_3NO$, is formed predominantly by fast primary steps, such as dissociative electron capture reaction 11. Consumption of nitrosomethane dimer at room temperature, on the other hand, occurs only as a result of relatively very slow secondary reactions. The observation that the sum $[CH_3ONO] + 2[cis\text{-}(CH_3NO)_2]$ is a linear function of dose (Figure 5) suggests that all of the nitrosomethane consumed by secondary reactions at room temperature is converted to methyl nitrite. Observations of Gowenlock and Trotman[19] lead one to anticipate conversion of a portion of the *cis* dimer to formaldoxime and to the *trans* dimer in the absence of nitrogen oxides at room temperature, as shown in the following diagram[20]

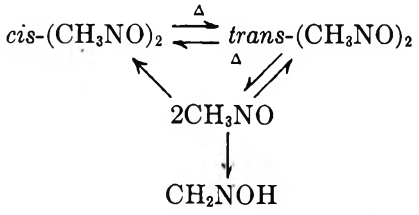


Absence of the *trans* dimer initially as well as after long standing of irradiated samples and the smallness of the formaldoxime yield[4] suggest, therefore, that nitrogen oxides are responsible for consumption of nitrosomethane at room temperature. Batt and Gowenlock[20] have observed that NO promotes disappearance of nitrosomethane in the gaseous phase. Existence of transient species of the form $R(NO)_3$, at or near equilibrium with aliphatic nitroso compounds and NO has been suggested,[21] as, for example

$$CH_3NO + 2NO \rightleftharpoons CH_3(NO)_3 \qquad (20, 21)$$

and Burrell[15] has reported lifetimes for the cyclohexyl analog of $R(NO)_3$ of the order $10^{-1}$ sec in solutions of NO in cyclohexane at room temperature. Energetically feasible alternative reactions of the $CH_3(NO)_3$ intermediate are

$$CH_3(NO)_3 \longrightarrow CH_3ONO + N_2O \qquad (22)$$

$$\longrightarrow CH_3O\cdot + NO + N_2 \qquad (23)$$

$$\longrightarrow CH_3ONO_2 + N_2 \qquad (24)$$

Reaction 23 contributes to formation of methyl nitrite *via* the methoxyl radical and reactions 18 and 19. Reactions 20–22 rationalize the observation that $N_2O$ is formed only at higher doses. The behavior of the yields of $N_2O$, $N_2$, and $CH_3ONO_2$ with respect to dose is also qualitatively consistent with this mechanism. The abundance of these products is, however, insufficient to permit more than about 70% of the observed enhancement in the methyl nitrite yield to occur through reactions 20–24. The behavior of the NO yield is—at least superficially—inconsistent with

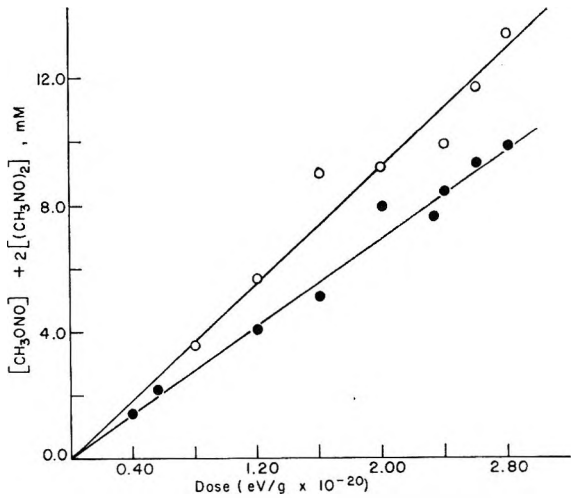


Figure 5. Variation of the sum $[CH_3ONO] + 2[cis\text{-}(CH_3NO)_2]$ with respect to dose at room temperature and 0°.

(18) H. W. Brown and G. C. Pimentel, *J. Chem. Phys.*, 29, 883 (1958).

(19) B. G. Gowenlock and J. Trotman, *J. Chem. Soc.*, 4190 (1955).

(20) L. Batt and B. G. Gowenlock, *Trans. Faraday Soc.*, 56, 682 (1960).

(21) L. G. Donaruma and D. J. Carmody, *J. Org. Chem.*, 22, 635 (1957).

FIRST CLASS
PERMIT No. 1411-R
WASHINGTON, D. C.

BUSINESS REPLY MAIL
No Postage Stamp Necessary if Mailed in the United States

— POSTAGE WILL BE PAID BY —

AMERICAN CHEMICAL SOCIETY
1155 Sixteenth Street, N.W.
Washington, D.C. 20036

ATTN. H. C. SPENCER

the proposed mechanism. Ignorance of the nature and positions of equilibria among the nitrogen oxides and of the fate of $NO_2$ precludes satisfactory rationalization of the dose dependence of $G(NO)$ at room temperature. The observation that the initial presence of $NO_2$ prevents formation of nitrosomethane while accelerating the rates of formation of NO and HCHO is consistent with reaction 13. Provision for partial consumption of $NO_2$, for conversion of nitrosomethane to methyl nitrite without formation of $N_2$ and $N_2O$, and for acceleration of NO formation with increasing dose may be made by suggesting reactions 25–27. The

$$NO_2 + NO \rightleftharpoons N_2O_3 \qquad (25, 26)$$

$$N_2O_3 + CH_3NO \longrightarrow CH_3ONO + 2NO \qquad (27)$$

possibility that the $ONONO_2$ dimer[22] serves as a source of NO molecules in equilibrium with $O_2NNO_2$ is also plausible and may also introduce the strongly oxidizing species, $NO_3$, as a possible precursor of $CO_2$, CO, and $CH_3ONO_2$, for example

$$2NO_2 \rightleftharpoons O_2NNO_2 \rightleftharpoons ONONO_2 \rightleftharpoons NO_3 + NO$$

An alternative source of $NO_3$ suggested by Donaruma and Carmody[21] and by Cundall, *et al.*,[4] is reaction 28. This is, however, much more strongly endothermic

$$CH_3NO + 2NO \longrightarrow CH_3\cdot + N_2 + NO_3 \qquad (28)$$

than are the products of steps 22–24 with respect to the same reactants, if gaseous phase heats of formation are pertinent,[23] and it seems highly unlikely that heats of solvation among the species involved would favor reaction 28 in the liquid phase.

Evidence concerning the fate of $CH_3$ radicals is largely negative. Effects of temperature, the initial presence of $NO_2$, and dose rate indicate that the methyl radical is not an important precursor of either $(CH_3NO)_2$ or $CH_3ONO$. Significant product formation *via* atomic abstraction steps by $CH_3$ radicals is inconsistent with the observed product distribution and effects of temperature. Furthermore, the yield of $C_2H_6$ is small at both high- and low-dose rates and is independent of dose, indicating that combination of $CH_3$ radicals does not occur. It appears that the net radiolytic yield of $CH_3$ radicals is quite small (*ca.* 0.1 radicals/100 eV), possibly because its predominant fate is back-reaction with $NO_2$.

As yet unidentified ionic species, the nitrosomethane monomer, and the $CH_2NO_2$ radical appear to be most significant among plausible primary organic intermediates. Effects of temperature indicate that fast reaction steps form all nitrosomethane monomer near zero dose. Absence of an effect of dose rate on the initial yield of the dimer demonstrates that the dimerization step has no competitor at low concentrations of nitrogen oxides. Since only half of the initial yields of $CH_3ONO$ and HCHO are attributable to fast reactions, it may also be concluded that a significant fraction of fast ionic reactions produces neutral reactive fragments, probably including the $CH_2NO_2$ radical.

Formation of substantial amounts of HCHO in radiolysis and its virtual absence among photolysis products[4–6] may be tentatively attributed to the fact that $CH_2NO_2$ radicals can be formed only by abstraction steps in photolysis at 253.7 nm and longer wavelengths. Similarly, the much larger proportion of nitrosomethane dimer formed in radiolysis may be largely attributed to reactions which are not energetically possible in photolysis, most notably dissociative electron attachment (reaction 11). Finally, the absence of the thermal dark reaction after photolysis must be attributed to the virtual absence of nitrosomethane.

*Acknowledgments.* The authors are grateful to Professor Brian Gowenlock of the University, Nottingham, England, for providing a pure sample of *trans* dimer of nitrosomethane as well as helpful information. This work was partially supported by the U. S. Atomic Energy Commission under provisions of Contract No. AT(11-1)-1116.

(22) W. G. Fateley, H. A. Bent, and B. Crawford, *J. Chem. Phys.*, 31, 204 (1959); H. A. Bent, *Inorg. Chem.*, 2, 747 (1963).

(23) The least endothermic among products of steps 22, 23, 24, and 28 are those of step 24, with steps 22, 23, and 28 following in order of increasing endothermicity. Step 28 may be estimated to be 28 kcal/mol more endothermic than step 23. Estimated standard gaseous phase heats of formation at 25° are taken from tabulations presented in the appendix of J. G. Calvert and J. N. Pitts, Jr., "Photochemistry," John Wiley & Sons, New York, N. Y., 1966.

# The Photochemistry of Cyclopentanone in the Gaseous Phase

by Chup Yew Mok[1]

*Contribution from the Department of Chemistry, University of Texas at Austin, Austin, Texas 78712*
*(Received November 4, 1969)*

The mechanism of the photochemical reactions of cyclopentanone has been investigated by obtaining quantum yields of products (CO, $C_2H_5$, *c*-$C_5H_8$, 4-pentenal) as a function of pressure, of temperature, and to a lesser extent of wavelength. At 3130 Å the pentenal decreases with increase in temperature and increases with increase in pressure, thus showing in agreement with earlier work by others that this product is formed mainly from low vibrational levels of an excited state. The ratio $C_2H_4$/*c*-$C_4H_8$ at 3130 Å is independent of all variables, but there may be a slight increase at low pressures at 2537–2654 Å. This latter point is not very definite. Ratios of rate constants for several steps in the proposed mechanism are given. There is no kinetic proof that the triplet state plays any part in this gas phase photolysis. 1,3-Pentadiene (*trans*) seems to exert no other effect than that of vibrational relaxation, and there seems to be no detectable *cis–trans* isomerization of the pentadiene. By analogy with other similar molecules one might expect those molecules which do not react in the singlet state to cross over to the triplet state. In the present case there is no proof that electronic relaxation to the ground state occurs *via* the triplet rather than directly by internal conversion, but steps must be included in the mechanism for destruction of the singlet state which are first order and do not lead to products.

## Introduction

The photochemistry of cyclopentanone has been the subject of active investigation since 1935,[2-11] and a summary up to 1963 has been given by Srinivasan.[12]

Upon irradiation with ultraviolet light gaseous cyclopentanone decomposes to give ethylene, cyclobutane, and carbon monoxide;[3,4] it also rearranges to form 4-pentenal[5]

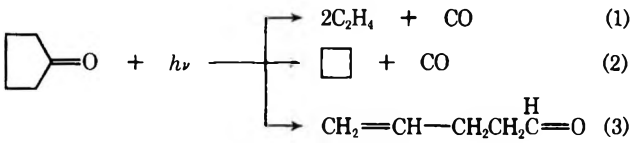


It has been found[6] that at 3130 Å, while the yield of disappearance of the ketone remained roughly constant, process 3 becomes increasingly important at the expense of processes 1 and 2 with decreasing temperature and with increasing pressure, but the ratio of ethylene to cyclobutane shows little change. There may, however, be a slight increase in this ratio at pressures below about 5 Torr. Addition of oxygen up to 275 Torr shows effects comparable to those of other added gases commonly regarded as inert, and there was virtually no exchange with $O^{18}$–$O^{18}$. These results have been interpreted as indicating that all three processes occur from the excited singlet state, with processes 1 and 2 requiring higher vibrational energy than 3.[6]

On the other hand, a detailed analysis[11] of the results of the benzene sensitization of cyclopentanone photolysis indicates that the processes which yield CO may arise from the excited singlet state, but that pentenal may come from the triplet state. This does not prove, of course, that pentenal comes from the triplet state in the ordinary unsensitized photolysis. In the liquid phase photolysis[10] pentenal is the only major product, and its formation is significantly quenched by adding oxygen or pentadiene, an observation which is consistent with a mechanism involving the triplet state.

In agreement with the findings of the liquid phase photolysis, fluorescence as well as phosphorescence of cyclopentanone have been observed in condensed media, but only fluorescence could be detected in the gas phase[13-15] although the yield is very low.

It thus appears that the role of multiplicity in the photochemical processes during direct photolysis is not fully resolved.

In the present work, attempts have been made to establish the mechanism by which the various processes

(1) Correspondence should be sent to the author's present address: Department of Chemistry, Nanyang University, Jurong Road, Singapore 22.

(2) (a) M. Saltmarsh and R. G. W. Norrish, *J. Chem. Soc.*, 445 (1935); (b) C. H. Bamford and R. G. W. Norrish, *ibid.*, 1521 (1938).

(3) S. W. Benson and G. B. Kistiakowsky, *J. Amer. Chem. Soc.*, **64**, 80 (1942).

(4) F. E. Blacet and A. Miller, *ibid.*, **79**, 4327 (1957).

(5) R. Srinivasan, *ibid.*, **81**, 1546 (1959).

(6) R. Srinivasan, *ibid.*, **83**, 4344 (1961).

(7) R. Srinivasan, *ibid.*, **83**, 4348 (1961).

(8) J. N. Butler, A. T. Drake, J. C. Mitchell, and P. Singh, *Can. J. Chem.*, **41**, 2704 (1963).

(9) R. F. Klemm, D. N. Morrison, P. Gilderson, and A. T. Blades, *ibid.*, **43**, 1934 (1965).

(10) P. Dunion and C. N. Trumbore, *J. Amer. Chem. Soc.*, **87**, 4211 (1965).

(11) E. K. C. Lee, *J. Phys. Chem.*, **71**, 2804 (1967).

(12) R. Srinivasan, *Advan. Photochem.*, **1**, 83, 1963.

(13) S. R. LaPaglia and B. C. Roquitte, *J. Phys. Chem.*, **66**, 1739 (1962).

(14) S. R. LaPaglia and B. C. Roquitte, *Can. J. Chem.*, **41**, 287 (1963).

(15) E. K. C. Lee, private communication.

of excited cyclopentanone take place through the determination of quantum yields, and the study of effects of pressure, added gases, temperature, and wavelength of exciting light.

## Experimental Section

*Material.* Cyclopentanone was obtained from Matheson Coleman and Bell. It was purified with preparative gas chromatography. The final product was better than 99% pure, but contained an impurity which had a retention time slightly shorter than that of cyclohexanone with a capillary MBMA (mixture of *m*-bis-*m*-phenoxyphenoxybenzene and apiezon L) column. The compound was degassed by several freeze–pump–thaw cycles before being admitted to the photolysis cell.

*trans*-Pentadiene (Aldrich Chemical Co., Inc.) originally contained a trace of the *cis* isomer but after purification with preparative gc no *cis* isomer could be detected with a Perkin-Elmer F11 chromatograph. The *trans*-diene was degassed before use.

Spectrograde acetone (Eastman Kodak) was used without further purification but was degassed before use.

The monatomic gases listed below were used without further treatment, except for degassing in the case of xenon: argon (Matheson, 99.98%); helium (Matheson 99.995%) krypton and xenon (Matheson research grade, 99.995%).

*Apparatus.* A grease-free, mercury-free Pyrex glass vacuum line equipped with Hoke 413 and 413-A metal valves in the manifold and large Veeco valves in the main line was employed. Two Wallace and Tiernan metal gauges were used for pressure reading: Model FA-160150 for the pressure range 0.1–20 Torr, and Model FA-160240 for 0 to 800 Torr. A cold cathode gauge in the main line provided assurance that the system pressure did not exceed $10^{-4}$ Torr for all runs.

The photolysis cell was made of quartz and was cylindrical, 10 cm long with end windows of 45 mm i.d. Dead space was about 30% of the total volume up to the metal valve. The cell and the dead space were encased in an oven made of asbestos boards with heating tapes attached to the rear wall. The oven had two circular quartz windows for passage of the light beam. Fluctuations of temperature in the vicinity of the cell were usually less than 1°.

The light source was a Hanovia S-100 mercury lamp. A filter combination of 5 cm of $CoSO_4$–$NiSO_4$ mixed solution and 1 cm of potassium biphthalate solution was used to isolate light essentially of 3130 Å. Another filter system of 5 cm of the $CoSO_4$–$NiSO_4$ solution, 1 cm of $KI_3$ solution, and 5 cm of chlorine gas at atmospheric pressure provided a means for isolating the 2537-Å line,[16,17] but some 2654-Å light is also included. Usually the solutions were renewed after a run. The light was collimated with a quartz lens to form a beam which filled the cell. Light intensity was monitored with an RCA 935 phototube connected to a Keithley 410 micromicroammeter. Before reaching the active surface of the phototube, the beam passed through a glass filter (Corning 9863) and then through a sodium salicylate plate, which fluoresced with intensity proportional to that of the beam.[18,19]

*Actinometry.* Acetone at 130° and 45 Torr was used as a chemical actinometer for photolysis at 3130 Å.[16] Under such conditions the quantum yield of carbon monoxide is unity. Condensables were trapped with liquid nitrogen, and CO was collected for analysis by mass spectrometry.

*Mixing and Photolysis Procedure.* Generally cyclopentanone was trapped in the cold finger; added gas was then either expanded to the cell or subsequently trapped in the cold finger. Thus mixing with less than 100 Torr Ar or He involved trapping cyclopentanone at liquid nitrogen temperature and expanding the inert gas to the cell. For higher pressures of Ar or of Kr, the ketone was trapped with a Dry Ice–acetone mixture. Xenon and pentadiene, as added gases, were condensed with the ketone at liquid nitrogen temperature. The components were then allowed to mix in the gas phase for several hours if the partial pressure of one gas was not more than ten times that of the other, otherwise mixing time was extended to about 10 hr (overnight).

Photolysis at 3130 Å usually lasted for 60 to 90 min and was carried out to 2–3% conversion.

*Sampling and Analysis.* Carbon monoxide was separated as a gas from other compounds at −196°. It was analyzed with a CEC mass spectrometer, Model 21-110, by using known amounts of Ar as a reference. For most runs CO was not analyzed and was pumped off.

Ethylene and cyclobutane were isolated from 4-pentenal and the ketone by trapping the latter two compounds at the temperature of Dry Ice. Small amounts of isobutane at about 0.5 Torr were introduced to serve as a carrier, and the gas mixture was condensed at −196° in a capillary tube which was inserted into a gas chromatograph (Aerograph Model 600-C) with a solid injector. A column of dimethylsulfolane on fire brick, 6.1 mm long and 2.5 mm i.d., gave good separation. The isobutane besides being a carrier was also a reference.

4-Pentenal was analyzed with a Perkin-Elmer F11 gas

(16) J. G. Calvert and J. N. Pitts, Jr., "Photochemistry," John Wiley & Sons, New York, N. Y., 1966.

(17) M. Kasha, *J. Amer. Opt. Soc.*, **38**, 929 (1948).

(18) R. Allison, J. Burns, and A. J. Tuzzolino, *ibid.*, **54**, 747 (1964).

(19) The plate was prepared by spraying a solution of sodium salicylate in methanol on a Corning 7740 glass filter, until a uniform layer of about 2 mg/sq cm had deposited. See also the Ph.D. Thesis of F. S. Wettack, The University of Texas at Austin, 1968.

chromatograph. An MBMA capillary column, 17 m in length and 0.5 mm i.d., was employed.

## Results

Since no evidence was found for polymer formation and no products other than those appearing in eq 1–3 could be detected, the yield (in micromoles) of carbon monoxide should be equal to 0.5 the yield of ethylene plus the yield of cyclobutane. This relationship was found to be true, within experimental error, for a few runs for which the amounts of all the three products were determined. For most runs the amount of CO was calculated.

Table I shows the results for experiments where only cyclopentanone was present initially. The data indicate that the ratio pentenal/CO increases as the temperature is lowered, or as the pressure is increased, in accord with previous results.[6,7] This ratio varies linearly with cyclopentanone pressure within experimental error and in the absence of foreign gas. Furthermore, $1/\Phi_{CO}$ *vs.* pressure of cyclopentanone is linear within experimental error. On the other hand, Figure 1 shows that $1/\Phi$ (pentenal) *vs.* $1/P$ cyclopentanone shows a curvature but may become linear at high pressure.

**Table I:** Variation of Product Quantum Yields with Pressure and Temperature; λ 3130 Å

| Pressure of cyclopentanone, Torr | $\Phi_{pentenal}$ | $\Phi_{CO}$[a] | $C_2H_4/\square$ | Pentenal/CO |
|---|---|---|---|---|
| | | Temp = 26° | | |
| 2.46 | 0.22 | 0.23 | 3.40 | 0.98 |
| 4.44 | 0.21 | 0.19 | 3.26 | 1.13 |
| 6.39 | 0.24 | 0.18 | 2.96 | 1.28 |
| 7.77 | 0.26 | 0.17 | 3.07 | 1.50 |
| 9.31 | 0.27 | 0.16 | 2.86 | 1.68 |
| | | Temp = 65° | | |
| 2.10 | 0.17 | 0.37 | 3.07 | 0.46 |
| 2.23 | 0.16 | 0.39 | 3.28 | 0.42 |
| 2.66 | 0.20 | 0.38 | 3.11 | 0.52 |
| 3.99 | 0.18 | 0.35 | 2.83 | 0.52 |
| 5.18 | 0.19 | 0.32 | 2.87 | 0.58 |
| 5.19 | 0.20 | 0.34 | 2.98 | 0.57 |
| 7.14 | 0.21 | 0.29 | 2.74 | 0.73 |
| 7.21 | 0.20 | 0.27 | 3.01 | 0.73 |
| 9.72 | 0.21 | 0.24 | 3.23 | 0.85 |
| 10.28 | 0.22 | 0.27 | 2.91 | 0.81 |
| 11.05 | 0.18 | 0.25 | 3.13 | 0.70 |
| 14.7 | 0.24 | 0.24 | 3.2 | 1.03 |
| 27.3 | 0.26 | 0.17 | 2.90 | 1.52 |
| 37.4 | 0.34 | 0.15 | 3.10 | 2.28 |
| 38.4 | 0.31 | 0.16 | 2.79 | 2.01 |
| 53.1 | 0.36 | 0.11 | 3.08 | 3.15 |
| 69.0 | 0.35 | 0.086 | 3.63 | 4.06 |
| | | Temp = 106° | | |
| 3.34 | 0.18 | 0.52 | 2.86 | 0.34 |
| 8.88 | 0.18 | 0.47 | 2.80 | 0.38 |
| 14.52 | 0.22 | 0.41 | 3.03 | 0.54 |
| 27.0 | 0.24 | 0.37 | 3.08 | 0.64 |

[a] The yield of CO was calculated from those of $C_2H_4$ and c-$C_4H_8$, *i.e.*, $\Phi_{CO} = {}^1/_2\Phi_{C_2H_4} + \Phi_{c\text{-}C_4H_8}$.

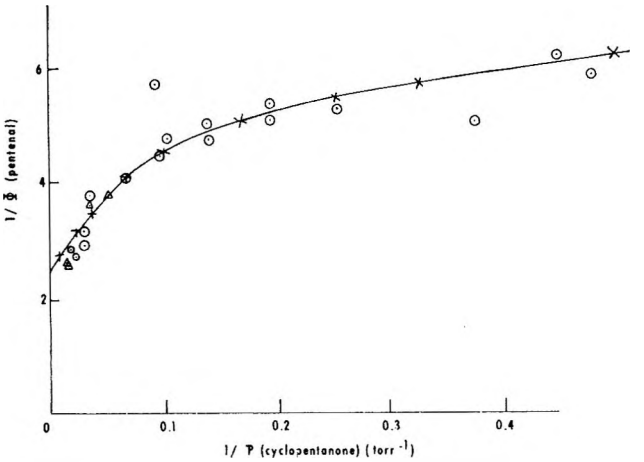


Figure 1. Plot of $1/\Phi$ (pentenal) *vs.* $1/P$ (cyclopentanone) at 25°. ⊙, Cyclopentanone only; △, added gas: 1,3-pentadiene; ×, points calculated by eq 6.

The ratio of ethylene to cyclobutane is virtually invariant to changes in temperature and pressure except possibly at low pressures. The mean value is 3.05. The average deviation from the mean is 0.16, which is about 5%, and is about the magnitude of experimental error.

A check on the possibility of a dark reaction at 65° was made by heating 10.87 Torr of cyclopentanone at that temperature in the cell for a period of 208 min. No products were found.

Results of the added gas study are shown in Table II. The presence of relatively large amounts of foreign gas generated some difficulties in product sampling.[20] For this reason the data are more incomplete and less precise than those given in Table I. Nevertheless they indicate that the effects of pressure on product distribution and quantum yields are of the same nature as those manifested in Table I. This is further illustrated in Figures 2, 3, and 4.

The presence of *trans*-1,3-pentadiene during photolysis did not lead to the formation of any detectable amount of *cis* isomer, even though one part of *cis* in a thousand parts of the *trans* could have been readily determined. A run was made in which a mixture of 46.1 Torr of the ketone and 6.20 Torr of *trans*-diene was photolyzed at 3130 Å and 65° for 65 min. No *cis* isomer was formed.

Three runs were made for light which contained almost exclusively the two lines at 2537 and at 2654 Å.

(20) For instance if He, Ar, and Kr were removed by pumping at liquid nitrogen temperature after photolysis, significant amounts of $C_2H_4$ and c-$C_4H_8$ might be stripped off.

**Table II:** Effects of Added Gases

| Pressure of cyclopentanone, Torr | Pressure of added gas, Torr | $\Phi_{pentenal}$ | $\Phi_{CO}$ | $C_2H_4/c\text{-}C_4H_8$ | Pentenal/CO |
|---|---|---|---|---|---|
| | | λ 3130 Å, temp = 65° | | | |
| 10.64 | 106 (He) | 0.25 | 0.18 | 3.11 | 1.38 |
| 10.55 | 209 (He) | 0.28 | 0.15 | 3.72 | 1.94 |
| 10.34 | 57 (Ar) | 0.25 | 0.19 | 2.56 | 1.33 |
| 10.67 | 107 (Ar) | 0.24 | 0.15 | 2.75 | 1.62 |
| 10.55 | 225 (Ar) | 0.32 | 0.13 | 3.52 | 2.53 |
| 10.60 | 372 (Ar) | 0.41 | 0.11 | 3.12 | 3.64 |
| 10.57 | 478 (Ar) | 0.41 | 0.081 | 3.00 | 5.07 |
| 10.55 | 110 (Kr) | 0.23 | 0.17 | 2.91 | 1.36 |
| 10.43 | 233 (Kr) | 0.33 | | | |
| 10.55 | 113 (Xe) | 0.26 | 0.15 | | 1.73 |
| 10.60 | 454 (Xe) | 0.36 | | | |
| 10.50 | 454 (Xe) | 0.41 | | | |
| 10.70 | 11.9 (*trans*-pentadiene) | 0.26 | 0.21 | 3.00 | 1.23 |
| 10.70 | 25.7 (*trans*-pentadiene) | 0.28 | 0.17 | 2.83 | 1.65 |
| 10.75 | 41.2 (*trans*-pentadiene) | | 0.13 | | |
| 10.55 | 83 (*trans*-pentadiene) | 0.37 | | | |

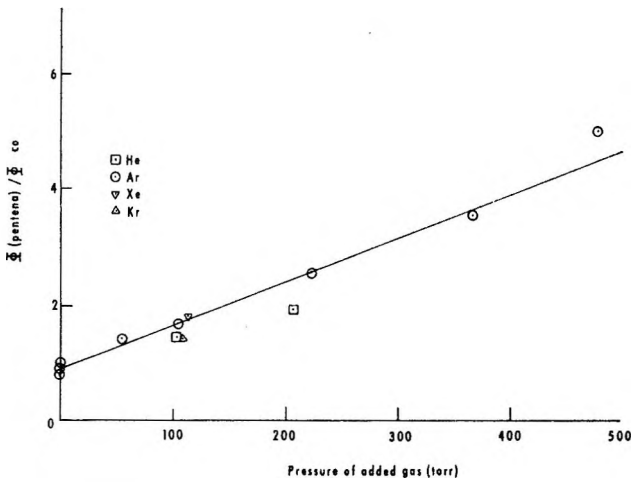


Figure 2. Ratio of pentenal to carbon monoxide yields as a function of pressure at 25° during photolysis of cyclopentanone.

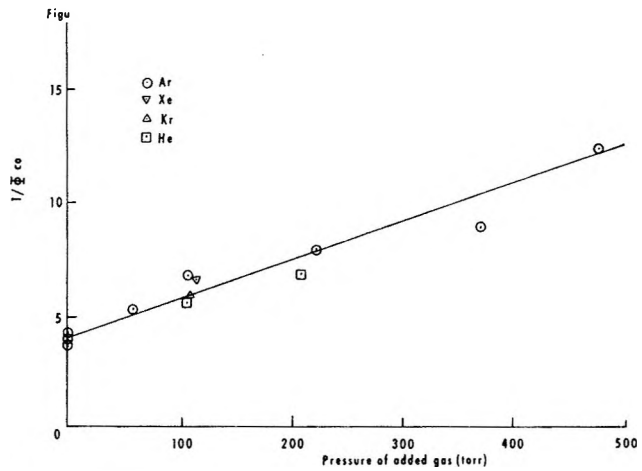


Figure 3. Reciprocal of carbon monoxide yield *vs.* pressure of added gas at 25° during photolysis of cyclopentanone.

**Table III:** Photolysis of Cyclopentanone at 2537–2654 Å, 26°

| Pressure of cyclopentanone, Torr | 2.33 | 5.37 | 9.17 |
|---|---|---|---|
| Time, min | 1225 | 1272 | 1257 |
| Relative incident light intensity | 3.09 | 3.15 | 3.02 |
| 4-Pentenal, mol | 0.072 | 0.17 | |
| $C_2H_4$, mol | 0.442 | 0.836 | 1.43 |
| $c\text{-}C_4H_8$, mol | 0.118 | 0.251 | 0.492 |
| $C_2H_4/c\text{-}C_4H_8$ | 3.75 | 3.33 | 2.91 |
| Pentenal/CO[a] | 0.21 | 0.26 | |

[a] The yield of CO was calculated from the amounts of $C_2H_4$ and $c\text{-}C_4H_8$.

A medium pressure mercury arc and filters were used. The results are shown in Table III.

## Discussion

It has been established that triplet–triplet energy transfer to olefin molecules may lead to *cis–trans* isomerization of the latter.[21–23] The energy transfer process is a very efficient one provided it is exothermic.[22] Thus conjugated dienes such as 1,3-pentadiene may be useful for mechanistic diagnosis in view of the fact that they have relatively low-lying triplets and are capable of geometrical isomerization. The lowest triplet state of cyclopentanone is situated at least a few kcal/mol above that of pentadiene,[13,14,22] and yet the

(21) G. S. Hammond, P. A. Leermakers, and N. J. Turro, *J. Amer. Chem. Soc.*, **83**, 2396 (1961).

(22) G. S. Hammond, N. J. Turro, and P. A. Leermakers, *J. Phys. Chem.*, **66**, 1144 (1962).

(23) R. B. Cundall, F. J. Fletcher, and D. G. Milne, *J. Chem. Phys.*, **39**, 3536 (1963).

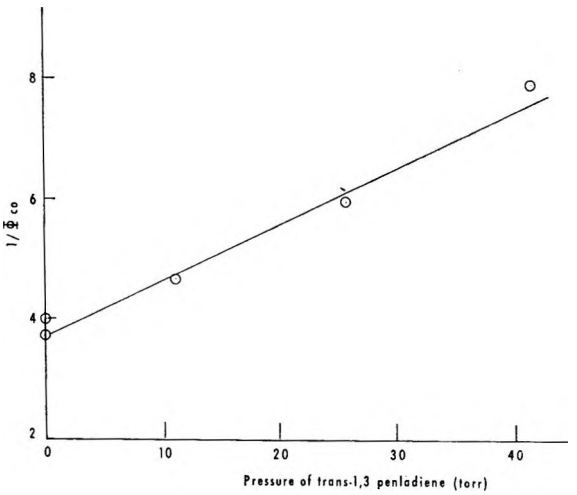


Figure 4. Reciprocal of carbon monoxide yield *vs.* pressure of *trans*-1,3-pentadiene (Torr) at 25° during photolysis of cyclopentanone.

first excited singlet state of the ketone is roughly 44 kcal/mol lower than that of the diene.[14,22] This makes the triplet energy transfer from the ketone to the diene favorable. The absence of *cis* isomer when photolysis of gaseous cyclopentanone was carried out in the presence of *trans*-1,3-pentadiene indicates that intersystem crossing to the triplet is not important.

It has been shown by Rebbert and Ausloos[24] that 1,3-pentadiene is inefficient in quenching the triplet state of acetone, and the same could well be true for other simple ketones such as cyclopentanone. However, 1,3-pentadiene is effective in producing vibrational relaxation and in some instances in quenching singlet states even though direct electronic energy transfer by a simple collision of the second kind is impossible. Thus the use of 1,3-pentadiene to identify effects due to triplet states must always be studied very carefully. In the present instance since isomerization of the pentadiene does not occur the results may not be used either to prove or to disprove the role of the triplet state during photolysis of cyclopentanone.

If the intersystem crossing in cyclopentanone is collisionally induced, then it may be dependent on the mass of the colliding partner, due to the heavy atom effect on spin–orbital coupling.[25,26] Hence if any of the photodecomposition or photoisomerization processes occurred from the triplet state, introducing a heavy colliding partner might enhance that process. The data in Table II show that addition of the monatomic gases He, Ar, Kr, and Xe, with significant variance in mass, leads to little difference, if any, in the effects of added gas on product distribution.

Since noble gases even though inefficient cause some vibrational relaxation, the change in the ratio of pentenal to carbon monoxide could be due entirely to this factor, and xenon is no more effective than the others.

The present results therefore support the original assertion[6] that in direct photolysis, all three processes take place from the singlet state, and that decarbonylation processes occur from upper vibrational levels as the data in the tables imply. However, although the ratio pentenal/CO increases linearly with pressure, there is no such relationship between $1/\Phi$ (pentenal) and $1/P$, as shown in Figure 1, the appearance of which can be anticipated if not all of the pentenal is formed from the thermally equilibrated vibrational levels of the excited singlet state.

The ratio $C_2H_4/c\text{-}C_4H_8$ is virtually constant regardless of variations in pressure and temperature. The value of 3.05 is in good agreement with the values of 3.26 and about 3.10 obtained by Benson and Kistiakowsky,[3] and Lee,[11] respectively, but is lower than that obtained by Klemm, Gilderson, Morrison, and Blades.[9] The latter have observed a falloff in the ratio $c\text{-}C_4H_8/C_2H_4$ at 100° at pressures below about 4 Torr. The data in Table III show a trend in qualitative agreement with this observation. Thus the possibility of some dissociation of a vibrationally "hot" cyclobutane may not be excluded.

At pressures above a few Torr, ethylene and cyclobutane seem to arise[5] from two concurrent processes. The present data, as well as previous ones,[6,9] indicate that both processes take place from upper vibrational levels of an excited (almost certainly singlet) state and that the ratio of their rate constants is independent of changes in pressure above pressures of 5 Torr, of temperature, and of exciting wavelength. A complete theory of this dissociation may not at present be given.

The results can therefore be explained in terms of the following simplified scheme

$$\text{cp} \xrightarrow{h\nu} {}^1\text{cp}^* \qquad \text{(a)}$$

$${}^1\text{cp}^* \xrightarrow{k_b} \begin{cases} \xrightarrow{k_{b1}} 2C_2H_4 + CO & (b_1) \\ \xrightarrow{k_{b2}} c\text{-}C_4H_8 + CO & (b_2) \end{cases}$$

$${}^1\text{*cp} \xrightarrow{k_c} \text{4-pentenal} \qquad \text{(c)}$$

$$\xrightarrow{k_d} \text{cp} \qquad \text{(d)}$$

$${}^1\text{cp} + \text{M} \xrightarrow{k_e} {}^1\text{cp} + \text{M} \qquad \text{(e)}$$

$${}^1\text{cp} \xrightarrow{k_f} \text{4-pentenal} \qquad \text{(f)}$$

$$\xrightarrow{k_g} \text{cp} \qquad \text{(g)}$$

where cp denotes ground-state cyclopentanone, ${}^1\text{cp}^*$ and ${}^1\text{cp}$ denote the excited singlet ketone with and without excess vibrational energy, respectively, beyond that at thermal equilibrium. M is a colliding molecule,

(24) R. E. Rebbert and P. Ausloos, *J. Amer. Chem. Soc.*, **87**, 5569 (1965).

(25) M. Kasha, *J. Chem. Phys.*, **20**, 71 (1952).

(26) M. Kasha and S. P. McGlynn, *Ann. Rev. Phys. Chem.*, **7**, 403 (1956).

**Table IV:** Ratios of Rate Constants

| Temp, °C | $k_c/k_b$ | $k_d/k_b$ | $k_f/(k_f + k_g)$ | $k_e/k_b$, Torr$^{-1}$ | Pentadiene, $k_e/k_b$, Torr$^{-1}$ | Ar, $k_e/k_b$, Torr$^{-1}$ |
|---|---|---|---|---|---|---|
| 26 | 0.66 | 2.0 | 0.39 | 0.28 | | |
| 65 | 0.36 | 1.2 | 0.38 | 0.12 | 0.10 | 0.017 |
| 106 | 0.28 | 0.5 | 0.43 | 0.035 | | |

either cyclopentanone or added gas. $k_b = k_{b_1} + k_{b_2}$ and $k_{b_1}/k_{b_2} = 3.05/2$.

At 3130 Å the ratio $C_2H_4/c\text{-}C_4H_8$ is essentially independent of temperature and of pressure. This must mean that small changes in vibrational level are unimportant. There may be a slight increase in this ratio at 2537 Å at low pressures, and thus one must reserve judgment as to the role which may be played by large amounts of vibrational energy.

Steps d and g are unimolecular processes which can be either fluorescence or internal conversion, possibly a combination of both. Data for most molecules of this type indicate that internal conversion from a first excited singlet state into the ground singlet state does not occur, but in the present instance it is impossible on kinetic evidence to draw such a positive conclusion. One may only say that (d) and (g) do not give recognizable products. In the case of cyclobutanone the preferred mechanism does not need to include internal conversion.[27]

Fluorescence of cyclopentanone has been studied in the gas phase,[14,15] but the yield is very low. An attempt was made in this work to observe fluorescence but without success. The lower limit of sensitivity would be a yield of about 0.01.

The following equations can be derived

$$1/\Phi_{CO} = 1 + \frac{k_c + k_d}{k_b} + \frac{k_e(cp)}{k_b} + \frac{k_e^A(A)}{k_b} \quad (4)$$

and

$$\frac{\Phi_{pentenal}}{\Phi_{CO}} = \frac{k_c}{k_b} + \frac{k_f}{k_b(k_f + k_g)}(k_e(cp) + k_e^A(A)) \quad (5)$$

where A represents an added gas.

Ratios of rate constants can be calculated from slopes and intercepts of plots of $1/\Phi_{CO}$ and of (pentenal)/(CO) *vs.* $P$, respectively. The results are in Table IV.

As can be anticipated, $k_c \lesssim k_e^{diene} > k_e^{Ar}$, since in general the efficiency to remove vibrational energy increases with complexity of colliding molecules. The fact that the ratio $k_f/(k_f + k_g)$ is independent of temperature is to be expected if both processes f and g require very small or similar energies of activation. The ratios $k_c/k_b$, $k_d/k_b$, and $k_e/k_b$ all decrease with increasing temperature, indicating that the dissociative processes require higher energies of activation than the other processes. The data are not precise enough to warrant a detailed discussion in terms of activation parameters.

From the ratios given in Table IV, the quantum yield of 4-pentenal can be calculated at different pressures. Since

$$\Phi_{pentenal} = \left[k_c + \frac{k_f k_e(M)}{k_f + k_g}\right] \frac{1}{k_b + k_c + k_d + k_e(M)} \quad (6)$$

The calculation was performed by using the ratios at 65°, for the case where no added gas is present. The calculated values agree well with those obtained experimentally, as shown in Figure 1, in which the line was drawn according to the calculated values. This is not in reality an independent check of the data.

The results of the present work are thus consistent with a mechanism by which all three chemical processes take place from the excited singlet state. This of course does not mean that these processes cannot occur from the triplet state.

Although some previous results seem to indicate that exothermic triplet energy transfer occurs on every collision between a triplet molecule and a molecule such as pentadiene,[22] more recent work indicates that this may not be true.[24] In the liquid phase it has been shown that the formation of 4-pentenal takes place from the triplet state,[10,28] with a rate constant of $1.1 \times 10^8$ sec$^{-1}$. It can be anticipated that in the gas phase the rate constant probably is of the same order of magnitude, yet no quenching was observed. The benzene-sensitized photolysis[11] of cyclopentanone showed that only 40% of the triplet state cyclopentanone molecules undergo rearrangement to pentenal. The remainder probably return to the ground state through intersystem crossing, since no phosphorescence has been observed in the gas phase. If rearrangement is so fast as to avoid quenching, so must be intersystem crossing. The present data indicate that the excited singlet lives long enough to experience collisional relaxation of vibrational energy, implying that intersystem crossing from excited singlet to triplet if it occurs should not be too much faster than the collision frequency.

While benzene triplet energy transfer to cyclopentanone gave rise to formation of the aldehyde,[11] triplet mercury-sensitized photolysis of 2-methylcyclohexa-

(27) T. H. McGee, *J. Phys. Chem.*, **72**, 1621 (1968).

(28) P. J. Wagner and R. W. Spoerkes, *J. Amer. Chem. Soc.*, **91**, 4437 (1969).

none[29] and 2-ethylcyclopentanone[30] produces largely decarbonylated products. It has been pointed out[11,30] that this difference in behavior may be connected with the fact that triplet mercury possesses about 1 eV of transferable energy more than triplet benzene and that the factor that determines the mode of reaction therefore appears to be the "energy content,"[20,6] rather than the "multiplicity" of the species. The results of the present work are in line with this view.

It is impossible to state with certainty whether or not triplet state molecules play an important role in the direct, unsensitized photolysis of cyclopentanone but if they do their mean lifetimes must be very short.

*Acknowledgment.* The author wishes to express his appreciation to Dr. A. T. Blades of the Research Council of Alberta, Edmonton, Alberta, and to Dr. E. K. C. Lee of the University of California at Irvine for helpful discussions and suggestions. The guidance offered by Professor W. A. Noyes, Jr., and financial support for this work provided by The Robert A. Welch Foundation are gratefully acknowledged.

(29) C. C. Badcock, M. J. Perona, G. O. Pritchard, and B. Rickbron, *J. Amer. Chem. Soc.*, 91, 543 (1969).

(30) R. Srinivasan and K. A. Hill, *ibid.*, 87, 4988 (1965).

# Interaction of the Benzene Molecule with Liquid Solvents. Fluorescence Quenching Parallels (0–0) Ultraviolet Absorption Intensity

**by J. W. Eastman and S. J. Rehfeld**

*Shell Development Company, Emeryville, California 94608* *(Received April 21, 1969)*

The fluorescence yield and uv absorption of benzene have been measured in 40 polar and nonpolar liquids. At 25° the total rate of all nonradiative transitions from the fluorescent state of benzene is found to increase systematically with increasing intensity in the solvent-induced (0–0) component of the 2600-Å absorption band.

## Introduction

When benzene is dissolved in liquids the fluorescence is thermally quenched with an activation energy of about 2000 $cm^{-1}$.[1] Also at a given temperature the yield depends on the solvent, and the Debye reorientation rate of the solvent is not the determining factor.[1] In attempting to find out why the yield depends on the particular liquid used as solvent, we have measured the uv absorption and fluorescence yield of benzene dissolved in 40 different liquids, both polar and nonpolar.

## Experimental Section

The benzene used in this experiment was a zone-refined product (purity greater than 99.9%) obtained from James Hinton (358 Chicago Ave., Valparaiso, Fla. 32580). The solvents used were all of research grade, purity of 99.5+ mol %, and of Spectrograde. All solutions were prepared under nitrogen. References to the experimental methods are given in Table I.

## Results

*Integrated Uv Absorption Intensity.* Absorptivities, $\epsilon_{max}$, at the uv absorption maximum, $\lambda_{max}$, and oscillator strengths for the 2600-Å transition of benzene dissolved in various solvents are given in Table I. Oscillator strengths, $f$, are calculated as

$$f = 4.32 \times 10^{9} \int \epsilon d\nu$$

where $\epsilon$ is the molar absorptivity in $(M\ cm)^{-1}$ and the frequency $\nu$ is in reciprocal centimeters. The absorptivities reported here are an average of 20% above those of Bayliss and Hulme,[2] but this may be caused by our using narrower slit widths, since the integrated intensities of the present work agree with theirs.

Except when benzene is dissolved in carbon tetrachloride (ref 2) and chloroform (this work and ref 2), the oscillator strength of the 2600-Å band is independent of solvent (precision ±5%, absolute magnitude ±10% in this work). The present measurements coincide with those of Bayliss and Hulme.[2]

The oscillator strengths, as well as the peak absorptivities, of benzene in carbon tetrachloride and chloroform are anomalously high. The peaks are especially

(1) J. W. Eastman, *J. Chem. Phys.*, 49, 4617 (1968).

(2) N. S. Bayliss and L. Hulme, *Aust. J. Chem.*, 6, 257 (1953).

**Table I:** Some Uv Spectroscopic Properties of Benzene as a Function of Solvent

| No.[a] | Solvent | Refractive index, $n$[b] | Symbol[c] | Wavelength, $\lambda_{max}$ Å ±1 | $10^{-3}\times$ frequency ($10^{-3}\times$ [$\nu_{00}$ + 522]), cm$^{-1}$ | Absorptivity,[d] $\epsilon_{max}$, ($M$ cm)$^{-1}$ ±4 | Line width, $\Delta\nu$ (9/10), cm$^{-1}$ | Oscillator strength,[d] $10^3\times f$ | $\epsilon_s/\epsilon_v$ | Fluorescence yield, $\Phi$,[e] at 25° | $10^{14}$ $\langle\nu^{-3}\rangle$ | $\int(\epsilon/\nu)d\nu$ | $10^{-8}\Sigma_i k_i$,[f] sec$^{-1}$ |
|---|---|---|---|---|---|---|---|---|---|---|---|---|---|
| 1a | Vapor | 1.000 | ● | 2529 | 38.61 | ... | 0 | 2.0[g] | 0 | 0.18[i] | $h$ | ... | 0.114[j] |
| 13b | Perfluoro-$n$-hexane | 1.2514 | | 2530 | 38.61 | 325 | 27 | ... | 0.049 | ... | ... | ... | ... |
| 27c | Methanol | 1.331 | ⊗ | 2543 | 38.42 | 268 | 70 | 1.85 | 0.095 | 0.027 | 2.33 | 10.7 | 0.90 |
| 40d | $D_2O$ | 1.338 | ⊗ | 2537 | 38.51 | 179 | 114 | 1.90 | 0.257 | 0.0052 | $h$ | 10.8 | 5.0 |
| 39e | Water | 1.333 | ⊗ | 2539 | 38.49 | 188 | 120 | 1.89 | 0.224 | 0.0058 | 2.31 | 10.8 | 4.3 |
| 36f | Acetonitrile | 1.346 | ◇ | 2543 | 38.43 | 227 | 89 | 1.77 | 0.166 | 0.029 | 2.35 | 10.2 | 0.84 |
| 2g | 2-Methylbutane | 1.351 | ○ | 2542 | 38.42 | 267 | 76 | 1.83 | 0.029 | 0.044 | $h$ | 10.5 | 0.54 |
| 23h | Diethyl ether | 1.350 | △ | 2543 | 38.42 | 262 | 80 | 1.87 | 0.088 | 0.047 | $h$ | 10.8 | 0.51 |
| 4i | $n$-Pentane | 1.357 (15°) | ○ | 2542 | 38.43 | 258 | 79 | 1.78 | 0.050 | 0.054 | $h$ | 10.3 | 0.44 |
| 14j | Tetramethylsilane | 1.359 (19°) | ● | 2543 | 38.40 | 267 | 73 | 1.88 | 0.058 | 0.054 | $h$ | 10.8 | 0.44 |
| 22k | Ethanol | 1.359 | ⊗ | 2544 | 38.40 | 265 | 77 | 1.83 | 0.091 | 0.033 | 2.36 | 10.6 | 0.73 |
| 5l | $n$-Hexane | 1.375 | ○ | 2543 | 38.40 | 259 | 73 | 1.74 | 0.049 | 0.058 | 2.36 | 10.0 | 0.41 |
| 20m | 2-Propanol | 1.375 | ⊗ | 2543 | 38.42 | 263 | 82 | 1.80 | 0.087 | 0.037 | $h$ | 10.4 | 0.65 |
| 21n | 1-Propanol | 1.384 | | 2545 | 38.39 | 245 | 87 | 1.70 | 0.097 | ... | ... | ... | ... |
| 16o | 2-Methyl-2-propanol | 1.384 | ⊗ | 2544 | 38.40 | 262 | 84 | 1.77 | 0.082 | 0.031 | $h$ | 10.2 | 0.78 |
| 35p | Dimethyl sulfate | 1.387 | | 2540 | 38.45 | 221 | 89 | 1.79 | 0.176 | ... | ... | ... | ... |
| 3q | 2,2,4-Trimethylpentane | 1.392 | ○ | 2543 | 38.42 | 251 | 89 | 1.69 | 0.059 | 0.057 | $h$ | 9.8 | 0.41 |
| 18r | 2-Methyl-1-propanol | 1.398 | ⊗ | 2544 | 38.39 | 258 | 88 | 1.81 | 0.084 | 0.042 | $h$ | 10.5 | 0.57 |
| 6s | $n$-Octane | 1.398 | ○ | 2544 | 38.40 | 248 | 89 | 1.78 | 0.058 | 0.057 | $h$ | 10.3 | 0.41 |
| 10t | Cyclopentane | 1.404 | ○ | 2544 | 38.40 | 261 | 80 | 1.75 | 0.052 | 0.056 | $h$ | 10.1 | 0.42 |
| 19u | 1-Butanol | 1.399 | ⊗ | 2545 | 38.37 | 256 | 93 | 1.89 | 0.081 | 0.045 | $h$ | 10.8 | 0.53 |
| 7v | $n$-Nonane | 1.405 | ○ | 2546 | 38.37 | 232 | 95 | 1.72 | 0.031 | 0.059 | $h$ | 9.9 | 0.40 |
| 15w | 3-Methyl-1-butanol | 1.408 | ⊗ | 2446 | 38.37 | 238 | 81 | 1.97 | 0.071 | 0.045 | $h$ | 11.4 | 0.53 |
| 8x | Methylcyclohexane | 1.424 | ○ | 2544 | 38.39 | 258 | 95 | 1.82 | 0.032 | 0.046 | $h$ | 10.5 | 0.52 |
| 11y | Cyclohexane | 1.424 | ○ | 2545 | 38.39 | 261 | 102 | 1.84 | 0.035 | 0.061 | 2.37 | 10.6 | 0.38 |
| 33z | 2-Methoxyethanol | 1.402 | | 2546 | 38.36 | 232 | 111 | 1.86 | 0.131 | ... | ... | ... | ... |
| 31$\alpha$ | 2-Ethoxyethanol | 1.408 | | 2546 | 38.37 | 240 | 108 | 1.96 | 0.117 | ... | ... | ... | ... |
| 32$\beta$ | 1,4-Dioxane | 1.423 | △ | 2544 | 38.39 | 241 | 119 | 1.96 | 0.131 | 0.044 | 2.37 | 11.3 | 0.54 |
| 28$\gamma$ | 2-(2-Ethoxyethoxy)-ethanol | | | 2546 | 38.36 | 233 | 116 | 1.94 | 0.121 | ... | ... | ... | ... |
| 17$\delta$ | 1-Octanol | 1.429 | | 2546 | 38.36 | 260 | 120 | 1.78 | 0.052 | ... | ... | ... | ... |
| 25$\epsilon$ | 1,2-Propanediol | 1.433 | ⊗ | 2547 | 38.34 | 206 | 110 | 1.81 | 0.095 | 0.029 | $h$ | 10.3 | 0.84 |
| 9$\zeta$ | $n$-Hexadecane | 1.432 | ○ | 2547 | 38.36 | 217 | 112 | 1.70 | 0.023 | 0.063 | $h$ | 9.7 | 0.37 |
| 12$\eta$ | 1-Dodecanol | | | 2546 | 38.36 | 230 | 130 | 1.75 | 0.040 | ... | ... | ... | ... |
| 30$\theta$ | Dichloromethane | 1.425 | □ | 2548 | 38.34 | 205 | 133 | 1.80 | 0.138 | 0.031 | $h$ | 10.4 | 0.78 |
| 26$\iota$ | 1,2-Ethanediol | 1.432 | ⊗ | 2547 | 38.33 | 192 | 123 | 1.65 | 0.112 | 0.029 | $h$ | 9.5 | 0.84 |
| 29$\kappa$ | 1,2-Dichloroethane | 1.448 | □ | 2548 | 38.33 | 206 | 131 | 1.74 | 0.134 | 0.031 | $h$ | 10.1 | 0.78 |
| 34$\lambda$ | 1,2,3-Propanetriol | 1.473 | ⊗ | 2549 | 38.30 | 197 | 133 | 1.87 | 0.163 | 0.025 | 2.38 | 10.8 | 0.98 |
| 37$\mu$ | Chloroform | 1.448 | □ | 2551 | 38.26 | 225 | 169 | 2.27 | 0.213 | 0.0049 | $h$ | | 5.1[f] |
| 24$\nu$ | Benzene | 1.498 | ● | 2552 | 38.24 | 202 | 153 | 1.76 | 0.091[j] | ... | ... | ... | ... |
| 38$\xi$ | Carbon tetrachloride | 1.604 (15°) | | 2557 | 38.20 | 261 | 183 | ... | 0.271 | ... | ... | ... | ... |

[a] Solvents are listed ($a$–$\xi$) in order of refractive index, absorption frequency, and line width. The numbers (1–40) give the order of solvent-induced (0–0) absorption and radiationless conversion. [b] Determined at the sodium D-line at $T$ = 20°. Bayliss and Hulm[2] and Sverdlova[6] have correctly used the refractive index at 2500–2540 Å, which is about 4% greater, for most solvents, than the value given here. [c] Symbols are the key to Figure 3. [d] Solutions prepared by weight + volumetric dilution, great care being taken to avoid evaporation loss of benzene. Absorption spectra measured with a Cary Model 14 spectrophotometer. [e] Determined as in ref 1. See J. W. Eastman, *Photochem. Photobiol.*, **6**, 55 (1967), and unpublished report (1968). [f] Spontaneous emission rate assumed to be $k_0$ = 2.5 × $10^6$ sec$^{-1}$. This is the average value of the rate calculated for benzene in the 23 solvents where $\int(\epsilon/\nu)d\nu$ was measured. [g] F. Almasy and H. Laemmel, *Helv. Chim. Acta*, **34**, 462 (1951). [h] For undetermined samples, $10^{14}\langle\nu^{-3}\rangle$ = 2.35 has been used. [i] W. A. Noyes, Jr., W. A. Mulac, and D. A. Harter, *J. Chem. Phys.*, **44**, 2100 (1966); and W. A. Noyes, Jr., and D. A. Harter, *ibid.*, **46**, 674 (1967). [j] Benzene crystal gives $\epsilon_s/\epsilon_v \approx 0.25$ [V. L. Broude, *Sov. Phys. Usp.* (English Transl.), **4**, 584 (1962)].

high when account is taken of their broad vibrational structure. The reason for this apparently stems from the presence of a charge-transfer absorption, which adds to the total intensity measured in the 2600-Å spectral

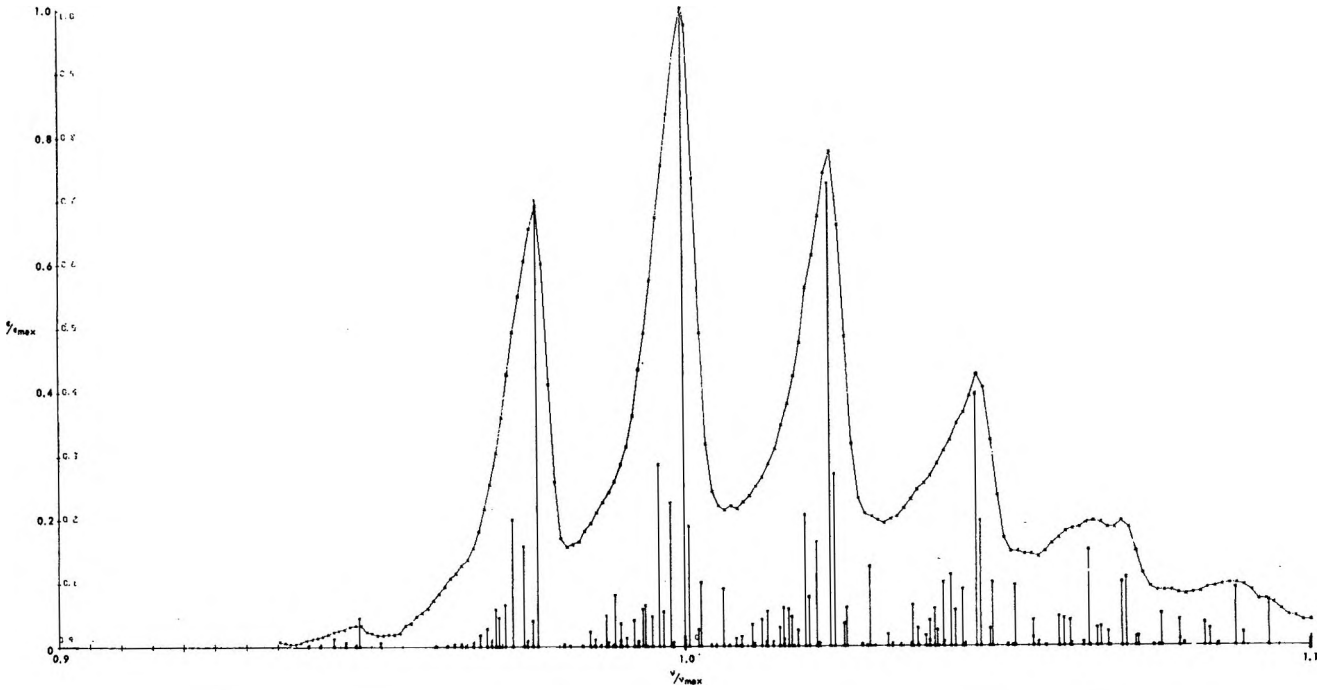

Figure 1. The 2600-Å absorption spectrum at 25° of benzene dissolved in 2-methyl-1-propanol, normalized both in frequency and amplitude at the absorption maximum. The stick plot is the spectrum of benzene vapor at 25° derived from data given or referred to by J. H. Callomon, T. M. Dunn, and I. M. Mills, *Phil. Trans. Roy. Soc.* (London), **259**, 499 (1966).

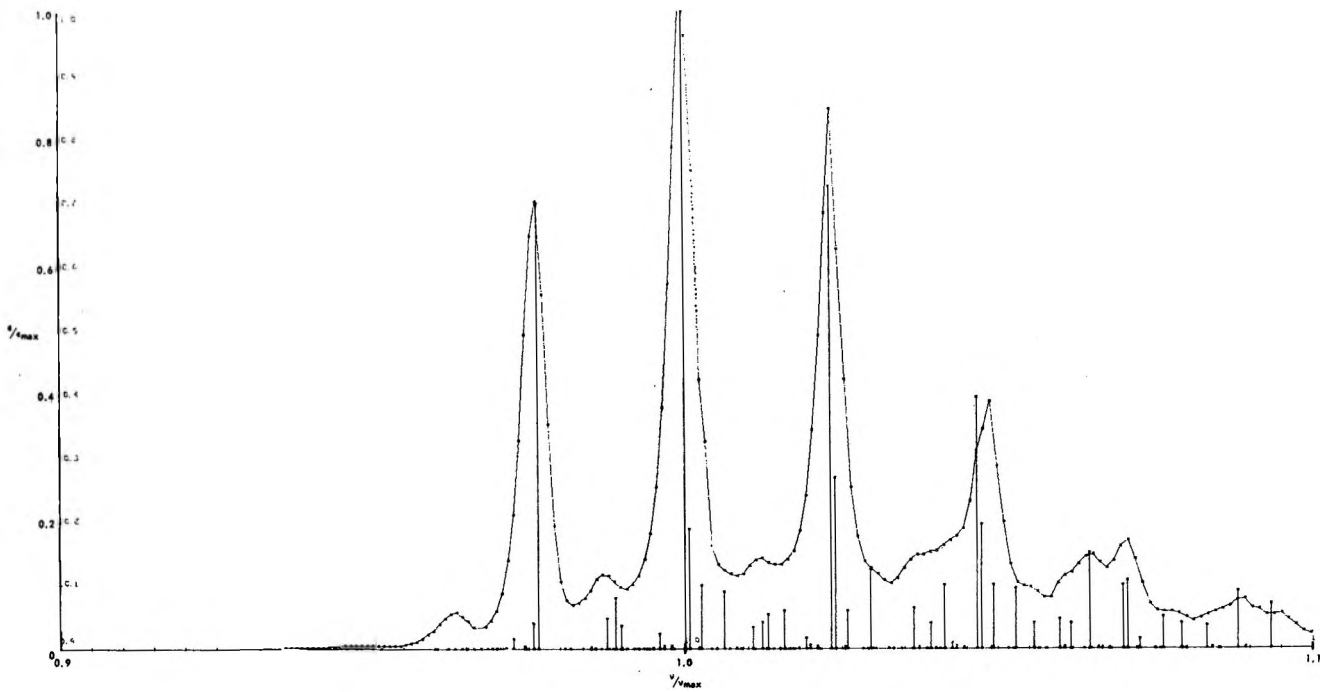

Figure 2. The 2600-Å absorption spectrum at about −140° of benzene dissolved in 2-methyl-1-propanol, normalized both in frequency and amplitude at the absorption maximum. The stick plot has been calculated for the spectrum of benzene vapor at −140°.

region.[3] These are the only two solvents studied that show evidence for charge-transfer complexes in the ground state.

*Uv Absorption Frequency and Line Width.* It will be shown below that the solvents such as water and chloroform that effectively quench the fluorescence of benzene also produce a strong enhancement of the (0–0) absorption band. To test this apparent correlation quantitatively, it is first necessary to correct the

(3) R. F. Weimer and J. M. Prausnitz, *J. Chem. Phys.*, **42**, 3643 (1965).

absorption line shape for the effects of varying frequency and line width, which are also solvent dependent.[2,4-10] To accomplish a complete line shape analysis, the absorption spectra were plotted with the normalized scale given in Figures 1 and 2. With spectra prepared in this way it was possible to rank the absorption frequencies and line widths for the vibrational fine structure, as in Table I. The reported frequency ($\nu_{00}$ + 522) is that of the first major peak in the vibronic spectrum, which occurs at *ca.* 522 $cm^{-1}$ above the electronic (0–0) origin. The line width was read at $^9/_{10}$ the maximum in absorptivity units, $(^9/_{10})\epsilon_{max}$. (By reading at $^9/_{10}$ maximum, the interference of the solvent-induced band is avoided in most solvents.)

The absorption frequency decreases and the line width of the vibrational fine structure increases with increasing refractive index, in agreement with the results of Bayliss,[2,4] Sverdlova,[6,9] and others. (Water and $D_2O$ have anomalously broad absorption peaks, and low absorptivity maxima. This may be caused by an experimental complication: interference by the solvent-induced (0–0) band, which is intense in water.) In mixtures of solvents or in solutions that are high in the concentration of benzene, the frequency and line width have been found to be determined by the refractive index of the mixed solvent.

Two numbering systems are given in Table I. The letter designations give the order for solvent effects in the uv absorption frequency and line width of the vibrational structure, both correlated with the refractive index. The number designations give the order for solvent-induced (0–0) absorption and for fluorescence quenching, as presented in the following.

*Solvent-Induced (0–0) Absorption Intensity.* Our results confirm and extend the observations of Bayliss and Cant[11] and those of Koyanagi and Kanda.[12,13] To accurately locate the solvent-induced band, low-temperature spectra were determined and compared with the spectra measured at 25°. At reduced temperatures the solvent-induced band is clearly resolved, even in such weakly interacting solvents as *n*-hexane and perfluoro-*n*-hexane.

To eliminate the effect of line width variations from our results, in Table I we have tabulated the solvent-induced intensity at the (0–0) frequency, $\epsilon_S$, relative to the normal vibronically allowed intensity at [$\nu_{00}$ + 522] $cm^{-1}$, $\epsilon_V$, *i.e.*, as $\epsilon_S/\epsilon_V$. The ratio is then the ratio of oscillator strengths, $f_s/f_v$, for the two-component bands if the line widths are the same. Using the normalized spectra discussed above (*e.g.*, Figures 1 and 2) the absorption tail of the vibronic peak ($\epsilon_v$) has been subtracted to obtain the induced peak ($\epsilon_s$).

*Fluorescence Quenching.* The fluorescent state is constituted of vibrational levels in thermal equilibrium, and since the oscillator strength for the 2600-Å absorption is a constant and the fluorescence spectrum is the mirror image of the absorption,[14] we may calculate the spontaneous emission rate from the absorption spectrum.[15,16] The spontaneous emission rate in cyclohexane calculated for the Franck–Condon state by Berlman is $k_0 = 2.46 \times 10^6$ $sec^{-1}$.[17] The present work gives $k_0 = 2.5 \times 10^6$ $sec^{-1}$ for the average of 23 solvents. Using the $\tau = 29$ nsec lifetime measured by Berlman in cyclohexane[17] and our most recently measured quantum yield of 0.061 for the same solvent, we calculate a spontaneous emission rate for the fluorescent state of $k_0 = \Phi/\tau = 2.1 \times 10^6$ $sec^{-1}$. The difference between the value calculated for the Franck–Condon state and that observed for the fluorescent state is within the present experimental uncertainty (±20% in the quantum yield). Based on the constancy of the oscillator strength for the benzene absorption, the spontaneous emission rate was calculated for the Franck–Condon state.[15,16] The rate of radiationless conversion obtained from this value and the experimental quantum yield are presented in Table I.

We note that charge-transfer absorption is not necessary for intense (0–0) absorption intensity or fluorescence quenching. Water and acetonitrile are two examples of solvents that are effective fluorescence quenchers, but that have no charge-transfer absorption in the 2600-Å region. We also note that there is no clear correlation of either the (0–0) absorption intensity or fluorescence quenching with the frequency, $\nu_{00}$, of the uv absorption,

(4) N. S. Bayliss, *J. Chem. Phys.*, **18**, 292 (1950).

(5) W. W. Robertson and F. A. Matsen, *ibid.*, **23**, 2468 (1955).

(6) O. V. Sverdlova, *Opt. Spectrosk.*, **6**, 223 (1959).

(7) B. Oksengorn, "Perturbation par la pression du spectre d'absorption de quelques composes aromatiques dans l'ultraviolet proche," Paris, 1959.

(8) B. Vodar, *Proc. Roy. Soc.* (London), **A255**, 44 (1960).

(9) O. V. Sverdlova, *Opt. Spectrosc. Suppl. 2* (English Transl.), 15 (1966).

(10) N. G. Bakhshiev, O. P. Girin, and I. V. Piterskaya, *Opt. Spectrosc.* (USSR) (English Transl.), **24**, 483 (1968).

(11) N. S. Bayliss and N. W. Cant, *Spectrochim. Acta*, **18**, 1287 (1962).

(12) M. Koyanagi and Y. Kanda, *ibid.*, **20**, 993 (1964).

(13) M. Koyanagi, *J. Mol. Spectrosc.*, **25**, 273 (1968).

(14) S. Leach, R. Lopez-Delgado, and F. Delmas, *ibid.*, **7**, 304 (1961).

(15) At the present time there is a controversy about the inclusion of the refractive index $n$ in calculations of spontaneous emission rates from integrated absorption spectra. For example, the work of S. J. Strickler and R. A. Berg, *J. Chem. Phys.*, **37**, 814 (1962), in which a factor $n^2$ is included, may be compared to that of W. Liptay, *Z. Naturforsch.*, **21a**, 1605 (1966), in which $n^2$ is omitted. The significance of this difference may be noted in the report of W. R. Ware and P. T. Cunningham, *J. Chem. Phys.*, **43**, 3826 (1965). In the present work we assume that there is a cancellation of errors in the usual formula (Strickler and Berg and ref 16), so that although the refractive index should be omitted in principle, in practice the correct rates for radiationless conversion in liquids ($n^2 \simeq 2$) can be calculated when the factor ×2 is included. If it is later proved that a correction for changes in refractive index is necessary, the rate calculated here for the vapor should be reduced by one-half, with a corresponding decrease of the rates given in Figures 3 and 4.

(16) J. B. Birks and D. J. Dyson, *Proc. Roy. Soc.* (London), **A275**, 135 (1963).

(17) I. B. Berlman, "Handbook of Fluorescence Spectra of Aromatic Molecules," Academic Press, New York, N. Y., 1965.

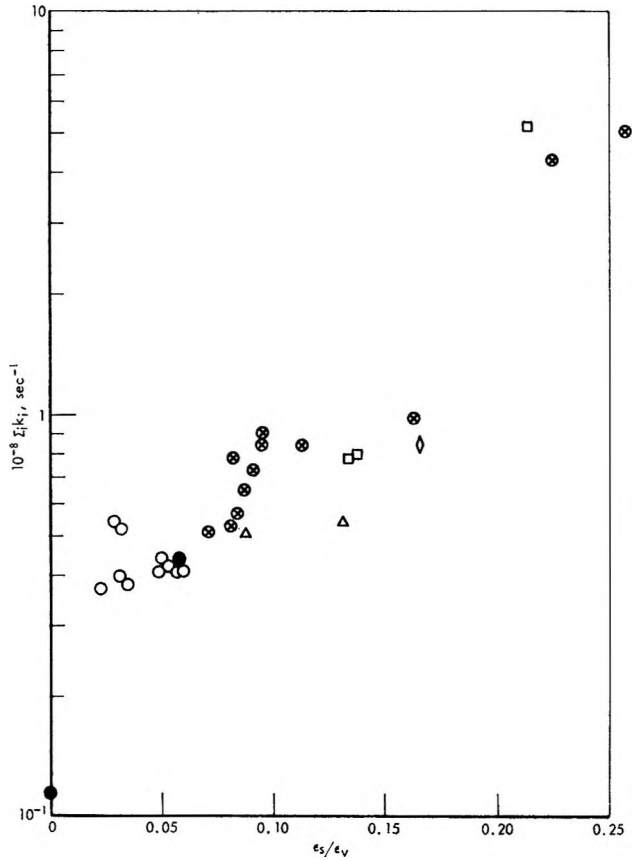


Figure 3. Correlation of solvent-induced fluorescence quenching at 25° with solvent-induced (0–0) uv absorption. The total radiationless conversion rate is plotted as a function of the (0–0) absorption intensity $\epsilon_s$, measured relative to the usual vibronic intensity $\epsilon_v$ (experimental points are keyed to Table I).

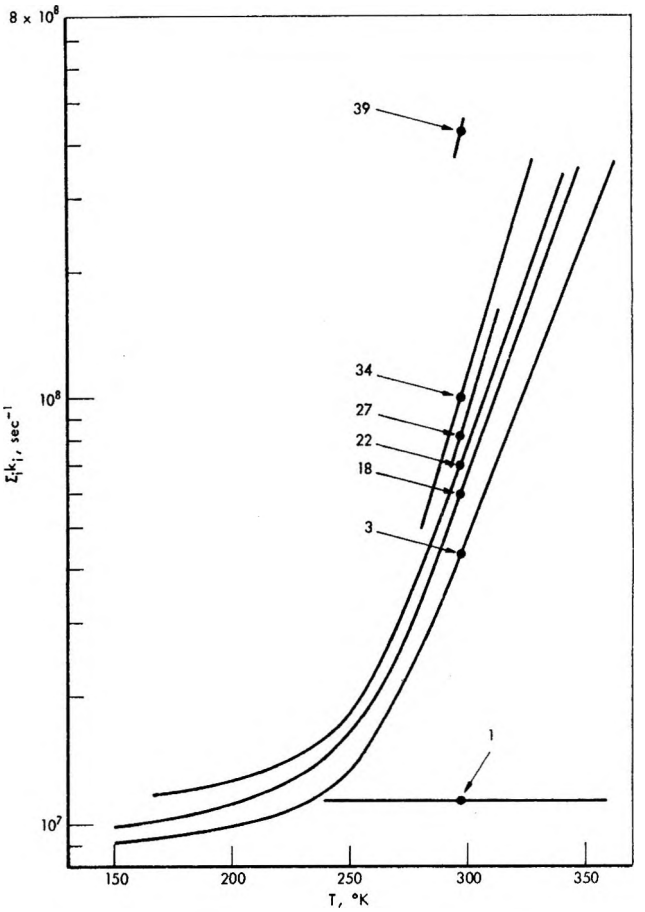


Figure 4. Total radiationless conversion rate as a function of temperature for a few solvents (keyed to Table I).

or with the width of the vibrational fine structure, $\Delta\nu \cdot (^9/_{10})$. These depend on the refractive index.

*Concentration Dependence.* When suitable account is taken of the change in line width that occurs when solvents are mixed (dependent on the refractive index of the mixed solvent), the authors have found that the (0–0) absorption intensity depends almost linearly on the volume fraction of the solvents. This agrees with the results of Koyanagi and Kanda.[12]

*Temperature Dependence.* Although the intensity of some bands in aromatic molecules has been found to depend on the temperature,[18] measurements made in the present work indicate that for benzene in liquid solutions the temperature dependence of the oscillator strength is negligible between 100 and 300°K. A small increase was found in the relative solvent-induced (0–0) absorption intensity, $\epsilon_S/\epsilon_V$, as the temperature was reduced (to *ca.* 190°K), although the change was well within the limits of experimental uncertainty (*ca.* ±25%).

The temperature dependence of fluorescence quenching is illustrated for a few solvents in Figure 4. Quantum yields similar to that of benzene vapor are reached in all liquids when the thermal excitation of the active levels is quenched (below *ca.* 200°K).

## Conclusions

The results of the present work show that the spontaneous emission rate, $k_0$, calculated for the Franck–Condon state is the same as that determined experimentally for the fluorescent state in cyclohexane (±20%).[15] This indicates that both fluorescence and radiationless processes arise from the same excited electronic state and that this state is similar to the Franck–Condon state produced directly by absorption. This is in keeping with the assumption that all the absorption in the 2400–2600-Å region arises from transitions to a single excited electronic state and that different vibrational sublevels giving fluorescence and nonradiative decay are in thermal equilibrium.

The oscillator strength of the 2600-Å transition is independent of solvent, so that the spontaneous emission rate is constant, and the dependence of fluorescence quenching on solvent arises from the effect of solvent on the radiationless conversion rate. The rate of radiationless conversion does not closely parallel the solvent

(18) V. P. Klochkov and S. M. Korotkov, *Opt. Spectrosc. Suppl. 2* (English Transl.), 11 (1966).

dependence of the (0–0) absorption frequency or the line width of the vibrational fine structure, both of which depend on the refractive index. Also there is no observable solvent dependence in the 522 and the 914-$cm^{-1}$ vibrational frequencies of the fluorescent state. The only clear empirical correlation for the fluorescence quenching was found with the (0–0) absorption intensity (Figure 3). The correlation suggests that the induced quenching depends on the same intermolecular forces that are responsible for the induced absorption. The latter are the average London-dispersion and dipole-induced dipole forces, as shown by Koyanagi.[13]

Little temperature dependence (100–300°K) was found in the (0–0) absorption intensity, a measure of the average intermolecular force. Thus the thermal quenching of the fluorescence in this same temperature region appears to arise from the thermal population of active vibrational levels above the zero-point level in the fluorescent state of benzene. In any case, only the total rate of all nonradiative transitions has been determined. Because the measured thermal quenching may arise from any number of thermally excited vibrations,[19] a single Arrhenius activation energy has only a limited quantitative significance. For this reason the authors have presented the temperature dependence of the fluorescence in graphical form (Figure 4).

The (0–0) absorption depends on the volume fraction of components in several mixed solvents, so we conclude that no special conformation of benzene with solvent is necessary to explain the solvent-induced radiationless conversion, which correlates with the (0–0) absorption. However, the formation of complexes, which may occur in chloroform, can greatly enhance any effects that the induced-dipole and dispersion interactions exert on the nonradiative transitions.

From the correlation between solvent-induced (0–0) absorption and fluorescence quenching (Figure 3) it is possible to estimate the fluorescence quantum yield of monomer benzene in liquid benzene at 25° as $\Phi = 0.040$.

*Acknowledgments.* The authors wish to acknowledge the helpful discussions of Drs. D. J. Meier, K. Loos, F. S. Mortimer, and J. W. Otvos, as well as the persistent and careful experimental work of C. A. Augustin and R. Woolley.

(19) S. H. Lin, *J. Chem. Phys.*, **44**, 3759 (1966).

# Dielectric Properties of Liquid Propylene Carbonate[1a]

**by Larry Simeral and Ralph L. Amey[1b]**

*Department of Chemistry, Occidental College, Los Angeles, California 90041* *(Received September 16, 1969)*

The equilibrium dielectric permittivity, density, and refractive index of liquid propylene carbonate (4-methyl-1,3-dioxolan-2-one) have been measured over the temperature range $220.15 \leq T \leq 293.15$°K. The Kirkwood correlation factor is essentially unity over this temperature range. The results suggest that propylene carbonate behaves as a normal polar liquid with strong dipole–dipole interactions but with little or no specific association present. The effects of concentration and temperature on the ir and nmr spectra provide further evidence which is consistent with the dielectric results. Its ability to supercool is due to molecular asymmetry.

## Introduction

The nature and extent of association in aprotic solvents is of considerable interest and has been open to much discussion in recent literature.[2] Kempa and Lee, in determining the dipole moments of several cyclic carbonates,[3] suggested the possibility of intermolecular association in the pure compounds.

As part of a general study of local structure in aprotic solvents of high dipole moment being conducted in this laboratory, an investigation of several cyclic carbonates has begun. The usefulness of dielectric measurements to establish the extent of association in aprotic systems has been shown both in this laboratory[4] and elsewhere.[5] It has been demonstrated that little or no self-association occurs in liquid dimethyl sulfoxide.[4] Similar studies by Meighan, *et al.*, of dimethylformamide have shown it to exhibit properties which are largely due to

(1) (a) A portion of this work was presented at the 158th National Meeting of the American Chemical Society, New York, N. Y., Sept 8, 1969. (b) To whom correspondence should be addressed.

(2) A. J. Parker, *Chem. Rev.*, **69**, 1 (1969).

(3) R. Kempa and W. H. Lee, *J. Chem. Soc.*, 1936 (1958).

(4) R. L. Amey, *J. Phys. Chem.*, **72**, 3358 (1968).

(5) R. M. Meighan and R. H. Cole, *ibid.*, **68**, 509 (1964).

nonspecific dipole–dipole interactions.[5] These results are consistent with the findings of infrared studies.[6]

The related properties and extensive liquid range (224.3–515°K) of propylene carbonate (4-methyl-1,3-dioxolan-2-one) have led us to begin with an examination of its dielectric behavior. Because of its increasing use as a solvent and reaction medium, an understanding of its local liquid structure should prove valuable.

## Experimental Section

*Materials.* Propylene carbonate was obtained from Matheson Coleman & Bell and dried by passage through a 1-ft column of Linde type 4A molecular seive under a nitrogen atmosphere. The effluent was vacuum distilled in a 3-ft spinning-band column at a pressure of 4–7 Torr. The middle 70% was collected under dry nitrogen and subsequently used for study. Purity was determined by gas chromatography; matched 4.5-ft ($^1/_8$ in. o.d.) columns filled with Poropak Q (100–120 mesh) were used with dual thermal conductivity detectors in a Beckman GC 5 gas chromatograph. The water content, determined by standard additions method, was found to be less than 20 ppm.

*Permittivity Measurements.* Capacitance measurements were made on a General Radio 1615A capacitance bridge in conjunction with a Rhode & Schwarz tunable indicating amplifier and a Hewlett-Packard 200 CD wide-range oscillator. The dielectric cell used was a three-terminal guarded concentric electrode assembly attached to the bridge with 0.085-in. o.d. Teflon coaxial cable. The cell was immersed in propylene carbonate contained within a jacketed vessel. The latter was thermostated by circulating methanol as the refrigerant. Temperature control was maintained by a Lauda TK-30 Ultra Kryomat to ±0.02°. The cell constant was determined over the temperature range of interest. The temperature of the liquid sample in immediate thermal contact with the cell was determined by a calibrated copper–constantan thermocouple and recorded on a 1-mV recorder.

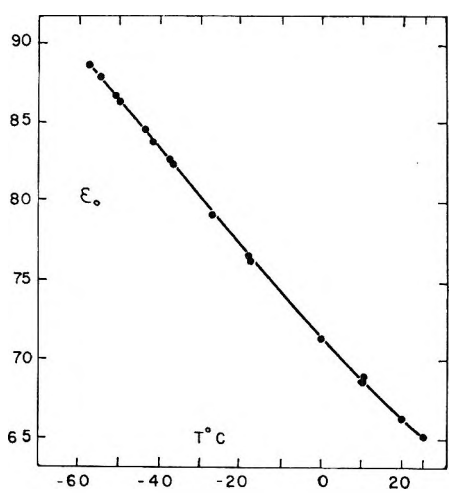


Figure 1. Dielectric permittivity of liquid propylene carbonate as a function of temperature.

Densities were determined with a Sprengle–Ostwald pycnometer calibrated with water and absolute methyl alcohol. Refractive indices were determined with an Abbe precision refractometer. The latter was calibrated with Cargille master calibration liquids.

*Other Measurements.* Nmr data were obtained with a Jeolco C-60HL spectrometer operated in the external lock frequency sweep mode. Variable-temperature controller Model JESVT-3 was used to obtain the desired temperature operation. Chemical shifts relative to the methyl proton signal were measured with a Beckman Model 7360RU frequency counter. Infrared measurements were made with a Perkin-Elmer Model 237 spectrophotometer. Sample temperature was approximately 25° during each run.

## Results

The density of liquid propylene carbonate was determined over the temperature range $220.15 \leq T \leq 293.15$°K. A relation of the following form was obtained from the data by least-squares analysis

$$\rho = 1.541 - 1.148 \times 10^{-3}T$$

where $T$ is the Kelvin temperature and $\rho$ is in g cc$^{-1}$. The uncertainty in $\rho$ is estimated to be ±0.001 g cc$^{-1}$.

The refractive index was found to behave linearly over the temperature range $220.15 \leq T \leq 293.15$°K. The corresponding relation is $n_D = 1.5314 - 3.752 \times 10^{-4}T$, with a maximum uncertainty in $n_D$ of $\pm 4 \times 10^{-4}$.

The dielectric permittivity was measured at 10 kHz and was found to be a nonlinear function of temperature. Some representative values are listed in Table I. A plot of permittivity *vs.* temperature is shown in Figure 1.

**Table I:** Static Dielectric Permittivity for Propylene Carbonate at Several Temperatures

| $\epsilon_0$ | Temp, °K | $\epsilon_0$ | Temp, °K |
|---|---|---|---|
| 61.7[a] | 313.15 | 76.9 ± 0.1 | 253.15 |
| 66.1 ± 0.3 | 293.15 | 80.0 ± 0.1 | 243.15 |
| 68.4 ± 0.1 | 283.15 | 83.0 ± 0.1 | 233.15 |
| 71.0 ± 0.2 | 273.15 | 86.1 ± 0.1 | 223.15 |
| 73.9 ± 0.1 | 263.15 | 89.3 ± 0.3 | 213.15 |

[a] From ref 3.

## Discussion

No subambient data have been reported in the literature for liquid propylene carbonate. However, Sax[7]

(6) A. Allerhand and P. Schleyer, *J. Amer. Chem. Soc.*, **85**, 1715 (1963).

(7) N. I. Sax, "Dangerous Properties of Industrial Materials," 2nd ed, Reinhold Publishing Corp., New York, N. Y., 1963, p 1139.

at 20°, Kempa and Lee,[3] Harris,[8] Kronick and Fuoss,[9] and Wu and Friedman[10] at 25° have all reported density values which agree with our corresponding high-temperature results.

Similarly, Kempa and Lee[3] and others[11] have published refractive index data at 25 and 20°, respectively, which are somewhat lower than values reported here.

The static dielectric permittivity at 25° has been reported by several workers,[8,9,12,13] the value by Fuoss, *et al.*, being in closest agreement with ours. A value reported by Kempa and Lee[3] at 40° agrees very well with our extrapolated value at that temperature.

Examination of association character through dielectric behavior is particularly useful in that local liquid structure can be inferred from appropriate calculations based on dielectric measurements.[14,15] The Kirkwood equation[16]

$$\frac{V(\epsilon_0 - \epsilon_\infty)(2\epsilon_0 + \epsilon_\infty)}{\epsilon_0(\epsilon_\infty + 2)^2} = \frac{4\pi N_0 \mu_0^2}{9kT} g$$

permits a description of those polar liquids having specific short-range forces which hinder rotation of the molecule. The limiting dielectric permittivities at low and high frequencies are $\epsilon_0$ and $\epsilon_\infty$, respectively, $\mu_0$ is the permanent dipole moment of the free molecule, and $V$ is the molar volume measured at temperature $T$. The correlation factor $g$ is a measure of the short-range effects which hinder orientation of a molecule with its surrounding neighbors. For systems in which specific intermolecular forces orient neighboring dipole vectors in a parallel fashion, $g$ is greater than unity; for an antiparallel configuration of dipoles, $g$ is less than unity. For systems with nonspecific intermolecular forces, $g$ equals unity and Kirkwood's equation reduces to the Onsager expression for a normal polar liquid.[17] From a calculation of the correlation factor with available dielectric data as a function of temperature, it is thus possible to provide a measure of the association present in a polar liquid. Figure 2 shows the results of such a calculation of $g$ for propylene carbonate over the temperature range of this study. It can be seen that within the estimated experimental error the correlation factor remains near unity. This temperature dependence is consistent with the behavior of a polar liquid with very strong, but nonspecific, dipole–dipole attractive forces.[4]

It should be noted that the value of $g$ is sensitive to the $\epsilon_\infty$ chosen for calculation of eq 1. For comparison purposes, $\epsilon_\infty$ was represented at each temperature by the usual but arbitrary approximation, $\epsilon_\infty = 1.1n^2$, where $n$ is the refractive index measured at optical frequencies. It is readily shown that larger assumed values for $\epsilon_\infty$ will result in somewhat reduced $g$ values.[18] A notable characteristic of most associated liquids is a strongly temperature-dependent correlation factor. Correlation factors with small temperature coefficients have been observed for some liquids in which association is

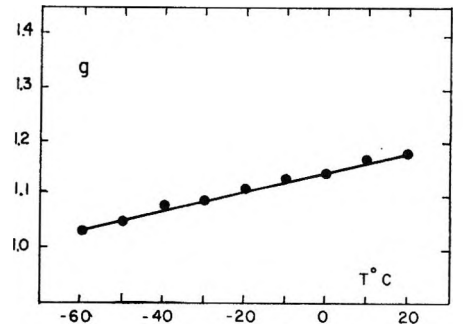


Figure 2. Kirkwood correlation factor of liquid propylene carbonate as a function of temperature.

believed to occur.[19] However, these instances are rare and to our knowledge are consistent with models which generate rather small equilibrium constants. For example, if the Dannhauser–Cole model for $n$-mer association is applied to our propylene carbonate data, an equilibrium constant of $9.8 \times 10^{-3}$ l. mol$^{-1}$ at 20° is obtained. From the temperature dependence of $K$, thermodynamic functions may be calculated: $\Delta H^\circ = +2.2$ kcal/mol, $\Delta S^\circ = -1.4$ eu/mol, $\Delta G^\circ = +2.6$ kcal/mol. The sign of $\Delta H^\circ$ is obviously inconsistent with a reasonable model for association[20] and leads us to conclude that if self association is occurring it is not of the linear $n$-mer type.

Because of the sensitivity of spectroscopic techniques to the presence of association species in liquids both ir and nmr measurements were made on propylene carbonate. The ir data were obtained on the pure liquid and on several dilute carbon tetrachloride solutions. Due to the limited solubility of propylene carbonate in nonpolar solvents it was necessary to compromise in the choice of an "inert" solvent for the study. The results are shown in Table II. Nmr measurements were made on the pure liquid over the temperature range $373 \leq T \leq 303$. These are reported in Table III relative to the high-field peak of the methyl proton doublet. As can be seen from the data, essentially

(8) W. Harris, Report UCRL-8381, USAEC, Berkeley Radiation Laboratory, 1958.

(9) P. Kronick and R. Fuoss, *J. Amer. Chem. Soc.*, **77**, 6114 (1955).

(10) Y. Wu and H. Friedman, *J. Phys. Chem.*, **70**, 501 (1966).

(11) Technical Bulletin, Jefferson Chemical Co., Houston, Texas, 1960, p 1.

(12) M. Watanabe and R. Fuoss, *J. Amer. Chem. Soc.*, **78**, 527 (1956).

(13) R. Seward and E. Vierira, *J. Phys. Chem.*, **62**, 127 (1958).

(14) J. B. Hasted, *Progr. Dielectrics*, **3**, 103 (1961).

(15) A. D. Buckingham, *Discuss. Faraday Soc.*, **43**, 205 (1967).

(16) J. G. Kirkwood, *J. Chem. Phys.*, **7**, 911 (1939).

(17) R. H. Cole, *Progr. Dielectrics*, **3**, 70 (1961).

(18) J. Middlehoek and C. J. F. Böttcher in "Molecular Relaxation Processes," Academic Press, London, 1966, p 69.

(19) W. Dannhauser and A. F. Flueckinger, *J. Phys. Chem.*, **68**, 1814 (1964).

(20) G. C. Pimentel and A. L. McClellan, "The Hydrogen Bond," W. H. Freeman and Co., San Francisco, Calif., 1960, p 210.

**Table II:** Infrared Absorption Frequencies of Propylene Carbonate in Carbon Tetrachloride

| Concn, mol $l.^{-1}$ | C=O str, $cm^{-1}$ | Skeletal str, $cm^{-1}$ | C—H str, $cm^{-1}$ |
|---|---|---|---|
| Neat | 1805 ± 2 | 1176 ± 2 | 2940 ± 5 |
| | | | 2930 ± 5 |
| 0.2 | 1825 ± 2 | 1165 ± 2 | ... |
| 0.04 | 1825 ± 2 | 1165 ± 2 | 2940 ± 5 |
| | | | 2920 ± 5 |
| 0.02 | 1825 ± 2 | 1165 ± 2 | 2940 ± 5 |
| | | | 2920 ± 5 |
| 0.004 | 1828 ± 2 | 1165 ± 2 | ... |
| 0.001 | 1825 ± 2 | 1165 ± 2 | 2940 ± 5 |
| | | | 2925 ± 5 |

no shifts are observed in either spectrum. The slight shift in the carbonyl stretch near 1820 $cm^{-1}$ and the skeletal stretch near 1160 $cm^{-1}$ in the ir spectra can be attributed to solvent interaction.[21] Again we are led to believe that this indicated the presence of little or no specific association in the liquid.

Recent nmr analysis of propylene carbonate has shown that its molecular skeleton is planar in the liquid state.[22] This is consistent with the observed dielectric permittivity, refractive index, and density results, all of which show smooth behavior through the melting point into the supercooled liquid region. Thus the supercooled state in propylene carbonate is not the result of specific association, but rather, is due simply to the low symmetry of the planar skeleton.

**Table III:** Nmr Chemical Shifts[a] for Liquid Propylene Carbonate at Various Temperatures

| Temp, °K | $\nu_a$, Hz | $\nu_b$, Hz | $\nu_c$, Hz |
|---|---|---|---|
| 373 | 215 ± 2 | 191 ± 1 | 158 ± 1 |
| 348 | 214 ± 2 | 190 ± 1 | 158 ± 1 |
| 328 | 215 ± 1 | 190 ± 1 | 158 ± 1 |
| 303 | 214 ± 1 | 192 ± 1 | 160 ± 1 |

[a] Relative to the high-field peak of the methyl proton doublet.

*Acknowledgment.* Acknowledgment is made to the donors of the Petroleum Research Fund, administered by the American Chemical Society, the Research Corp., and the National Science Foundation for partial support of this work.

(21) C. L. Angell, *Trans. Faraday Soc.*, **52**, 1178 (1956).
(22) H. Finegold, *J. Phys. Chem.*, **72**, 3244 (1968).

# Binding of Counterions to Polyacrylate in Solution

**by R. J. Eldridge and F. E. Treloar**

*Physical Chemistry Department, University of Melbourne, Parkville, Victoria, 3052, Australia*
*(Received September 26, 1969)*

Ultraviolet spectrophotometric measurements on solutions containing $[Co(NH_3)_6](ClO_4)_3$, fully neutralized poly(acrylic acid) of molecular weight $7 \times 10^5$, and added electrolyte show the occurrence of intimate binding of the trivalent cation, analogous to ion pairing. The extent of this binding is inversely proportional to the cube of the concentration of added $LiClO_4$ or $NaClO_4$, and $LiClO_4$ reduces the binding more effectively than $NaClO_4$. This leads to the conclusion that the alkali metal cations compete with $[Co(NH_3)_6]^{3+}$ for binding sites on the polyanion.

Since the hypothesis of site binding in polyelectrolyte solutions was first introduced,[1] evidence has been obtained that association of this nature does in fact occur in many cases.

Mandel[2] has pointed out that more than one type of ion-association can occur in a given polyelectrolyte solution and that experimental methods differ in their sensitivity to the different kinds of association. He emphasized that a variety of techniques must be used before the nature of the counterion–polyion interaction in any polyelectrolyte system can be made clear. Thu transference[3,4] and dilatometric[5] measurements on solutions of alkali metal polyacrylates have been interpreted

(1) F. E. Harris and S. A. Rice, *J. Phys. Chem.*, **58**, 725, 733 (1954).
(2) M. Mandel, *J. Polym. Sci.* (C), **16**, 2955 (1967).
(3) S. J. Gill and G. V. Ferry, *J. Phys. Chem.*, **66**, 995, 999 (1962).
(4) L. A. Noll and S. J. Gill, *ibid.*, **67**, 498 (1963).
(5) U. P. Strauss and Y. P. Leung, *J. Amer. Chem. Soc.*, **87**, 1476 (1965).

as evidence for site binding, while infrared absorption measurements[6] provided no such evidence.

Ultraviolet spectroscopy should be sensitive to the occurrence of intimate site binding, analogous to ion pairing, in solutions containing an absorbing counterion, but not to more diffuse binding. This technique has been used to study complexation of transition metal ions by polymeric carboxylates but in this work we studied the binding by polyacrylate of the hexaamminecobalt(III) cation (M), which should be extensively and intimately bound because of its high charge, but will not undergo inner-sphere coordination.

Other workers have shown that the formation of ion pairs ("outer-sphere coordination") between M and an ions such as sulfate[7] or the halides[8] enhances the absorbance of M in the region of its charge-transfer band. Matthews[9] has used this effect to study the association of M with biological macroanions; he concluded that this is analogous to Langmuir adsorption behavior.

However, this conclusion may not be valid since the equation which Matthews used to test his data contains an algebraical mistake; we were unable to derive his eq 6 from his eq 4.

We have studied the binding of M to fully neutralized poly(acrylic acid) (PAA) in solutions containing added electrolyte.

## Experimental Section

$[Co(NH_3)_6]Cl_3$ was prepared by the method of Bjerrum and McReynolds,[10] and after two recrystallizations converted to the perchlorate by precipitation with $HClO_4$. A further recrystallization was then carried out from dilute $HClO_4$. (*Anal.* for $NH_3$, 22.03% and for Co (by electrodeposition), 13.17%. Calculated for $CoN_6H_{18}Cl_3O_{12}$: $NH_3$, 22.23%; Co, 12.82%.)

PAA was prepared by the method of Kandanian.[11] Fifty-seven $cm^3$ of glacial acrylic acid, distilled under reduced pressure, was dissolved in 325 $cm^3$ of butanone and 0.19 g of 2,2′-azo-*i*-butyronitrile added. Oxygen-free nitrogen was bubbled through the mixture for 1.25 hr and the temperature raised until polymerization commenced as seen by precipitation of the polymer. After 1 hr the mixture was cooled and the product collected and washed with butanone. The PAA was freeze-dried from water redistilled from $KMnO_4$; yield, about 50%.

The molecular weight was determined by viscosity measurements in 1,4-dioxane solution at 30.0°. A plot of $C/\eta_{sp}$ against $C^{1/2}$ was linear, giving $[\eta] = (71.7 \pm 1)$ $dm^3$ $kg^{-1}$. Hence, by comparison with published data,[12] weight-average molecular weight is $7.1 \times 10^5$.

Aqueous solutions of PAA were neutralized to the phenolphthalein end point with NaOH or LiOH under a blanket of nitrogen.

$NaClO_4$ and $LiClO_4$ were prepared as aqueous solutions by neutralizing $Na_2CO_3$ and LiOH with $HClO_4$.

Six series of solutions were prepared containing $5 \times 10^{-4}$ mol $dm^{-3}$, $[Co(NH_3)_6](ClO_4)_3$, NaPA or LiPA at (3–36) $\times 10^{-3}$ monomol $dm^{-3}$, and $NaClO_4$ or $LiClO_4$ to make the concentration of alkali metal 0.26, 0.41, or 0.51 mol $dm^{-3}$. The pH of all solutions was between 7 and 8. The absorbance of each solution was measured at 235.8 nm and 30.0° against $5 \times 10^{-4}$ mol $dm^{-3}$ $[Co(NH_3)_6](ClO_4)_3$ as a reference. (The molar absorbance of the complex salt is not affected by added perchlorate at the concentrations used.) The absorbance of NaPA and LiPA was also measured in solutions of the same ionic strength. Small corrections for the absorbance of the perchlorate were made in all cases. The instrument used was a Hilger and Watts Uvispek, fitted with a circulating-water thermostat.

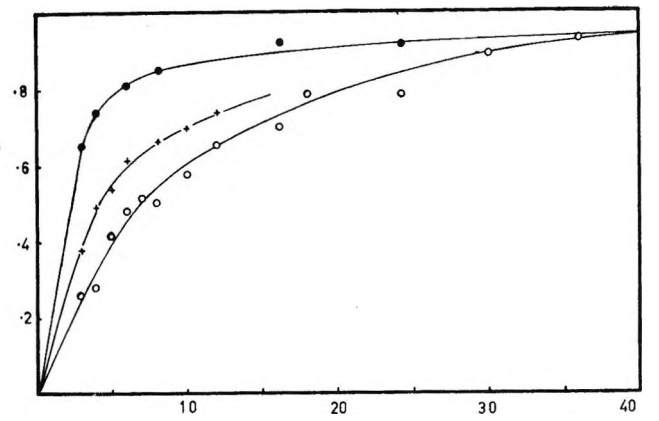


Figure 1. Spectrophotometric measurements on NaPA–$NaClO_4$–$[Co(NH_3)_6](ClO_4)_3$ solutions. Ordinate, absorbance increment Δ; abscissa, (stoichiometric polymer concentration $C_p$) $\times 10^3$, monomol $dm^{-3}$; (-●-, $C_{NaClO_4}$ = 0.26; -+-, 0.41; -○-, 0.15 mol $dm^{-3}$).

The range of concentrations of added salt was restricted by precipitation of the polyanion complex cation adduct at lower concentrations, and of the hexaamminecobalt(III) perchlorate at higher concentrations of added perchlorate. Under the conditions used no turbidity was observed, nor did the absorbance of the solutions change with time.

## Results and Discussion

The absorbance difference measured as described above is shown, after subtraction of the absorbance of the appropriate stoichiometric concentration of polymer, as a function of polymer concentration in Figures

(6) J. C. Leyte, L. H. Zuiderweg, and H. J. Vledder, *Spectrochim. Acta*, **23A**, 1397 (1967).

(7) H. Taube and F. A. Posey, *J. Amer. Chem. Soc.*, **75**, 1463 (1953); **78**, 15 (1956).

(8) M. G. Evans and G. H. Nancollas, *Trans. Faraday Soc.*, **51**, 793 (1955).

(9) M. B. Matthews, *Biochim. Biophys. Acta*, **37**, 288 (1960).

(10) J. Bjerrum and J. P. McReynolds, *Inorg. Syn.*, 216 (1946).

(11) A. Y. Kandanian, Dissertation Polytechnic Institute of Brooklyn, Brooklyn, N. Y., 1964, p 18.

(12) S. Newman, W. R. Krigbaum, C. Laugier, and P. J. Flory, *J. Polym. Sci.*, **14**, 451 (1954).

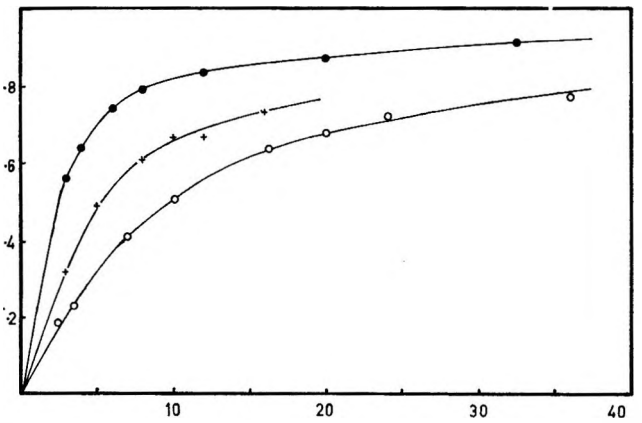


Figure 2. Spectrophotometric measurements on LiPA–$LiClO_4$–$[Co(NH_3)_6](ClO_4)_3$ solutions. Ordinate: absorbance increment Δ; abscissa: (stoichiometric polymer concentration $C_p$) × $10^3$, monomole $dm^{-3}$; —●—, $C_{LiClO_4}$ = 0.26; –+–, 0.41; –○–, 0.51 mol $dm^{-3}$).

1 and 2. We conclude from the magnitude of the absorbance increment that extensive site binding of the hexaamminecobalt(III) ion occurs. At higher polymer concentrations the absorbance increment Δ approaches a constant value for all six series of solutions, showing that the trivalent ion is virtually completely bound.

Increasing concentrations of added electrolyte decrease the degree of binding, and $LiClO_4$ is obviously more effective than $NaClO_4$ in doing this. This is in accord with the observation of other workers that the extent of binding of the alkali metal cations to the anions of weak polyacids increases with decreasing radius of the *unhydrated* cation.[3,4,13–15] This fact has been attributed to intimate binding accompanied by disruption of the hydration sheath of the cation.[4,13,14]

In order to calculate the extent of binding of $[Co(NH_3)_6]^{3+}$, we assume the binding reaction to be represented by $M^{3+} + nCOO^- \rightleftharpoons MS$ where $M^{3+}$ represents a "free," and MS a site-bound $[Co(NH_3)_6]^{3+}$ ion. The absorbance increment will then be

$$\Delta = [MS]\epsilon_{MS} + [M^{3+}]\epsilon_{M^{3+}} + [COO^-]\epsilon_p - C_{M^{3+}}\epsilon_{M^{3+}} - C_p\epsilon_p \quad (1)$$

where the ε are molar absorbances, the $C$ stoichiometric concentrations, and the subscript p indicates polyacrylate.

If a fraction $f$ of the $M^{3+}$ ions are site-bound

$$f \equiv [MS]/C_{M^{3+}} \quad (2)$$

and

$$\Delta = fC_{M^{3+}}\{\epsilon_{MS} - \epsilon_{M^{3+}} - n\epsilon_p\} \quad (3)$$

Thus $f$ can be found for any $C_p$ by dividing the observed Δ by the limit of Δ at high $C_p$, where $f$ approaches unity.

If now the binding of each trivalent ion can be regarded as outer-sphere coordination by three carboxylate groups (*i.e.*, we assume $n = 3$), and is accompanied by the release of three univalent cations from the polymer domain, giving for the binding reaction $M^{3+} + S \rightleftharpoons MS + 3M^+$ then we can define an association constant

$$K \equiv \frac{[M^+]^3[MS]y^3_{M^+}y_{MS}}{[M^{3+}]^{1/3}[COO^-]y_{M^{3+}}y_S} \simeq \frac{3C^3_{M^+}f}{(1-f)(C_p - 3fC_{M^{3+}})} \quad (4)$$

neglecting the activity coefficients $y$.

We believe that this neglect is justified since $y^3$ for a singly charged cation should be approximately equal to $y$ for a triply charged cation and because the activity coefficients of the polyanion including bound complex ion or including bound singly charged cation should be very similar.

Equation 4 assumes that the carboxylate groups binding each trivalent ion are attached to the one polymer molecule. If this assumption is valid then a plot of $f/(1-f)$ against $[COO^-] = C_p - 3fC_{M^{3+}}$ will be linear.

Equation 4 was tested in two ways. Figure 3 shows $f/(1-f)$ as a function of $C_p - 3fC_{M^{3+}}$ for each of the six series; the gradient $m$ of the best line through the origin for each series and $mC_{M^+}{}^3$ are shown in columns 2 and 3 of Table I.

**Table I:** Test of the Dependence of the Degree of Site Binding of $[Co(NH_3)_6]^{3+}$ on Polymer and Alkali Metal Concentration

| Concn $C_{M^+}$ of added electrolyte, mol $dm^{-3}$ | Gradient $m$ of plot of eq 4, $dm^3$ $mol^{-1}$ | $mC^3_{M^+}$, $mol^2$ $dm^{-6}$ | Reciprocal gradient $m'$ of plot of eq 5, $dm^3$ $mol^{-1}$ | $m'C^3_{M^+}$, $mol^2$ $dm^{-6}$ |
|---|---|---|---|---|
| 0.26 $NaClO_4$ | 1480 | 26.1 | 1280 | 22.5 |
| 0.41 $NaClO_4$ | 330 | 22.8 | 316 | 21.8 |
| 0.51 $NaClO_4$ | 191 | 25.4 | 181 | 24.1 |
| 0.26 $LiClO_4$ | 824 | 14.5 | 722 | 12.7 |
| 0.41 $LiClO_4$ | 240 | 16.6 | 228 | 15.7 |
| 0.51 $LiClO_4$ | 131 | 17.4 | 114 | 15.3 |

Equation 4 also leads to

$$1/f = \frac{3C^3_{M^+}}{K(C_p - 3fC_{M^{3+}})} + 1 \quad (5)$$

This relation is tested in Figure 4 which shows $1/f$ plotted against $(C_p - 3fC_{M^{3+}})^{-1}$; the reciprocal $m'$ of the gradient of the best line with unit intercept and

(13) U. P. Strauss, D. Woodside, and P. Wineman, *J. Phys. Chem.*, **61**, 1353 (1957).

(14) U. P. Strauss and P. D. Ross, *J. Amer. Chem. Soc.*, **81**, 5295, 5299 (1959).

(15) J. Bourdais, *J. Chim. Phys.*, **56**, 194 (1959).

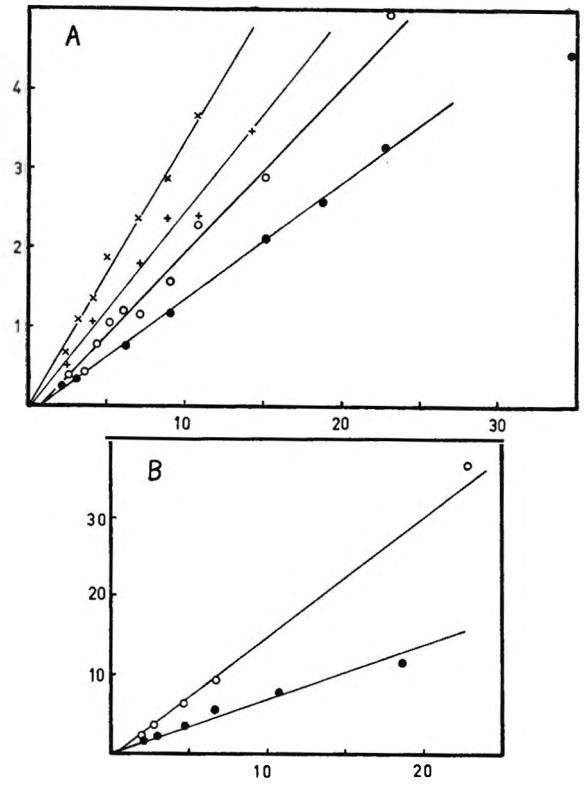


Figure 3. Test of eq 4. Ordinate: $f/(1-f)$; abscissa: (concentration of "free" carboxylate groups, $(C_p - 3fC_{M^{3+}}) \times 10^3$, monomole dm$^{-3}$; (A: -●-, 0.51 mol dm$^{-3}$ $LiClO_4$; -+-, 0.41 mol dm$^{-3}$ $LiClO_4$; -O-, 0.51 mol dm$^{-3}$ $NaClO_4$; -×-, 0.41 mol dm$^{-3}$ $NaClO_4$; B: -●-, 0.26 mol dm$^{-3}$ $LiClO_4$; -⊙-, 0.26 mol dm$^{-3}$ $NaClO_4$).

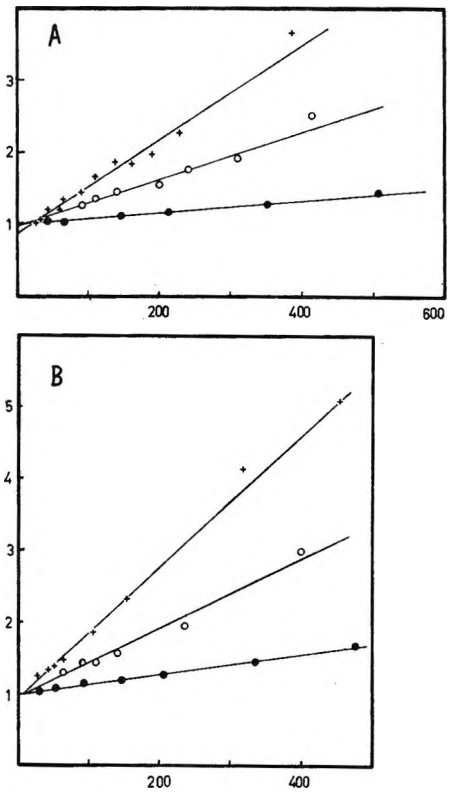


Figure 4. Test of eq 5. Ordinate: 1/f; abscissa: reciprocal of concentration of "free" carboxylate groups, $1/(C_p - 3fC_{M^{3+}})$, dm$^3$ monomol$^{-1}$. (A: -●-, $C_{Na^+} = 0.26$; -O-, 0.41; -+-, 0.51 mol dm$^{-3}$; B, -●-, $C_{Li^+} = 0.26$; -O-, 0.41; -+-, 0.51 mol dm$^{-3}$).

$m'C^3_{M^+}$ are shown for each series in columns 4 and 5 of Table I.

Because of the constancy of the figures obtained for each alkali metal, we conclude that three univalent ions are indeed released from the polymer domain during the binding of one trivalent ion, and because the "association constant" for $[Co(NH_3)_6]^{3+}$ is greater in the case of $Na^+$, we further conclude that the alkali metal cations are also site bound. (The stronger binding of $Li^+$ to the polymer cannot be explained by a model based on the interaction of the counterion's charge with the electrostatic potential well of the polyanion. An explanation of the observed dependence on ionic radius of the binding of the alkali metal cations requires the assumption that binding is to one or perhaps a few of the polymer chain's charged groups, and involves partial dehydration of the cation. There is experimental evidence for the occurrence of such a process in a number of systems. Thus the volume changes[5] accompanying the binding of $Li^+$, $Na^+$, $K^+$, $Mg^{2+}$, and $Ca^{2+}$ ions to several polyelectrolytes suggest that strongly electrostricted water is released in the binding process, almost certainly from the hydration sheath of the cation. Nmr studies[16] of solutions containing polyacrylate and $Co^{2+}$ ions show changes in the average chemical shift of the water protons attributable to the loss of water molecules from the hydrated cobalt cation when binding occurs.)

Finally, the results provide some evidence that the carboxylate groups composing a binding site are close together on the polymer molecule. If they were widely spaced and binding of a trivalent ion required the formation of large rings, then it is hard to see how up to one third of the carboxylate groups could be involved in site binding, as is observed at low polymer and perchlorate concentrations. The binding of a few trivalent ions would so severely restrict the possible conformations of the polymer chain that the requirements for the formation of more large chelate rings would prove almost impossible to meet. Thus the binding ability of the polyelectrolyte would be small and would decrease at low polymer-to-trivalent ion ratios. The plots of Figure 3 would then not be linear at low polymer concentrations.

It is hoped that studies now being carried out of hexaamminecobalt(III) binding by partly neutralized and partly esterified PAA will provide a test of this postulate.

(16) D. G. Williams and F. E. Treloar, unpublished results.

# Ion-Pair Association of Cesium and Tetraethylammonium Perchlorates in Ethanol–Acetone Mixtures at 25°

by Gianfranco Pistoia and Gianfranco Pecci

*Istituto Elettrotecnico, Università di Roma, Rome, Italy* *(Received August 20, 1969)*

Equivalent conductances of $CsClO_4$ and $Et_4NClO_4$ in the practically isodielectric mixtures ethanol–acetone are reported at 25°. The log $K_A$ *vs.* $1/D$ plot does not increase with the decrease of the dielectric constant. This is explained in terms of degradation of the ethanol structures by the added acetone and the subsequent production of simpler alcohol forms active in ionic solvation. Log $K_A$ *vs.* mixture composition plots are also reported and compared with those obtained for NaCl and CsCl in the same solvent mixtures. The Walden products, showing minima at about 70 wt % acetone, seem to confirm the occurrence of an anion–alcohol dipole relaxation effect having a maximum at this concentration.

Recent studies of Kay and coworkers on the conductivity of several alkylammonium halides in methanol and ethanol[1,2] have clearly shown the influence of the solvent on the association of ion pairs.

The effect of solvent is twofold. (a) It can stabilize the pairs due to the hydrogen bond chains in the alcohol. (b) It can solvate anions by hydrogen bonding,[3] so that the expected $K_A$ value's order (increasing with anionic radius for salts with the same cation) is inverted.

The participation of alcohols in the ion-pair formation equilibrium, therefore, should involve both steric effects and coulombic effects.

On the basis of this approach, the structure modifications of the alcoholic polymers generated by added solvents should result in a variable influence of the alcohol molecules on the ion-pair association of electrolytes. Consequently, the $K_A$ values in mixed solvents should vary with the mixture composition in a different way from that expected on the basis of the short range ion–ion interactions which depend only on the dielectric constant of the solvent.

Studies on various electrolytes in alcohol–dipolar aprotic solvent mixtures such as methanol–acetonitrile,[4] methanol–pyridine,[5] and ethanol–acetone[6] have indeed given astonishing results for $K_A$ values, explainable only by assuming that changes in the alcohol structures affect $K_A$ values much more than the changes in the dielectric constant. Particularly, in the practically isodielectric mixtures ethanol ($D$ = 24.3)–acetone ($D$ = 20.7), the plots log $K_A$ *vs.* $1/D$ for the cesium and sodium chlorides showed a minimum at a value of $1/D$ corresponding to 15–20 wt % acetone.[6] This was explained on the basis of a depolymerizing effect of acetone on ethanol and of the consequent build-up of simpler forms of the alcohol. These forms should be more efficient than the polymeric ones on the ionic solvation and, consequently, should produce lower $K_A$ values.

In this work the behavior of $CsClO_4$ and $Et_4NClO_4$ in ethanol–acetone mixtures has been investigated.

In this case also, the results indicate that in these mixtures the controlling factors for $K_A$ are, to a great extent, the changes produced on the alcohol chains by the added aprotic solvent.

## Experimental Section

$Et_4NClO_4$ (Erba reagent grade) was crystallized twice from *n*-butyl alcohol. $CsClO_4$ was prepared by double exchange reaction from CsCl and $HClO_4$ 60% (both B.D.H. Analar products) and crystallized four times from a water–methanol mixture. Both of the perchlorates were dried at 170° under vacuum ($10^{-3}$ to $10^{-4}$ mm) and were handled in a drybox.

The commercial ethanol (Erba RP product) contained about 0.1% $H_2O$ (Karl Fischer method).

After purification, following Kay's technique,[7] the water concentration was reduced to 0.004–0.005%. Its density (0.78514 g/cm$^3$) and specific conductivity (2–3 $\times$ $10^{-8}$ ohm$^{-1}$ cm$^{-1}$) were in good agreement with those reported by Kay.[7]

Acetone (Merck product) was purified by two fractional distillations on Drierite, according to the procedure recommended by Weissberger and Proskauer.[8] The water content, which initially was about 0.05–0.08%, was reduced to 0.003–0.004%. The density (0.78453 g/cm$^3$) and the specific conductivity (4–5 $\times$ $10^{-8}$ ohm$^{-1}$ cm$^{-1}$) were in good agreement with the data

(1) R. Kay, C. Zawoyski, and D. F. Evans, *J. Phys. Chem.*, **69**, 4208 (1965).

(2) D. F. Evans and P. Gardam, *ibid.*, **72**, 3281 (1968).

(3) A. Parker, *Quart. Rev.* (London), **63**, 163 (1962).

(4) F. Conti and G. Pistoia, *J. Phys. Chem.*, **72**, 2245 (1968).

(5) F. Conti, P. Delogu, and G. Pistoia, *ibid.*, **72**, 1396 (1968).

(6) G. Pistoia, *Ric. Sci.*, **38**, 1250 (1968).

(7) J. Hawes and R. Kay, *J. Phys. Chem.*, **69**, 2420 (1965).

(8) A. Weissberger and E. Proskauer, "Technique of Organic Chemistry," Vol. II, Interscience Publishers, New York, N. Y., 1963, p 382.

of Sears.[9] The instrumentation (based on a Tinsley conductivity bridge) and the dilution technique used to prepare the mixtures have been previously described.[6] The conductivity cells, obtained from a 250-cm³ erlenmeyer flask, were of the type described by Kraus[10] and standardized by solutions of KCl crystallized three times, using the Lind, Zwolenik, and Fuoss constants.[11]

A cell with a constant of (0.50265 ± 0.00006) $cm^{-1}$ was used for the mixtures rich in acetone, because of their low resistance values. For the mixtures rich in ethanol, which have higher resistance values, a cell with a constant of (0.15191 ± 0.00002) $cm^{-1}$ was used. The Parker effect was almost negligible for all the mixtures, as the difference between the value of $R$ at 1000 cps and that extrapolated to infinite frequency was equal to 0.01–0.02 % of $R$ over the range of operation.

For each set of measurements a sample of salt (100–130 mg) was directly added to solvent of known conductivity in the cell. After a constant value of $R$ was reached, 50–60 cm³ of solution was siphoned off and an equal volume of the mixture of the two solvents was added to the cell. In contrast to CsCl and NaCl in the same mixtures,[6] the salts dissolved rapidly but the equilibrium after each dilution process was reached slowly. Measurements of certain sets were not concluded in one day and this probably explains why the precision of the data, even if satisfactory as shown by $\sigma_\Lambda$ values in Table I, is slightly inferior to that obtained with NaCl and CsCl.

The ir spectra were obtained with a Perkin-Elmer spectrophotometer Model 337 using air as reference and a regular slit.

## Results

The physical properties of the mixtures examined are shown in Table II. Dielectric constants ($D$) and viscosities ($\eta$) were obtained by interpolation from the data of Celiano[12] and Dunstan,[13] respectively. Densities ($d$) were obtained by interpolation of data determined in this laboratory. The equivalent conductivities ($\Lambda$) and the corresponding concentrations in equivalents/liter are reported in Table III.

The data were analyzed by a UNIVAC 1108 computer using the Fuoss–Onsager[14] equation in the form

**Table I:** Derived Constants

| No. | $\Lambda_0$ | $K_\Lambda$ | $a$, Å | $\sigma_\Lambda$ |
|---|---|---|---|---|
| | | $CsClO_4$ | | |
| 1 | 98.6 ± 0.1 | 263 ± 16 | (10 ± 2) | 0.004 |
| 2 | 136.4 ± 0.3 | 177 ± 10 | 4.3 ± 0.3 | 0.008 |
| 3 | 145.7 ± 0.2 | 173 ± 7 | 4.3 ± 0.2 | 0.01 |
| 4 | 162.2 ± 0.3 | 154 ± 5 | 3.9 ± 0.1 | 0.01 |
| 5 | 199.9 ± 0.2 | 223 ± 4 | 3.7 ± 0.1 | 0.01 |
| | | $Et_4NClO_4$ | | |
| 6 | 68.0 ± 0.2 | 164 ± 14 | 4.0 ± 0.9 | 0.01 |
| 7 | 110.8 ± 0.2 | 74 ± 8 | 3.9 ± 0.3 | 0.01 |
| 8 | 135.5 ± 0.2 | 69 ± 9 | 4.2 ± 0.3 | 0.01 |
| 9 | 153.1 ± 0.3 | 62 ± 9 | 4.0 ± 0.3 | 0.01 |
| 10 | 198.8 ± 0.1 | 84 ± 3 | 4.5 ± 0.1 | 0.01 |

**Table II:** Properties of Ethanol–Acetone Mixtures at 25°

| Wt % $CH_3COCH_3$ | $D$ | $\eta$ poise | $d$, g/ml |
|---|---|---|---|
| 30.24 | 21.90 | 0.00625 | 0.78615 |
| 54.70 | 20.75 | 0.00445 | 0.78594 |
| 61.40 | 20.60 | 0.00415 | 0.78584 |
| 74.10 | 20.35 | 0.00372 | 0.78552 |
| 100.00 | 20.70 | 0.00305 | 0.78453 |
| 5.90 | 23.70 | 0.00980 | 0.78577 |
| 36.30 | 21.55 | 0.00565 | 0.78611 |
| 51.80 | 20.85 | 0.00460 | 0.78598 |
| 64.08 | 20.50 | 0.00405 | 0.78578 |
| 93.70 | 20.50 | 0.00325 | 0.78487 |

**Table III:** Conductance of $CsClO_4$ (No. 1–5) and $Et_4NClO_4$ (No. 6–10) in Ethanol–Acetone Mixtures at 25°

| $10^4c$, equiv/l. | $\Lambda$, ohm$^{-1}$ cm² equiv$^{-1}$ | $10^4c$, equiv/l. | $\Lambda$, ohm$^{-1}$ cm² equiv$^{-1}$ | $10^4c$, equiv/l. | $\Lambda$, ohm$^{-1}$ cm² equiv$^{-1}$ |
|---|---|---|---|---|---|
| 1 | | 5 | | 8 | |
| 8.144 | 81.594 | 39.900 | 122.480 | 20.605 | 105.546 |
| 6.656 | 83.250 | 33.725 | 126.830 | 13.877 | 110.610 |
| 5.605 | 84.566 | 25.710 | 133.848 | 10.037 | 114.323 |
| 3.921 | 87.080 | 22.410 | 137.340 | 7.509 | 117.347 |
| 2.929 | 88.870 | 22.169 | 137.583 | 5.694 | 119.815 |
| 2 | | 18.550 | 142.102 | 9 | |
| 22.212 | 97.541 | 15.320 | 146.839 | 24.061 | 117.317 |
| 16.148 | 102.550 | 10.510 | 155.545 | 19.010 | 120.940 |
| 13.494 | 105.240 | 8.070 | 161.190 | 15.751 | 123.656 |
| 11.401 | 107.652 | 6 | | 10.581 | 128.899 |
| 9.208 | 110.599 | 22.839 | 49.768 | 7.968 | 132.263 |
| 3 | | 17.297 | 51.947 | 10 | |
| 24.206 | 102.801 | 12.603 | 54.275 | 20.519 | 153.693 |
| 17.256 | 108.530 | 10.195 | 55.733 | 16.713 | 157.662 |
| 13.146 | 112.893 | 8.686 | 56.733 | 12.828 | 162.500 |
| 9.912 | 117.121 | 7 | | 9.560 | 167.470 |
| 7.604 | 120.818 | 27.609 | 82.861 | 7.957 | 170.298 |
| 4 | | 22.033 | 85.504 | | |
| 32.085 | 109.066 | 14.697 | 89.928 | | |
| 23.585 | 115.132 | 11.560 | 92.340 | | |
| 17.111 | 121.296 | 8.724 | 94.841 | | |
| 12.184 | 127.347 | | | | |
| 10.160 | 130.374 | | | | |

(9) P. Sears, E. Wilhoit, and L. Dawson, *J. Phys. Chem.*, **60**, 169 (1956).

(10) H. Daggett, E. Bair, and C. Kraus, *J. Amer. Chem. Soc.*, **73**, 799 (1951).

(11) J. Lind, J. Zwolenik, and R. Fuoss, *ibid.*, **81**, 1557 (1959).

(12) A. Celiano, P. Gentile, and M. Cefola, *J. Chem. Eng. Data*, **7**, 391 (1962).

(13) A. Dunstan, *J. Chem. Soc.*, **85**, 817 (1904).

(14) R. Fuoss and F. Accascina, "Electrolytic Conductance," Interscience Publishers, Inc., New York, N. Y., 1959, p 234.

$$\Lambda = \Lambda_0 - S(c\gamma)^{1/2} + Ec\gamma \log (c\gamma) + (J - B\Lambda_0)c\gamma - K_A c\gamma f^2 \Lambda \quad (1)$$

The term $B$ which accounts for the viscosity increment due to the added salt was assumed to be equal to 0.0 for $CsClO_4$ and 0.5 for $Et_4NClO_4$, the latter value having been used in the methanol–pyridine mixtures[5] for the same salt. It has already been pointed out that $B$ does not appreciably influence the $\Lambda_0$ and $K_A$ values.[1] Choosing system number 9 as a control, it was found that on varying $B$ from 0.0 to 0.5, $\Lambda_0$ remained unchanged while $a$ and $K_A$ varied 1.2% and 0.2%, respectively, values much less than experimental errors.

Table I shows the values of the derived constants $\Lambda_0$, $K_A$, and $a$ together with $\sigma_\Lambda$, the average of the percentage differences between the experimental values of $\Lambda$ and the ones calculated by (1).

It was not possible to measure the conductivity of $CsClO_4$ in a mixture containing more than 70 wt % acetone because of the extremely low solubility of the salt in ethanol.

The $a$ value for $CsClO_4$ in the mixture containing 30 wt % acetone, (10 ± 2) Å, is extremely high. Similar high values of $a$ have already been obtained for alkali and alkylammonium halides in various solvents.[15,16] $K_A$ for $Et_4NClO_4$ in pure ethanol was obtained from recalculation of the data of Hartley.[17]

## Discussion

Figure 1 shows the behavior of the log $K_A$ for the two perchlorates *vs.* $1/D$. The dotted lines were obtained by using the theoretical equation[14]

$$K_A = K_0 \exp(e^2/aDkT) \quad (2)$$

where $a$ is 4.1 Å for $CsClO_4$ and 6.4 Å for $Et_4NClO_4$.

Examination of the curves shows the following two characteristics. (1) Log $K_A$ does not linearly increase with $1/D$, as expected on the basis of eq 2, and both the perchlorates show two $K_A$ values for the same $1/D$ (because of the slight minimum in the $D$ *vs.* mixture composition plot, systems number 5 and number 10 have the same $1/D$ of systems at less acetone concentration). (2) In the ethanol-rich mixtures the log $K_A$ values are appreciably greater than those calculated theoretically, this being more marked for $Et_4NClO_4$ than for $CsClO_4$. In particular, $K_A$ for $Et_4NClO_4$ in pure ethanol is one order of magnitude greater than that obtained from eq 2 and, in spite of the higher $D$, it is greater than the extrapolated value in pure acetone.

The peculiar variations of the $K_A$ values with the changes in the composition of the mixtures are further evident in Figure 2. At a concentration of 60–70 mol % acetone ($D \simeq 20.4$) the curves show a minimum. For comparison the curves of NaCl and CsCl in ethanol–acetone mixtures[6] are also reported. These curves,

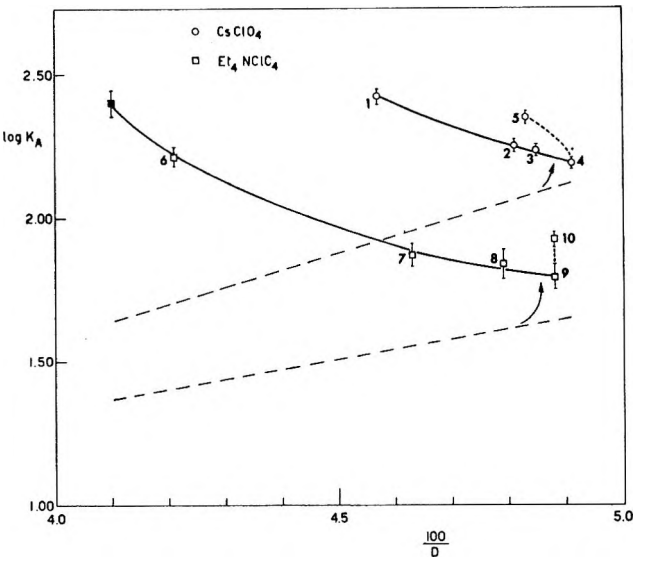


Figure 1. Dependence of association constants on dielectric constant: dotted lines, association constants calculated from eq 2; ■, Hartley's datum.[17]

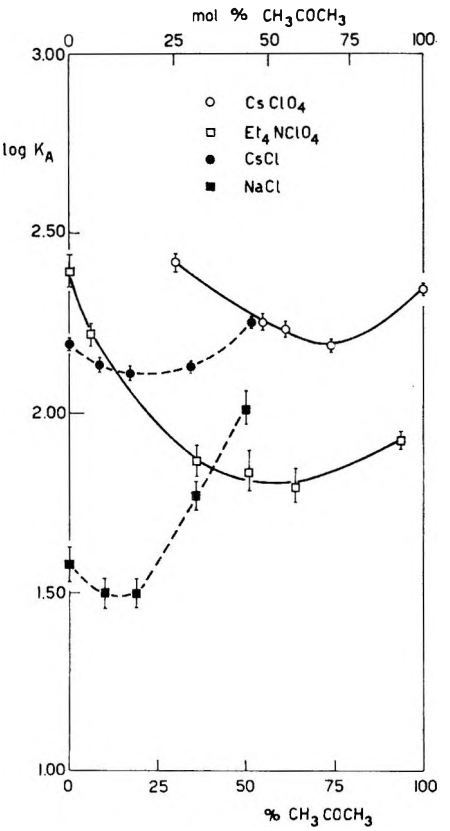


Figure 2. Dependence of association constants on mixture composition.

(15) P. Walden, H. Ulich, and G. Busch, *Z. Phys. Chem.*, **123**, 429 (1926).

(16) A. Harkness and H. Daggett, *Can. J. Chem.*, **43**, 1215 (1965).

(17) M. Barak and H. Hartley, *J. Phys. Chem.* (Leipzig), **A165**, 273 (1933).

covering only half the composition range because of the low solubility of the chlorides in acetone, show minima too at concentration values close to 15 mol % acetone.

The observed behavior is clearly to be ascribed not so much to changes in $D$, which for the most part varies directly with the composition of the mixtures, but to modifications produced on the ethanol structures by the acetone additions and therefore to the varying influence of the solvent on the ion-pair formation.

Ethanol is a solvent highly associated by hydrogen bonds with polymeric aggregates similar to those present in methanol.[18,19] As suggested by Kay for various alkylammonium halides in methanol,[1] it is possible that pure ethanol can stabilize the pairs formed by the two perchlorates as the result of the molecular chains created by hydrogen bondings. In any case, it cannot be assumed that appreciable ionic solvation, which should be of the ion–dipole type for the salts examined,[20] takes place in pure ethanol, due to the large size of the ions and to the low number of active alcohol forms in ionic solvation. Therefore the factors which stabilize the ion pairs seem to dominate those which hinder them.

The addition of acetone, an aprotic solvent having a relatively high dielectric constant, induces alcohol depolymerization with production of less associated forms. Ir spectra obtained in our laboratory on some ethanol–acetone mixtures show (Figure 3) a progressive decrease in intensity of the absorption band of the polymeric alcohol (at 3440–3500 $cm^{-1}$) with increasing acetone concentration. The ir spectra also show the absence, even at high acetone concentrations, of the characteristic band of the free monomer (at about 3630 $cm^{-1}$),[18] noted also by Freymann.[21]

The sharp band at 3400 $cm^{-1}$ (absent in a $C_2H_5OH$–$CCl_4$ mixture having a similar alcohol content) can be ascribed to the formation of mixed associated species, as already pointed out by previous Raman[19,22] and ir[21,23] studies. Ethanol and acetone can interact by hydrogen bondings to produce a one-to-one complex[19] $(CH_3)_2—C=O\rightarrow H—O—C_2H_5$.

This interaction, though contributing to the degradation of the alcohol structure, also creates mixed associated forms, thus limiting the concentration of free monomers.

The decrease of the association constants with decreasing ethanol concentration could therefore be explained by both the progressive reduction of the ethanol structures which stabilize the ion pairs and by the onset of a type of ionic solvation by the simpler forms of the alcohol. This solvation, as suggested by pmr measurements on $CsClO_4$ and $Et_4NClO_4$ in methanol,[24] should be related mainly to the anion and should be of the anion–alcohol dipole type,[20] considering the weak tendency of acetone to solvate anions.[3]

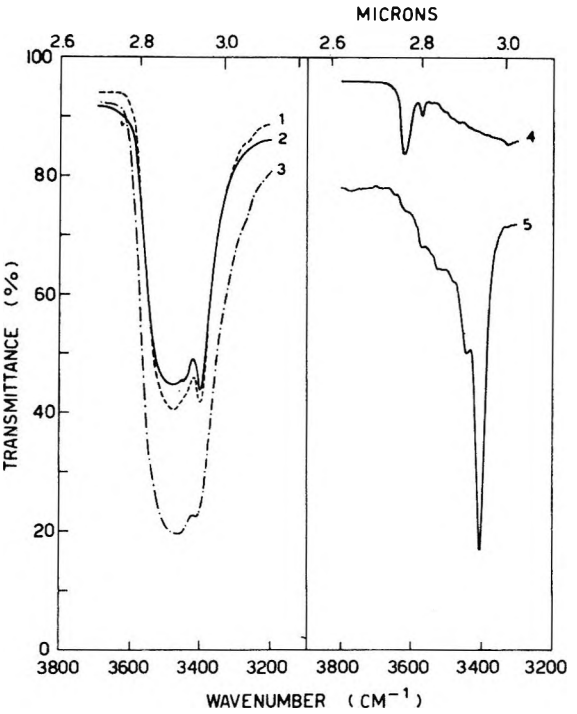


Figure 3. Infrared absorption spectra of some ethanol–acetone mixtures (mol % acetone: 1, 93.8; 2, 96.5; 3, 87.8; 5, 99.4), plus one ethanol–carbontetrachloride mixture for comparison (4, 98.7 mol % $CCl_4$). Cell path 0.05 mm for left side curves and 0.1 mm for right side curves.

At acetone concentration values of 60–70 mol %, the factors which stabilize the ion pairs seem to reach a minimum and after exceeding this concentration, the curves (Figure 2) begin to rise toward the log $K_A$ values of the salts in pure acetone.

A similar behavior occurs for NaCl and CsCl, for which minima in the log $K_A$ *vs.* mixture composition plots are seen at low concentration of added acetone. The $K_A$ values for the chlorides, however, are influenced by the change of the solvent composition in a different way from those of the perchlorates. In fact, for the former, one must consider both the absence or the relative unimportance of stabilizing effect on the ion pairs[6] and that, while the solvation of large ions is mainly determined by the dipole moment of the alcohol,[20] for small ions such as $Cl^-$ the solvation is mainly of the hydrogen bonding type.[3]

The Walden product of the perchlorates shows a minimum (much more pronounced for $Et_4NClO_4$) at about 65–75 wt % acetone (Figure 4), despite the

(18) E. Becker in "Hydrogen Bonding," Pergamon Press, London, 1959, p 152.

(19) A. Sundara Rao, *J. Indian Chem. Soc.*, **22**, 260 (1945).

(20) R. Kay, B. Hales, and G. Cunningham, *J. Phys. Chem.*, **71**, 3925 (1967).

(21) M. Freymann and R. Freymann, *Bull. Soc. Chim.*, **4**, 944 (1937).

(22) P. Puranik, *Proc. Indian Acad. Sci.*, **37A**, 499 (1953).

(23) W. Gordy, *Phys. Rev.*, **50**, 1151 (1936).

(24) R. Butler and R. Symons, *Chem. Commun.*, **2**, 71 (1969).

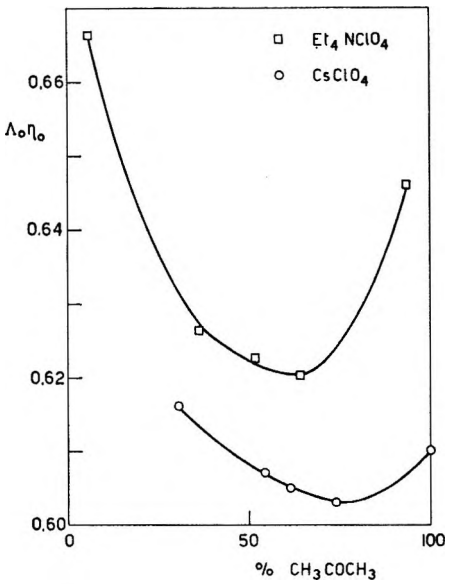


Figure 4. Walden products *vs.* mixture composition.

fact that $\eta$ is a directly varying function of the mixture composition. This seems to confirm the existence of an anion–alcohol dipole relaxation phenomenon which increases with increasing acetone concentration up to about 70 wt %.

As already found in pure ethanol,[25] $Cs^+$ has a mobility slightly less than that of $Et_4N^+$ in the ethanol–acetone mixtures, while for these large ions the order expected on the basis of the crystallographic radii (1.7 Å for $Cs^+$ and 4.0 Å for $Et_4N^+$) might be expected.

On the other hand, the average contact distance $a$, obtained from (1), is equal for the two salts (4.1 Å), thus indicating that the actual radius in solution of the $Et_4N^+$ ion is similar to that of the $Cs^+$ ion.

The $a$ value for $Et_4NClO_4$, very low with respect to the crystallographic datum (6.4 Å), is comparable with the (4.2 ± 0.2) Å value found by Evans[2] for several alkylammonium halides in ethanol.

## Conclusion

The results of the present investigation and those obtained from the studies on association constants of $KClO_4$ and $CsClO_4$ in methanol–acetonitrile,[4] $Et_4NClO_4$ in methanol–pyridine,[5] NaCl and CsCl in ethanol–acetone,[6] permit the following observations. (a) For none of the salts examined in these alcohol–dipolar aprotic solvent mixtures does log $K_A$ linearly increase with $1/D$, as expected from the theoretical eq 2. (b) All the salts show a minimum in the $K_A$ *vs.* mixture composition plots (a discontinuity for $CsClO_4$ in $CH_3OH$–$CH_3CN$ mixtures).[4] The position of this minimum in a given mixture depends on the specific electrolyte. In particular, in ethanol–acetone mixtures the minimum does not vary significantly, for a given anion, as the cation is changed.

These results confirm that the discontinuity of the solvents in the area near the ions produces anomalous $K_A$ values when the structure of the solvent which more strongly affects these values is drastically changed by addition of another solvent of relatively high dielectric constant.

(25) R. Kay and D. F. Evans, *J. Phys. Chem.*, **70**, 2325 (1966).

# Heats of Mixing. I. Temperature Dependence of Aqueous Electrolytes with a Common Anion[1]

by Henry L. Anderson and Linda A. Petree

*Department of Chemistry, University of North Carolina at Greensboro, Greensboro, North Carolina 27412*
*(Received September 4, 1969)*

The heats of mixing of $LiCl-(CH_3)_4NCl-H_2O$, $KCl-(CH_3)_4NCl-H_2O$, $LiCl-KCl-H_2O$, $LiCl-NaCl-H_2O$, $HCl-NaCl-H_2O$, and $NaCl-KCl-H_2O$ at constant total ionic strength have been measured at 40, 60, and 80°. The first three mixtures had heats of mixing independent of the temperature whereas the latter three had heats of mixing dependent on the temperature. The results have been interpreted in terms of the solute–solvent structural properties.

## Introduction

Aqueous electrolyte solutions have received considerable attention in recent years with much of this attention being stimulated by the need to develop an efficient and relatively inexpensive method of converting sea water to potable water.

Over the years, a wealth of experimental and theoretical information has been amassed concerning electrolyte solutions and from an *a priori* point of view the Debye–Hückel limiting law has been firmly established. Unfortunately, efforts to make *a priori* calculations of thermodynamic properties of electrolyte solutions in real concentration ranges often fall short of the desired level of understanding. A large contribution to this lack of success can be attributed to an incomplete understanding of the specific role water plays in influencing ionic interactions in aqueous solutions.[2]

Recently,[3] it has been shown that determination of the excess thermodynamic properties of aqueous mixed electrolyte solutions is an excellent way of studying specific ion interactions. For example, mixing aqueous salt solutions at constant ionic strength, $I$, according to the scheme

$$MX(I) + NX(I) \rightarrow \text{mixture}(I)$$

has the advantage of canceling effects due to the ionic atmosphere. Further, in the presence of a common ion (*e.g.*, the common "X" anion) the effects due to oppositely charged pair interactions cancel, and one observes phenomena due only to like-charged pair and higher order interactions.

Young, Wu, and Krawetz[4] observed that for common ion mixtures the sign of the heat of mixing could be predicted by classifying the ions into two groups. When ions of like classification are mixed, the heat of mixing is endothermic and when ions of unlike classification are mixed, the heat of mixing is exothermic. Wood and Anderson[5,6] have shown that this classification should be made on the basis of the ion–water structural relationship. They used the classification of Frank, Evans, and Wen[7,8] where an ion is classified as either a structure maker or a structure breaker.

In order to gain more specific information concerning the nature of the solute–solvent interaction, the present work was undertaken. Since water structure is strongly temperature dependent,[9] the temperature dependence of the heats of mixing should shed considerable light on the role water plays in determining the nature of the specific ion interactions upon mixing.

There has been considerable discussion in the literature concerning the nature of specific ion interactions. On the one hand, the Brønsted specific ion interaction principle has been defended by Scatchard[10] and on the other hand it has been refuted by Friedman[11] and Wood and coworkers.[3,12] Stern and coworkers[13,14] measured the heat of mixing of $HCl-NaCl-H_2O$ and $HCl-KCl-H_2O$ from 0 to 40°. Both mixtures showed a decrease in absolute magnitude in the heat of mixing as tempera-

(1) This study was aided by a grant from the Office of Saline Water, U. S. Department of the Interior.

(2) See, for example, J. L. Kavanau, "Water and Solute-Water Interactions," Holden-Day, Inc., San Francisco, Calif., 1964.

(3) R. H. Wood and R. W. Smith, *J. Phys. Chem.*, **69**, 2974 (1965).

(4) T. F. Young, Y. C. Wu, and A. A. Krawetz, *Discuss. Faraday Soc.*, **24**, 37 (1957).

(5) R. H. Wood and H. L. Anderson, *J. Phys. Chem.*, **71**, 1869 (1967).

(6) R. H. Wood and H. L. Anderson, *ibid.*, **71**, 1871 (1967).

(7) H. S. Frank and M. W. Evans, *J. Chem. Phys.*, **13**, 507 (1945).

(8) H. S. Frank and W. Y. Wen, *Discuss. Faraday Soc.*, **24**, 133 (1957).

(9) Seef for example: (a) G. E. Walrafen, *J. Chem. Phys.*, **36**, 1035 (1962); (b) O. D. Bonner and G. B. Woolsey, *J. Phys. Chem.*, **72**, 899 (1968).

(10) G. Scatchard, *J. Amer. Chem. Soc.*, **83**, 2636 (1961).

(11) H. L. Friedman, *J. Chem. Phys.*, **32**, 1134 (1960).

(12) R. H. Wood and H. L. Anderson, *J. Phys. Chem.*, **70**, 992 (1966).

(13) J. H. Stern and A. A. Passchier, *ibid.*, **67**, 2420 (1963).

(14) J. H. Stern, C. W. Anderson, and A. A. Passchier, *ibid.*, **69**, 207 (1965).

ture increased, although the former did so at a much larger rate than the latter. Stern and coworkers discussed their heats of mixing data in terms of deviations from the Brønsted specific ion interaction principle. They interpreted the decrease in the heats of mixing as temperature increased as a reduction in the deviation from the specific ion interaction principle approaching the Brønsted prediction of a zero heat of mixing. They recognized that 40° was not a high enough temperature to make a prediction as to whether or not the heat of mixing would actually go to zero.

The present work was designed to go to higher temperatures to see if in fact the heat of mixing does decrease to zero as temperature is increased.

## Experimental Section

*Calorimeter.* Common ion heats of mixing are quite small (10–40 cal/kg of solvent for the mixtures in this study) and require a solution calorimeter having a sensitivity in the microdegree range. Because of the required sensitivity it was decided to set an upper limit of 80° in this initial investigation.

A schematic diagram of the calorimeter constructed for this research is given in Figure 1. The "double calorimeter"[15] construction has an advantage in that twice as many experiments can be performed during a given run. This is especially advantageous when experiments are carried out at temperatures greatly different from ambient temperatures, because considerable time is spent in bringing the calorimeter to the desired experimental temperature.

Although the calorimeter incorporates many of the ideas presented elsewhere,[16,17] its configuration from the point of view of high-temperature utility and simplicity warrants some comment.

The calorimeter consisted of a 240-ml dewar flask[18] (I) cemented with silicon rubber cement to a brass collar (D). The collar was bolted to a brass lid (C) and sealed with a rubber "O ring" (K). The brass lid was silver-soldered to the brass superstructure (B). Each lid supported a stirrer bearing (L), a calibration (G) and rough heater (F), thermistor probe (E), and a pipet holder (H). All of the probes (except the stirrer) exited the calorimeter *via* the superstructure and were protected from the water bath. The portion of the superstructure directly attached to the lid was a half-cylinder (B). The stirrer bearing (precision-bore 5-mm glass tubing) was housed outside the half-cylinder, allowing the heat generated during stirring to dissipate directly into the water bath. The stirrer was mounted off-center so that a large pipet could be used. The pipets consisted of 15 × 65 mm glass tubing blown out on two sides. Each end of the pipet had a Teflon sleeve attached with epoxy cement and sealed with Teflon plugs equipped with "O rings" which fit into the Teflon sleeves. The Teflon plugs were attached to a 3-mm glass tube by epoxy cement. A 5-mm glass tube

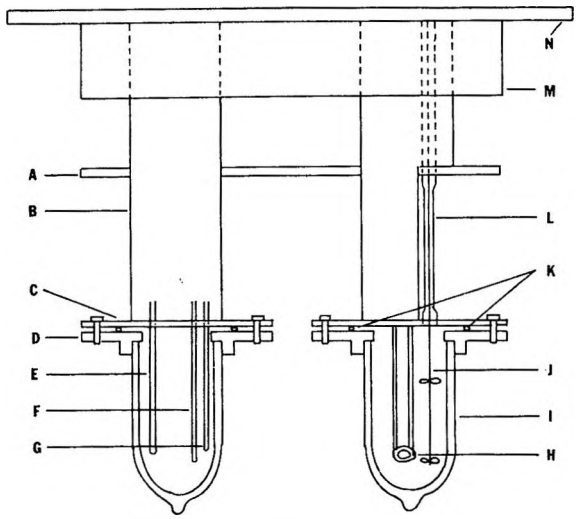


Figure 1. A schematic diagram of the calorimeter: A, 12 × 8 × 1/4 in. brass plate; B, half-cylinder brass superstructure; C, brass lid; D, brass collar; E, thermistor; F, rough heater; G, calibration heater; H, Teflon pipet support; I, 10-oz dewar flask,[18] J, glass stirrer; K, "O rings"; L, 5-mm precision-bore bearing; M, styrofoam; N, 20 × 12 × 1/2 in. plywood. Note: right calorimeter is rotated 90°.

was attached to the pipet plunger above the lid and exited through a 5-mm precision-bore glass bearing. The pipets were supported in the vessel by a Teflon ring suspended from the lid by Teflon-coated wire. To establish pressure equilibrium, a small capillary venting tube was mounted in the top Teflon plug. The pipets had a volume of approximately 17 ml and during the course of this work gave heats of opening varying between 0.000 and 0.008 ± 0.004 cal. (For some of the 80° work the heat of opening was as high as 0.034 ± 0.008 cal.)

The temperature monitoring was performed with a 10-kilohm thermistor using a bridge similar to that described by Jeckel, Criss, and Cobble.[16] The calibration heat circuit was identical with that described by Wood, *et al.*[17]

In designing the calorimeter, every effort was made to keep the volume of space above the solution in the calorimeter to a minimum so as to minimize the loss of solvent on reaching vapor equilibrium at the higher temperatures.

The experimental procedure for carrying out heats of mixing has been reported in the literature by several authors.[3,4] The calibration of the chemical heat of mixing is performed by comparing each individual heat of mixing experiment with a known amount of heat

(15) Two identical, independent calorimeters mounted on a common superstructure.

(16) E. C. Jeckel, C. M. Criss, and J. W. Cobble, *J. Amer. Chem. Soc.*, 86, 5404 (1964).

(17) R. H. Wood, H. L. Anderson, J. D. Beck, J. R. France, W. E. deVry, and L. J. Soltzberg, *J. Phys. Chem.*, 71, 2149 (1967).

(18) Thermos replacement filler No. 50 F, The American Thermos Bottle Co., Norwich, Conn.

**Table I:** Aqueous Heats of Mixing Parameters

| Mixture | $I$ | 25° $RTh_0$ | 40° $RTh_0$ | 40° $RTh_1$ | 60° $RTh_0$ | 60° $RTh_1$ | 80° $RTh_0$ | 80° $RTh_1$ |
|---|---|---|---|---|---|---|---|---|
| LiCl–KCl | 1.0 | −64.2[a] | −63.9 ± 0.7 | −3.3 ± 1.0 | −63.0 ± 0.3 | −2.8 ± 0.5 | −61.1 ± 1.6 | 4.7 ± 2.3 |
| LiCl–$(CH_3)_4NCl$ | 0.5 | −160.8[b] | −157.1 ± 1.9 | −5.5 ± 2.8 | −161.3 ± 1.5 | −6.6 ± 2.1 | −162.8 ± 4.5 | ... |
| KCl–$(CH_3)_4NCl$ | 0.5 | 118.9[b] | 118.4 ± 1.0 | ... | 114.7 ± 1.4 | ... | 112.9 ± 6.5 | ... |
| NaCl–KCl | 1.0 | −38.1[c] | −36.6 ± 0.4 | ... | −35.1 ± 0.3 | ... | −31.2 ± 0.6 | ... |
| LiCl–NaCl | 1.0 | 84[a] | 64.2 ± 0.3 | 3.8 ± 0.4 | 44.5 ± 0.4 | 2.4 ± 0.6 | 33.0 ± 1.1 | ... |
| HCl–NaCl | 1.0 | 124[c] | 112.3 ± 0.8 | 8.0 ± 1.0 | 95.5 ± 1.1 | 5.6 ± 1.4 | 82.2 ± 1.1 | 3.6 ± 1.5 |

[a] R. H. Wood and R. W. Smith, *J. Phys. Chem.*, **69**, 2974 (1965). [b] R. H. Wood and H. L. Anderson, *ibid.*, **71**, 1871 (1967). [c] Y. C. Wu, M. B. Smith, and T. F. Young, *ibid.*, **69**, 1868 (1965).

provided by a calibration heater. To check the validity of the calibration heaters a chemical experiment of a known heat of reaction was determined. The calibration was performed with the neutralization of tris(hydroxymethyl)aminomethane (Tris) by hydrochloric acid at 25°. The neutralization was carried out according to the procedure outlined and discussed by Gunn.[19] Four determinations resulted in a value of 59.0 ± 0.1 cal/g of THAM. This compares with Gunn's value of 58.67 cal/g of Tris.

*Materials.* Approximately 5 *m* stock solutions of Mallinckrodt sodium chloride, hydrochloric acid, and potassium chloride, Research Inorganic Chemical lithium chloride, and Eastman tetramethylammonium chloride were prepared and analyzed as described previously[3,20] and stored in polyethylene bottles.

*Results and Treatment of Data.* The experimental heats of mixing were fitted by the method of least squares to the equation[11]

$$\Delta_m H \text{ (cal/kg of solvent)} = RTI^2y(1 - y)[h_0 + (1 + 2y)h_1] \quad (1)$$

where $R$ is the universal gas constant, $T$ is the temperature, $I$ is the total molal ionic strength, $y$ is the mole fraction of the component having the largest formula weight, $h_0$ is the magnitude of the interaction, and $h_1$ is a measure of asymmetry from the quadratic relation with respect to mole fraction.

The parameters for eq 1 are listed in Table I. In general, $RTh_1$ is very small compared to $RTh_0$. A statistical "F" test (95% confidence level) was performed on each mixture to test for the significance of $RTh_1$. In those cases where the inclusion of $RTh_1$ was not justified, $RTh_1$ was set equal to zero and the data were refitted using just $RTh_0$.

For each determination of the heat of mixing, from 10 to 16 experimental determinations were made between 0–0.2 and 0.8–1.0 mol fraction. It has been shown[3,4] that this is sufficient to determine the mixing parameters.

## Discussion

The heats of mixing of symmetrical mixtures of electrolytes at constant ionic strength have been studied extensively at 25°.[3-6,12-14,20,21] In the concentration range of 0.1–1.0 *m* total strength, the magnitude of the skew term, $RTh_1$, is small. In fact, the mole fraction at the maximum heat of mixing ($y$ at $d(\Delta_m H)/dy = 0$) for all known mixtures lies between 0.47 and 0.53 mole fraction unit. For the mixtures studied in this work, similar results have been obtained indicating that those interactions contributing to skew do not gain in importance at higher temperatures. In terms of the conclusions drawn by Wood and Anderson[12] concerning skew this means that triplet interactions involving like-charged ions or higher order interactions do not gain in importance at the higher temperatures. In fact, since the heats of mixing do not change dramatically with

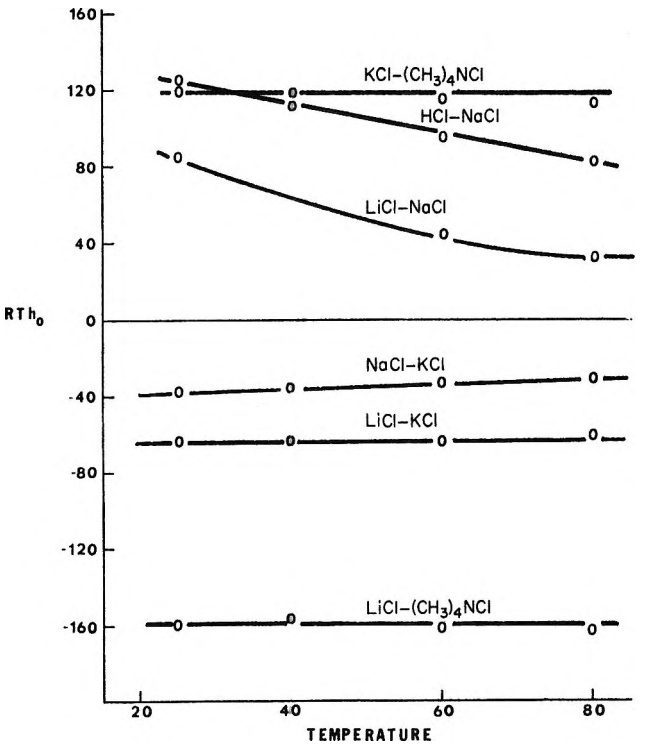


Figure 2.

(19) S. R. Gunn, *J. Phys. Chem.*, **69**, 2902 (1965).
(20) R. H. Wood and H. L. Anderson, *ibid.*, **71**, 1871 (1967).
(21) J. H. Stern and C. W. Anderson, *ibid.*, **68**, 2528 (1964).

temperature, one can conclude that whatever the interactions are, they are changing only in degree rather than in kind.

*Solute–Solvent Structure.* The temperature dependence of the heats of mixing is best illustrated by Figure 2. For three of the mixtures ($LiCl–KCl–H_2O$, $LiCl–(CH_3)_4NCl–H_2O$, $KCl–(CH_3)_4NCl–H_2O$) the heats of mixing are constant within experimental error. This means that each of the excess free energies of mixing for these three systems is a simple linear function in temperature which can be represented as

$$\Delta_m G^E(t_2) = \Delta_m G^E(t_1) - \Delta_m S^E(t_1)\Delta T \qquad (2)$$

by simplifying eq 3 as given below. This suggests that the water–solute structural interactions or mixing are temperature independent for these systems, indicating that the interaction energies are greater than the available thermal energy. These three mixtures involve three rather different ions in that $Li^+$ is a small structure-making ion, $K^+$ is a medium-sized structure-breaking ion, and $(CH_3)_4N^+$ is a large structure-breaking ion. It seems unreasonable to expect for such a diversity of mixings that the lack of temperature dependence in the heats of mixing is accidental. It is always tempting to explain one's experimental observations on a molecular level, the present authors included.[22]

Previous interpretations of the heats of mixing of electrolyte solutions at 25° have been made using the Frank–Evans–Wen[7,8] structure-making, structure-breaking model for ions in water. This model assumes the ions to be surrounded immediately by a region of structure-made (water strongly associated with the ion, *i.e.*, the primary hydration sphere), followed by a region of structure-broken water lying between the structure-made water around the ion and the bulk water.

The present results can be explained by the Frank–Evans–Wen model by assuming that the specific interactions observed upon mixing involve ion–solvent interactions in the region of the primary hydration sphere. For reasons that will be mentioned later, it is suggested that the water involved in these interactions is in the region of the interface between the primary hydration sphere and the disordered water in the structure-broken region.

The assumption that the interactions have to occur in the region of the primary hydration sphere is based upon the insensitivity of this primary hydration sphere to temperature. Walrafen[9a] has shown by Raman investigations in this temperature range that the primary hydration sphere of ions appears to be temperature independent. On the other hand, it is well recognized that bulk water structure is reasonably temperature sensitive. For example, Bonner and Woolsey[9b] have estimated that the amount of unstructured water (monomer water) increases by about 50% in the 25–80° temperature range.

The reason for suggesting that the interactions probably occur at the interface between the structure-made and structure-broken region is based on the results of the mixings $HCl–NaCl–H_2O$, $LiCl–NaCl–H_2O$, and $NaCl–KCl–H_2O$. All three of these mixtures show a temperature dependence outside of the experimental error (see Figure 2.). For two of the systems this dependence is large, although there does not appear to be a tendency for these systems to go to zero within any reasonable temperature. All three of these mixtures involve the sodium ion, which has been recognized as a borderline ion in the structure-making, structure-breaking classification scheme. For example, Frank and Evans[7] considered the sodium ion to be a structure breaker (entropy of hydration argument), whereas from fluidity measurements[23] the sodium ion is classified as a structure maker. It seems plausible that the interface between the structure-making and structure-breaking region is less well defined and susceptible to temperature changes. This, of course, would be reflected in the heats of mixing. The explanation based on this work can only be tentative, but currently a wider variety of ions is being investigated by the present method to test the validity of the conclusions drawn.

*Thermodynamics.* The results of this work can be used to calculate the temperature variation of the excess free energy of mixing. For example, one can write[24]

$$\Delta_m G^E(t_2) = \Delta_m G^E(t_1) + \Delta_m C_p]_{t_1}^{t_2}\Delta T - \Delta_m S^E(t_1)\Delta T - T_2\Delta_m C_p]_{t_1}^{t_2} \ln (T_2/T_1) \qquad (3)$$

where

$$\Delta_m C_p = \frac{\Delta_m H(t_2) - \Delta_m H(t_1)}{\Delta T}$$

The $\Delta_m C_p$ values can be determined directly from the present results. In order to calculate $\Delta_m G^E(t_2)$ one needs $\Delta_m G^E(t_1)$ at some reference temperature.

There have been a number of investigations of the activities of mixed electrolyte solutions, with most of the information coming from emf measurements of $HX–MX_n–H_2O$ mixtures where X is a halide and M is an alkali or alkaline earth cation or from isopiestic measurements of $MX–NX–H_2O$ mixtures. Extreme care is required in both methods in order to obtain reliable

(22) Thermodynamic measurements do not provide for a method of looking at molecular structure in the same sense that one "sees" structure by spectroscopic methods. One should quite properly expect that structure in electrolyte solutions should depend on the time scale of the experimental probe. Compared to spectroscopic measurements, the time scale of free energies or enthalpies of mixed electrolyte solutions is, of course, infinite. Keeping this in mind, it is not surprising to find that there are widely diverging pictures concerning the structure of electrolyte solutions.[2] It is necessary to discover the important structural features from a thermodynamic point of view because any *a priori* calculation of thermodynamic properties of electrolyte solutions is going to have to account for these features. Of course, the ultimate goal would be to understand structure on all time scales in a consistent and unifying way.

(23) E. C. Bingham, *J. Phys. Chem.*, **45**, 885 (1941).

(24) See, for example, C. M. Criss and J. W. Cobble, *J. Amer. Chem. Soc.*, **86**, 5385 (1964).

data for the excess free energies of mixing in the 1.0 $m$ total ionic strength range. Using the values of $\Delta_m G^E(25°)$ found in the literature, $\Delta_m G^E$ and $\Delta_m S^E$ have been calculated at 40, 60, and 80° and recorded in Table II. It should be pointed out that the calculation

**Table II:** Excess Thermodynamic Properties at $y = 0.5, I = 1.0$

| Mixture | Temp, °C | $\Delta_m H$ | $\Delta_m G^E$ | $\Delta_m S^E$ |
|---|---|---|---|---|
| HCl–NaCl–$H_2O$ | 25 | 32.5[e] | 8.7[a] | 0.80 |
| | 40 | 28.1 | 7.6 | 0.65 |
| | 60 | 23.9 | 6.4 | 0.53 |
| | 80 | 20.6 | 5.4 | 0.43 |
| NaCl–KCl–$H_2O$ | 25 | −9.53[f] | −4.0[b] | −0.018 |
| | 40 | −9.15 | −3.7 | −0.017 |
| | 60 | −8.78 | −3.4 | −0.016 |
| | 80 | −8.05 | −3.1 | −0.013 |
| LiCl–KCl–$H_2O$ | 25 | −15.8[e] | −9.4[c] | −0.021 |
| | 40 | −15.8 | −9.1 | −0.021 |
| | 60 | −15.8 | −8.7 | −0.021 |
| | 80 | −15.8 | −8.2 | −0.022 |
| LiCl–NaCl–$H_2O$ | 25 | 21.0[e] | 3.6[d] | 0.058 |
| | 40 | 16.0 | 2.9 | 0.042 |
| | 60 | 11.0 | 2.1 | 0.027 |
| | 80 | 8.3 | 1.5 | 0.019 |

[a] See ref 25. [b] A. K. Covington, T. H. Lilly, and R. A. Robinson, *J. Phys. Chem.*, **72**, 2759 (1968). [c] B. B. Owen and T. F. Cooke, *J. Amer. Chem. Soc.*, **59**, 2273 (1937). [d] R. A. Robinson and C. K. Lim, *Trans. Faraday Soc.*, **49**, 1144 (1953). [e] See ref 4. [f] See ref 3.

of $\Delta_m G^E(25°)$ involves a relation of the type[25]

$$\Delta_m G^E(25°) = -2.303RTy(1 - y)I^2[\alpha_{23} + \alpha_{32} - 2(m_3\beta_{23} - m_2\beta_{32} + {}^2/_3(\beta_{23} - \beta_{32})(m_2 - m_3)]$$

The leading term, $\alpha_{23} + \alpha_{32}$, is actually the difference between two small numbers, making the calculation of $\Delta_m G^E(25°)$ extremely difficult.[26] However, once $\Delta_m G^E(25°)$ is known, it is a simple matter to extend the calculations to higher temperatures *via* eq 3 since the heats of mixing as a function of temperature are

**Table III:** Free Energies for HCl–NaCl–$H_2O$ ($I = 1.0$)

| Temp, °C | $\Delta_m G^E$ (calcd) | $\Delta_m G^E$ (exptl)[25] |
|---|---|---|
| 0 | | 10.0 |
| 10 | | 9.1 |
| 20 | | 8.7 |
| 25 | | 8.7 |
| 30 | | 8.5 |
| 40 | 7.60 | 9.0 |
| 50 | | 9.4 |
| 60 | 6.40 | |
| 80 | 5.35 | |

comparatively easy to measure with a relatively high degree of accuracy.[27] For comparison, the excess free energies of mixing calculated from this work are compared with Harned's experimentally determined values in Table III. Harned's data indicate that the excess free energy of mixing goes through a minimum between 30 and 40°, whereas the values calculated from this work indicate that the excess free energy of mixing decreases over the entire temperature range studied.

*Acknowledgment.* The authors wish to thank Miss Danne Smith for performing an experimental check on the heat of mixing of HCl–NaCl–$H_2O$ at 40°.

(25) H. S. Harned, *J. Phys. Chem.*, **63**, 1299 (1959).

(26) For a discussion of the problems in calculating $\Delta_m G^E$ from experimental data, see H. S. Harned and R. A. Robinson in "The International Encyclopedia of Chemistry and Chemical Physics," Topic 15, Vol. 2, R. A. Robinson, Ed., Pergamon Press, New York, N. Y., 1968, Chapters 4 and 5.

(27) Stern and Anderson[21] have measured the heats of mixing for HCl–NaCl–$H_2O$ from 0 to 40°. Their value of 22 cal/kg compared to our value of 28.1 cal/kg represents a difference of about 20%, well beyond normal experimental error. These measurements have been repeated recently in our laboratory by a different worker about 1 year after the initial measurements and they agree with our initial value of 28 cal/kg. As undesirable as this disagreement is, it does not greatly affect the calculation of $\Delta_m G^E(t_2)$ because the second and fourth terms on the right side of the eq 3 are almost self-compensating. Using Stern's value for the heat of mixing at 40° gives a value of 7.80 cal/kg for $\Delta_m G^E(40°)$. Although this is 0.2 cal/kg different from the value in Table III, it is within the uncertainty of the excess free energy of mixing at 25°.

# The Solubility and Partial Molar Volume of Nitrogen and Methane in Water and in Aqueous Sodium Chloride from 50 to 125° and 100 to 600 Atm[1]

by Thomas D. O'Sullivan and Norman O. Smith

*Department of Chemistry, Fordham University, New York, New York 10458* *(Received March 11, 1969)*

The solubility of nitrogen and of methane in water, 1 *m* NaCl, and 4 *m* NaCl at 51.5, 102.5, and 125.0° has been measured at pressures from 100 to 600 atm using a stirred autoclave and a direct sampling technique. The results for methane in the salt solutions differ from the only previous studies. At the lowest temperature, where the water vapor content of the gas phase can be ignored, ln $(f/X)$ for the dissolved gas is linear with total pressure, and the isobaric Henry's law applies up to the highest pressure for both gases. At the higher temperatures a curvature develops with rise in temperature, pressure, and, in general, salt concentration, but Henry's law may still apply. The data are interpreted in terms of the partial molar volume of dissolved gas and its variation with pressure, temperature, and salt concentration. Increase in NaCl concentration enhances the temperature coefficient of the partial molar volume of the dissolved gas. It also causes the latter to decrease at 51.5° but, in general, to increase at 102.5 and 125.0°, except at the highest pressure and temperature. Salting-out coefficients are tabulated and found to be nearly the same for both gases, to be approximately independent of pressure, to pass generally through a minimum with rise in temperature, and to show a decrease with increase in salt concentration. At a pressure of 200 atm the solubility of methane in water, 1 *m* NaCl, and 4 *m* NaCl passes through a minimum at 79 ± 2, 72 ± 3, and 69 ± 5°, respectively.

The solubility of naturally occurring gases such as nitrogen and methane in sodium chloride solution, and its variation with pressure, temperature, and salt concentration is of interest not only to the physical chemist but to the geochemist, for both gases occur associated with brine in the earth's crust and are doubtless transported subterraneously in solution from high to low pressure regions. Very few studies of "permanent" gas in aqueous salt solution at pressures of hundreds of atmospheres have been reported. The most extensive high-pressure solubility data for nitrogen in water are those of Wiebe, Gaddy, and Heins[2] up to 100° and of Krase and co-workers,[3,4] but the only studies of its solubility in aqueous sodium chloride at pressures other than atmospheric are from this laboratory: a preliminary one[5] at 30°, confined to pressures below 70 atm and involving a comparatively inaccurate technique, and an incomplete one[6] confined to 1 *m* NaCl over a smaller temperature range. The most important measurements for pure methane in water are those of Culberson and McKetta,[7] while its solubility in aqueous sodium chloride has been determined by Michels, Gerver, and Bijl[8] up to 220 atm and in this laboratory[9] at pressures not exceeding 65 atm. The measurements reported in the present paper have an accuracy much greater than that of the last two studies mentioned and extend to pressures of 600 atm. No partial molar volumes of gases dissolved in simple salt solutions appear to be available in the literature.

## Experimental Section

The gases were obtained from The Matheson Co., Inc., their purity given as 99.996% for the $N_2$ and 99.95% for the $CH_4$. The solubility equilibria were obtained in a 1-gallon, 316 stainless steel stirred, packless autoclave, the temperature of which was controlled to ±0.5° by a Minneapolis-Honeywell Electr-O-Pulse unit and Electronik 18 recorder, except for brief but unavoidable excursions of ±2°. An iron–constantan thermocouple, calibrated against a certified thermometer, was used to measure the autoclave temperature. The water used was distilled, passed through

(1) Taken from the Ph.D. dissertation of T. D. O. Portions of this paper were presented before the Division of Physical Chemistry at the 151st National Meeting of the American Chemical Society, Pittsburgh, Pa., March 1966, and before the Geochemical Society in San Francisco, Calif., Nov 1966.

(2) R. Wiebe, V. L. Gaddy, and C. Heins, Jr., *Ind. Eng. Chem.*, **24**, 97 (1932); *J. Amer. Chem. Soc.*, **55**, 947 (1933).

(3) J. B. Goodman and N. W. Krase, *Ind. Eng. Chem.*, **23**, 401 (1931).

(4) A. W. Saddington and N. W. Krase, *J. Amer. Chem. Soc.*, **56**, 353 (1934).

(5) N. O. Smith, S. Keleman, and B. Nagy, *Geochim. Cosmochim. Acta*, **26**, 921 (1962).

(6) T. D. O'Sullivan, N. O. Smith, and B. Nagy, *ibid.*, **30**, 617 (1966).

(7) O. L. Culberson and J. J. McKetta, *Trans. Am. Inst. Mech. Engr.*, **192**, 223 (1951); *J. Petrol. Technol.*, **2**, 319 (1950).

(8) A. Michels, J. Gerver, and A. Bijl, *Physica*, **3**, 797 (1936).

(9) J. R. Duffy, N. O. Smith, and B. Nagy, *Geochim. Cosmochim. Acta*, **24**, 23 (1961).

an ion-exchange column, and $N_2$ or $CH_4$ bubbled through it overnight. The salt solutions were prepared in a similar manner using Baker Analyzed Reagent grade NaCl previously dried at 115°. They were made up by weight, but analyzed after a run by evaporation to dryness, as a check. The water, or solution, was transferred to the autoclave by suction, flushed with $N_2$ or $CH_4$ at atmospheric pressure to remove any residual air, saturated with the gas at 50–100 atm, the pressure reduced, and the system again flushed. Gas was again admitted and the pressure and temperature brought to the desired values. High pressures were attained by means of a 1.5-hp compressor and compression cylinder. The pumping liquid was water, saturated with the gas being studied. Autoclave pressure was measured with a precision Heise–Bourdon gauge, 0 to 15,000 psi with an accuracy of ±0.05%, calibrated frequently with a dead-weight tester and found to exhibit a hysteresis of about 0.1%. It is estimated that the maximum possible error in the pressures quoted in the tables is 0.5 atm below 100 atm and 1 atm at 600 atm. All connecting tubing ($^1/_8$ in. i.d. except for the sampling tubes which were $^1/_{16}$ in.) and valves were of stainless steel. At least 8 hr was allowed for the attainment of equilibrium, and the same results were obtained when approached from higher and lower pressures. When equilibrium had been reached, 15–30 ml of saturated liquid sample was withdrawn at the rate of 0.5–1 ml/min into an evacuated, calibrated, water-jacketed buret system using mercury as leveling fluid and similar to that used elsewhere,[2] whereupon the gas flashed out of solution giving two phases in the burets. The first sample was always discarded. Results were found to be independent of the rate of sample withdrawal. During the sampling the equilibrium pressure in the autoclave was maintained by admitting more gas from the compression cylinder. By manipulation of the leveling bulbs mercury was cascaded through the liquid phase until no more gas bubbles were seen. Since at no time had the pressure in the burets exceeded 0.05 atm it was assumed that only a negligible amount of gas remained in solution. The pressure in the burets was now raised to atmospheric, and the volumes of the liquid and gas phases and the temperature and atmospheric pressure recorded. After correcting for aqueous pressure[10] and meniscus curvature, the number of moles of gas was calculated from the gas volume with the aid of tables of molar volume.[11] The number of moles of liquid was calculated from its volume, composition, and density.[10] For each pressure three or more separate samples were withdrawn for analysis and the results averaged. Their average deviation was about 0.4%. The pressure was changed to a new value without replacing the liquid contents of the autoclave, the volume of which was never allowed to be less than 1500 cc. Measurements were made in this way for water, 1 *m* NaCl, and 4 *m* NaCl at 51.5, 102.5, and 125.0°. These isothermal runs were supplemented by isobaric ones; the solubility of methane (only) in the same three liquids was measured at a number of temperatures under an estimated fixed partial pressure of methane of 200 atm in an effort to study quantitatively the effect of dissolved salt on the temperature of minimum solubility.

## Results and Discussion

The results of the isothermal work are given in Table I, where $P$ is total pressure (atm) and $X_2$ is mole fraction of dissolved gas. $X_2$ was calculated for the salt solutions as if the salt were *undissociated*. The solubilities for nitrogen in water agree with those of Wiebe, *et al.*,[2] within about 1.5% at 51.5° and 1.8% at 102.5°. The values for methane in water differ from those interpolated from the work of Culberson and McKetta[7] by about 1% at 51.5°, 1.5% at 102.5°, and 8% at 125.0°. The results for methane in both water and salt solution differ seriously from those of Michels, *et al.*,[8] obtained by an inaccurate pressure decline technique.

**Table I:** Solubility of $N_2$ and $CH_4$ in $H_2O$, 1.000 *m* NaCl, and 4.00 *m* NaCl (Mole Fraction of Dissolved Gas × $10^4$)

| $P$, atm | $H_2O$ | | 1 *m* NaCl | | 4 *m* NaCl | |
|---|---|---|---|---|---|---|
| | $X_{N_2}$ | $X_{CH_4}$ | $X_{N_2}$ | $X_{CH_4}$ | $X_{N_2}$ | $X_{CH_4}$ |
| | | | 51.5° | | | |
| 100.0 | 7.99 | 14.27 | 5.93 | 10.76 | ... | ... |
| 200.0 | 14.54 | 22.79 | 10.76 | 16.95 | 5.00 | 8.05 |
| 300.0 | 20.17 | 28.7 | 14.97 | 21.38 | 7.00 | 9.97 |
| 400.0 | 24.9 | 33.4 | 18.60 | 25.0 | 8.78 | 11.54 |
| 500.0 | 29.2 | 37.3 | 22.16 | 27.9 | 10.34 | 13.03 |
| 600.0 | 33.5 | 40.9 | 25.3 | 30.7 | 11.79 | 14.44 |
| | | | 102.5° | | | |
| 101.0 | 7.77 | 13.55 | 6.03 | ... | ... | ... |
| 201.0 | 14.47 | 22.05 | 11.13 | 16.93 | 5.23 | 8.26 |
| 302.0 | 20.05 | 28.7 | 15.38 | 22.19 | 7.31 | 10.79 |
| 403.0 | 25.2 | 33.3 | 19.20 | 25.7 | 8.99 | 12.11 |
| 503.0 | 29.8 | 38.5 | 22.52 | 28.9 | 10.47 | 13.19 |
| 604.0 | 33.7 | 41.9 | 26.0 | 32.0 | 12.05 | 14.33 |
| | | | 125.0° | | | |
| 103.0 | 8.08 | 14.34 | 6.32 | 10.58 | ... | ... |
| 204.0 | 14.92 | 23.21 | 11.02 | 17.52 | 5.67 | 8.25 |
| 305.0 | 20.47 | 29.6 | 15.33 | 22.23 | 7.40 | 10.05 |
| 405.0 | 25.7 | 34.3 | 18.83 | 26.0 | 9.21 | 11.64 |
| 507.0 | 30.6 | 39.6 | 22.31 | 29.4 | 10.41 | 13.22 |
| 608.0 | 35.1 | 43.0 | 25.5 | 32.5 | 12.27 | 14.38 |

In determining the extent to which Henry's law applies for each of the systems at each temperature it may be noted that $P/X_2$ increases with $P$ even at 51.5° where the partial pressure of water, $p_{H_2O}$, contributes negligibly to $P$. At larger pressures the condition of

(10) "International Critical Tables," Vol. 3, McGraw-Hill Publications, New York, N. Y., 1928.

(11) F. Din, "Thermodynamic Functions of Gases," Vol. 3, Butterworth and Co. Ltd., London, 1961.

constant *total* pressure, which is inherent in Henry's law, becomes important. In addition, fugacity should be used in place of partial pressure of permanent gas. Krichevsky and Kasarnovsky,[12] and later Kobayashi and Katz,[13] showed that by combining Henry's law

$$f_2 = kX_2(T, P \text{ constant}) \quad (1)$$

(where $f_2$ is the fugacity of the solute gas and $X_2$ its mole fraction) with other thermodynamic relations, and assuming $\bar{V}_2$, the partial molar volume of dissolved gas, to be independent of $P$

$$\ln (f_2/X_2) = \ln k^* + (P\bar{V}_2/RT) \quad (2)$$

where $k^*$ is the limiting value of $f_2/X_2$ as $P$ is reduced indefinitely, or the Henry's law constant. Although this result is correct, both pairs of investigators derived it by arguments involving the mutual cancellation of errors. In ref 12 an essential part of the derivation is the use of the approximation $d\mu_2 = RT\, d \ln X_2$ (where $\mu_2$ is chemical potential), which implies the absence of any dependence of $\mu_2$ on $P$. It is this very dependence that forms the basis for the article. In ref 13 $d\mu_2 = \bar{V}_2 dP$, valid only for fixed composition, is equated to $d\mu_2 = RT\, d \ln f_2$ and integrated, and then the concentration is permitted to vary. These difficulties can be avoided as follows. Since $\mu_2 = \mu_2(T, P, X_2)$, $d\mu_{2T} = (\partial\mu_2/\partial X_2)_{T,P}\, dX_2 + \bar{V}_2\, dP_T$. At any one temperature, however, $d\mu_2 = RT\, d \ln f_2$ so $(\partial\mu_2/\partial X_2)_{T,P} = RT(\partial \ln f_2/\partial X_2)_{T,P}$. Moreover, by eq 1, valid only for $dT = dP = 0$, $(\partial \ln f_2/\partial X_2)_{T,P} = 1/X_2$ or $(\partial\mu_2/\partial X_2)_{T,P} = RT/X_2$. It follows that for isothermal changes $RT\, d \ln f_2 = (RT/X_2)\, dX_2 + \bar{V}_2\, dP = RT\, d \ln X_2 + \bar{V}_2\, dP$ or

$$[\partial \ln (f_2/X_2)/\partial P]_T = \bar{V}_2/RT \quad (3)$$

Integration between $P = P^*$, a very small pressure (where $X_2 = X_2^*$, $f_2 = f_2^*$) and $P = P$ (where $X_2 = X_2$, $f_2 = f_2$), assuming $\bar{V}_2$ independent of $P$, yields eq 2. Thus when the isobaric Henry's law holds and $\bar{V}_2$ is independent of $P$ a plot of $\ln (f_2/X_2)$ *vs.* $P$ is linear with a slope of $\bar{V}_2/RT$ and an intercept of $\ln k^*$. It is to be noted also that if the isobaric Henry's law holds, $\bar{V}_2$ must be independent of $X_2$ at constant total pressure and equal to the value at infinite dilution, $\bar{V}_2^0$. Experimentally, however, it is virtually impossible to separate the effects of the variables $X_2$ and $P$ on $\bar{V}_2$.

At 51.5° the gas phase is essentially pure nitrogen (or methane) so the gas partial pressure is given by $P$, from which $f_{N_2}$ and $f_{CH_4}$ can be determined by reference tables.[11,14] Figure 1 is a plot of $\ln (f_2/X_2)$ *vs.* $P$. The lines are straight within experimental error. The evidence is strong, therefore, that at this temperature Henry's law holds for all three solvents up to 600 atm for both gases and that $\bar{V}_2$ is independent of $P$.

At the higher temperatures, however, it is possible only to estimate the fugacities. The gas phase now has a water vapor content that cannot be ignored,

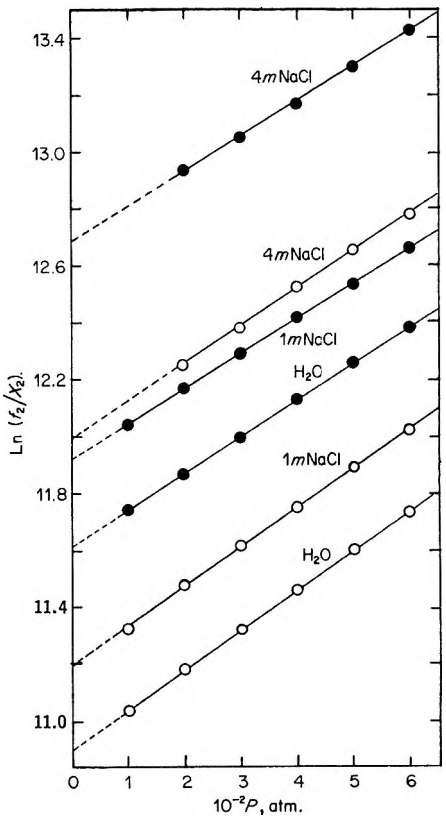


Figure 1. Solubility of $N_2$ and of $CH_4$ in $H_2O$, 1 *m* NaCl, and 4 *m* NaCl at 51.5°: ●, $N_2$; ○, $CH_4$.

but the analyses of previous investigators do not always agree, as comparisons of the data for nitrogen[4,15,16] and methane[16,17] show. The Gibbs–Poynting equation, $(\partial \ln p_{H_2O}/\partial P)_T = \bar{V}_2/RT$, cannot be relied upon to give a quantitative answer because of the nonideality of the gas–water vapor mixture.[18] Even when the gas-phase composition is known, there is still the problem of finding the fugacity of the permanent gas. The Lewis and Randall rule[19] can be used but is not reliable, again because of gas mixture nonideality. Nevertheless the fugacities at 102.5 and 125.0° were estimated by finding them for the pure gas at the same pressure and temperature[11,14] and multiplying these by the mole fraction of water as given in the literature.[4,16,17] This mole fraction is greatest for the highest temperatures and the lowest pressures, being 0.030 for methane at 125.0° and 103.0 atm. The fugacity of pure methane under

(12) I. R. Krichevsky and J. S. Kasarnovsky, *J. Amer. Chem. Soc.*, **57**, 2168 (1935).

(13) R. Kobayashi and D. L. Katz, *Ind. Eng. Chem.*, **45**, 440 (1953).

(14) W. E. Deming and L. E. Shupe, *Phys. Rev.*, **37**, 638 (1931).

(15) E. P. Bartlett, *J. Amer. Chem. Soc.*, **49**, 65 (1927).

(16) M. Rigby and J. M. Prausnitz, *J. Phys. Chem.*, **72**, 330 (1968).

(17) R. H. Olds, B. H. Sage, and W. N. Lacey, *Ind. Eng. Chem.*, **34**, 1223 (1942).

(18) N. O. Smith, *J. Chem. Educ.*, **40**, 317 (1963).

(19) G. N. Lewis and M. Randall, "Thermodynamics," rev. by K. S. Pitzer and L. Brewer, McGraw-Hill Publications, New York, N. Y., 1961, p 295.

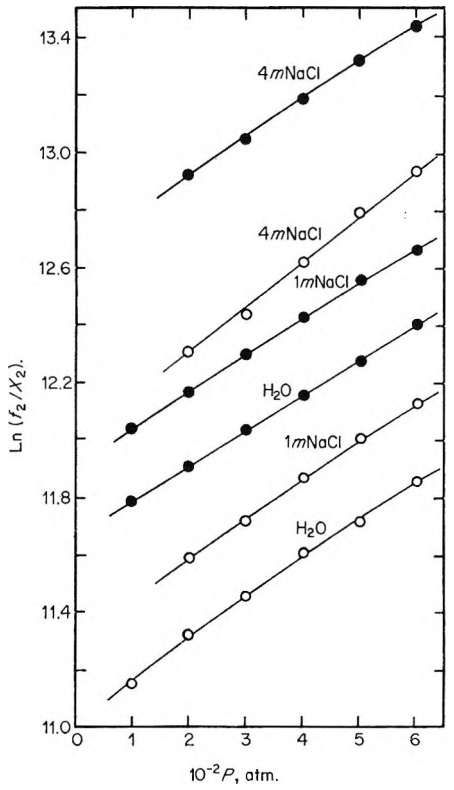


Figure 2. Solubility of $N_2$ and of $CH_4$ in $H_2O$, 1 $m$ NaCl, and 4 $m$ NaCl at 102.5°: ●, $N_2$; ○, $CH_4$.

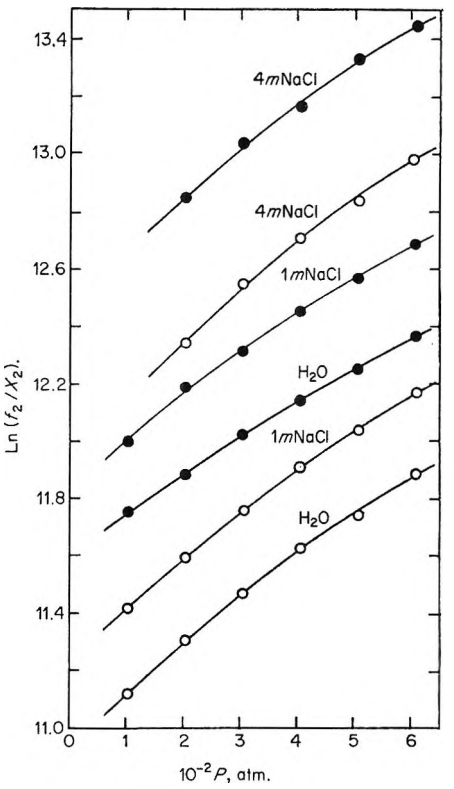


Figure 3. Solubility of $N_2$ and of $CH_4$ in $H_2O$, 1 $m$ NaCl, and 4 $m$ NaCl at 125.0°: ●, $N_2$; ○, $CH_4$.

these conditions is 99.1 atm, so $f_{CH_4}$ is estimated to be 0.970(99.1) = 96.1 atm, and ln $(f_{CH_4}/X_{CH_4})$ = 11.11. The resulting graphs are shown in Figures 2 and 3 for 102.5 and 125.0°, respectively. It is evident that at these temperatures there is more scatter in the data, the increased difficulty of controlling the temperature of the large mass of the autoclave and the greater sensitivity of pressure to temperature being largely responsible. For this reason the location of the lines is uncertain, but it is clear that a curvature develops with rise in pressure, temperature, and, generally, salt concentration. This is the first time such curvature has been pointed out, although the data of Culberson and McKetta[7] for methane in water at 102.5° (interpolated), for example, suggest it. It was apparently not considered by Kobayashi and Katz[13] in their treatment of the same data.

Curvature could conceivably be caused by one or more of the following: (1) inapplicability of Henry's law, (2) erroneous estimation of fugacities from faulty gas composition data and/or failure of the Lewis and Randall rule, (3) variation of $\bar{V}_2$ with $P$. Since, however, Henry's law is valid at 51.5° and would be expected to become more, rather than less, valid with rise in temperature, it seems reasonable to suppose that the curvature does not lie in (1). Validity of Henry's law means that $\bar{V}_2$ is independent of $X_2$ at fixed $P$. It is likewise possible to eliminate (2) since the lines are curved in the same direction even when no correction is made to the fugacities for the presence of water vapor, and the corrections, even if known accurately, would reduce the uncorrected values of ln $(f_2/X_2)$ more at the lower pressures than at the higher ones, thus making the curvature greater. It appears, therefore, that the curvature must be attributed to decrease of $\bar{V}_2$ with increase in $P$. Such a decrease in $\bar{V}_2$ is entirely to be expected. Furthermore, the increased curvature with rise in $T$ requires that $[\partial(\bar{V}_2/RT)/\partial P]_T = (1/RT)\cdot(\partial\bar{V}_2/\partial P)_T$ become more negative with increase in $T$. This, in turn, requires that $(\partial\bar{V}_2/\partial P)_T$ become more negative—a reasonable possibility since $(\partial V/\partial P)_T$ does so for pure liquids. Thus the observed curvature can be accounted for qualitatively on the basis of the behavior of $\bar{V}_2$.

In order to apply eq 3 to the results it would have been helpful to have low-pressure data to reduce the uncertainty of extrapolation to zero pressure. However, because of the paucity of such data at all temperatures and the inherent difficulty of fugacity measurements at higher temperatures, where the gas phase has an appreciable water content, only the data of the present study were used. The data for 51.5° were fitted to ln $(f_2/X_2) = a + bP$ and those for 102.5 and 125.0° to ln $(f_2/X_2) = a' + b'P + c'P^2$ (with the two exceptions indicated), giving the parameters shown in Table II. They generally reproduce the experimental values of ln $(f_2/X_2)$ within 0.05, 0.06, and 0.07% at the three temperatures, respectively. Table III gives the

**Table II:** Parameters in Ln $(f_2/X_2) = a + bP$ and Ln $(f_2/X_2) = a' + b'P' + c'P^2$

| Gas | Temp, °C | $H_2O$ $a$ | $H_2O$ $10^3b$ | 1 *m* NaCl $a$ | 1 *m* NaCl $10^3b$ | 4 *m* NaCl $a$ | 4 *m* NaCl $10^3b$ |
|---|---|---|---|---|---|---|---|
| $N_2$ | 51.5 | 11.615 | 1.278 | 11.923 | 1.230 | 12.688 | 1.221 |
| $CH_4$ | 51.5 | 10.905 | 1.393 | 11.195 | 1.394 | 11.964 | 1.374 |

| Gas | Temp, °C | $H_2O$ $a'$ | $H_2O$ $10^3b'$ | $H_2O$ $10^7c'$ | 1 *m* NaCl $a'$ | 1 *m* NaCl $10^3b'$ | 1 *m* NaCl $10^7c'$ | 4 *m* NaCl $a'$ | 4 *m* NaCl $10^3b'$ | 4 *m* NaCl $10^7c'$ |
|---|---|---|---|---|---|---|---|---|---|---|
| $N_2$ | 102.5 | 11.662[a] | 1.222[a] | | 11.899 | 1.384 | −1.93 | 12.644 | 1.389 | −1.32 |
| $CH_4$ | 102.5 | 11.001 | 1.647 | −3.94 | 11.286 | 1.507 | −1.75 | 11.973[a] | 1.598[a] | |
| $N_2$ | 125.0 | 11.604 | 1.450 | −3.25 | 11.826 | 1.807 | −6.58 | 12.409 | 2.405 | −12.2 |
| $CH_4$ | 125.0 | 10.943 | 1.905 | −5.99 | 11.224 | 1.919 | −6.09 | 11.888 | 2.473 | −11.3 |

[a] Parameters for ln $(f_2/X_2) = a' + b'P$.

**Table III:** Henry's Law Constants and Partial Molar Volumes of Dissolved Gas at 51.5°

| | $H_2O$ $N_2$ | $H_2O$ $CH_4$ | 1 *m* NaCl $N_2$ | 1 *m* NaCl $CH_4$ | 4 *m* NaCl $N_2$ | 4 *m* NaCl $CH_4$ |
|---|---|---|---|---|---|---|
| $10^5k$*, atm | 1.108 | 0.544 | 1.507 | 0.728 | 3.238 | 1.570 |
| $\bar{V}_2$, cm³ mol⁻¹ | 34.05 | 37.10 | 32.76 | 37.12 | 32.52 | 36.61 |

**Table IV:** Partial Molar Volumes of Dissolved Gas (cm³ mol⁻¹)

| *P*, atm | $H_2O$ $N_2$ | $H_2O$ $CH_4$ | 1 *m* NaCl $N_2$ | 1 *m* NaCl $CH_4$ | 4 *m* NaCl $N_2$ | 4 *m* NaCl $CH_4$ |
|---|---|---|---|---|---|---|
| | | | 102.5° | | | |
| 200 | 37.7 | 45.9 | 40.3 | 44.3 | 41.2 | 49.3 |
| 400 | 37.7 | 41.1 | 37.9 | 42.1 | 39.6 | 49.3 |
| 600 | 37.7 | 36.2 | 35.5 | 40.0 | 38.0 | 49.3 |
| | | | 125.0° | | | |
| 200 | 43.1 | 54.4 | 50.5 | 54.7 | 62.7 | 66.1 |
| 400 | 38.9 | 46.6 | 41.9 | 46.8 | 46.7 | 51.3 |
| 600 | 34.6 | 38.7 | 33.2 | 38.8 | 30.8 | 36.5 |

limiting Henry's law constants and partial molar volumes (pressure and composition independent) at 51.5° determined from the parameters. At the higher temperatures, where extrapolation was deemed too uncertain, and where curvature indicated a pressure dependence of $\bar{V}_2$, only the latter was calculated, and this for rounded pressures, not infinite dilution (Table IV).

The Henry's law constant of Table III for nitrogen in water at 51.5° may be compared with the following obtained by interpolation of the results of low-pressure solubility measurements: 1.109 (ref 20) and 1.117 × $10^5$ atm (ref 10), and that in 1 *m* NaCl with 1.441 × $10^5$ (ref 20). Those for methane in water may, similarly, be compared with 0.580 (ref 20), 0.585 (ref 10), and 0.581 × $10^5$ (ref 21), and in 1 *m* NaCl with 0.763 × $10^5$ (ref 20). The high-pressure data of Wiebe, *et al.*,[2] for nitrogen yield 1.103 × $10^5$ and those of Culberson and McKetta[7] for methane 0.541 × $10^5$ (both in water) at this temperature—in support of the present values rather than of some of the data of low-pressure studies. One wonders whether lower temperature Henry's law constants, determined by linear extrapolation of good high-pressure data, are not actually the more reliable. Similar doubt of the validity of certain commonly used techniques for determining gas solubilities at low pressures has been expressed by Horiuti.[22]

It is possible to estimate, from the data of Table I, that 1 ft³ of sedimentary rock, of 20% porosity, saturated with brine (50,000 ppm NaCl), can accommodate about 1 mol of methane in solution when in equilibrium with that gas at the pressure and temperature existing at a depth of 10,000 ft.

Nearly all of the previously published partial molar volumes at temperatures of 50° and higher have been obtained by extrapolation of high-pressure data. The values in Table III are in excellent agreement with those obtained by others[12,13] using the same method. Direct experimental measurements of $\bar{V}_2^0$ at these temperatures have been attempted by Krichevski and Il'nskaya,[23] who claimed that the experimental values did not agree with those obtained by the use of eq 2. They attributed this to the failure of the isobaric Henry's law and consequent invalidity of eq 2 as a means of finding $\bar{V}_2^0$. This seems unlikely, however, in view of the arguments presented above. Glew[24] suggests that the values of $V_2^0$ measured directly[23] are in error as a result of ignoring the difference between apparent and partial molar volumes, even in such dilute solutions. At the higher temperatures only partial molar volumes obtained by extrapolation of high-pressure data are available: 36.2[12,13] cm³ mol⁻¹ for nitrogen in water at 100° (using the same data[2]), and 40.6[13] and 40.2[24] for methane at 102° (using the same data[7]).

(20) T. J. Morrison and F. Billet, *J. Chem. Soc.*, 3819 (1952).

(21) S. K. Shoor, R. D. Walker, Jr., and K. E. Gubbins, *J. Phys. Chem.*, **73**, 312 (1969).

(22) J. Horiuti, *Sci. Papers Inst. Phys. Chem. Res. Tokyo*, **17**, 125 (1931).

(23) I. R. Krichevski and A. Il'nskaya, *Acta Physicochim. URSS*, **20**, 327 (1945).

(24) D. N. Glew, *J. Phys. Chem.*, **66**, 606 (1962).

**Table V:** Salting-out Coefficients ($k_{NaCl}$)

| Temp, °C | $m$ | Approx $P$, atm 100 | 200 | 300 | 400 | 500 | 600 |
|---|---|---|---|---|---|---|---|
| | | | | Nitrogen | | | |
| 51.5 | 1 | 0.129 | 0.131 | 0.129 | 0.126 | 0.120 | 0.122 |
| 51.5 | 4 | ... | 0.116 | 0.115 | 0.113 | 0.113 | 0.113 |
| 102.5 | 1 | 0.110 | 0.114 | 0.115 | 0.118 | 0.121 | 0.113 |
| 102.5 | 4 | ... | 0.111 | 0.110 | 0.112 | 0.113 | 0.112 |
| 125.0 | 1 | 0.107 | 0.132 | 0.126 | 0.135 | 0.137 | 0.139 |
| 125.0 | 4 | ... | 0.105 | 0.110 | 0.111 | 0.117 | 0.114 |
| | | | | Methane | | | |
| 51.5 | 1 | 0.122 | 0.128 | 0.128 | 0.126 | 0.127 | 0.125 |
| 51.5 | 4 | ... | 0.111 | 0.115 | 0.115 | 0.114 | 0.113 |
| 102.5 | 1 | ... | 0.115 | 0.111 | 0.114 | 0.125 | 0.117 |
| 102.5 | 4 | ... | 0.103 | 0.106 | 0.110 | 0.116 | 0.107 |
| 125.0 | 1 | 0.132 | 0.122 | 0.124 | 0.120 | 0.129 | 0.122 |
| 125.0 | 4 | ... | 0.112 | 0.117 | 0.117 | 0.119 | 0.119 |

For methane in water at 125° one finds 41.4[13] and 40.0[24] in treatments of the same data[7] by different authors. Clearly, much depends on how the extrapolation is made. If one recognizes the curvature shown in Figures 2 and 3 the four last-quoted values are probably all low (*cf.* Table IV). If, due to intermolecular forces, the activity coefficient of the permanent gas in the gas–water vapor phase were seriously different from unity at the higher temperatures both $k^*$ and $\bar{V}_2^0$, obtained by extrapolation, would require further correction.

Examination of Tables III and IV shows that, for both gases, $\bar{V}_2$ (1) increases appreciably with temperature in water and salt solution, (2) decreases slightly with salt concentration at 51.5°, and (3) generally increases markedly with salt concentration at 102.5 and 125.0°—if one accepts the argument given above that $\bar{V}_2$ is independent of concentration at a given pressure and temperature. The large temperature coefficient of $\bar{V}_2$ corresponds to the general belief that water becomes a more "normal" liquid as the temperature is raised. The larger partial molar volume of a dissolved gas in a solvent more normal than water is well documented.[25] Apparently the presence of salt in water enhances the return to normalcy in this respect.

The effect of change of salt concentration at a given temperature may be accounted for as follows. At lower temperatures the salt ions are surrounded by a shell of oriented water molecules which induce an icelike, and therefore open, structure in the water adjacent to the periphery of the shell—even more open than in the bulk liquid—thus slightly reducing $\bar{V}_2$. At the higher temperature, however, where the bulk hydrogen-bonded network has largely disintegrated, and the water structure collapsed, addition of salt tightens the structure even more, and solution of gas therein produces considerable expansion and large values of $\bar{V}_2$. At 600 atm, however, especially for nitrogen, the pressure is high enough to counteract this effect.

**Table VI:** Solubility of $CH_4$ in $H_2O$, 1.000 $m$ NaCl, and 4.00 $m$ NaCl at a Partial Pressure of Methane of 200 Atm (Mole Fraction of Dissolved Gas × $10^4$)

| Temp, °C | $P$, atm | $X_{CH_4}$ $H_2O$ | 1 $m$ NaCl | 4 $m$ NaCl |
|---|---|---|---|---|
| 51.5 | 200.0 | 22.79 | 16.95 | 8.05 |
| 60.0 | 200.0 | ... | 16.57 | 7.92 |
| 65.0 | 200.0 | 21.51 | ... | 7.96 |
| 70.0 | 200.3 | 21.44 | 16.25 | 7.91 |
| 75.0 | 200.3 | 21.36 | 16.30 | 7.97 |
| 80.0 | 200.3 | 21.33 | 16.40 | 8.03 |
| 85.0 | 200.7 | 21.48 | ... | ... |
| 90.0 | 200.7 | 21.72 | 16.74 | 8.08 |
| 102.5 | 201.0 | 22.05 | 16.93 | 8.26 |
| 115.0 | 202.7 | 22.76 | 17.47 | 8.22 |
| 125.0 | 204.0 | 23.21 | 17.52 | 8.25 |

The unsmoothed results for the salt solutions given in Table I are restated as salting-out coefficients ($k_{NaCl}$) in Table V where $k_{NaCl} = \log (S^\circ/S)/m$, $S^\circ$ and $S$ being the gas solubilities in water and salt solution of molality $m$. (Apart from the work of Morrison and Billet,[20] there is no previous study with which to compare these results. For 1 $m$ NaCl at 50° interpolation of their data gives $k_{NaCl} = 0.11$ for both gases from low-pressure data.) The following general conclusions can be drawn. NaCl has approximately the same coefficient for both $N_2$ and $CH_4$ over a considerable range of temperature and pressure, and for both gases it is practically independent of pressure, seems to pass through a minimum with rise in temperature, and shows an appreciable decrease with increase in salt concentration. The variation of the coefficient with salt concentration is not surprising since several other gases, even at lower pressures, also show poor constancy.[26] The

(25) See, for example, K. W. Miller and J. H. Hildebrand, *J. Amer. Chem. Soc.*, 90, 3001 (1968).

low-pressure data of Braun[27] for nitrogen in the same salt up to 2 $M$ at 25° show an even greater variation. Expressing the data of Table V in terms of molarity instead of molality makes no significant improvement in the constancy. Although McDevit and Long[28] found $k_{NaCl}$ to be independent of salt concentration up to 4 $M$ when the solute is benzene, it appears that this is not in general true for small molecules like nitrogen and methane.

Table VI gives the results of the isobaric runs for methane. The total pressures used and quoted were estimated as giving an approximately constant partial pressure of methane of 200 atm. The data reveal that, at this pressure, its solubility passes through a minimum with rise in temperature at 79 ± 2, 72 ± 3, and 69 ± 5° for $H_2O$, 1 $m$ NaCl, and 4 $m$ NaCl, respectively. The location of the minimum for $H_2O$ agrees excellently with ref 7. (Michels, *et al.*,[8] found no minimum for water or salt solutions.) The decrease, with rise in temperature, of the solubility of slightly soluble gases in water as contrasted with the increase in more normal solvents is well known.[29] In water, as well as in salt solutions, more normal behavior may be expected as the temperature is raised. Thus the existence of the minimum in solubility may be explained. The small decrease in the temperature of the minimum with increasing salt concentration seems to be outside the limits of experimental error and suggests that the addition of salt confers some "normalcy" on the water, in agreement with the observation made earlier.

*Acknowledgment.* The authors wish to acknowledge with thanks the assistance of a grant from the Earth Sciences Section of the National Science Foundation.

(26) M. Randall and C. P. Failey, *Chem. Rev.*, **4**, 271 (1926).

(27) L. Braun, *Z. Phys. Chem.*, **33**, 721 (1900).

(28) W. F. McDevit and F. A. Long, *J. Amer. Chem. Soc.*, **74**, 1773 (1952).

(29) J. H. Hildebrand and R. L. Scott, "Regular Solutions," Prentice-Hall, Inc., Englewood Cliffs, N. J., 1962.

# Hydration of the Alkali Ions in the Gas Phase. Enthalpies and Entropies of Reactions $M^+(H_2O)_{n-1} + H_2O = M^+(H_2O)_n$

**by I. Džidić and P. Kebarle**

*Chemistry Department, University of Alberta, Edmonton, Canada* *(Received September 2, 1969)*

The equilibrium constants $K_{n-1,n}$ for the gas-phase reactions $M^+(H_2O)_{n-1} + H_2O = M^+(H_2O)_n$ were determined at different temperatures and water pressures in the Torr range for all alkali ions. Values for the enthalpies and entropies $\Delta H_{n-1,n}$, $\Delta S^\circ_{n-1,n}$ were obtained for $n$ up to about 6. The measurements were done with a mass spectrometer incorporating a high-pressure ion source. The enthalpies are compared with potential energies of the clusters $M^+(H_2O)_n$ calculated on the basis of an electrostatic model. Comparison of the absolute values does not prove very meaningful; however, comparison of the relative values indicates that some covalent bonding is present in the $Li^+(H_2O)$ and $Na^+(H_2O)$. The electrostatic calculations also indicate the approximate $n$ at which the water molecules become nonequivalent, *i.e.*, the point where a transition to a new structure occurs. Calculated entropies $\Delta S_{0,1}$ based on statistical mechanics equations and parameters of the electrostatic calculations are found in good agreement with the experimental values. The experimental $-\Delta S_{n-1,n}$ are found to increase with increase of $n$ for all alkali ions. This is taken as evidence for loss of freedom in the complex due to crowding.

## Introduction

In a series of papers published over the past few years[1-6] we have tried to show that important information on the solvation of ions can be obtained by measurement of reaction equilibria involving gaseous ions and molecules of a given "solvent" vapor. An example of such an equilibrium is the clustering of water molecules around an alkali ion $M^+$. The method relies on

$$M^+(H_2O)_{n-1} + H_2O = M^+(H_2O)_n \quad (n-1,n)$$

mass spectrometric determination of the intensities of the reactant ions escaping through a small leak from a

(1) P. Kebarle, S. K. Searles, A. Zolla, J. Scarborough, and M. Arshadi, *J. Amer. Chem. Soc.*, **89**, 6393 (1967).

(2) S. K. Searles and P. Kebarle, *J. Phys. Chem.*, **72**, 742 (1968).

(3) P. Kebarle and R. M. Haynes, *J. Amer. Chem. Soc.*, **89**, 5753 (1967).

reaction chamber containing a known pressure of solvent vapor. Comprehensive investigations of the systems $H^+(H_2O)_n$,[1] $NH_4^+(NH_3)_n$[2] have been published as well as some experiments describing the competitive solvation of the proton by methanol and water[3] and the $NH_4^+$ ion by $NH_3$ and $H_2O$. The kinetics and rate constants involved in the formation of $H^+(H_2O)_n$ in $N_2$ and $O_2$ have also been studied[6] and on basis of these results the time required for the achievement of the clustering equilibrium can be predicted with some certainty for a variety of conditions.

The hydration of halide negative ions has also been examined,[5] but only at a single temperature. Experiments at different temperature allowing the determination of $\Delta H_{n-1,n}$ and $\Delta S^\circ_{n-1,n}$ for the halide ions are described in a subsequent paper of this issue. The study of the hydration of the positive alkali ions follows quite logically from the work described above. Since the alkali ions are spherical, one might expect that their hydration energies should be most amenable to classical calculations based on ion dipole interactions. Thus comparison of experiment with simple theory would be meaningful. Also the alkali and halide ions have played an important role in attempts to evaluate single ion hydration energies. Thus Latimer, Pitzer, and Slanski[7] and many others have based their approach on the heats of hydration of the alkali halides. A comparison between the present gas-phase results for the hydration of the alkali and halide ions and the single ion hydration energies evaluated by other means is given in the following paper.[8]

The information obtained by measuring gas-phase hydration equilibria for the alkali ions is of interest not only for liquid solutions but obviously of importance also to the many gas-phase systems where these ions occur. Hydrated alkali ions have been observed in the ionosphere,[9] in flames,[10] mobility experiments,[11] etc. In many gas-phase situations the alkali ions are the ultimate ions since due to their low ionization potential, once charge is transferred to them, it is retained. If the gas phase contains traces of water, as is often the case, the ultimate ion becomes $M^+(H_2O)_n$. The increase of interest in alkali ion gas-phase chemistry is evident from the number of papers devoted to it in recent symposia.[12]

In order to measure hydration equilibria involving the alkali ions, one must first find a way of creating these ions in the gas phase under conditions where thermal and clustering equilibrium could be achieved. Ionization by fast electrons, protons or $\alpha$ particles, which had been used before, could not be applied, since no compounds containing the alkali atoms and having sufficient vapor pressure could be found. Therefore a method depending on thermionic emission of positive ions from a filament painted with an alkali salt was developed and described in a previous publication[13] which dealt with the hydration of the potassium ion. The present experiments are thus a continuation of this earlier work extending the measurements to include $Li^+$, $Na^+$, $Rb^+$, and $Cs^+$.

## Experimental Section

The measurements were done with a high-pressure mass spectrometer containing a thermionic alkali ion source attached to the reaction chamber. The experimental arrangement has been described previously.[13] The principle is as follows. The alkali ions, created by thermionic emission from a filament painted with a suitable salt containing the desired ion, drift under the influence of an applied field between the filament and the orifice of the reaction chamber to the reaction chamber. Both filament chamber and reaction chamber contain the desired pressure of water vapor. The clustering reactions are completed in the field-free reaction chamber. The ionic concentrations in the reaction chamber are sampled by bleeding the gas through a narrow slit into the ion accelerating and mass analysis section, which is maintained at a pressure less than $10^{-4}$ Torr by a high-capacity pumping system.

Checks made to establish that the clustering equilibrium is not affected by the temperature of the filament and the presence of the drift field are described in the previous publication.[13]

The Kunsman mixture[14] on a Pt ribbon filament was used for the production of $Na^+$, $K^+$, $Rb^+$, and $Cs^+$. For $Li^+$ the most satisfactory source found was $\beta$-eucryptite ($1Li_2O \cdot 1Al_2O_3 \cdot 2SiO_2$) suggested by Blewett and Jones.[15] $\beta$-Eucryptite was made by melting $Li_2CO_3$, $Al(NO_3)_3 \cdot 9H_2O$, and pure powdered quartz together at about 1400°. The melts were then powdered and remelted two times. The compound was finally powdered and mounted as a thin layer on the 1 × 0.3-cm filament made of platinum gauze.

(4) A. M. Hogg and P. Kebarle, *J. Chem. Phys.*, **43**, 449 (1965).

(5) P. Kebarle, M. Arshadi, and J. Scarborough, *ibid.*, **49**, 817 (1968); **50**, 1049 (1969).

(6) A. Good, D. A. Durden, and P. Kebarle, accepted for publication in *J. Chem. Phys.*

(7) W. M. Latimer, K. S. Pitzer, and C. M. Slanski, *J. Chem. Phys.*, **7**, 108 (1935). One of the most recent compilations of single-ion hydration energies for the alkali and halide ions is to be found in J. E. Desnoyers, "Modern Aspects of Electrochemistry," Vol. 5, J. O. M. Bockris, Ed, Plenum Press, New York, N. Y., 1969, Chapter 1.

(8) M. Arshadi, R. Yamdagni, and P. Kebarle, *J. Phys. Chem.*, **74**, 1475 (1970).

(9) R. S. Narcisi and A. D. Bailey, *J. Geophys. Res.*, **70**, 3687 (1965).

(10) A. N. Hayhurst and T. M. Sugden, *Proc. Roy. Soc.*, **A293**, 36 (1966).

(11) R. J. Munson and A. M. Tundall, *ibid.*, **A172**, 28, (1939); L. B. Loeb, "Basic Processes of Gaseous Electronics," University of California Press, Los Angeles, Calif., 1961, Chapter 1.

(12) "Symposium on Physics and Chemistry of the Upper Atmosphere," Stanford Research Institute, June 1969.

(13) S. K. Searles and P. Kebarle, *Can. J. Chem.*, **47**, 2619 (1969).

(14) R. O. Jenkins and W. G. Trodden, "Electron and Ion Emission from Solids," Routledge and Kegan Paul, Ltd., London, 1965, Chapter 7.

(15) J. P. Blewett and E. J. Jones, *Phys. Rev.*, **50**, 464 (1936).

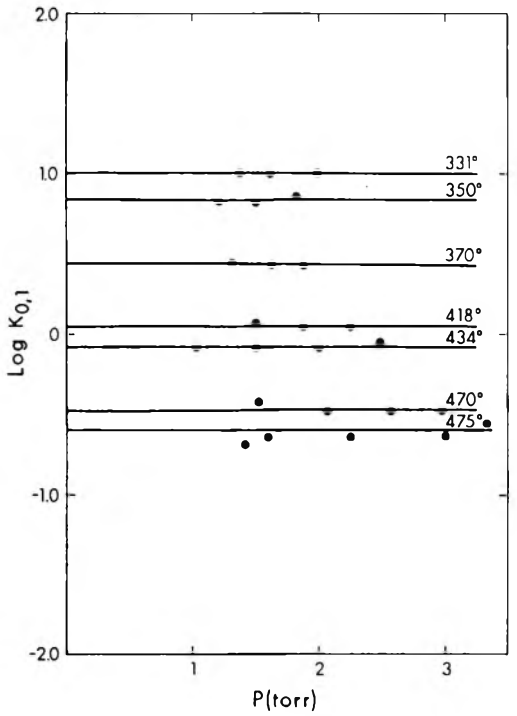


Figure 1. Plots of equilibrium constant $K_{0,1}$ for reactions $Na^+ + H_2O = Na^+(H_2O)$ *vs.* $H_2O$ pressure. Plot shows that equilibrium constants taken at a given temperature remain constant with pressure.

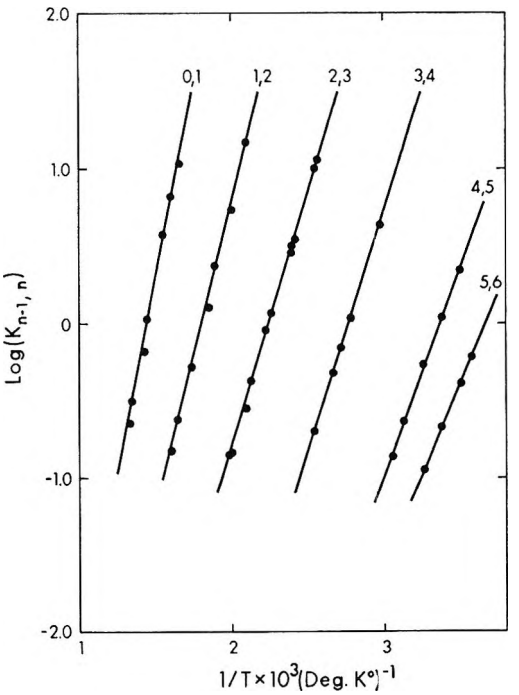


Figure 2. van't Hoff plots for equilibrium constants $K_{n-1,n}$ of reactions $Na^+(H_2O)_{n-1} + H_2O = Na^+(H_2O)_n$.

In general a positive ion current of about $10^{-6}$ to $10^{-7}$ A was obtained from the filaments. The maximum emission was not affected unfavorably by the presence of water vapor.

## Results and Discussion

Some of the equilibrium constants obtained for the reaction

$$Na^+ + H_2O \underset{\leftarrow}{\overset{M}{\rightleftharpoons}} Na^+(H_2O) \qquad (0,1)$$

are shown in Figure 1 as a function of water pressure. The equilibrium constants were calculated by means of eq I. $I_0$ and $I_1$ correspond to the measured intensities of the $Na^+$ and $Na^+(H_2O)$ ion, and $P$ is the measured water pressure in the reaction chamber. Equation I is

$$K_{0,1} = \frac{I_1}{I_0 P} \qquad (I)$$

based on the assumption that the ion intensities are proportional to the ion concentrations in the reaction chamber, with the same proportionality constant. This assumption is justified by the fact that the clustering reactions inside the reaction chamber are fast compared with the time taken for the ions to travel to the exit slit. Thus no discrimination should occur in the reaction chamber. The discriminations outside the reaction chamber are dependent on the mass of the ions and are small for the ions involved in the measurements.

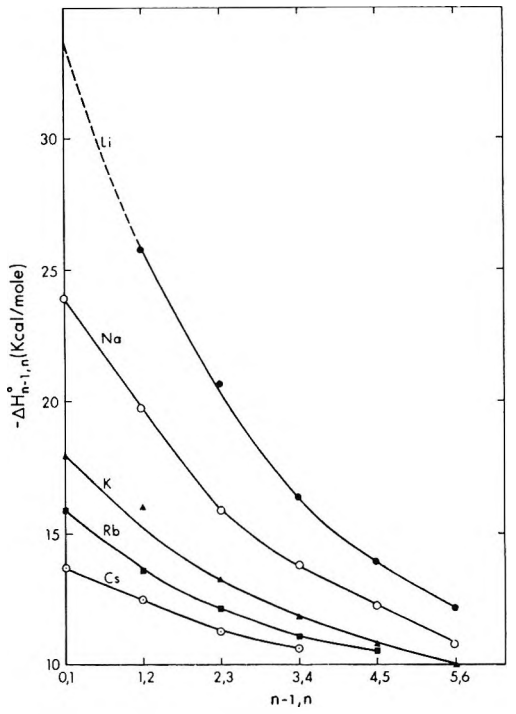


Figure 3. Enthalpies for clustering reactions $M^+(H_2O)_{n-1} + H_2O = M^+(H_2O)_n$.

It can be seen from Figure 1 that the equilibrium constants remain constant for a 3–4-fold variation of the water pressure. Similar results were obtained for the other alkali ions and higher hydration equilibria.

van't Hoff plots of the equilibrium constants for the sodium hydrates are shown in Figure 2. The con-

**Table I:** Thermodynamic Values for the Gas-Phase Reactions[a] $M^+(H_2O)_{n-1} + H_2O \rightleftarrows M^+(H_2O)_n$

| $-\Delta H^\circ_{n-1,n}$ | $Li^+$ | $R_{3,1}$[c] | $Na^+$ | $R_{3,1}$ | $K^+$ | $R_{3,1}$ | $Rb^+$ | $R_{3,1}$ | $Cs^+$ | $R_{3,1}$ |
|---|---|---|---|---|---|---|---|---|---|---|
| 0,1 | 34.0[b] | 1.92 | 24.0 | 2.26 | 17.9 | 2.60 | 15.9 | 2.76 | 13.7 | 2.98 |
| 1,2 | 25.8 | 1.94 | 19.8 | 2.28 | 16.1 | 2.60 | 13.6 | 2.76 | 12.5 | 2.98 |
| 2,3 | 20.7 | 1.96 | 15.8 | 2.30 | 13.2 | 2.62 | 12.2 | 2.76 | 11.2 | 2.98 |
| 3,4 | 16.4 | 2.02 | 13.8 | 2.34 | 11.8 | 2.66 | 11.2 | 2.76 | 10.6 | 2.98 |
| 4,5 | 13.9 | 2.10 | 12.3 | 2.38 | 10.7 | 2.68 | 10.5 | 2.78 | | 3.00 |
| 5,6 | 12.1 | 2.16 | 10.7 | 2.44 | 10.0 | 2.74 | | 2.84 | | 3.06 |
| $A \times 10^6$,[d] kcal × Å$^{12}$ | 0.19 | | 0.95 | | 3.9 | | 7.37 | | 15.87 | |
| $-\Delta G^\circ_{n-1,n}$ | $Li^+$ | | $Na^+$ | | $K^+$ | | $Rb^+$ | | $Cs^+$ | |
| 0,1 | 25.5 | | 17.6 | | 11.4 | | 9.6 | | 7.9 | |
| 1,2 | 18.9 | | 13.2 | | 8.9 | | 7.0 | | 5.9 | |
| 2,3 | 13.3 | | 9.3 | | 6.3 | | 5.0 | | 4.2 | |
| 3,4 | 7.5 | | 6.3 | | 4.4 | | 3.8 | | 3.0 | |
| 4,5 | 4.5 | | 3.9 | | 3.2 | | 2.8 | | | |
| 5,6 | 2.5 | | 2.9 | | 2.3 | | | | | |

[a] All energy values in kcal/mol. Free energy values for standard state 1 atm and 298°K. [b] Extrapolated value from plot in Figure 3. [c] $R_{3,1}$ (Å) corresponds to distance between $M^+$ and oxygen nuclei in cluster $M^+(OH_2)_n$ obtained from calculations in which the $A$ value was selected to give $\Delta E_{0,1} = \Delta H_{0,1}$. [d] $A$ values for term $AR_{3,1}^{-12}$ in electrostatic calculations obtained by setting $\Delta H_{0,1} = \Delta E_{0,1}$.

**Table II:** Entropy Changes[a] for Reactions $M^+(H_2O)_{n-1} + H_2O = M^+(H_2O)_n$

| | $Li^+$ | $Na^+$ | $K^+$ | $Rb^+$ | $Cs^+$ |
|---|---|---|---|---|---|
| $\Delta S_{0,1}^\circ$ | 23.0[d] | 21.5 | 21.6 | 21.2 | 19.4 |
| $\Delta S_{0,1}$[b] | 23.0 | 22.7 | 21.6 | 22.0 | 21.2 |
| $\Delta S_{0,1}$[c] | 23.0 | 22.9 | 22.0 | 22.0 | 21.3 |
| | (835°K) | (667°K) | (570°K) | (455°K) | (445°K) |
| $\Delta S_{1,2}$ | 21.1 | 22.2 | 24.2 | 22.2 | 22.2 |
| $\Delta S_{2,3}$ | 24.9 | 21.9 | 23.0 | 24.0 | 23.7 |
| $\Delta S_{3,4}$ | 29.9 | 25.0 | 24.7 | 24.8 | 25.4 |
| $\Delta S_{4,5}$ | 31.4 | 28.1 | 25.2 | 25.7 | ... |
| $\Delta S_{5,6}$ | 32.0 | 26.0 | 25.7 | ... | ... |

[a] Entropy values in eu. [b] Entropy values calculated at 298°K. [c] Entropy values calculated at the temperatures shown in brackets corresponding to middle of van't Hoff plot temperature range from which experimental $\Delta S$ values were obtained. [d] $\Delta S$ value obtained by extrapolation of experimental $\Delta G^\circ_{n-1,n}$ and $\Delta H^\circ_{n-1,n}$ for $Li^+(OH_2)_n$.

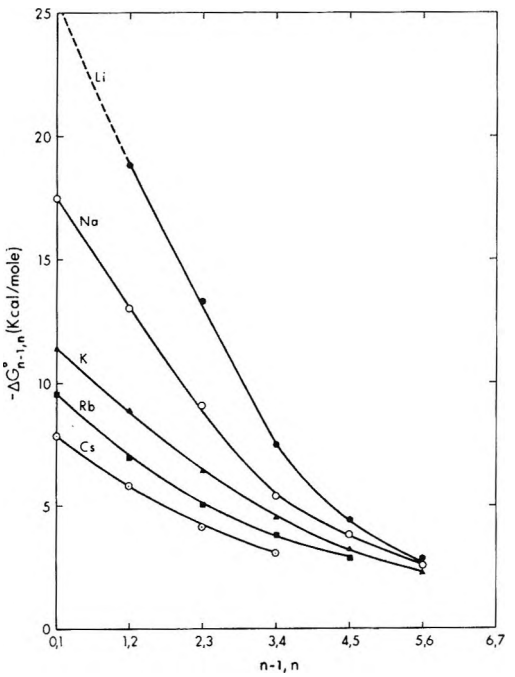


Figure 4. Free energies of clustering reactions $M^+(H_2O)_{n-1} + H_2O = M^+(H_2O)_n$.

stant slopes of these plots lead to $\Delta H_{n-1,n}$ for the sodium reactions. Similar results were obtained for the other alkali ions. The resulting $\Delta H^\circ_{n-1,n}$, $\Delta G^\circ_{n-1,n}$ and $\Delta S^\circ_{n-1,n}$ are shown in Table I and II and in Figures 3 and 4.

In Figure 3 the $\Delta H^\circ_{n-1,n}$ for the ions are shown for the different clustering steps $(n-1,n)$. It is found, for a given alkali ion, that $-\Delta H^\circ_{n-1,n}$ decreases as $n$ and thus the size of the cluster increases. Comparing the different alkali ions one finds that the $-\Delta H^\circ_{n-1,n}$ are largest for $Li^+$ and smallest for $Cs^+$. Both results are reasonable and agree with what one would have expected. The $\Delta G^\circ_{n-1,n}$ values of Figure 4 exhibit similar trends.

The (0,1) values for $Li^+$ were not measured experimentally since at the high temperatures required to observe the equilibrium ($T > 900$°K) large impurity emission of $K^+$ ions interfered with the reliability of the measurements. While the $Li^+$ equilibrium could be probably measured with the use of suppressor grids and other refinements, the additional effort involved was not considered worth it for the present time since a fairly accurate value for $\Delta H_{0,1}$ of $Li^+$ can be obtained by extrapolation from the other $\Delta H^\circ_{n-1,n}$ of this ion.

The consistency of the relative $\Delta H^\circ_{n-1,n}$ values for the different alkali ions with available thermodynamic data is checked in Figure 5 which gives a plot of $\Delta H_{0,n}$.

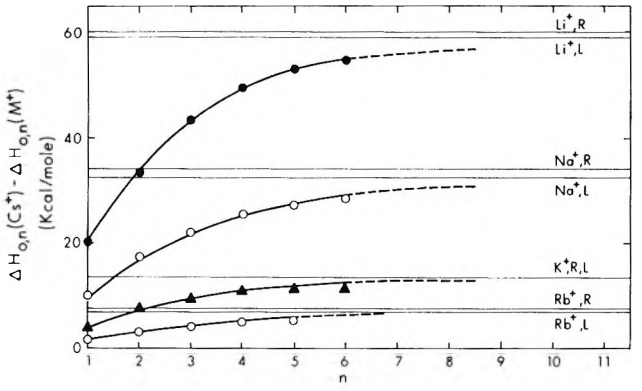


Figure 5. Plot of $\Delta H_{0,n}(Cs^+) - \Delta H_{0,n}(M^+)$ *vs.* $n$ showing that above differences approach differences of total single ion heats of hydration obtained by Randles (R) and Latimer (L).[7]

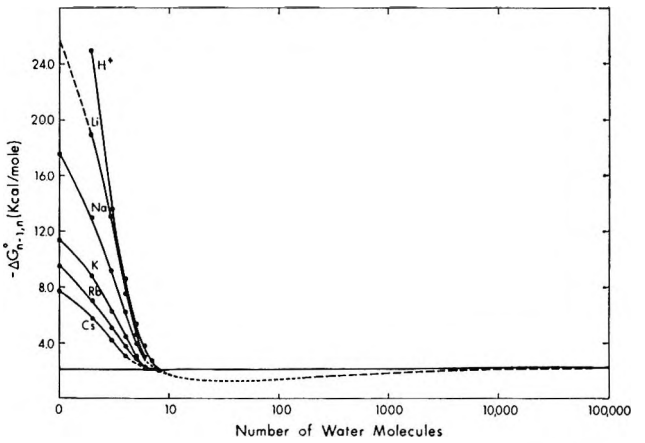


Figure 6. Comparison of free energy of hydration $\Delta G^\circ_{n-1,n}$ with free energy of evaporation of 1 mol of water molecules from 1 mol of water droplets carrying a single ionic charge. Number of molecules contained per droplet given in the abscissa. Free energy of evaporation calculated from Thompson formula.[16]

$(Cs^+) - \Delta H_{0,n}(M^+)$ *vs.* $n$. It is to be expected that for large $n$ the above difference should approach the difference between the single ion heats of hydration: $\Delta H_h(Cs^+) - \Delta H_h(M^+)$. Indicated on the figure are the values for these differences obtained from the single ion hydration enthalpies of Latimer, Pitzer, and Slanski[7] and Randles. The plot clearly shows that the present data are consistent with the single ion hydration differences.

In Figure 6 the $-\Delta G^\circ_{n-1,n}$ values at 298°K are plotted *vs.* $n$ but using a logarithmic scale for $n$ in order to be able to accommodate a large increase of $n$. The dashed line represents calculated $\Delta G^\circ_{evap}$ using the Thompson formula,[16] eq (II), for the evaporation of water from a spherical droplet of radius $r$ carrying a

$$\Delta G^\circ_{evap} = RT \ln \frac{P_\infty}{P_r} = -\frac{M}{\rho}\left(\frac{2\theta}{r} - \frac{e^2}{8\pi\epsilon r^4}\right) \quad \text{(II)}$$

single centrally located charge. $P_r$ is the vapor pressure over the droplet while $P_\infty$ is the vapor pressure of water with a flat surface. $\rho$ and $M$ are the density and the molecular weight while $\theta$, $e$, and $\epsilon$ are the surface tension, electronic charge, and dielectric constant. The surface tension and dielectric constant are assumed independent of the radius. Equation II is still used in cloud chamber practice.[16] The first term in the equation represents the lowering of the $-\Delta G^\circ$ with decreasing radius of the droplet. This effect is due to the operation of surface tension. The second term expresses the increase of $-\Delta G^\circ$ with decreasing radius due to the increased attraction between the charge and the water dipoles. As the radius of the droplet decreases the distinction between charged water droplets and water clusters, $M^+(H_2O)_n$ becomes less pronounced and $\Delta G^\circ_{evap}$ (for 1 mol of water molecules from "1 mol of water droplets") begins to approach $\Delta G^\circ_{n-1,n}$. The dashed line given in Figure 6 was obtained with the macroscopic values for $\rho$, $\theta$, and $\epsilon$.

It is interesting to note that the experimentally determined $\Delta G^\circ_{n-1,n}$ values for all ions are consistent with the predictions of eq II since the $\Delta G^\circ_{n-1,n}$ for all ions extrapolate smoothly for high $n$ into the calculated curve.

Figure 6 also illustrates the fact that there is a theoretical limit for $n$ beyond which clustering equilibria cannot be measured. Thus when $-\Delta G^\circ_{n-1,n}$ becomes smaller than $-\Delta G^\circ_{evaporation} = 2.03$ kcal/mol at 298°K (normal free energy of evaporation from a flat water surface, indicated by black horizontal line in Figure 6) condensation to bulk liquid water becomes theoretically possible. However, in the absence of other nucleation catalysts, condensation will not occur and ion clustering equilibria will exist (at water pressures above saturation pressure) until $n$ becomes about equal to 20. Beyond this point the $-\Delta G^\circ_{n-1,n}$ (dashed curve) begins to increase, which means that clusters with higher $n$ become thermodynamically more stable and growth of the clusters becomes spontaneous ending in bulk water.

In experiments done up to the present we found that clustering equilibria could not be measured beyond $n \approx 7$ due to condensation of water in the ion source. According to the above discussion, the condensation must have been catalyzed by some other nucleating agents (*i.e.*, active points on the metal surfaces of the walls, *etc.*). Thus application of special techniques as, for instance, used in cloud chamber experiments coupled with rapid mass scanning might allow equilibria to be measured for $n$ up to about 20, but not higher.

It was considered of interest to compare the experimental enthalpy and entropy values with theoretically calculated energies and entropies. The potential energy $E_n$ of a cluster consisting of a central ion and $n$

(16) J. J. Thompson, "Applications of Dynamics to Physics and Chemistry," Vol. I, McMillan & Co., London, 1888, p 165; C. M. York, "Cloud Chambers," Sect. 3, Vol. XLV, "Handbuch der Physik," Springer-Verlag, Berlin, 1958.

ligand molecules relative to the energy for the ion and the ligands at infinity was calculated by eq III.

$$E_n = \text{EDIP} + \text{EPOL} + \text{EDIS} + \text{RDIP} + \text{REL} \quad \text{(III)}$$

EDIP stands for the energy due to the ion–permanent dipole attractions, EPOL for the ion–induced dipole attractions, and EDIS is the energy due to attractive van der Waals or dispersion forces between the ion and the ligands and the ligands themselves. RDIP is the energy term representing dipole–dipole repulsion forces. The dipole–dipole repulsion forces are those due to permanent dipole and induced dipole repulsions. The last term, REL, stands for the electronic repulsion between the ion and the ligand molecules. The electronic repulsions between the ligand molecules themselves were neglected.

For clusters with $n > 2$, a number of structures can be assumed. We used for $n = 3$ a trigonal planar structure. A tetrahedron, a trigonal bypyramid, and an octahedron were used for $n = 4$, 5, and 6. The metal ion was located in the center while the water molecules were at the corners of the regular polyhedra mentioned above. The water molecules were so oriented that the central ion was lying on the extension of the bisector of the HOH angle with the oxygen pointing toward the ion.

The terms EDIP and EPOL were calculated as described in the previous publication dealing with the hydration of potassium.[13] In these calculations a point charge model was used to represent the water dipole. The atomic polarizabilities of hydrogen and oxygen were used to represent the polarizability of water.

The individual terms whose sum gives the total dispersion energy EDIS were calculated from eq IV which has been used by Muirhead-Gould and Laidler[17] for similar evaluations

$$\text{EDIS}_{ij} = -{}^3/_2 \frac{\alpha_i \alpha_j}{r_{ij}^6} \frac{I_i I_j}{I_i + I_j} \quad \text{(IV)}$$

$\alpha_i$ is the (point dipole) polarizability and $I_i$ the ionization potential of molecule i. $r_{ij}$ is the distance between the molecules. The distance between the ion and the water molecules was taken as equal to the distance from the ion nucleus to the oxygen nucleus ($R_{1,3}$) plus 0.3 Å. The distances between the water molecule themselves were measured from center to center assuming the center to lie on the bisector of the $OH_2$ angle and 0.3 Å from the oxygen nucleus. The total dispersion energy was obtained by summing over all appropriate molecules. The ionization potentials and polarizabilities were the same as those used by Muirhead-Gould and Laidler.

For the calculation of the terms due to permanent dipole–permanent dipole repulsion the point charge model for the water molecule was used. However, the point charge model becomes too cumbersome in the calculation of the permanent dipole–induced dipole and induced dipole–induced dipole interactions. Therefore these were calculated by using the point dipole and point polarizability of water.

The selection of the numerical value for the constant $A$ in the term $\text{REL} = AR^{-12}$ representing the electronic repulsions is probably the most critical step in electrostatic calculations of the type used here. Thus, the nature of the central ion $Li^+$, or $Na^+$, etc., finds expression in the calculation essentially only through the value of $A$. The dispersion terms also depend on the nature of the ion but these terms are quite small. A first set of calculations was made in which the constants $A$ for the repulsion between the alkali ions and the water molecules were evaluated from $A$ values for the noble gases.[18,19] The $A$ constants for the noble gases which were used[18] are a well established set based on second virial coefficients. The procedure used to obtain the required $A$ values for the alkali ions from those of the noble gases is given in the Appendix, and the actual $A$ values used are given in Table III.

**Table III:** Potential Energies of Clusters $M^+(H_2O)_n$ from Electrostatic Calculations Using Repulsion Terms $AR^{-12}$ [a]

| $-\Delta E_{0,n}$ | $Li^+$ | $Na^+$ | $K^+$ | $Rb^+$ | $Cs^+$ |
|---|---|---|---|---|---|
| 0,1 | 53.3 | 42.9 | 31.2 | 28.1 | 23.1 |
| $R_{3,1}$ | 1.56 | 1.74 | 2.04 | 2.16 | 2.38 |
| 0,2 | 95.9 | 79.1 | 58.8 | 53.6 | 44.4 |
| $R_{3,1}$ | 1.60 | 1.76 | 2.06 | 2.18 | 2.38 |
| 0,3 | 119.6 | 102.7 | 79.8 | 73.7 | 62.0 |
| $R_{3,1}$ | 1.66 | 1.80 | 2.08 | 2.20 | 2.42 |
| 0,4 | 129.7 | 116.5 | 94.9 | 89.1 | 76.3 |
| $R_{3,1}$ | 1.72 | 1.86 | 2.12 | 2.24 | 2.44 |
| 0,5 | 123.8 | 117.4 | 101.6 | 97.5 | 85.4 |
| $R_{3,1}$ | 1.84 | 1.94 | 2.18 | 2.28 | 2.48 |
| 0,6 | 118.4 | 116.0 | 105.9 | 103.6 | 92.6 |
| $R_{3,1}$ | 1.96 | 2.04 | 2.24 | 2.34 | 2.52 |
| $A \times 10^5$ kcal $\times$ Å$^{12}$ | 0.0298 | 0.0861 | 0.4200 | 0.8400 | 2.100 |

[a] Repulsion term determined according to procedure described in the Appendix from noble gas $A$ values, van der Waals radii of noble gases, and Stokes radii of $M^+$. $\Delta E_{0,n}$ in kcal/mol; $R_{3,1}$ in Å corresponds to distance from center of ion to nucleus of oxygen atom of water molecule.

The potential energies $E_n$ as a function of the parameter $R_{3,1}$ (oxygen–ion distance) were then calculated for all ions with an IBM 360/67 computer. The po-

(17) J. S. Muirhead-Gould and K. J. Laidler, *Trans. Faraday Soc.*, **63**, 944 (1967).

(18) J. O. Hirschfelder, C. F. Curtis, and R. B. Bird, "Molecular Theory of Gases and Liquids," John Wiley & Sons, New York, N. Y., 1954, p 1110.

(19) E. A. Mason and J. I. Vanderslice in "Atomic and Molecular Processes," D. R. Bates, Ed., Academic Press, New York, N. Y., 1967, Chapter 17.

tential energy minima found are given in Table III where the notation $\Delta E_{0,n}$ is used in analogy with the notation for the experimental ($\Delta H$) values. Given in Table IV are the values of the individual energy

**Table IV:** Individual Energy[a] Contributions to Potential Energy Calculations of Cluster $Na^+(OH_2)_n$

| $n$ | −EDIP | −EPOL | −EDIS | RDIP | REL |
|---|---|---|---|---|---|
| 1 | 36.871 | 14.982 | 2.283 | 0 | 11.180 |
| 2 | 72.243 | 28.741 | 4.425 | 6.810 | 19.494 |
| 3 | 104.064 | 39.720 | 6.531 | 25.236 | 22.330 |
| 4 | 130.794 | 47.015 | 8.353 | 49.490 | 20.117 |
| 5 | 151.423 | 50.385 | 10.680 | 80.234 | 15.149 |
| 6 | 165.773 | 50.341 | 11.608 | 104.830 | 9.946 |

[a] All values in kcal/mol.

terms: EDIP, EPOL, *etc.*, for sodium in order to illustrate the relative magnitude of each contribution. Figure 7 gives a plot of $-\Delta E_{0,n}$ and the experimentally measured $-\Delta H_{0,n}$ for sodium. It can be seen from the figure and the tables that in all cases the calculated values are considerably larger than the experimental values. In general the calculated $\Delta E_{0,1}$ and $\Delta E_{0,2}$ are about 70% larger than the corresponding enthalpy values. We consider it unlikely that the experimental determinations can be in error by such a large margin. It is more likely that some assumptions made in the calculation were inappropriate. The term that is most suspect is REL = $AR^{-12}$. In the Appendix it is demonstrated that the present choice of $A$ values is consistent with the accepted set of Lennard-Jones parameters for the inert gases. These parameters were determined from second virial coefficients which are due to weak intermolecular interactions. Assuming that these parameters are correct in the weak interaction range, they will be applicable to stronger interactions (smaller intermolecular distances) only if the Lennard-Jones potential function is of the correct form. It would be desirable to obviate the use of the Lennard-Jones six–twelve potential by dropping both these terms (EDIS and EREP) from the potential energy expression and replacing them with experimentally determined potentials based on molecular beam scattering experiments.[19] The scattering in relatively high kinetic energy beams is due to strong interactions occurring at close distances betwen the colliding partners. Unfortunately, experimental potential functions for the present pairs $Li^+\cdots H_2O$, $Na^+\cdots H_2O$ are not available. However, as shown in the Appendix the interaction for the pair Ne···Ne appears to be a good approximation for that between $Na^+$ and $H_2O$. Therefore calculations were made for sodium using the potential term $7190/r9.99$ kcal/mol[20] instead of EDIS and REL. The results from these calculations gave

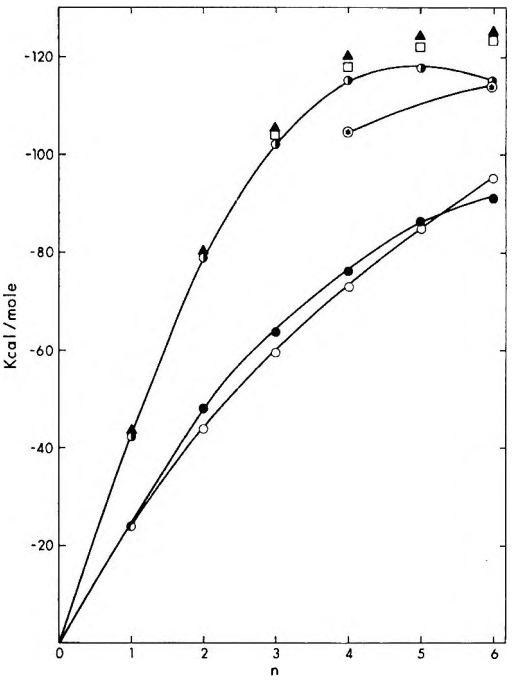


Figure 7. Comparison between experimental enthalpies $\Delta H_{0,n}$ and potential energies $\Delta E_{0,n}$ obtained on basis of electrostatic type calculations, for sodium hydrates $Na^+(H_2O)_n$. ○, experimental $\Delta H_{0,n}$; ●, $\Delta E_{0,n}$ calculated by adjusting value of constant $A$ in repulsion term $AR^{-12}$ so as to make $\Delta H_{0,1} = \Delta E_{0,1}$; ◐ $\Delta E_{0,n}$ with $A$ value for $Na^+\cdots O$ repulsion obtained from Stokes radius for $Na^+$ van der Waals radius of oxygen. □, calculated with $A$ value for $Na^+$–$H_2O$ repulsion set equal to $A$ value for Ne–Ne repulsion;[18] ▲, calculated with $A$ value for $Na^+$–$H_2O$ repulsion based on Stokes radius of $Na^+$ and $A$ value for water–water repulsion[18] (see Appendix); ⊙, $\Delta E_{0,n}$ calculated by Garrick.[21]

$-\Delta E_{0,n}$ which were even somewhat higher than the $-\Delta E_{0,n}$ calculated previously.

At present we cannot understand too well why all classes of $A$ values lead to $-\Delta E_{0,n}$ which are too high (see Figure 7). An idea about a possible cause for the discrepancy is given in the Appendix. It is interesting to note that the early calculation of Garrick[21] which also used a Lennard-Jones function with parameters based on the noble gases also predicts considerably higher $-\Delta E_{0,4}$ and $-\Delta E_{0,6}$ energies (Figure 7). Values for $-\Delta E_{0,1}$ and $-\Delta E_{0,2}$ obtained from Garrick's equations turn out quite close to those of the present calculations; *i.e.*, they are also much higher than the experimental results.

An alternative often adopted is to retain the Lennard-Jones six–twelve potential but to determine the constant $A$ in the repulsion term by some semiempirical method. Thus Muirhead-Gould and Laidler[17] adjusted the value of $A$ so as to give a distance between the ion and the water molecules equal to the sum of the Goldsmith ionic radius and a radius for the water mole-

(20) I. Amdur and E. A. Mason, *J. Chem. Phys.*, **23**, 415 (1955).
(21) F. J. Garrick, *Phil. Mag.*, **9**, 131 (1930); **10**, 76 (1930).

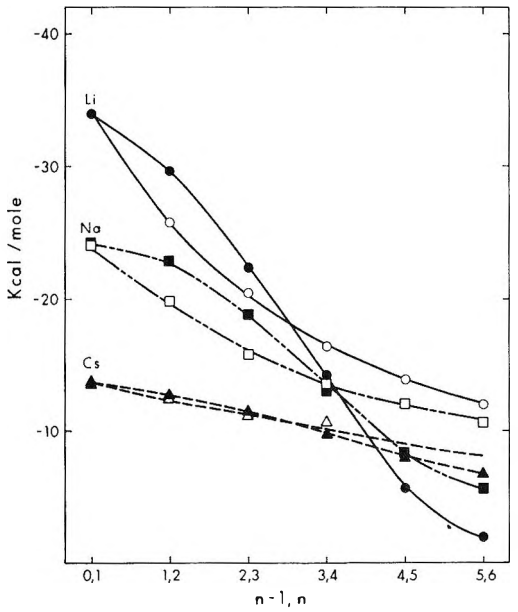


Figure 8. Comparison of experimental $\Delta H_{n-1,n}$ and calculated potential energy differences $\Delta E_{n-1,n}$ for alkali ion clusters $M^+(OH_2)_n$: ○, $\Delta H$ of $Li^+$; ●, $\Delta E$ of $Li^+$; □, $\Delta H$ of $Na^+$; ■, $\Delta E$ of $Na^+$; △, $\Delta H$ of $Cs^+$; ▲, $\Delta E$ of $Cs^+$.

cule. The calculations of Muirhead-Gould and Laidler give results which are in closer agreement with the present experimental values. Unfortunately, only incomplete sets for $Li^+$ and $Rb^+$ are available from that source.

In order to compare the change of $\Delta H_{n-1,n}$ for a given ion with calculated results we chose a procedure already used in a previous paper.[13] The $AR^{-12}$ form was retained and an empirical value for $A$ was determined for each ion by setting $\Delta E_{0,1} = \Delta H_{0,1}$. The $\Delta E_{0,n}$ values obtained by this procedure were then used to evaluate: $\Delta E_{n-1,n} = \Delta E_{0,n} - \Delta E_{0,n-1}$. Some of the data obtained are shown in the composite Figure 8 which illustrates the observed effects for the small ion $Li^+$, the medium sized ion $Na^+$, and the large ion $Cs^+$. For small $n$ ($n = 2$ and 3) it is found that $-\Delta E_{n-1,n}$ falls off less rapidly than the $-\Delta H_{n-1,n}$. This effect is most pronounced for $Li^+$ and almost not noticeable for $Cs^+$. The more rapid initial drop off of the $-\Delta H_{n-1,n}$ terms could be due to the presence of chemical (nonelectrostatic) bonding in the $M^+OH_2$ complex. This bonding should occur only for the attachment of the first water molecule and be completely or almost completely absent for the other water molecules. Such a state of affairs would exist if a certain amount of dative bonding between the oxygen lone pair and the lowest empty orbital of the alkali ion occurred. The oxygen lone pair electrons would then partly screen the positive charge from the other water molecules.[22] The effect should be largest in lithium which has most covalent character and weakest with cesium. This is what is observed in Figure 8.

At higher $n$ the $-\Delta E_{n-1,n}$ curve is found to decrease more rapidly and cross the $-\Delta H_{n-1,n}$. For $Li^+$ and $Na^+$, $-\Delta E_{4,5}$ and $-\Delta E_{5,6}$ are very much smaller than the corresponding $\Delta H$ (Figure 8). As mentioned before, the calculations are made under the assumption that all water molecules are equidistant from the ion. For $Li^+$ and $Na^+$ which are small ions, this assumption is probably inadequate at $n = 5$ and $n = 6$. Thus the crossover at $n = 4$ should indicate that at this point a change to a new structure occurs in which all water molecules are not equivalent. The $-\Delta E_{4,5}$ and $-\Delta E_{5,6}$ for Cs are somewhat smaller than the corresponding $\Delta H$ values. However, the differences between the calculated and experimental values are very small so that one may conclude that the data do not indicate a change of structure at $n = 4$ or 5 but a persistence of the equivalence of all water molecules to about $n = 6$. This is, of course, consistent with the larger radius of $Cs^+$.

Entropy change calculations for the reaction 0,1 were performed following the procedures described in the earlier publication.[13] The parameters used and the results obtained are shown in Table II. The parameters used were obtained from the calculations where the constant $A$ was adjusted to give agreement between $-\Delta H_{0,1}$ and $-\Delta E_{0,1}$. As can be seen from Table II, relatively good agreement is obtained between the calculated and observed $-\Delta S_{0,1}°$ values. Calculations for the other reactions are possible but would involve an increasing number of assumptions. Therefore they were not made.

It is interesting to note that the experimental $-\Delta S_{n-1,n}$ increase with increase of $n$. The same result is obtained for the halide ions as shown in the following paper.[8] The increase of the $-\Delta S$ values occurs even though the bonding forces (represented for instance by $-\Delta H_{n-1,n}$) decrease. It is reasonable to assume that the increase of the $-\Delta S$ terms reflects the gradual loss of freedom due to crowding of the molecules around the central ion. The study of the $H^+(H_2O)_n$ clusters[1] showed that the $-\Delta S_{n-1,n}$ values decrease somewhat with increase of $n$. This difference of behavior between the clusters around centrally located (large) ions and water clusters containing an extra proton may be considered as evidence for the mobility or nonlocalization of the charge in the hydrates $H^+(H_2O)_n$.

The following paper[8] contains results for the hydration of the halide ions. A comparison between the hydration energies of the alkali and halide ions is given there.

## Appendix

*Selection of Values for the Constant A in the Electronic Repulsion Term REL = $AR^{-12}$ used in the Electrostatic Calculations.* For determination of the values of the

(22) L. B. Magnusson, *J. Chem. Phys.*, 39, 1953 (1963).

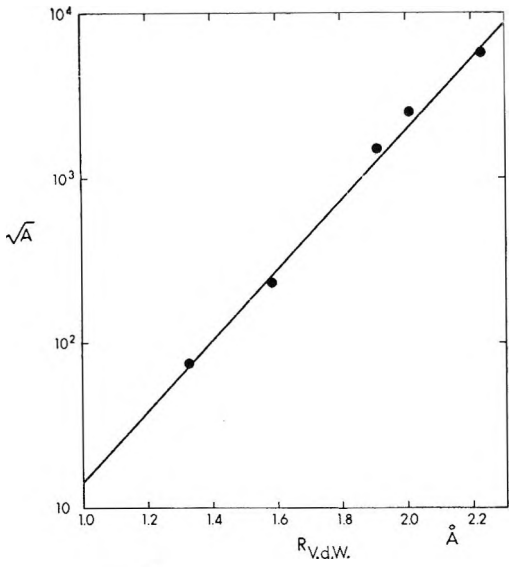


Figure 9. Plot of $A^{1/2}$ on a logarithmic scale *vs.* the van der Waals radius. $A$ is the constant in the repulsive energy term REL = $AR^{-12}$. Points shown on the graph represent $A^{1/2}$ values for repulsion between the inert gas atoms He···He, Ne···Ne, etc.

constant $A$ the following procedure was adopted. The values of $A$ for the repulsions between Ne···Ne, Ar···Ar, etc., were calculated from the six–twelve potential function of Lennard-Jones using the equation $A = 4\epsilon\sigma^{12}$. $\epsilon$ is the depth of the potential well and $\sigma$ is the interatomic distance for zero potential energy. The values for $\epsilon$ and $\sigma$ were taken from Hirschfelder, Curtis, and Bird.[18] It has been observed[19] that the $A$ values for the interactions between two nonidentical noble gas atoms like Ne···Ar can be approximated quite well by taking the geometric means of the $A$ values for Ne···Ne and Ar···Ar. Thus $A_{Ne,Ar} \approx A^{1/2}_{Ne,Ne} \times A^{1/2}_{Ar,Ar}$. This property was the basis of the selection of $A$ values for the present purposes. Figure 9 shows a plot of $A^{1/2}$ for the inert gases plotted on a logarithmic scale *vs.* their respective van der Waals radii. The straight line obtained allows one to select an $A^{1/2}$ value for any species for which an appropriate radius is available. It is important to realize that the selected radius must be consistent with the van der Waals radii used for the inert gases. Thus the radius for the isoelectronic positive alkali ion should be smaller than that of the corresponding inert gas atom and the radius of the halide ion should be larger. One set of $A^{1/2}$ values for the alkali ion–water repulsions was obtained by using the van der Waals radii for the alkali ions obtained by Stokes,[23] who determined these radii by quantum mechanical scaling of the van der Waals radii of the corresponding isoelectronic inert gas atoms. In one set of calculations the $A^{1/2}$ term representing the water molecules was taken as the $A^{1/2}$ term of the oxygen atom. The van der Waals radius of oxygen 1.4 Å was used. The radius in the $AR^{-12}$ term corresponded in this case to $R_{1,3}$, the distance between the alkali and oxygen nuclei. The resulting $A$ values for the $M^+\cdots O$ repulsions are given in Table III. The $M^+\cdots H$ repulsions were neglected. The potential energies $\Delta E_{0,1}$ from these $A$ values are given in Table III and Figure 7.

A second set of calculations was made with the $A^{1/2}$ values of the alkali ions as determined above and the $A^{1/2}$ value for water–water molecule repulsions given in the literature, (p 214, ref 18). The radius in the $AR^{-12}$ term in this case corresponded to $R_{1,3}$ + 0.3 Å. The potential energies calculated with these $A$ values were very similar to those obtained above (see Figure 7).

A third set of calculations was made for Na $(OH_2)_n$ in which the $A$ value was taken to be the same as that for the Ne···Ne repulsions. The justification for this procedure lies in the observation that $Na^+$ should be somewhat smaller than Ne while $H_2O$ should be somewhat larger and an approximate cancellation of the two errors might be expected. The potential energies obtained with this choice of $A$ are also shown in Figure 7 and are also in close agreement with the other two calculations.

At present, we do not understand too well why all choices of $A$ values lead to $-\Delta E_{0,n}$ results which are too high (see Figure 7). The following may be an explanation. All choices of $A$ depend on a certain assumed size parameter (radius) for the positive ion and the water molecule. However, since the electron cloud of the positive ion is compressed because of the excess nuclear charge, the electronic repulsive forces in a strong collision between the positive ion and the neutral should be larger than those occurring in a collision of two neutrals of the same size. This stiffness of the electron cloud of the alkali ion is not taken into account in the present choices of $A$. An empirical way of correcting for the greater stiffness of the positive ion is to choose a bigger radius. For example, the radii of Pauling[24] or Gourary and Adrian[25] might have been selected. The difficulty in such a procedure lies in the correlation of the ionic radii with the radii of the inert gases which are the basis of the plot in Figure 9.

(23) R. H. Stokes, *J. Amer. Chem. Soc.*, **86**, 979 (1964).

(24) L. Pauling, "The Nature of the Chemical Bond," Cornell University Press, Ithaca, N. Y., 1948.

(25) B. S. Gourary and F. J. Adrian, *Solid State Phys.*, **10**, 127 (1960).

# Hydration of the Halide Negative Ions in the Gas Phase. II. Comparison of Hydration Energies for the Alkali Positive and Halide Negative Ions

by M. Arshadi, R. Yamdagni, and P. Kebarle

*Chemistry Department, University of Alberta, Edmonton, Canada* *(Received September 2, 1969)*

The $\Delta H_{n-1,n}$, $\Delta G_{n-1,n}$, and $\Delta S_{n-1,n}$ for the gas-phase reactions $X^-(H_2O)_{n-1} + H_2O = X^-(H_2O)_n$ where $X^- = F^-$, $Cl^-$, $Br^-$, $I^-$ were measured for $n = 1$ to $n = 4$ or 5. The method of measurement depends on mass spectrometric sampling of the ions $X^-(H_2O)_n$ emerging from an ion source containing water vapor. Comparison of the enthalpies of $X^-(H_2O)_n$ with the enthalpies of the isoelectronic alkali $M^+(H_2O)_n$ shows that the isoelectronic positive ion gives stronger hydration interactions for small $n$. The difference between $\Delta H_{n-1,n}$ for the positive and negative isoelectronic ions decreases as $n$ increases. Electrostatic calculations of the potential energies of $X^-(H_2O)_n$ indicate that the relatively stronger interactions of the negative ions at high $n$ are probably due to a gradual change-over in the attachment mode of the water molecules to the negative ion. For small $n$ the water molecule "touches" the ion with both H atoms; at higher $n$ crowding is relieved by attachment through only one of the H atoms. The determined enthalpies for the halide and alkali ions are shown to be consistent with the total single ion hydration energies based on the Randles Volta measurements.

## Introduction

The gas-phase hydration energies for the alkali positive ions are described in the preceding paper[1] of this issue. The present work deals with the hydration energies of the halide ions in the reactions $(n - 1,n)$ occurring in the gas phase where $X^- = F^-$,

$$X^-(H_2O)_{n-1} + H_2O = X^-(H_2O)_n \quad (n - 1,n)$$

$Cl^-$, $Br^-$, and $I^-$. The principle of the determination of the hydration equilibria and the temperature dependence of the equilibrium constants $K_{n-1,n}$ was the same as that used in the preceding paper.[1]

The present work is a continuation of an earlier study[2] of the halide ions. In the earlier study equilibrium determinations were done only at room temperature so that no $\Delta H_{n-1,n}$ values could be obtained. Also the set of $(n - 1,n)$ reactions observed was more restricted. The study of the halide ions is a logical continuation of the alkali ion investigation. Both sets represent spherically symmetrical ions with noble gas electronic shells. However, since the orientation of the water molecules is different in the positive and negative ions, the hydration energies might show some specific differences. In an earlier comparison[2] of the hydration of the alkali and halide ions, which was restricted by the availability of a complete set of $\Delta G^\circ_{3,4}$ data only, we concluded that the gas-phase hydration energies are consistent with the single ion hydration energies based on Volta measurements by Randles.[3] The present results which are more detailed allow interesting elaborations to be made on the above conclusion.

The gas-phase hydration equilibria of the halide ions should also be of primary interest in the many fields of study involving ions at pressures from about $10^{-3}$ Torr to atmospheric pressure. Thus in electrical phenomena in the troposphere and ionosphere, drift and mobility experiments with gaseous ions, gas discharges, ionic reactions induced by ionizing radiation, flames, etc., water, and other polar molecules are often natural constituents, deliberate admixtures, or chance impurities. Clustering of the polar molecules around the ion occurs in such systems and has important effects on the mobility, recombination coefficients, and reactivity of the ions.

## Experimental Section

Most of the measurements were made with a magnetic mass spectrometer incorporating a high-pressure ion source. A 2000-eV electron beam was used as ionizing medium. Both ion source and electron gun were mounted in separate ports of an 8-in. pumping lead (Figure 1). The electron beam produced by a thoriated iridium filament is electrostatically focused by an electrode system similar to that employed in cathode ray tubes. The ion source machined out of

(1) I. Džidic and P. Kebarle, *J. Phys. Chem.*, **74**, 1466 (1970).

(2) P. Kebarle, M. Arshadi, and J. Scarborough, *J. Chem. Phys.*, **49**, 817 (1968); **50**, 1049 (1969).

(3) J. E. Desnoyers, in "Modern Aspects of Electrochemistry," Vol. 5, J. O. M. Bockris, Ed., Plenum Press, New York, N. Y., 1969, Chapter 1.

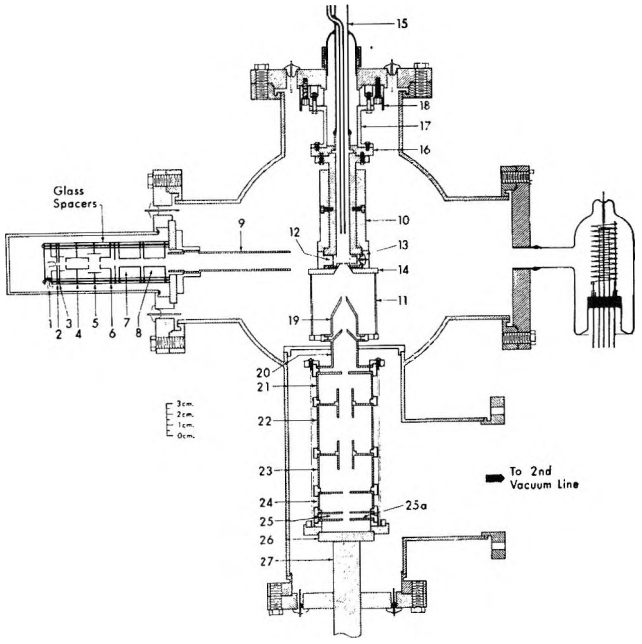


Figure 1. Electron beam high-pressure ion source: 1, electron filament; 2–6, electrodes for electrostatic focusing of electron beam; 7,8, deflection electrodes; 9, magnetic and electrostatic shielding of electron beam; 10, ion source with copper heating mantle; 11, electrostatic shielding of ions; 12, electron entrance slit; 13, electron trap; 14, copper lid holding ion exit slit flange; 15, gas inlet and outlet; 16–18, ion source supports and insulation; 19–26, ion beam acceleration and focusing; 27, mass spectrometer tube to 90° magnetic sector.

stainless steel had a port carrying the electron entrance slit (2 × 0.015 mm) and another port at right angles carrying the ion exit slit (2 × 0.015 mm). The vertical distance between the plane of the electron beam and the ion exit slit was 4 mm. All parts of the ion source were sealed with gold gaskets. This allowed operation of the source up to 500°. The ion source block was surrounded by a thick copper mantle which carried the heater wells.

The ions escaping from the exit slit were accelerated to the first cone electrode (Figure 1) where they entered a differentially pumped acceleration and focusing region. Mass analysis was obtained in a 90°, 15-cm radius magnetic sector tube which was also differentially pumped. The electron pulses produced in a secondary multiplier were counted with a counting system. The above arrangement of ion source and electron gun is very similar to that described in an earlier publication by Durden, Kebarle, and Good.[4] An improvement in the present setup is the high-temperature capability of the ion source.

The electron beam could be pulsed and the ion detection could be gated in a manner similar to that used in the Durden apparatus. Shown in Figure 2 is the detected total ion intensity with time after a 50-μsec electron pulse. The ion source contained 3 Torr of water vapor. It can be seen that the average time which an ion spends in the ion source is some 2–3 msec. One can calculate on the basis of clustering reaction rate constants for the hydration of the proton determined recently[5] that clustering equilibria in that system are achieved in less than 100 μsec at water pressures larger than 0.2 Torr. Assuming that the rate constants for the clustering equilibria of the halides are of a similar order of magnitude, it follows that the equilibria for these ions are also achieved within the source residence time of the average sampled ion. All clustering equilibria measurements were made under continuous electron irradiation and ion detection since under these conditions the intensity of the detected signal is highest.

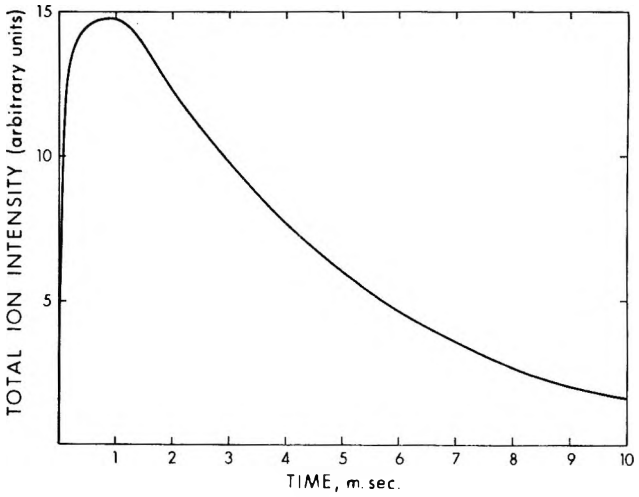


Figure 2. Total ion intensity detected with mass spectrometer after electron pulse of 50-μsec duration. Curve shows that ion residence time of the average ion is considerably longer than 100 μsec.

Some of the measurements were made with the α-particle mass spectrometer which has been described previously.[2] In order to be able to increase the temperature of the ion source without increasing the temperature of the α source a modification was made to the earlier apparatus. The α source was mounted in a separate hermetically sealed compartment which was not in physical contact with the ion source. Both the α particle compartment and ion source α entrance port were sealed by 0.0001-in. stainless steel foils. The arrangement is shown in Figure 3.

The measurement of water pressure and other experimental conditions were very similar to those described in previous publications.

The compounds used to produce the halide ions were the same as those used in the earlier work.[2]

(4) D. A. Durden, P. Kebarle, and A. Good, *J. Chem. Phys.*, **50**, 805 (1969).

(5) A. Good, D. A. Durden, and P. Kebarle, *ibid.*, in press.

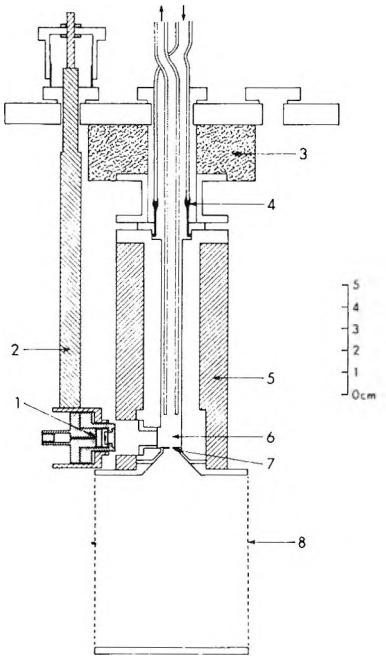


Figure 3. $\alpha$-Particle high-temperature ion source: 1, $\alpha$ source in double container with two foil windows and two porous stainless steel plugs for pressure equalization; 2, copper rod carrying $\alpha$ source container and allowing vertical motion of $\alpha$ source; 3, insulation; 4, double gas inlet for allowing gas circulation; 5, copper heating mantle; 6, ion source; 7, ion exit slit; 8, shielding electrode and copper bottom of ion source.

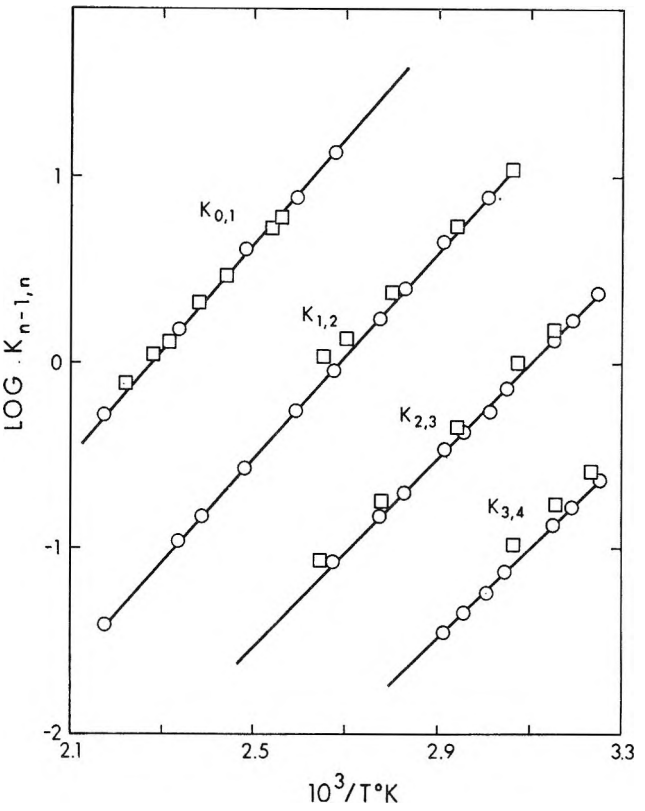


Figure 5. van't Hoff plots of the equilibrium constants $K_{n-1,n}$ for the gas-phase hydration of $Cl^-$: ○, electron beam mass spectrometer; □, $\alpha$ particle mass spectrometer.

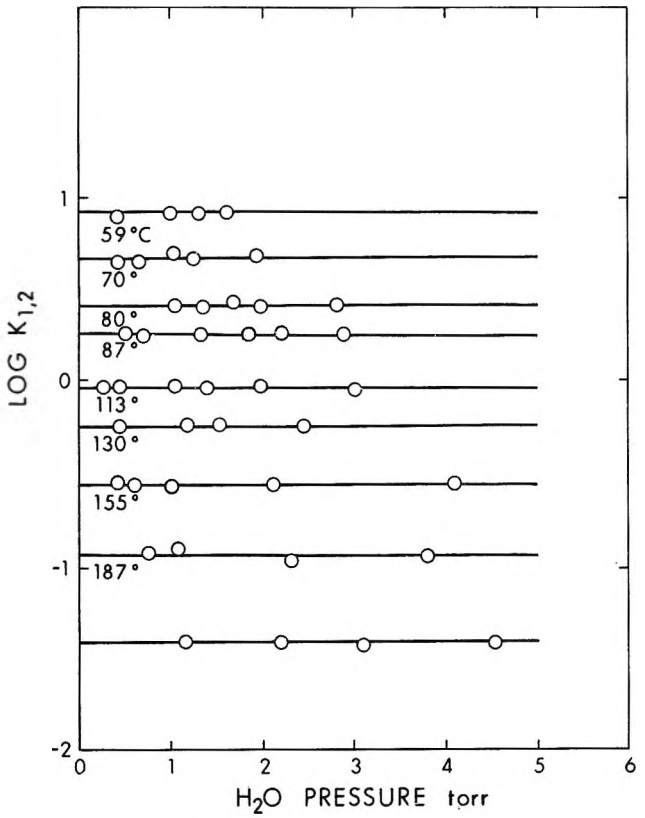


Figure 4. Plots of log $K_{1,2}$ for the gas-phase hydration of $Cl^-$ at various constant temperatures *vs.* pressure of $H_2O$.

## Results and Discussion

*A. Results for the Halide Ions.* An example of some typical determinations of the equilibrium constants $K_{n-1,n}$ is given in Figure 4 which shows $K_{1,2}$ for $Cl^-$ as a function of water pressure and reaction temperature. The equilibrium constants were determined from the measured ion ratio $I_n/I_{n-1}$ and the known water pressure $p$ using the equation $K_{n-1,n} = I_n/(I_{n-1}p)$. The data in Figure 4 demonstrate that the equilibrium constants do not change with water pressure. van't Hoff plots of the equilibrium constants of $Cl^-$ are given in Figure 5 showing the straight lines obtained whose slopes lead to the determination of $\Delta H_{n-1,n}$. Results of similar appearance were obtained also for the other halides. The experimental $\Delta H_{n-1,n}$, $\Delta G^\circ_{n-1n}$, and $\Delta S^\circ_{n-1,n}$ for the halide ion hydrations are summarized in Table I and Table II.

The $\Delta H_{n-1,n}$ of the halide ions are also shown in Figure 6 plotted *vs.* $n$. The figure shows that the $-\Delta H_{n-1,n}$ are highest for $F^-$ and lowest for $I^-$ as would be expected from the relative size of the ions. The variation of $\Delta H_{n-1,n}$ with $n$ will be considered below in connection with electrostatic calculations.

The consistency of the relative $\Delta H_{n-1,n}$ values for the different halides with available thermodynamic data is checked in Figure 7 which gives a plot of $\Delta H_{0,n}(I^-) - \Delta H_{0,n}(X^-)$ *vs.* $n$, where $X^- = F^-$, $Cl^-$,

**Table I:** Experimentally Determined Enthalpies and Calculated Potential Energies for Hydration Reactions of the Halide Ions.[a] $X^-(H_2O)_{n-1} + H_2O = X^-(H_2O)_n$

| | $F^-$ | | | $Cl^-$ | | | $Br^-$ | | | $I^-$ | | |
|---|---|---|---|---|---|---|---|---|---|---|---|---|
| $(n-1,n)$ | $-\Delta H$ | $-\Delta E$ (sym) | $-\Delta E$ (nonsym) | $-\Delta H$ | $-\Delta E$ (sym) | $-\Delta E$ (nonsym) | $-\Delta H$ | $-\Delta E$ (sym) | $-\Delta E$ (nonsym) | $-\Delta H$ | $-\Delta E$ (sym) | $-\Delta E$ (nonsym) |
| (0,1) | 23.3 | 18.8 | 12.6 | 13.1 | 13.2 | 8.7 | 12.6 | 12.7 | 8.4 | 10.2 | 9.7 | 6.4 |
| (1,2) | 16.6 | 16.9 | 12.0 | 12.7 | 12.3 | 8.4 | 12.3 | 11.9 | 8.1 | 9.8 | 9.2 | 6.2 |
| (2,3) | 13.7 | 13.3 | 10.6 | 11.7 | 10.5 | 7.7 | 11.5 | 10.3 | 7.4 | 9.4 | 8.2 | 5.8 |
| (3,4) | 13.5 | 10.5 | 9.5 | 11.1 | 9.2 | 7.1 | 10.9 | 9.0 | 6.9 | ... | 7.5 | 5.4 |
| (4,5) | 13.2 | 5.8 | 8.3 | ... | 6.3 | 6.4 | ... | 6.3 | 6.2 | ... | 5.6 | 5.1 |
| (5,6) | ... | 2.1 | 7.2 | ... | 4.2 | 5.8 | ... | 4.4 | 5.7 | ... | 4.5 | 4.7 |
| $R(X^-H_2O)$,[b] Å | ... | 2.46 | 3.05 | ... | 2.92 | 3.48 | ... | 2.97 | 3.54 | ... | 3.37 | 3.92 |
| $A$,[c] Å$^{12}$ kcal mol$^{-1}$ | | $5.06 \times 10^4$ | | | $2.746 \times 10^5$ | | | $3.445 \times 10^5$ | | | $1.181 \times 10^6$ | |

[a] All energy values in kcal/mol. [b] $R$ corresponds to the distance between the centers of the negative ion and the water molecule for the case $n = 1$. [c] Value of constant in term $AR^{-12}$ used for electronic repulsion between hydrogen atom of water molecule and halide ion.

**Table II:** Gas-Phase Free Energies and Entropies for Hydration Reaction of Halide Ions.[a] $X^-(H_2O)_{n-1} + H_2O = X^-(H_2O)_n$

| | $-\Delta G°_{n-1,n}$, kcal/mol | | | | $-\Delta S°_{n-1,n}$, eu | | | |
|---|---|---|---|---|---|---|---|---|
| $n-1,n$ | $F^-$ | $Cl^-$ | $Br^-$ | $I^-$ | $F^-$ | $Cl^-$ | $Br^-$ | $I^-$ |
| 0,1 | 18.1 | 8.2 | 7.0 | 5.4 | 17.4 (22.5)[b] | 16.5 (20.9) | 18.4 (20.0) | 16.3 (17.7) |
| 1,2 | 11.0 | 6.5 | 5.5 | 4.2 | 18.7 | 20.8 | 22.9 | 19.0 |
| 2,3 | 7.6 | 4.5 | 4.1 | 3.1 | 20.4 | 23.2 | 24.8 | 21.3 |
| 3,4 | 5.5 | 3.4 | 2.9 | ... | 36.9 | 25.8 | 26.8 | ... |
| 4,5 | 7.1 | ... | ... | ... | 30.7 | ... | ... | ... |

[a] Standard state 1 atm, $T = 298°K$. [b] Values in parentheses correspond to $-\Delta S_{0,1}$ calculated using bond distances and vibrational frequencies, based on electrostatic calculations.

and $Br^-$. It is to be expected that for large $n$ the above difference should approach the difference between the single ion heats of hydration $\Delta H_h(I^-) - \Delta H_h(X^-)$. Indicated on the figure are the values for these differences obtained from the single ion hydration enthalpies of Latimer, Pitzer, and Slanski and Randles.[3] The $\Delta H_{n-1,n}$ values used in the plot are those directly measured when available or extrapolated values from Figure 7. The plot shows that the present determinations are consistent with the single ion hydration enthalpies since the $\Delta H_{0,n}$ differences extrapolate approximately to the single ion hydration differences. For $F^-$ and $Cl^-$ the single ion hydration differences calculated from the Latimer and Randles data are quite close. However, for the case of $Br^-$ there is an appreciable difference. This difference should be due to the use of different values for the electron affinity of Br in the Born cycles involved in the evaluations.[6a] It will be noted in Figure 7 that the Br $\Delta H_{0,n}$ difference curve crosses the Latimer line and is asymptotic to the Randles line. Therefore the present results are consistent with the Randles data which were evaluated with use of more recent and better electron affinities.

*B. Electrostatic Calculations for the Negative Ions and Comparison of Calculations with Experimental Results.* Electostatic calculations of the potential energy $E_n$ of the clusters $X^-(H_2O)_n$ were made since it was believed that a comparison of the calculations with the $\Delta H_{n-1,n}$ will help in the interpretation of the experimental results. The potential energy $E_n$ was expressed according to eq I as a sum of the attractive potential energy

$$E_n = \text{EDIP} + \text{EPOL} + \text{EDIS} + \text{RDIP} + \text{REL} \quad \text{(I)}$$

terms EDIP, EPOL, and EDIS standing for the ion–dipole, ion–induced dipole, and ion–water molecule dispersion forces interactions. The repulsive interactions considered were RDIP and REL standing for the dipole–dipole repulsions between the water molecules and the repulsion between the charge clouds of the ion and the water molecules. The procedures followed in the calculations were the same as those given in the preceding paper.[1] All water molecules were placed in equivalent positions. For the negative ions, two orientations of the water molecules may be considered. In one orientation the negative ion lies on the extension of the bisector of the HOH angle

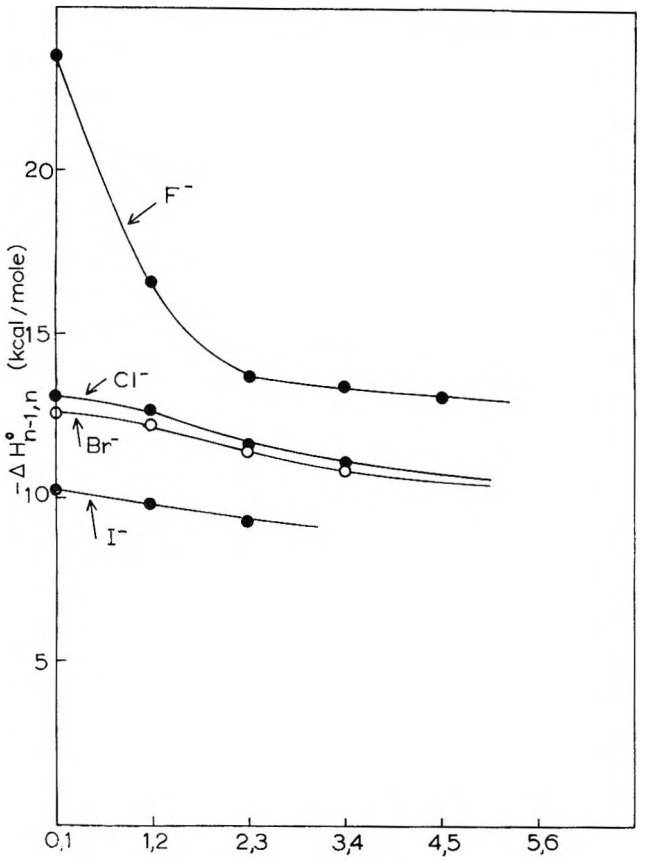


Figure 6. $\Delta H_{n-1,n}$ *vs.* $n$ for hydration of halide ions.

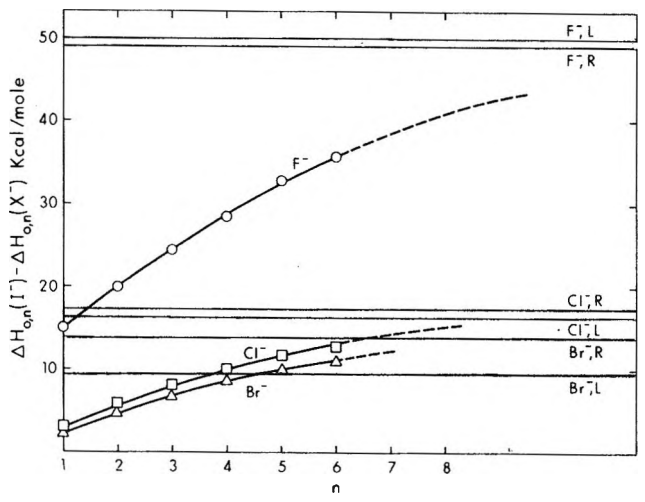


Figure 7. Comparison of experimental $\Delta H_{0,n}$ with total single ion heats of hydration of Latimer, Pitzer, and Slanski (L) and Randles (R).

and the two hydrogens are symmetrically "touching" the ion. This orientation we will call symmetric. In the second nonsymmetric orientation the negative ion lies on the extension of the H–O bond with one hydrogen atom touching the ion and the other rotated around the X---H–O axis to a position of minimum potential energy.

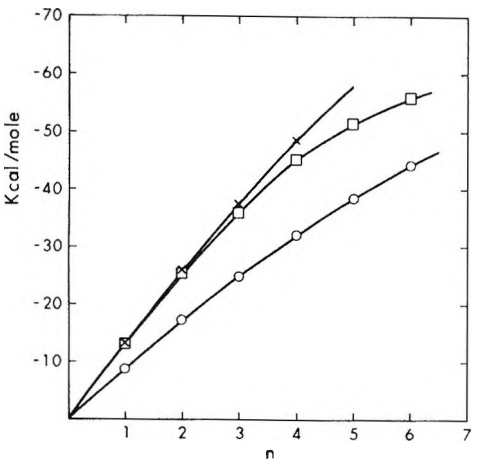


Figure 8. Comparison of calculated potential energy $\Delta E_{0,n}$ and experimental $\Delta H_{0,n}$ for $Cl^-(H_2O)_n$: ×, $\Delta H_{0,n}$; □, $\Delta E_{0,n}$ (sym); ○, $\Delta E_{0,n}$ (nonsym).

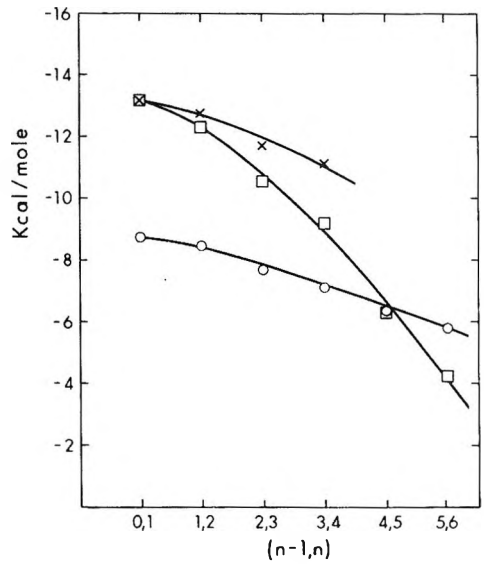


Figure 9. Comparison of calculated potential energy $\Delta E_{n-1,n}$ and experimental $\Delta H_{n-1,n}$ for $Cl^-(H_2O)_n$: ×, $\Delta H_{n-1,n}$; □, $\Delta E_{n-1,n}$ (sym); ○, $\Delta E_{n-1,n}$ (nonsym).

The electronic repulsion energies REL were calculated under the assumption that only the repulsions between the ion and the hydrogen atoms "touching" it are important. The repulsive term REL was set equal to $2A/R^{12}$ for the symmetric structure and $A/R^{12}$ for the nonsymmetric structure. $R$ is the distance between the ion and hydrogen nuclei. The selection of the constant $A$ was obtained by the procedure outlined in the Appendix of the preceding paper.[1] As distance parameters for Figure 9 of the Appendix, in ref 1, the Stokes van der Waals radii were used for the halide ions: $F^-$ (1.909 Å), $Cl^-$ (2.252 Å), $Br^-$ (2.298 Å), $I^-$ (2.548 Å), and the van der Waals radius for hydrogen H (1.2 Å). The resulting values for $A$ are given in Table I.

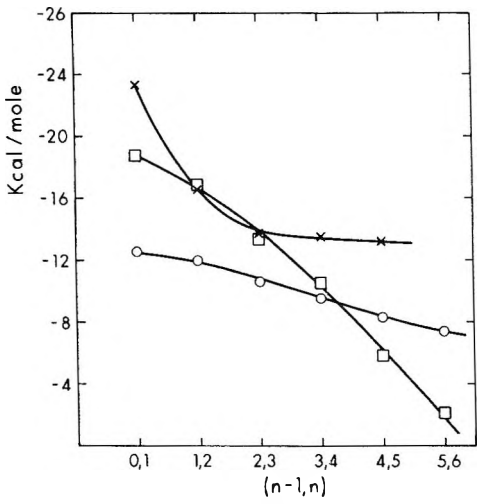


Figure 10. Comparsion of calculated potential energy $\Delta E_{n-1,n}$ and experimental $\Delta H_{n-1,n}$ for $F^-(H_2O)_n$: ×, $\Delta H_{n-1,n}$ □, $\Delta E_{n-1,n}$ (sym); ○, $\Delta E_{n-1,n}$ (nonsym).

The results of the calculations are given in Table I and Figures 8, 9, and 10. In Figure 8 a comparison is made between the experimental $\Delta H_{0,n}$ and the calculated $\Delta E_{0,n}$ (sym) and (nonsym) for the medium sized ion $Cl^-$. The figure shows that there is very good agreement between the $\Delta H_{0,1}$ and $\Delta H_{0,2}$ and the calculated symmetric values. For higher $n$, the calculated $-\Delta E_{0,n}$(sym) become somewhat smaller than the experimental results. The $-\Delta E_{0,n}$ (nonsym) are considerably lower for all $n$. However, the fall-off in slope with increase of $n$ in the nonsymmetric case is slower than that of the symmetric case. This tendency is shown more clearly in Figure 9 which gives $\Delta H_{n-1,n}$ and $\Delta E_{n-1,n}$. The fall-off of the $-\Delta E_{n-1,n}$ (sym) is much faster than that of the experimental or the nonsymmetric values. The slower fall-off observed for the nonsymmetric case must be due to the fact that the nonsymmetric arrangement allows more molecules to be fitted around an ion of given radius, *i.e.*, this arrangement minimizes the repulsions between the water molecules. Probably in the actual clusters, the first water molecules go in the symmetric positions, but as the cluster grows some molecules assume symmetric and others nonsymmetric positions or positions intermediate between symmetric and nonsymmetric.

The calculations for the larger ions $Br^-$ and $I^-$ reveal trends which are very similar to the trends in the $Cl^-$ ion; therefore they will not be discussed. However, the $F^-$ ion shows an interesting deviation which should be mentioned. In Figure 10 one finds that the $-\Delta H_{0,1}$ is considerably larger than the calculated $-\Delta E_{0,1}$. Since the symmetric $\Delta E_{0,1}$ were in good agreement with $\Delta H_{0,1}$ for all other ions, the discrepancy observed in the $F^-$ case indicates that the bonding in $F^- \cdot H_2O$ is not well approximated by the electrostatic model. The additional bonding probably comes about from an F–H bond formation. Thus the electronic structure of the monohydrate is probably a hybrid of the mesomeric structures I, II, and III. The fact that this effect does not occur

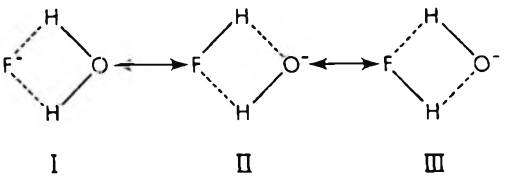


to such a large extent with the other halides is easily understood. The tendency for H–X bond formation is by far the largest for fluorine. This is illustrated by the very high bond dissociation energy in hydrogen fluoride $D$(H–F) = 135 kcal/mol as compared with $D$(H–Cl) = 103 and $D$(H–I) = 71 kcal/mol.

The close agreement between the absolute values of the calculated $\Delta E_{0,1}$ and $\Delta E_{1,2}$(sym) and the corresponding experimental $\Delta H_{0,1}$ and $\Delta H_{1,2}$ is probably not significant.

We do not believe that the electrostatic calculation is capable of producing such close agreement with experiment. In the preceding paper[1] dealing with the alkali ions, rather poor agreement was found between the electrostatic calculations and experiment. In that place reasons were given as to why the $A$ values selected by the procedure used in the Appendix of ref 1 might be effectively too low for the positive ions. If these reasons are valid, the $A$ values selected for the negative ions should be too low and thus lead to $-\Delta E_{0,n}$ which are too low. We think that absolute values of the electrostatic calculations for positive and negative ions do not have any great significance and that only the relative changes with $n$ are instructive.

*C. Comparison between the Hydration Energies of the Alkali and Halide Ions.* The experimental enthalpies $\Delta H_{n-1,n}$ for the alkali and the halide ions are shown together in Figure 11 plotted *vs.* $(n-1, n)$. The hydration interactions of these spherical ions are probably best examined if one compares the hydration energies of isoelectronic pairs like $K^+$ and $Cl^-$, $Rb^+$ and $Br^-$, etc. Since the nuclear charge of the negative ion in the isoelectronic pair is two units lower, the size of the electron cloud of the isolated negative ion will be definitely larger than that of the positive ion. Therefore, if one considers only the effect of ionic size (*in vacuo*) one would definitely predict that the positive isoelectronic ion should have higher $-\Delta H_{n-1,n}$. Examining the enthalpies of the larger ions like $K^+$ and $Cl^-$, $Rb^+$ and $Br^-$, and $Cs^+$ and $I^-$, for which the effect of any covalent bonding to water should be small, we notice (Figure 11) that in all cases the isoelectronic positive ion has considerable higher $-\Delta H_{n-1,n}$. Thus the prediction based only on the size of the ions is borne out at least qualitatively

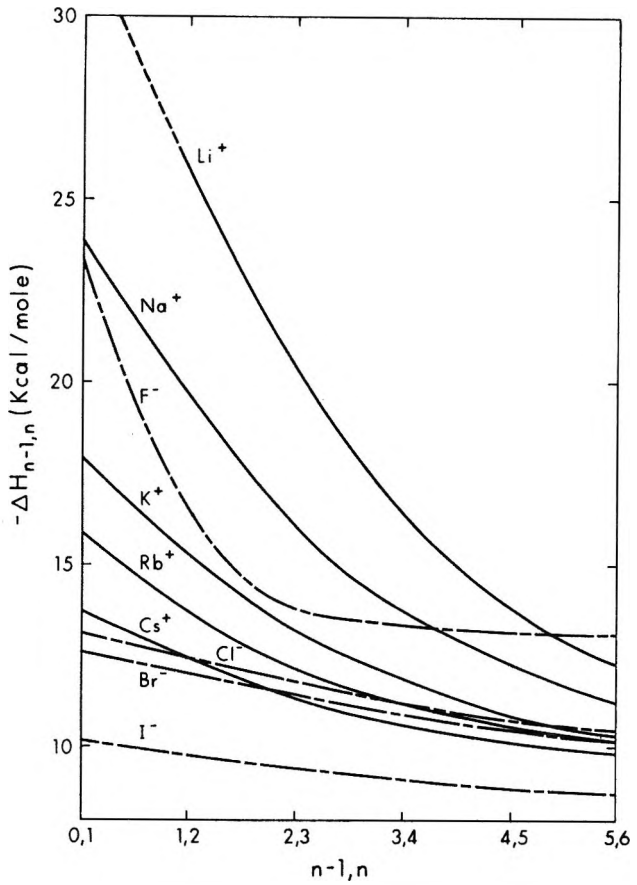


Figure 11. Comparison of $\Delta H_{n-1,n}$ for hydration of alkali positive and halide negative ions.

by the results. It is interesting to note that the difference between the $\Delta H_{n-1,n}$ of the isoelectronic pairs decreases as $n$ becomes larger and that in the cases of $Na^+$ and $F^-$, $K^+$ and $Cl^-$, $Rb^+$ and $Br^-$ a crossover is observed within the range of the figure in which the $-\Delta H_{n-1,n}$ of the negative ion becomes higher. Furthermore, the smaller the size of the ions the sooner does the crossover occur. For the $Na^+$, $F^-$ it occurs at about $n = 4$, for $K^+$,$Cl^-$ at $n \approx 5.5$ and for $Ru^+$,$Br^-$ at $n \approx 6$. These observations can be explained on basis of the electrostatic calculations which indicated that the slower decrease of $-\Delta H_{n-1,n}$ of the negative ions is due to the ability of the water molecules to assume nonsymmetric positions in which only one of the hydrogen atoms "touches" the negative ion. These nonsymmetric arrangements result in lower water–water repulsions for ligands in the same shell and become of importance when the shell becomes crowded. Of course crowding occurs sooner in the smaller ions.

It is of interest to examine at this point the correlation of the present results with the total single ion hydration enthalpies. Values for the total enthalpies of hydration have been obtained by several authors on the basis of thermodynamic cycles and experimental and semiempirical evaluations of the energies required in the various steps of the cycle. Two sets of data which have found wide acceptance are those of Latimer, Pitzer, and Slanski and Randles.[3] Data from these two sets were used earlier in the paper for a correlation of the relative heats of hydration of negative ions. Examining the values that the Latimer set gives for the alkali and halide ions, one finds that the $-\Delta H_h$ for the negative ion is substantially larger than that for the positive isoelectronic ion. Thus $-\Delta H_h$ ($Br^-$) = 81.4 kcal/mol while $-\Delta H_h$ ($Rb^+$) = 69.2 kcal/mol. Therefore Latimer's heats of hydration are exactly of opposite magnitudes to those expected from the standpoint of electron cloud size of the gaseous alkali and halide ions. Two basically different reasons have been put forward to explain the Latimer data. The first explanation which exists in several variations[6] proposes that the arrangement of water molecules around the negative ion and (or) in the transition from the hydrated ion to the bulk of the liquid is more favorable. The second suggestion has been that water molecules have an electrical quadrupole moment which is of such a size that it leads to an attraction with negative and repulsion with positive ions.[7] On the basis of the present results which give higher energies of interactions for the positive ions, it is possible to eliminate the quadrupole theory since the effect of the quadrupole should be particularly large exactly at close range, *i.e.*, in the gaseous clusters. It should be pointed out that the present results do not prove that a quadrupole moment is completely absent. They only show that a water quadrupole moment of the magnitude required to explain the Latimer data cannot be present. In any event, as is shown in the subsequent discussion, the present results cannot be reconciled with the very strong hydration interaction for negative ions predicted by the Latimer data.

The Randles total hydration energy set assigns a slightly higher $-\Delta H_h$ for $F^-$ than for $Na^+$ but for the larger ions the $-\Delta H_h$ of the positive isoelectronic ions are somewhat larger than those of the negative ions. The Randles data are thus closer to expectations based on the present results. A correlation of the present data and the single ion hydration energies of Latimer and Randles is given in the composite Figures 12a,b which shows plots of $[-\Delta H_{0,n}(M^+)] - [-\Delta H_{0,n}(X^-)]$ for isoelectronic pairs. The plots are based on the experimental $\Delta H_{n-1,n}$ whenever these were available (low $n$). For higher $n$, values extrapolated on basis of Figure 11 were used. Also indicated in Figure 12 (as two horizontal lines) are the differences of the total single ion hydration energies

(6) (a) E. T. Verwey, *Rec. Trav. Chim.*, **61**, 127 (1942); (b) D. R. Rosseinsky, *Chem. Rev.*, **65**, 467 (1965).

(7) A. D. Buckingham, *Discussions Faraday Soc.*, **24**, 151 (1957); F. Vaslow, *J. Phys. Chem.*, **67**, 2773 (1963).

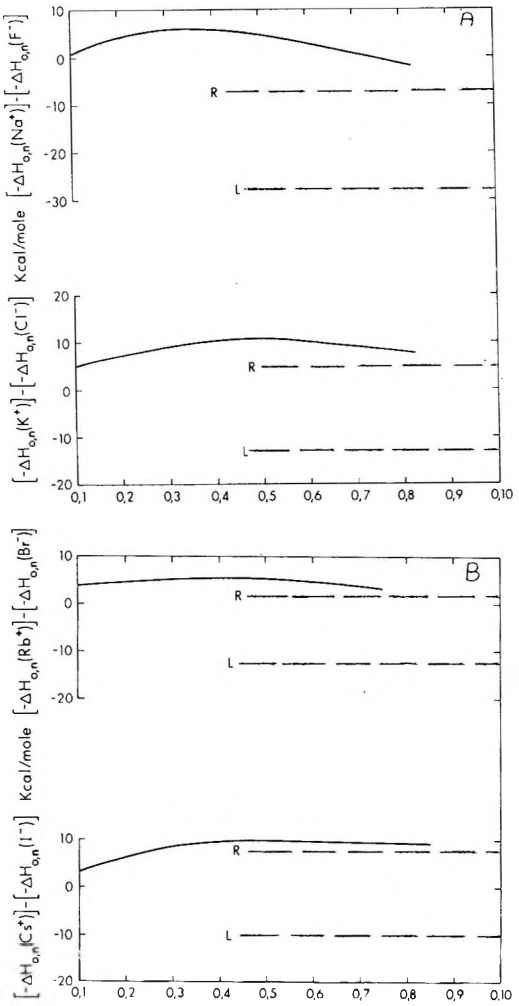


Figure 12. Comparison of $\Delta H_{0,n}$ hydration of alkali and halide ions with total enthalpies of hydration of Latimer, Pitzer, and Slanski (L) and Randles (R).

for the isoelectronic pairs based on the data of Latimer and Randles. It can be seen that the $\Delta H_{0,n}$ differences are in all cases much closer to the Randles differences; moreover, the $\Delta H_{0,n}$ differences seem to extrapolate for high $n$ into the Randles differences. Of course by definition the $\Delta H_{0,n}$ differences should become equal to the $\Delta H_h$ differences for very high $n$.

We can summarize the observations on positive and negative isoelectronic pairs as follows. In the initial hydration interactions ($n$ small) the positive ion gives higher energies of interaction as would be expected from its smaller size. As the cluster grows, interactions in the negative ion become gradually more favorable (Figures 11 and 12). This is probably due to the ability of the negative ion to pack the water molecules more closely without too large water–water repulsions. Extrapolation of the data to moderately high $n$ seems to lead to an asymptotic approach to the Randles data. Thus the present results are in support of the Randles data and also indicate that the decisive interactions determining the total heats of hydration occur during the attachment of the first 8–12 molecules. One may consider the further path toward the formation of a liquid solution as a single step in which the large clusters are fitted into the bulk of the liquid. The present results indicate that the hydration energy for this final "step" will be quite similar for a positive or negative cluster containing the corresponding isoelectronic ion.

*D. Entropies of Hydration Reactions.* The experimentally determined entropies are summarized in Table II. The Table also includes values for $\Delta S_{0,1}$ which were calculated from the translational, rotational, and vibrational entropy changes in the 0,1 reaction using the well known formulas of statistical mechanics. The rotational entropies were determined on basis of the $X^-$–$H_2O$ distances obtained from the electrostatic calculations. The vibrational entropy changes were calculated by assuming three new vibrational modes in the complex $X^-$–$H_2O$. The force constants for these vibrations were obtained from the electrostatic calculations. The procedure was essentially identical with that used for $K^+(OH_2)$ which has been described in greater detail in ref 8.

Comparing the experimental and calculated $\Delta S_{0,1}$ one finds that the agreement is only fair. The theoretical $-\Delta S_{0,1}$ are generally larger. The agreement between calculated and experimental values for the alkali hydrates was very much better.[1] It is difficult to say whether the differences between the present calculated and experimental results reveal structural features in the complexes not taken into account by the calculation or whether they are due to experimental error in the $\Delta S_{0,1}$ determinations. Unfortunately, the $\Delta S$ determinations are obtained from the differences of two large terms $\Delta G$ and $\Delta H$ and are therefore subject to greater error.

Examining the changes of $\Delta S_{n-1,n}$ with increase of $n$, one finds that the $-\Delta S$ values increase as $n$ increases. The same trend was observed with the alkali hydrates. The increase of the negative entropies should reflect the gradual loss of freedom of the water molecules in the complex due to crowding in the cluster.

*Acknowledgments.* This work was supported by the Canadian National Research Council. Figure 2 in the text was obtained by Mr. J. Payzant, a graduate student in our laboratory.

(8) S. K. Searles and P. Kebarle, *Can. J. Chem.*, **47**, 2619 (1969).

# Hydration of $OH^-$ and $O_2^-$ in the Gas Phase. Comparative Solvation of $OH^-$ by Water and the Hydrogen Halides. Effects of Acidity

by M. Arshadi and P. Kebarle

*Chemistry Department, University of Alberta, Edmonton, Canada* *(Received September 2, 1969)*

The thermodynamic quantities $\Delta H_{n-1,n}$, $\Delta G^\circ_{n-1,n}$ and $\Delta S^\circ_{n-1,n}$ for the reactions $OH^-(H_2O)_{n-1} + H_2O = OH^-(H_2O)_n$ and the analogous reaction but involving $O_2^-$ have been determined for $n$ up to 5,($OH^-$) and $n$ up to 3,($O_2^-$) with a mass spectrometer utilizing a high-pressure source made for the study of clustering equilibria. Comparison of the $\Delta H_{n-1,n}$ values with those of $F^-$ which were determined previously shows that both ions have very similar hydration interactions. The $-\Delta H_{0,1}$ of $F^-$ is slightly higher than that of $OH^-$; however the $-\Delta H_{n-1,n}$ of $OH^-$ becomes slightly higher for larger $n$. The results show a specifically high $-\Delta H_{0,1}$ for both $F^-$ and $OH^-$ which must be due to the partial covalent bonding in the monohydrates. The results indicate that the total enthalpies of hydration of $F^-$ and $OH^-$ should be very similar with $-\Delta H_h$-($OH^-$) probably higher. The changes of $\Delta H$ for the gas-phase solvation reactions $OH^- + HX = (OHHX)^-$ where X = OH, F, Cl, Br, I, can be calculated from available experimental data. The exothermicity of the reactions increases in the order given above. The energy values can be correlated with the acidity of HX.

## A. Hydration of $OH^-$ and $O_2^-$ in the Gas Phase

A recent mass spectrometric study[1] of the gas-phase hydration reactions of the halide ions has been extended to the $OH^-$ and $O_2^-$ ions. The mass spectrometer which has a high-pressure ion source and utilizes 2000-eV electrons for the ionization has been described in ref 1. All techniques used were similar to those given in ref 1.

The $OH^-$ and its hydrates $OH^-(H_2O)_n$ were observed in water vapor containing traces of hydrogen peroxide and in pure water vapor. The hydrates of $O_2^-$ were observed in oxygen containing a known partial pressure of water. Total pressures were in the 1–5 Torr range. The water vapor partial pressures in the determinations of $O_2^-(H_2O)_n$ varied from 0.1 to 0.8 Torr. Equilibrium constants $K_{n-1,n}$ for the reactions

$$OH^-(H_2O)_{n-1} + H_2O = OH^-(H_2O)_n$$

$$O_2^-(H_2O)_{n-1} + H_2O = O_2^-(H_2O)_n$$

which were constant with water pressure in the experimental range were obtained for both ions. Figure 1 shows a van't Hoff plot of the equilibrium constants for the $OH^-$ hydration reactions. The $\Delta H_{n-1,n}$ and corresponding $\Delta G^\circ$ and $\Delta S^\circ$ data for both ions are shown in Table I.

The $\Delta H_{0,1}$ value for $OH^-$ can be compared with the results of an electron detachment study by Golub and Steiner.[2] These authors obtained 2.95 ± 0.15 eV as the required energy for the reaction

$$H_3O_2^- \longrightarrow OH + H_2O + e$$

Using 1.8 eV for the electron affinity of $OH^-$ they calculated a value of 1.2 eV or 27.6 kcal/mol for the sum of the kinetic energy of the separating particles and the binding energy between $H_3O_2^-$ relative to $OH^-$ and $H_2O$. The present experimental value $\Delta H_{0,1} = -22.5$ kcal/mol would indicate that the kinetic energy contribution was 5 kcal.

**Table I:** Experimental Thermodynamic Values for the Reactions

| Reaction $n-1,n$ | $-\Delta H^\circ_{n-1,n}$, kcal/mol | $-\Delta G^\circ_{n-1,n(298)}$,[b] kcal/mol | $-\Delta S^\circ_{n-1,n(298)}$,[b] eu |
|---|---|---|---|
| $OD^-(D_2O)_{n-1} + D_2O \rightleftharpoons OD^-(D_2O)_n$[a] | | | |
| 0,1 | 22.5 | 16.9 | 19.1 |
| 1,2 | 16.4 | 10.7 | 19.3 |
| 2,3 | 15.1 | 7.73 | 24.8 |
| 3,4 | 14.2 | 5.45 | 29.5 |
| 4,5 | 14.1 | 4.22 | 33.2 |
| $O_2^-(H_2O)_{n-1} + H_2O \rightleftharpoons O_2^-(H_2O)_n$ | | | |
| 0,1 | 18.4 | 12.5 | 20.1 |
| 1,2 | 17.2 | 9.71 | 25.1 |
| 2,3 | 15.4 | 7.02 | 28.2 |

[a] In order to avoid overlap of the mass of $OH^-(H_2O)$ (35) with the mass of $Cl^-$ (35) which was present as a small impurity, $OD^-$ and $D_2O$ were used in the experiments. The thermodynamic values for the protonated species should be practically the same. [b] Standard state 1 atm.

(1) M. Arshadi, R. Yamdagni, and P. Kebarle, *J. Phys. Chem.*, **74**, 1475, (1970).

(2) S. Golub and B. Steiner, *J. Chem. Phys.*, **49**, 5191 (1968).

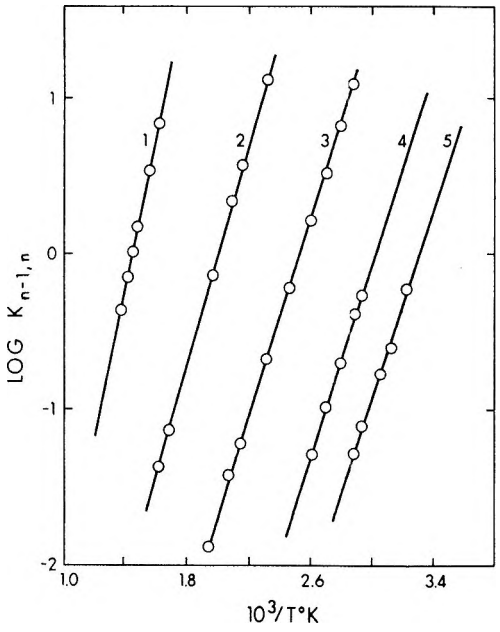


Figure 1. van't Hoff type plots of the equilibrium constants $K_{n-1,n}$ for the gas-phase hydration of $OH^-$. Numbers in figure correspond to $n$.

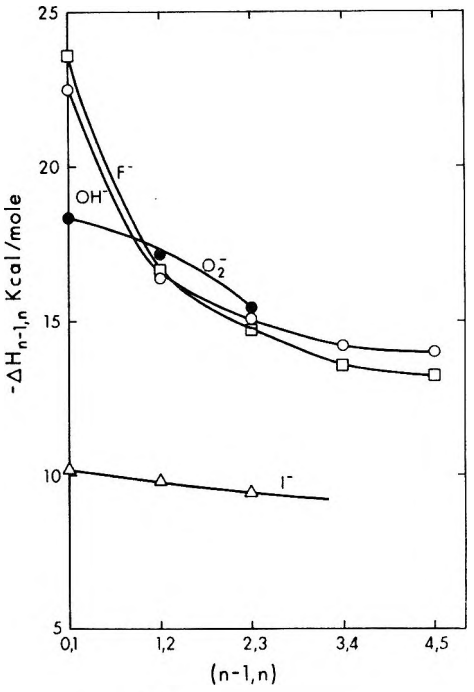


Figure 2. Plots of $-\Delta H_{n-1,n}$ for hydration reactions in the gas phase. $F^-$ and $I^-$ are added to the figure for comparison purposes. □, $F^-$; ○, $OH^-$; ●, $O_2^-$; △, $I^-$.

The enthalpies $\Delta H_{n-1,n}$ of $OH^-$ and $O_2^-$ are shown in Figure 2 in function of $n$. Included in the figure for comparison are the corresponding values for $F^-$ which is a small ion of the size of $OH^-$ and $I^-$ which is a large negative ion. The $\Delta H$ values of the halide ions come from ref 1. Comparing first $OH^-$ and $F^-$ we notice that $-\Delta H_{0,1}$ for $F^-$ is somewhat higher but that for higher $n$ the $-\Delta H_{n-1,n}$ of $OH^-$ become slightly bigger. Both ions show a very large drop-off between $-\Delta H_{0,1}$ and $\Delta H_{1,2}$, which indicates specially strong bonding in the monohydrate complex. The strong bonding in the monohydrate complex in $F^-$ was explained as partly due to covalent bonding. Similar reasons should apply also for the $OH^-$ ion. The resonance structures probably contributing to the bonding in both cases are shown below

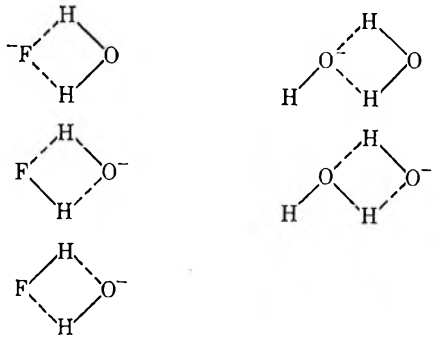

On the basis of the $\Delta H_{n-1,n}$ values for $F^-$ and $OH^-$ shown in Figure 2, one would have expected that the total single ion heats of hydration $\Delta H_h(F^-)$ and $\Delta H_h(OH^-)$, corresponding to the enthalpy changes for the process: ion(gas phase) → ion(aqueous solution), should be about the same, the $-\Delta H_h(OH^-)$ being perhaps larger. However, the accepted tabulations of the total heats of hydration[3] give $-\Delta H_h(OH^-) = 101$ and $-\Delta H_h(F^-) = -113.3$ kcal/mol; *i.e.*, the $-\Delta H_h$ of $F^-$ is given as being larger. An examination of the origin of the tabulated data shows that they are based on a calculation by Halliwell and Nyburg[4] based on crystal lattice energies of the alkali hydroxides calculated by Waddington.[5] However, Waddington's lattice energies lead to the electron affinity of OH, $EA(OH) = 65$ kcal/mol which is equal to a value determined by Page.[6] However, the value of Page is incorrect. The presently accepted $EA(OH) = 42$ kcal/mol.[7] Therefore the lattice energies of Waddington are probably too low by some 23 kcal, which would lead to a $-\Delta H_h(OH^-) \approx 124$ kcal/mol, a value that appears too high. On basis of the present experimental results we think that the best estimate for the $-\Delta H_h(OH^-)$ is that it should be a few kilocalories higher than that of $F^-$.

The higher hydration interactions of $OH^-$ for high $n$ need not be surprising if one assumes that this ion fits better in the total structure of the water cluster.

(3) D. R. Rossinsky, *Chem. Rev.*, **65**, 467 (1955); J. E. Desnoyers in "Modern Aspects of Electrochemistry," Vol. 5, J. O'M. Bockris, Ed., Plenum Press, New York, N. Y., 1969, Chapter 1.

(4) H. F. Halliwell and S. C. Nyburg, *Trans. Faraday Soc.*, **59**, 1126 (1963).

(5) T. C. Waddington, *Adv. Inorg. Chem. Radiochem.*, **1**, 158 (1959).

(6) F. M. Page, *Discussions Faraday Soc.*, **19**, 87 (1955).

(7) L. M. Branscomb, *Phys. Rev.*, **148**, 11 (1966).

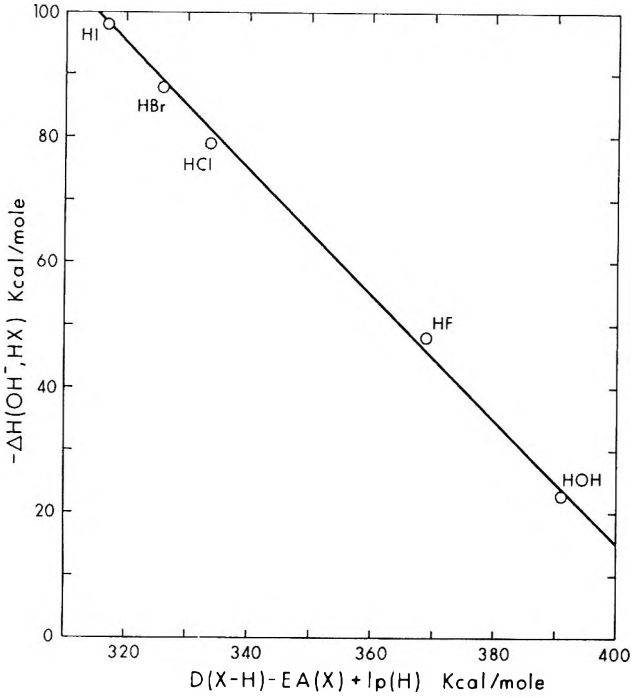


Figure 3. Plot of $-\Delta H_{0,1}$ ($OH^-$,HX) corresponding to enthalpy change for reaction $OH^- + HX \rightarrow (OHHX)^-$ *vs.* $D(XH) - EA(X) + I_p(H)$ which can be defined as a measure of the "gas-phase acidity" of HX.

The $\Delta H_{n-1,n}$ of $O_2^-$ show a characteristically different change with $n$ than the enthalpies of the $OH^-$ and $F^-$ since the $\Delta H_{0,1}$ and $\Delta H_{1,2}$ of this ion are so close. This result is expected in view of the electronic structure of the $O_2^-$ ion. According to the simple molecular orbital description, $O_2^-$ should have its three outer electrons in the doubly degenerate orbital $2p\pi_u$ which spreads the electronic charge to the two ends of the molecule.

The $O_2^-$ hydration equilibria should be of interest in the atmospheric electricity and lower ionosphere research fields since the hydrated $O_2^-$ ion is certainly an important negative species in the troposphere and the lower ionosphere.

### B. Correlation of Gas-Phase Acidity and Strength of Solvating Interactions of Compounds HR with the $OH^-$ Ion

The $\Delta H_{0,1}$ enthalpy values for the hydration of the halide ions can be used together with available thermodynamic data for the evaluation of the enthalpies for the reaction

$$OH^- + HX \longrightarrow (OHHX)^- \qquad (1)$$

The $\Delta H_1$ will be called $\Delta H_{0,1}$($OH^-$,HX) since it corresponds to the $\Delta H_{0,1}$ of $OH^-$ solvated by HX. The evaluation of these enthalpies allows one to make some interesting comparisons between the acidity and the solvating ability of the hydrogen halides and water.

In order to evaluate $\Delta H_{0,1}$($OH^-$, HX) one needs the heat of formation of the reactants participating in (1). $\Delta H_f(OH^-)$ can be calculated from $EA(OH)$ = 42 kcal/mol[7] and $\Delta H_f(OH)$ = 2.3 kcal/mol.[8] The heats of formation of the hydrogen halides are well known.[8] The heat of formation of $(OHHX)^-$ can be evaluated from the enthalpies for reaction 2

$$OH_2 + X^- = (OHHX)^- \qquad (2)$$

which corresponds to $\Delta H_{0,1}$($X^-$,$H_2O$) and was determined previously.[1] The heats of formation of $X^-$ were evaluated from bond dissociation energies in ref 8 and the electron affinities of the halide atoms.[9]

Shown in Figure 3 are the $\Delta H_{0,1}$($OH^-$,HX) determined by the procedure outlined above. Plotted on the abscissa are the values for: $D$(H–X) − $EA$(X) + $I_p$(H). This quantity corresponds to the heterolytic dissociation energy of HX, *i.e.*, the energy required to dissociate HX to $H^+$ and $X^-$ in the gas phase. This energy may be considered as a measure of the "acidity" of HX in the gas phase. As seen from Figure 3 an approximately linear correlation is obtained between the $\Delta H_{0,1}$($OH^-$, HX) and the heterolytic dissociation energy or gas phase acidity. Since the electron affinities of the halogens do not change much, the strongest interaction observed between $OH^-$ and HI is due to a gradual decrease of the bond dissociation energies $D$(H–X) from HF to HI.

Of course reaction 1 is in a sense a neutralization reaction and the correlation in Figure 3 is therefore not surprising. Experiments on the solvation of $Cl^-$ by compounds HR to be reported in the future[10] show that the solvation interactions also for this ion follow to a certain extent the acidities of HR. These results are in line with the findings for $OH^-$ discussed above. In the case of $Cl^-$ one must also consider the negative ion to be in a sense a gas-phase Brönsted base and HR the gas-phase acid. The formation of the complex in the gas phase can be considered as involving only partial proton donation by the HR or HX.

(8) V. I. Vedeneyev, L. V. Gurvich, V. N. Kondratyev, V. A. Medredev, and Ye. L. Frankevich, "Bond Energies, Ionization Potentials and Electron Affinities," Translated from Russian, Edward Arnold, London, 1962.

(9) R. S. Berry and C. W. Reimann, *J. Chem. Phys.*, **38**, 1540 (1963).

(10) R. Yamdagni and P. Kebarle, submitted for publication.

# The Reversible Hydration of Pyruvic Acid. II. Metal Ion and Enzymatic Catalysis[1]

by Y. Pocker[2] and J. E. Meany

*Department of Chemistry, University of Washington, Seattle, Washington 98105* *(Received September 16, 1969)*

The hydration of pyruvic acid and the dehydration of 2,2-dihydroxypropionate anion were followed at 0.0° using a spectrophotometric method. The dehydration of 2,2-dihydroxypropionate anion was investigated with respect to its sensitivity to catalysis by the zinc metalloenzyme carbonic anhydrase from bovine erythrocytes and by various transition metal ions in diethylmalonate buffers at pH 6.7. The magnitude of metal ion catalysis follows the order $Cu^{2+} > Zn^{2+} > Ni^{2+} > Co^{2+} > Cd^{2+} > Mn^{2+}$, an order presumably dictated by the ability of the substrate to chelate to these divalent metal ions. The enzymatically catalyzed dehydration of 2,2-dihydroxypropionate anion to pyruvate anion has not previously been demonstrated, and the anion hydrate represents the first known substrate analog of $HCO_3^-$. The hydration of pyruvic acid was studied in the pH range 1.2 to 2.1 and these investigations allowed the determination of the spontaneous and the hydronium ion rate constants ($k_0 = 2\ min^{-1}$, $k_{H_3O^+} = 104\ l.\ mol^{-1}\ min^{-1}$).

## Introduction

The physiological importance of pyruvic acid lies in its intermediacy in the metabolism of both proteins and carbohydrates.[3] Our interest in this compound is associated with its reversible hydration. Eigen, *et al.*,[4] and Strehlow[5] have studied this process but only at relatively low pH.[6]

We have shown in part I of this series[7] that the ratio of 2,2-dihydroxypropionic to pyruvic acid at equilibrium is dependent on the third power of the water concentration, eq 1, and took this as an indication that the mini-

$$CH_3COCO_2H + (x + 1)\ H_2O \rightleftharpoons (CH_3C(OH)_2CO_2H)\cdot xH_2O \quad (1)$$

mum stoichiometric composition of the hydrate in its ground state is $CH_3C(OH)_2\cdot CO_2H\cdot 2H_2O$.

The pyruvate anion, however, has little tendency to hydrate since the electron withdrawing influence of the carboxyl group has been rendered ineffective with deprotonation. Consequently, as the pH of the reaction media exceeds the $pK_a$ of pyruvic acid ($pK_a = 2.18$ at 25.0°)[8] the dehydration of 2,2-dihydroxypropionic acid becomes dominant

$$(CH_3C(OH)_2CO_2H)\cdot xH_2O \rightleftharpoons CH_3COCO_2^- + H_3O^+ + xH_2O \quad (2)$$

Finally, when the pH of the reaction media exceeds the $pK_a$ of 2,2-dihydroxypropionic acid ($pK_a = 3.6$ at 25.0°[8]), one is able to follow the dehydration of the 2,2-dihydroxypropionate anion

$$(CH_3C(OH)_2CO_2^-)\cdot xH_2O \rightleftharpoons CH_3COCO_2^- + (x + 1)H_2O \quad (3)$$

The present work delineates the sensitivity of this latter process, (eq 3), toward metal ion and enzymatic catalysis. These studies were prompted by the proximity of the carbonyl and carboxyl groups in pyruvic acid. Thus the relative positions of the oxygens associated with the carbonyl and carboxyl groups allow pyruvic acid to act as a bidentate ligand and promote the formation of complexes between pyruvic acid and various metal ions.[9-11] With the metalloenzyme carbonic anhydrase, it has become increasingly clear that its efficiency as a hydrating and hydrolyzing catalyst[12,13] is not a property of the metal ion alone nor of the protein alone. The dehydration of 2,2-dihydroxypropionate by carbonic anhydrase further exemplifies the vast catalytic versatility of this enzyme.

(1) This work was supported by U. S. Public Health Service Grants from the National Institutes of Health.

(2) Author to whom correspondence should be addressed.

(3) D. M. Greenberg, "Metabolic Pathways," Academic Press, London, Vol. 1 (1960) and Vol. 2 (1961).

(4) M. Eigen, K. Kustin, and H. Strehlow, *Z. Phys. Chem.*, 31, 140 (1962).

(5) H. Strehlow, *Z. Elektrochem.*, 66, 3921 (1962).

(6) Measurements of the rapid reversible hydration of pyruvic acid[4,5] indicate that reaction 1 is catalyzed by hydronium ions, pyruvic acid molecules, and pyruvate ions. There is also a spontaneous rate of hydration which by comparison with the results of other hydration reactions seemed to the authors[4,5] to be too large to be interpreted entirely from catalysis by water molecules alone.

(7) Y. Pocker, J. E. Meany, B. J. Nist, and C. Zadorojny, *J. Phys. Chem.*, 73, 2879 (1969).

(8) G. Kortüm, W. Vogel, and K. Andrussow, "Dissociation Constants of Acids in Aqueous Solution," Butterworth and Co., Ltd., London, 1961, p 335.

(9) E. Ferrell, J. M. Ridgion, and H. L. Riley, *J. Chem. Soc.*, 1442 (1934).

(10) W. Franke, *Ann. Chem.*, 475, 39 (1929).

(11) D. L. Leussing, *Talanta*, 11, (2), 189 (1964).

(12) Y. Pocker and J. E. Meany, *Biochemistry*, 4, 2535 (1965).

(13) Y. Pocker and D. R. Storm, *ibid.*, 7, 1202 (1968).

## Experimental Section

*Materials.* Reagent grade pyruvic acid was an Eastman Organic Chemicals product which was twice distilled under reduced pressure through a short Vigreux column in an atmosphere of nitrogen gas, bp (18 mm) 60–69°. The substrate was always distilled directly before use in order to minimize polymerization. The second distillation was carried out because small amounts of acetic acid were detected in the distillate from early fractions. Thus, the nmr spectrum of aqueous solutions of these early fractions showed the two expected signals arising from the methyl hydrogens associated with pyruvic acid (2.5 ppm) and its conjugate hydrate (3.5 ppm) as well as a third peak in between (3.0 ppm), the intensity of which increased upon addition of small quantities of acetic acid.[7]

The preparation and purification of diethylmalonic acid has been described in an earlier paper.[11] All other buffer components were commercially available in analytical or reagent grade. Metal ion solutions were prepared in the form of their nitrates or chlorides as obtained from Baker and Adamson in reagent grade. Bovine carbonic anhydrase was a product of Mann Research Laboratories and was assayed at 2900 Philpot units/mg. Zinc ion analysis of the enzyme was carried out as in our earlier work.[14] The enzyme was stored dry at −20°.

*Apparatus.* The reactions were followed on a Gilford high-speed recording spectrophotometer, Model 2000, which was equipped with a specially constructed bath, thermostated to 0.0 ± 0.02° by means of the apparatus described earlier.[12] Measurements of pH were carried out on a Beckman 101900 research pH meter. Ultraviolet scanning employed a Cary 14 recording spectrophotometer. All nmr measurements were obtained on a Varian DA-60 IL instrument.

*Method.* Because pyruvate ion remains essentially unhydrated around neutral pH,[7] it is necessary to follow the dehydration of 2,2-dihydroxypropionate in this region. At very low values of pH, an appreciable amount of the acid hydrate exists in aqueous solutions.[13] Thus, an equilibrated solution of pyruvic acid and its hydrate resulted from an aqueous solution of pyruvic acid (32% v/v) and small amounts of concentrated HCl which were added to obtain a pH around 0.35. A calibrated Hamilton syringe was employed to inject 0.01 ml of this solution into 3 ml of the solution to be tested. The total pyruvate concentration was then 0.015 *M*. An instantaneous decrease in pH of about 0.3 unit was observed upon addition of the pyruvic acid to 3 ml of 0.1 *M* diethylmalonate buffer. The final pH of 6–8 was reached long before any appreciable dehydration was recorded.

The dehydration was monitored by following the increase in absorbancy at either 762 or 340 mμ. The ultraviolet scanning of pyruvic acid in THF reveals two maxima, one at 276 mμ and a more intense peak at 388 mμ. In acidic aqueous solutions, only one maximum at 327 mμ was observed which was much less intense than that observed at 338 mμ in THF solvent. The pseudo-first-order rate constants were determined from the slope of the straight line obtained by plotting log $(A_\infty - A_t)$ *vs.* time (Figure 1). The results obtained at the two wavelengths were identical to within experimental error (±2%).

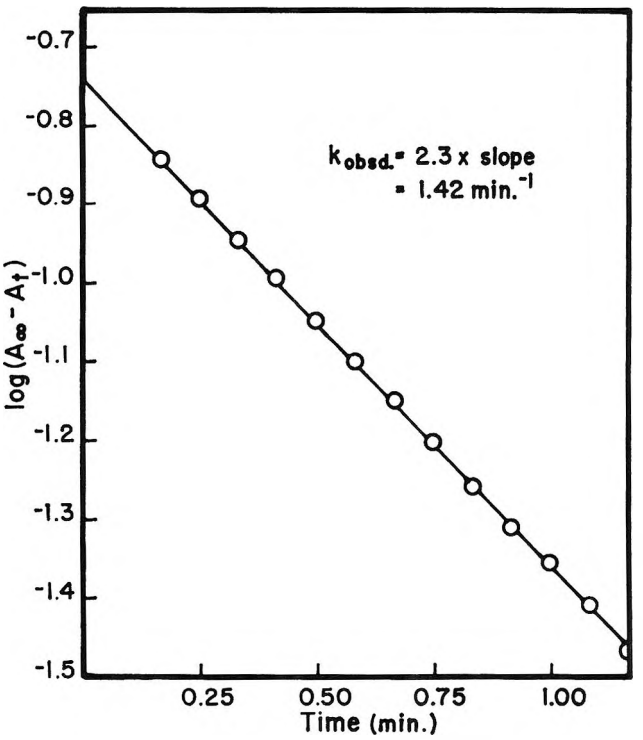


Figure 1. Typical kinetic run for the dehydration of 2,2-dihydroxypropionate with $4 \times 10^{-4}$ *M* $Zn^{2+}$ in 0.10 *M* diethylmalonate buffer at pH 6.7 and 0.0°.

The hydration of pyruvic acid at low pH (pH <2.1) was initiated by injecting 0.01 ml of neat pyruvic acid into water the pH of which had been adjusted by the addition of appropriate amounts of sodium hydroxide or hydrochloric acid. The pH of these solutions was determined after each run. Alternatively, the pH was controlled by employing 0.05 *M* phosphoric acid buffers ($pK^{0.0°} = 2.05$[15]) or 0.1 *M* diethylmalonic acid buffers ($pK_1^{0.0°} = 2.21$[8]). Since in these reasonably dilute solutions the catalysis by the corresponding buffer components was negligibly small relative to the "spontaneous" hydration, the data obtained in the presence of, as well as in the absence of, these buffer components were identical to within experimental error.

The hydration was monitored by following the decrease in absorbancy at 340 mμ. The experimental rate constants were deduced from the slopes of the straight lines resulting from plots of log $(A_t - A_\infty)$ *vs.* time ($k_{obsd} = 2.3 \times$ slope). The observed rate con-

(14) Y. Pocker and J. E. Meany, *Biochemistry*, 6, 239 (1967).
(15) L. F. Nims, *J. Amer. Chem. Soc.*, 56, 1110 (1934).

stants for the hydration are actually a sum of the first-order rate constants for the forward, $k^f$, and for the reverse, $k^r$, processes. These data were converted to the forward rate constants by multiplying $k_{obsd}$ by the fraction of hydration, $\chi$, according to the pH at which the reaction had taken place. These fractions of hydration were determined by nmr measurements[7] by comparing the relative areas of the methyl hydrogen peaks associated with pyruvic acid and its conjugate hydrate

$$\chi = \frac{\text{Area}_{\text{Hydrate}}}{\text{Area}_{\text{Hydrate}} + \text{Area}_{\text{Pyruvic acid}}}$$

## Results and Discussion

The dehydration of 2,2-dihydroxypropionate was followed in various buffer solutions of moderate pH in the absence of metal ions or enzyme for the purpose of evaluating the background catalysis arising from the respective buffer components. From the data given in Table I, the following conclusions may be drawn. (a) For the runs made in diethylmalonate buffers, it would appear from entries 3 and 4 that alteration of the total buffer concentrations of diethylmalonate results in essentially no change in the experimental rate constant. This implies that catalytic contribution from the mono- and dianions of diethylmalonate are negligible at these concentrations. It will also be noted that the rate constants show little variation in the pH range studied in diethylmalonic buffers. Consequently, it may be assumed that the value of the spontaneous rate for this process is very close to $k_0 = 0.055$ min$^{-1}$. (b) A comparison between the data observed in phosphate and diethylmalonate buffers implies that as with other reversible hydration reactions,[16,17] the components of phosphate buffers are considerably more catalytic than those of diethylmalonate buffers. Furthermore, this comparison suggests that this process like other hydration–dehydration processes is subject to general catalysis. The experimental rate constants observed in 0.1 $M$ acetate buffers at pH 5.2 may be represented by the expression

**Table I:** Observed Rate Constants for the Dehydration of 2,2-Dihydroxypropionate in Various Buffers at 0.0°

| Entry | Buffer | Total concn, mol l.$^{-1}$ | pH | $k_{obsd}$, min$^{-1}$ |
|---|---|---|---|---|
| 1 | DEM | 0.1 | 7.2 | 0.055 |
| 2 | DEM | 0.1 | 6.7 | 0.055 |
| 3 | DEM | 0.1 | 6.4 | 0.055 |
| 4 | DEM | 0.05 | 6.4 | 0.055 |
| 5 | Phosphate | 0.05 | 7.2 | 0.340 |
| 6 | Phosphate | 0.05 | 6.1 | 0.320 |
| 7 | Acetate | 0.1 | 5.2 | 0.400 |

$$k_{obsd} = k_0 + k_{H_3O^+}[H_3O^+] + k_{HOAc}[HOAc] + k_{OAc^-}[OAc^-] \quad (4)$$

Assuming a mean activity coefficient of $f_\pm = 0.77$ at an ionic strength of 0.1,[18] the concentration of hydronium ion is

$$\frac{1}{0.77}\,\frac{1}{\text{antilog pH}} = 8.2 \times 10^{-6} \text{ mol l.}^{-1}$$

Inasmuch as the catalytic components of acetic acid and acetate ion are small in comparison to the component due to hydronium ion catalysis at this pH,[19] the value of $k_{H_3O^+}$ may be deduced from eq 5

$$k_{H_3O^+} = \frac{0.400 - 0.055}{8.2 \times 10^{-6}} = 4.2 \times 10^4 \text{ l. mol}^{-1} \text{ min}^{-1} \quad (5)$$

The dehydration of 2,2-dihydroxypropionate was found to be very sensitive toward catalysis by various divalent transition metal ions. The total pyruvate concentration employed in these kinetic runs was 0.015 $M$ and the concentrations of the respective metal ions studied were varied over a rather wide range due to their vastly different catalytic efficiencies. The overall rate constants, $k_{obsd}$, deduced from these kinetic runs consist of a sum of catalytic terms as given in eq 6

$$k_{obsd} = k_0 + k_{H_3O^+}[H_3O^+] + k_{OH^-}[OH^-] + k_A[A] + k_B[B] + k_{M^{2+}}[M^{2+}] \quad (6)$$

where A and B represent the acid and base components of the buffer.[20] The catalytic coefficients for the metal ions were determined from a series of runs in which only the metal ion concentration was varied.

Because the dehydration of 2,2-dihydroxypropionate is a reversible process, the experimentally determined rate constants, $k_{obsd}$, refer to a sum of rate constants, $k_{hyd} + k_{dehyd}$. Consequently, the catalytic coefficients associated with the various catalysts studied for this process were obtained by multiplying the slopes of the lines in Figures 2, 3, and 4 by the respective fractions of dehydration.[7] In general, the specific rates of dehydration of 2,2-dihydroxypropionate appear to be linear with metal ion concentration.[19,21] We take this to

(16) Y. Pocker and D. G. Dickerson, *Biochemistry*, 7, 1995 (1968).

(17) Y. Pocker and J. E. Meany, *J. Phys. Chem.*, 71, 3113 (1967).

(18) The value $f = 0.77$ was calculated from the expression: $\log f_z = -0.49\, z^2 I^{1/2}/(1 + 1.5\, I^{1/2})$, where $I$ and $z$ stand for the ionic strength and charge, respectively.

(19) A fourfold variation in the concentration of buffer components (from 0.05 to 0.2 $M$ acetate buffer) at pH 5.2 led to no perceptible change in rate.

(20) Also included in the catalytic terms associated with the buffer components would be those corresponding to catalysis by pyruvate anion and 2,2-dihydroxypropionate anion which, however, would be very small since the initial pyruvate concentration was only 0.015 $M$.

(21) The slope associated with $Cu^{2+}$ catalysis appears to decrease slightly with increasing metal ion concentration. The value reported to copper ion catalysis refers to data obtained at low copper ion concentration.

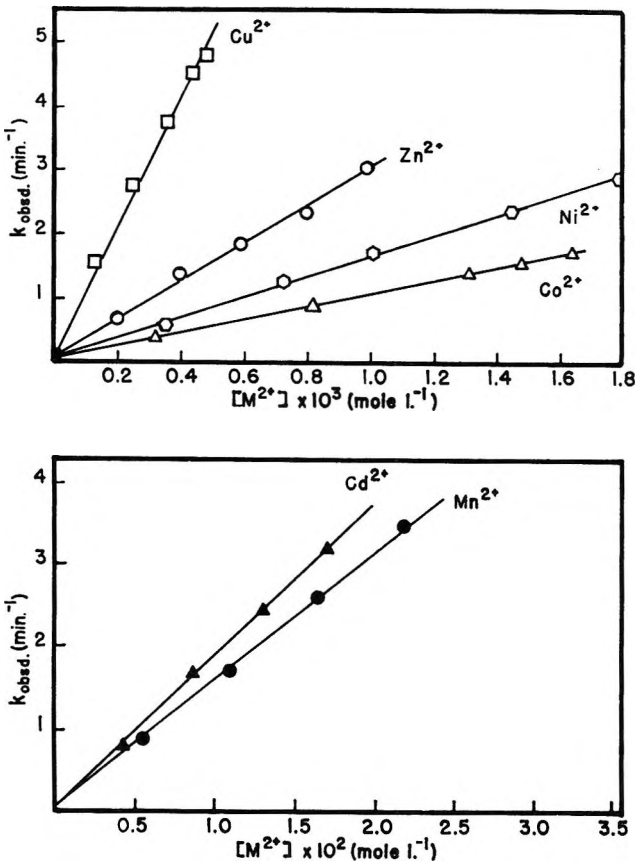


Figure 2. Metal ion catalysis of the dehydration of 2,2-dihydroxypropionate in 0.10 *M* diethylmalonate buffer at pH 6.7 and 0.0°.

imply that on the average, one metal ion promotes the dehydration of one molecule of substrate, *i.e.*, that the stoichiometric composition of these activated complexes is: 2,2-dihydroxypropionate, $M^{2+}$, and $xH_2O$. The catalytic coefficients associated with the various metal ions are given in Table II and show that the order of effectiveness by which these ions catalyze the process under investigation is

$$Cu^{2+} > Zn^{2+} > Ni^{2+} > Co^{2+} > Cd^{2+} > Mn^{2+}$$

Earlier work in these laboratories involving the catalytic efficiencies of these same metal ions with respect to the hydration of 2-pyridinecarboxaldehyde resulted in a similar order[22]

$$Cu^{2+} > Co^{2+} > Ni^{2+} > Zn^{2+} > Cd^{2+} > Mn^{2+}$$

In both series, catalysis by copper ion is considerably greater than of all other metal ions in this series while that due to cadmium or manganese is relatively poor. Although the two series differ in the positions of cobalt, nickel, and zinc ions, these three ions have almost the same catalytic efficiency toward the hydration of 2-pyridinecarboxaldehyde (Table III). We may also add that the stability constants of metal complexes of N,N′-di-(2-hydroxybenzyl)-ethylenediamine-N,N-diacetic acid follow the order[23]

$$Cu^{2+} > Ni^{2+} > Co^{2+} > Zn^{2+} > Cd^{2+} > Mn^{2+}$$

an order which resembles that followed by the ability of these same ions to catalyze the dehydration of 2,2-dihydroxypropionate and the hydration of 2-pyridinecarboxaldehyde.

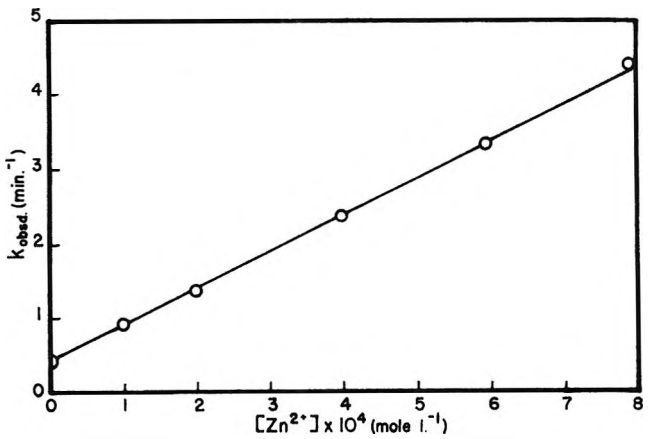


Figure 3. Zinc ion catalysis of the dehydration of 2,2-dihydroxypropionate in 0.1 *M* acetate buffer at pH 5.2 and 0.0°.

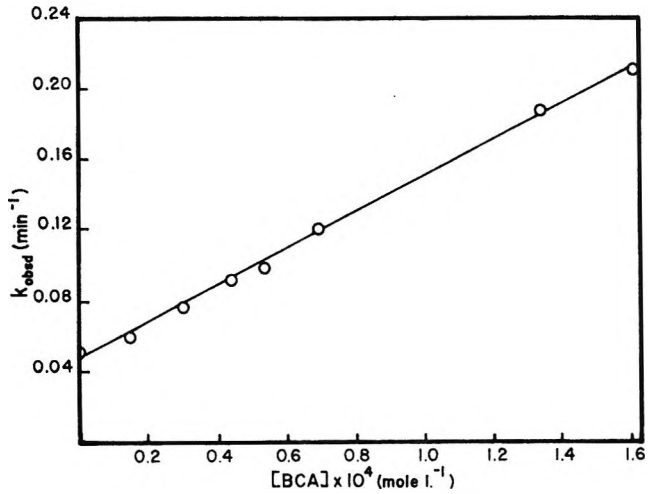


Figure 4. Bovine carbonic anhydrase catalysis of the dehydration of 2,2-dihydroxypropionate in 0.1 *M* diethylmalonate buffer at pH 6.7 and 0.0°.

For the hydration of 2-pyridinecarboxaldehyde, we have postulated that the special arrangement of the ring nitrogen and aldehydic group is necessary for the powerful catalysis afforded by divalent transition metal ions.[22] On the other hand, the corresponding hydration of 4-pyridinecarboxaldehyde, where the proximity of the ring nitrogen and aldehydic group is absent, is not appreciably susceptible to metal ion catalysis.[22] It has also been observed that the hydrations of aliphatic aldehydes which lack such a special

(22) Y. Pocker and J. E. Meany, *J. Phys. Chem.*, **72**, 655 (1968).

(23) F. L. Eplattenier, I. Murase, and A. E. Martell, *J. Amer. Chem. Soc.*, **74**, 2036 (1952).

**Table II:** Catalysis of 2,2-Dihydroxypropionate Dehydration by Bovine Carbonic Anhydrase and Various Metal Ions at 0.0°

| Species | Buffer | pH | $k_{cat}$, l. mol$^{-1}$ min$^{-1}$ |
|---|---|---|---|
| $Cu^{2+}$ | 0.1 *M* DEM | 6.7 | 10,300 |
| $Zn^{2+}$ | 0.1 *M* DEM | 6.7 | 3,020 |
| $Zn^{2+}$ | 0.1 *M* DEM | 6.4 | 3,060 |
| $Zn^{2+}$ | 0.1 *M* Acetate | 5.2 | 4,920 |
| $Ni^{2+}$ | 0.1 *M* DEM | 6.7 | 1,580 |
| $Co^{2+}$ | 0.1 *M* DEM | 6.7 | 1,050 |
| BCA | 0.1 *M* DEM | 6.7 | 1,040 |
| BCA | 0.1 *M* Acetate | 5.3 | 3,250 |
| $Cd^{2+}$ | 0.1 *M* DEM | 6.7 | 185 |
| $Mn^{2+}$ | 0.1 *M* DEM | 6.7 | 150 |

**Table III:** Comparison of Metal Ion Catalysis in the Dehydration of 2,2-Dihydroxypropionate and the Hydration of 2-Pyridinecarboxaldehyde

| Species | 2,2-Dihydroxypropionate, $(k_{M^{2+}}/k_{H_2O})^b$ | 2-Pyridinecarboxaldehyde,[a] $(k_{M^{2+}}/k_{H_2O})^b$ |
|---|---|---|
| $Cu^{2+}$ | $1.04 \times 10^7$ | $2.44 \times 10^8$ |
| $Zn^{2+}$ | $3.05 \times 10^6$ | $6.22 \times 10^6$ |
| $Ni^{2+}$ | $1.59 \times 10^6$ | $6.88 \times 10^6$ |
| $Co^{2+}$ | $1.06 \times 10^6$ | $7.33 \times 10^6$ |
| $Cd^{2+}$ | $1.86 \times 10^5$ | $1.11 \times 10^6$ |
| $Mn^{2+}$ | $1.51 \times 10^5$ | $1.02 \times 10^3$ |

[a] See ref 13. [b] $k_0 = k_{H_2O}$ [55.5]; $k_0$ for 2,2-dihydroxypropionate is taken as 0.05 min$^{-1}$; that for 2-pyridinecarboxaldehyde was taken as 0.25 min$^{-1}$.

arrangement of basic groups are not accelerated by metal ions except when in the presence of specific environments, such as imidazole buffers.[17] In the present work, we have chosen a substrate for which several metal ion complexes are known.[9-11] Again, their ability to chelate to these cations may parallel the accelerative effect these ions have on the process under investigation. One may envisage two limiting possibilities for metal ion assistance. (a) Participation by the direct transfer of water

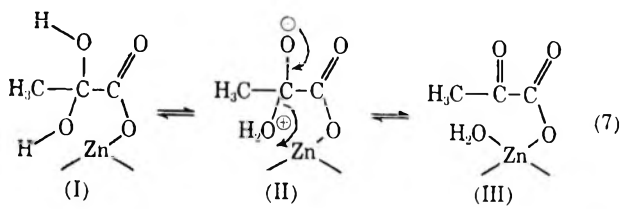


(7)

(b) (i) Participation by acting as a conveniently located general acid

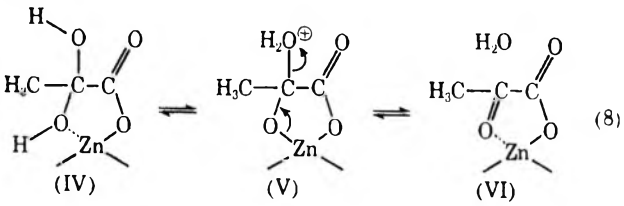


(8)

(ii) In a similar scheme, one may also invoke metal ion participation through the bridging of water (or hydroxide)

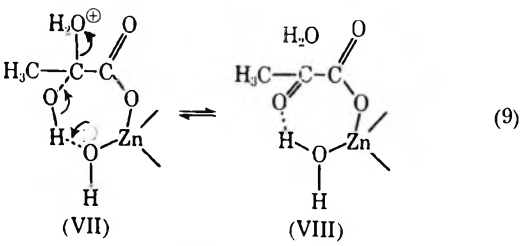


(9)

Any of the above mechanisms is consistent with the ability of the substrate to bind to these metal ions, the powerful catalysis afforded by these metal ions, and the principle of microscopic reversibility.

According to Table III, it is apparent that most of the ratios $k_{M^{2+}}/k_{H_2O}$ for metal ion catalysis are greater for the hydration of 2-pyridinecarboxaldehyde than for the dehydration of 2,2-dihydroxypropionate. This may be due in part to the fact that 2-pyridinecarboxaldehyde (and its hydrate) is more rigid than pyruvic acid (and its hydrate) thus enhancing the very special orientation required in the metal ion-substrate complex.

Zinc ion catalysis in 0.1 *M* acetate buffers at pH 5.2 (Figure 3, Table II) is appreciably more powerful than in 0.1 *M* diethylmalonate buffer at pH 6.7. There are two major variables which must be taken into account in this comparison. It is conceivable that zinc ions are less available for catalysis in diethylmalonate buffers due to chelation to diethylmalonate dianion.[22,24] It is also possible that zinc ion catalysis is a function of pH, the catalysis of the dehydration process being more powerful at lower values of pH. We are presently considering metal ion catalysis in a variety of buffers at various values of pH which should lead to a more definitive explanation of these data.

The zinc metalloenzyme carbonic anhydrase from bovine erythrocytes was also found to catalyze the dehydration of 2,2-dihydroxypropionate. The catalytic coefficients, $k_{enz}$, were evaluated for this process from the results of a series of runs in 0.1 *M* diethylmalonate buffers at pH 6.7 in which only the concentration of the enzyme was varied. A plot of $k_{obsd}$ against enzyme concentration gave a straight line, the slope of which is defined as $k_{enz}$ (Figure 4, Table II). This enzymatic acceleration affords the first example of a carbonic anhydrase catalyzed dehydration yielding the anion of a keto acid.

It should be noted that the concentrations of diethylmalonate and acetate buffers used in the present work were necessarily *ca.* ten times higher than those ordi-

(24) V. S. K. Nair and G. H. Nancollas, *J. Chem. Soc.*, 4367 (1961); V. S. K. Nair, *ibid.*, 1450 (1965).

narily employed in these laboratories for such enzymatic experiments.[12,14,16] The monoanions associated with the above buffers act as noncompetitive inhibitors of hydrase and esterase activity but as competitive inhibitors of dehydrase activity.[25] Thus, it is probable that the enzymatic activity shown in Figure 4 represents a partially inhibited rate. Nevertheless, since the respective inhibitory potencies of these two buffer anions are very similar,[25] the $k_{enz}$ values reported in the two buffers (Table II) probably represent rates inhibited by nearly proportional amounts.[16]

We find in the present work that the value of $k_{enz}$ in the dehydration of 2,2-dihydroxypropionate anion to pyruvate anion at pH 5.3 ($k_{enz}$ = 3250 l. mol$^{-1}$ min$^{-1}$) is 3.1 times larger than the corresponding value at pH 6.7 ($k_{enz}$ = 1040 l. mol$^{-1}$ min$^{-1}$). It is of considerable interest that the enzyme retains this much activity at low pH. In general, the pH–rate profiles associated with the enzymatic hydration of $CO_2$[26] and of aliphatic aldehydes[12,16] and with the hydrolysis of esters[13,27,28] are defined as sigmoid curves having points of inflection around neutrality, showing maximum activity at high values of pH and decreasing to almost negligible values of $k_{enz}$ at lower values of pH. These pH–rate profiles were found to be consistent with the view that the turnover rate, in all these reactions, varies as though dependent on the ionization of a group in the enzyme with p$K_a$ around 7.0, only the basic form of which is active. On the other hand, the enzymatic dehydration of bicarbonate anion is again a sigmoid curve but of opposite shape,[29,30] having a similar point of inflection around pH 7 but showing a high plateau around pH 5–6 and a negligible rate at pH 8. Here the enzymatic rate varies as though dependent on the ionization of a group in the enzyme with the same p$K$ value (~7.0), only the *acid* form of which is active.[29,30] It is interesting to note that the enzymatic dehydration of bicarbonate anion is also faster at pH 5.3 than at pH 6.7 but by a factor of only 2.[29,30] Work now in progress attempts to deduce the complete pH–rate profile as well as the kinetic parameters associated with the various elementary steps. Enzyme modification studies in our laboratory strongly indicate that the acidic form of an imidazole group in a histidine residue of the enzyme may play a key role as a proton donor in the catalytic dehydration of both bicarbonate and 2,2-dihydroxypropionate anions. However, this does not diminish the significance of coordination between anion and the essential zinc atom. Indeed, such an association would facilitate a general acid (*e.g.*, imidazolium) promoted dehydration of $HCO_3^-$ (*e.g.*, *via* scheme IX) or of $CH_3C(OH)_2CO_2^-$ (*e.g.*, *via* scheme X).

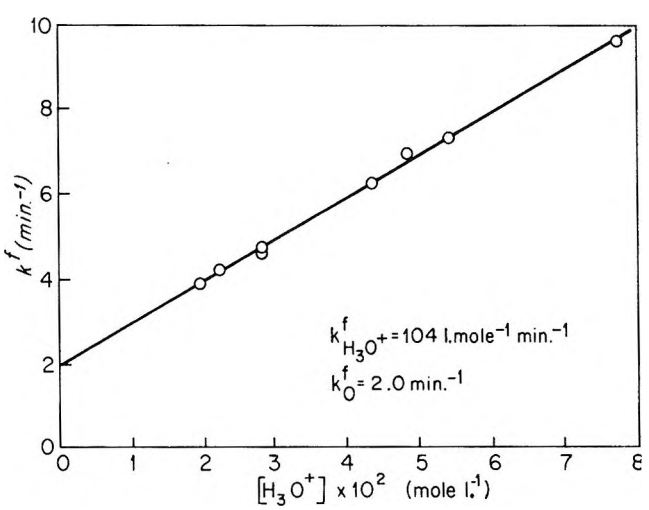


Figure 5. Catalysis of the hydration of pyruvic acid by $H_2O$ and $H_3O^+$ at 0.0°.

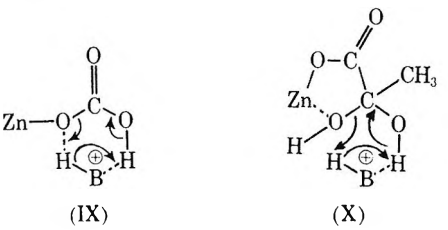


(IX) (X) (10)

Actually, it may be sufficient to have these anions interact with zinc through a water molecule which would function as a bridge.[16] In any case the $Zn^{2+}X^-$ or $Zn^{2+}(OH_2)X^-$ ion-pair complexes would be additionally stabilized by interaction with a neighboring imidazolium ($BH^+$) group.[16] Significantly, the inhibitory effects of anions and the binding of $HCO_3^-$ both decrease with increasing pH as if the cationic binding site lies close to the zinc and has an apparent p$K_a$ around 7.0.[25,27]

The hydration of pyruvic acid was investigated in the pH range 1.2–2.1. The experimental rate constants, $k_{obsd}$, were converted to the respective forward rate constants, $k^f$, by multiplying the values of $k_{obsd}$ by the fraction of hydration corresponding to the pH at which each kinetic run was carried out (Table IV). The fractions of hydration, $\chi$, were deduced as a function of pH by means of nuclear magnetic resonance spectra.[7] The catalytic coefficients, $k^f_0$ and $k^f_{H_3O^+}$, were evaluated from the forward rate constants as a function of hydronium ion concentration (Figure 5). Similar studies have been carried out by Strehlow[5] at 25.0° and our results appear to accord qualitatively with his to the extent that the spontaneous rate coefficient appears to be relatively large in comparison to the catalytic coefficient associated with hydronium ion. The data listed in Table V[31] compare ratios of $k_{H_3O^+}/k_0$ for several reversible hydration processes. Strehlow[5] attributes

(25) Y. Pocker and J. T. Stone, *Biochemistry*, 7, 2936 (1968).
(26) J. C. Kernohan, *Biochim. Biophys. Acta*, 81, 346 (1964).
(27) Y. Pocker and J. T. Stone, *Biochemistry*, 6, 668 (1967).
(28) Y. Pocker and J. T. Stone, *ibid.*, 7, 4139 (1960).
(29) J. C. Kernohan, *Biochim. Biophys. Acta*, 96, 304 (1965).
(30) Y. Pocker, L. Guilbert, and R. Reaugh, unpublished results.
(31) Y. Pocker and D. G. Dickerson, *J. Phys. Chem.*, 73, 4005 (1969).

**Table IV:** Hydronium Ion Catalysis of the Hydration of Pyruvic Acid

| $[H_3O^+] \times 10^2$,[a] mol l.$^{-1}$ | 1.89 | 2.17 | 2.83 | 2.83 | 4.31 | 5.85 | 5.48 | 7.80 |
|---|---|---|---|---|---|---|---|---|
| $\chi$[b] | 0.78 | 0.79 | 0.79 | 0.79 | 0.84 | 0.84 | 0.84 | 0.86 |
| $k_{obsd}$, min$^{-1}$ | 5.42 | 5.82 | 6.42 | 6.46 | 7.98 | 8.74 | 9.11 | 11.67 |
| $k^f$, min$^{-1}$ | 4.22 | 4.60 | 5.07 | 5.10 | 6.70 | 7.34 | 7.65 | 10.03 |

[a] The average ionic strength for these runs was 0.06. Correspondingly, hydronium ion concentrations were deduced by dividing the experimentally determined values of $a_{H_3O^+}$ by a mean activity coefficient of 0.82. [b] The fractions of hydration, $\chi$, refer here to a pyruvic acid concentration of 0.0479 *M*. It is important to note that the stoichiometric composition of the hydrate includes 2 additional molecules of water, and the fractions of hydration as determined by nmr vary significantly with the absolute concentration of water and hence of pyruvic acid (ref 7).

**Table V:** A Comparison of Catalysis of $k_{H_3O^+}/k_0$ for Various Reversible Hydration Reactions

| Substrate | $k_{H_3O^+}/k_0$ | Reference | Substrate | $k_{H_3O^+}/k_0$ | Reference |
|---|---|---|---|---|---|
| $CH_3CHO$ | 120,000 | 17 | 2-PA | 44,000 | 11 |
| $CH_3CH_2CHO$ | 130,000 | 31 | 4-PA | 168,000 | 11 |
| $(CH_3)_2CHCHO$ | 194,000 | 31 | Pyruvic acid | 52 | *a* |
| $(CH_3)_3CCHO$ | 251,000 | 31 | | | |

[a] Data from the present study.

the relatively powerful spontaneous rate to intramolecular acid catalysis by the carboxyl group.

Interestingly, our studies involving the dehydration of 2,2-dihydroxypropionate show very powerful catalysis by the various metal ions as discussed earlier. One might presume in this reaction, and its reverse, both of which involve anions, that the metal ion merely takes the place of a hydrogen ion which is responsible for the comparatively large spontaneous rate of hydration of pyruvic acid. (See Structure VI, eq 8.) However, it must be remembered that, relative to protons, divalent metal ions are weak Lewis acids, and therefore the added role of the metal ion in facilitating hydration may be found either in its strongly polarizing effect on the carbonyl group of pyruvate or in its capacity to participate in the transfer of water by acting both as a bridging group and activator of a properly positioned water molecule in its hydration shell.

# Kinetics and Mechanism of Ethylene Oxidation. Reactions of Ethylene and Ethylene Oxide on a Silver Catalyst

by Robert E. Kenson[1] and M. Lapkin[2]

*Chemicals Group Research Laboratory, Olin Corporation, New Haven, Connecticut 06504* *(Received June 9, 1969)*

The kinetics of the reactions of ethylene and ethylene oxide on a supported silver catalyst were investigated. The principal reaction of ethylene oxide on silver between 200 and 285° was isomerization to acetaldehyde, which underwent rapid oxidation to carbon dioxide and water when oxygen was present. The rate law was determined to be

$$-dC_2H_4O/dt = 3.9 \times 10^{-4} (C_2H_4O)^{1.0}$$

at 200°, while $E_a$ and $\Delta S^{\pm}$ were 9.8 ± 0.6 kcal/mol and −55 ± 2 eu, respectively. The results were interpreted in terms of chemisorption of ethylene oxide as the rate-determining step of the isomerization reaction. Ethylene was oxidized by the same catalyst in a flow system to ethylene oxide or carbon dioxide and water. The activation energy of carbon dioxide formation was 7.6 ± 15 kcal higher than that of ethylene oxide formation, which correlates with the difference in stability of atomic and molecular oxygen complexes, respectively, on the silver catalysts. The mechanism of ethylene oxidation is believed to involve formation of ethylene oxide by reaction with molecular oxygen, and formation of carbon dioxide and water by reaction with atomic oxygen.

## Introduction

The reactions of ethylene oxide over a silver catalyst were first investigated by Twigg.[3,4] His discovery that ethylene oxide was isomerized to acetaldehyde at temperatures comparable with those used for the silver-catalyzed oxidation of ethylene oxide led to further interest in this reaction,[5-7] the purposes of which were to determine the significance of ethylene oxide isomerization in the formation of carbon dioxide. The Twigg reaction scheme postulates three routes for the oxidation of ethylene. These were

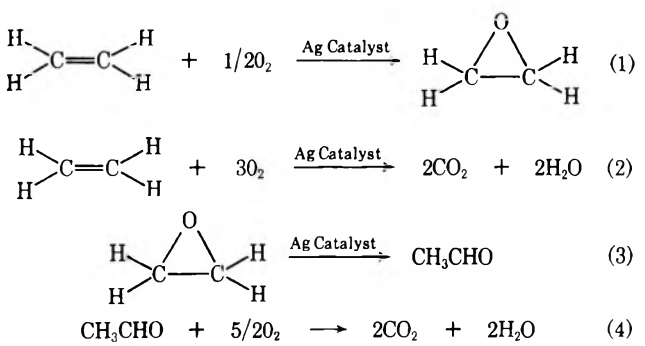


This generalized oxidation reaction scheme has been explicitly or implicitly accepted by most investigators[5-13] of these reactions. The microscopic details of the mechanism are steeped in controversies concerning the relative importance of reaction 3 and the involvement of different adsorbed oxygen species in reactions 1 and 2, which have decidedly different activation energies.[3,4]

Twigg concluded that reaction 3 was a minor source of carbon dioxide in the oxidation of ethylene. The results of Orzechowski and MacCormack,[5] who oxidized ethylene oxide in a flow reactor, and Margolis and Roginski,[6] who oxidized C-14 labeled ethylene and unlabeled ethylene oxide, supported the original conclusion that reaction 3 was too slow to account for most of the carbon dioxide formed. The possibility existed, however, as conceded by Orzechowski and MacCormack, that reaction 3 was really part of reaction 2 and that ethylene oxide adsorbed on the catalyst, after its formation, could be further oxidized to carbon dioxide. Recently, however, Ide[7] and coworkers, concluded that acetaldehyde was the intermediate by which ethylene was oxidized to carbon dioxide. With the exception of Ide, all investigators have made an important assumption about the physical state of the ethylene oxide which is isomerized. There is no ques-

(1) Research and Development Department, Engelhard Industries, Newark, N. J. 07105.

(2) To whom all correspondence should be addressed. Olin Corporation, Thompson Plastics, Assonet, Mass. 02702.

(3) G. H. Twigg, *Proc. Roy. Soc.*, **A188**, 92 (1946).

(4) G. H. Twigg, *Trans. Faraday Soc.*, **42**, 284 (1946).

(5) A. Orzechowski and K. E. MacCormack, *Can. J. Chem.*, **32**, 388 (1954).

(6) L. Ya. Margolis and S. Z. Roginski, *Probl. Kinet. Katal., Akad. Nauk SSSR* **9**, 107 (1957).

(7) Y. Ide, T. Takagi, and T. Keii, *Nippon Kagaku Zasshi*, **86**, 1249 (1965).

(8) K. E. Hayes, *Can. J. Chem.*, **38**, 2256 (1960).

(9) A. I. Kurilenko, N. V. Kul'kova, L. P. Baranova, and M. I. Tempkin, *Kinet. Katal.*, **3**, 177 (1962).

(10) F. McKim and A. Cambron, *Can. J. Res.*, **27B**, 813 (1949).

(11) K. E. Murray, *Aust. J. Sci. Res.*, **A3**, 2143 (1950).

(12) G. R. Schultze and H. Theile, *Erdoel Kohle*, **5**, 552 (1952).

(13) S. Wan, *Ind. Eng. Chem.*, **45**, 234 (1953).

tion that gas-phase ethylene oxide is isomerized slowly to acetaldehyde within the temperature range used for ethylene oxidation. Adsorbed ethylene oxide, however, would be isomerized more rapidly than gas-phase ethylene oxide, if the slow step in this process is the adsorption of the ethylene oxide on the catalyst.[14,15] Hence, the isomerization of ethylene oxide to acetaldehyde, followed by its oxidation, could be the major route to carbon dioxide relative to direct oxidation of ethylene. Therefore, if the rate-determining step in the isomerization of ethylene oxide to acetaldehyde could be established, the true importance of reaction 3 in carbon dioxide formation as compared with reaction 2 would be determined. It was decided that an investigation of the kinetics and thermodynamics of ethylene oxide isomerization and oxidation over a silver catalyst be undertaken to resolve this question.

The involvement of oxygen in the oxidation of ethylene has been an area of disagreement among various investigators. If reactions 1 and 2 are accepted as being discrete and separate reactions leading to ethylene oxide and carbon dioxide, respectively, then it is most likely that these reactions involve different oxygen species adsorbed on the silver catalyst. Two major oxygen species have been discovered on silver catalysts at temperatures required for ethylene oxidation.[16-20] Although disagreement exists as to the velocity of interconversion of the species as determined by the use of isotopic oxygen,[17,18] evidence points to one of these species being molecular (O–O bonds present) and the other being atomic (absence of O–O bonds). Attempts to determine the product obtained from reaction of ethylene with atomic oxygen produced from $N_2O$ adsorption on silver were made by Schultze and Theile.[12] The results were however ambiguous, since decomposition of $N_2O$ on catalytic surfaces leads to both atomic and molecular oxygen species.[21]

The adsorption of ethylene on silver is known to be weak[3] and therefore could not contribute much to the known activation energy difference between ethylene oxide (1) and carbon dioxide formation (2). The major contribution to this difference ought to be the relative energy states of the two oxygen species adsorbed on the silver catalyst. It should then be possible to correlate the difference in activation energies of reactions 1 and 2 and thermodynamics of oxygen adsorption on silver[16-20] at low surface coverage. Flow studies of the relative rates of reactions 1 and 2 at various temperatures were therefore undertaken to determine the activation energy difference.

## Experimental Section

*Catalyst.* The catalysts utilized for the isomerization of ethylene oxide and the oxidation of ethylene were the same. They consisted of 0.475 cm × 0.475 cm fused alumina pellets (Norton SA-101) coated with silver, the pellets containing 10% by weight silver. The catalyst was prepared outside this laboratory by reduction at 250° by hydrogen of silver nitrate impregnated onto the alumina *in vacuo* at 25°. All results were obtained with the same catalyst batch.

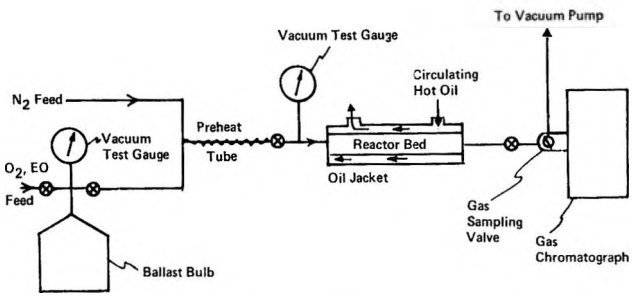


Figure 1. Schematic diagram of reactor for ethylene oxide isomerization studies in a static system.

*Apparatus. Static System.* Figure 1 illustrates the static reaction apparatus used in the isomerization studies. It consisted of a feed system and mixing bulb for the reactants, the reactor, and a vapor phase chromatograph to analyze the products and reactants. The reactant feed system consisted of gas-tight 0.635-cm o.d. stainless steel tubes and fittings. Needle valves were used to control gas flows. The gases were premixed in a stainless steel flask fitted with a Bourdon tube vacuum test gauge to read the pressures of the gases. The tubing leading to the reactor from the mixing bulb was heated by means of a heating tape to preheat the gases before they reached the reactor.

The reactor itself consisted of a 3.34-cm o.d. carbon steel tube jacketed by a 5.08-cm o.d. carbon steel tube containing a heat transfer fluid. This fluid was circulated through the jacket and to a thermostated bath by an electric-powered pump. The heat transfer fluid was a silicone oil which, for the 200° bath, was Dow-Corning mold release fluid, and for the higher temperature runs was General Electric SF-96 silicone fluid. Teflon-packed toggle valves were used to isolate the reactor from the preheat section and the vapor phase chromatograph. The reactor volume of 470 cc was totally filled by 543 g of catalyst.

(14) Physical adsorption, of course, would presumably be rapid and probably obey a Langmuir–Hinshelwood adsorption isotherm, as noted by Ide in ref 7. Chemisorption of a molecule on a catalytic surface can involve an appreciable activation energy and, therefore, be a rate-determining process.[15]

(15) B. M. W. Trapnell, "Chemisorption," Academic Press, Inc., New York, N. Y., 1955, pp 49–86.

(16) A. W. Czanderna, *J. Chem. Phys.*, **68**, 2765 (1964).

(17) R. G. Meisenheimer, A. W. Ritchie, D. O. Schissler, D. P. Stevenson, H. H. Voge, and J. N. Wilson, *Proc. 2nd. Intern. Congr. Surface Activity*, **2**, 299 (1957).

(18) Y. L. Sandler and D. D. Durigon, *J. Phys. Chem.*, **69**, 4201 (1965).

(19) W. W. Smeltzer, E. L. Tollefson, and A. Cambron, *Can. J. Chem.*, **34**, 1046 (1956).

(20) J. T. Kummer, *J. Phys. Chem.*, **63**, 460 (1959).

(21) H. B. Charmon, R. M. Dell, and S. S. Teale, *Trans. Faraday Soc.*, **59**, 453 (1963).

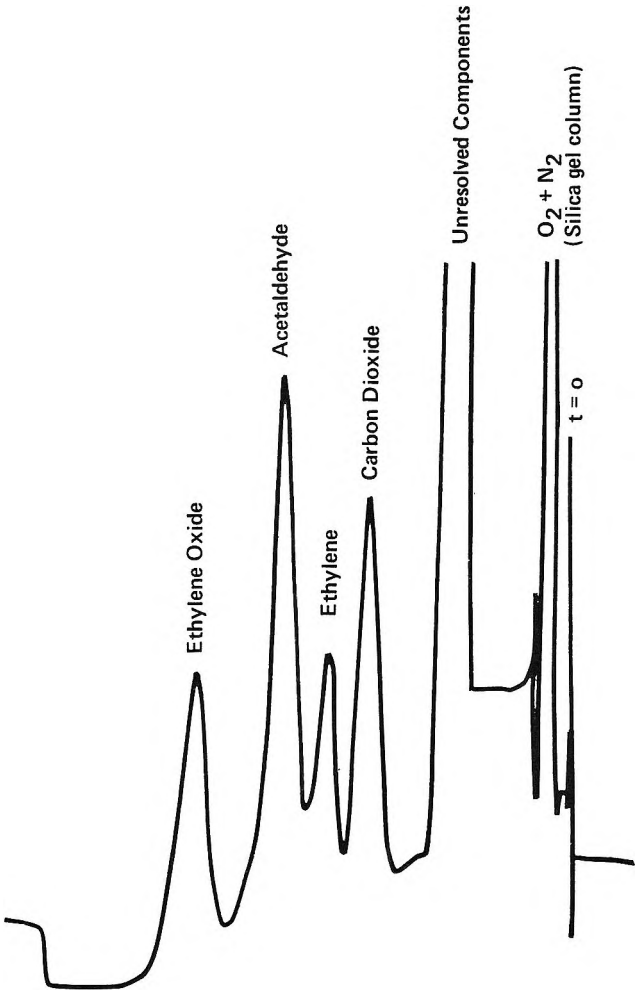


Figure 2. Typical chromatogram for isomerization of ethylene oxide.

The vapor phase chromatograph was a Perkin-Elmer Model 154D equipped with a thermistor detector. Sampling was accomplished by means of a Beckman gas sampling valve which contained two calibrated 1.0-ml gas loops. The complete analysis of the reaction gas mixture required a 1:1 splitting of each sample between two parallel chromatographic columns. Air, carbon dioxide, and ethylene were determined on a silica gel column, while ethylene oxide and acetaldehyde were determined on a Kel-F on Fluoropak column. When acetaldehyde was not required to be analyzed, ethylene oxide was determined on a $\beta,\beta'$-oxydipropionitrile on Chromasorb W column. Response factors were determined for all reactants and products in order to do quantitative analyses. A typical chromatogram is shown in Figure 2. Samples removed approximated 1% of the total gas. Volume change corrections were employed when required.

The entire system was kept under vacuum by a Welch dual-stage mechanical pump with a liquid nitrogen cold trap. All results were obtained at reduced pressures in order to give a proper sample size for the chromatographic columns and also to avoid problems due to the explosive limits of ethylene oxide and oxygen mixtures.

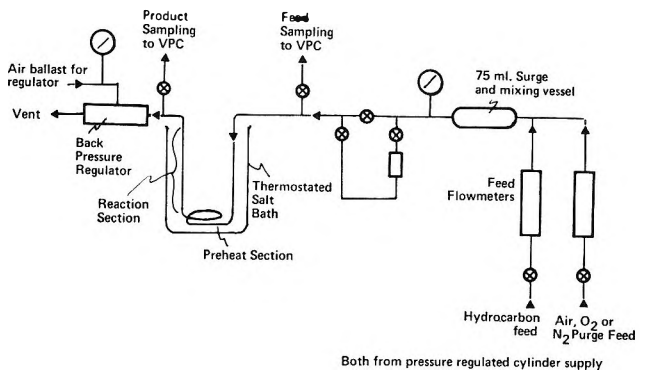


Figure 3. Schematic diagram of ethylene oxidation flow reactor.

*Apparatus. Flow System.* Figure 3 illustrates the apparatus used for the oxidation of ethylene in the flow reactor. The catalyst bed occupied 12 in. of the 0.635-cm i.d. carbon steel tube used as a reactor. A preheat section of 0.475-cm diameter alumina spheres was packed into the other end of the steel tube. The catalyst bed volume was 9.7 cc. Flowmeters were calibrated for delivery of the feed stream gases, ethylene, and air at 50 psig.

At a flow rate of 100 cc/min of gas feed at standard conditions, a mixture of 55% ethylene and 45% air was used as a reactor feed composition. The analyses were obtained by use of the same vapor phase chromatograph as in the isomerization studies.

*Materials.* Chromatographic response factors were obtained by the use of a pure sample of each reaction component to be analyzed. The ethylene used was Matheson CP grade gas and the carbon dioxide was Matheson Bone Dry grade. The acetaldehyde was Fisher CP, and the ethylene oxide was Matheson (99.7%) compressed liquid distilled from the cylinder into a cold trap. The same ethylene oxide was used as a reactant in the isomerization studies. For the isomerization studies, Matheson Ultra-Pure analyzed oxygen and Linde H. P. dry nitrogen were employed. Matheson CP grade ethylene again was used for the oxidation studies, as was Matheson dry compressed air.

*Procedures.* The studies of the isomerization of ethylene oxide required premixing of the reactants. Nitrogen was bled into the mixing bulb through a needle valve and its pressure read on a vacuum test gauge. Next the oxygen was bled into the bulb through a needle valve and its pressure read by difference. Ethylene oxide was distilled under vacuum from a cylinder at 26° to an aerosol test bottle thermostated at 0°. The bottle was warmed to above the boiling point of ethylene oxide, 10.7°, and some of the gas bled into the bulb through a needle valve. The

pressure was read to determine the concentration of ethylene oxide just as those of oxygen and nitrogen had been determined. The preheat section was heated to 160° in the meantime.

The silver catalyst was oxygenated before each experiment by maintaining 150 millimeters pressure of oxygen in the closed reactor at the experimental temperature for 1 hr. No change in the pressure of oxygen was noted, yet when the catalyst bed was evacuated, adsorbed oxygen was removed from the catalyst, as detected by the gas chromatograph. Contacting the silver catalyst with oxygen for 5–6 hr did not affect the kinetic results; therefore, it was felt that the maximum amount of chemisorption of oxygen on the catalyst was reached within 1 hr.

To start a kinetic run, the catalyst bed was evacuated to as low a pressure as possible to remove physically adsorbed oxygen and the toggle valve leading to the gas sampling valve closed. The pressure was read on the vacuum test gauge attached to the reactor after the reaction mixture was introduced and equilibrium attained; then the toggle valve to the preheat section was closed. This was considered as time zero in the reaction. Samples were then admitted into a sampling loop and injected into the vapor phase chromatograph at regular intervals.

Concentrations of reactants and products were determined by multiplying the area under a chromatographic peak due to a component by that component's response factor. The factors were found to be essentially constant over the time period of these studies. Calibration of the 1:1 column flow split was accomplished daily by determination of the relative areas of air peaks from the two columns.

For the studies of ethylene oxidation, the reactor (Figure 3) was pressured up to 50 psig and the flows adjusted to give the proper gas feed composition. The reactor was heated to 175° and the system allowed to equilibrate overnight. A 1-cc sample of the exit gas stream was then analyzed to obtain the yield of ethylene oxide and the conversion of ethylene. The temperature was raised and points taken until the selectivity of ethylene oxide fell toward 50%.

The selectivity for ethylene oxide was calculated from the analysis of the exit stream ethylene oxide and carbon dioxide (eq 5a) while the conversion of ethylene was

$$\text{Selectivity } (\%) = \frac{100[C_2H_4O]}{[C_2H_4O] + {}^1/_2[CO_2]} \quad (5a)$$

calculated from the ethylene concentration at the reactor exit as well as the ethylene oxide and carbon dioxide concentrations (eq 5b).

$$\text{Conversion } (\%) = \frac{100([C_2H_4O] + {}^1/_2[CO_2])}{[C_2H_4] + [C_2H_4O] + {}^1/_2[CO_2]} \quad (5b)$$

## Results

Nine experiments were conducted for the study of the isomerization of ethylene oxide to acetaldehyde. The results are summarized in Table I. A typical concentration *vs.* time plot is shown in Figure 4. Kinetic run EO-1 was run under conditions similar to those employed by Twigg,[4] with oxygen absent. Behavior similar to that observed by both Twigg[4] and Ide[7] was observed in this experiment. The major product of ethylene oxide destruction was acetaldehyde, but some ethylene and carbon dioxide were formed. When oxygen was preadsorbed and then excess oxygen pumped off, as in all subsequent runs, the ethylene formation was diminished. Runs EO-2 and

**Table I:** Kinetic Results for Ethylene Oxide Isomerization

| Expt no. | $T$, °C | $[C_2H_4O]_0$, mm | $[O_2]_0/[C_2H_4O]_0$ | $k_1 \times 10^{-4}$, sec$^{-1}$ |
|---|---|---|---|---|
| EO-1 | 200 | 33.4 | 0 | 4.03 |
| EO-2 | 200 | 15.1 | 1 | 4.03 |
| EO-3 | 200 | 18.3 | 1 | 3.83 |
| EO-4 | 250 | 15.7 | 0 | 9.20 |
| EO-5 | 250 | 16.4 | 1 | 8.78 |
| EO-6 | 250 | 16.8 | 3 | 8.48 |
| EO-7 | 250 | 9.6 | 6 | 9.17 |
| EO-8 | 285 | 17.3 | 3 | 19.3 |
| EO-9 | 285 | 13.6 | 3 | 18.4 |

$k_1$ av at 200° = $3.96 \times 10^{-4}$ sec$^{-1}$
$k_1$ av at 250° = $8.91 \times 10^{-4}$ sec$^{-1}$
$k_1$ av at 285° = $1.89 \times 10^{-3}$ sec$^{-1}$

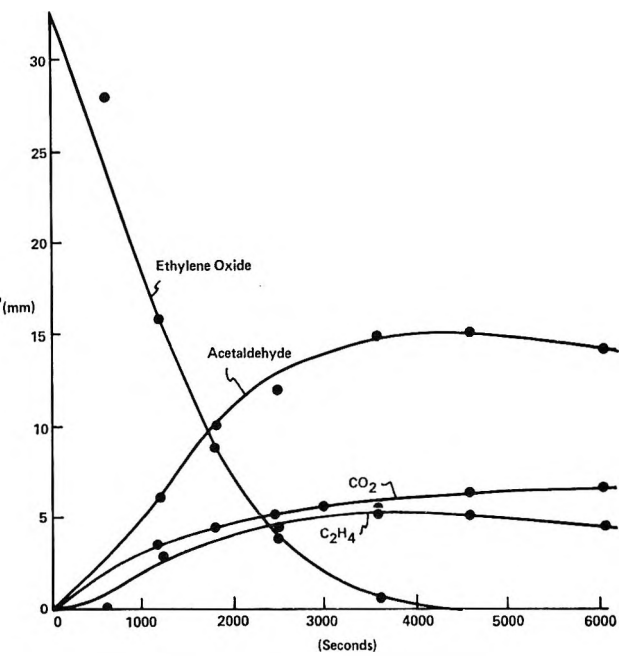


Figure 4. Plot of concentrations of reactants and products *vs.* time of kinetic run EO-1.

EO-3 were conducted at about half the initial concentration of run EO-1 so that the order of the reaction in ethylene oxide could be determined. The order, as determined by plotting the log of the rate of initial ethylene oxide loss *vs.* the log of the initial ethylene oxide concentration, was 1.03 ± 0.04. In these two experiments, oxygen was also added, equivalent to the concentration of ethylene oxide. The major product was then carbon dioxide, and the rate of its formation was twice that of ethylene oxide disappearance. This first-order rate law was obeyed through the first 90% of reaction.

Four experiments, EO-4 through EO-7, were run at 250° to determine the rate of ethylene oxide isomerization and oxidation at a higher temperature. Variation of the initial ethylene oxide concentration confirmed the first-order dependence in ethylene oxide. It was also found, by varying the initial oxygen concentration at constant initial ethylene oxide concentration, that the rate of oxidation of ethylene oxide is independent of the oxygen concentration. Two more experiments were run at 285° and the results were consistent with the previous results.

Thermodynamic variables were then determined from the kinetic data. Pressure measurements before and after $t = 0$ indicated that the adsorption of ethylene oxide on the catalyst was very small in magnitude. The desorption of product was rapid enough that the rate of reactant disappearance was equal to the rate of product formation; therefore, the surface concentration of chemisorbed species would be low. It was then possible to express the thermodynamic variables in a simple Langmuir–Hinshelwood[22] form rather than having recourse to an Elovitch isotherm.[23] The energy of activation for isomerization of ethylene oxide, $E_a$, was 9.8 ± 0.6 kcal/mol, and the enthalpy of activation at 200°, $\Delta H^{\ddagger}_{200°}$, was 8.9 ± 0.6 kcal/mol. The value of the entropy of activation, $\Delta S^{\ddagger}$, as determined from the 200° data was found to be −56 ± 2 eu. The oxidation of ethylene to ethylene oxide and carbon dioxide and water was also studied. In each experiment a new catalyst bed was utilized; therefore the results (Table II) show some variance. Orzechowski and McCormack[5] noted that prolonged periods of ethylene oxidation were required to bring such catalysts to equilibrium. The high selectivity of the ethylene oxidation was shown by the fact that over a tenfold increase in per cent ethylene reacted and over a 65° temperature range, the ethylene oxide selectivity only decreased from 79% to 59%. This could be shown by a plot of conversion of ethylene *vs.* ethylene oxide selectivity as shown for run 1 in Figure 5.

In fuel-rich oxidations, such as that of ethylene in this study, the reaction order approaches zero in ethylene and 1 in oxygen for both ethylene oxide and carbon dioxide formation. At an ethylene/oxygen ratio of over 6, the rate equation in terms of the Orzechowski and McCormack treatment[5] (6) will approach the first-order case (7).

**Table II:** Data for Oxidation of Ethylene

| Run no. | $T$, °C | Yield $C_2H_4O$, % | Conversion $C_2H_4$, % | Conversion $O_2$, % |
|---|---|---|---|---|
| 1 | 180 | 78 | 1.15 | 3.0 |
| | 200 | 78 | 2.0 | 5.25 |
| | 210 | 76 | 3.8 | 10.45 |
| | 225 | 71 | 6.4 | 19.5 |
| | 235 | 64 | 8.9 | 31.2 |
| | 245 | 59 | 10.0 | 35.6 |
| 2 | 180 | 79 | 1.4 | 3.6 |
| | 190 | 76 | 2.5 | 6.9 |
| | 200 | 73.5 | 4.15 | 12.0 |
| | 210 | 72 | 5.8 | 17.4 |
| | 220 | 69 | 7.6 | 24.2 |
| | 230 | 66 | 9.3 | 31.4 |
| | 240 | 62.5 | 10.8 | 38.6 |
| 3 | 175 | 81 | 0.6 | 1.4 |
| | 180 | 79.5 | 1.1 | 2.8 |
| | 190 | 77 | 1.85 | 4.95 |
| | 200 | 75 | 2.8 | 7.9 |
| | 220 | 71.5 | 5.3 | 16 |
| | 225 | 69.5 | 5.9 | 18.6 |
| | 245 | 59 | 9.7 | 37 |
| 4 | 175 | 80 | 0.95 | 2.4 |
| | 180 | 79 | 1.35 | 3.45 |
| | 190 | 75 | 2.0 | 5.75 |
| | 200 | 74 | 3.2 | 9.2 |
| | 210 | 72 | 4.4 | 13.2 |
| | 215 | 69 | 5.5 | 17.5 |
| | 220 | 68 | 5.8 | 18.9 |
| | 225 | 64 | 6.6 | 23.1 |
| | 240 | 64 | 7.4 | 25.9 |
| | 245 | 63 | 7.4 | 26.4 |
| 5 | 175 | 80 | 0.95 | 2.4 |
| | 180 | 79 | 1.2 | 3.1 |
| | 190 | 79 | 2.0 | 5.1 |
| | 200 | 72 | 3.5 | 10.5 |
| | 210 | 69 | 5.3 | 16.8 |
| | 220 | 67.5 | 6.6 | 21.6 |
| | 235 | 64.5 | 9.8 | 34.1 |
| | 245 | 63 | 10.2 | 36.4 |
| | 250 | 61 | 11.2 | 41.5 |
| 6 | 175 | 80 | 0.9 | 2.25 |
| | 190 | 75 | 2.3 | 6.5 |
| | 200 | 73.5 | 3.8 | 11.0 |
| | 210 | 71 | 5.8 | 17.6 |
| | 225 | 69 | 7.8 | 24.8 |
| | 235 | 68 | 8.7 | 28.3 |
| | 240 | 65 | 9.4 | 32.3 |
| | 250 | 61 | 10.5 | 38.7 |
| 7 | 175 | 82.5 | 0.65 | 1.5 |
| | 180 | 81 | 0.9 | 2.2 |
| | 190 | 77.5 | 1.45 | 3.85 |
| | 200 | 77 | 2.5 | 6.7 |
| | 210 | 74.5 | 3.6 | 10.25 |
| | 225 | 73 | 6.0 | 17.6 |
| | 240 | 69 | 8.0 | 25.5 |
| | 250 | 63 | 9.3 | 33.2 |

(22) I. Langmuir, *J. Amer. Chem. Soc.*, **40**, 1361 (1918).
(23) M. J. D. Low, *Chem. Rev.*, **60**, 267 (1960).

**Table III:** Typical Results for the Rate of Ethylene Oxide Formation

| Run no. | 1 | 2 | 3 | 4 | 5 | 6 | 7 | Av |
|---|---|---|---|---|---|---|---|---|
| $k_1 \times 10^2$ at 200°[a,b] | 0.59 | 1.25 | 0.82 | 0.94 | 1.01 | 1.14 | 0.71 | 0.91 ± 0.24 |
| $k_1 \times 10^2$ at 225°[a,b] | 2.82 | ... | 2.26 | 3.70 | ... | 4.24 | 2.33 | 3.07 ± 0.94 |

[a] $k_1$ obtained from $\ln [O_2]_0/[O_2]_t = (0.5\ k_1 + 1.5\ k_2)t$ where $t$ = 16 sec and $k_1 = k_{C_2H_4O}$, $k_2 = k_{CO_2}$. [b] In sec$^{-1}$.

$$\frac{d[C_2H_4O]}{dt} = \frac{k'}{1 + \frac{A}{[C_2H_4]} + \frac{B}{[O_2]}} \quad \begin{matrix} B > A \\ B \gg 1 \end{matrix} \qquad (6)$$

$$\frac{k'}{B}[O_2] = k[O_2]$$

$$\frac{d[C_2H_4O]}{dt} = k[O_2] \text{ for } [C_2H_4] > [O_2] \qquad (7)$$

The reaction would be pseudo-zero order in ethylene at this ethylene–oxygen ratio of 6, as only 10% or less of the ethylene was reacted during any kinetic run. Equation 6 has been applied successfully to other studies of ethylene oxidation where fractional orders in ethylene and oxygen are encountered. Absolute rate constants for ethylene oxide formation were determined from (8) which follows from (7) and the reaction

$$\ln ([O_2]_0/[O_2]_t) = (0.5k_{C_2H_4O} + 1.5k_{CO_2})t \qquad (8)$$

stoichiometries (1) and (2). The reaction is first order in oxygen and approximately zero order in ethylene for both ethylene oxide and carbon dioxide formation. Variations at constant $T$ were about ±30% (Table III), consistent with behavior encountered in many kinetic studies of ethylene oxidation.

Calculation of activation energies from each experiment for ethylene oxide formation indicated that consistent results could be obtained from each set of kinetic data, which gave an average value of 21.4 ± 0.8 kcal/mol.

The activation energy for carbon dioxide formation was obtained from the relative rate data ($k$ relative = $k_{C_2H_4O}/k_{CO_2}$). A plot of the log of $k$ (relative) *vs.* $1/T$ was made to determine $\Delta E_a$, where $\Delta E_a$ is $E_{a\ C_2H_4O} - E_{a\ CO_2}$ and $k$ (relative) is $C_2H_4O$ selectivity/2(100–$C_2H_4O$ selectivity). $\Delta E_a$ was determined to be −7.6 ± 1.5 kcal/mol; therefore, the average $E_a$ for carbon dioxide formation is 29.0 ± 1.7 kcal/mol as determined by subtraction of $\Delta E_a$ from the $E_a$ for ethylene oxide formation. A value for $\Delta S_{C_2H_4O}^{\ddagger} - \Delta S_{CO_2}^{\ddagger}$, or $\Delta\Delta S^{\ddagger}$, of −10.4 eu was determined from the same relative rate data.

## Discussion

Two mechanisms to explain the kinetic data for the isomerization and oxidation of ethylene oxide are proposed. Thermodynamic data were used to establish the most reasonable one. The first mechanism (designated above as reactions 8a–8d) postulates

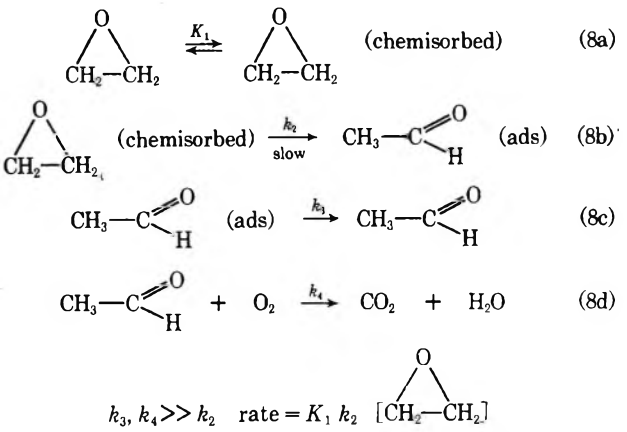


that the rate-determining step is the isomerization of ethylene oxide adsorbed on the catalyst to acetaldehyde. This step would be preceded by rapid chemisorption of ethylene oxide on the catalyst. The acetaldehyde would then be oxidized by oxygen to carbon dioxide and water. The value of the apparent $\Delta S^{\ddagger}$, which in this case would be the sum of $\Delta S_1 + \Delta S_2^{\ddagger}$, is quite reasonable in relation to literature values for chemisorptive processes.[24-26] In order to rationalize the value of $E_a$, less reasonable partitionings of energy must be employed. In order for $E_a$ to be about 10 kcal/mol, $q_1$, which is the sum of $q$ adsorption + $q$ chemisorption, must be negative and at least of the order of magnitude of $E_a$

$$E_a = E_a \text{ (true)} + q_1 \qquad (9)$$

but $q$ adsorption should be approximately thermoneutral.[27] $Q$ chemisorption would, therefore, have to be at least about 10 kcal for mechanism 8a–8d to be valid. Since ethylene oxide is only very weakly adsorbed[28,29] and $q$ chemisorption is therefore small,

(24) $\Delta S_1$ is the entropy change for the equilibrium chemisorption ($K_1$) and $\Delta S_2^{\ddagger}$ is the entropy of activation for the isomerization. Chemisorptive entropies determined for ethylene on copper and gold,[25] for example, are −33.4 and −42.5 eu at low surface coverage ($\theta$ = 0.1). The same magnitude of equilibrium entropy should be obtained for the chemisorption of ethylene oxide on silver. The entropy of activation for the ethylene oxide isomerization should be close to that for thermal isomerization of ethylene oxide to acetaldehyde,[26] which is −1.98 eu.

(25) B. M. W. Trapnell, *Proc. Roy. Soc.*, A218, 566 (1953).

(26) M. L. Neufeld and A. T. Blades, *Can. J. Chem.*, 41, 2956 (1963).

(27) A value of $q$ isosteric can be computed from data on kinetic runs at 200 and 250° where the surface coverage, $\theta$, was approximately constant. Application of the Clausius–Clapeyron relation yielded a value of $q$ = −2.3 kcal/mol.

(28) J. A. Allen and P. H. Scaife, *Aust. J. Chem.*, 20, 837 (1967).

this route for oxidation of ethylene oxide is unsatisfactory.

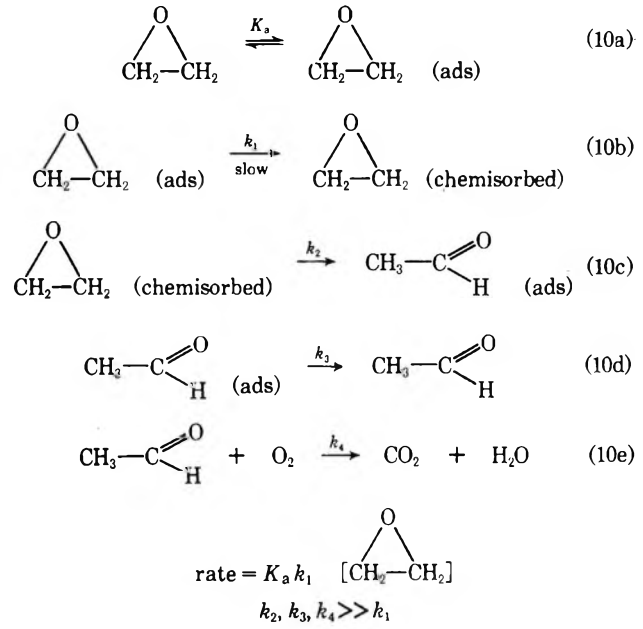

(10a)

(10b)

(10c)

(10d)

(10e)

$$\text{rate} = K_a k_1 \quad [\text{CH}_2\text{—CH}_2]$$

$$k_2, k_3, k_4 >> k_1$$

The second mechanism (eq 10a–10e) involves the same sequence of steps as (8a–8b), except the rate-determining step is postulated as the chemisorption (10b) of ethylene oxide on the catalyst. This assumes that the isomerization to acetaldehyde is rapid and that desorption of chemisorbed ethylene oxide is not significant. The chemisorption of a molecule on a catalyst has been shown in many cases to be an activated process,[15] and therefore it can be the rate-determining step in a heterogeneous reaction. The low value for the activation energy would be consistent with this mechanism. The high negative value of $\Delta S^{\ddagger}$ ($-56 \pm 2$ eu) is quite common with activated chemisorption, especially in the case of a very localized reactant–catalyst site complex.[30] The activated complex can be depicted as a silver atom bonded through oxygen to the ethylene oxide.

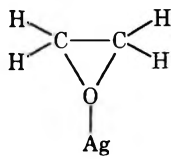

(11)

All translational entropy would be lost, as well as some of the rotational entropy.[24]

The most consistent explanation of the kinetic and thermodynamic data, therefore, is that the rate-determining step of the isomerization and subsequent oxidation of ethylene oxide is activated chemisorption of ethylene oxide on the silver catalyst. On the basis of this conclusion, no significant amount of gaseous ethylene oxide is adsorbed, isomerized, and subsequently oxidized, which is in agreement with previous investigations.[5,6]

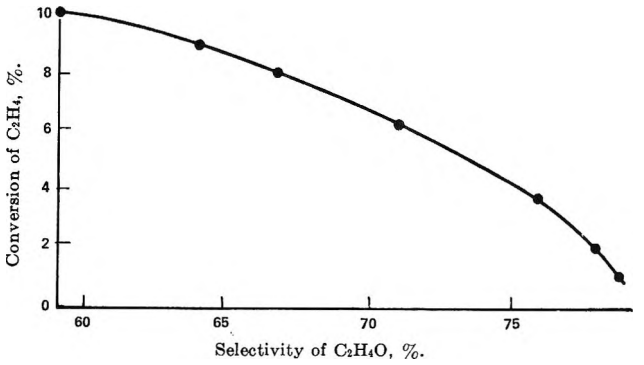


Figure 5. Conversion–yield plot of data from run 1.

As the rate-determining step is the activated chemisorption, the subsequent isomerization step is fast enough to account for the quantity of carbon dioxide produced by ethylene oxidation.[31] The reactivity of chemisorbed ethylene oxide toward isomerization to acetaldehyde accounts for the rate of formation of carbon dioxide and the concomitant loss of ethylene oxide yield in the oxidation of ethylene. This is equivalent to merging reactions 2 and 3 of the generalized ethylene oxidation mechanism.

The relevancy of this study to previous work should be obvious. Previous investigators[5,6] concluded that because of the slow rate of ethylene oxide isomerization to acetaldehyde, this was not an important route of carbon dioxide formation in ethylene oxidation over silver. This conclusion was founded upon the incorrect assumption that the rate-determining step of ethylene oxide isomerization was the isomerization reaction.

Further evidence in support of the conclusions reached in this study was obtained by employing the same catalyst for the oxidation of ethylene. The activation energy determined for ethylene oxide formation (21.4 kcal/mol) appeared to fit previous results.[3,13,32] The activation energy varies from catalyst to catalyst because of the presence of promoters, intentional or unintentional, in the silver. Twigg, with a silver catalyst deposited on glass wool, obtained a value of 23 kcal/mol. The measured activation energy for ethylene oxide formation is dependent on both the

(29) Allen and Scaife reported a nonactivated process similar to that observed by Twigg[3,4] and the present authors. The major route of ethylene oxide adsorption between 250 and 373°K was an activated process. Quantitative comparisons with higher temperature studies may not be possible because of catalyst differences and the use of a different form for the adsorption isotherm than used in many of the studies of ethylene oxide adsorption on silver.[3,4,7]

(30) Calculation of $\Delta S^{\ddagger}$ from a localized complex model (11) for the interaction of silver and ethylene oxide confirms the nature of the ethylene oxide adsorption on silver, as the $\Delta S^{\ddagger}$ calculated from the model is $-58 \pm 12$ eu while the experimental value is $-56 \pm 2$ eu.

(31) At 200° $k_{CO_2} \approx 5 \times 10^{-3}$ sec$^{-1}$, while $k_1$ (chemisorption) is $\approx 4 \times 10^{-4}$ sec$^{-1}$. If we make the reasonable assumption that chemisorption step is at least 100-fold slower than the isomerization itself ($k_2 \approx 10^2 k_1$) then $k_2$ is $\approx 4 \times 10^{-2}$ sec$^{-1}$, or $k_{CO_2}[O_2] \leq k_2[C_2H_4O]$.

(32) J. T. Kummer, *J. Phys. Chem.*, 60, 666 (1956).

purity of the silver catalyst, where unintentional promoters may be present, and the rate-determining step, as the measured activation energy is a sum of several equilibrium heats of reaction and the true activation energy in a catalytic reaction. We would presume then that the Twigg studies involved basically the same catalyst and rate-determining step as the present study. The activation energy for carbon dioxide formation in the present study was calculated to be 29 kcal/mol. The difference in activation energies between the reactions leading to carbon dioxide and to ethylene oxide is only 7.6 kcal/mol. Such a difference is not surprising, as the selectivity to ethylene oxide from the oxidation of ethylene only varied from about 80% to 60% over a 60–70° temperature range. It has been proposed in the past that the two reactions, 1 and 2, involve the same transition state and are identical in most reaction steps except for their final products. The difference in activation energies between the ethylene oxide and carbon dioxide forming reactions, however, precludes a common transition state. The selectivity is higher than in many other studies of ethylene oxidation because of the low ethylene conversion (1–10%) and high pressure (50 psig) employed. Good agreement was obtained with the ethylene oxide selectivity results of Twigg at low ethylene conversion. The large difference in activation energy between ethylene oxide and carbon dioxide formation indicates that a different rate-determining step may be found in the present study.

Isotopic[17–20] and gravimetric methods have proven the existence of two major oxygen species on the catalyst surface, one molecular (O–O bonds present) and one atomic (O–O bonds absent) in nature. Any mechanism proposed for the oxidation of ethylene therefore has to meet the criteria of accounting for: (I), the high selectivity of the reaction; (II), the roles of the two different oxygen species present on the catalyst; (III), the activation energy difference in the two ethylene oxidation routes; and (IV) the ethylene oxide isomerization results.

The most logical explanation is that the formation of ethylene oxide occurs by reaction of ethylene with the molecular oxygen–silver complex (12) analogously to liquid phase oxidation of olefins.[33–36]

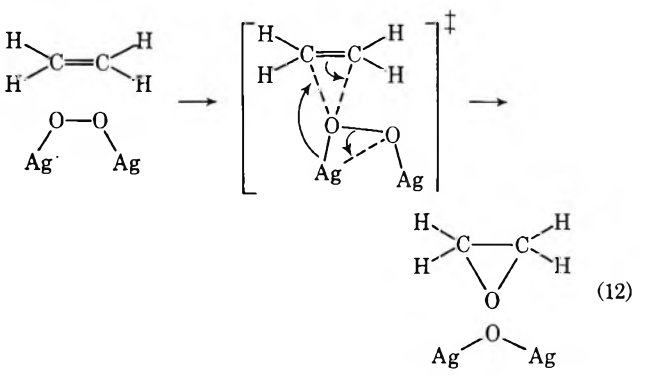

(12)

This results in the formation of ethylene oxide and $Ag_2O$, which is the most probable configuration of the atomic oxygen–silver complex. This complex is also reactive to ethylene, but leads to a formation of ethylene oxide in a *chemisorbed* state (13)

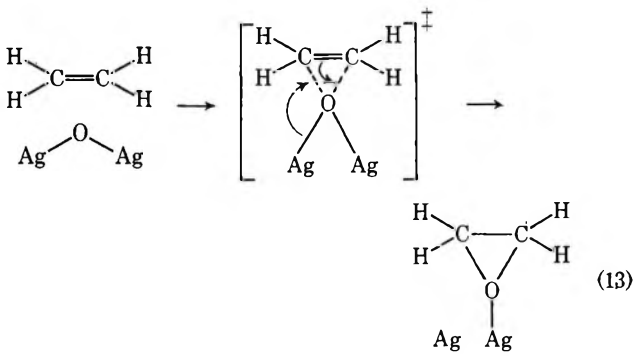

(13)

Isomerization of the chemisorbed ethylene oxide to acetaldehyde occurs quite easily (14) and the resultant acetaldehyde is rapidly oxidized to carbon dioxide and water, as shown by the ethylene oxide isomerization studies.[31] High yields of ethylene oxide are obtainable in spite of the apparent prediction by the proposed mechanism of a limiting yield of 50%. One factor is the higher reactivity of the ethylene oxide-forming

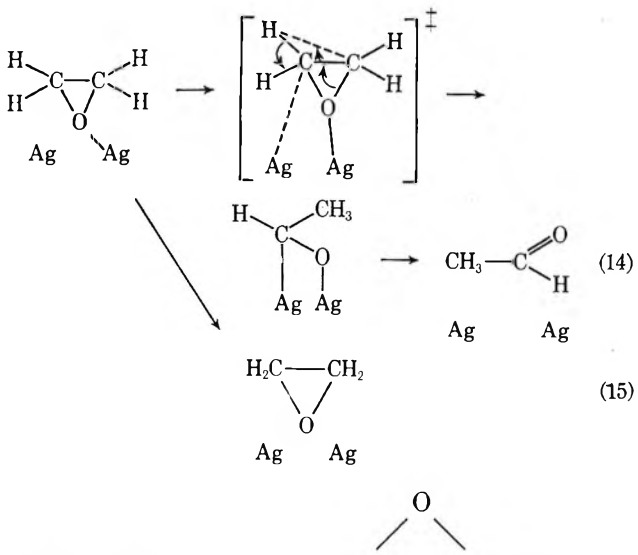

(14)

(15)

catalyst sites, relative to the Ag Ag sites. The lower reactivity of the atomic oxygen complex results from its facile migration to form $Ag_2O_2$ complexes by recombination with another $Ag_2O$ complex. The activation energy for this step is lower than for reaction with ethylene. A second factor is the competition of

(33) The exact structure and stoichiometry of the molecular oxygen silver complex is not known. Stoichiometries of $AgO_2$, $Ag_2O_3$, and $Ag_2O_2$ have all been reported in the literature.[34–36] The structure of $Ag_2O_2$ does not infer in our mechanism an exact structure, but simply a peroxidic silver–oxygen species.

(34) M. W. May and J. W. Linnett, *J. Catal.*, **7**, 324 (1967).

(35) Von M. Feller-Kniepmeier, H. G. Feller, and E. Titzenthaler, *Ber. Bunsenges. Phys. Chem.*, **71**, 606 (1967).

(36) L. Ya. Margolis, *Advan. Catal.*, **14**, 463 (1963).

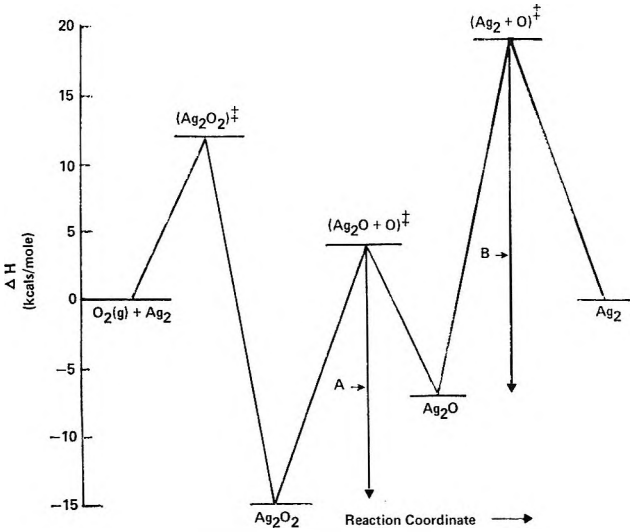


Figure 6. Thermodynamic diagram for ethylene oxidation.

the desorption (15) of chemisorbed ethylene oxide with the isomerization of ethylene oxide (14). A third factor is the higher proportion of peroxide sites, only a fraction of which have reacted in any given time interval to produce $Ag_2O$ sites. Higher pressures of oxygen or the use of selective poison (small concentration of an S or Cl containing compound) would then decrease the rate of isomerization of chemisorbed ethylene oxide because the oxygen or selective poison would be able to effectively compete for the silver catalyst site adjacent to the chemisorbed ethylene oxide.

Thermodynamically, the difference in activation energies for the two reactions is related to the stabilities of the two oxygen–silver complexes. Ethylene adsorption is very weak; therefore, it will contribute little to the activation energies. The thermodynamic diagram for oxygen–silver systems is found in Figure 6.

The values for the thermodynamic variables, such as the heat of activation for $Ag_2O$ decomposition,[37] the activation energies for oxygen adsorption and mobility,[16] and the heat of oxygen adsorption,[38] were obtained from the literature. The heat of formation of $Ag_2O$ was obtained from NBS data.[39]

The activation energy difference between the ethylene oxide and carbon dioxide forming reaction will depend upon the stabilities of the oxygen–silver complexes and the transition states for their decomposition. From the data, it is apparent that the $Ag_2O_2$ species is 8 kcal/mol more stable than $Ag_2O$. The $Ag_2O_2$ transition state, however, is about 17 kcal/mol lower in energy than $Ag_2O$ as determined from Czanderna's data.[16,40]

The higher the transition state energy, the higher is the activation energy. From the equation $\Delta E_a = \Delta E_{\text{transition state}} - \Delta E_{\text{ground state}}$, $\Delta E_a$ was calculated as $-9$ kcal/mol, in good agreement with the experimental value of $-7.6 \pm 1.5$ kcal/mol determined in this study. The absolute values for the activation energies for ethylene oxide and carbon dioxide formation were determined from the data, Figure 6. The value of energy level A, 21 kcal/mol, was equivalent to the activation energy for formation of ethylene oxide from ethylene and $Ag_2O_2$, and it compared well with a value of 21.4 kcal/mol calculated from the kinetic data for ethylene oxide formation. The value of energy level B, 30 kcal/mol, was equivalent to the activation energy for ethylene oxide formation from ethylene and $Ag_2O$, and was very close to the value calculated from the $E_a$ for ethylene oxide formation minus $\Delta E_a$, 29 kcal/mol. This is also comparable with the previously determined value of the heat of activation of $Ag_2O$ decomposition of 28 kcal/mol.[37]

The resultant values for the activation energies of ethylene oxide and carbon dioxide formation are unfortunately not uniquely determined by use of reactions 12–15. Using the same thermodynamic diagram, reasonable values for these respective activation energies can be calculated for several alternative mechanisms for ethylene oxidation.[3,5,6,8,39,41] This mathematical exercise does, however, lead to the conclusion that the rate-determining step for ethylene oxidation to either ethylene oxide or carbon dioxide and water involves primarily the breaking of one or more silver–oxygen bonds. This means that except for the extreme cases, ($[C_2H_4] \gg [O_2]$ or $[O_2] \gg [C_2H_4]$), the surface reaction of a silver–oxygen complex with adsorbed ethylene is rate determining in the oxidation of ethylene to ethylene oxide or carbon dioxide. The value of $\Delta\Delta S^{\ddagger}$ indicates that the oxidation of ethylene to ethylene oxide has a more ordered transition state than oxidation to carbon dioxide. This evidence would favor ethylene oxide arising from reaction of ethylene with a molecular oxygen–silver complex. It is possible that preferential adsorption at "kink" and "ledge" sites would lead to this negative $\Delta\Delta S^{\ddagger}$.[42]

In summary, the selectivity of the reaction is explained by the coupled nature of the reactions. The activation energy difference of the two oxygen species involved in these reactions is related to the difference in their thermodynamic stabilities and those of the

(37) B. D. Averbukh and G. I. Chufarov, *Zh. Fiz. Khim.*, **23**, 37 (1949).

(38) A. F. Benton and L. C. Drake, *J. Amer. Chem. Soc.*, **56**, 255 (1934).

(39) "Selected Values of Chemical Thermodynamic Properties," National Bureau of Standards Circular No. 500, U. S. Government Printing Office, Washington, D. C., 1950.

(40) The relative energy state of $[Ag_2O]^{\ddagger}$ was calculated as equal to the difference in activation energies between molecular and atomic adsorption on silver, this 5 kcal/mol being taken as equivalent to the energy for forming $[Ag\overset{O}{\diagdown\diagup}Ag]^{\ddagger}$. The relative energy state of $[Ag_2 + O]^{\ddagger}$ was taken to be equal to the activation energy required for migration of an oxygen atom, 22 kcal/mol.

(41) H. H. Voge and C. R. Adams, *Advan. Catal.*, **17**, 171 (1967).

(42) O. Knacke and I. N. Stranski, "Progress in Metal Physics," Vol. VI, Pergamon Press, London, 1956, pp 214–216.

transition states. By examination of the relative activation energies, it was determined that the ethylene oxide formation is caused by reaction of ethylene with the molecular oxygen–silver complex. Carbon dioxide can then be produced by reaction of ethylene with the atomic oxygen–silver complex which forms. This gives a chemisorbed ethylene oxide, which can rapidly isomerize to acetaldehyde and subsequently is oxidized to carbon dioxide and water. The reaction of these silver–oxygen complexes with adsorbed ethylene is the rate-determining step in the oxidation of ethylene to ethylene oxide or to carbon dioxide and water.

*Acknowledgments.* The authors wish to thank the Vapor Phase Chromatography Laboratory, Analytical Department, for the development of the analytical separations. We thank Mr. Roger Polak for the flow system experimental results. The authors also wish to express their appreciation to Dr. John Churchill for many helpful comments and stimulating discussions.

# Mechanism of the Catalytic Isomerization of Cyclopropane over Brønsted Acid Catalysts[1]

**by Z. M. George and H. W. Habgood**

*Research Council of Alberta, Edmonton 7, Alberta, Canada* *(Received September 22, 1969)*

The isomerization of cyclopropane over a Brønsted acid catalyst takes place *via* a protonated cyclopropane intermediate, which on ring opening gives propylene probably through a primary propyl cation. With a deuterated catalyst the propylene product is randomly deuterated and, for a fully deuterated catalyst, the extent of monodeuteration during isomerization is 85%, which is close to $^6/_7$ as expected for complete mixing with no isotope effect of one D with 6 H's. These results suggest that the $c$-$C_3H_6D^+$ ion probably has sufficient time to equilibrate among its various isotopic forms before the ring opens. A lower degree of deuteration during the isomerization step may be found if the catalyst is incompletely deuterated, and this was found to be the case for NaY catalyst equilibrated with $D_2O$ at 300°. Some catalytically active sites which do not readily exchange with $D_2O$ form a significant fraction of the acid sites on a catalyst of low acidity such as NaY. These peculiar sites are of negligible importance in practical catalysts such as NaHY zeolite which have much higher total acidity.

## Introduction

The mechanism of the Brønsted acid catalyzed isomerization of cyclopropane to propylene is of interest in connection with current studies of this reaction as a possible test reaction for measuring catalyst Brønsted acidity. A previously published study from this laboratory[2] had given results inconsistent with what is probably the simplest mechanism

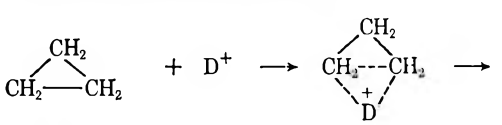

$$[\overset{+}{C}H_2—CH_2—CH_2D] \longrightarrow CH_2{=}CH—CH_2D + H^+ \quad (1)$$

In these experiments slugs of cyclopropane were passed over an NaY zeolite catalyst that was maintained in deuterated form by a low constant partial pressure of $D_2O$. The catalytic sites on the sodium zeolite are probably the result of some hydrolysis of the sodium ions and also some crystal defects. It was found that about 26% of the propylene produced by the isomerization reaction did not have any deuterium whereas eq 1 would lead to 100% exchange during the isomerization step. To account for these results, Bartley, Habgood, and George[2] proposed two alternative mechanisms, each involving an intramolecular hydride transfer during the ring-opening step.

Meanwhile, Hall and Hightower[3] carried out a different sort of experiment in which the coisomerization of a 50:50 mixture of cyclopropane-$d_0$ and cyclopropane-$d_6$ over silica–alumina was studied. A plot of hydrogen atoms exchanged per molecule gave a value of between 0.45 and 0.50 on extrapolation to zero conversion, and this indicated that there was one,

(1) Contribution No. 475 from the Research Council of Alberta.

(2) B. H. Bartley, H. W. Habgood, and Z. M. George, *J. Phys. Chem.*, **72**, 1689 (1968).

or nearly one, intermolecular hydrogen transfer per isomerization. From these and related results Hall and Hightower[3,4] concluded that the mechanism of eq 1 applied.

Although the existence of different mechanisms for this reaction on dry silica–alumina and on wet zeolite would not be too improbable, the results of Hightower and Hall have given us additional incentive to carry out further tracer experiments with the zeolite catalyst. Mechanism I leads to deuteration exclusively on carbon 3 whereas the two alternatives proposed by Bartley, *et al.*, would give deuteration on carbon 3 and carbon 2, respectively. Our previous work involved mass spectrometric measurements of the deuterated propylenes; these spectra give no useful information on the *location* of the deuterium. We have now obtained nmr spectra of the exchanged propylene in order to determine the distribution of deuterium within the molecule.

Furthermore, we have critically examined the degree to which the Brønsted sites of the zeolite catalyst were maintained in a deuterated form. In the previous work it was assumed that a steady stream of $D_2O$ vapor sufficient to maintain a ratio of adsorbed $D_2O$ to adsorbed cyclopropane of at least 100:1 would be adequate to ensure that all sites were effectively deuterated.

The results we have now obtained remove much of the apparent previous contradiction. The nmr results indicate an equilibration among the various possible isomers of $c\text{-}C_3H_6D^+$ that leads to mixing among all hydrogens prior to ring opening which may then proceed *via* the primary propyl cation as indicated in eq 1. The *minimum* degree of deuteration during the isomerization step should be 86% (6/7) depending on the relative extent of the equilibration of $c\text{-}C_3H_6D^+$. We found that our NaY catalyst contained a small concentration of catalytically active sites that are difficult to deuterate with $D_2O$ but when these sites are deuterated the expected 86% deuteration during the isomerization step is achieved.

## Theory

As previously discussed,[2] the various exchange and isomerization reactions occurring when cyclopropane-$d_0$ ($A_0$) is passed over a deuterated catalyst may be summarized in the following reaction scheme where A

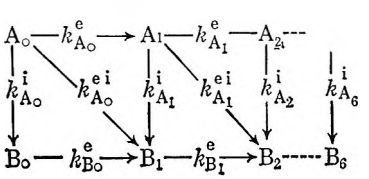

(2)

represents cyclopropane, B propylene, the subscripts refer to the number of deuterium atoms, and each rate constant is identified by a superscript as a reaction of exchange (e), isomerization without exchange (i), or isomerization with exchange (ei) and by a subscript indicating the reactant. If the reaction proceeds by mechanism 1, $k_{A_0}^{i}$, $k_{A_1}^{i}$, $k_{A_2}^{i}$, etc., will turn out to be zero.

Under our experimental conditions[2,5] the maximum extent of significant deuteration is 3 deuterium atoms per propylene molecule. Consequently, we require expressions for the amounts of each of the various B species up to $B_3$ formed from the slug of $A_0$ injected at the inlet of the catalyst column under the conditions of the microcatalytic chromatographic reactor. Each of the B species may be formed by several different reaction routes; for example, $B_2$ is produced by $A_0 \rightarrow B_0 \rightarrow B_1 \rightarrow B_2$, $A_0 \rightarrow A_1 \rightarrow B_2$, $A_0 \rightarrow A_1 \rightarrow B_1 \rightarrow B_2$, $A_0 \rightarrow A_1 \rightarrow A_2 \rightarrow B_2$, and $A_0 \rightarrow B_1 \rightarrow B_2$ as given in the reaction scheme, eq 2. Each reaction route will yield a characteristic isotopic distribution in the product and the final distribution will depend on the relative contributions of the various routes. Any one reaction route is a series of consecutive first-order reactions; because the reactions are first order the various routes may be treated independently. In developing expressions for the amount of product from each route the only distinctive feature is the need to take account of the difference in the rates of elution of the A and B species along the catalyst column. The pulse of A travels with a contact time $t_A$ and the product B has a contact time on the catalyst ranging from 0 for isomerization occurring at the column outlet to $t_B$ for isomerization at the inlet. The total amount of B is then the integrated sum of the various increments formed from A all along the column. The previous paper illustrated the derivational procedure.

The actual isotopic distribution expected for any one route depends on the assumptions made concerning each step. It is reasonable to assume that exchange of cyclopropane will introduce D randomly in all positions and that exchange of propylene will introduce D randomly into the 5 H positions on C1 and C3. Different assumptions can then be made concerning deuteration during isomerization in line with the different proposed mechanisms.

Of the various rate constants occurring in eq 2, it is possible to determine experimentally only $k_{A_0}^{i}$, $k_{A_0}^{ei}$, $k_{A_0}^{e}$, and $k_{B_0}^{e}$.[2] It was also shown that

$$k_{A_0}^{ei} + k_{A_0}^{i} = k_{A_1}^{ei} + k_{A_1}^{i} = \cdots = k^{i} \qquad (3)$$

where $k^i$ is the experimentally determined rate constant for the surface reaction A → B. To estimate the remaining individual rate constants involved in the reactions up to $B_3$ the following assumptions have been made. Hydrogen–deuterium exchange in cyclopropane

(3) J. W. Hightower and W. K. Hall, *J. Amer. Chem. Soc.*, 90, 851 (1968).

(4) J. W. Hightower and W. K. Hall, *J. Phys. Chem.*, 72, 4555 (1968).

(5) H. W. Habgood and Z. M. George, Molecular Sieves (Conference), Society of Chemical Industry, London, 1968, p 130.

**Table I:** Expressions for Calculating Relative Amounts of Various Propylene (B) Species Formed from Cyclopropane-$d_0$ ($A_0$) by Different Routes over a Deuterated Catalyst

| Species | | Route | Expression[a] |
|---|---|---|---|
| $B_0$ | 1: | $A_0 \rightarrow B_0$ | $B_0/A_0^0 = k_{A_0}{}^i t_A F(k_{B_0}{}^e t_B, k_{A_0} t_A)$ |
| $B_1$ | 2: | $A_0 \rightarrow B_1$ | $B_1/A_0^0 = k_{A_0}{}^{ei} t_A F(k_{B_1}{}^e t_B, k_{A_0} t_A)$ |
| | 3: | $A_0 \rightarrow A_1 \rightarrow B_1$ | $B_1/A_0^0 = 6k_{A_0}{}^i t_A [F(k_{B_1}{}^i t_B, k_{A_1} t_A) - F(k_{B_1}{}^e t_B, k_{A_0} t_A)]$ |
| | 4: | $A_0 \rightarrow B_0 \rightarrow B_1$ | $B_1/A_0^0 = 5k_{A_0}{}^i t_A [F(k_{B_1}{}^e t_B, k_{A_0} t_A) - F(k_{B_0}{}^e t_B, k_{A_0} t_A)]$ |
| $B_2$ | 5: | $A_0 \rightarrow B_1 \rightarrow B_2$ | $B_2/A_0^0 = 4k_{A_0}{}^{ei} t_A [F(k_{B_2}{}^e t_B, k_{A_0} t_A) - F(k_{B_1} t_B, k_{A_0} t_A)]$ |
| | 6: | $A_0 \rightarrow A_1 \rightarrow B_2$ | $B_2/A_0^0 = 6k_{A_1}{}^{ei} t_A [F(k_{B_2}{}^e t_B, k_{A_1} t_A) - F(k_{B_2}{}^e t_B, k_{A_0} t_A)]$ |
| | 7: | $A_0 \rightarrow A_1 \rightarrow A_2 \rightarrow B_2$ | $B_2/A_0^0 = 15k_{A_2}{}^i t_A [F(k_{B_2}{}^e t_B, k_{A_0} t_A) - 2F(k_{B_2}{}^e t_B, k_{A_1} t_A) + F(k_{B_2}{}^e t_B, k_{A_2} t_A)]$ |
| | 8: | $A_0 \rightarrow A_1 \rightarrow B_1 \rightarrow B_2$ | $B_2/A_0^0 = 24k_{A_1}{}^i t_A [F(k_{B_2}{}^e t_B, k_{A_0} t_A) + F(k_{B_2}{}^e t_B, k_{A_1} t_A) - F(k_{B_1}{}^e t_B, k_{A_0} t_A) - F(k_{B_1}{}^e t_B, k_{A_1} t_A)]$ |
| | 9: | $A_0 \rightarrow B_0 \rightarrow B_1 \rightarrow B_2$ | $B_2/A_0^0 = 10k_{A_0}{}^i t_A [F(k_{B_0}{}^e t_B, k_{A_0} t_A) - 2F(k_{B_1}{}^e t_B, k_{A_0} t_A) + F(k_{B_2}{}^e t_B, k_{A_0} t_A)]$ |
| $B_3$ | 10: | $A_0 \rightarrow A_1 \rightarrow A_2 \rightarrow B_3$ | $B_3/A_0^0 = 15k_{A_2}{}^{ei} t_A [F(k_{B_3}{}^e t_B, k_{A_0} t_A) - 2F(k_{B_3}{}^e t_B, k_{A_1} t_A) + F(k_{B_3}{}^e t_B, k_{A_2} t_A)]$ |

[a] $F(X, Y) = e^{-X} - e^{-Y}/Y - X$; $A_0^0$ is amount of $A_0$ injected.

was assumed to occur randomly among all 6 hydrogen positions with no isotope effect. Hence on purely statistical grounds the following relations are obtained

$$k_{A_1}{}^e = {}^5/_6 k_{A_0}{}^e; \quad k_{A_2}{}^e = {}^4/_6 k_{A_0}{}^e; \quad \text{etc.} \tag{4}$$

Similarly, for propylene exchange, assuming random exchange among the 5 hydrogen positions of carbons 1 and 3

$$k_{B_1}{}^e = {}^4/_5 k_{B_0}{}^e; \quad k_{B_2}{}^e = {}^3/_5 k_{B_0}{}^e; \quad \text{etc.} \tag{5}$$

Estimation of the individual rate constants $k_{A_1}{}^i$ and $k_{A_1}{}^{ei}$, etc., relative to $k^i$ is somewhat dependent on the mechanism proposed for the isomerization. For example, one of the mechanisms proposed by Bartley *et al.*, requires an isotope effect of 1.5 in the final step and mixing of the added $D^+$ with 2 hydrogens on what becomes the methyl carbon; assuming no isotope effect in the intramolecular hydrogen shift, we obtain the value 0.65 for the ratio of $k_{A_1}{}^{ei}$ to $(k_{A_1}{}^{ei} + k_{A_1}{}^i)$. By the other mechanism (mixing with one hydrogen on the number 2 carbon and an isotope effect of 3.0 for the loss of $H^+$ or $D^+$) we obtain a value of 0.68. Taking the average and similarly for the reactions of $A_2$ gives

$$k_{A_1}{}^{ei}/(k_{A_1}{}^{ei} + k_{A_1}{}^i) = 0.66 \tag{6}$$

$$k_{A_2}{}^{ei}/(k_{A_2}{}^{ei} + k_{A_2}{}^i) = 0.57 \tag{7}$$

Once values are obtained for the rate constants $k_{A_0}{}^e$, $k_{A_0}{}^i$, $k_{A_0}{}^{ei}$, and $k_{B_0}{}^e$ the relations of equations 3 to 7 permit the assignment of values to the remaining rate constants for the various reactions giving $B_0$ to $B_3$.

The final set of expressions used to calculate the amounts of the various B species is summarized in Table I. The first term of each of the expressions for a route involving more than a single step has already been simplified by means of the relations listed in eq 3 and 4. Only one route leading to $B_3$ is included in the Table. Contributions to $B_3$ by the other 6 routes either were neglected or else were estimated, in both cases on the basis of an extrapolation of the pattern of contribution to the species $B_0$ to $B_2$.

## Experimental Section

The gas chromatographic microcatalytic reactor, the experimental details for the activation, regeneration, and equilibration of the catalyst with $D_2O$ or $H_2O$, and the measurements of conversion and retention are described in previous papers from this laboratory.[2,5]

The isotopic compositions of the propylene product and the unreacted cyclopropane were determined mass spectrometrically. Initially the spectra were measured on a modified MS2 spectrometer using 70 (and occasionally 20) V ionizing electrons and obtaining the best fit for the peaks of all $C_3$ fragments.[2] Later a Veeco GR4 spectrometer was used with an ionizing voltage of 14 V which, for this instrument, was the maximum that would give no fragmentation of either compound. In this case, analyses were based on the intensities of the parent peaks with corrections for $C^{13}$ and for the variation in parent-peak intensity with isotopic substitution. This latter was determined by carefully prepared mixtures of $d_0$ and $d_6$ compounds (prepared manometrically using a quartz-spiral Bourdon gauge to an estimated accuracy of 1%) and with correction for the small amount of $d_5$ impurity. The observed intensity of the $d_6$ compound was 91% of that of $d_0$ for both cyclopropane and propylene and the variation was assumed linear with degree of deuteration. The intensity of the peak for cyclopropane was 70% of that for propylene.

The positional distribution of deuterium within the propylene molecule was estimated on the basis of of nmr spectra. Approximately 0.1 mmol of propylene product, separated gas chromatographically from $D_2O$, cyclopropane, and any impurities, was mixed with 30% cyclopropane as an internal nmr standard. The mixture was analyzed by glc before being condensed

into an nmr tube with chloroform solvent (80% deuterated to provide a "locking" signal without giving interference to the vinyl proton signal of propylene). The nmr spectrum was scanned at 100 MHz and at −60° on a Varian HA 100 instrument equipped with a 15-in. magnet. The extent of exchange at C1, C2, and C3 positions of propylene was determined by measuring the integrated peak areas of the three different hydrogens in the nmr absorption spectrum and comparing them with the 2:1:3 values expected for propylene-$d_0$ on the basis of the observed signal for cyclopropane internal standard and the known composition of the mixture.

Most of the experiments reported here were carried out on a 2.0-g sample of NaY zeolite (Linde Lot SK40 51-31) which had been treated with NaCl, as reported previously.[2] On a fully dehydrated basis, it had the formula $Na_{0.96}Ca_{0.006}AlO_2 \cdot 2.39SiO_2$. One set of experiments was carried out on a partially hydrogen-exchanged sample, NaHY, which was obtained by treating 10 g of the original sample (NaY SK40) with 1 l. of $10^{-2}$ $M$ $NH_4Cl$ for 72 hr at room temperature with gentle agitation. Before deammination, this sample had the composition $Na_{0.675}(NH_4)_{0.227}Ca_{0.028}AlO_2 \cdot 2.31SiO_2$.

Cyclopropane and propylene were obtained from Matheson and $D_2O$ and deuterated compounds from Merck Sharpe and Dohme, Ltd.

## Results and Discussion

The deuterium distribution in the propylene product from the isomerization of cyclopropane-$d_0$ over a deuterated NaY catalyst was determined and compared with predicted values. Deuterated NaY catalyst was prepared as in previous work[2] by saturating the helium stream with $D_2O$ at 0° and passing the wet helium over the catalyst for several hours at the reaction temperature of 285°. The $D_2O$ stream was continued during the reactions and it was assumed that this would maintain the catalyst in a deuterated condition even during exchange with cyclopropane and propylene. The partial pressure of $D_2O$ over the catalyst was about 2.8 Torr and a separate experiment with 3.6 Torr of $D_2O$ showed that the catalytic activity is independent of $D_2O$ pressure in this range.

In order to obtain sufficient propylene for the nmr analysis, 10 successive slugs of cyclopropane (each 10 ml at 100 Torr) were passed over the catalyst and the separated propylene fractions were combined. The conversions of the successive slugs at 285° were substantially the same, 20.4 ± 1.0%. The rate constant for the surface reaction (equal to $k_{A_0}{}^{i} + k_{A_0}{}^{ei}$) calculated from the conversion and the contact time, $t_A$ = 11.1 sec, was 0.0210 $sec^{-1}$. This was close to the value 0.0217 predicted from the previous results for this temperature and consequently it was felt justified to use the previous results to estimate the values for the other rate constants: $k_{A_0}{}^{i}$ 0.0053, $k_{A_0}{}^{ei}$ 0.0157, $k_{A_0}{}^{e}$ 0.0680, $k_{B_0}{}^{e}$ 0.0345, and the value of $t_B$ 13.7 sec.

Using these rate constants the composition of the propylene product was calculated by the equations of Table I; the resultant values are summarized in Table II along with the experimentally determined composition and the total degree of deuteration as determined from the nmr results. The agreement between observed and predicted composition is good for $B_1$, the principal deuterated species; the higher than expected value for $B_0$ suggests a somewhat greater proportion of isomerization without exchange than the 26% obtained in the previous paper and on which the rate constants were based. Table III shows the deuteration on each of the three carbons of propylene during the isomerization step. This is obtained as the difference between the total deuteration on each carbon as obtained by nmr and the calculated deuteration by exchange of cyclopropane and exchange of propylene (assumed to introduce D randomly into all 6 H positions of cyclopropane and randomly into the 5 H positions on C1 and C3 in propylene. There is indeed some exchange into the C2 position of propylene[6] but this is small enough to be negligible here.) The data show the deuteration during isomerization to be random among all hydrogen positions in propylene.

**Table II:** Conversion to Various Deuterated Propylenes

| Species | | Reaction route | Fractional composition of propylene: Calcd | | Obsd |
|---|---|---|---|---|---|
| $B_0$ | 1 | $A_0 \rightarrow B_0$ | | 0.136 | 0.228 |
| $B_1$ | 2 | $A_0 \rightarrow B_1$ | 0.426 | | |
| | 3 | $A_0 \rightarrow A_1 \rightarrow B_1$ | 0.069 | 0.531 | 0.507 |
| | 4 | $A_0 \rightarrow B_0 \rightarrow B_1$ | 0.036 | | |
| $B_2$ | 5 | $A_0 \rightarrow B_1 \rightarrow B_2$ | 0.093 | | |
| | 6 | $A_0 \rightarrow A_1 \rightarrow B_2$ | 0.143 | | |
| | 7 | $A_0 \rightarrow A_1 \rightarrow A_2 \rightarrow B_2$ | 0.015 | 0.266 | 0.211 |
| | 8 | $A_0 \rightarrow A_1 \rightarrow B_1 \rightarrow B_2$ | 0.009 | | |
| | 9 | $A_0 \rightarrow B_0 \rightarrow B_1 \rightarrow B_2$ | 0.006 | | |
| $B_3$ | 10 | $A_0 \rightarrow A_1 \rightarrow A_2 \rightarrow B_3$ | 0.022 | | |
| | 11 | $A_0 \rightarrow A_1 \rightarrow A_2 \rightarrow A_3 \rightarrow B_3$ | 0.002 | 0.050 | 0.048 |
| | 12 | $A_0 \rightarrow A_1 \rightarrow B_2 \rightarrow B_3$ | 0.016 | | |
| | 13 | $A_0 \rightarrow B_1 \rightarrow B_2 \rightarrow B_3$ | 0.010 | | |
| | B total | | | 0.983 | 1.000 |
| | Extent of deuteration, fractional | | | 0.212 | 0.180 |
| | | | | | 0.171 (nmr) |

Random exchange among all hydrogen positions of the propylene product almost certainly must occur before ring opening of the cyclopropane. The most

(6) Z. M. George and H. W. Habgood, unpublished results.

**Table III:** Deuteration of Various Hydrogen Positions in Product Propylene

| | Fractional deuteration per H | | |
|---|---|---|---|
| | C1 | C2 | C3 |
| Predicted | | | |
| (1) *Via* exchange of A,[a] routes 3, 6, 7(2x), 8, 10(2x), 11(3x), 12 | 0.053 | 0.053 | 0.053 |
| (2) *Via* exchange of B,[b] routes 4, 5, 8, 9(2x), 12, 13(2x) | 0.037 | | 0.037 |
| Total *via* exchange separate from isomerization | 0.090 | 0.053 | 0.090 |
| Observed (from nmr areas) | 0.173 | 0.127 | 0.185 |
| Deuteration during isomerization | | | |
| By difference | 0.083 | 0.074 | 0.095 |
| Predicted, routes 2, 5, 6, 10, 12, 13 | ...average 0.118... | | |

[a] Assumed to introduce deuterium randomly in all 6 hydrogens in the resulting propylene. [b] Assumed to introduce deuterium randomly in the 5 hydrogens on C1 and C3 of propylene.

probable mechanism is a rapid isomerization among all of the possible forms of edge-protonated cyclopropane. The degree of exchange in the propylene product should then be substantially independent of the exact mechanism of isomerization. Assuming no isotope effect for the loss of $H^+$ or $D^+$ from the carbonium ion, the degree of exchange during isomerization, $k_{A_0}^{ei}/(k_{A_0}^{i} + k_{A_0}^{ei})$ should be $^6/_7$ or 86%. A normal isotope effect would give a higher value. The results of Hightower and Hall indicated close to 100% exchange during isomerization. Galeski and Hightower[7] have recently obtained a value of about 84% in microcatalytic experiments over a $D_2O$–wet silica–magnesia catalyst in which they varied the flow rate and extrapolated to zero conversion.

The question then remains as to why we obtain only 74% or less exchange during isomerization. We have explored two possible explanations. (a) Redeuteration of a catalytic site by exchange with $D_2O$ following reaction is slow relative to a fresh reaction on the same site even though the concentration of adsorbed $D_2O$ was at least 100 times the concentration of adsorbed cyclopropane. (b) The technique for preparing a deuterated catalyst–exchange with $D_2O$ at the reaction temperature of 285° for some reason does not deuterate all reactive sites.

In order to check on the first possibility, several experiments were carried out at different partial pressures of cyclopropane while maintaining the partial pressure of $D_2O$ at about 2.8 Torr. Constant flow rather than slug experiments were used here in order to specify the actual partial pressures more completely. The range of inlet partial pressure of cyclopropane was from 0.017 Torr to 1.75 Torr and the results are summarized in Table IV. The experiment at 1.75 Torr showed a small but significant increase in the fraction of undeuterated propylene indicating that at this partial pressure redeuteration of catalyst sites is not complete. A slug experiment, however, with a 30-Torr, 10-ml slug gave results identical with the lower pressure flow experiments. This indicates that the requirements for redeuteration are much less serious for a slug than for steady flow.

Attempts were then made to see whether a more complete initial deuteration of the catalyst was possible. The first approach was to carry out the exchange with $D_2O$ at a higher temperature. The catalyst was heated to 500° in the flowing $D_2O$ stream (2.8 Torr) for 4 hr, then cooled to reaction temperature (294°) and equilibrated at this temperature. The first slug injected (Table V) gave a propylene composition corresponding to 86% deuteration during isomerization. The second and subsequent slugs gave the usual value, about 75%.

A second approach to complete initial deuteration was to carry out an injection of cyclopropane-$d_6$ (in this case over the dry catalyst) in the hope that this would lead to the deuteration of all active sites. The catalyst was then equilibrated with $D_2O$ in the usual manner and the first subsequent injection of a slug of cyclopropane-$d_0$ gave products corresponding to 87.5% exchange with isomerization. The second and succeeding slugs showed a marked increase in the relative amount of isomerization without deuteration (Table V).

Following the experiments described in the preceding two paragraphs, a standard reaction in $D_2O$–wet helium at 289° showed that the catalytic activity had not been impaired ($k^i$ = 0.0236 $sec^{-1}$ compared with the previous value of 0.0240 $sec^{-1}$) and measurements of the retention volume of cyclopropane agreed with previous values.

These experiments, therefore, have demonstrated the existence on this NaY catalyst of some protonic sites which are highly reactive with cyclopropane yet are exchangeable with $D_2O$ only with difficulty. In fact, for reaction temperatures around 300° these anomalous sites do not significantly exchange with $D_2O$, although, as shown by the flow experiments, the remaining sites exchange fast enough to be maintained in deuterated form during all of the experiments previously reported.

We have no specific suggestions to offer concerning the nature of these sites that react (and exchange) readily with cyclopropane but do not exchange with water. We attempted to learn something of their importance to zeolite catalysis generally by investigating a sample of NaHY containing about 30% replacement of Na by H. These acid sites are predominantly the ones that are of practical interest

(7) J. B. Galeski and J. W. Hightower, presented to the Third Canadian Symposium on Catalysis, Edmonton, Canada, October 20, 1969.

**Table IV:** Effect of Variation of Partial Pressure of Cyclopropane-$d_0$ in Flow Experiments Over a Deuterated Catalyst[a]

| Catalyst temp | Partial pressure above catalyst, Torr | He flow rate, ml/sec | Conversion % | Isotopic composition of product propylene, % $d_0$ | $d_1$ | $d_2$ | $d_3$ | $d_4$ |
|---|---|---|---|---|---|---|---|---|
| 274 | 1.75 | 0.72 | 9.9 | 0.201 | 0.653 | 0.139 | 0.007 | |
| 276 | 0.182 | 0.72 | 11.4 | 0.150 | 0.666 | 0.161 | 0.023 | |
| 274 | 0.017 | 0.72 | 10.8 | 0.156 | 0.654 | 0.160 | 0.030 | |
| 274 | Cyclopropane slug, 10 ml at 30 Torr | 0.72 | 11.8 | 0.149 | 0.631 | 0.189 | 0.029 | |

[a] Partial pressure of $D_2O$, 2.8 Torr.

**Table V:** Summary of Experiments with "Drastic" Deuteration of the NaY Catalyst

| Catalyst treatment | Slug no. | Conversion, % | $B_0/\Sigma B$ | $k_{A_0}^i/(k_{A_0}^i + k_{A_0}^{ei})$ |
|---|---|---|---|---|
| Regenerated catalyst equilibrated with $D_2O$ at 500°, cooled in $D_2O$ vapor to 294°, and equilibrated with $D_2O$ at this temperature | 1 | 22.0 | 0.084 | 0.138 |
| | 3[a] | 22.8 | 0.176 | 0.290 |
| Regenerated catalyst cooled to 288°, a slug (10 ml at 10 Torr) of cyclopropane-$d_6$ was injected and catalyst equilibrated with $D_2O$ at 288° | 1 | 20.2 | 0.072 | 0.125 |
| | 3[a] | 19.8 | 0.152 | 0.315 |

[a] The second slug in each experiment was $B_0$. For both $A_0$ slugs, the results from a single $B_0$ slug were used to calculate $k_{A_0}^i/(k_{A_0}^i + k_{A_0}^{ei})$. $k_{B_0}^e$ was 0.04 in both experiments, compared to 0.05 in the previous paper.[2]

in catalysis and it would be important to know if a large fraction of them showed this high catalytic activity coupled with reluctance to undergo H–D exchange with water.

The NaHY catalyst was equilibrated with 2.8 Torr of $D_2O$ at 139° and the reaction was carried out in the same manner as before. The lower reaction temperature was necessary because of the greater reactivity of the NaHY catalyst. The concentration of adsorbed $D_2O$ was estimated[5] to be about 10 molecules per cavity (as compared with 1 molecule per cavity at 300°) and the ratio of adsorbed $D_2O$ to that of adsorbed cyclopropane was approximately 200:1 as compared with 100 to 1. Table IV showed the results to be substantially independent of the ratio of $D_2O$/cyclopropane so that the 200:1 ratio here would not of itself be expected to change the effective degree of deuteration of the catalyst. The rate constants are summarized in Table VI. The proportion of cyclopropane isomerizing without exchange ($k_{A_0}^i/(k_{A_0}^i + k_{A_0}^{ei})$) is seen to be 15%. This is similar to the value found for the first slug on a "drastically" deuterated NaY catalyst and is approximately the fraction expected for complete mixing in the $c$-$C_3H_6D^+$ ion. The 26% nonexchange observed with the NaY catalyst under the steady-state conditions of a $D_2O$ stream must then reflect the presence of a small number of atypical sites that are of negligible importance in catalysts of practical importance.

**Table VI:** Rate Constants for the Isomerization of Cyclopropane over NaHY Catalyst in the Presence of $D_2O$ at 139°

| $k^i$ | $k_{A_0}^e$ | $k_{A_0}^i$ | $k_{A_0}^{ei}$ | $k_{B_0}^e$ |
|---|---|---|---|---|
| $5.0 \times 10^{-3}$ | $3.6 \times 10^{-2}$ | $0.75 \times 10^{-3}$ | $4.3 \times 10^{-3}$ | $1.1 \times 10^{-2}$ |

The rate constant for isomerization, $k^i$, for NaHY is about 100 times the value extrapolated from the previous measurements with NaY. This reflects the expected increase in catalytic activity with the increase in concentration of the acid sites. The ratio of exchange of cyclopropane to isomerization, $k_{A_0}^e:k^i$, is approximately 7 for NaHY as compared with about 2 for NaY. This difference could correspond to a difference in activation energy for isomerization and for exchange of 3.6 kcal/mol. Although this is somewhat outside the experimental scatter of the previous measurements such a difference would then be a measure of the asymmetry of the potential-energy surface around the metastable $c$-$C_3H_7^+$ cation. Otherwise this difference in ratio indicates a difference in the environments of Brønsted sites on the two catalysts so that the potential energy surface is different at different sites.

We feel that the results reported here have confirmed the most plausible mechanism of cyclopropane isomerization to be that of eq 1 with the addition of an equilibration step among the various possible forms of protonated cyclopropane carbonium ion. In subsequent work, to be reported separately, we are studying

the reaction of cyclopropane over dry deuterated catalyst in an attempt to measure the concentration of active sites and to learn more about the initial reaction step of cyclopropane with the catalyst.

*Acknowledgments.* The nmr spectra were recorded by G. Bigam, Chemistry Department, University of Alberta. Excellent technical assistance was provided by J. J. Mendiuk.

# Electron Paramagnetic Resonance of Nickel Acetate. Irradiation-Induced Spin Pairing

**by D. A. Morton-Blake**[1]

*Division of Molecular Science, National Physical Laboratory, Teddington, Middlesex, England* *(Received July 14, 1969)*

Single crystals of X-irradiated nickel acetate tetrahydrate were investigated by epr at 77°K. The spectra of several $S = {}^1/_2$ species were observed, indicating that one of the electron spins in the $Ni^{2+}$ ion had paired with a free spin created in one of the ligands. Using a single mounting position of the crystal and assuming cylindrical $g$-tensor symmetry, a least-squares computation gave the components $g_{||} = 2.463 \pm 0.002$, $g_{\perp} = 2.076 \pm 0.002$ for the main species formed. However, there is some evidence for the presence of an appreciable rhombic component which would introduce an uncertainty of 0.02 in $g_{||}$.

## Introduction

Recently it was shown[2] that X-irradiation of cupric acetate monohydrate $[(CH_3CO_2)_2Cu \cdot H_2O]_2$ crystals results in partial spin pairing within the $S = 1$ magnetic triplet species. This was evidenced by the presence of an $S = {}^1/_2$ species whose spin was centered on one of the two copper atoms, as revealed by the epr spectrum. The inference drawn was that the irradiation had removed an H atom from one of the four acetate ligands, and that the resulting radical had spin-paired with the nearest cupric ion, leaving a free spin on the remaining cupric ion.

This result suggested the possibility of partial spin pairing in other paramagnetic species for which $S > {}^1/_2$ and this paper describes a similar investigation of irradiated nickel acetate tetrahydrate, $(CH_3CO_2)_2Ni \cdot 4H_2O$. $Ni^{2+}$ has a $3d^8$ shell, and normally forms a ground-state $S = 1$ triplet. The crystal structure[3] shows that the $Ni^{2+}$ ion is surrounded by six O atoms in the form of a slightly distorted octahedron. Four of the oxygens, which are in $H_2O$ ligands, form an approximate square in an "equatorial plane" at $\pm 2.06$ and $\pm 2.11$ Å from the $Ni^{2+}$ ion at the origin, while the other two oxygens, which are in two different acetate anions, are at $\pm 2.12$ Å along the "polar" directions.

An irradiation mechanism similar to that supposed to occur in cupric acetate would be expected to eliminate an H atom in one acetate ligand, converting it to the radical anion, $\dot{C}H_2CO_2^-$. Describing this acetate radiolysis by the reaction $A^- \longrightarrow \mathfrak{A}^{\cdot -} + H$, the irradiation of nickel acetate can, in principle, create any of the species represented schematically on the right-hand side of the reactions

$$A^-\text{–}\overset{2+\ \uparrow\uparrow}{Ni(d^8)}\text{–}A^- \xrightarrow{-H} \begin{cases} \longrightarrow A^-\text{–}\overset{2+\ \uparrow\uparrow\ \ \uparrow}{Ni(d^8)}\text{–}\mathfrak{A}^{\cdot -} & \text{(1a)} \\ \longrightarrow A^-\text{–}\overset{+\ \ \uparrow}{Ni(d^9)}\text{–}\mathfrak{A} & \text{(1b)} \\ \longrightarrow A^-\text{–}\overset{3+\ \uparrow\uparrow\ \ \uparrow\downarrow}{Ni(d^7)}\text{–}\mathfrak{A}^{2-} & \text{(1c)} \end{cases}$$

If there were no metal–ligand spin interaction, the epr spectrum of species (1a) would be merely the $S = {}^1/_2$ spectrum of $\mathfrak{A}^{\cdot -}$ superposed upon that of nickel acetate ($S = 1$). Interaction of the spins would produce an $S = {}^3/_2$ quartet or $S = {}^1/_2$ doublet, and spin delocalization on metal or ligand would produce the species (1b) or (1c) in which the nickel ion is isoelectronic, respectively, with $Cu^{2+}(d^9)$ or with $Co^{2+}(d^7)$, and should possess very similar paramagnetic properties ($g$ values and relaxation times).

Unlike cupric acetate which has an $S = 0$ ground state, the only appreciably populated state in nickel acetate is the triplet. Therefore any paramagnetic species created by the irradiation is subject to spin

(1) Chemistry Department, Trinity College, Dublin 2, Ireland.

(2) D. A. Morton-Blake, *J. Phys. Chem.*, **73**, 2964 (1969).

(3) J. N. van Niekerk and F. R. L. Schoening, *Acta Cryst.*, **6**, 609 (1953).

exchange with neighboring triplet species, with consequent line-broadening. Irradiated nickel acetate crystals gave epr line widths of 35 to 40 G. In order to obtain narrow lines and therefore better resolution, nickel-doped crystals of magnesium acetate tetrahydrate were used.

## Experimental Section

Crystals of magnesium acetate tetrahydrate (monoclinic space group $P2_1/c$) containing 1% nickel acetate tetrahydrate were grown from dilute acetic acid. A crystal irradiated with 150-kV X-rays to a dosage of 5 Mrads was mounted in an $H_{101}$ rectangular cavity with the (011) face on the narrow vertical wall, so that the $b$ axis was in the plane of the magnetic field. Measurements were made at 77°K, and since there was evidence that some of the radiogenic species were unstable a single crystal setting was used as described previously,[2] the spectra being recorded every 10° over the magnet rotation range $\chi = 0$ to 170°. The spectra were calibrated by a variable-frequency proton resonance probe. The frequency of the X-band superheat spectrometer used in the investigation was 8859.7 MHz.

## Calculation

The results indicate that all the observed paramagnetic species created by the irradiation are described by formula 1b. This may be thought of as a pseudocupric complex consisting of a $3d^9$ ion at the center of a distorted octahedron of oxygen atoms.

Distortions in octahedral complexes may have various causes, but the most important one in $d^9$ complexes is that due to a Jahn–Teller effect which lifts the orbital degeneracy of the $e_g$ orbital (with which the spin is associated) by removing some of the symmetry elements of the octahedron.[4] The result of this distortion is either (i) (usually) to increase the distances of both ligands on one of the *three* $C_2$ axes of the octahedron, so as to produce tetragonal ($\tilde{\mathfrak{D}}_{4h}$) symmetry, or (ii) (occasionally) to compress the ligands about one of the *four* $C_3$ axes so as to produce trigonal ($\tilde{\mathfrak{D}}_{3d}$) symmetry. In either case a unique symmetry axis is imposed on the complex formed from one of the *seven* possible directions described. This axis, which we shall refer to as the Jahn–Teller (or J–T) axis, becomes a principal axis for susceptibility, $g$, and hyperfine tensors.

We assume that all our radiogenic species contain such a unique axis of cylindrical symmetry, and so we can use the least-squares procedure described in ref 2 to evaluate the spectral parameters

$$G \equiv (g_{||}^2 - g_{\perp}^2) \sin^2 \theta \tag{2a}$$

and

$$\Gamma \equiv g_1^2 \tag{2b}$$

The quantities $g_{||}$ and $g_{\perp}$ have their usual meanings for a complex with cylindrical symmetry, and $\theta$ is the angle

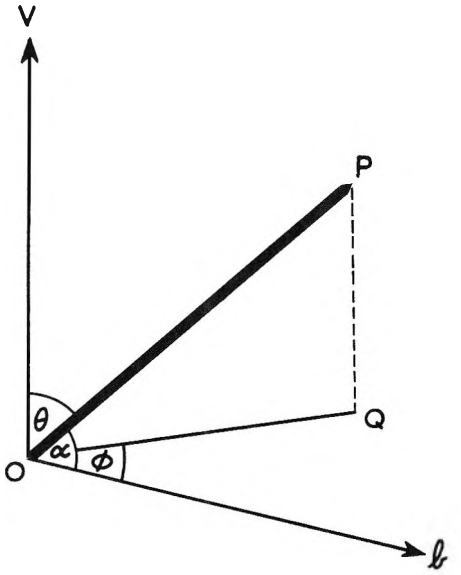


Figure 1. Symmetry (J–T) axis OP and its projection onto the plane of rotation of the magnetic field which includes the direction of the $b$ axis.

made between the axis of the complex and the vertical direction (*i.e.*, that about which the magnetic field is rotated).

$\theta$ is known approximately from the crystal setting, and Figure 1 shows that it is related to the two other angles $\alpha$ and $\phi$. $\alpha$ is the angle between the $b$ axis and the *seven* possible J–T axes OP described above, and $\phi$ is the angle between $b$ and the projection of OP onto the plane of rotation of the magnetic field. Clearly the relationship is

$$\cos \alpha = \sin \theta \cos \phi \tag{3}$$

Since the $b$ axis is in the plane of rotation of the field $\phi$ can be found directly from the spectra, the $g$ value is a maximum (or in some cases a minimum) along the projection OQ of the J–T axis; $\phi$ is therefore the angle between such a position and the $b$ axis. The seven possible angles $\alpha$ can be easily calculated from the crystal structure.

A computer was programmed to calculate values of $\phi$ for each of the seven angles $\alpha$, and for each of a set of $\theta$ values within a reasonable range. By comparing calculated and observed values of $\phi$ the J–T axes and their directions $\theta$ with the vertical could thus be assigned to the six species. In many of the species there were considerable shifts (~20°) in the directions of the J–T axes from those of the parent axes as a result of the radiolysis. Since the crystallographic values of $\alpha$ used related to the unirradiated complex, the $\theta$ calculated *via* (3) were subject to some uncertainty, and in such cases the calculation of $g_{||}$ was not attempted. For the main species, however, the J–T axis apparently lay quite close to one of the symmetry axes of the nickel acetate

(4) A. D. Liehr and C. J. Ballhausen, *Ann. Phys.*, **3**, 304 (1958).

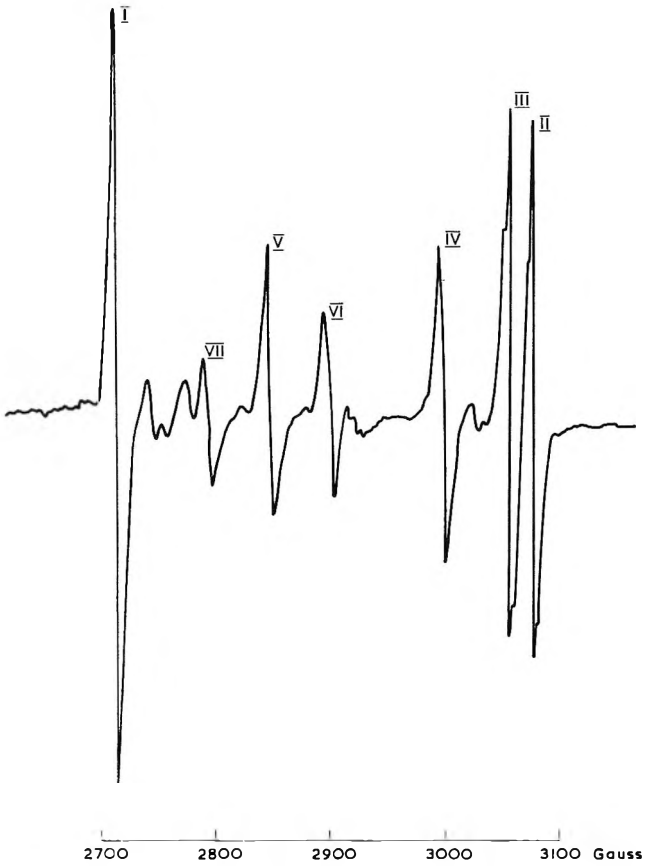


Figure 2. Epr spectrum of X-irradiated nickel acetate at 77°K. Field along $b$ axis.

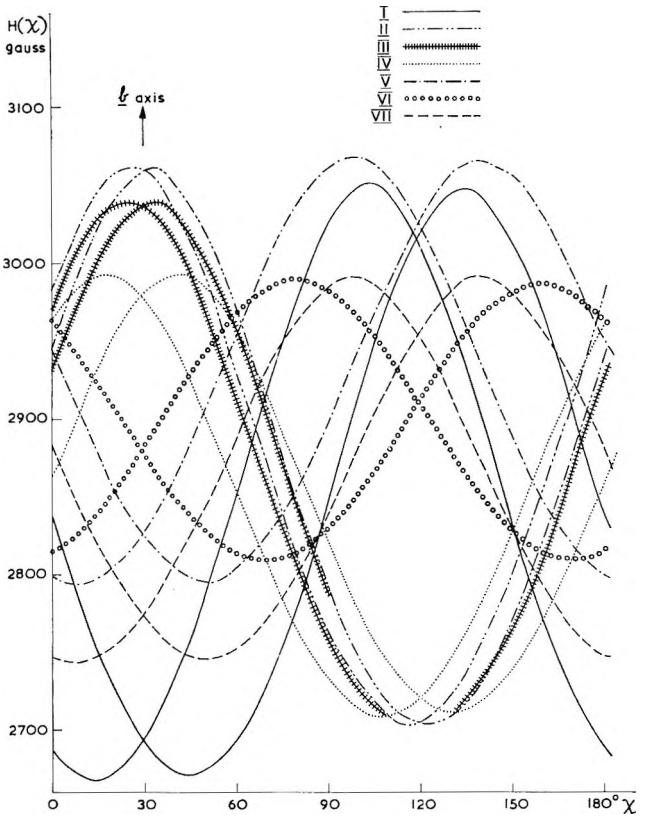


Figure 3. Resonant field curves for the seven observed paramagnetic species in X-irradiated nickel acetate.

complex, and so the value of $\theta$ obtained by this procedure was used to calculate $g_{||}$ *via* the relation $g_{||}^2 = \Gamma + G/\sin^2\theta$.

## Results

The spectra, one of which is shown in Figure 2, revealed the existence of several distinguishable paramagnetic species, seven of which were sufficiently resolvable to follow their resonances over the field-direction range. The resonant fields were all between 2670 and 3065 G, which fact strongly suggested that all the paramagnetic species observed were of the kind $S = {}^1/_2$ and possessed effective $g$ values in the range $g = 2.06$ to 2.38 for this crystal setting. From this $Cu^{2+}$-like $g$ value it would appear that the species were of type (1b) rather than (1c) since the $Co^{2+}$ ion ($d^7$) has much larger and more anisotropic $g$ values, and its epr spectra can only be well resolved at low temperatures (4–20°K) due to its short spin–lattice relaxation time. All the species gave rise to probably equal line widths of 4.5 to 6 G; for some lines apparent widths of 10 G were observed, but at certain orientations there was evidence for the presence of two or more species with almost-parallel J–T axes. All possessed roughly similar degrees of $g$-value anisotropy and showed site splittings which were consistent with monoclinic crystal symmetry, as seen from the H($\chi$) resonant field curves in Figure 3. These curves and the resonance lines in Figure 2 are numbered from I to VII in the order of decreasing concentration of paramagnetic species as estimated roughly from the relative intensities of the spectra.

Table I shows the J–T axes assigned to the seven paramagnetic species, their relative concentrations, and where possible the $g$-value components. It was not possible to evaluate $g_{||}$ accurately for these species which had a $C_3$ J–T axis for two reasons. Firstly, for the crystal setting used, the angles $\alpha$ and $\phi$ were in the region 78 to 90° thus limiting the accuracy of (3) to calculate $\theta$ (which itself turned out to be rather small for $C_3(1)$ and so in its turn imposed an inaccuracy on $g_{||}$ as calculated by (2)). Secondly, the $H_2O$ ligands in the Ni complex are involved in intramolecular hydrogen bonding with the nonligand oxygen atoms of the acetate groups and in intermolecular hydrogen bonding with such oxygen atoms of neighboring complexes.[3] As a result of the hydrogen bonding it is unlikely that a Jahn–Teller distortion would occur precisely along an octahedral $C_3$ axis. In order to obtain the true directions of the distortion axes and the $g$-value components, two or three crystal setting positions would have to be used. The instability of some of the species precluded the use of this method here.

If species I, V, and VII are indeed chemically identical and differ only by a shift in the directions of the

**Table I:** J–T Axes and $g$-Value Components of the Radiogenic Species from Nickel Acetate Tetrahydrate

| Species | Rel. concn | $g$ | $g_{\|\|}$ | J–T axis |
|---|---|---|---|---|
| I | 13 | 2.076 ± 0.002 | 2.463 ± 0.002 | (Ac)O–Ni–O(Ac) |
| V | 4 | 2.064 ± 0.002 | probably the same | |
| VII | 2 | 2.117 ± 0.002 | | |
| II | 9 | 2.069 ± 0.002 | | |
| III | 9 | 2.080 ± 0.002 | — | $C_3(1)$ |
| IV | 5 | 2.115 ± 0.002 | | |
| VI | 3 | 2.116 ± 0.002 | ~2.34(?) | $C_3(2)$ |

J–T axes we should have to face the presence of an appreciable rhombic component at right angles to these axes. This is shown by the relatively large range of $g$ values observed, namely from 2.064 to 2.117, and may be caused by differences in bond lengths and/or angles involving the two pairs of water ligands. Such a rhombic component would introduce some inaccuracy in our single-mounting-position theory, since the use of eq 2a is valid only for cylindrical symmetry. A correction for the rhombic component would lead to the value $g_{||} = 2.47 \pm 0.01$ for species I, V, VII, with $g_{\perp} = 2.06$ to 2.12.

## Discussion

An X-irradiated crystal of undoped magnesium acetate tetrahydrate shows two main multiplets which at most orientations are recognizable as 1:2:1 triplets;[5] this result therefore supports the identification of the radical $\mathfrak{a}^{\cdot -}$ as $\dot{C}H_2COO^-$ which was made in the introduction. The results of the present experiment Indicate that the X-radiolysis of nickel acetate is analogous to that of cupric acetate. The free spin on the acetate radical $\mathfrak{a}^{\cdot -}$ clearly finds an energy trough in the 3d shell of the nickel ion leaving a spin-paired, neutral group $CH_2CO_2$, the complete paramagnetic species being represented by formula 1b. The removal of the negative charge from one of the acetate anion ligands and of one of the positive charges on the nickel cation causes the electrostatic attraction between cation and the *other* acetate anion to be reduced to one-half its value in the parent complex, while that between $Ni^+$ and $\mathfrak{a}$ is considerably less (the actual amount depends on the degree of polarization of $\mathfrak{a}$ by the $Ni^+$ cation). This must result in an increase in the Ni–O bond lengths in these directions, the $Ni^+$–$\mathfrak{a}$ bond length being greater than that of $A^-$–$Ni^+$. Similarly, the $H_2O$–$Ni^+$ bond lengths will also be increased by amounts roughly equal to that of the $A^-$–$Ni^+$ bond extension.

The lengthening of the nickel cation radius as a result of its chemical reduction $Ni^{2+} \rightarrow Ni^+$ by the irradiation is about equal to the lengthening in the step $Ni^{3+} \rightarrow Ni^{2+}$ which is 0.1 Å.[6] The lengthening of the ligand O atom in the $A^- \rightarrow \mathfrak{a}$ step is probably about the same. Since the ground state of the unirradiated $Ni^{2+}$ complex is already an orbital singlet (symmetry $A_1$) a Jahn–Teller distortion does not occur and the complex approaches octahedral symmetry more closely than do spin-doublet species such as $Cu^{2+}$ or $Ni^+$. However, the conversion of a $Ni^{2+}(^3F)$ complex into a $Ni^+(^2D)$ requires the selection of a distortion axis, and we are not surprised to find that the radiogenic species formed with highest concentration (species I) is one which has as its J–T axis the unique octahedral direction $A^-$–$Ni^+$–$\mathfrak{a}$. The length of this axis, between the pair of "polar" oxygen ligands is now 4.54 Å as a result of the irradiation; the new "equatorial" axial lengths (between the two pairs of water ligands) are 4.32 and 4.44 Å; we should therefore not expect these directions to form normal J–T axes.

It is not so obvious that some species would be created possessing a J–T axis of *trigonal* symmetry, but as has been suggested this could be caused by hydrogen bonding which does in fact make the octants of the octahedron inequivalent. However, the reason for the selection, by the complex, of the particular axes $C_3(1)$ (which is directed between the ligands $H_2O$ (1), $H_2O$ (2) and $O_1$ in the notation of van Niekerk and Schoening[3]) and $C_3$ (2) (which is directed between $H_2O$ (1), $H_2O$ (2) and $\bar{O}_1$) is still not clear, and the calculation of crystal forces of distortion is difficult.

The striking similarity between the $g$ components of species I in Table I and those of $^2$D-cupric acetate[2] ($g_{||} = 2.458$, $g_{\perp} = 2.075$) indicates that in our $^2$D-nickel acetate complex too we have a high degree of spin population on the metal cation. If the values of $\lambda$ and $\Delta E$ in the expression $g = g_e - 8\lambda/\Delta E$ are similar to those for $^2$D-cupric acetate, the spin population is about 90–95%, which is measurably greater than in similar complexes involving formate ligands.[7,8]

*Acknowledgment.* My thanks are due to Mr. E. Bullock for preparing the crystals and to Miss R. H. Colton for identifying the crystal axes. This work forms part of the research program of the Division of Molecular Science of the National Physical Laboratory.

(5) D. A. Morton-Blake, unpublished observations.

(6) L. Pauling, "The Nature of the Chemical Bond," Cornell University Press, Ithaca, N. Y., 1960, p 518.

(7) G. R. Wagner, R. T. Schumacher, and S. A. Friedberg, *Phys. Rev.*, **150**, 226 (1966).

(8) J. M. Barbour, D. A. Morton-Blake, and A. L. Porte, *J. Chem. Soc., A*, 878 (1968).

# An Electron Paramagnetic Resonance Study of Y-Type Zeolites.

# I. $O_2^-$ on Alkaline Earth Zeolites

by Katherine M. Wang and Jack H. Lunsford

*Department of Chemistry, Texas A&M University, College Station, Texas 77843* *(Received August 20, 1969)*

Interactions between the adsorbed $O_2^-$ species and alkaline earth Y-type zeolites have been studied by means of epr spectroscopy. The adsorbed $O_2^-$ was formed by uv or $\gamma$ irradiation of the zeolites in oxygen. The results show that there are three or more different adsorption sites on each of the cationic zeolites. The spectra have been placed into three groups according to their $g$ values and response to the two types of irradiation. Within each group there does not appear to be any significant trend in the energy splitting, $\Delta$, of the $2p\pi_g^*$ levels of the $O_2^-$ ion as one goes up the series from BaY to MgY. The CaY zeolite was also studied after extensive $\gamma$ irradiation of the sample under vacuum. Three paramagnetic centers were also formed under these conditions; two were identified as V-type centers and the other as an F-type center.

## Introduction

Pickert, *et al.*,[1] calculated the electrostatic field for a number of points in purely ionic models of CaX and CaY zeolites. In these models, several restrictions were made. The net negative charge associated with each $AlO_4$ tetrahedron was assumed to reside on the Al ion; each 6-ring contained exactly two aluminums, and these two aluminums must be apart as far as possible; a "double basket" unit of structure was formed by the pairs of adjacent sodalite units with their associated calcium ions of sites I and II, and this "double-basket" unit has zero net electric charge and zero dipole moment. According to their results the electrostatic field is much stronger for an occupied site than it is near an unoccupied site. The effective field for polarization is stronger at a shorter distance of approach; therefore, a stronger field should be expected for a smaller cation. Also, they proposed that the electrostatic field was responsible for the catalytic activity of the zeolites.

A number of attempts have been made to verify experimentally the presence of these unusually large fields and to show that they varied in a systematic manner as predicted. One of the most convincing pieces of evidence is from the work of Kasai,[2] who used epr spectroscopy to show that the energy splitting of the $2p\pi_g^*$ levels of the superoxide ion, $O_2^-$, was exactly twice as large with divalent BaY as with monovalent NaY. The epr spectrum is particularly sensitive to the ion's environment and has been used to determine interactions on a number of systems including decationated (HY) zeolites,[3] MgO,[4] ZnO,[4] $TiO_2$,[5] and supported sodium.[6]

In the present study an attempt was made to determine whether any systematic change in crystal field effect on the adsorbed $O_2^-$ species could be detected as one goes up the group IIa series from BaY to MgY zeolites. In addition, it was of interest to learn of the general location of the adsorption site, the effect of varying the extent of exchange, and the possibility that more than one site was present.

## Experimental Section

The alkaline earth Y-type zeolites were prepared by exchanging the sodium from a Linde type Y zeolite with the cations from a nitrate solution of the desired cation. The percentage exchange of these divalent zeolites is shown in Table I. An analysis of the NaY zeolite which was washed in deionized water showed that the ratio of $Na_2O/Al_2O_3$ was only 0.93, which is less than the stoichiometric ratio of 1.000. The original NaY had an $Na_2O/Al_2O_3$ ratio of 0.992.

**Table I:** The Percentage Exchange of the Divalent Zeolites on Dehydrated Basis

| Zeolite | % exchanged |
|---|---|
| MgY | 65 |
| CaY-1 | 92 |
| CaY-2 | 65 |
| CaY-3 | 43 |
| SrY | 92 |
| BaY | 79 |

(1) P. E. Pickert, J. A. Rabo, E. Dempsey, and V. Schomaker, "Proceedings of the Third International Congress on Catalysis," North-Holland Publishing Co., Amsterdam, 1964.

(2) P. H. Kasai, *J. Chem. Phys.*, **43**, 3322 (1965).

(3) K. M. Wang and J. H. Lunsford, *J. Phys. Chem.*, **73**, 2069 (1969).

(4) J. H. Lunsford and J. P. Jayne, *J. Chem. Phys.*, **44**, 1487 (1965).

(5) R. D. Iyengar, M. Codell, and J. Turkevich, *J. Catal.*, **9** (3), 305 (1967).

(6) J. Turkevich and T. Sato, The First North American Meeting of the Catalysis Society, Atlantic City, N. J., Feb 1969.

The samples were broken into chips with a 1-mm maximum dimension and then placed in a Vycor sample tube which contained a quartz side arm of 18-cm length with a 3-mm inside diameter. The samples were degassed under vacuum ($10^{-5}$ Torr) to 500° with a heating interval of 100°/hr. During the degassing process, the side arm was heated for at least 5 min to complete the degassing procedure. After 5 hr degassing, the samples were heated in 1 atm of $H_2$ at 500° for 2 hr, and the hydrogen gas was removed by evacuation for at least 30 min. After cooling to room temperature, the zeolite chips were tapped into the side arm and an epr spectrum was obtained at −196°. In the unreduced sample, a low-field background spectrum was observed; however, reduction in $H_2$ removed this spectrum. It did not reappear upon the subsequent treatment used to form the $O_2^-$ species. Oxygen at pressures ranging from 10 to 400 Torr was distilled onto the sample from the liquid state while the sample was at 23°.

The samples were then either irradiated by means of a uv lamp with a maximum wavelength of 2537 Å or by using $^{60}Co$ $\gamma$ rays. For $\gamma$ irradiation, the samples were sealed in the quartz side arm, and two different dose rates were used, $4.74 \times 10^2$ rads/min and $8.73 \times 10^4$ rads/min.

After irradiation, the samples were tapped into one end of the quartz side arm and the other end was heated with a flame for at least 5 min to remove any color centers that may have formed in the quartz tube. Then, the samples were cooled in liquid nitrogen for at least 15 min before the epr spectrum was obtained. Sometimes the $\gamma$-irradiated samples were transferred under a nitrogen atmosphere into a sample tube fitted with a stopcock so that the gas-phase $O_2$ could be removed by evacuation. Other samples which had never been exposed to oxygen were irradiated under vacuum.

A Varian spectrometer (Model 4502) with a $T.E._{102}$ mode cavity was employed. Low microwave powers were obtained with the Varian matching low power cavity. Spin concentrations and $g$ values of the $O_2^-$ spectra were obtained by using a phosphorus-doped silicon standard. The estimated error in spin concentration is ±50%. The experimental error in $g$ values is ±0.002 along the $z$ direction, ±0.001 along the $x$ direction, and ±0.001 along the $y$ direction.

## Results

*Spectra of the $O_2^-$ Species.* The spectra shown in Figure 1 are typical of the $O_2^-$ spectra which were obtained at −196° when CaY-1 was uv-irradiated and $\gamma$-irradiated ($1.4 \times 10^6$ rads total dosage) in the presence of oxygen. The lines that appeared were characterized by $g$ values which are due to the interaction between the external magnetic field and the electron spin along three principal axes ($x$, $y$, and $z$).

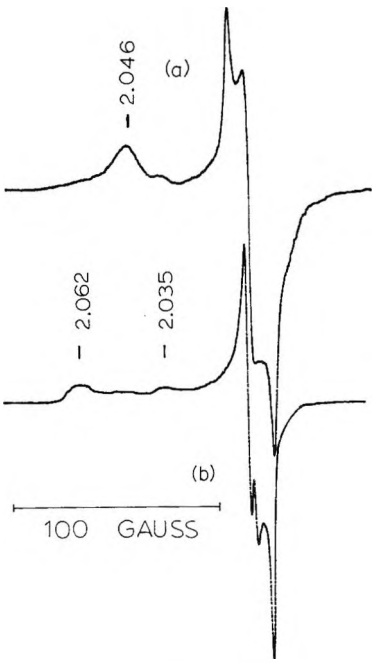


Figure 1. Epr spectrum of $O_2^-$ on CaY-1 zeolite formed by: a, uv irradiation; b, $\gamma$ irradiation.

Here, $z$ is chosen along the internuclear axis while $x$ and $y$ are along the $p\pi$ functions. Several low-field lines which correspond to different $g_{zz}$ values are the result of $O_2^-$ in different crystal field environments. The lines corresponding to different $g_{xx}$ and $g_{yy}$ are overlapped to some extent.

The spectrum of the adsorbed $O_2^-$ on CaY-1 zeolite after $\gamma$ irradiation with a total radiation dosage of $1 \times 10^8$ rads is somewhat different from the one which is $\gamma$-irradiated with less radiation dosage ($1.4 \times 10^6$ rads). The former has a spin concentration of $2 \times 10^{19}$ spins/g of zeolite and has a predominant peak at $g_{zz} = 2.046$ while the latter has a predominant peak at $g_{zz} = 2.063$.

The spectra in Figure 2 show the effect of heating CaY-1 after uv irradiation in the presence of oxygen. After the sample was heated to 400°, the intensity of the spectrum was reduced to $^1/_{20}$ of that which was obtained before heating. The most predominant line having $g_{zz} = 2.046$ was reduced faster than that of $g_{zz} = 2.040$. The latter became the most intense line after heating at 400°. From Figure 2, one can see a $g_{xx}$ line that was reduced concomitantly with the line at $g_{zz} = 2.046$, after heating to 400°. Hence, a set of lines with $g_{zz} = 2.046$, $g_{xx} = 2.011$, and $g_{yy} = 2.0017$ was recognized.

In the presence of 150 Torr of $O_2$ measured at 23° all the low-field lines except the one with a $g_{zz} = 2.049 \pm 0.002$ were broadened. The broadening effect is due to the dipolar interaction between spins. The change in field at electron 1, the $O_2^-$ species, due to the dipole 2, molecular oxygen, is given by $\Delta H = \mu_2/r_{12}^3$ G, where $\mu_2$ is the magnetic moment of dipole 2 and $r_{12}$ is

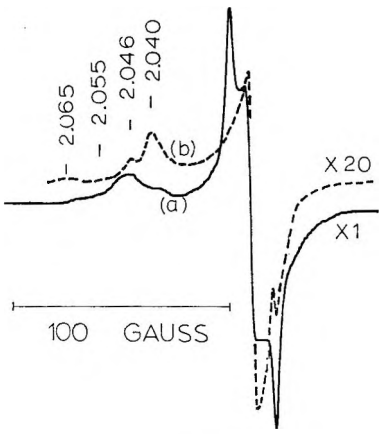


Figure 2. Epr spectrum of $O_2^-$ on CaY-1 zeolite after: a, uv irradiation; b, uv irradiation and heating the sample to 400°.

the crystallographic distance between electron 1 and dipole 2. At the low temperature of the experiment the gas-phase $O_2$ is adsorbed in the supercages of the zeolite. The degree of interaction between molecular $O_2$ and $O_2^-$ in the supercage is greater than that between molecular $O_2$ and $O_2^-$ in the sodalite unit or in the hexagonal prism because the average distance is greater in the latter case. So, we may conclude that the site which has $g_{zz}$ of 2.049 is hidden, either in the sodalite unit or in the hexagonal prism of CaY zeolites. This broadening is reversible since all lines appeared again after the samples were evacuated for 10 min to remove the $O_2$.

When $9.8 \times 10^{18}$ molecules $H_2O$/g of sample were adsorbed on the 92% exchanged CaY-1, the site with $g_{zz} = 2.049$, as well as the remainder of the $O_2^-$ spectrum, was almost completely destroyed. However, after uv irradiation for 24 hr in 200 Torr of oxygen, part of the $O_2^-$ spectrum appeared again, but with an amplitude of $^1/_2$ the original spectrum.

A series of CaY with different percentage exchange (92, 65, and 43%) was investigated after the samples were uv-irradiated in the presence of oxygen. The epr spectra showed that all of the samples possessed the same sites except for a low field line at $g_{zz} = 2.072$ which appeared only on the 65- and 43%-exchanged CaY. This site was also present on NaY that was $\gamma$-irradiated in the presence of oxygen.

The spectra shown in Figure 3, where only low-field lines are shown, were obtained at −196° after the divalent zeolites had been $\gamma$-irradiated with a total radiation dosage of $1.4 \times 10^6$ rads in the presence of oxygen at a pressure of 20 Torr. The spin concentration is estimated to be about $10^{18}$ spins/g of zeolite. The most intense low-field peak of the $O_2^-$ center, which corresponds to an average $g_{zz}$ value of 2.062 ± 0.002, was seen on all the divalent zeolites. The other sites, which have $g_{zz}$ values of 2.049 and 2.035, also appear on MgY, CaY, and SrY zeolites. BaY showed

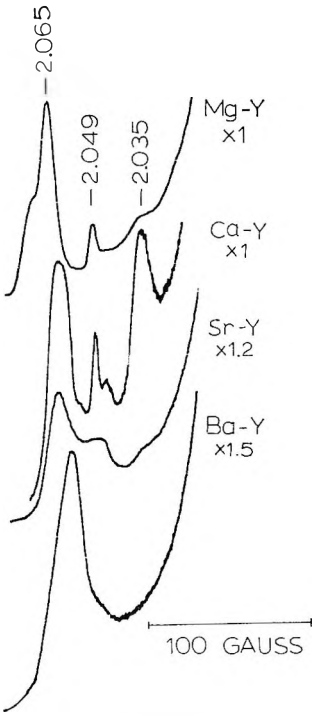


Figure 3. Epr spectra of $O_2^-$ on $\gamma$-irradiated alkaline earth zeolites.

only the single low-field line ($g_{zz} = 2.059 \pm 0.002$) after $\gamma$ irradiation, but a site corresponding to $g_{zz} = 2.040$ began to grow after the $\gamma$-irradiated BaY sample was uv-irradiated. This site at $g_{zz} = 2.040$ also appeared on a $\gamma$-irradiated NaY sample with the same radiation dosage.

The spectrum of $\gamma$-irradiated NaY zeolite in the presence of oxygen showed several low-field lines with $g_{zz}$ values of 2.098, 2.074, 2.040; $g_{xx} = 2.007$; and $g_{yy} = 2.002$. The most intense of these $g_{zz}$ maxima was at 2.040. No line was ever observed at $g_{zz} = 2.113$, though repeated attempts were made to find it.

The spectra shown in Figure 4 reveal the $g_{zz}$ values that were obtained when the divalent zeolites were uv-irradiated in the presence of 400 Torr of oxygen. A predominant low-field peak with a $g_{zz}$ value of 2.049 ± 0.002 appeared on CaY and SrY zeolites. This line appeared on BaY with a peak of the same intensity at a $g_{zz}$ value of 2.058, the predominant line on the $\gamma$-irradiated BaY sample. The spectrum of MgY zeolite showed a low-field line at $g_{zz} = 2.024$ after being irradiated in uv light, but the line decreased in intensity after setting for 24 hr. A very broad line at $g_{zz} = 2.0037$ was observed which was similar to the line which appeared for the decationated zeolite; however, the six-line hyperfine structure could not be resolved.

Table II summarizes the results from both uv-and $\gamma$-irradiated divalent zeolites in the presence of oxygen.

*Spectra of Zeolites Irradiated under Vacuum.* The spectra shown in Figure 5a, b were obtained at −196° and room temperature, respectively, after CaY-1 had

**Table II:** Average[a] $g_{zz}$ Values for Irradiated Divalent Zeolites in the Presence of Oxygen

| | | | | | | |
|---|---|---|---|---|---|---|
| MgY | 2.070[b] | 2.065 (s–$\gamma$)[e] | | 2.049 | 2.035[d] | 2.024 |
| CaY | 2.072[b] | 2.064 (s–$\gamma$) | 2.056[c] | 2.048 (s–uv)[f] | 2.038 | |
| SrY | | 2.064 (s–$\gamma$) | | 2.050 (s–uv) | 2.035 | |
| BaY | | 2.059 (s–$\gamma$) | | 2.050 | 2.040 | |
| Average | 2.070 | 2.062 ± 0.002 | 2.056 | 2.049 ± 0.002 | 2.037 ± 0.002 | 2.024 |
| Δ, eV | 0.40 | 0.46 | 0.52 | 0.60 | 0.82 | 1.28 |

[a] Average $g_{zz}$ value for uv and $\gamma$ irradiation. [b] Only appeared for divalent zeolites exchanged less than 70%. [c] Only appeared on a $\gamma$-irradiated CaY with $1 \times 10^8$ rads radiation dosage or after heating a uv-irradiated CaY zeolite. [d] The broad line with $g_{zz}$ = 2.037 was not included. [e] s–$\gamma$ represents the strongest peak after $\gamma$ irradiation. [f] s–uv represents the strongest peak after uv irradiation.

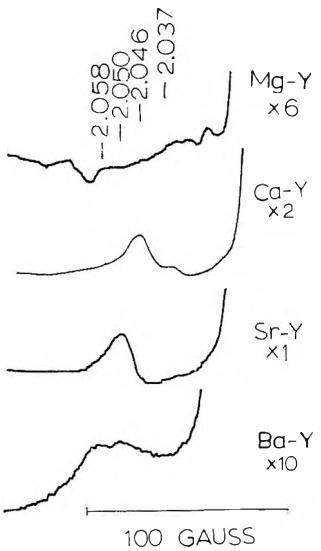


Figure 4. Epr spectra of $O_2^-$ on uv-irradiated alkaline earth zeolites.

been $\gamma$-irradiated at a total radiation dosage of $1 \times 10^8$ rads in the absence of oxygen. Three different types of magnetic centers were formed. The first magnetic center has $g_\perp = 2.046$, $g_{||} = 2.0011$ and a spin concentration of $3 \times 10^{17}$ spins/g of zeolite; the second center has a $g$ value of 1.999 and a spin concentration of $1.5 \times 10^{17}$ spins/g of zeolite; the third center has a $g$ = 2.015 and a spin concentration of $6 \times 10^{17}$ spins/g of zeolite. The first center and the second center have almost the same number of spins but the intensity of the latter appears smaller in Figure 5 because of saturation with microwave power. Spectra were also recorded at much lower microwave powers. Figure 5b shows that the peak of the third center is not observable at room temperature due to a short spin–lattice relaxation time. The spectrum shown in Figure 5c was obtained at −196° with 150 Torr of oxygen on the $\gamma$-irradiated CaY-1 sample. Figure 5d shows an $O_2^-$ center that appeared after evacuation for 10 min to remove all the gas-phase $O_2$. The spectrum of the CaY-1 zeolite irradiated in the absence of oxygen at a lower radiation dosage ($1.4 \times 10^6$ rads) appeared as a very weak peak at $g$ = 2.0017.

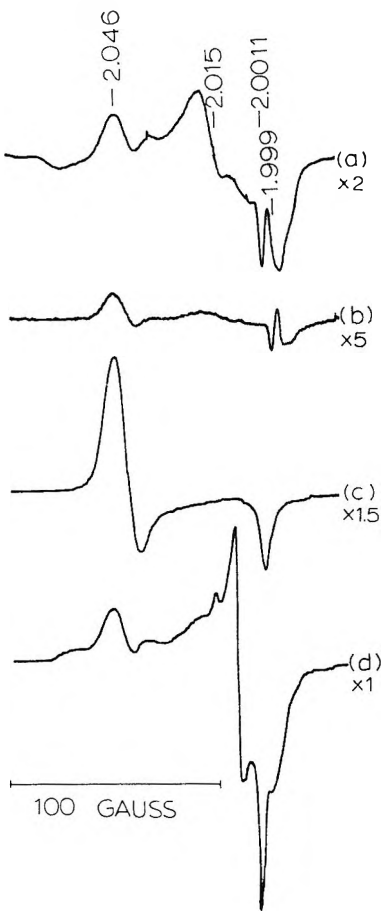


Figure 5. Epr spectrum of CaY-1 zeolite following $\gamma$ irradiation under vacuum: a, epr spectrum at −196°; b, epr spectrum at room temperature; c, epr spectrum at −196° with molecular oxygen; d, epr spectrum at −196° after molecular oxygen removed.

## Discussion

*Spectra of the $O_2^-$ Species.* Kanzig and Cohen[7] have derived the equations which are used to calculate the energy splitting Δ of the $2p\pi_g^*$ levels of the $O_2^-$ ion from $g$ tensors. The calculated values of energy splitting, due to the different crystal field interactions, are shown in Table II. At least two common sites exist

(7) W. Kanzig and M. H. Cohen, *Phys. Rev. Lett.*, **3**, 509 (1959).

in all the divalent zeolites: the site at $g_{zz} = 2.062 \pm 0.002$ which appeared as the most intense peak on all the $\gamma$-irradiated divalent zeolites; and the site at $g_{zz} = 2.049 \pm 0.002$ which appeared as the most intense peak on the uv-irradiated CaY and SrY zeolites. This peak also appeared on $\gamma$-irradiated MgY and uv-irradiated BaY zeolites. From Table II, one cannot see any clear trend of energy splitting, $\Delta$, when one goes from BaY to MgY zeolites. This indicates that there is no significant variation in the crystal field interactions on the divalent zeolites.

A set of $g$ values for $\gamma$-irradiated BaY zeolite was observed at $g_{zz} = 2.058$, $g_{xx} = 2.0087$, and $g_{yy} = 2.0047$ which is similar to the set of Kasai's[2] reported values at $g_{zz} = 2.057$, $g_{xx} = 2.009$, and $g_{yy} = 2.0046$. In addition, he reported a set of $g$ values for a $\gamma$-irradiated NaY zeolite at $g_{zz} = 2.113$, $g_{xx} = 2.0066$, and $g_{yy} = 2.0016$. In the present work values of $g_{xx} = 2.007$ and $g_{yy} = 2.002$ were observed for $\gamma$-irradiated NaY zeolite, but instead of $g_{zz} = 2.113$, several low-field lines at $g_{zz} = 2.098$, 2,074, and 2.040 were observed. The difference may be due to variations in stoichiometry; however, the value of $\Delta$ as determined by Kasai was based upon $g_{zz} = 2.113$. It now appears that this adsorption site is not a general property of NaY zeolites.

The infrared spectra of the decationated zeolites and multivalent ion-exchanged zeolites have been studied recently by two groups of investigators.[8,9] The conclusion of their work is that the electrostatic fields associated with the cation causes dissociation of adsorbed water to produce acidic hydroxyl groups. Ward,[8] who studied the infrared spectra of the divalent zeolites, found that the frequencies of the adsorption bands due to the $M(OH)^+$ groups increase with the decrease of cation radii. This result is expected from the calculations of Pickert, *et al.*;[1] *i.e.*, the smaller the cation, the stronger the electrostatic field, and the higher the frequency. Upon mild dehydration, it is possible that the alkaline earth oxide MO [10] or $M^+$–O–$M^+$ [9] is formed, and most of the $O_2^-$ species are held at such sites. At the same time, a few $M^{2+}$ species probably exist due to the dehydroxylation of $M(OH)^+$.

It has been observed that the adsorption bands due to the silanol groups are at frequencies similar to those observed in the decationated zeolites and, hence, probably of the same type.[8,11] Ward[10] as well as Hall and coworkers[11] have shown that these hydroxyl groups are able to protonate pyridine just as the hydroxyl of the decationated zeolites. The concentration of these hydroxyl groups is much less than that in the decationated (HY) zeolites.

Similarly, the concentration of decationated type sites on CaY zeolites is only about $^1/_{50}$ the concentration of HY zeolites as determined from the epr spectra of adsorbed nitric oxide.[12,13] If one takes $^1/_{50}$ the amplitude of $g_{zz}$ for $O_2^-$ on the HY zeolite and compares it with the amplitude in the spectra of Figure 1, it is clear that the HY-type spectrum would be relatively small and difficult to detect in the presence of the other spectrum. Perhaps the rather broad line at $g_{zz} = 2.038$ which appears in the spectrum of uv-irradiated MgY zeolite is the HY-type spectrum; however, the results are not conclusive since the $^{27}Al$ hyperfine lines could not be resolved.

The $O_2^-$ species is formed when the lattice electron is excited by irradiation and then combines with the $O_2$ molecule. The ultimate concentration of the $O_2^-$ ion depends upon the ionization potential of the electron donor, the energy of the radiation, the dose rate, the total dosage, and the cross section of $O_2$ for the capture of an electron. Since Mg has the greatest ionization potential among the group IIa cations, MgY zeolite needs higher radiation energy to excite the lattice electron. This apparently is the reason why the characteristic spectrum following ultraviolet irradiation was not observed for MgY zeolites.

*Spectra of Zeolites Irradiated under Vacuum.* The epr spectrum of $\gamma$-irradiated CaY-1 without $O_2$ reveals the presence of certain defect sites on the dehydrated zeolite. By varying the temperature and microwave power and from results of the oxygen broadening experiment it is clear that the spectrum shown in Figure 5a is actually due to three overlapping spectra. One of these is a narrow, symmetric line which is easily saturated with microwave power. It has a $g$ value of 1.999. These characteristics are typical of F-type centers, which result when an electron is trapped at an anion vacancy. This F-type center in the zeolite shows no hyperfine structure and is irreversibly destroyed by oxygen. The electron apparently leaves the trap and forms the $O_2^-$ species.

A second center was less easily saturated with microwave power, and the spectrum has a very asymmetric shape with $g_\perp = 2.046$ and $g_{||} = 2.0011$. These characteristics are typical of V-type centers, which result when a hole is trapped at a cation vacancy. This V-type center shows no hyperfine structure and is not broadened by oxygen.

The spectrum of the third center with an apparent $g$ value of 2.015 was quite broad, and the center was very difficult to saturate with microwave power because of a short relaxation time. These results suggest that this is also a V-type center. The broadened spectrum may be the result of small dipole interactions or unresolved hyperfine interactions between the unpaired electron and the nucleus of either $^{27}Al$ or $^{23}Na$. Upon addition

(8) J. W. Ward, *J. Phys. Chem.*, **72**, 4211 (1968).

(9) J. B. Uytterhoeven, R. Schoonheydt, B. V. Liengme, and W. K. Hall, *J. Catal.*, **13**, 425 (1969).

(10) J. W. Ward, *ibid.*, **10**, 34 (1968).

(11) L. G. Christner, B. V. Liengme, and W. K. Hall, *Trans. Faraday Soc.*, **64**, 1679 (1968).

(12) J. H. Lunsford, *J. Phys. Chem.*, **72**, 4163 (1968).

(13) J. H. Lunsford, *ibid.*, **74**, 1518 (1970).

of 150 Torr of $O_2$, the spectrum became still broader because of dipole interactions with molecular oxygen. This means that the center is on the surface of the supercage.

While it is not possible to make a positive identification of the irradiation-induced centers from these results, one can speculate as to the types of defects that might be involved. The dehydration process will ultimately remove hydroxyl groups from the $M(OH)^+$ and -Si-OH species. If the dehydration reaction is according to

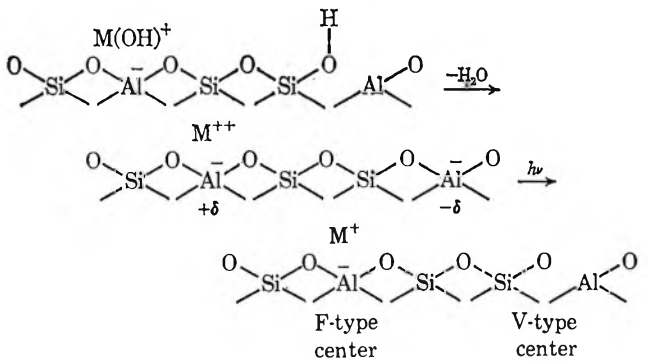


then a positive region will be formed around the cation and a negative region around the cation vacancy at the aluminum.

During the irradiation process, the negative region will lose an electron forming a trapped hole or V-type center such as that with $g = 2.015$ and the positive region will accept, or trap, an electron to become an F-type center. The V-type center may have a certain amount of interaction with the adjacent aluminum ion which could lead to the broad spectrum. On the other hand, the electron will be localized on the cation, which in the three-dimensional zeolite may not be as close to the aluminum as shown in the above figure. Both of these centers would be located on the surface of the supercage and subject to strong magnetic interactions with molecular oxygen.

Stamires and Turkevich[14] observed the spectrum of a similar V-type center on $\gamma$-irradiated NaY zeolites. The $g$ value, however, was 2.020 instead of 2.015. They attributed the center to a hole located at the oxygen atom in the lattice site between two ($SiO_{4/2}$) units. These authors also observed a six-line spectrum in decationated zeolites which they attributed to an electron trapped at an $AlO_{3/2}$ defect, where the Al is part of the zeolite lattice. They reported, however, that there was no interaction between this center and molecular oxygen. This observation is indeed difficult to reconcile with their proposed center, since all of the lattice aluminum ions are on the surface of the supercage and would be accessible to molecular oxygen.

Infrared and X-ray evidence has indicated that the predominant dehydroxylation process may lead to an $M^+$–O–$M^+$ configuration where an oxide in the sodalite unit bridges a Site I′ cation with a Site II′ cation. One can then imagine a cation defect such as $Ca^+$–O– which would trap a hole to form the V-type center with $g_\perp = 2.046$ and $g_{||} = 2.0011$. This V-type center is similar to the $V_1$ center formed in MgO with $g_\perp = 2.0385$ and $g_{||} = 2.0032$.[15] Since the center is not broadened with the addition of oxygen, the vacancy is apparently inside the sodalite cage at the Site I′ position.

## Conclusions

Results of this investigation indicate that $O_2^-$ is adsorbed at three or more different sites on each of the alkaline earth Y-type zeolites; all of these zeolites appear to have two sites in common. There does not appear to be any significant trend in crystal field interaction as one goes up the series from BaY to MgY.

The CaY zeolite contains defects that are able to trap electrons or holes upon $\gamma$ irradiation. One F-type center and one V-type center are located at the surface of the supercage, whereas another V-type center is located inside the sodalite unit or the hexagonal prism.

*Acknowledgment.* The authors wish to acknowledge the contribution of Dr. J. D. Sherman in obtaining an analysis of the zeolite and Dr. J. W. Sutherland for the extensive $\gamma$ irradiation. This work was supported by National Science Foundation Grant GP-8319.

(14) D. N. Stamires and J. Turkevich, *J. Amer. Chem. Soc.*, **86**, 757 (1964).

(15) J. H. Lunsford, *J. Phys. Chem.*, **68**, 2312 (1964).

# An Electron Paramagnetic Resonance Study of Y-Type Zeolites.

# II. Nitric Oxide on Alkaline Earth Zeolites

by Jack H. Lunsford

*Department of Chemistry, Texas A&M University, College Station, Texas 77843* *(Received August 20, 1969)*

The epr spectrum of the adsorbed nitric oxide molecule was used to study the alkaline earth Y-type zeolites. Results show that two types of sites existed on MgY, CaY, and SrY zeolites that had been degassed at 500°, but only one type of site was detected for the BaY zeolite. The spectrum on BaY was characterized by $g_\perp = 1.994$, $g_\parallel = 1.89$, and $a_\perp = 30$ G for the N hyperfine splitting. A like spectrum was observed for the other zeolites; however, it was partially obscured by an overlapping spectrum, which showed no distinct hyperfine structure and a value of $g_\parallel = 1.95$. This spectrum was similar to that previously observed on dehydroxylated HY zeolites. The spectrum of NO on CaY was observed as a function of dehydration temperature and extent of cation exchange. The HY-type site began to develop after dehydration at 300° and after 64% of the $Na^+$ ions had been exchanged.

## Introduction

Since the early work of the Linde[1,2] group on the alkaline earth Y-type zeolites, there has been considerable interest in explaining the high activity and the systematic change in the catalytic behavior of these materials. It is now known that for a variety of reactions the activity increases as one moves up the series from Ba to Mg. At least three basic theories have been used to explain the experimental results. It was first proposed that strong electrostatic fields, emanating from the cations, polarize the reactants to the extent that they become pseudocarbonium ions.[1,2] Next, it was suggested that the cations influence structural hydroxyl groups, thereby creating more acidic protons.[3,4] Finally, it has been postulated that the divalent cations are able to produce acidic sites through the hydrolysis of water which is held at the cation.[5,6] The proton liberated in this process becomes attached to a lattice oxide ion where it forms the following type site

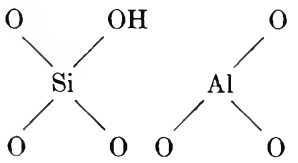


which is identical with that proposed for decationated zeolites.[7] The ability to form these sites in cationic zeolites depends upon the hydrolyzing power of the cation.

In an earlier paper from this laboratory on decationated (HY) zeolites, it was suggested that hydroxyl defect sites[8]

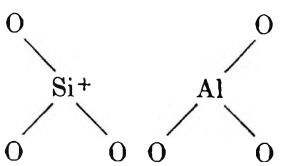


may form strong acids through their influence on adjacent SiOH groups.[9] A similar mechanism may be operative for the cationic form, if indeed the same hydroxyl defect sites exist.

Infrared data have shown that structural hydroxyl groups do occur on certain cationic Y zeolites, and there is growing infrared and X-ray evidence that lattice oxide ions are involved in the formation of water during the dehydroxylation process.[5,6,10,11] In the dehydroxylation process; however, there are a number of alternate mechanisms that may occur, and it is very likely that several different reactions are proceeding to some extent.

The present study has been carried out to determine the types of sites that exist on zeolites with divalent cations and to establish from epr data whether any Y–[OH] sites are formed upon dehydration. The electron paramagnetic resonance (epr) spectrum of the nitric oxide molecule was used to determine the crystal

(1) P. E. Pickert, J. A. Rabo, J. A. Dempsey, and V. Schomaker, *Proc. Int. Congr. Catal., 3rd, Amsterdam, 1964*, 714 (1965).

(2) J. A. Rabo, C. L. Angell, P. H. Kasai, and V. Schomaker, *Discussions Faraday Soc.*, **41**, 328 (1966).

(3) A. E. Hirschler, *J. Catal.*, **2**, 428 (1963).

(4) J. T. Richardson, *ibid.*, **9**, 182 (1967).

(5) J. W. Ward, *J. Phys. Chem.*, **72**, 4211 (1968); *J. Catal.*, **10**, 34 (1968).

(6) L. G. Christner, B. V. Liengme, and W. K. Hall, *Trans. Faraday Soc.*, **64**, 1679 (1968).

(7) J. B. Uytterhoeven, L. G. Christner, and W. K. Hall, *J. Phys. Chem.*, **69**, 2117 (1965).

(8) For simplicity in nomenclature, the symbol [OH] will be used to denote a hydroxyl vacancy. If the vacancy is part of the Y zeolite lattice, the symbol Y–[OH] will be used; whereas, if the vacancy is on the cation M, the symbol M–[OH] will be used. A similar symbolism (X–[OH], $Al_2O_3$–[OH], etc.) could be extended to other systems.

(9) J. H. Lunsford, *J. Phys. Chem.*, **72**, 4163 (1968).

(10) J. B. Uytterhoeven, R. Schoonheydt, B. V. Liengme, and W. K. Hall, *J. Catal.*, **13**, 425 (1969).

(11) D. H. Olson, *J. Phys. Chem.*, **72**, 1400 (1968).

and magnetic interactions at the surface. A particularly distinguishing feature in this spectrum is the line shape that results from the hyperfine interaction of NO with an $^{27}Al$ nucleus. This interaction is available at the Y–[OH] site, but at all other adsorption sites the small aluminum ion is apparently hidden by large oxide ions.

## Experimental Section

The zeolites used have been described in the preceding paper.[12] They were degassed by heating the samples under vacuum for 1 hr at 100° intervals, usually up to 500°. Following such pretreatment the zeolites were either (a) used in this form, (b) reduced for 2 hr in $H_2$ at 500°, or (c) oxidized in $O_2$ for 2 hr at 500° and then reduced for 2 hr in $H_2$ at 500°. The samples were evacuated at the high temperature for 30 min after exposure to $H_2$ or $O_2$. After each pretreatment suitable epr spectra were obtained.

Purified nitric oxide was admitted onto the samples at room temperature and usually at a pressure of 10 Torr. The samples were cooled by immersing the quartz sample tube slowly into liquid nitrogen. An alternate procedure which gave more uniform adsorption involved first cooling the sample tube in pentane at its freezing point (−130°), and then rapidly transferring the tube to liquid nitrogen. All spectra were recorded at −196°.

Determination of the $g$ values and spin concentrations were essentially the same as described in earlier work.[9,12] Because of the relatively weak amplitude of the spectra, the error in the absolute concentration is estimated to be ±50%.

## Results

The spectra shown in Figure 1 were observed when NO was adsorbed on the respective Y-type zeolite that had been degassed at 500°, treated with oxygen, and then reduced with hydrogen. Each of the spectra show the $^{14}N$ hyperfine splitting from which $a_\perp$ was determined to be 30 ± 1 $G$. It is clear, however, that as one moves up the series from BaY to MgY, the three line hyperfine structure shows less resolution. This loss in resolution may be ascribed to the presence of a second broad peak, such as that observed for NO on dehydroxylated HY zeolites[9] and silica–alumina.[13] In the latter cases the broad line was due to aluminum hyperfine interaction with the NO molecule. In addition to the loss in resolution, one may observe from Figure 1 that a high-field minimum is present for SrY, CaY-1, and MgY zeolites at $g$ = 1.95, which is the same as the value of $g_{||}$ for NO on HY and silica–alumina. Only a very weak minimum at $g$ = 1.89 was observed for BaY.

Still a third overlapping spectrum was observed at $g$ = 2.008 for SrY. This narrow line, like the major NO spectrum, can be removed by brief evacuation of the sample at room temperature. It is much less prominent at a lower surface concentration of nitric oxide.

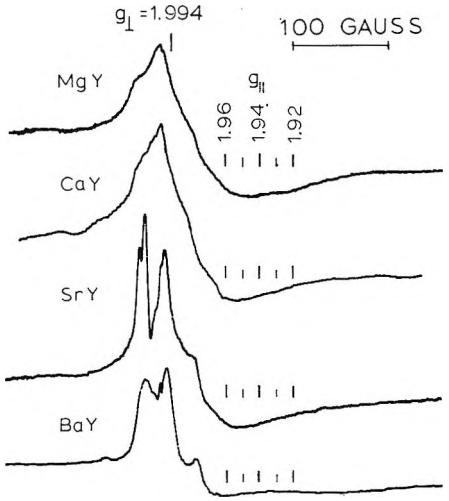


Figure 1. Epr spectra of NO adsorbed on alkaline earth Y-type zeolites.

The spin concentration, from the spectra of Figure 1, was about 5 × $10^{17}$ spins/g. This concentration, which constitutes only a small fraction of the total NO concentration on the zeolite, was not increased upon increasing the pressure above 10 Torr.

A comparison in Figure 2 of the spectra for $^{15}NO$ and $^{14}NO$ on CaY-1 shows that the nitrogen hyperfine splitting changes as expected for the two isotopes. The $^{14}N$ isotope has a spin of 1, whereas the $^{15}N$ isotope has a spin of $^1/_2$. For $^{15}NO$ the presence of the broad line can be more clearly seen at a low magnetic field where there is less interference from a nitrogen hyperfine line. The steep slope of the hyperfine line is also convincing evidence that the loss in resolution is not due to broadening of the nitrogen hyperfine lines, but rather to an interfering spectrum.

The similarity in the spectra of NO on CaY and HY zeolites may be seen by comparing the curves in Figures 2b and 2c. The spectrum of NO on silica–alumina shows somewhat less structure than that in Figure 2c. Though not shown here, the spectrum of $^{15}NO$ on HY zeolites is likewise compatible with the spectrum of Figure 2a.[9]

It was of interest to study changes in the spectra as the dehydration temperature was increased. In this process the sample was heated under vacuum but no $O_2$ or $H_2$ was employed. After the dehydration of CaY-1 at 100° and addition of 10 Torr NO the spectrum shown in Figure 3a was observed. Under these conditions only the nitrogen hyperfine lines along with a weak minimum at $g$ = 1.92 were detected. It is interesting to note that a shoulder also appeared at this same $g$

(12) K. M. Wang and J. H. Lunsford, *J. Phys. Chem.*, **74**, 1512 (1970).

(13) J. H. Lunsford, *J. Catal.*, **14**, 379 (1969).

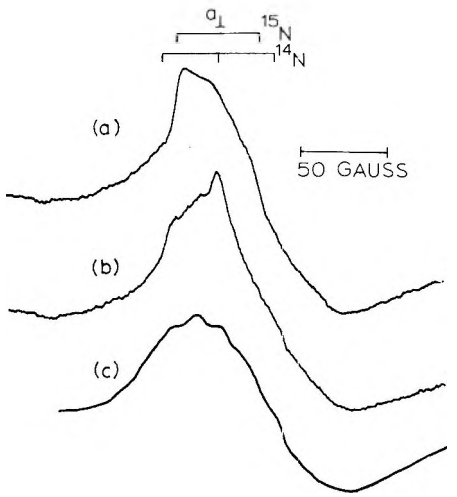


Figure 2. Spectra of: a, $^{15}NO$ adsorbed on CaY-1; b, $^{14}NO$ adsorbed on CaY-1; c, $^{14}NO$ adsorbed on a HY zeolite.

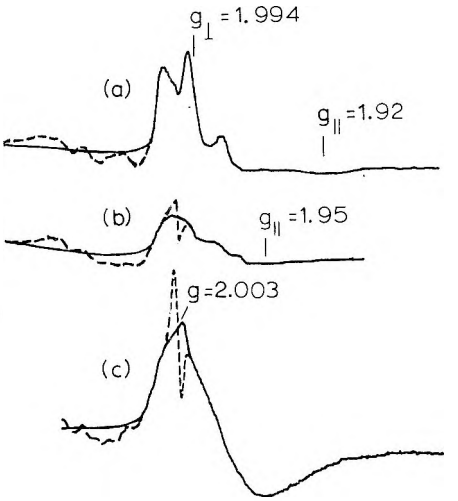


Figure 3. Spectra of NO on CaY-1 following dehydration at: a, 100°; b, 300°; c, 500°.

value in the spectrum of MgY as shown in Figure 1. The dashed line in Figure 3 denotes a low-field impurity signal which could be removed by reduction with $H_2$ at elevated temperatures.

Following a maximum dehydration temperature of 300°, the weak and poorly resolved spectrum in Figure 3b was detected. Here it appears that the broad spectrum was beginning to develop. The presence of the high-field minimum at $g = 1.95$ was also observed. The sharp line at $g = 2.003$ is an additional part of the background spectrum. It is probably the result of carbonaceous material on the zeolite since it may be removed by the oxygen treatment. In addition, a very weak line at $g = 1.96$, which is sometimes observed, is part of the $NO_2$ spectrum.[14]

When the same sample was dehydrated at a maximum temperature of 500°, the spectrum shown in Figure 3c was recorded. One should note that the amplitude was about twice that observed for the spectrum in Figure 3b. Apart from the background, the spectrum in Figure 3c is the same as was shown for NO on CaY-1 in Figures 1b and 2c. Dehydration at higher temperatures did not significantly alter the shape or the amplitude of the spectrum.

In an attempt to explore the reversibility of this dehydration procedure $2 \times 10^{20}$ molecules of water per gram of zeolite were added back to the previous sample at 23°. This sample had been degassed to remove residual oxides of nitrogen. After addition of water, the sample was heated under vacuum for 1 hr at 100°, and the NO spectrum was recorded under the usual conditions. The spectrum was quite similar to that shown in Figure 3b and did not revert back to the spectrum of Figure 3a. In a separate experiment the sample was degassed at 23° after rehydration and the subsequent NO spectrum was similar to that in Figure 3a. Following dehydration at 500° the spectrum was essentially the same as that shown in Figure 3c.

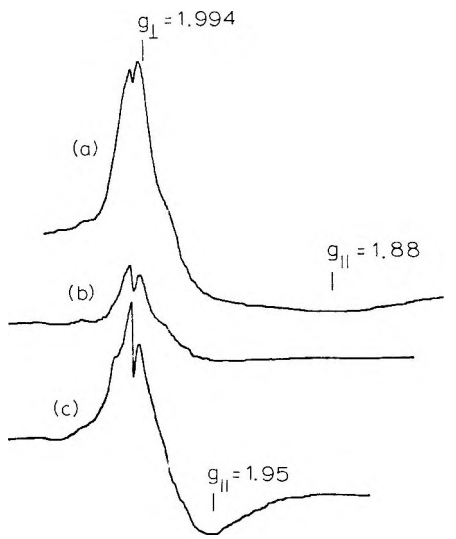


Figure 4. Spectra of NO on: a, CaY-3 (43% exchanged); b, CaY-2 (65%) exchanged); c, CaY-1 (92% exchanged).

Since the catalytic activity and adsorption properties of the divalent zeolites are dependent upon the degree of exchange,[1,15] a study was made to determine the effect of this parameter upon the NO spectrum. Samples of CaY-1, CaY-2, and CaY-3 were dehydrated at a maximum temperature of 500° and reduced in $H_2$. The spectrum of NO on CaY-3 (43% exchanged) is shown in Figure 4a. This curve has much in common with the spectrum of NO on NaY zeolite.[9] The poorly resolved $^{14}N$ hyperfine structure is thought in this case to result from a weak magnetic interaction of the NO molecule with a $^{23}Na$ nucleus. A value of $g_\parallel = 1.88 \pm 0.01$ may be compared with a value of $g_\parallel = 1.86 \pm 0.01$ for NO on NaY. The amplitude of the curve in

(14) J. H. Lunsford, *J. Colloid Interfac. Sci.*, **26**, 355 (1968).
(15) S. E. Tung and E. McInninch, *J. Catal.*, **10**, 166 (1968).

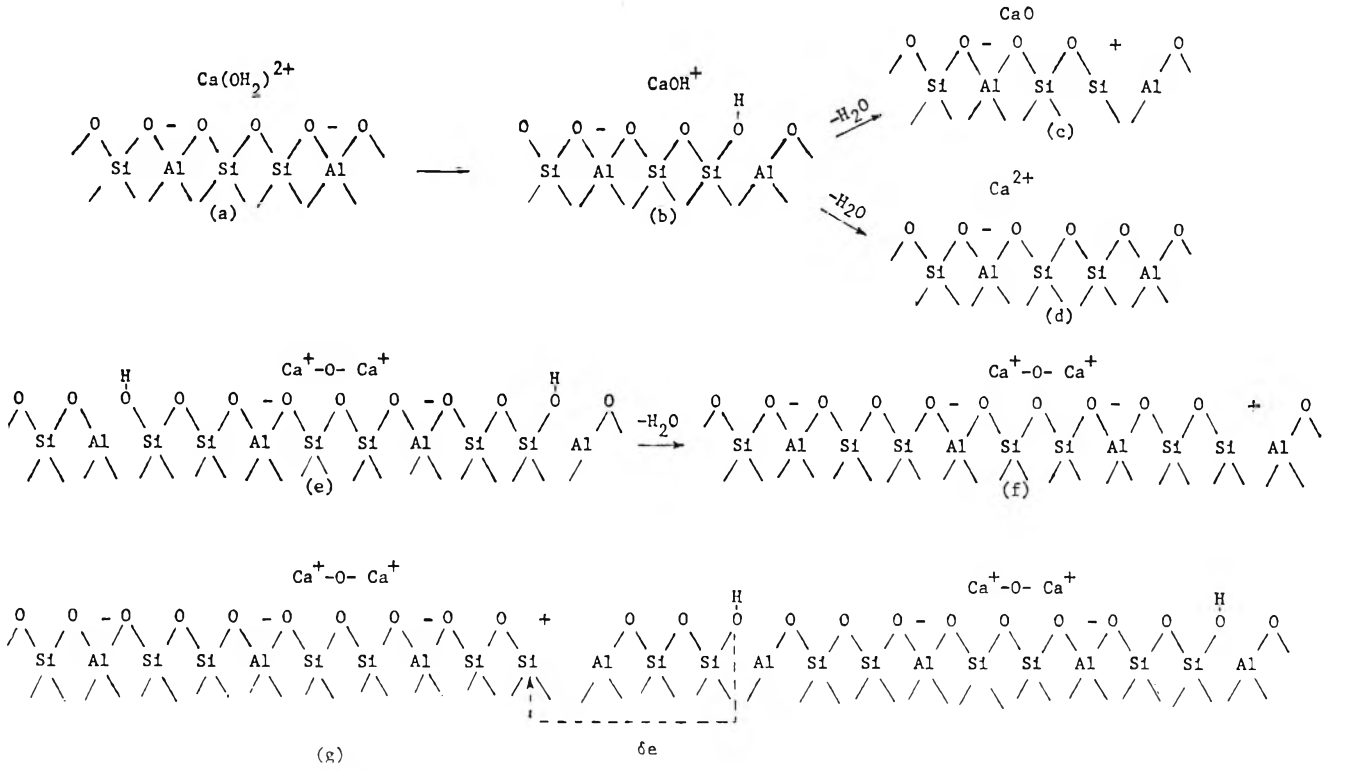


Figure 5. Proposed mechanisms for dehydroxylation of a CaY zeolite.

Figure 4a was less than the amplitude of the NO spectrum on pure NaY. For CaY-2 (65% exchanged) the intensity of the spectrum decreased by almost a factor of 3, and the apparent value of $g_{||}$ shifted to 1.95 as shown in Figure 4b. This suggests that some Y-[OH] sites were formed. The typical spectrum of CaY-1 (92% exchanged), shown in Figure 4c, reveals a large increase in the number of Y–[OH] sites.

## Discussion

The role of the cation in hydrolyzing water to form the lattice hydroxyl is clear from infrared data.[5,6] The OH stretching band at a nominal 3640 $cm^{-1}$ has been generally assigned to this particular group. Recent work by Ward[5] has shown that this band was quite prominent in the ir spectra of MgY, CaY, and SrY, but not in BaY zeolites. The hydrolysis reaction and subsequent dehydration as proposed by Ward are shown in Figures 5a, 5b, and 5c, using CaY as an example. According to this mechanism, dehydroxylation results in the Y–[OH] defect. Ward[5] concluded that the electrostatic field associated with the barium cation was insufficient to bring about the dissociation of the adsorbed water to any appreciable extent. The BaY situation is somewhat ambiguous, however, since Hall and coworkers[6,10] observed a weak band at 3650 $cm^{-1}$ following dehydration at 250°.

All infrared work on the cationic zeolites shows that the 3640-$cm^{-1}$ band, when observed, rapidly decreases in amplitude upon heating the sample above 400°. This means that lattice protons are involved in the formation of water during dehydration, but it does not necessarily mean that lattice oxide ions are involved. An example of the latter case is shown in Figure 5d. Recently, Uytterhoeven, Schoonheydt, Liengme, and Hall[10] pointed out that the infrared band associated with $M(OH)^+$ ions is more sensitive to dehydroxylation than the –Si–OH groups. They suggested that the early stages of dehydroxylation lead to a product similar to that shown in Figure 5e. If this is true, during the latter stages of dehydroxylation (Figure 5f) lattice oxide ions would be removed and the Y–[OH] defect would be formed.

One may reason from the epr results that upon dehydration of MgY, CaY, and SrY zeolites a lattice oxygen is removed as molecular water is formed. This oxide vacancy uncovers a trigonal aluminum which is capable of adsorbing nitric oxide. The magnetic interaction between the aluminum and a nitric oxide molecule leads to the broad line which is depicted in Figure 2. The spectrum of NO on BaY indicates that few, if any, Y–[OH] defects were formed upon dehydration. This result would be expected from the ir data of Ward since the –Si–OH group is a precursor of the Y–[OH] defect. It is clear from the data presented here and in a previous paper[11] that more than one type of adsorption site is involved, but only one type of adsorption site is characterized by the aluminum hyperfine interaction.

The one-dimensional zeolite in Figure 5g illustrates

the type of interaction which may be operating in these zeolites to produce a very acidic proton. The electron induction may be even stronger here than in partially dehydroxylated HY since a cation is compensating for part of the negative charge which is formally placed on the aluminum. It should be emphasized that, acccording to this model, the active center for Brönsted acidity includes both the Y–[OH] defect and an adjacent hydroxyl group. Inclusion of the hydroxyl group as part of the active site is consistent with the loss in catalytic activity for certain reactions upon excessive dehydration.[16] It was interesting to note that the Y–[OH] defect could be reproduced following addition of water to a dehydrated sample. A similar reversible behavior has been noted in the infrared and catalytic data for cationic zeolites.[5,17,18]

Likewise, there is favorable agreement between the formation of the Y–[OH] center and the onset of catalytic activity,[1,15] beginning when roughly 60% of the sodium ions are exchanged and increasing until more than 90% of the sodium ions are exchanged with calcium ions. The calcium ions in the dehydrated zeolite strongly prefer site I and will tend to fill all of those sites (57% exchanged) before the site II positions begin to fill. Apparently the Y–[OH] defect is promoted by the site II divalent cations or by a cooperative effect of the site II′ and site I′ cations such as that shown in Figure 5f. The 3640-$cm^{-1}$ band has been detected in divalent Y zeolites for all exchange levels tested, including 42 and 64% exchanged CaY. The observation of this band at low $Ca^{2+}$ levels is difficult to reconcile with the epr data unless one assumes that at these low exchange levels dehydration does not involve removal of oxide ions from the lattice.

If one assumes that the spin concentration is linearly proportional to the site concentration, then it follows that the number of Y–[OH] sites on the divalent zeolites is about $^1/_{50}$ the number found for dehydroxylated HY.[9] This is in agreement with the reported concentration of hydroxyl groups on these materials.[5] The spin concentration is several orders of magnitude less than the active site concentration as determined by catalytic poisoning experiments,[19] but it is also several orders of magnitude greater than the site concentration as calculated from transition state theory.[4]

While a study of the reaction of NO to form $N_2O$ and $NO_2$ has not been the purpose of this paper, it is perhaps worthwhile to state that this reaction has been observed to occur on the zeolites reported here. Addison and Barrer[20] were the first to report that the reaction occurred on sodium and calcium faujasites as well as on other zeolites. Infrared evidence indicated the formation of $N_2O$, $NO_2$, and $NO_3^-$ groups on cationic X zeolites when NO was adsorbed.[21] There may, in fact, be competition for certain sites between NO and $N_2O$ or $NO_2$. This competition for sites by oxides of nitrogen could explain why the NO spin concentration was much less than the maximum $O_2^-$ spin concentration on the same divalent zeolites. It should be recalled that the $O_2^-$ species was largely on sites other than the Y–[OH] defect.[11] These sites (sites II cations, for example) may stabilize the $O_2^-$ ion but cause the NO molecule to react. On the HY zeolites the NO spin concentration[9] exceeds the $O_2^-$ spin concentration, and both species are primarily at the Y–[OH] defect.[22] This may mean that the Y–[OH] site adsorbs NO in the molecular form and does not promote further reaction.

## Conclusions

The work presented here strongly suggests that lattice oxide ions are removed upon extensive dehydration of MgY, CaY, and SrY zeolites. The resulting defect sites, which adsorb NO, are quite similar to those found on dehydroxylated HY zeolites. Other investigators have reached a similar conclusion based mainly upon infrared data.

A second type of adsorption site which does not involve aluminum ions is present on MgY, CaY, SrY, and BaY zeolites.

*Acknowledgment.* The author wishes to acknowledge the support of this work by The Robert A. Welch Foundation under Grant No. A-257.

(16) P. D. Hopkins, *J. Catal.*, 12, 325 (1968).

(17) J. W. Ward, *J. Phys. Chem.*, 72, 2689 (1968).

(18) C. S. Plank, *Proc. Int. Congr. Catal., 3rd, Amsterdam, 1964*, 727 (1965).

(19) J. Turkevich, F. Nozaki, and D. Stamires, *ibid.*, 516 (1965).

(20) W. E. Addison and R. M. Barrer, *J. Chem. Soc.*, 757 (1955).

(21) A. V. Alekseyev, V. N. Filimonov, and A. N. Terenin, *Dokl. Akad. Nauk SSSR*, 147, 1392 (1962).

(22) K. M. Wang and J. H. Lunsford, *J. Phys. Chem.*, 73, 2069 (1969).

# A Study of the Behavior of Polyoxyethylene at the Air–Water Interface by Wave Damping and Other Methods[1]

by R. L. Shuler and W. A. Zisman

*Laboratory for Chemical Physics, Naval Research Laboratory, Washington, D. C. 20390* *(Received November 6, 1969)*

The behavior of monomolecular films of polyoxyethylene with an average molecular weight of 90,000 has been investigated at the air–water interface at 20° by measuring the wave-damping coefficient ($k$), the film pressure ($F$), and the surface potential ($\Delta V$), as a function of monomer area ($A$). There was excellent agreement in the $F$ *vs.* $A$ graphs of films spread with various spreading solvents, indicating that the films were spread as stable monolayers. The $F$ *vs.* $A$ curves of polymer films compressed not more than 20 Å/monomer were both reversible and reproducible, but when a film was compressed below that value of $A$, a decided difference was found between the $F$ *vs.* $A$. curves of compression and expansion. However, the $F$ *vs.* $A$ curve obtained when a film compressed more than 20 Å²/monomer was allowed to expand was once more reversible and reproducible upon subsequent compression and expansion. The experimental results on the behavior of polyoxyethylene films upon compression at the air–water interface has been interpreted as follows: (a) at low compressions the polymer contains tightly bound water molecules and occupies a monomer area of 28 Å²; (b) at higher compressions the bound water is displaced from the film leaving the polymer with a monomer area of 20 Å²—in this state the polymer is in conformation (I); (c)there is a transformation of conformation (I) into a new conformation (II) when the molecules are compressed to an area of 16 Å²/monomer; and finally (d) the film starts to collapse when the molecules are compressed below 16 Å²/monomer. The above interpretation has been supported by the construction of two plausible molecular models representing conformations (I) and (II) with monomer areas corresponding to those deduced from the experiments. The oxygen atoms in both of these models were on one side of the molecule with the two methylene groups on the other giving the molecule both a hydrophilic and hydrophobic surface. Compressing conformation (I) into the more compact conformation (II) greatly increased the rigidity of the chain, and the greater steric hindrance in conformation (II) is thought to be the main cause of the irreversibility of the change from conformation (I) to (II). In addition, the atoms were packed closer together in conformation (II), and the resulting stronger intramolecular cohesive forces helped to stabilize that configuration. The sensitivity of the graphs of $k$ *vs.* $A$ to molecular packing, association, or conformational changes was remarkable and gave us a powerful surface chemical tool for this investigation.

## Introduction

In a very recent investigation, Garrett and Zisman,[2] working with adsorbed insoluble monolayers of the polydimethylsiloxanes and the polydimethylphenylsiloxanes at the air–water interface, demonstrated the profound effect the nature of an adsorbed film can have on its wave-damping properties. They found that if the wave-damping coefficient ($k$) was plotted against the area per molecule ($A$), as many as 3 or 4 maxima and 3 minima appeared in the curves, and they were able to relate these to changes in the conformation of the adsorbed molecules which had been deduced previously from film pressure *vs.* area ($F$ *vs.* $A$) relations.[3] Especially interesting here was their observation that the wave-damping method was a far more sensitive tool for detecting these changes than was the $F$ *vs.* $A$ graph obtained with the Langmuir–Adam film balance.

In view of their findings, it was decided to investigate by the wave-damping method spread films of another relatively simple homopolymer, polyoxyethylene, whose surface spreading behavior and adsorbed state at the air–water interface needed investigation and elucidation. The polyoxyethylenes are linear open-chain polymers like the trimethylsylyl end-blocked polydimethylsiloxanes, but one would expect less freedom of motion in the former type of molecular chain because of the replacement of the larger silicon atoms in the polydimethylsiloxanes by the smaller carbon atoms in the polyoxyethylenes. It was also of interest to determine the effect such decreased molecular flexibility would have on the wave damping and other surface properties of the polymer.

Polyoxyethylene, with its hydrophobic–hydrophilic character, would seem to be a suitable material for surface spreading studies at the air–water interface, but surprisingly little work has been done on the subject. In almost all of the reported investigations, derivatives of polyoxyethylene, such as ethylene oxide adducts of fatty alcohols, have been used rather than polyoxyethylene itself.[4–7] Based on past investigations, there

(1) From a dissertation submitted by R. L. Shuler to the Graduate School of Georgetown University in partial fulfillment of the requirements for the degree of Doctor of Philosophy, June 1969.

(2) W. D. Garrett and W. A. Zisman, "Damping of Capillary Waves by Monomolecular Films of Polyorganosiloxanes," submitted for publication in *J. Phys. Chem.*

(3) H. W. Fox, P. W. Taylor, and W. A. Zisman, *Ind. Eng. Chem.*, **39**, 1401 (1947).

(4) A. L. Meader and D. W. Criddle, *J. Colloid Sci.*, **8**, 170 (1953).

was ample evidence that the films of such polymers spread at the air–water interface as monolayers with the hydrophilic ethylene oxide monomeric chain lying flat in the interface with every ether oxygen atom in the water whereas the hydrophobic group was oriented away from the surface and into the atmosphere. However, in films adsorbed from solution in water, Schick's data[6] indicated that the ethylene oxide chains, instead of lying flat in the water surface as was true of insoluble films, formed coils in the aqueous phase with the hydrophobic part of each monomer above the interface as in spread films of the adducts.

Some investigations have also been made using unsubstituted polyoxyethylenes,[8–10] but these have been devoted to the study of the properties of films adsorbed from solution in water instead of insoluble films spread upon the surface of the water which is the subject of this investigation. Although there has not been complete agreement reached by the various authors concerning the surface structure of the adsorbed polymer molecules, the weight of the evidence is that at least some portion of the polyoxyethylene chain is oriented away from the interface, possibly directed into the aqueous solution.

This investigation was undertaken to learn more about the surface behavior of polyoxyethylene molecules spread as insoluble films on aqueous substrates. We have used as a new research tool the damping of capillary water waves by surface films as a function of area per monomer ($A$) and also have employed the more commonly used measurements of the film pressure ($F$) *vs.* $A$ and the vertical component ($\mu_p$) of the surface potential *vs.* $A$. This was the first time that all three of these methods were used in an investigation on an insoluble monolayer. Since the experimental results obtained with these three methods could be correlated well with each other, more firm conclusions could be drawn regarding film structure and behavior.

## Experimental Section

The polyoxyethylene research sample used was obtained from the research laboratory of the Union Carbide Corp. at Tarrytown, N. Y., and it was identified as POLYOX PEO WSR-N10. According to the supplier, the sample had an average molecular weight of 90,000 and the terminal groups were mainly hydroxyl groups and initiator fragments. In one series of experiments, an attempt was made to purify the polymer by extraction with acetone. The extraction procedure consisted of dissolving the polymer in slightly warm analytical grade acetone and allowing the solute to precipitate overnight. Then the supernatant liquid was discarded, and the entire procedure was repeated twice.

The ACS analytical grade ammonium sulfate added to the distilled water to make up the aqueous substrate in one film experiment was found to grossly contaminate

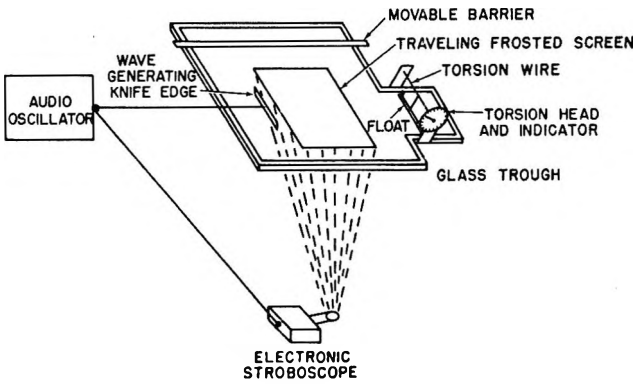


Figure 1. Schematic of film balance and instrumentation used to generate capillary waves and measure their amplitudes.

the water surface. To remove the film-forming impurities, the salt was treated as follows with activated vegetable charcoal (Darco Type G-60, 325 mesh powder). The ammonium sulfate solution containing about 1 g of charcoal per liter was heated to boiling and the charcoal was filtered off while the solution was still hot. This charcoal treatment proved to be very effective in removing the surface contaminants because the 35% ammonium sulfate solution so treated was as free from surface contaminants (according to film balance tests) as the pure water used in other experiments.

The organic liquids used as spreading solvents were each ACS analytical grade. In most of the work, the water used as the substrate was distilled once through a tin-lined still. In some experiments, the water was triply distilled, once through a tin-lined still and twice through an all-quartz still; however, a later comparison of the $F$ *vs.* $A$ graphs of the polyoxyethylene films spread on the once- and triply distilled water showed no detectable difference. Therefore, in the remainder of the experiments singly distilled water was used.

The basic experimental arrangement for wave-damping measurements was similar to that described by Garrett and Zisman.[2] However, instead of the ring tensiometer used by them to calculate $F$, the film pressure was measured directly with a modified Langmuir–Adam film balance made by using the torsion head and float of a Cenco "Hydrophil Balance" which was then fitted with a Monel torsion wire 0.01 in. in diameter and a pair of 0.001 in. thick polyethylene foil "end loops." This film balance was made an integral part of the wave-damping trough in order to expedite the experimental procedure and also make it possible

(5) H. Lange, *Kolloid-Z.*, **182**, 123 (1962).
(6) M. J. Schick, *J. Colloid Sci.*, **17**, 801 (1962).
(7) M. J. Shick, *ibid.*, **18**, 378 (1963).
(8) E. L. Lovell and H. J. Hibbert, *J. Amer. Chem. Soc.*, **62**, 2144 (1940).
(9) A. Couper and D. D. Eley, *J. Polym. Sci.*, **3**, 345 (1948).
(10) J. E. Glass, *J. Phys. Chem.*, **72**, 4459 (1968).

to measure film pressures simultaneously with either wave amplitudes or surface potentials. The schematic in Figure 1 shows the resulting modified film balance together with the instrumentation used to generate and measure the amplitudes of capillary water waves. The torsion head and float system spanned a 6 × 6 in. part of the glass trough extending away from the main portion which was 18 × 24 in. so as to accommodate the wave-generating apparatus. The sensitivity of the film balance was 0.342 dyne per centimeter of film pressure per degree of rotation of the torsion wire, and the torsion scale was read to the nearest 0.01° of arc.

A box-shaped cover with movable Lucite sides and a glass top protected the water surface from contamination by airborne particles during experiments of long duration. The entire trough could not be covered, however, because a small part of one side of the cover had to be left open to allow either the wave-generating or surface potential apparatus to be inserted through it and placed close to the water surface.

Construction of a glass trough sturdy enough to contain the aqueous substrate without contaminating it presented problems. Several attempts to build a trough using paraffin wax to secure glass bars around the edge of the thick, glass, base plate did not work satisfactorily on the large trough because the wax adhered so poorly to the glass that the glass border bars broke away from the base plate fairly easily. A more successful method of constructing the trough was developed. Each glass strip 1 × 1 cm in cross section was positioned along the border of the base plate and made to adhere by wrapping the top and sides with strips of Teflon tape. The resulting Teflon-coated surface was then completely covered with molten clean paraffin wax (mp 65–70°). The glass bars used as compression barriers were also covered with paraffin-coated Teflon tape. This use of wax-coated Teflon tape offered three advantages over the application of paraffin alone: (a) the slider moved easily over the side walls of the trough, (b) the wax could be applied more smoothly and evenly to the surface of the Teflon tape than to the glass, and (c) the wax coating on top of the tape less frequently cracked to cause leaks than did the wax coating applied directly to the glass walls.

Capillary water waves were generated and their amplitudes were measured by the same method used earlier,[2] and the main parts of the system are shown schematically in Figure 1. The capillary waves were generated by means of a T-shaped polystyrene dipper 6 in. long with the lower part having a flat edge 2 mm wide which just touched the water surface. The dipper was connected to the coil of a loudspeaker and was made to vibrate perpendicularly to the water surface at 60 cps by driving the loudspeaker with an audio frequency oscillator. Power from that oscillator was also fed to an electronic stroboscope; thus, the on–off frequency of the light from the stroboscope was the same as the frequency of the capillary ripples on the water surface. The light rays from the stroboscope were passed up through the bottom of the glass trough, were refracted by the wave crests, and then projected onto a frosted glass screen maintained parallel to and at a controllable distance above the water. Therefore, the observer could see a system of parallel lines corresponding to the crests of the system of standing waves. Since each of the wave crests acted as an approximately cylindrical lens, the light passing through the crest was refracted and focused at some position in the plane above the water surface.

From the geometrical optics of the system, the amplitude ($a$) of the capillary wave was estimated from the relation

$$a = 0.075\lambda^2\left(\frac{1}{L_1} + \frac{1}{L_2}\right) \quad (1)$$

where $\lambda$ is the wavelength of the system of parallel transverse water waves, $L_1$ is the distance from the water surface to the light source, and $L_2$ is the focal length of the cylindrical lens equivalent to a wave crest. The derivation of this equation was given in ref 2. The focal length of each cylindrical lens was found by raising or lowering the frosted screen until the rectilinear image of a given wave appeared sharpest and brightest. The wavelength was estimated by placing the screen just above the water surface and measuring the distance between the successive wave images.

The amplitudes of the ripples, $a_1$, $a_2$, etc., theoretically should and experimentally did decrease exponentially with distance $x$ from the source according to

$$a = a_0e^{-kx} \quad (2)$$

in which $a_0$ is the amplitude of the wave at the source. The damping coefficient ($k$) will be used to express wave-damping results. If eq 2 is expressed in logarithmic form, the familiar equation is obtained

$$\ln a = \ln a_0 - kx \quad (3)$$

which permitted $k$ to be determined from the slope of a linear plot of log $a$ *vs.* $x$.

The well known radioactive electrode method was used to determine the surface potential difference ($\Delta V$) at the air–water interface. The system employed consisted of an Americium$^{241}$ air electrode used in conjunction with a Keithley 610 electrometer. The aqueous substrate was grounded through a polished platinum foil electrode dipped into the water of the trough. The radioactive electrode was a 2-in. square brass plate on which the radioactive material had been deposited by the manufacturer (United Radium Corp., Morristown, N.J.). The electrode was supported about 3 mm above the water surface by the top of the protective cover. To provide shielding from extraneous electrostatic effects, a grounded, cubical,

copper wire screen cage was placed around the sides and above the radioactive electrode. An Amphenol RG shielded cable connected the radioactive electrode to the electrometer. A strip-chart recorder (Varian Model G-11A) was connected to the electrometer so that the potential difference between the radioactive electrode in the air and the platinum electrode immersed in the aqueous solution could be recorded directly. The recorder could be read reliably to 1 mV, and the reproducibility of the $\Delta V$ measurements was within $\pm 1\%$.

The stability of $\Delta V$ was determined by measuring periodically $\Delta V$ of a polyoxyethylene monolayer on water spread so that $A$ was 25 Å$^2$/monomer. In general, $\Delta V$ drifted only 3 mV in 5.5 hr, the maximum duration of any one experiment in this study. Therefore, the uncertainty in the perpendicular component ($\mu_p$) of the surface dipole moment per monomer calculated from the Helmholtz equation (see eq 5) is about 2 (mD) at this area/monomer, which was considered acceptable for this investigation.

In general, the experimental procedure consisted of leaving the aqueous substrate in the trough for 1 hr to allow any film-forming impurities to rise to the surface. Next, the water surface was swept clean with waxed barriers several times, and the freedom of the final surface from organic films was verified by pushing the movable barrier close to the float of the film balance. If there resulted a rise in pressure less than 0.15 dyne/cm, the cleanliness was acceptable. An aliquot of the spreading solution containing about 0.5 mg of polymer/ml of solution was placed on the surface with a micrometer-driven hypodermic syringe fitted with a glass needle. Generally, the film area was reduced in steps by slow sliding movements of the barrier over the water surface. The film subsequently reached a constant pressure usually within 2 min, so that the $F$ *vs.* $A$ isotherms based on such time intervals were not time dependent. By reversing the direction of motion of the barrier, film reversibility could be studied. However, the total range of values of $A$ over which the film could be examined was limited by the total area of the water surface in the hydrophil trough. In one experiment it was desired to study the film over a wider range of values of $A$ and for this purpose the film was further compressed by adding more polymer to the water surface using the syringe and a known solution of polymer.

## Results and Discussion

*Force vs. Area Relations of Polyoxyethylene Films.* In Figures 2a, 2b, and 2c are shown $F$ *vs.* $A$ curves for polyoxyethylene films compressed and expanded on distilled water at pH 3 over three ranges of $A$. The film compressed to a minimum monomer area of 20 Å (Figure 2a) was reversible, but the other two films showed hysteresis when they were expanded after the

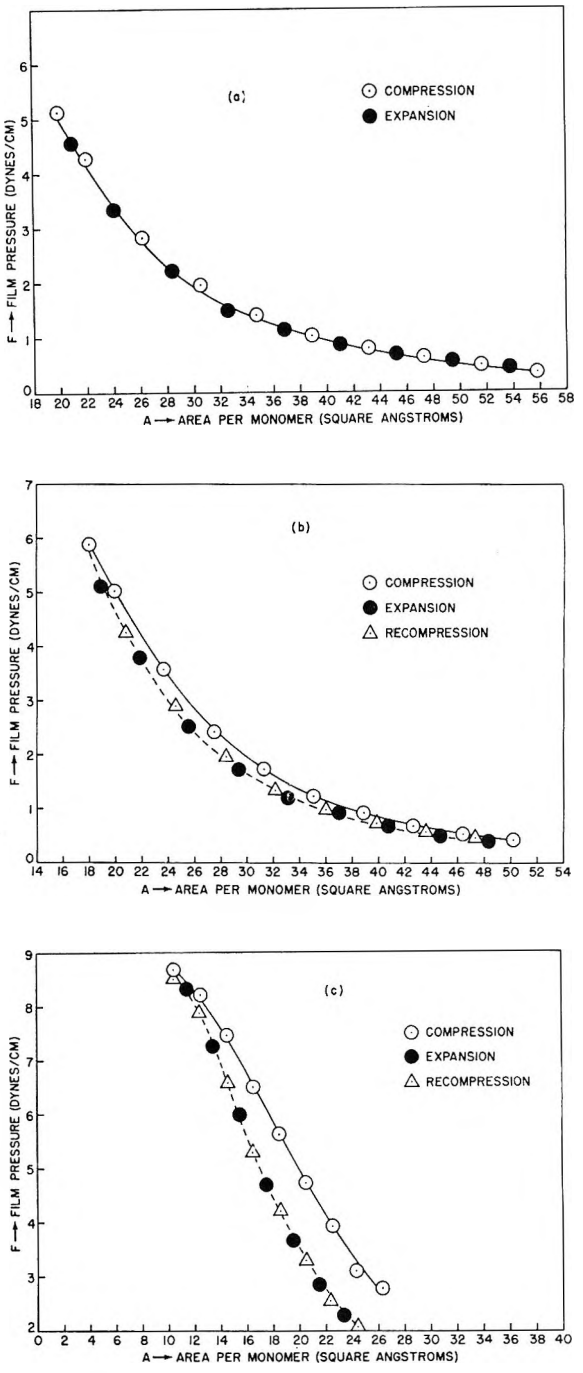


Figure 2. Film pressure *vs.* area per monomer curves of polyoxyethylene (on distilled water at 20° and pH 3).

first compression to 18 Å$^2$/monomer and 10 Å$^2$/monomer, respectively (Figures 2b and 2c). However, when the latter two films were recompressed, the $F$ *vs.* $A$ curves were the same as those obtained when the films were expanded, showing that after the first compression the films were once more reversible. Thus it appeared that film properties had been permanently altered by the initial compression. It may be noted also that the film compressed to 10 Å$^2$/monomer (Figure 2c) showed more hysteresis when expanded than the one compressed to 18 Å$^2$/monomer (Figure 2b) so that the

amount of hysteresis in the polyoxyethylene film was related to the lowest area per monomer to which the film was first compressed.

A possible cause for the observed hysteresis in films compressed below 20 Å²/monomer is that compression forced some of the film into the aqueous substrate, since polyoxyethylene is miscible with bulk water in all proportions at room temperature. Moreover, the polymer sample used in this study had a distribution of molecular weights, and compression of the film could have displaced some of the lower molecular weight components from the surface causing hysteresis upon decompression. In an attempt to determine whether hysteresis was caused by dissolution of some of the film in the substrate, a film was spread on a 35% ammonium sulfate solution to take advantage of its salting-out effect.[11] However, the *F vs. A* curve of this film was like that obtained when the film was spread on water at pH 3. Therefore, it was unlikely that some of the film was dissolving in the substrate to cause hysteresis.

To examine further the possibility that the hysteresis in the *F vs. A* curve might have been caused by the loss of components of the film into the underlying water, *F vs. A* curves were obtained using a polymer extracted with pure acetone. This treatment should have purified the polymer to some degree and perhaps narrowed its molecular weight range by removing some of the lower molecular weight fraction. However, since the *F vs. A* curve of the polymer extracted in this way was essentially identical, under comparable experimental conditions, with that of a film of the unextracted polymer, it was concluded that hysteresis was not caused by extraction of some of the polyoxyethylene by the aqueous substrate.

The reproducibility of the initial compression curve of the extracted polymer was investigated by spreading the polymer with each of four different pure solvents, chloroform, carbon tetrachloride, water, and benzene. The resulting *F vs. A* graphs were in excellent agreement; thus, there was convincing evidence that the films were fully spread and were identical. It is noteworthy that water could be used as one of the spreading solvents, an example of a water-soluble polymer being spread on the surface from an aqueous solution. For this to occur the free energy of the system must have been reduced by the spreading process, and this could have been accomplished by an unfolding of the polymer at the interface. From the above experiments it was concluded that the polyoxyethylene films had each spread on the aqueous substrate without loss of material to form a stable, adsorbed, insoluble monolayer at the air–water interface.

*Compressibility Curves.* An alternative explanation for the observed lack of reversibility or hysteresis is that the polymer molecule undergoes an irreversible structural change as the film is compressed. If this occurs, a change should be evident at the point of

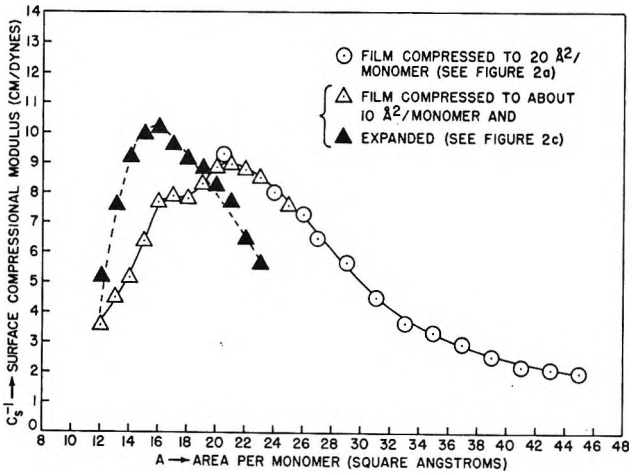


Figure 3. Compressibility modulus curves of polyoxyethylene films (on distilled water at 20° and pH 3).

structural transition because a well defined change in film compressibility has long been associated with either a phase change or some change in the structure of the film.[12,13] Therefore, the compressibility ($C^s$) of each polyoxyethylene film was carefully studied. Especially helpful were plots of the reciprocal of the compressibility, or the surface compressional modulus ($C_s^{-1}$), calculated as usual by

$$C_s^{-1} = -A\left(\frac{\partial F}{\partial A}\right)_T \qquad (4)$$

When $C_s^{-1}$ is plotted against $A$, a maximum in the curve gives the area and pressure at which the film is least compressible.

Values of $C_s^{-1}$ were calculated from the slopes of the *F vs. A* curves in Figures 2a and 2c and are plotted against $A$ in Figure 3. The values of $C_s^{-1}$ denoted by circles in curve $C$ were calculated from the *F vs. A* curve of the film compressed to 20 Å²/monomer and expanded (Figure 2a). Since this film was reversible, the $C_s^{-1}$ values were the same for compression and expansion. The triangles in curves $C$ and $E$ were obtained from the *F vs. A* curves of the film compressed and expanded over the area-per-monomer range of about 26 Å² to 10 Å² (Figure 2c). This film evidently behaved irreversibly and, as a result, the $C_s^{-1}$ *vs. A* curves of compression (curve C) and expansion (curve E) were definitely different. As may be seen in the graph, a maximum appeared in curve C at about 20 Å²/monomer but it disappeared when the film which had been compressed to about 10 Å²/monomer was allowed to expand (curve E). The $C_s^{-1}$ *vs. A* curves of the film of the acetone-extracted polymer and the film spread on a 35% ammonium sulfate solution also

(11) F. E. Bailey, Jr., and R. W. Collard, *J. Appl. Polymer Sci.*, **1**, 56 (1959).

(12) D. G. Dervichian, *J. Chem. Phys.*, **7**, 931 (1939).

(13) H. B. Bull, *J. Amer. Chem. Soc.*, **67**, 4 (1945).

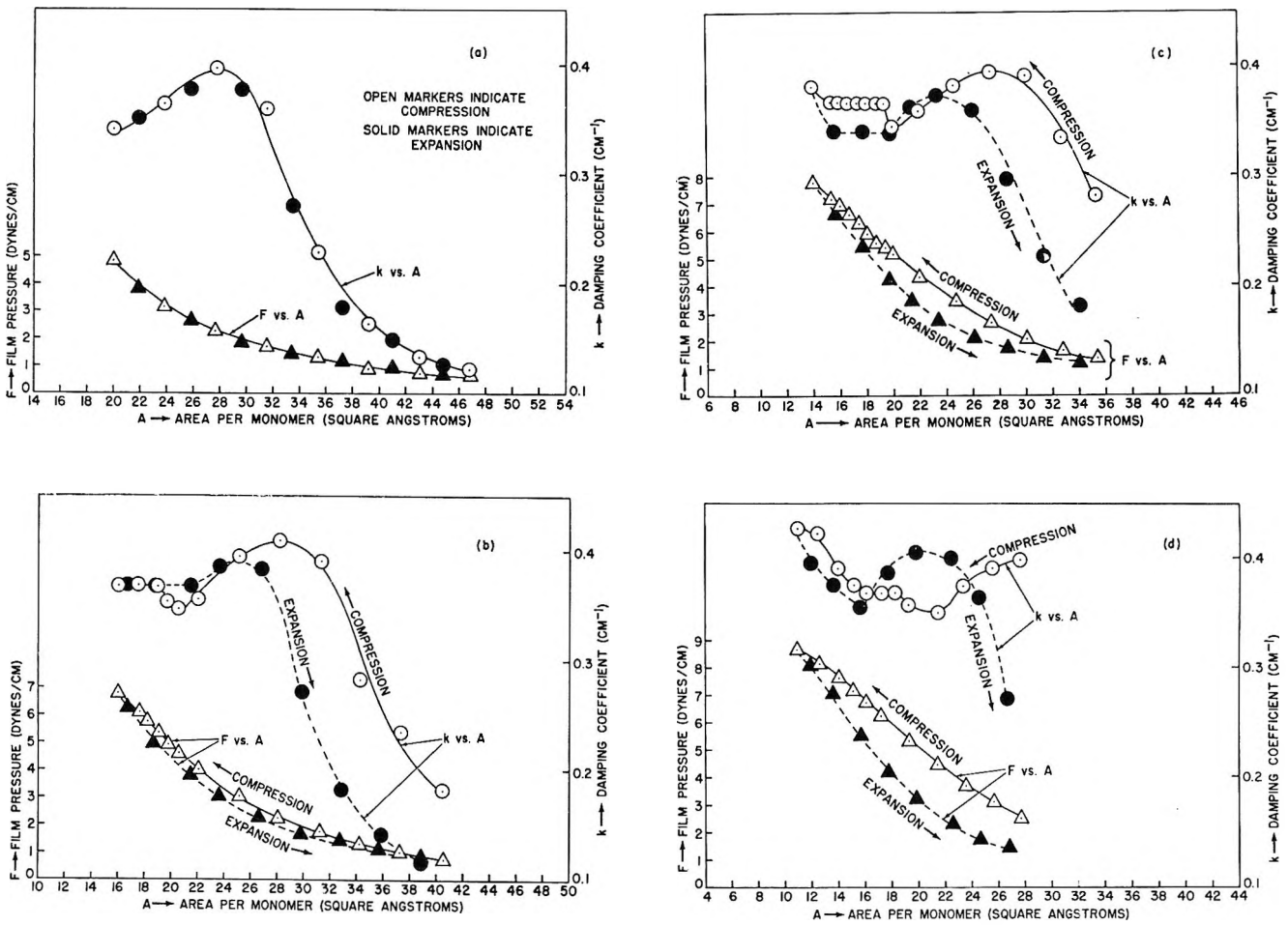


Figure 4. Damping coefficient and film pressure as function of area per monomer for polyoxyethylene (on distilled water at 20° and pH 3).

showed a similar maximum at about 20 Å²/monomer. Evidently, 20 Å/monomer is a critical value in the compression of these monolayers, and it was assumed that at this area per monomer, the molecules became sufficiently close packed to form a highly condensed film. In such a situation, the molecules would be expected to be oriented in a nonrandom manner and to lie flat on the surface of the water. This polymer structure will hereafter be referred to as conformation (I).

Compression of the film to less than 20 Å²/monomer appeared to cause the monolayer to collapse in some way or to change its structure because the maximum in the compression curve at that area disappeared when the film was expanded. However, a collapse of the film seemed to be ruled out because the *F vs. A* curve shown in Figure 2c did not bend toward the horizontal at this point. The film compressed to about 10 Å²/monomer showed an inflection point (or shoulder) at about 16 Å²/monomer and a maximum at nearly the same area when the film was decompressed. It was assumed that the inflection point in curve C represented the close-packed area of the molecules in a new structure, hereafter identified as conformation (II). The elimination of the maximum at 20 Å²/monomer when the film was decompressed suggested that conformation (II), once formed, did not revert spontaneously to conformation (I) when the pressure was allowed to decrease.

*Wave-Damping Studies.* Any rearrangement of adsorbed molecules on a liquid surface, because it can (and usually does) alter the free surface energy of the system, should be manifested by a change in the wave-damping properties of the film. Therefore, it was considered probable that wave-damping measurements would furnish confirmatory evidence of any molecular rearrangements, or structural changes, experienced by the polyoxyethylene monolayers adsorbed at the air–water interface. In an early series of experiments both wave-damping *vs. A* and surface pressure *vs. A* measurements were made simultaneously in the film trough. Surface pressure measurements were made also without wave generation and were found to be the same in both circumstances. Usually the wave train had vanished before it reached the mica float of the film balance, and no evidence of vibration of the float was seen when the wave generator was operating.

Damping coefficient *vs.* area per monomer (*k vs. A*) and *F vs. A* curves of films compressed to progressively

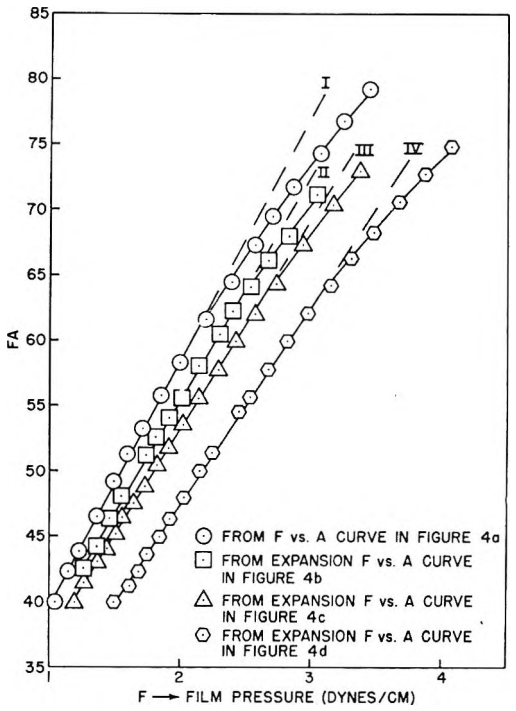


Figure 5. *FA vs. F* plots of polyoxyethylene films.

smaller monomer areas are shown in Figures 4a through 4d. As seen in Figure 4a, both curves were reversible for the film compressed to only 20 Å²/monomer as would be expected if the polymer molecules retained the same molecular structure as when spread, *i.e.*, had not yet started to go into another conformation. Once a film was compressed below 20 Å²/monomer (Figures 4b, 4c, and 4d), hysteresis was exhibited because as *A* was decreased below that value, the monolayer started to undergo an irreversible conformational change.

When each of the films compressed below a monomer area of 20 Å² was expanded, a peak appeared in the wave-damping curve which shifted to smaller areas as the film was compressed further. The significance of these peaks was indicated by plotting the product *FA* against *F*, a method used to characterize gaseous monolayers.[14] A linear relationship at low pressures is taken as evidence of an imperfect gaseous film showing increasing lateral cohesion as *F* inceases. The *FA vs. F* plots of four films are shown in Figure 5. Line I was constructed from the *F vs. A* curve in Figure 4a whereas lines II, III, and IV were obtained from the expansion *F vs. A* curves in Figures 4b, 4c, and 4d. Figure 5 shows that in all of the plots good straight lines were obtained up to a certain film pressure. The *FA vs. F* curve for the film compressed to a monomer area of 20 Å² began to deviate from linearity at about $F = 2.2$ dyn/cm or, from Figure 4a, at a monomer area of about 28 Å². This is the area at which the maximum appeared in the *k vs. A* curve; it appears to be the maximum which marks the point of transition from a gaseous to a more closely packed film. The monomer areas at which the other *FA vs. A* curves departed from linearity were found to be about 25, 23, and 20 Å²/monomer for the films represented by lines II, III, and IV, respectively. These values also correspond to the areas at which the maxima appeared in the respective *k vs. A* curves when these films were expanded. This correlation between the wave damping and surface pressure data is good evidence that the first maximum in the *k vs. A* curve when a film is compressed and the last maximum when the film is expanded is an indication of when the film is either leaving or entering the gaseous region.

The minimum in the *k vs. A* curve at 20 Å²/monomer when the films were compressed (Figures 4b, 4c, and 4d) must correspond to the maximum in the modulus of compressibility curve of Figure 3. Since this area has been proposed as representing the monomer area of conformation (I), it becomes necessary to explain the structure of the film at 28 Å²/monomer where the film molecules are apparently in close proximity. A clue as to the form of the molecule at this area is obtainable from the findings of Rosch,[15] who obtained from viscosity data good evidence of the association on the average of two water molecules with each oxygen in polyoxyethylene. The influence of these bound water molecules would be to increase the surface area of the polymer molecule and possibly also increase intermolecular cohesion. It is conceivable, therefore, that the polymer molecule with the two bound water molecules per monomer occupies an area of about 28 Å²/monomer while the polymer molecule without these hydrogen-bonded water molecules occupies only 20 Å²/monomer.

As the film was compressed beyond a monomer area of 28 Å², the two bound molecules of water could have been squeezed out of the interface, or the hydrogen bonds broken, until, at 20 Å²/monomer, only the polymer molecule remained in the interface with much weaker hydrogen bonding with the bulk aqueous substrate. This interpretation is in agreement with the ideas expressed by Henry Bull[13,16] about proteins. Bull had postulated that a major effect of the compression of proteins was dehydration of the molecule, and a hydrated molecule would be expected to be more compressible than the simple molecule. It is possible that the form of polyoxyethylene with two water molecules attached to each ether oxygen is so compressible, or elastic, that no distinct change of slope at 28 Å²/monomer was discernible in the compressibility curve. On the other hand, the wave-damping method is probably more sensitive to changes occurring in the monolayer and, as a consequence, a well-defined peak

(14) R. K. Schofield and E. K. Rideal, *Proc. Roy. Soc.*, **A109**, 58 (1925).

(15) M. Rosch, *Kolloid-Z.*, **147**, 78 (1956).

(16) H. B. Bull, *Advan Protein Chem.* **3**, 95 (1947).

appears in the $k$ *vs.* $A$ curve which corresponds to the external work done to cause dehydration.

According to the theory proposed from the $F$ *vs.* $A$ plots shown in Figure 2, compressing the film beyond a monomer area of 20 Å$^2$ causes the molecule to assume conformation (II). It is reasonable to expect that the molecule does not readily go into this conformation because an energy barrier generally has to be overcome before a molecule can be transformed into a more stable conformation. Thus it appears that the polymer molecules do not immediately begin to form conformation (II) at 20 Å$^2$/monomer; instead the film must be compressed to almost 19 Å$^2$/monomer before the energy barrier has been overcome. According to this concept, the polymer molecules acquire the energy necessary to initiate the formation of conformation (II) as the film is compressed from 20 to almost 19 Å$^2$/monomer. However, once that necessary work has been done when $A$ has decreased to about 19 Å$^2$/monomer, there appears to be a smooth transition to configuration (II) as shown by the constant value of $k$ between 19 and 16 Å$^2$/monomer.

The constancy of $k$ in the transition region of about 19 to 16 Å$^2$/monomer may seem surprising since this indicates no appreciable change in the mode of attachment of the polymer molecule to the aqueous substrate. This may be reasonable, however, if the position of the oxygens in the polymer relative to the water surface is not very different in the two conformations. It will be suggested later that these atoms are situated on one side of the polyoxyethylene molecule so as to anchor it firmly to the water surface. The oxygen atoms are believed to remain essentially in the same plane, adsorbed on the water, as the molecule is rearranged into the new conformation. As a result, and because the polymer molecule is already free of any tightly bound water, there may be little difference in the two conformations insofar as the strength of the attractive forces between the oxygenated group in the polymer and the aqueous substrate molecules is concerned. On the other hand, compression of the film up to 20 Å/monomer should, as observed, cause definite changes in the wave-damping coefficient. The increase in $k$ as the film is compressed to an area per monomer of 28 Å$^2$ is obviously caused by the wave energy consumed as the polymer molecules are being pushed closer together. The decrease in $k$ from 28 to 10 Å$^2$/monomer is the result of the removal of the two attached water molecules from each monomer as well as the decrease in $A$, thus decreasing the water drag caused by the wave-induced lateral movement of the polymer. Therefore, if the proposed interpretation is correct, the extent of hydrogen-bonded association between the film and the water molecules is continuously changing as the film is compressed down to a monomer area of 20 Å$^2$.

It is worth noting that when the film was compressed to at least 16 Å$^2$/monomer the minimum in the $k$ *vs.* $A$ curve at 20 Å$^2$/monomer disappeared as the film was expanded and the necessary work done was supplied by the wave energy (Figures 4b, 4c, and 4d). Clearly whatever caused the minimum was eliminated by the compression of the film below 20 Å$^2$/monomer. These results agree with the compressibility data shown in Figure 3 and corroborate the view that, once conformation (II) begins to film, the polymer molecules do not pass back into conformation (I) on decreasing the film pressure.

Compression of a film to less than 16 Å$^2$/monomer probably causes it to collapse in some manner because the $F$ *vs.* $A$ curve starts to curve toward the horizontal at about this monomer area (Figure 4d). Additional evidence of film collapse is furnished by the $k$ *vs.* $A$ curves of films compressed below this area. Figure 4c shows that when a film compressed to 14 A$^2$/monomer was allowed to expand, $k$ dropped substantially. This result may be contrasted with the $k$ *vs.* $A$ curve of the film which had been compressed to only 16 Å$^2$/monomer (Figure 4b). When this film was expanded, $k$ remained the same as it had been during the last stages of compression. A simple interpretation of these results is that as the film was finally being compressed, it started to collapse irreversibly at a monomer area of 16 Å$^2$ accompanied presumably by the expulsion of some of the polymer molecules from the water surface. It is possible that some of the monomers were depressed below the surface of the aqueous substrate upon compression below 16 Å$^2$/monomer. If such were the case, the film compressed to 14 Å$^2$/monomer would contain fewer monomers when expanded than the film compressed to only 16 Å$^2$/monomer. Accordingly, the wave-damping ability (or $k$) of the film compressed to 14 Å$^2$/monomer would be less, at corresponding values of $A$, when it was expanded because there would be less hydrodynamic drag than during compression.

Since film collapse means a drastic change is occurring in the structure of the polymer film adsorbed at the interface, we should expect external work would be needed, and concomitant changes would occur in the wave-damping properties of the film. In line with that expectation, $k$ increased fairly rapidly as $A$ decreased below 16 Å$^2$/monomer for the films during compression (Figures 4c and 4d).

In the next experiment, the results of which are shown in Figure 6, a film was compressed to lower areas than previously by adding more polymer to the surface, thus allowing the film to be studied over a wider range of values of $A$ in a single experiment than was possible using the movable barriers. In addition to the maximum and minimum shown in the previous $k$ *vs.* $A$ plots, the $k$ *vs.* $A$ curve is seen to have a peak at about 11 Å$^2$/monomer, indicative most likely of film collapse. The $F$ *vs.* $A$ curve began to level off at about 16 Å$^2$/monomer to reach a maximum surface pressure of about 10 dyn/cm. The gradual transition to a col-

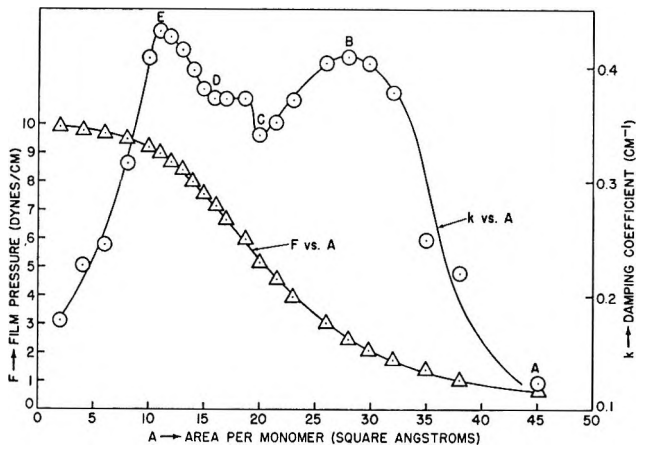


Figure 6. Variation of damping coefficient and film pressure with area per monomer for polyoxyethylene (on distilled water at 20° and pH 3).

lapsed state is consistent with the behavior of other horizontally oriented polar polymers, and the low collapse pressure is characteristic of a film whose intermolecular forces are weak.

Based on the curves in Figure 6 and the other evidence already given, the behavior of a polyoxyethylene film at the air–water interface may be visualized in the following way using the wave-damping curve of Figure 6 as a guide. At low pressures, the film behaves as an imperfect gaseous monolayer and is composed of polymer molecules with two water molecules on the average attached to each ether oxygen by hydrogen bonds. The part of the curve marked AB represents the compression of this form of the film molecules. As the film is compressed beyond point B, the area of closest packing of the polymer molecules with the two adsorbed water molecules per oxygen, the two water molecules are gradually squeezed out of the interface as the film pressure rises until, at point C, only the simple polymer molecules in conformation (I) remain adsorbed on the water surface. The film has shown no hysteresis up to this point. As the film is compressed beyond point C, the molecules begin to condense and rearrange somewhat to assume a more compact structure until, at point D, the resulting condensed film is composed almost entirely of molecules in conformation (II). The described change in conformation is not reversible and, as a result, decompressing a film which has been compressed beyond point C will produce a hysteresis curve. The film after being compressed beyond point D begins to collapse in some way which requires external work extracted from the wave energy and this is exhibited by the second peak at point E.

*Proposed Molecular Conformations.* The ideas expressed above were well supported by assigning reasonable molecular structures to the important monomer areas of 20 and 16 Å$^2$. Stuart and Briegleb molecular models were used because they generally give a good representation not only of the size but also the flexibility of a molecule.

As a beginning, the zigzag and meander conformations that were postulated for polyoxyethylene in solution by Staudinger[17] have been examined. Above a degree of polymerization of 9, Staudinger believed that the zigzag conformation was twisted into the more compact meander conformation due to increased intramolecular attractive forces. The areas occupied by the zigzag and meander conformations were calculated from molecular models to be 18.7 and 14 Å$^2$/monomer, respectively. These areas are considered to differ enough from the monomer area values of 20 and 16 Å$^2$ deduced from our experiments to remove them from consideration as possible structures for polyoxyethylene adsorbed on the surface of water.

Considering the strong hydrogen-bonding ability of the oxygen atom in polyoxyethylene and the hydrophobic nature of the rest of the molecule, it is reasonable to expect the oxygen atoms to be directed toward and the hydrocarbon group away from the aqueous substrate. Therefore, the oxygens were arranged on one side of the molecular model as shown in Figure 7, which is a view looking up from the adsorbing surface, to give a hydrophilic and hydrophobic surface to the molecule. This structure has a calculated area of 20.1 Å$^2$/monomer and seems to be a logical choice for the basic form of the molecule when spread. Consequently, it is proposed as the structure of conformation (I) mentioned earlier. The regular array of the water-attracting oxygen atoms should anchor the molecule firmly to the substrate. If two models representing water molecules are placed on an oxygen atom in accordance with Rosch's conclusions, the oxyethylene unit and water molecules together occupy an area of roughly 28 Å$^2$.

Conformation (I) became a more attractive possibility when it was discovered that by applying pressure from the ends the model could be compressed into an orderly, close-packed model with a monomer area of 16.1 Å$^2$ without removing the oxygens from the plane of the water surface. This model, which corresponds to conformation (II) mentioned previously, is shown in Figure 8. It may be noted that in this conformation the molecule is packed as closely as possible, and this may represent the smallest structure that the molecule can assume as long as it remains planar with the hydrophilic oxygen atoms on one face so as to attach the molecule to the underlying water. Thus, a polyoxyethylene film compressed beyond 16 Å$^2$/monomer on an aqueous substrate would be expected to begin to collapse as has been suggested by *k vs. A* and *F vs. A* curves.

If the postulated conformational change is not reversible, it becomes necessary to explain the greater

(17) H. Staudinger, "Die Hochmolekularen Organischen Verbindungen," Springer-Verlag, Berlin, 1960.

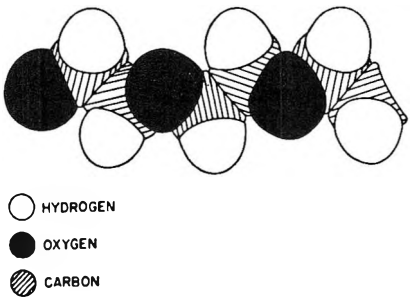


Figure 7. Sketch of molecular model of conformation (I) of polyoxyethylene lying in the surface viewed from the water phase.

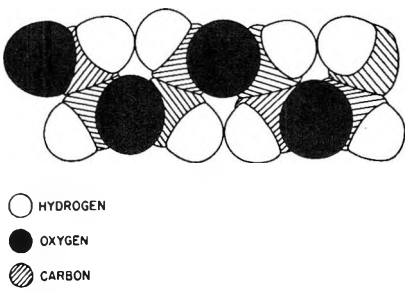


Figure 8. Sketch of molecular model of conformation (II) of polyoxyethylene lying in the surface viewed from the water phase.

stability of conformation (II) as opposed to conformation (I). An examination of the molecular models proved to be very helpful on this point. Conformation (I) is loose and flexible, but compressing it into the compact conformation (II) tends to lock the chain in one position resulting in a sterically hindered and more rigid structure. In fact, the arrangement is such that, as long as the atoms remain in the same plane, the chain can be expanded only slightly without breaking the ball-model bonds. Since the great affinity of the oxygen atoms for water would be expected to keep the adsorbed molecule anchored in the water surface, it is easy to imagine that neither the release of pressure nor kinetic agitation would be sufficient to cause the molecule to go back to conformation (I) if the molecular model gives an accurate representation of the rigidity of the actual polyoxyethylene chain in conformation (II).

Conformation (II) may have been further stabilized by an increase in the intramolecular forces. For example, the hydrogen atoms in conformation (II) are paired so that each hydrogen touches another one. The mutual cohesion between these atoms due to London dispersion forces should be another factor in making conformation (II) more stable than conformation (I).

The polyoxyethylene sample used in this study was in the high-molecular weight range and therefore the polymer molecules should be in the meander form when dissolved. In order for the molecule to assume the expanded conformation (I) on the surface, it would have to unfold. This seems to be a distinct possibility for the following reason. The polymer can be spread with an aqueous solution and, as mentioned earlier, this requires that the free energy of the system be reduced by the spreading process. This could be accomplished by the molecule unfolding at the surface.

*Film Behavior at Higher Temperatures.* The combination of increased chain rigidity and stronger internal cohesive forces probably means that molecules in conformation (II) must overcome an energy barrier before they can revert to conformation (I). An attempt was made to provide the necessary energy for this conformation change by raising the temperature of the film. A film was compressed at 20° until the polymer molecules were in conformation (II) and the film was then heated to 56°, about the highest temperature to which the substrate could be raised without danger of melting the paraffin wax in the trough. The film was then decompressed at this higher temperature and, judging from compressibility data, the film molecules remained in conformation (II). Clearly the thermal energy of agitation at 56° was not sufficient to allow the polymer molecule to overcome the energy barrier and to go back to conformation (I).

*Surface Potential Studies.* A further series of experiments was carried out on polyoxyethylene films by measuring surface potential differences between the air and water across the interface. The surface potential difference, $\Delta V$, due to a uniform plane film of $n$ dipoles per square centimeter is given by the classic Helmholtz equation

$$\Delta V = 4\pi n\mu_p \text{ statvolts}$$
$$= 300(4\pi n\mu_p) \text{ volts} \quad (5)$$

where $\mu_p$ is the perpendicular component of the dipole moment expressed in esu as it exists in contact with the adsorbing surface. In this study the dipole moment $\mu_p$ will be that of the adsorbed monomer and the number of monomers per square centimeter of surface will be $10^{16}/A$, since $A$ is the area of surface occupied per monomer in square Ångstroms. Hence, we can rewrite eq 5 as follows

$$\Delta V = 300(4\pi)\left(\frac{10^{16}}{A}\right)\mu_p \quad (6)$$

In order to express $\mu_p$ in debyes, eq 6 is divided by $10^{18}$ (1 D = $10^{-18}$ esu) to give the final equation

$$\Delta V = \frac{12\pi\mu_p}{A} \text{ or } \mu_p = \frac{A(\Delta V)}{12\pi} \quad (7)$$

Although water molecules and ions in the water beneath the surface film will contribute to the observed value of $\mu_p$, this term should (and usually does) give a useful indication of the orientation of the polar ether group at the water surface.

As in the wave-damping study, films were compressed

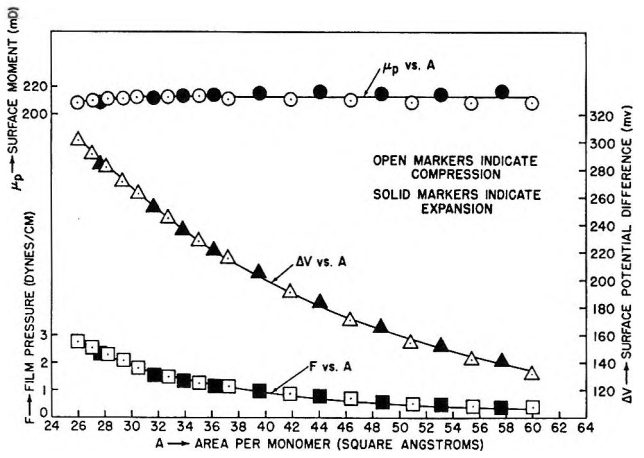


Figure 9. Surface moment, surface potential, and film pressure as function of area per monomer for polyoxyethylene (on distilled water at 20° and pH 3).

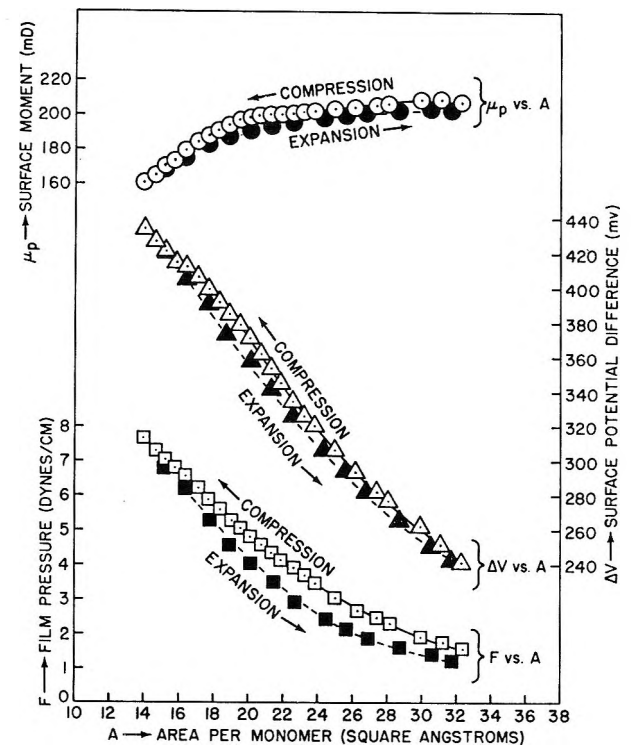


Figure 10. Surface moment, surface potential, and film pressure as function of area per monomer for polyoxyethylene (on distilled water at 20° and pH 3).

to various monomer areas and expanded. The *F vs. A*, $\Delta V$ *vs. A*, and $\mu$ *vs. A* curves of two of the films studied are shown in Figures 9 and 10. As expected, the film compressed to 26 Å²/monomer (Figure 9) was reversible with respect to all three quantities, *F*, $\Delta V$, and $\mu_p$. The surface dipole moment was essentially constant down to about 28 Å²/monomer where it seemed to decline slightly. We can conclude that in the region where $\mu_p$ is constant no significant reorientation of the polar groups was taking place. Since the film was apparently gaseous to about 28 Å²/monomer, the film dipoles were probably free to orient at the surface and the polymer chains were most likely stretched out flat on the surface since this was the probable position of minimum potential energy.

It may be seen in Figure 10 that, below an area of 28 Å²/monomer where the hydrated molecules were in close contact, $\mu_p$ began to decline gradually down to a monomer area of about 20 Å² after which it dropped more steeply. The change in the slope of the $\mu_p$ *vs. A* curve in the region of 28 to 20 Å²/monomer, since it was relatively small, suggests that the orientation of the polar ether group at the surface was not changing appreciably. What was changing, however, was the contribution of the water molecules associated with the oxygen atom in the polymer to the net observed surface dipole moment. The hydrogen atoms in the waters of hydration were undoubtedly linked to the oxygen in the polymer by hydrogen bonds and this would have caused the hydrogens in the water to be oriented upward toward the surface. The presence of these hydrogens at the surface would naturally make $\mu_p$ more positive, and the breaking of the hydrogen bonds would lower $\mu_p$ as observed.

The commencement of the transformation of the polymer molecule into a new conformation was reflected in the relatively large fall in $\mu_p$ at approximately 20 Å²/monomer. At this area the polar ether groups themselves were being compressed for the first time causing a more pronounced change in $\mu_p$. This marked drop in $\mu_p$, since it does not denote film collapse, gives additional confirmation of a reorientation of the polymer molecule at the surface.

The $\mu_p$ *vs. A* curve decreased smoothly past 20 Å²/monomer and gave no definite indication that the transition from one polymer conformation to another was complete at about 16 Å²/monomer. In this region the $\Delta V$ *vs. A* curve can probably be looked at more advantageously. As may be seen in Figure 10, $\Delta V$ appears to have increased linearly between 20 and 16 Å²/monomer. At 16 Å²/monomer the curve started to slope toward the horizontal and, as discussed earlier, this probably marked the beginning of film collapse.

*Surface Dipole Moments and Molecular Orientation.* Usually, it is impractical to attempt any quantitative interpretation of surface dipole moments of polar molecules on water since all of the factors which are contributory are so little understood. Nevertheless, an attempt was made in this study to relate the observed changes in the surface dipole moment in the transition region of 20 to 16 Å²/monomer to a change from conformation (I) to conformation (II).

As a first step, the surface dipole moment of the film at 20 and 16 Å²/monomer was taken from five different $\mu_p$ *vs. A* plots, including that shown in Figure 10. The average value of $\mu_p$ at the former area was 194 mD whereas the value at the latter area was 173 mD. These values represented, of course, the experimental

surface dipole moments of the proposed conformations (I) and (II), respectively. The observed change in $\mu_p$ due to the conformational change was accordingly 194 − 173 = 21 mD.

It is now necessary to compare the observed change in $\mu_p$ to that expected on the basis of the two proposed molecular models of Figures 7 and 8. For this purpose, conformation (I) was assigned the experimentally determined value of $\mu_p$ of 194 mD, and $\mu_p$ for conformation (II) was calculated from this value. At 20 Å$^2$/monomer the polymer molecule in conformation (I) presumably was lying flat on the surface with every oxygen atom immersed in the substrate, and it was assumed that at this area the C–O dipole was free to orient in the electrostatic field normal to the water surface.

Compression of the molecular models revealed that, in going from conformation (I) to conformation (II), the ether group was twisted so that in conformation (II) it was almost 20° from the vertical. Hence, the surface dipole moment of conformation (I) should be diminished by the factor cos 20° and the moment of conformation (II) is calculated to be 182 mD. The calculated change in the surface dipole moment based on the $\mu_p$ values of the proposed conformations is thus 194 − 182 = 12 mD compared to the experimental change of 21 mD. There are a number of factors which may be responsible for this discrepancy in the two values. In the above calculation involving the two proposed conformations, only the change expected in the intrinsic moment of the surface molecule as a result of the tilting of the polar ether group was taken into account. Actually, however, the reorientation of the polymer molecule on an aqueous substrate probably causes changes in the interactions between the ether group and the oriented water molecules beneath, between the ether groups themselves, and between the hydrocarbon groups and their immediate environment. These changes are not likely to be negligible and, since we cannot make corrections for them, it is not surprising that there is not better agreement between the calculated and experimental changes in the surface dipole moment as the polymer undergoes a conformational change at the air–water interface.

## Conclusions

Of the three experimental methods used in this study, measurements of wave damping, surface pressure, and surface potential, the wave-damping method was found to be the most sensitive to molecular structural and other changes occurring in the polyoxyethylene films adsorbed on water. Whereas it was sometimes necessary to rely on small changes in the slope of the $F$ *vs.* $A$ and $\Delta V$ *vs.* $A$ curves to detect these changes, very distinct maxima and minima or inflection points appeared in the $k$ *vs.* $A$ curve when the film was undergoing some type of change. By comparing the areas at which these peaks appeared with the calculated areas of molecular models, experimental results were obtained which could be interpreted more fully than heretofore had been possible. Strong evidence has been found for a well defined irreversible-conformational change in the polymer molecule as it was compressed appropriately at the air–water interface.

Since polyoxyethylenes of even higher average molecular weights are completely soluble in water, it might be anticipated a monolayer of the polymer used would be unstable at the air–water interface especially when the film was compressed. However, we have demonstrated that the polyoxyethylene film, once spread on the surface, did not dissolve in the aqueous substrate except perhaps at the surface pressures high enough to cause film collapse. Our polyoxyethylene specimen once spread as a monolayer on the water surface must have been in a lower energy state than when dissolved in bulk water.

In addition to the inherent hydrophobic–hydrophilic (or surface-active) properties of polyoxyethylene, which are evidently favorable for spreading and adsorption of the polymer at the air–water interface, the size of these higher polyoxyethylene molecules probably contributed to the stability of the films studied here. Crisp,[18] in an early survey of the $F$ *vs.* $A$ properties of linear polymers on water, pointed out that surface-active polymers, since they contain many monomers which can be adsorbed simultaneously on the water surface, spread under different circumstances than simple surface-active molecules. Before a polymer molecule as a whole can pass into the aqueous substrate, every monomer unit must be desorbed simultaneously, but the chances of this happening to a high polymer are small. Consequently, such a surface-active polymer as high molecular weight polyoxyethylene, even though water soluble, can form well-spread films at the air–water interface. As a matter of fact, readily spread, insoluble monolayers of polyvinyl alcohol and un-ionized polyacrylic acid have been reported by Crisp.[19]

(18) D. J. Crisp in "Surface Phenomena in Chemistry and Biology," J. F. Danielli, K. G. A. Pankhurst, and A. C. Riddiford, Ed., Pergamon Press, Inc., Elmsford, N. Y., 1958, p 24.

(19) D. J. Crisp, *J. Colloid Sci.*, **1**, 161 (1946).

# Interfacial Tensions against Water of Some $C_{10}$–$C_{15}$ Hydrocarbons with Aromatic or Cycloaliphatic Rings

by Joseph J. Jasper, Marta Nakonecznyj, C. Stephen Swingley, and H. K. Livingston

*Department of Chemistry, Wayne State University, Detroit, Michigan 48202* *(Received August 7, 1969)*

Interfacial tensions against water were determined for the $C_5$, $C_6$, $C_7$, and $C_9$ *n*-alkylbenzenes at 30–75° by the drop-volume method and for bicyclopentyl and bicyclohexyl at 30° by the horizontal capillary method. For a homologous series of hydrocarbons, there is a limit beyond which Antonov's rule does not apply to the hydrocarbon–water interfacial tension. This limit falls near the $C_7$ in *n*-alkylbenzenes. For the bicycloalkyls, both bicyclopentyl and bicyclohexyl are near this limit. Dispersion forces alone cannot be used to explain the observed interfacial tension data. The discrepancy between the experimental tensions and tensions calculated by combining dispersion forces may be due to the increase in thickness of the interface that results when the hydrocarbon molecules do not pack well, as they do not in the case of bicycloalkyls and long-chain alkylbenzenes.

## Introduction

During the past twenty years a series of studies of interfacial tensions at the organic liquid–water surface have been carried out in these laboratories.[1] All these measurements employed the drop-volume method with the helical spring technique for controlling the rate of drop formation that was first described by Adinoff.[2] Improvements in technique and apparatus design have occurred over the years. Jasper and Duncan[1] gave the status of the improved procedure at the time the present work was initiated. Most of the previous papers in this series deal with the interfacial tension of halogenated organic compounds against water, but also included are data for the lower members of the alkylbenzene series $RC_6H_5$, where R was methyl, ethyl, *n*-propyl, and *n*-butyl.[3] In all cases, interfacial tension was determined as a function of temperature over a substantial range, which was in some cases as broad as from 20 to 80°.

The recent work of Jasper and Duncan[1] was distinctive in that data were obtained for the first time for hydrocarbons with more than ten carbon atoms. This represented our first venture into the molecular weight range encountered in practical lubricating oils and surface-active agents. That study dealt only with the $C_{13}$–$C_{16}$ $\alpha$-olefins. In the present work we are extending our measurements to alkylbenzenes of higher molecular weight than those investigated by Jasper and Seitz[3] and presenting the first interfacial tension measurements on hydrocarbons with two unfused rings, specifically bicyclopentyl and bicyclohexyl.

## Experimental Section

Two special features of the experimental techniques used in the present work should be mentioned.

1. The drop-volume method has been used with some further refinements. These have made it possible to study time effects in drop formation in detail.

2. The evident importance of allowing time for equilibrium in drop formation has led us to substitute for the drop-volume method the horizontal capillary method in some measurements. This method has had very little use since it was first proposed by Ferguson and Kennedy in 1932.[4] It does not require the determination of densities of the mutually saturated phases. This permitted us to satisfy the conditions of loan of the highly purified hydrocarbon samples which the custodians of the American Petroluem Institute Standard Samples of research hydrocarbons kindly sent to us. We actually used only 3 g of the loan samples. While methods of measuring saturated densities with very small samples and no chance of contamination could no doubt have been devised, it was considered preferable to avoid this problem completely.

Some modifications were made in the Ferguson–Kennedy technique. The capillary was placed in a jacket through which water at 30 ± 0.05° was circulated. One end of the capillary, which was polished to have a face perpendicular to the bore of the capillary, projected out of the jacket. The other was attached to an open-end manometer and a source of pressure (Figure 1). One source of error that had to be avoided

(1) J. J. Jasper and J. C. Duncan, *J. Chem. Eng. Data*, **12**, 257 (1967), and previous references cited there.

(2) B. Adinoff, "Thermodynamics of Hydrocarbon Surfaces," Ph.D. Thesis, University of Chicago, 1943; see also W. D. Harkins and A. E. Alexander, "Techniques of Organic Chemistry," Vol. 1, Weissberger, Ed., Interscience Publishers, New York, N. Y., 1959, p 757.

(3) J. J. Jasper and H. R. Seitz, *J. Phys. Chem.*, **63**, 1429 (1959).

(4) A. Ferguson and S. J. Kennedy, *Proc. Phys. Soc.* (London), **44**, 511 (1932).

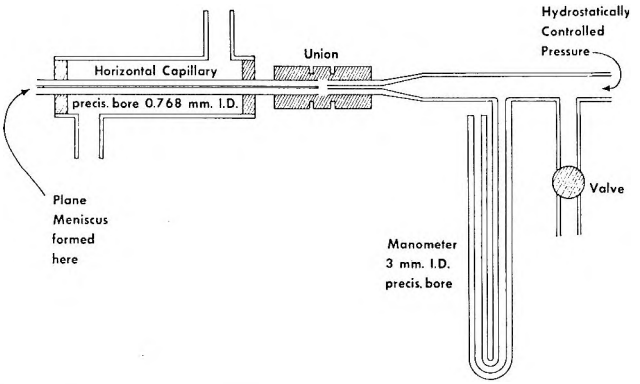


Figure 1. Apparatus for measuring interfacial tensions by the horizontal capillary method.

was the possible oxidation of the hydrocarbons by atmospheric oxygen. Oxidation would form surface-active substances capable of lowering the interfacial tension. The samples of bicyclopentyl and bicyclohexyl were therefore handled under nitrogen in being transferred to the capillary. The capillary and accessories were in a plastic box that was kept under a positive pressure from cylinder nitrogen having a purity of 99.999%.

An essential feature of the experimental procedure was the use of the technique recommended by Ferguson and Kennedy[4] for determining the condition of planarity in the meniscus. They reported that planarity could be determined with great sensitivity by their method, and we confirm this observation. Several readings were taken; each time the pressure was adjusted back and forth beyond the planar meniscus by about 1 mm of water pressure. The planarity of the meniscus was easily detected by the transposition of the image from the filament of the flashlight bulb used to illuminate the meniscus into a broad, bright band across the face of the capillary. When the pressure was too low, the concave hemisphere of liquid in the bore showed an inverted image of the filament much smaller than the band across the face. When the pressure was too great, the convex hemisphere of liquid gave an uninverted image, also reduced.

The principles of the drop-volume method were accurately presented by Lohnstein.[5] Later workers, such as Harkins and his students,[2,6] have rephrased Lohnstein's conclusions, extended his calculations to give greater accuracy, and provided some detailed experience with the method (or the closely related drop-weight method) for surface tension measurements.

The subject of time effects has not been neglected. Harkins and Brown[6] in describing their surface tension measurements comment that one should form each drop over a 5-min interval. They reported that the surface tension of water was high by 0.3% if the drops were formed as fast as possible. We have found the calculated interfacial tension of benzene against water to be 1.7% higher at 2 drops/min than it is at

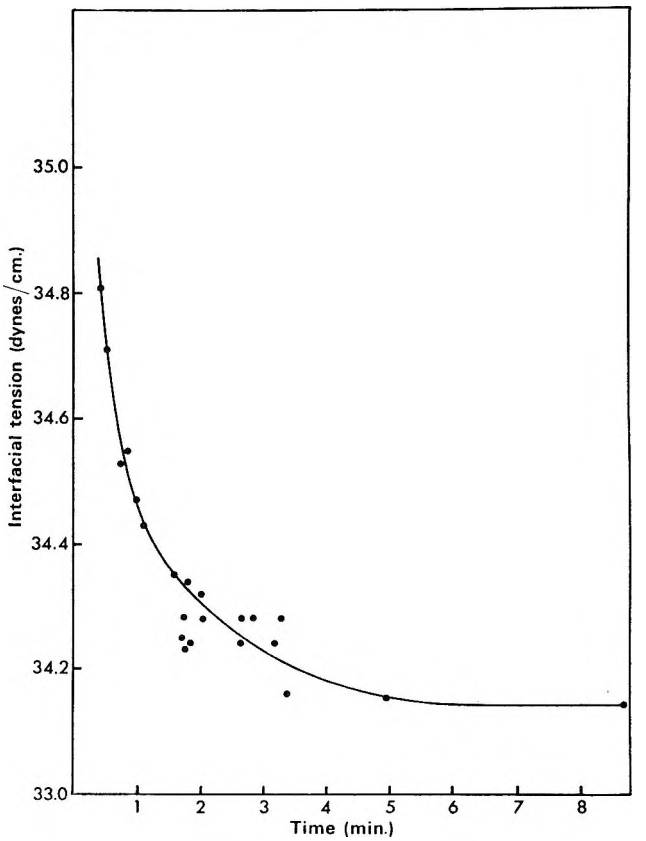


Figure 2. The apparent interfacial tension at the benzene–water interface as a function of time (drop-volume method; 25°).

1 drop/7 min. For interfacial tension measurements with water and benzene 1 drop/5 min is the maximum rate that we consider to give reliable results (Figure 2).

For the substituted benzenes, the following variation in procedure was actually used: 90% or more of the volume of a drop was formed rapidly by raising the pipet. The pipet was then lowered until the drop just started to retreat into the tip. The pipet was then raised very slightly, and the drop allowed to grow slowly until it detached. Results with this procedure corresponded with those obtained for uniform drop growth at a rate of 1 drop/5 min. Matthews[7] had previously observed that this time-saving variant had no effect on results.

Lohnstein's theoretical treatment[5] is based on equilibrium conditions, which means that in any experiment sufficient time must be allowed for equilibrium to be established. The drop-volume method for interfacial tension measurement will not yield the maximum accuracy unless time effects are considered in the experimental work.

(5) T. Lohnstein, *Ann. Phys.* (Leipzig), **20**, 237, 606 (1906).

(6) W. D. Harkins and F. E. Brown, *J. Amer. Chem. Soc.*, **41**, 499 (1919).

(7) J. B. Matthews, *Trans. Faraday Soc.*, **35**, 1113 (1939).

The hydrocarbons whose interfacial tensions against water were measured came from several sources. The alkylbenzenes were tested for purity by vapor-phase chromatography. *n*-Amylbenzene from Beacon Chemical Industries and *n*-heptylbenzene and *n*-nonylbenzene from Orgmet were of high purity and were used as received. *n*-Hexylbenzene from Beacon was purified by two vacuum fractionations through a 10-in. column, 0.75 in. wide, packed with single-turn glass helices. Bicyclopentyl and bicyclohexyl were American Petroleum Institute Research samples and were used without further purification. As noted above, they were handled under nitrogen at all times.

## Results

The measurements of alkylbenzene interfacial tensions against water were all made by the drop-volume method with a tip of radius 0.2966 ± 0.0001 cm and 16–20 drops collected. The results, which cover the range 30–75.5°, fit equations of the form $\gamma = A - Bt - Ct^2$, where $t$ is the temperature in °C. Least-square values for the constants are given in Table I.

**Table I:** Constants of the Equation $\gamma = A - Bt - Ct^2$ Giving Alkylbenzene–Water Interfacial Tension as a Function of Temperature in °C

| *n*-Alkylbenzene | *A*, dyn/cm | *B*, dyn/(cm deg) | *C*, dyn/(cm deg²) |
|---|---|---|---|
| Amylbenzene | 42.2318 | 0.05490 | $3.333 \times 10^{-7}$ |
| Heptylbenzene | 42.9581 | 0.002869 | $5.256 \times 10^{-4}$ |
| Nonylbenzene | 43.0988 | −0.05026 | $1.118 \times 10^{-3}$ |

The greatest deviation of observed interfacial tension from the value calculated by this equation was 0.07 dyn/cm.

An essential part of the drop-volume method was the determination of the density of water saturated with each alkylbenzene and each alkylbenzene saturated with water over the temperature range 30–75.5°. The densities of the aqueous phases were virtually identical with the known densities of pure water at the temperatures investigated. The water-saturated hydrocarbons had densities given by equations of the form $\rho = Z - yt$, and the constants of the equations are given in Table II.

**Table II:** Constants of the Equation $\rho = Z - Yt$ Giving Density of Water-Saturated Alkylbenzenes as a Function of Temperature in °C

| *n*-Alkylbenzene | *Z*, g/cm³ | *Y*, g/(cm³ deg) |
|---|---|---|
| Amylbenzene | 0.8744 | 0.0078 |
| Heptylbenzene | 0.8723 | 0.0074 |
| Nonylbenzene | 0.8697 | 0.0074 |

At 30° the interfacial tensions of these $C_5$–$C_9$ alkylbenzenes against water are approximated by the equation $\gamma = 36.9 + 0.76\,n$, where $n$ = number of carbon atoms in the alkyl group. The greatest deviation of the experimental values from those indicated by the equation is 0.18 dyn/cm. This equation agrees reasonably well with the water–alkylbenzene data obtained for the shorter-chain alkylbenzenes by Bartell, Case, and Brown,[8] but are higher than the interfacial tensions reported by Jasper and Seitz[3] for shorter-chain alkylbenzenes.

The horizontal capillary method was used only at 30°, and the results obtained were: interfacial tension bicyclopentyl–water: 41.2 dyn/cm; interfacial tension bicyclohexyl–water: 38.8 dyn/cm.

The only interfacial tension measured by both methods was that of benzene against water. We obtained 32.5 dyn/cm at 30° by the horizontal capillary method and 34.1 dyn/cm at 25° by the drop-volume method. These can be compared with values of 32.5–35.1 at 25° and 32.3–34.6 at 30° that have been found by previous investigators.[9,10]

## Discussion Based on the Tensions at Surfaces

Much discussion of interfacial tensions has been devoted (and properly so) to the balance of tensions at the liquid–liquid–vapor interface where a lens of the lighter liquid rests atop the surface (*i.e.*, liquid–vapor interface) of the heavier liquid. In the present case we are dealing with pairs of liquids with very little mutual solubility. When solubility is substantial and the surface tensions of the two saturated phases (solutions) are significantly different from the surface tensions of the pure liquids, Antonov's rule[11] is generally applicable. This states that $\gamma_1' - \gamma_2' = \gamma_{12}$ where the primes refer to saturated solutions (Component 1 saturated with Component 2 and Component 2 saturated with Component 1, respectively). Donahue and Bartell[12] have given a very reasonable treatment of Antonov's rule, pointing out that there is one class of systems, which they call Class I, for which $\gamma_{12} + \gamma_2 > \gamma_1$. All their examples of Class I have water

(8) F. E. Bartell, L. O. Case, and H. Brown, *J. Amer. Chem. Soc.*, **55**, 2769 (1933).

(9) The high values are from E. Hutchinson, *J. Colloid Sci.*, **3**, 235 (1948), and are extrapolated between his 25° and his 40° measurements.

(10) The low values are from A. S. Michaels and E. A. Hauser, *J. Phys. Chem.*, **55**, 408 (1951), and are extrapolated between their 23° and 46° measurements. Interfacial tensions at 25° having values between these extremes have been reported by L. F. Transue, *et al.*, *J. Amer. Chem. Soc.*, **64**, 274 (1942), F. E. Bartell and C. W. Bjorklund, *J. Phys. Chem.*, **56**, 454 (1952), D. J. Donahue and F. E. Bartell, *ibid.*, **56**, 480 (1952), and J. E. Shewmaker, *et al.*, *ibid.*, **58**, 945 (1954). The one previous measurement made with a horizontal capillary (Ferguson and Kennedy, ref 4) was at 15°. Depending on the temperature coefficient assumed, it is within 0–0.5 dyn/cm of our horizontal capillary value.

(11) G. N. Antonov, *J. Chim. Phys.*, **5**, 372 (1907).

(12) D. J. Donahue and F. E. Bartell, *J. Phys. Chem.*, **56**, 480 (1952).

as Component 1 and hydrocarbons as Component 2. Shifting to the more convenient subscripts W and H, one can observe that $\gamma_W > \gamma_W'$ and $\gamma_H \simeq \gamma_H'$, so it is a necessary condition of Class I systems that $\gamma_{WH} + \gamma_H' > \gamma_W'$ and Antonov's rule cannot be obeyed.

Donahue and Bartell[12] made solubility measurements on their systems. All the Class I hydrocarbons had extremely low solubility in water and dissolved very small amounts of water. In the homologous series of *n*-alkanes, as the molecular weight increased, $\gamma_{WH} + \gamma_H$ first approached, then became greater than $\gamma_W$. We note the same behavior in our own data (Table III) for the *n*-alkylbenzenes. The bicycloalkyls are very close to the limit of Class I systems in that $\gamma_{WH} + \gamma_H \simeq \gamma_W$. Thus we have extended to two new series of hydrocarbons the observation of Donahue and Bartell that Antonov's rule only applies above a certain critical level of solubility.

**Table III:** Comparison of Surface Tensions and Interfacial Tensions in an Approximate Test of Antonov's Rule (at 30°)

| Hydrocarbon | $\gamma_H$, surface tension, dyn/cm | $\gamma_{WH}$, interfacial tension against water, dyn/cm | $(\gamma_{WH} + \gamma_H)$ | $(71.2 - \gamma_{WH} - \gamma_H)$[a] |
|---|---|---|---|---|
| Bicyclopentyl | 29.8[b] | 41.2 | 71.0 | 0.2 |
| Bicyclohexyl | 31.8[b] | 38.8 | 70.6 | 0.6 |
| *n*-Amylbenzene | 28.5[b] | 40.6 | 69.1 | 1.1 |
| *n*-Hexylbenzene | 29.1[b] | 41.6 | 70.7 | 0.5 |
| *n*-Heptylbenzene | 29.5[c] | 42.4 | 71.9 | −0.7 |
| *n*-Nonylbenzene | 30.2[c] | 43.6 | 73.8 | −2.6 |

[a] 71.2 dyn/cm is the surface tension of water at 30°. The magnitude of the tabulated value is therefore a measure of the approach to that limit of any homologous series of organic compounds for which Antonov's rule ceases to be applicable. [b] Surface tension data taken from J. J. Jasper's compilation being prepared for the National Bureau of Standards under Project CST-357. [c] Extrapolated from data for *n*-alkylbenzenes with $C_1$–$C_6$ alkyl groups.

## Discussion Based on Dispersion Forces at Interfaces

The Girifalco–Good–Fowkes[13,14] calculation of interfacial tensions is based on the concept that the interfacial tension is the sum of the individual surface tensions minus that part of the work of adhesion between the two liquids that arises from surface dispersion forces only. Fowkes[14,15] has had great success with the equation

$$\gamma_{12} = \gamma_1 + \gamma_2 - 2\sqrt{\gamma_1^d \gamma_2^d}$$

to calculate the interfacial tension $\gamma_{12}$ of liquid 1 against liquid 2. For the water interface with saturated hydrocarbons he postulates[15] $\gamma_H = \gamma_H^d$ and calculates, based on $\gamma_{WH}$ for seven saturated hydrocarbons, that $\gamma_W^d$ is 21.8 dyn/cm at 20°.

We have used the Fowkes equation for our own data, which requires correcting $\gamma_W^d$ to 30°. Since this dispersion force should depend only on packing, it is reasonable to use the temperature-independent parameter devised by Sugden[16] and known as the parachor. Then

$$(\gamma_W^d)_{30°}/(\gamma_W^d)_{20°} = [(\rho)_{30°}/(\rho)_{20°}]^4$$

This calculation gives 21.6 dyn/cm for $(\gamma_W^d)_{30°}$.

Based on Fowkes, original suggestion, one would assume that $\gamma_{WH}$ for bicyclopentyl and bicyclohexyl could be obtained by calculating the value of $\gamma_W + \gamma_H - 2\sqrt{21.6\gamma_H}$. Also, $\gamma_{WH}$ for alkylbenzenes might be expected to approach this value as the length of the alkyl chain increased so that the saturated hydrocarbon portion of the molecule would be more significant than the phenyl group. Table IV shows that this is not the case. Fowkes in his earlier work[15] observed that there was a discrepancy of 13–16 dyn/cm between calculated and observed $\gamma_{WH}$ for aromatic hydrocarbons. He based this conclusion on data given by Girifalco and Good[13] for benzene and mono-, di-, and trisubstituted benzenes with short alkyl groups. He ascribed the discrepancy as being due to forces other than dispersion forces and suggested $\pi$ bonds as a possible source of these forces.

In Table IV we have included data for a branched alkane, 2,7-dimethyloctane, which were available in the Girifalco–Good compilation[13] but not cited by Fowkes.[17] It seems very likely that the molecular packing of branched alkanes and of the bicyclic saturated hydrocarbons bicyclopentyl and bicyclohexyl has a major effect on the dispersion forces. Molecular models of the two bicyclic molecules that we have studied readily assume a "clamshell" conformation that would make the surface packing almost certainly looser than that of cyclohexane or decahydronaphthalene.

The conformation of amyl- to nonylbenzene molecules also may lead to looser packing than would be expected for *n*-pentane to *n*-nonane hydrocarbons. The steady decrease in the discrepancy between the calculated and observed interfacial tensions with chain length suggests that the discrepancy might vanish at about *n*-hexadecylbenzene.

The data in the previous section provide an alternative method for evaluating dispersion forces at

(13) L. A. Girifalco and R. J. Good, *J. Phys. Chem.*, **61**, 904 (1957).

(14) F. M. Fowkes, *ibid.*, **66**, 382 (1962).

(15) F. M. Fowkes, *ibid.*, **67**, 2538 (1963).

(16) S. Sugden, "The Parachor and Valency," Routledge, London, 1930.

(17) We note that Fowkes[14] also did not select the pentane and isopentane data from Girifalco and Good's compilation.[13] While these data lend some support to the ideas developed here, we are aware of the experimental difficulties encountered in making measurements with such volatile materials and therefore agree with Fowkes that these data should not be used as a basis for theoretical conclusions.

**Table IV:** Comparison of Observed Interfacial Tensions with Interfacial Tensions Calculated on the Assumption that Dispersion Forces Are Constant at Water–Hydrocarbon Interfaces

| Hydrocarbon | Temp, °C | $\gamma_W$, dyn/cm | $\gamma_H$, dyn/cm | $\gamma_W{}^d$, dyn/cm | $\gamma_H{}^d$, dyn/cm | $\gamma_{WH}$, calcd | Dyn/cm, exptl |
|---|---|---|---|---|---|---|---|
| *n*-Hexane | 20 | 72.8 | 18.4[a] | 21.8[b] | 18.4[b] | 51.2 | 51.1[a] |
| *n*-Heptane | 20 | 72.8 | 20.4[a] | 21.8[b] | 20.4[b] | 51.1 | 50.2[a] |
| *n*-Octane | 20 | 72.8 | 21.8[a] | 21.8[b] | 21.8[b] | 51.0 | 50.8[a] |
| *n*-Decane | 20 | 72.8 | 23.9[a] | 21.8[b] | 23.9[b] | 51.1 | 51.2[a] |
| *n*-Tetradecane | 20 | 72.8 | 25.6[a] | 21.8[b] | 25.6[b] | 51.1 | 52.2[a] |
| Cyclohexane | 20 | 72.8 | 25.5[a] | 21.8[b] | 25.5[b] | 51.1 | 51.4[a] |
| Decahydronaphthalene | 20 | 72.8 | 29.9[a] | 21.8[b] | 29.9[b] | 51.7 | 51.3[a] |
| 2,7-Dimethyloctane | 20 | 72.8 | 22.2[a] | 21.8[b] | 22.2 | 51.0 | 46.8[a] |
| Bicyclopentyl | 30 | 71.2 | 29.8[c] | 21.6 | 29.8 | 50.2 | 41.2 |
| Bicyclohexyl | 30 | 71.2 | 31.8[c] | 21.6 | 31.8 | 50.7 | 38.8 |
| *n*-Amylbenzene | 30 | 71.2 | 28.5[c] | 21.6 | 28.5 | 49.8 | 40.6 |
| *n*-Hexylbenzene | 30 | 71.2 | 29.1[c] | 21.6 | 29.1 | 49.9 | 41.6 |
| *n*-Heptylbenzene | 30 | 71.2 | 29.5[d] | 21.6 | 29.5 | 50.1 | 42.4 |
| *n*-Nonylbenzene | 30 | 71.2 | 30.2[d] | 21.6 | 30.2 | 50.2 | 43.6 |

[a] L. A. Girifalco and R. J. Good, *J. Phys. Chem.*, **61**, 904 (1957). [b] F. M. Fowkes, *ibid.*, **67**, 2538 (1963). [c] Surface tension data taken from J. J. Jasper's compilation being prepared for the National Bureau of Standards under Project CST-357. [d] Extrapolated from data for *n*-alkylbenzenes with $C_1$–$C_6$ alkyl groups.

interfaces. In any homologous series of hydrocarbons, solubility in water decreases with increasing molecular weight. The sum of hydrocarbon surface tension and interfacial tension against water ($\gamma_H + \gamma_{WH}$) approaches the surface tension of water ($\gamma_W$). The Fowkes equation[15] for saturated hydrocarbons

$$\gamma_{WH} = \gamma_H + \gamma_W - 2\sqrt{\gamma_H \gamma_W{}^d}$$

where $\gamma_W{}^d$ is considered to be a constant can therefore have $\gamma_W{}^d$ evaluated simply from surface and interfacial tension data for a homologous series. Those systems that present the equality $\gamma_W = \gamma_H + \gamma_{WH}$ must have $\gamma_H = \gamma_W{}^d$. Inspection of the data for the *n*-alkane homologous series, as tabulated by Donahue and Bartell,[12] shows that $\gamma_W = \gamma_H + \gamma_{WH}$ for *n*-octane, for which hydrocarbon $\gamma_H = 21.8$ dyn/cm at 20°. This is Fowkes' preferred value for $\gamma_W{}^d$ at 20°.

The two bicycloalkyls that we have studied do not have $\gamma_W{}^d = \gamma_H$, even though $\gamma_{WH} + \gamma_H \simeq \gamma_W$. Fowkes' generalization that $\gamma_H = \gamma_H{}^d$ for saturated hydrocarbons has been stated too broadly. It probably should be restated as applying to those saturated hydrocarbons that can pack closely at the water–hydrocarbon interface. 2,7-Dimethyloctane, bicyclopentyl, and bicyclohexyl cannot pack closely, as judged by molecular models, and therefore have $\gamma_H{}^d$ values of 26.5 at 20°, 41.0 at 30°, and 47.2 dyn/cm at 30°, respectively.

## Conclusions

The classification which Donahue and Bartell have proposed, based on Antonov's rule, provides the most useful means of systematizing water–hydrocarbon interfacial tension data such as those obtained in the present work. The Fowkes equation fits the new experimental data, since it has two adjustable parameters. If one parameter, assigned to the dispersion forces on the water side of the interface, is considered to be a constant, the other parameter is qualitatively related to the packing of the hydrocarbons at the interface. There is not enough known about packing at interfaces to permit a quantitative interpretation of this second parameter.

*Acknowledgments.* This work was supported in part by the Petroleum Research Fund and the Atomic Energy Commission. The loan of Standard Samples of bicyclopentyl and bicyclohexyl by the American Petroleum Institute is also gratefully acknowledged.

# A Carbon Monoxide–Oxygen Molten Polyphosphate Fuel-Type Cell[1]

by Leslie Gutierrez and James L. Copeland

*Department of Chemistry, Kansas State University, Manhattan, Kansas 66502* *(Received December 16, 1968)*

An electrochemical cell of the type: CO(Pt); $Na_4P_2O_7$, $NaPO_3$; $(Pt)O_2$ has been studied with the objective of electrochemically determining thermodynamic properties associated with the high-temperature formation of $CO_2$ from CO. The respective anode and cathode reactions may be: anode, $CO(g) + P_2O_7^{-4} = CO_2(g) + 2PO_3^- + 2e^-$; cathode, $0.5O_2(g) + 2PO_3^- + 2e^- = P_2O_7^{-4}$; and net reaction, $CO(g) + 0.5O_2(g) = CO_2(g)$. Mixtures of CO and $CO_2$, at various partial pressure ratios, served as the anode, and $O_2$ at atmospheric pressure served as cathode. The partial pressure ratios of $CO_2$ to CO studied were 0.258, 0.656, 1.00, 3.17, and 9.00, in addition to a run involving pure CO. These gases were introduced over Pt substrates into separate wells of a Vycor cell which contained an electrolytic melt of 33 wt % $Na_4P_2O_7$, 67 wt % $NaPO_3$. The emf's generated by the cell at each partial pressure ratio of $CO_2$ to CO were measured from 650 to 750°. The $\Delta G$, $\Delta H$, $\Delta S$, and $K$ (equilibrium constant) values for the oxidation of CO to $CO_2$ were calculated in the usual way and compared to their predicted values from literature thermochemical tabulations. Deviations of less than 10% from predicted were found for $\Delta G$, with $\Delta S$ possessing the largest deviation from its predicted value (30–50%). Although the cell was found not to behave entirely reversibly, it possesses interesting possibilities as a fuel cell.

## Introduction

In recent years attempts have been made to study electrochemical cells with molten salt electrolytes in which the net chemical reaction represents only the consumption of $O_2$ and C and the formation of $CO_2$.[2-5] Such cells could have significance in two areas: (a) they might be used to determine electrochemically the thermodynamic functions associated with the high-temperature formation of $CO_2$, and (b) they may have fundamental importance in fuel cell research.

Unfortunately, such studies have not met with extensive success because of either the irreversible behavior of the electrode system or mechanical problems associated with the corrosive nature of most electrolyte melts at operational temperatures.

It had been assumed that emf data could be obtained very near the theoretical values if one could find a suitable electrolyte system compatible with the cell container and alter some previous procedures. This, in turn, could enable calculations of the thermodynamic properties of high-temperature formation of $CO_2$ nearer their theoretical values. It was in the light of this assumption that the present work has resulted. Although we were not able to confirm this assumption, interesting results were nevertheless obtained.

The investigation has extended previous work by using a molten polyphosphate system as the electrolyte and CO (rather than C) as the reductant. The work involves potentiometric study of the electrochemical oxidation of CO at high temperatures and includes (a) emf measurements as a function of temperature from 650 to 750°, (b) emf measurements as a function of various partial pressure ratios of $CO_2$ to CO, (c) the ability of the simple system to generate a sustained electrical current, (d) calculation of *apparent* high-temperature thermodynamic functions associated with the formation of $CO_2$ from CO and $O_2$, and (e) interpretation of the results by comparison with theoretical thermodynamic properties and possibilities of the system as a potential fuel cell.

## Experimental Section

*Materials and Apparatus.* Reagent grade $NaPO_3$ and $Na_4P_2O_7 \cdot 10H_2O$ were obtained from the Baker and Adamson Co. The $Na_4P_2O_7 \cdot 10H_2O$ was dehydrated as completely as possible by heating in a porcelain casserole over a burner for *ca.* 2 hr. This sample, as well as the $NaPO_3$, was oven-dried at *ca.* 130° for an additional 72 hr. The samples were cooled in a Drierite-containing desiccator before being used. It had been established earlier by accurate pre- and post-weighings that this procedure quantitatively converted the decahydrate to $Na_4P_2O_7$.

Carbon monoxide was obtained from the Matheson Co., and $CO_2$ and $O_2$ were from the National Cylinder Gas Co. The CO was CP grade (99.5% min. purity), the $O_2$ was USP grade, and the $CO_2$ was (at the time) of unknown purity. Mass spectrometric analyses established the gases to be of actual high purity. All gases were passed through $Mg(ClO_4)_2$ drying towers prior to entry into the cell.

Reagent grade dibutyl phthalate was obtained from the Baker and Adamson Co., and was used as the manometric fluid in constructed flowmeters.

(1) This paper was presented in part at the fourth Midwest Regional Meeting of the American Chemical Society, Manhattan, Kan., Nov 1968.

(2) F. R. Duke and J. L. Copeland, USAEC Report IS-665 (1963).

(3) L. A. King and F. R. Duke, *J. Phys. Chem.*, **68**, 1536 (1964).

(4) G. J. Young and R. B. Rozelle, *J. Chem. Educ.*, **36**, 68 (1959).

(5) J. Weissbart, *ibid.*, **38**, 276 (1961).

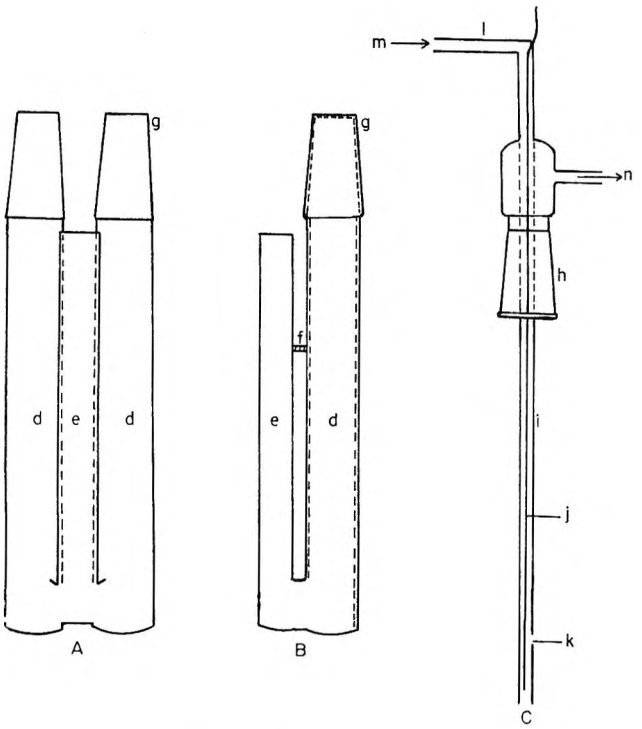


Figure 1. Vycor cell and gas electrode. A and B are front and side views of the cell container, respectively, and C is a gas electrode. Electrode wells are designated by d, e is a thermocouple well, f is a brace, g is an inner Vycor standard taper joint, h is an outer Vycor standard taper joint, i is a gas delivery tube, j is a Pt wire, k is the gas exit orifice, l is a Pyrex tube, m is the gas inlet, and n is the gas outlet.

The cell, shown in Figure 1, consisted of a U-shaped, 17-mm o.d. Vycor tube with 30-cm limbs. The latter terminated in 24/40 standard taper Vycor inner joints, and when in place the limbs extended upward out of a vertical, cylindrical electrical resistance furnace with a 2-in. Alundum core. A 13-mm Vycor tube extended upward from the center of the cell to allow introduction of a chromel–alumel thermocouple. All three limbs were commonly joined at the bottom of the cell. Figure 1 also includes a drawing of the $CO$–$CO_2$ and $O_2$ electrodes. Vycor gas delivery tubes, 6-mm o.d., extended 31 cm down from the ring seals in the outer 24/40 standard taper Vycor joints. Vycor–Pyrex graded seals, 6-mm o.d., permitted the upper portions of the electrodes to terminate in 6-mm o.d. Pyrex tubing. Platinum wires, 24 gauge, which served as electrical contacts and electrode substrates, were sealed into the Pyrex at the upper ends of the electrodes and extended downward to within 1.5 cm of the ends of the delivery tubes. Small holes were placed 3.8 and 3.2 cm above the ends of the $CO_2$–$CO$ and $O_2$ electrodes, respectively, to allow the gases to exit from the delivery tubes without forcing the melt out of the ends of them.

Gas flowmeters were constructed from 7-mm o.d. Pyrex tubing and 2-mm i.d. Pyrex capillary. Dibutyl phthalate was the manometric fluid, and the assemblies were calibrated using their respective gases, an electric timer, and a gas buret.

*Procedure.* The cell container was thoroughly washed with dichromate cleaning solution, and was rinsed repeatedly with distilled water and finally with deionized water. The electrodes were first cleaned with hot, concentrated $HNO_3$ and rinsed with distilled and deionized water. After the electrodes had dried, the Pt wires were heated to a red glow with an oxygen torch to remove any additional contamination.

A 33 wt % $Na_4P_2O_7$–67 wt % $NaPO_3$ mixture was prepared, corresponding to a eutectic whose melting point is 575°.[6] The solid mixture was placed in the Vycor cell and was fused. The level of the melt was such that the small gas exit orifice of the $O_2$ electrode was slightly below the level of the melt, and that of the $CO$–$CO_2$ electrode was slightly above it. Thus, only the $O_2$ would bubble into the melt. The $CO$–$CO_2$ gas mixture was not bubbled because of the difficulty in reading the appropriate flowmeters.

The gas flow system was constructed and employed as follows. Tygon tubing was used throughout when required for flexibility. Gases flowed from their respective cylinders through $Mg(ClO_4)_2$ drying towers, then through flowmeters, and finally into 250-ml erlenmeyer flasks before entering their respective electrodes. The flasks served as traps to prevent any dibutyl phthalate in the flowmeters from flowing into the cell in the event of any sudden change in flow rates. The $CO$ and $CO_2$ were mixed between their respective flowmeters and an erlenmeyer flask, before passage into the anode, by means of a 7-mm o.d. Pyrex Y-connector.

Initially only $CO$ and $O_2$ were passed into the cell and allowed to react at 750° to achieve stability, as indicated by potentiometric measurements with a Leeds and Northrup Type K-3 potentiometer. When such stability was achieved (after *ca.* 72 hr) the $CO$ flow rate was adjusted to 1.00 $cm^3\ sec^{-1}$, and the $O_2$ flow rate was set at a constant value of *ca.* 0.3 $cm^3\ sec^{-1}$. The reaction was allowed to equilibrate at these flow rates at 750°. The emf was determined from 750 to 650°, in intervals of 10°, and then from 650 back to 750° in intervals of 10°. Readings were repeated until reproducible values (within ±1.5 mV) were obtained. This procedure was repeated for five different runs, corresponding to different flow rate ratios of $CO_2$ to $CO$, with but the total rate of flow of $CO_2$ plus $CO$ always kept at 1.00 $cm^3\ sec^{-1}$. In all runs the $O_2$ flow rate was maintained constant. The $CO_2 \cdot CO$ flow rate ratios studied were 0.258, 0.656, 1.00, 3.17, and 9.00, in addition to a run involving pure $CO$.

(6) W. S. Ginell, "Molten Phosphate Reactor Fuel. I." AEC Report NAA-SR-5925 (Reactor Technology), Atomics International, A Division of North American Rockwell Corp., Sept 30, 1961.

For a quick estimate of power delivery and current density obtainable, a decade resistance box was placed across the electrode terminals with the cell operating at 750° with pure CO. The resistance was gradually decreased to the point at which the cell was just able to maintain a constant current for several hours, as measured by an in-series microammeter. The corresponding working voltage was ascertained by the potentiometer.

**Results**

It was *assumed*, for purposes of comparison, that the fundamental overall reaction occurring in the electrochemical process was

$$CO(g) \pm 0.5O_2(g) = CO_2(g) \quad (1)$$

by means of hypothetical half-cell reactions naively written as

$$CO(g) + P_2O_7^{-4} = CO_2(g) + 2PO_3^- + 2e^-$$

$$0.5O_2(g) + 2PO_3^- + 2e^- = P_2O_7^{-4} \quad (2)$$

Use of the high-temperature heat tables of Kelley,[7] together with $\Delta H^\circ_{298} = -67.636$ kcal and $\Delta G^\circ_{298} = -61.452$ kcal,[8] for the reaction of eq 1, yield by the usual thermodynamic treatment

$$\Delta H^\circ_T = -68{,}310 + 0.2T + 0.31 \times 10^{-3}T^2 + 1.75 \times 10^5 T^{-1} \text{ cal} \quad (3)$$

and

$$\Delta G^\circ_T = -68{,}310 - 0.2T \ln T - 0.31 \times 10^{-3}T^2 - 0.875 \times 10^5 T^{-1} + 23.3T \text{ cal} \quad (4)$$

for that reaction. The Nernst equation for the reaction is

$$E_T = E^\circ_T - (RT/2F) \ln (P_{CO_2}/P_{CO}P_{O_2}^{1/2}) \quad (5)$$

where $E_T$ is the emf at temperature $T$, $E^\circ_T$ is the standard emf, and the $P$'s are the appropriate partial pressures of the gases (taken as equal to fugacities). Thus, a predicted $E^\circ_T$ value may be found at each temperature with the use of eq 4 and the usual relationship

$$E^\circ_T = -\Delta G^\circ_T/2F \quad (6)$$

$E_T$ may then be predicted at any temperature and ratio of partial pressures from eq 5. Similarly, by the appropriate combinations of these equations and the Gibbs–Helmholtz equation, one may calculate *apparent* $\Delta H$, $\Delta G$, and $\Delta S$ values for eq 1 from experimental emf data, as well as an equilibrium constant, $K$, according to the usual

$$K = \exp(-\Delta G^\circ_T/RT) \quad (7)$$

If $P_{O_2}$ is maintained at 1 atm, then eq 5 reduces to

$$E_T = E^\circ_T - (RT/2F) \ln (P_{CO_2}/P_{CO}) \quad (8)$$

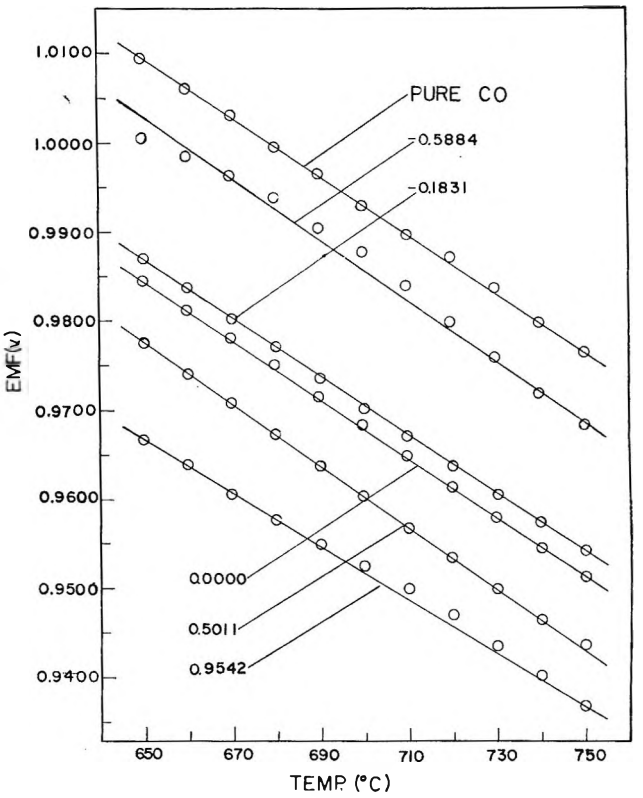


Figure 2. Experimental emf *vs.* temperature. Numbers labeled on curves are values of log $r$ corresponding to the five values of $r$ ratios investigated.

where the $P_{CO_2}/P_{CO}$ ratio ($r$) may be ascertained from the relative flow rates of these gases. In the present work, $O_2$ was always maintained at atmospheric pressure. Table I summarized the slopes of emf *vs.* temperature plots for the six $r$ ratios studied (including $r = 0$ for pure CO) and compares them to the predicted slopes. Figure 2 is the graph of these

**Table I:** Summary of Slopes of Emf *vs.* Temperature (°K) Plots at Various $P_{CO_2}/P_{CO}$

| $r$ | Exptl slope × $10^4$ | Predicted slope × $10^4$ |
|---|---|---|
| 0.258 | −3.33 | −4.02 |
| 0.656 | −3.24 | −4.42 |
| 1.00 | −3.31 | −4.60 |
| 3.17 | −3.46 | −5.10 |
| 9.00 | −2.94 | −5.55 |
| 0 (pure CO) | −3.25 | ... |

(7) K. K. Kelley, "Contributions to the Data on Theoretical Metallurgy. XIII. High-Temperature Heat-Content, Heat-Capacity, and Entropy Data for the Elements and Inorganic Compounds," Bulletin 584, U. S. Bureau of Mines, 1960.

(8) G. N. Lewis and M. Randall, "Thermodynamics," 2nd ed, revised by K. S. Pitzer and L. Brewer, McGraw-Hill Publications, New York, N. Y., 1961, pp 53–73, 158–183.

**Table II:** Summary of Experimental and Predicted Emf Data and Thermodynamic Properties at Various Temperatures with $P_{CO_2}/P_{CO} = r = 1.00$

| Temp, °K | $E°_T$, V, exptl | $E°_T$, V, theoret | $-\Delta G°_T$, exptl, kcal | $-\Delta G°_T$, theoret, kcal | $-\Delta H°_T$, exptl, kcal | $-\Delta H°_T$, theoret, kcal | $10^{10}$ $K$, expt, | $10^{11}$ $K$, theoret |
|---|---|---|---|---|---|---|---|---|
| 923 | 0.98430 | 1.04986 | 45.4 | 48.4 | 59.5 | 68.0 | 5.62 | 2.88 |
| 933 | 0.98120 | 1.04522 | 45.3 | 48.2 | 59.5 | 68.0 | 3.98 | 1.95 |
| 943 | 0.97830 | 1.04065 | 43.1 | 48.0 | 59.6 | 68.0 | 2.88 | 1.32 |
| 953 | 0.97520 | 1.03603 | 45.0 | 47.8 | 59.6 | 68.0 | 2.04 | 0.912 |
| 963 | 0.97180 | 1.03143 | 44.8 | 47.6 | 59.6 | 68.0 | 1.48 | 0.631 |
| 973 | 0.96850 | 1.02681 | 44.7 | 47.4 | 59.6 | 68.0 | 1.07 | 0.437 |
| 983 | 0.96510 | 1.02224 | 44.5 | 47.1 | 59.6 | 68.0 | 0.783 | 0.302 |
| 993 | 0.96170 | 1.01762 | 44.4 | 46.9 | 59.6 | 68.0 | 0.578 | 0.214 |
| 1003 | 0.95810 | 1.01303 | 44.2 | 46.7 | 59.5 | 68.0 | 0.425 | 0.151 |
| 1013 | 0.95480 | 1.00843 | 44.0 | 46.5 | 59.5 | 68.0 | 0.316 | 0.107 |
| 1023 | 0.95160 | 1.00385 | 43.9 | 46.3 | 59.5 | 68.0 | 0.237 | 0.077 |

$\Delta S°$(exptl) = −15.3 eu; $\Delta S°$(theoret) = −21.2 eu.

emf–temperature data with slopes as shown in the table.

Table II summarizes the emf–temperature results for the special case of $r = 1$, and the experimental, *apparent* values of $\Delta G°_T$, $\Delta H°_T$, $\Delta S°$, and $K$ together with the corresponding predicted values. Values of these properties have been calculated for the other $r$ ratios as well, but the data are far too numerous for inclusion here. The case of $r = 1$ is adequately representative. Experimental emf values represent averages of several readings taken over periods of several hours. Probable errors were calculated for the experimental, apparent thermodynamic values and were found to be: in $\Delta G_T$, ±0.1 kcal, in $\Delta H_T$, ±0.1 kcal, in $\Delta S$, ±0.1 eu, and these appear to be representative of the errors in these quantities at other temperatures and $r$ values. In comparing the experimental, apparent thermodynamic functions to the predicted values, as exemplified by Table II, for all $r$ values the best agreement is in the free energy changes. Errors of about 10% for this property are found for the smallest $r$ ratio of 0.258, with a trend toward better agreement as $r$ increases (errors of about 6–7% for $r = 1$, to negligible errors for $r = 9.00$). Lack of agreement between predicted and calculated $\Delta H$ values is worse, *ca.* 13%, and is essentially the same at all $r$ values. One interesting feature, however, is that both experimental and predicted enthalpy changes are fairly constant from 650 to 750°, not only within a particular $r$ value, but also with varying $r$ ratios. Agreement between calculated and predicted $\Delta S$ values varies from about 16% error at $r = 0.258$, to about 29% at $r = 1$, to nearly 50% at $r = 9$.

Table III summarizes the slopes of both predicted and experimental emf *vs.* log $r$ plots, with temperatures as indicated. These are least-squares slopes, and the data are graphed in Figure 3. The individual points are not shown for the sake of avoiding confusion because of their dense population. It is seen from Table III that the experimental slopes deviate considerably from the predicted values (*ca.* 75–80%).

**Table III:** Summary of Slopes of Emf *vs.* Log $r$ Plots at Various Temperatures

| Temp, °K | Exptl slope × $10^3$ | Predicted slope × $10^2$ |
|---|---|---|
| 923 | −2.0 | −9.16 |
| 933 | −2.1 | −9.26 |
| 943 | −2.1 | −9.36 |
| 953 | −2.2 | −9.46 |
| 963 | −2.1 | −9.56 |
| 973 | −2.1 | −9.66 |
| 983 | −2.0 | −9.75 |
| 993 | −2.0 | −9.85 |
| 1003 | −2.0 | −9.95 |
| 1013 | −2.0 | −10.05 |
| 1023 | −1.9 | −10.15 |

With this prototype cell, admittedly not yet designed to deliver significant current densities, it was possible at 750° to maintain a constant upper limit current delivery of 28 μA through a load of 28 kilohms at a voltage of 0.784 V for several hours, corresponding to a power of 22 μW. Each of the 24-gauge Pt wire electrodes was immersed in the melt to an extent of about 2 cm, giving an approximate surface area of 0.32 $cm^2$ of a single Pt wire in contact with liquid. Using this value for electrode surface, a current density of *ca.* 0.08–0.09 mA $cm^{-2}$ results. However, this may be low in view of the fact that the major contribution to the anode electrochemical reaction at the $CO$–$CO_2$ electrode is presumably localized at the very small, undeterminable surface area at the melt–metal–gas interface, where the liquid meniscus contacts the wire. This is because the $CO$–$CO_2$ mixture was not bubbled over the Pt, as was stated earlier. This power mea-

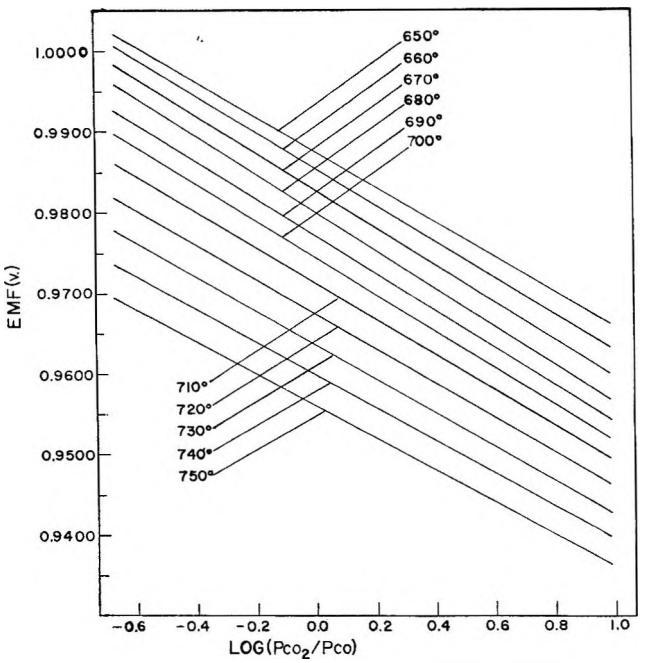


Figure 3. Experimental emf *vs.* common logarithm of the partial pressure ratios of $CO_2$ to CO (log $r$), with temperatures as indicated in °C.

surement was with pure CO, and represents a voltage drop of *ca.* 0.192 V from the open-circuit emf of 0.976 V at this temperature.

## Discussion

It is apparent from the tables and figures that the electrode system did not behave in a reversible manner. This is especially obvious from the large deviations of experimental slopes of $E$ *vs.* log $r$ plots from predicted values (Table III). It is seen from these latter data that the observed emf does not decrease nearly as rapidly with increasing $P_{CO_2}/P_{CO} = r$ ratio as it should if truly reversible. This is true at all temperatures. The implication is, of course, that the activity of CO is greater than indicated by its partial pressure in the entering gas, or that the activity of $CO_2$ is less than indicated by its partial pressure, either case resulting is a smaller effective $r$ value in eq 8. One possible explanation for this would be that the $CO_2$ is undergoing a chemical oxidation to $CO_3^{-2}$ with the melt. Such a path would reduce the effective activity of $CO_2$ below the calculated value to an extent dependent on the final position of the $CO_2$–$CO_3^{-2}$ equilibrium. As one goes to greater entering partial pressures of $CO_2$ relative to CO (greater $r$ values), the expectation would be for the equilibrium to be shifted further in favor of $CO_3^{-2}$ formation. Thus, interpreted in the light of this hypothetical mechanism, one would expect a flatter slope of $E$ *vs.* log $r$ than predicted as a result of the *effective* $r$ becoming ever smaller than expected with increasing $P_{CO_2}$. Other possible sources of error could be due to a small diffusion of $O_2$ from the cathode to anode chamber, or diffusion of air to the anode through the thermocouple well, etc.

Although the present work does not yet indicate feasibility of this system as a possible fuel cell, it does have some worthwhile characteristics for such applications. It was found to be stable, and the observed emf's were quite reproducible. The molten polyphosphate system also affords several advantages over other molten electrolytes, such as carbonates and mixtures of a salt and a corresponding oxide (*e.g.*, the $Na_2WO_4$–$WO_3$ system). With the electrochemical oxidation of CO in a molten carbonate electrolyte, $CO_2$ must always be added with the CO to regenerate the $CO_3^{-2}$ ion.[9] With electrolyte systems in which an oxide is added to a salt,[2,3] the problem of the oxide subliming out of the melt is encountered. The effect would be an ever-changing electrolyte system. In addition, the unusually high corrosive nature of many molten salts is not a characteristic of the polyphosphate system.

*Acknowledgment.* The authors gratefully acknowledge the support of the National Science Foundation, Grant GP-12002, and the Kansas State University Bureau of General Research. This paper is based on the thesis of Leslie Gutierrez, which has been accepted by the Graduate School of Kansas State University in partial fulfillment of the requirements for the degree of Master of Science.

(9) K. R. Williams in "An Introduction to Fuel Cells," K. R. Williams, Ed., American Elsevier Publishing Co., New York, N. Y., 1966, pp 1–13, 156–181.

# The Mesomorphic Behavior of Cholesteryl S-Alkyl Thiocarbonates

**by Wolfgang Elser and Reinhard D. Ennulat**

*U. S. Army Electronics Command, Night Vision Laboratory, Fort Belvoir, Virginia 22060* *(Received September 10, 1969)*

The first 20 members of the cholesteryl S-alkyl thiocarbonates were investigated under the microscope and in the capillary to identify mesomorphic phases and with the differential scanning calorimeter to determine the temperature and the latent heat of each phase transition. All compounds exhibit a cholesteric and, with the exception of the first four members of the series, a smectic mesophase. However, some of these compounds did not show cholesteric colors. The plots of transition temperatures and transition heats as a function of alkyl chain length reveal relationships typical of sterols with cholesteric and smectic mesophases.

Valuable information about the requirements for the existence of cholesteric mesophases as a function of molecular features has been obtained by studying homologous series.[1-5] These studies require extremely pure materials, so that the measurable effects cannot be linked to impurity content, and also require that all errors associated with the physical measurements be ascertained. This entails both a synthesis which yields a minimum amount of impurities and the complete removal of unavoidable side products.

## I. Preparation

Cholesteryl chloroformate[6] (**1**), alkanethiols, and pyridine as a base reacted to form the corresponding cholesteryl S-alkyl thiocarbonates (**2**), in analogy to the synthesis of cholesteryl alkyl carbonates.[2] Cholesterol, 3$\beta$-chlorocholest-5-ene, cholesta-3,5-diene, and dicholesteryl carbonate were formed as side products, while the yield of S-alkyl thiocarbonate was lower than the one obtained for cholesteryl carbonate. An excess of pyridine led to a higher amount of dicholesteryl carbonate. Since some of the formed impurities, especially larger amounts of dicholesteryl carbonate, are difficult to remove by conventional purification methods,[4] other tertiary amines were tried as the base. Because alkanethiols are more acidic than the corresponding alkanols, stronger bases were expected to improve the yields of cholesteryl S-alkyl thiocarbonates. The use of triethylamine resulted not only in a higher yield but also in a substantial lessening of cholesterol and dicholesteryl carbonate. Cholesteryl diethyl carbamate (**3**), another expected side product in the reaction with triethylamine as a base, could not be detected. As reported for stigmasteryl chloroformate,[7] it is formed by reaction of **1** with either triethylamine or an excess of diethylamine. The presence of the more acidic alkanethiol apparently prevents this side reaction.

For purification, the compounds were chromatographed on silica gel, which allowed a separation from cholesterol and dicholesteryl carbonate, as demonstrated by thin-layer chromatographic analysis (Figure 1). Because of the high effectiveness of this method in separating these impurities, all remaining contaminants must originate in the starting materials. This aspect, extensively covered in the Experimental Section, leads to the conclusion that the prepared series of cholesteryl S-alkyl thiocarbonates has a minimum purity of 98% with the exception of cholesteryl S-pentadecyl thiocarbonate, which may contain about up to 5% of the tetradecyl thiocarbonate. The physical properties, yields of analytically pure compounds, analytical

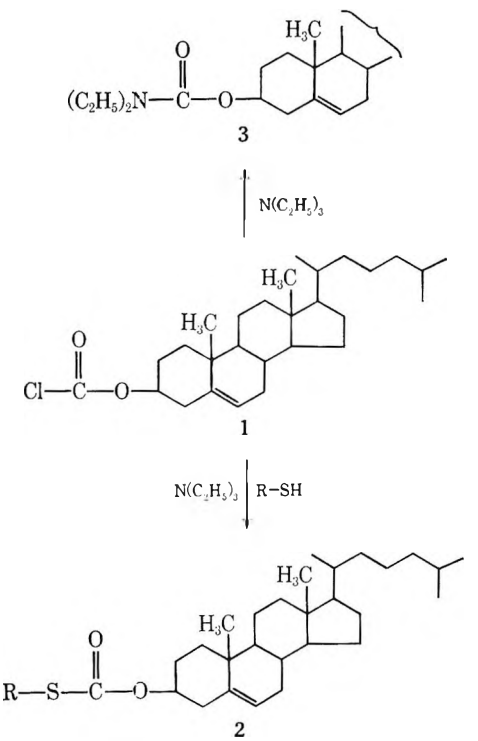


(1) R. D. Ennulat, *Mol. Cryst. Liq. Cryst.*, **8**, 247 (1969).
(2) W. Elser, *Mol. Cryst.*, **2**, 1 (1966).
(3) J. L. W. Pohlmann, *ibid.*, **2**, 15 (1966).
(4) J. L. W. Pohlmann and W. Elser, *Mol. Cryst. Liq. Cryst.*, **8**, 427 (1969).
(5) W. Elser, *ibid.*, **8**, 219 (1969).
(6) A. F. McKay and G. R. Vavasour, *Can. J. Chem.*, **31**, 688 (1953).
(7) J. A. Campbell, *J. Org. Chem.*, **22**, 1259 (1957).

**Table I:** Cholesteryl S-Alkyl Thiocarbonates

| R(alkyl) | Yield, % | Mp, °C | S–Ch,[a] °C | Ch–I,[b] °C | Formula | Mol wt | Anal. values, % Calcd C | Calcd H | Calcd S | Found C | Found H | Found S |
|---|---|---|---|---|---|---|---|---|---|---|---|---|
| Methyl | 84 | 101.2 | ... | 103.8 | $C_{29}H_{48}O_2S$ | 460.7 | 75.59 | 10.50 | 6.96 | 75.67 | 10.77 | 6.72 |
| Ethyl | 79 | 114.7 | ... | 97.1 | $C_{30}H_{50}O_2S$ | 474.8 | 75.89 | 10.62 | 6.75 | 76.02 | 10.68 | 6.66 |
| Propyl | 77 | 97.9 | ... | 90.3 | $C_{31}H_{52}O_2S$ | 488.8 | 76.17 | 10.72 | 6.56 | 75.90 | 10.53 | 6.33 |
| Butyl | 78 | 97.5 | ... | 93.3 | $C_{32}H_{54}O_2S$ | 502.8 | 76.43 | 10.80 | 6.37 | 76.31 | 10.63 | 6.53 |
| Pentyl | 75 | 92.9 | 40.3[c] | 87.3 | $C_{33}H_{56}O_2S$ | 516.8 | 76.69 | 10.90 | 6.20 | 76.57 | 10.73 | 6.02 |
| Hexyl | 75 | 94.1 | 58.0[c] | 85.4 | $C_{34}H_{58}O_2S$ | 530.8 | 76.93 | 11.01 | 6.04 | 76.66 | 11.07 | 6.21 |
| Heptyl | 82 | 61.0 | 68.2 | 84.2 | $C_{35}H_{60}O_2S$ | 544.8 | 77.15 | 11.10 | 5.89 | 77.42 | 10.82 | 5.85 |
| Octyl | 78 | 80.9 | 69.8 | 82.3 | $C_{36}H_{62}O_2S$ | 558.9 | 77.39 | 11.18 | 5.74 | 77.30 | 10.89 | 5.74 |
| Nonyl | 77 | 75.2 | 71.8 | 79.3 | $C_{37}H_{64}O_2S$ | 572.9 | 77.57 | 11.26 | 5.60 | 77.53 | 11.31 | 5.80 |
| Decyl | 74 | 78.1 | 71.3 | 77.9 | $C_{38}H_{66}O_2S$ | 586.9 | 77.77 | 11.33 | 5.46 | 77.51 | 11.23 | 5.47 |
| Undecyl | 75 | 72.5 | 69.7 | 74.8 | $C_{39}H_{68}O_2S$ | 600.9 | 77.94 | 11.41 | 5.34 | 77.78 | 11.42 | 5.40 |
| Dodecyl | 74 | 60.6 | 65.2 | 71.6 | $C_{40}H_{70}O_2S$ | 615.0 | 78.12 | 11.47 | 5.21 | 78.02 | 11.40 | 5.40 |
| Tridecyl | 80 | 55.2 | 63.6 | 69.3 | $C_{41}H_{72}O_2S$ | 629.0 | 78.27 | 11.53 | 5.10 | 78.34 | 11.78 | 5.11 |
| Tetradecyl | 76 | 59.4 | 60.8 | 67.6 | $C_{42}H_{74}O_2S$ | 643.0 | 78.45 | 11.60 | 4.99 | 78.49 | 11.51 | 5.20 |
| Pentadecyl | 76 | 62.7 | 61.9 | 67.6 | $C_{43}H_{76}O_2S$ | 657.1 | 78.59 | 11.66 | 4.88 | 78.84 | 11.89 | 4.83 |
| Hexadecyl | 73 | 47.1 | 57.2 | 63.6 | $C_{44}H_{78}O_2S$ | 671.1 | 78.74 | 11.72 | 4.78 | 78.73 | 11.69 | 4.92 |
| Heptadecyl | 73 | 68.3 | 55.8 | 62.4 | $C_{45}H_{80}O_2S$ | 685.2 | 77.88 | 11.77 | 4.68 | 78.73 | 11.69 | 4.82 |
| Octadecyl | 73 | 58.8 | 57.3 | 63.5 | $C_{46}H_{82}O_2S$ | 699.2 | 79.02 | 11.82 | 4.59 | 78.95 | 12.08 | 4.50 |
| Nonadecyl | 75 | 73.6 | 54.1 | 60.6 | $C_{47}H_{84}O_2S$ | 713.2 | 79.14 | 11.87 | 4.50 | 79.25 | 11.91 | 4.82 |
| Eicosyl | 77 | 64.8 | 54.2 | 60.4 | $C_{48}H_{86}O_2S$ | 727.2 | 79.27 | 11.92 | 4.41 | 79.38 | 12.06 | 4.53 |

[a] Smectic–cholesteric transition. [b] Cholesteric–isotropic transition. [c] Microscopical determination.

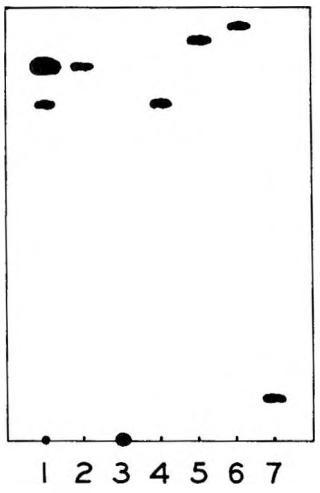


Figure 1. Thin-layer chromatography of products on Silica Gel HR (Merck), benzene–hexane 5:95 (v/v). (1) Cholesteryl S-heptyl thiocarbonate, crude reaction product; (2) cholesteryl S-heptyl thiocarbonate; (3) cholesterol; (4) dicholesteryl carbonate; (5) 3β-chlorocholest-5-ene; (6) cholesta-3,5-diene; cholesteryl diethyl carbamate.

data, and calorimetric determinations are summarized in Table I.

## II. Mesomorphic Behavior

For reasons discussed elsewhere,[8] we identified mesophases by optical means and determined temperatures of phase transitions by thermal analysis. The transition temperatures and transition heats were measured to determine their dependence on chain length.

*Types of Mesophases.* Using a polarizing microscope under conoscopic and orthoscopic operating conditions, we studied samples contained between thin glass cover slips in transmitted and reflected light and heated on a microscope stage. The difference of the optical sign shown by homeotropic textures and the difference of the sign of elongation exhibited by focal conic bands (*i.e.*, Friedel's "oily streaks")[9] permitted a clear distinction of the observed mesophases into smectic and cholesteric. However, several compounds (see Experimental Section) did not exhibit iridescent colors typical of cholesteric mesophases. This behavior may be caused by the failure of forces acting at the liquid crystal–substrate interface to favor the plane texture over coexisting birefringent textures or to align the plane texture sufficiently and thus reduce the diffuseness of selectively reflected light. It is also possible that the temperature-dependent repeat distance required for the interference effect in the visible may not be realized within the temperature range in which the cholesteric mesophases are observed. For example, cholesteryl S-pentyl thiocarbonate displays cholesteric colors only when the homeotropic texture is rapidly and excessively undercooled. In summary, the optical evidence establishes the existence of cholesteric mesophases from cholesteryl S-methyl to S-eicosyl thiocarbonate and a smectic mesophase, occurring at lower temperatures, for S-pentyl thiocarbonate and higher members of the series.

*Transition Temperatures.* The transition temperatures of these compounds were measured with an espe-

(8) R. D. Ennulat in "Analytical Calorimetry," R. S. Porter and J. F. Johnson, Ed., Plenum Publishing Corp., New York, N. Y., 1968, p 219.

(9) G. Friedel, *Ann. Phys.* (Paris), 18, 273 (1922).

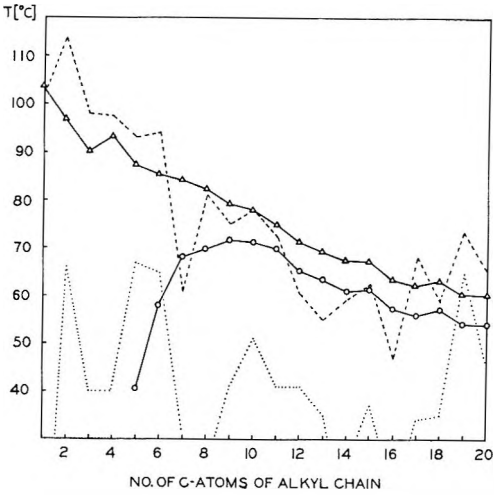


Figure 2. Transition temperatures of cholesteryl S-alkyl thiocarbonates: – – –, melting points; –Δ–, cholesteric–isotropic transitions; –O–, smectic–cholesteric transitions; · · ·, onset of freezing.

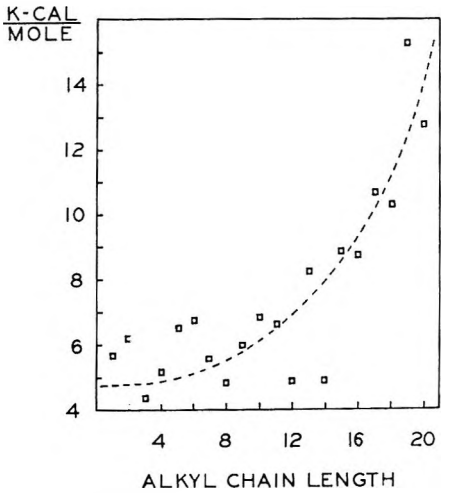


Figure 3. Heats of fusion.

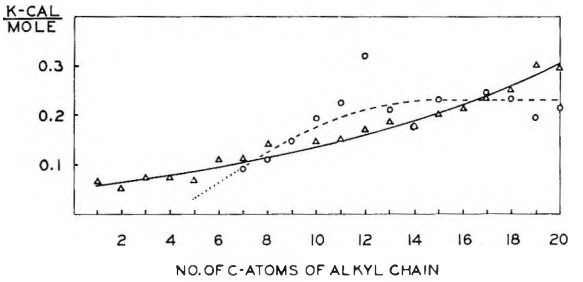


Figure 4. Heats of transitions in the melt: –Δ–, cholesteric–isotropic transitions; --O--, smectic–cholesteric transitions.

cially modified calorimeter[8] (DSC-1, Perkin-Elmer Corp.), with a maximum uncertainty of ±0.4° for transitions in the melt and, because of the higher heat flux, a larger uncertainty of ±1° for melting points. For details see Experimental Section.

In Figure 2 the transition temperatures of the cholesteryl S-alkyl thiocarbonates are plotted as a function of S-alkyl chain length.

As observed in other sterol series some of these compounds exhibit a high melting point after storage at room temperature for hours or days and a low melting point when the sample is immediately measured after solidification obtained at a cooling rate of 10° per minute. Depending on the compound these melting points differ by as much as 18°. We report only the high melting points, because they are presumably associated with the crystal modification stable at and above room temperature. To indicate the low-temperature limit of the melted state we also plotted the onset of freezing with a cooling rate of 10° per min. Both curves show the expected erratic behavior, while the curve of the clearing points and of the smectic–cholesteric transition temperatures indicate a definite relation to chain length. Probably the presence of unknown impurities causes the few major deviations. Because of intervening freezing and because of instrumental limitations of the calorimeter, the monotropic smectic–cholesteric transition temperatures of S-pentyl and S-hexyl thiocarbonate could only be estimated by optical means on rapidly undercooled samples.

*Transition Heats.* Since we were interested in the general trend of transition heats on chain length, we avoided the cumbersome high precision methods of adiabatic calorimetry and used the more expedient but less accurate differential scanning calorimeter. The latter permitted the determination of transition heats in the melt within less than ±20% (for details see Experimental Section). The much larger heats of fusion were measured with an uncertainty of a few per cent.

Figure 3 shows the dependence of the heat of fusion on the chain length. Although only the presumably more stable high melting phases were considered, the scattered data indicate only a general upward trend with chain length. Since no attempt was made to establish thermal equilibrium, a condition which might not even be achievable with the differential scanning calorimeter,[10] the data are unreliable and therefore should only be used qualitatively. In particular, Figure 4 shows that the heat of fusion is at least 40 times larger than the transition heats in the melt.

However, because of the independence of thermal history, the transition heats in the melted state should correspond to thermal equilibrium data at least within the uncertainty of the measurement. This does not contradict the results of light-scattering experiments,[11] which indicate a thermal equilibration time of up to 1 hr for a temperature change within a given mesophase. This time is needed to achieve the average equilibrium size of the ordered regions required for the new tem-

(10) Even much simpler organic compounds attain thermal equilibrium only after many hours of slow crystallization; see J. P. McCullough and G. Waddington, *Anal. Chim. Acta*, **17**, 80 (1957).

(11) L. M. Cameron, *Mol. Cryst. Liq. Cryst.*, **7**, 235 (1969).

perature and not to change the type of the structure during a phase transition. The apparently low viscosity of our melted samples results in a high molecular mobility, which does not permit such structural differences and structural instabilities to exist for long.[12]

Although the transition heats in the melt exhibit the same dependence on chain length observed for other homologous sterols, the scatter of the data is larger than the uncertainty. We assume that unknown nonhomologous impurities are responsible for the marked deviation of the smectic–cholesteric transition heats of dodecyl and tetradecyl thiocarbonate because this deviation cannot be caused by the small amount of homologous impurities in our samples. In spite of the repeated attempts to remove these nonhomologous impurities, we were not able to reduce these discrepancies. As expected, the fact that the pentadecyl thiocarbonate might have contained up to 5% of lower homologs did not cause a noticeable deviation from the general trend of the data. Obviously major and minor components of this material are so close in their molecular properties that the pliable mesophase can accommodate both types of molecules without apparent effect.

The extrapolation of the smetic–cholesteric curve of latent heats beyond $C_7$ toward lower chain length indicates that smectic phases could be expected down to $C_5$. Performing the similar operation on the corresponding transition temperature curve (Figure 2) we find that the transitions for $C_6$ and $C_5$ lie in the freezing region. Optical tests verified the temporary existence of the smectic mesophase in rapidly undercooled samples. However, for shorter chain lengths we observed no smectic mesophase even in cases for which the extrapolated transition temperature is above the freezing curve.

## III. Discussion

Following Gray's reasoning[13] that the purer the compounds the smoother the relationships between chain length and transition temperatures in the melt—and we extend this idea to include transition heats—and considering that the scatter of our data is larger than the measurement uncertainty, we must conclude that the impurity content of our compounds is not negligible. In spite of this shortcoming the extrapolation of our data indicates a definite relation between transition parameters and chain length. This justifies the comparison of our results with those obtained from other homologous series. Disregarding minor variations, the shape of the curves, shown in Figures 2 and 4, is typical for homologous series of sterols exhibiting smectic and cholesteric mesophases and showing no odd-even effects in their chain length dependence. The thermal stability of the cholesteric mesophase decreases with chain length while that of the smectic mesophase first increases and then decreases at about the same rate. This results in an almost constant temperature interval for the cholesteric mesophase from about $C_{10}$ on.

The beginning of the curves for smectic–nematic systems shows the same trend; the nematic clearing points decrease with chain length,[14] while the smectic mesophase, occurring from a certain chain length on, increases in thermal stability. However, with increasing chain length the temperature interval of the nematic mesophase steadily decreases until this phase does not exist. By considering the relative contributions of lateral and terminal forces to molecular interactions, Gray[13] was able to explain the behavior of smectic–nematic systems. However, for smectic–cholesteric series this approach fails. Of course, the increase of the thermal stability of the smectic mesophase can still be explained by the rise in polarizability of the alkyl chain and the resulting larger lateral attraction. But why does the smectic mesophase not displace the cholesteric mesophase? To answer this question we think that Gray's approximation of the molecular force field should be extended by adding a tensorial interaction force. We speculate that the source of this addition may be due to the same asymmetric molecular force field, which is responsible for the optical activity and thus in part for the cholesteric behavior. The latter is supported by the following empirical facts. 1. No nematogenic compound is known which has optically active centers resulting in net optical activity. 2. No cholesteric compound is known that is optically inactive. 3. Certain mixtures of dextro- and laevo-rotatory cholesteric mesophases exhibit nematic behavior at a temperature for which the optical activity vanishes.[9,13] 4. Minute additions of optically active compounds, which are not necessarily mesomorphic, to a pure nematic compound can induce cholesteric behavior of the mesophase.[15] Unfortunately we have no evidence clarifying the features which create the molecular force field essential for the occurrence of cholesteric mesophases. We think that the introduction of the tensorial force implied by optical activity may make the existence of a helical structural plausible. We will attempt empirically to link optical activity data with the chain length dependence of cholesteric transition temperatures.

## IV. Experimental Section

(*a*) *Preparation of Compounds.* The general procedure is exemplified by the first synthesis as outlined

(12) For example, the orientation relaxation time in nematic mesophases is about $10^{-5}$ sec; see ref 33, p 73.

(13) G. W. Gray, "Molecular Structure and Properties of Liquid Crystals," Academic Press, Inc., New York, N. Y., 1962.

(14) Gray mentions a few compounds for which the clearing points rise with chain length, ref 33, p 236. Since we do not know of a counterpart for cholesteric mesophases, we restrict our discussion to homologous series with falling clearing points.

(15) G. Friedel, *C. R. H. Acad. Sci.*, 176, 475 (1923).

below. The proportions of reactants and solvent were the same in all synthetic procedures. The reactions were carried out in a nitrogen atmosphere.

*Cholesteryl S-Ethyl Thiocarbonate* (**1**). A solution of 1.01 g (0.01 mol) of triethylamine in 10 ml of absolute benzene is added to a stirred solution of 4.49 g (0.01 mol) of cholesteryl chloroformate and 0.62 g (0.01 mol) of ethanethiol in 70 ml of absolute benzene within 30 min at room temperature. Stirring is continued for another 2 hr under reflux. Then the cooled reaction mixture is filtered, the solvent distilled off, the residue dissolved in benzene–hexane, and chromatographed on silica gel (45 × 350 mm). Elution with approximately 1500 ml of benzene–hexane (30/70), combination of the fractions containing the S-ethyl thiocarbonate, evaporation of the solvent, and recrystallization of the residue from acetone yields 3.77 g (79%) of colorless needles, mp 113–115°.

*Cholesteryl Diethyl Carbamate* (**2**) (*1*). A solution of 4.49 g (0.01 mol) of cholesteryl chloroformate in 50 ml of absolute benzene and 1.01 g (0.01 mol) of triethylamine is boiled under reflux for 5 hr. The solution is filtered, the solvent evaporated, and the residue twice recrystallized from acetone. Yield: 4.05 g (83.5%); mp 143–144°, not mesomorphic. *Anal.* Calcd for $C_{32}H_{55}NO_2$: C, 79.11; H, 11.41; N, 2.88. Found: C, 79.33; H, 11.81, N, 2.62. Mol wt 485.8.

(*2*) A solution of 4.49 g (0.01 mol) of cholesteryl chloroformate in 50 ml of absolute benzene and 1.46 g (0.02 mol) of diethylamine is heated under reflux for 3 hr. The white precipitate is filtered off, the filtrate evaporated to dryness, and the residue recrystallized twice from acetone. Yield: 4.0 g (82.5%) of material, melting at 143–144°, and identical in all respects with that of reaction 1.

(*b*) *Properties, as Observed in the Capillary of a Büchi Melting Point Apparatus.* (Temperatures are uncorrected and the readings were not adjusted for the thermal lag due to varying heating and cooling rates. These rates were chosen to facilitate observations rather than to obtain temperature equilibrium.)

Cholesteryl S-methyl thiocarbonate melts at 101° and gives a blue color at 103°, which disappears at 104°. On cooling a blue color appears at 104°, which changes to a light blue at 101°, and disappears at 99°, with the now turbid melt solidifying at room temperature.

Cholesteryl S-ethyl thiocarbonate melts at 113–115°. On cooling, a light blue color is exhibited between 96° and 86°.

Cholesteryl S-propyl and S-butyl thiocarbonate do not exhibit cholesteric colors on either heating or cooling.

Cholesteryl S-pentyl thiocarbonate melts at 91–92.5° and on cooling gives a blue color at 86°, which disappears at 52°. Further cooling gives violet at 44°, blue at 43°, green at 42.5°, yellow at 42°, and red at 41.5°, followed by solidification.

Cholesteryl S-hexyl thiocarbonate melts at 91.5–93° and on cooling gives a blue color at 84°, which disappears at 59°. On further cooling, the complete solar spectrum is exhibited between 56° and 53° for an undercooled sample.

Cholesteryl S-heptyl thiocarbonate melts at 62° and clears at 86°. On cooling blue appears at 68°, green at 67.5°, and red at 67°, followed by crystallization.

Cholesteryl S-octyl thiocarbonate melts at 79–80° and on cooling exhibits blue at 78°, followed by a brief green and red at 71.5°, which disappears at 71°.

Cholesteryl S-nonyl through S-tetradecyl thiocarbonate do not exhibit any cholesteric colors on either heating or cooling. However, they do show a slight blue haze on cooling.

Cholesteryl S-pentadecyl thiocarbonate melts at 62–65° and on cooling becomes turbid at 63°, and crystallizes near 40° without exhibiting colors. On rapid cooling the phenomenon of "crystal colors" can be noticed, *e.g.*, cholesteric colors in connection with crystallization.[5]

Cholesteryl S-hexadecyl thiocarbonate melts at 48° and clears at 58°, exhibiting the solar spectrum between 56° and 55° on cooling.

Cholesteryl S-heptadecyl thiocarbonate melts at 67–69° and on cooling turns turbid at 61° and crystallizes at 60°. On rapid cooling, with an air stream blown against the oil bath of the melting point apparatus, cholesteric colors can be observed at 58–57°.

Cholesteryl S-octadecyl thiocarbonate melts at 58.5° and clears at 62°. On cooling the solar spectrum is exhibited around 57.5°.

Cholesteryl S-nonadecyl thiocarbonate melts at 71–73.5°, becomes turbid on cooling to 65°, and starts to crystallize at 62°. On rapid cooling cholesteric colors appear at 52–51°.

Cholesteryl S-eicosyl thiocarbonate melts at 64–66°. On cooling it becomes turbid at 63° with the solar spectrum appearing at 57–56°.

(*c*) *Purification.* The crude compounds, prepared on a 0.01-mol scale, were chromatographed on silica gel (45 × 350 mm) and eluted with mixtures of *n*-hexane and benzene. Dicholesteryl carbonate was eluted first, followed by the thiocarbonate, with cholesterol being retained on the column. For the lower members (up to $C_8$) a 70:30 mixture of hexane–benzene was used, while an 85:15 mixture was sufficient for the higher members. The fractions were monitored by thin-layer chromatography for the presence of impurities, and then the materials were recrystallized from acetone or acetone–butanone for the higher members. No change in the transition temperatures was observed after several additional recrystallizations and thin-layer chromatography gave only one spot.

(*d*) *Detection of Impurities.* (*1*) *Thin-layer Chromatographic Methods.* Ascending thin-layer chromatography was performed on 0.25-mm layers of Silica Gel HR (Merck) and Aluminum Oxide H (Merck). The plates were activated for 1 hr at 120° before use.

As in the case of cholesteryl esters,[16,17] thin-layer chromatographic separation of the lower members is easily achieved. This technique, however, does not allow satisfactory separation of individual members from cholesteryl S-octyl through S-eicosyl thiocarbonate. By reversed-phase partition thin-layer chromatography cholesteryl esters of long-chain fatty acids can be separated[17,18] on silica gel layers impregnated with paraffins[19] or silicone oil.[20] This method gives a clear separation of cholesteryl hexadecanoate and cholesteryl octadecanoate, although the $R_F$ values are close together. However, cholesteryl heptadecanoate and cholesteryl octadecanoate are only slightly separated from each other. The same negligible separation was found for an attempted separation of cholesteryl S-nonyl and S-decyl thiocarbonate on silanized and tetradecane-impregnated layers of silica gel and aluminum oxide in the solvent systems benzene–hexane, acetonitrile–butanone, tetralin–hexane, and acetonitrile–acetic acid.

Two-dimensional thin-layer chromatography, using reversed-phase separation in the first dimension, followed by impregnation with silver nitrate before the second development, was also not conclusive. This procedure works well in the separation of cholesteryl esters[10] and fatty acid methyl esters,[21] which are separated according to chain length, structure, and configuration.

Gradient thin-layer chromatography,[22,23] with gradients between silica gel and aluminum oxide, and silica gel with up to 50% silver nitrate, respectively, also did not give a clear separation between adjacent homologs.

These results show that thin-layer chromatographic methods are of little value for the detection of minor contaminations of the higher members with close homologs.

(*2*) *Gas-Liquid Chromatography of Alkanethiols.* Because of thermal instability of cholesteryl S-alkyl thiocarbonates, a direct gas chromatographic analysis is ruled out. An alternative solution is the analysis of the starting materials. The alkanethiols, partially obtained from commercial sources and redistilled under nitrogen, and partially prepared from high-purity alkanols (99+%) *via* the bromide and the isothiuronium bromide,[24] were checked for purity by gas–liquid chromatography. The materials generally had a purity of about 98% with the following exceptions: pentadecanethiol contained about 5% tetradecanethiol, hexadecanethiol about 8% octadecanethiol, and octadecanethiol about 10% hexadecanethiol. The analyses were performed on 6-ft glass columns packed with 3% QF-1 and 15% Carbowax 20M, respectively, on silanized support. The instrument used was a Hewlett-Packard F & M Gas Chromatograph Model 5756B with electronic integrator.

As already outlined, a thin-layer chromatographic separation of cholesteryl S-hexadecyl and S-octadecyl thiocarbonate is achieved, and both compounds were uniform on thin-layer chromatography. The only remaining ambiguity is cholesteryl S-pentadecyl thiocarbonate, which may contain some of the tetradecyl thiocarbonate. This may, to some extent, explain the observed "crystal colors," although the same phenomenon has been observed in several stigmasteryl S-alkyl thiocarbonates.[5]

(*e*) *Stability.* The prepared cholesteryl S-alkyl thiocarbonates form a variety of products over a period of several months. The same behavior was also found in the series of cholesteryl alkyl carbonates. Only two of these products, cholesterol and dicholesteryl carbonate, could be identified by thin-layer chromatography and verified with authentic samples after chromatographic isolation. However, if the materials were kept in the cold (−35°) and in the dark, decomposition was not observed over a period of several months.

(*f*) *Infrared Spectra.*[25] Cholesteryl S-heptyl thiocarbonate shows infrared absorption at 1695 $cm^{-1}$ (C=O stretch) and 1160 $cm^{-1}$ (C—S stretch), in agreement with reported frequencies of thiol esters.[26,27] This is a distinct shift to longer wavelengths compared with those of cholesteryl alkyl carbon ates,[2,28] which absorb at 1735–1741 $cm^{-1}$ and 1265–1270 $cm^{-1}$.

(*g*) *Measurement Uncertainty of the Modified Scanning Calorimeter DSC-1.* (*1*) *Temperature.* Using reference materials with melting points known within ±0.1°, we obtained the calibration curve of the temperature scale, shown in Figure 5, for samples weighing

(16) H. Weicker, *Klin. Wochenschr.*, **37**, 763 (1959).

(17) H. P. Kaufmann, Z. Makus, and F. Deicke, *Fette, Seifen, Anstrichm.*, **63**, 235 (1961).

(18) Č. Michalec, M. Šulc, and J. Meštan, *Nature*, **193**, 63 (1962).

(19) H. P. Kaufmann and Z. Makus, *Fette, Seifen, Anstrichm.*, **62**, 1014 (1960).

(20) D. C. Malins and H. K. Mangold, *J. Amer. Oil Chem. Soc.*, **37**, 576 (1960).

(21) L. D. Bergelson, E. V. Dyatlovitskaya, and V. V. Voronkova, *J. Chromatogr.*, **15**, 191 (1964).

(22) E. Stahl, *Angew. Chem., Int. Ed., Engl.*, **3**, 784 (1964).

(23) C. G. Honegger, *Helv. Chim. Acta*, **47**, 2384 (1964).

(24) G. G. Urquhart, J. W. Gates, Jr., and R. Connor in "Organic Syntheses," Coll. Vol. III, E. C. Horning, Ed., John Wiley and Sons, New York, N. Y., 1955, p 363.

(25) The samples were examined in KBr disks and the spectra recorded on a Perkin-Elmer Model 421 double-beam grating spectrometer.

(26) A. W. Baker and G. H. Harris, *J. Amer. Chem. Soc.*, **82**, 1923 (1960).

(27) R. A. Nyquist and W. J. Potts, *Spectrochim. Acta*, **17**, 769 (1961).

(28) J. L. Hales, J. I. Jones, and W. Kynaston, *J. Chem. Soc.*, 618 (1957).

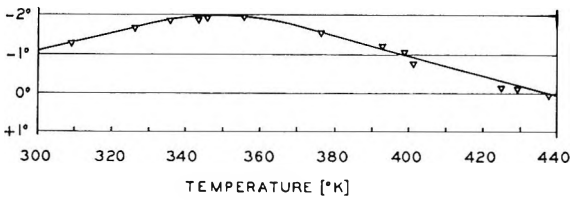


Figure 5. Calibration curve for differential scanning calorimeter. Temperature is corrected by adding value of ordinate to instrument reading. The following zone-refined materials were used—with increasing melting points: 2-methylnaphthalene; 4-nitrotoluene; cyclododecane; biphenyl; 1,4-diethoxybenzene; naphthalene; xanthene; 4,4′-azoxyanisole; *trans*-stilbene; benzamide; adipic acid; indium; benzanilide.

less than 1 mg. Repeated calibration tests revealed that unknown changes of the instrument caused a unidirectional parallel shift of this curve accumulating within several months to 0.2°. Correcting for this shift and considering that the temperature indication is reproducible with a standard deviation of ±0.2°,[29] we estimate for measurements of transition temperatures of the melted state a maximum uncertainty of ±0.4°.

The determination of melting points of samples weighing more than 1 mg requires an additional correction to allow for the temperature difference between the center of the sample and the temperature sensor of the instrument[30] caused by the much higher heat flux occurring during melting. The correction ranged from 0.6 to 0.9° and, due to variations of the thermal contact resistance between sample capsule and heating platform, had an uncertainty of ±50%. As a result the melting points of the homologous series were determined within ±1°. The sample weight was chosen to be large enough for the detection of small latent heats and small enough to obtain instrument limited operating conditions and thus a definable transition temperature. These conditions are fulfilled for any weight between 5 and 10 mg.

(2) *Transition Heats.* The scanning calorimeter records the heat flux entering or leaving the sample as a function of the time during which the temperature linearly increases or decreases. At the beginning of the phase transition the heat flux deviates from a constant value, rises almost linearly, and, at the end of the transition, drops back to a constant value. The area between this approximately triangular transition curve and the straight base line is proportional to the latent heat of the phase transition. By using the known heat of fusion of pure indium as a reference this instrument can be calibrated with a precision of a few per cent.[30] Based on the assumption that certain amplifiers in the instrument have a negative feedback of about 99% we estimate an additional uncertainty of ±1% of full scale.

Since transitions in the melt yield transition curves with peak heights ranging from 0.1 to 0.4 of full scale even for the most sensitive instrument settings,[31] we obtain uncertainties of between ±4 and ±10% with respect to the peak height. In addition spurious fluctuations of the recording prevent the precise location of the base line. This error of judgment is increased by the presence of sample impurities, which reduce the peak height and widen the base of the transition curve. We estimate a total uncertainty of less than ±20% for all compounds except for cholesteryl S-nonadecyl thiocarbonate. Since the smectic–cholesteric transition curve of the latter was superimposed on the beginning of the freezing curve, we could only estimate the lower limit of the latent heat.

*Acknowledgment.* The authors are grateful to Mr. A. J. Brown for obtaining the calorimetric data and to Dr. L. M. Cameron and Dr. J. L. W. Pohlmann for many valuable discussions.

(29) Thermal Analysis Newsletter, No. 5, Perkin-Elmer Corp., Norwalk, Conn.

(30) R. F. Schwenker, Jr., and J. C. Whitwell in "Analytical Calorimetry," R. S. Porter and J. F. Johnson, Ed., Plenum Publishing Corp., New York, N. Y., 1968, p 249.

(31) This modified instrument is ten times more sensitive than the standard version.

# The Thermal Decomposition of Solid Hexaamminecobalt(III) Azide. Kinetics of the Cobalt Nitride Reaction

by Taylor B. Joyner

*Research Department, Naval Weapons Center, China Lake, California 93555* *(Received March 14, 1969)*

The isothermal rates of the decomposition of solid hexaamminecobalt(III) azide to CoN have been measured in the temperature range of 95–150°. Samples ranging from microcrystalline powders to large single crystals all show induction periods. Both the final reaction and the induction periods in the absence of ammonia yield apparent activation energies of about 25 kcal/mol. Small quantities of ammonia prolong the induction period and give higher apparent activation energies. The final reaction is independent of ammonia. The induction period can be shortened by dusting the reactant with CoN or freshly prepared metallic cobalt. These observations and the similar kinetic parameters found for substituted cobalt(III) ammine azides suggest a rate-controlling step involving an interaction of the ionic, lattice azide with the solid product.

## Introduction

Solid cobalt(III) ammine azides can decompose to either cobalt(II) complexes or CoN. The rather complicated relationship of the two systems has been discussed qualitatively for hexaamminecobalt(III) azide,[1] and the kinetics of the cobalt(II) reaction have been analyzed.[2] Quantitative studies of the substituted azidopentaamminecobalt(III) azide[3] and *cis*- and *trans*-diazidotetraamminecobalt(III) azides[4,5] revealed analogous reactions and indicated that topography is particularly important in the CoN decomposition. This reaction

$$[Co(NH_3)_6](N_3)_3 \longrightarrow CoN + 6NH_3 + 4N_2 \quad (1)$$

has a well-defined induction period and a relatively fast, final reaction. Study of both periods permits some understanding and separation of the chemical and topographic aspects of the decomposition. This paper considers the former. These depend only on a quite general analysis and form the basis for the comparison with the substituted compounds upon which the subsequent discussion of mechanism will rest.

The experiments of this paper were designed to avoid the cobalt(II) reaction

$$[Co(NH_3)_6](N_3)_3 \longrightarrow Co(NH_3)_2(N_3)_2 + 4NH_3 + 1.5N_2 \quad (2)$$

It is, however, a potential competitor, and a full discussion should account for both it and the unusual form of the CoN reaction. A consideration of reaction topography (second paper in series[6]) can explain the existence of an induction period, its relationship to the observable CoN reaction, and the complex interplay of the cobalt(II) and CoN reactions. The model is applicable to all four compounds. A final paper[7] discusses mechanisms for the series.

## Experimental Section

*Preparation.* Preparation and purification have been described.[1] The usual recrystallization from warm water gives lathlike crystals ranging in size from about $1 \times 0.3 \times 0.1$ mm to $0.2 \times 0.1 \times 0.02$ mm. The kinetic study made extensive use of two such samples labeled "Crystals(A)" and "Crystals(B)." The latter was used in probing, in particular, the induction period, and detailed presentation of the data will be deferred until the following paper.[6] To study the effects of particle size, "Powder" with crystal sizes in the range of $10^{-4}$ to $10^{-3}$ mm was prepared by rapid precipitation of an aqueous solution with excess alcohol. (This particular sample was also the "Preparation B" in the study of the cobalt(II) reaction.[2]) Slower addition of the alcohol gave a sample, labeled "Small-crystals," with crystals up to *ca.* 0.01 mm in length but also containing smaller particles comparable to "Powder." Dark, room-temperature evaporation of an aqueous solution gave "Large-crystals" up to 13 mg in weight and roughly $3 \times 3 \times 1$ mm in size. All identities were checked by powder patterns.[8] During preparation particular attention was given to avoiding conditions which might lead to contamination with the double salt $[Co(NH_3)_6](N_3)_3 \cdot 3NaN_3$.[8] Storage was over $P_2O_5$ in an opaque vacuum desiccator.

*Procedure.* The apparatus and procedure have been described.[1,9] Again, "normal" runs began with the

(1) T. B. Joyner and F. H. Verhoek, *Inorg. Chem.*, **2**, 334 (1963).
(2) T. B. Joyner, *J. Phys. Chem.*, **72**, 4386 (1968).
(3) T. B. Joyner, *ibid.*, **69**, 1723 (1965).
(4) T. B. Joyner, *ibid.*, **71**, 3431 (1967).
(5) T. B. Joyner, *ibid.*, **72**, 703 (1968).
(6) T. B. Joyner, *ibid.*, **74**, 1558 (1970).
(7) J. B. Joyner, *ibid.*, **74**, 1563 (1970).
(8) T. B. Joyner, D. S. Stewart, and L. A. Burkardt, *Anal. Chem.*, **30**, 194 (1958).

system initially evacuated (to *ca.* $10^{-5}$ Torr) and the usual 10-mg sample exposed to only its own products. The useful "trapped-normal" runs had a liquid nitrogen trap present during the induction period and absent during the final reaction (the technique has been discussed[4]) so that a single run gave quantitative data on both periods. With recognition of the sensitivity of the induction period to ammonia, there was concern that the trap—even assisted by periodic venting—might not adequately remove ammonia from the solid. Thus "pumped-normal" runs exposed the solid to continuous pumping for the first 90 ± 5% of the induction period. The cold trap was then maintained until the initiation of the fast reaction. The results resemble trapped-normal runs, and the data are considered together in the calculations. A few runs were pumped continuously with progress crudely checked by intermittently isolating the trap and measuring the accumulated ammonia. The rather sparse data appeared to agree with trapped-normal runs but were inadequate for analysis. A large number of runs "trapped" throughout were made on four independently prepared samples during early stages of the study. These yield quantitative confirmation of the induction period and qualitative (due to slow diffusion of ammonia to the trap) support for the final reaction.

In "catalyzed" runs the surface of the hexaammine was dusted with CoN. A thin-stemmed, glass funnel was used to add fresh hexaammine to the residue from a previous run. The solids were very gently mixed taking care to avoid damaging the crystals. The system was evacuated, generally for 15 min, and the subsequent run commenced under trapped-normal conditions. Usually the catalyst was used the day of preparation or after standing overnight in the vacuum system. Two runs used metallic cobalt—a commercial powder and a sample freshly prepared by heating CoN[9]—as the catalyst.

The reaction has been studied isothermally between 95 and 150°. At 150° it is fast and warm-up time is a problem. Thermocouples in loose contact with the sample cup took about 100 sec to reach bath temperature. This is of no concern to the final reaction since even at 150° there is a 600-sec induction period. It is also insignificant for the induction periods at lower temperatures. It is, however, obviously of concern at the high temperatures; hence, those runs with induction periods under 1000 sec were omitted from the calculation of the apparent activation energies. The warm-up time was otherwise ignored. The tables report total, uncorrected times.

*Products.* Some additions to the early report[9] are necessary. The usual solid product is CoN. However, a few runs (at temperatures ranging from 95 to 140°) yielded products with relatively faint lines in the powder patterns indicating the presence of metallic cobalt as well. Careful observation of the solid upon first exposure to air also detected the pyrophoric reaction observed with the substituted compounds[4] but not previously reported for the hexaammine product. Again, it involved only a small portion of the solid.

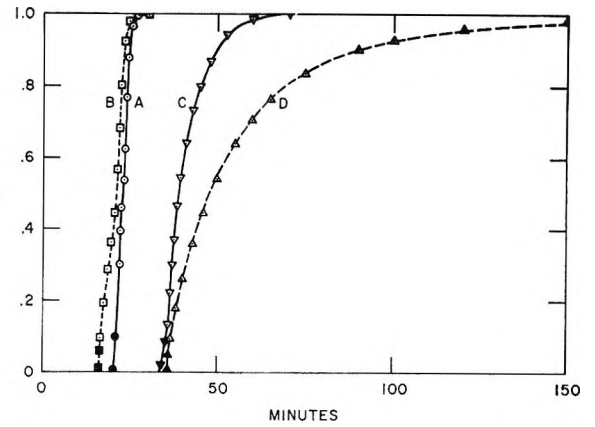


Figure 1. Representative reaction curves for the decomposition of $[Co(NH_3)_6](N_3)_3$ samples of various particle sizes; temp 130°: curve A, Powder; curve B, Small-crystals; curve C, Crystals(A); curve D, Large-crystals. The solid symbols indicate the presence of a liquid nitrogen trap in this and the following figures.

## Results

It is necessary to analyze both the induction period (when little of a directly observable nature is occurring) and the final reaction. These differ in their response to conditions. In particular, the former is very sensitive to ammonia while the latter is not. Particle-size effects and the competition between eq 1 and 2 are related to the ammonia dependence.[1] (Briefly, powders are prone to eq 2, and careful removal of self-generated ammonia is necessary for observation of the CoN reaction; larger crystals favor the CoN reaction.) The qualitative explanation of the rather complicated behavior[1] as amended[3] is believed to be essentially correct and will be elaborated on in the following paper.[6]

Figure 1 illustrates the reaction. The fraction reacted, $\alpha$, is plotted against time. Closed symbols indicate the presence of the cold trap, open symbols its absence. The induction period is obvious. The final reaction curves are generally deceleratory. There is a slight tendency towards sigmoidal curves at the lowest temperatures and with Large-crystals. The Small-crystals yield irregular curves probably because of the distribution of particle sizes.

The duration of the induction period, $\tau$, is arbitrarily defined as the time to reach $\alpha = 0.1$. It is quite reproducible (generally within 10%) for trapped-normal runs. In untrapped runs the extreme sensitivity to ammonia requires very careful control of condi-

(9) T. B. Joyner and F. H. Verhoek, *J. Amer. Chem. Soc.*, **83**, 1069 (1961).

**Table I:** Induction Periods ($\tau$) and Rate Constants ($k_u$) for Various Samples of $[Co(NH_3)_6](N_3)_3$

| Temp, °C | Conditions | $\tau$, sec | $k_u \times 10^4$, $sec^{-1}$ |
|---|---|---|---|
| | Crystals(A) | | |
| 150 | Trapped-normal | 645 | 123 |
| 150 | Trapped-normal | 587 | 131 |
| 150 | Pumped-normal | 610 | 114 |
| 140 | Trapped-normal | 1,149 | 55.6 |
| 140 | Trapped-normal | 1,106 | 53.8 |
| 140 | Pumped-normal | 1,080 | 56.6 |
| 140 | Pumped-normal | 1,153 | 53.5 |
| 130 | Trapped-normal | 2,151 | 24.6 |
| 130 | Trapped-normal | 2,178 | 23.3 |
| 130 | Trapped-normal | 2,040 | 26.4 |
| 130 | Trapped-normal | 2,355 | 22.6 |
| 130 | Pumped-normal | 2,364 | 24.0 |
| 130 | Pumped-normal | 2,191 | 26.4 |
| 120 | Trapped-normal | 6,090 | 10.0 |
| 120 | Trapped-normal | 5,169 | 11.2 |
| 110 | Trapped-normal | 13,020 | 5.41 |
| 100 | Trapped-normal | 24,615 | 2.48 |
| 95 | Trapped-normal | 60,300[a] | 1.46[a] |
| 95 | Pumped-normal | 60,000 | 1.48 |
| 150 | Normal | 598 | 104 |
| 150 | Normal | 616 | 107 |
| 140 | Normal | 1,388 | 52.6 |
| 130 | Normal | 4,094 | 25.4 |
| 120 | Normal | 14,117 | 12.2 |
| 110 | Normal | 65,586 | 5.26 |
| | Powder | | |
| 140 | Trapped-normal | 860 | Explosion |
| 130 | Trapped-normal | 1,302 | 215 |
| 120 | Trapped-normal | 2,826 | 124 |
| 110 | Trapped-normal | 6,900 | 36.4 |
| 100 | Trapped-normal | 17,400 | 20.8 |
| 95 | Trapped-normal | 29,640 | 13.8 |
| | Small-crystals | | |
| 150 | Trapped-normal | 445 | 352[b] |
| 140 | Trapped-normal | 705 | 172 |
| 130 | Trapped-normal | 1,017 | 153 |
| 120 | Trapped-normal | 2,160 | 118 |
| 110 | Trapped-normal | 8,028 | 45.0 |
| 100 | Trapped-normal | 19,680 | 9.60 |
| | Large-crystals | | |
| 150 | Trapped-normal | 567 | 28.2 |
| 150 | Trapped-normal | 573 | 33.7 |
| 140 | Trapped-normal | 1,200 | 13.3 |
| 130 | Trapped-normal | 2,640 | 4.08 |
| 130 | Trapped-normal | 2,211 | 7.82 |
| 120 | Trapped-normal | 7,800 | 1.68 |
| 120 | Trapped-normal | 7,500 | 1.45 |

[a] Composite of two runs. [b] The curves tend to be irregular. In general the constants represent only the last 50% of the decomposition. The 100 and 120° plots are particularly unsatisfactory.

tions to realize a similar reproducibility. Table I reports $\tau$'s.

The final reactions of trapped-normal and trapped runs have similar durations despite the obvious differences in ammonia pressures. This suggests an independence of ammonia. Confirmation was provided by a trapped run interrupted at $\alpha = 0.34$ (Figure 2, curve E). During the 5-min interruption the trap—which contained sufficient added ammonia to raise the pressure by 63 Torr—was warmed. The experiment was then completed as a normal run. The excess ammonia had no effect on the rate of the final reaction.

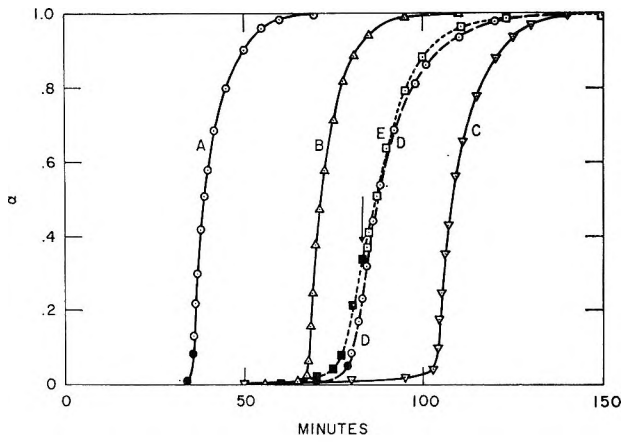


Figure 2. The effect of ammonia on the decomposition of $[Co(NH_3)_6](N_3)_3$. Crystals(A) at 130°: curve A, trapped-normal run; curve B, normal run; curve C, run in the presence of 50 Torr of added ammonia. Crystals(B) at 120°; curve D, trapped-normal run; curve E, an initially trapped run interrupted (arrow) and completed in the presence of its own products and 63 Torr of added ammonia.

In contrast, ammonia seriously alters the induction period. With "Powder" the self-generated ammonia suffices for a conversion to the cobalt(II) system.[1,2] With "Crystals" it prolongs the induction period prior to a typical, final CoN reaction (Table I and Figure 2, curve B). The CoN reaction can also occur—again with Crystals—under 50 Torr of added ammonia (Figure 2, curve C) with similar final rates but even longer induction periods. At higher pressures runs with crystals become too erratic for analysis with very long induction periods (during which cobalt(II) complexes can be observed) and eventual partial explosions or pressure bursts.[1]

The consistency of growth patterns at various temperatures was probed with split-temperature runs at 110 and 130°. (The extremes were avoided due to rapidity or inconvenient slowness.) A 110°, trapped-normal run was carried to $\alpha = 0.57$ (Figure 3, curve C) and cooled to room temperature for 19 min (represented by C′) while the bath was raised to 130°. Upon reinitiation the run took up a rate (Figure 3, curve C″) appropriate for 130° (Figure 2, curve A) indicating that the early decomposition had not imposed a growth pattern which would be abnormal for a 130° run. In a similar experiment, the induction period required 9000 sec at 110° and 446 sec at 130°. The times correspond to about 69 and 21% of the usual

**Table II:** Interrupted Runs with Crystals(A)

| Initial decomposition[a] | | | Interrupted at | | Interruption | | Final decomposition[a] | | |
|---|---|---|---|---|---|---|---|---|---|
| Conditions | $\tau$, sec | $k_u \times 10^4$, $sec^{-1}$ | Time, sec | $\alpha$ | Duration, min | Sample exposure | $\tau$,[b] sec | Conditions[b] | $k_u \times 10^4$, $sec^{-1}$ |
| Trapped-normal[c] | 2151 | 24.6 | | | | | | | |
| Normal[c] | 4094 | 25.4 | | | | | | | |
| Trapped-normal | 2417 | 21.4 | 2700 | 0.55 | 15 | Products | 0 | Normal | 20.1 |
| Trapped-normal | 2248 | 25.0 | 2490 | 0.55 | 15 | Pumping | 0 | Normal | 24.6 |
| Trapped-normal | 2075 | 26.5 | 2280 | 0.55 | 15 | Air | 1290 | Normal | 20.0 |
| Trapped-normal | 2335 | 22.7 | 2610 | 0.56 | 15 | Air | 660 | Trapped | 19.2 |
| Trapped-normal | 2200 | 24.0 | 2520 | 0.61 | 900 | Products | 702 | Normal | 24.0 |
| Trapped-normal | 2487 | 27.4 | 2760 | 0.55 | 3780 | Products | 1500 | Normal | 27.4 |
| Trapped-normal | 2447 | 22.7 | 2790 | 0.59 | 900 | Pumping | 990 | Normal | 23.3 |
| Trapped | ... | ... | 1800[d] | ~0 | 15 | Pumping | 714 | Trapped | 22.1 |
| Trapped | ... | ... | 2100[d] | ~0 | 930 | Pumping | 835 | Trapped | 24.8 |

[a] All experiments were at 130°. [b] The second $\tau$ is obtained under the indicated conditions. The final $k_u$'s are for normal conditions. [c] Check runs. [d] Interrupted during the induction period.

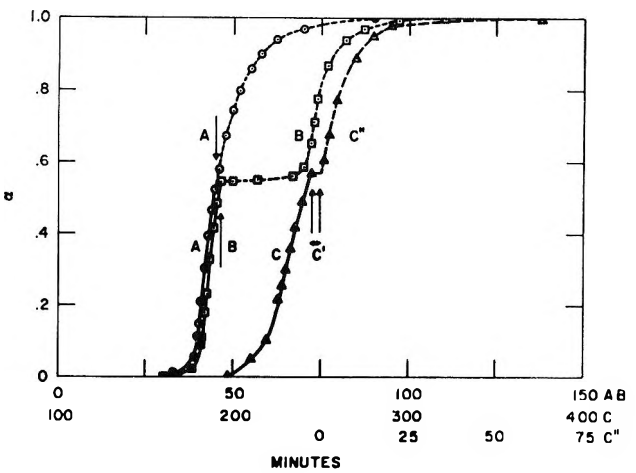


Figure 3. Interrupted and split-temperature runs with crystals (A): curve A, 130° run interrupted and cooled for 15 min; curve B, 130° run interrupted and cooled for 63 hr; curve CC'C'', split-temperature run commenced at 110° (C), interrupted and cooled for 19 min (a period represented by C'), and completed at 130° (C''). The time scales for C'' and curves A and B are identical. The arrows indicate the points of interruption.

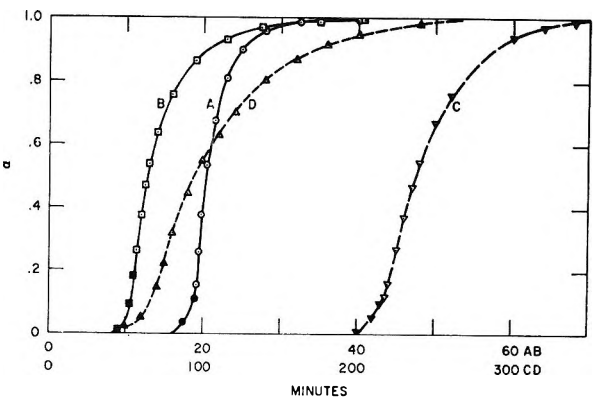


Figure 4. Comparison of runs catalyzed by dusting with CoN (curves B and D) and conventional, trapped-normal runs (curves A and C); temp: curves A and B, 140°; curves C and D, 110°; sample: Crystals (A).

induction periods at the respective temperatures with the total reasonably close to expectation. The final reaction was appropriate for 130°.

The absence of self-heating (a possibility in exothermic solid reactions) is indicated by the consistent analyses (following section) of both fast and very slow runs. As a further check, runs at 140 and 130° (Figure 3, curve A) were carried to $\alpha$ = *ca.* 0.5, cooled for 15 min while the solid was either subjected to pumping or left in contact with the product gases, and reinitiated. In all cases the run took up the previous rate indicating an absence of excessive temperatures prior to the interruption.

Exposure of the partially reacted solid to air or prolonged interruptions (with or without pumping) produced a second induction period. Figure 3, curve B is illustrative. Table II summarizes the experiments. The duration of the second induction period appears to be somewhat dependent on the length of the interruption. It is shorter (660 to 1500 sec) than the usual induction period under normal conditions (about 4100 sec). The two runs exposed to air indicate it can be shortened by trapping. Interruptions during the induction period seemed less serious although 930 min of pumping did cause some prolongation. The final reactions do not seem to be greatly altered by the various interruptions. These observations have not been pursued in detail.

Since the interrupted sample consists of unreacted hexaammine (confirmed by powder patterns) and the solid products, it seemed worthwhile to determine the effect of CoN on fresh material. These catalyzed runs were concurrent with the experiments of Table I; hence, the changes are not due to aging. The results are reported in Table III and illustrated by Figure 4. Dusting gives shortened induction periods, more sigmoidal and generally slower final reactions, and

irreproducibility in both $\tau$ and the final reaction. The CoN appears to maintain its catalytic ability after prolonged pumping or exposure to air although, perhaps, with some loss in efficiency. Shortening of $\tau$ was also observed with freshly prepared metallic cobalt but not with the commercial powder.

**Table III:** Catalyzed Runs[a] with Crystals(A)

| Temp, °C | $\tau$, sec | $k_u \times 10^4$, $sec^{-1}$ |
|---|---|---|
| 150 | 414 | 64.1 |
| 140 | 660 | 29.3 |
| 140 | 653 | 31.2 |
| 130 | 1,113 | 20.0 |
| 130 | 1,231 | 17.1 |
| 130 | 1,050 | 18.8 |
| 120 | 2,100 | 7.77 |
| 110 | 3,768 | 3.51 |
| 100 | 8,460 | 1.37 |
| 95 | 15,000 | 0.640 |
| 130[b] | 1,466 | 16.7 |
| 130[c] | 1,515 | 11.2 |
| 130[d] | 1,545 | 25.2 |
| 130[e] | 2,131 | 21.4 |

[a] The runs were made under trapped-normal conditions. The catalyst was CoN except as noted below. [b] The CoN was pumped on for 46 hr prior to use. [c] The CoN was exposed to air for 63 hr prior to use. [d] Freshly prepared cobalt(0) was used as the catalyst. [e] Commercial cobalt(0) powder was used as the catalyst.

## Discussion

*Analysis.* The trapped-normal runs with "Crystals-(A)" provide the most detailed data. Both the induction period and the final reaction can be analyzed. The latter is well described by the usual first-order (or "unimolecular") decay law

$$-\ln (1 - \alpha) = k_u t + c_u \qquad (3)$$

where $t$ is time and $k_u$ and $c_u$ are constants.[10,11] Figure 5 is illustrative; Table I reports rate constants. The induction period gives little direct evidence, either visual or by gas evolution, of the processes taking place. Fortunately, its duration is useful. Plots of both $\tau$ and $k_u$ against $1/T$ give good straight lines. The similarities in the apparent activation energies, $E_a$, and precxponentials, $A$, are apparent in Table IV. The treatment of $\tau$ as a measure of rate has been discussed.[3] It may be noted that the onset of the final reaction is so rapid that alternate definitions of $\tau$ in the approximate range $0.05 < \alpha < 0.2$ would not seriously alter the analysis. The final reactions of normal runs give similar results; the induction periods, however, have an apparent activation energy approaching the 46 kcal/mol of the cobalt(II) reaction under low ammonia.[2]

The Crystals(B) data and the early exploratory studies generally agree with the above. Thus the

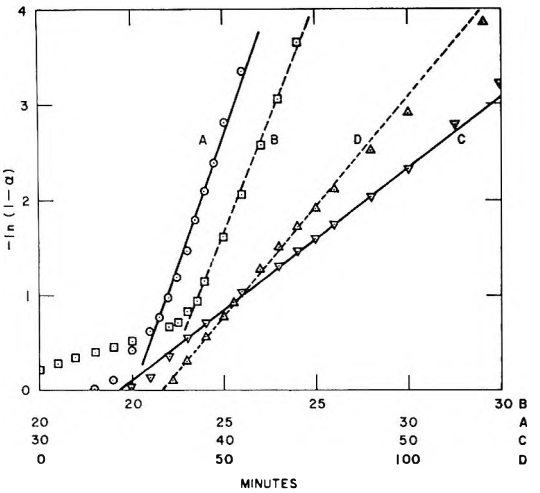


Figure 5. Illustrative kinetic treatments for samples of various particle sizes; temp, 130°: curve A, Powder; curve B, Small-crystals (the poor fit is apparent); curve C, Crystals(A); curve D, Large-crystals.

**Table IV:** Apparent Activation Energies ($E_a$) and Pre-exponentials ($A$) for Various Samples of $[Co(NH_3)_6](N_3)_3$

| Sample | Conditions | Treatment | $E_a$, kcal/mol | log $A$, $sec^{-1}$ |
|---|---|---|---|---|
| Crystals(A) | Trapped-normal[a] | $\tau$ | 26.3[b] | 10.75[b] |
| | | $k_u$ | 24.6 | 10.86 |
| Crystals(A) | Normal | $\tau$ | 40.4 | 18.25 |
| | | $k_u$ | 24.1 | 10.44 |
| Crystals(A) | Catalyzed, trapped-normal[c] | $\tau$ | 21.0 | 8.31 |
| | | $k_u$ | 25.2 | 10.85 |
| Crystals(B)[d] | Trapped | $\tau$ | 24.1 | 9.68 |
| Crystals(B) | Normal | $k_u$ | 20.6 | 8.80 |
| Powder | Trapped-normal | $\tau$ | 26.3 | 11.18 |
| | | $k_u$ | 23.9 | 11.28 |

[a] Includes pumped-normal runs. [b] All treatments are least squares. [c] Catalyzed runs were carried out under trapped-normal conditions. [d] Data for Crystals(B) will be more fully presented in the following paper.[6]

results are not peculiar to a single batch of crystals. Some variations are observed (Table IV). These reflect, it is thought, the importance of topography. (The model will suggest explanations. For now, the number and distribution of early reaction centers may influence growth patterns and hence the adequacy of the kinetic analysis and definition of $\tau$.) Table IV

(10) P. W. M. Jacobs and F. C. Tompkins in W. E. Garner, "Chemistry of the Solid State," Butterworth and Co., Ltd., London, 1955, Chapter 7.

(11) Equation 3 should be considered as descriptively useful rather than as evidence of a decomposition pattern. The reaction curves can also be quite adequately handled by a shrinking-cube treatment to yield a similar temperature dependence. This is often the case. Ideal shrinking-cube and first-order decay curves do not differ greatly. In practice, moreover, inherent features such as particle-size variations and the nucleation process can cause deviations from ideal behavior. It will be seen (following paper)[6] that the proposed model is a modified shrinking-volume decomposition.

indicates an uncertainty greater than that suggested by any single series of experiments. For instance, trapped-normal runs with Crystals(A)—probably the best series—give $E_a = 24.6 \pm 0.4$ kcal/mol and log $A = 10.75 \pm 0.20$ sec$^{-1}$, while the $k_u$'s from catalyzed runs (discussed below) scatter rather badly but still yield $E_a = 25.2 \pm 0.9$ kcal/mol and log $A = 10.85 \pm 0.50$ sec$^{-1}$. Although one is inclined to weigh the Crystals(A) data rather heavily, Table IV would suggest a conservative $E_a = 24 \pm 3$ kcal/mol as a generous margin of uncertainty.[12]

Catalyzed runs show considerable irreproducibility and a pronounced acceleratory period. Both are relevant to the model. The acceleratory period hinders the estimation of $\tau$ and is, itself, too short and irreproducible for useful analysis. However, the deceleratory portion of the curve, about the last 75%, is fit by eq 3 with the results discussed above. The slight decrease in $E_a$ given by the induction periods (Table IV) is of doubtful significance in view of the difficulties with $\tau$. (The lower temperature $\tau$'s, in particular, closely parallel the trapped-normal curve.) It thus seems likely that catalysis shortens the induction period but does not change the temperature dependence.

The remaining samples support the Crystals results. Powder, with probably uniform particles, yields good agreement. Large-crystals show an expected dependence on the particular crystal, making detailed treatment of the rather limited data of little value. The $\tau$'s and $k_u$'s do approximately parallel the results from Crystals and Powder. The Small-crystals data scatter badly, probably due to the distribution of particle sizes. (The smallest crystals may commence the final reaction early, produce ammonia, and so influence the larger particles.) The results are of little quantitative value—showing, at best, only rough agreement with the other samples—but of some qualitative interest in indicating the borderline conditions for the CoN and cobalt(II) reactions. Although the particles sizes are not greatly different, normal runs with Powder go to cobalt(II), while Small-crystals prefer the CoN reaction.

## Conclusions

The results of immediate interest are summarized.

(1) The similarity in the apparent activation energies for the induction period and final reaction suggests the same mechanism is responsible for both periods. (2) CoN can shorten $\tau$ indicating that the solid product is involved in the reaction mechanism of the induction period and, by (1), the final reaction as well. (3) The hexaammine reaction is quantitatively similar to those of the substituted compounds.[3-8] To anticipate the following paper,[6] during the induction period the CoN reaction is thought to grow a fixed distance on a microscopic scale prior to commencing the observable decomposition. Since the same reaction is responsible for both periods, similar activation energies are expected. Ammonia, added or self-generated, interferes with the microscopic CoN reaction. The early growth is then by the cobalt(II) reaction and the $\tau$'s, as observed for normal runs, yield the apparent activation energy of that reaction.

Apparently both CoN and metallic cobalt can shorten $\tau$. Some uncertainty is caused by the possible presence of some cobalt in the CoN catalyst and the conceivable survival of CoN in the freshly prepared cobalt. The contamination, however, should be minor, and it thus seems likely that both CoN and fresh cobalt can play a role in the reaction mechanism. (It is doubtful that a purely physical alternative—for instance, more efficient heat transfer to the reactant—could avoid altering the apparent activation energy.) Direct involvement of the product is also suggested by the interrupted runs. During a prolonged interruption intimate contact between the reactant and product may be ruptured by some slow process (crystal growth involving the agglomeration of CoN from the reactant surface with the bulk of the product can be envisioned) so that upon reinitiation a second induction period is needed to reestablish the reactant–product interface. Presumably rupture is assisted by oxidation since 15-min exposures to air produce the second induction period. An oxide coating might also explain the failure of the commercial cobalt to shorten the induction period.

The quantitative similarities in the reactions of the series of cobalt(III) ammine azides suggest a single mechanism. The compounds, particularly the cations, differ considerably but all have the common feature of at least one ionic azide. It seems reasonable to suggest a critical role for these azides and, specifically, to hypothesize a rate-controlling mechanism involving an interaction between the ionic azide and the solid product. This will be discussed in a summary paper.[7]

(12) It may be noted that Table IV provides a very clear warning of the danger in attaching too much precision to results from a single batch of crystals when reaction patterns are not known with certainty.

# The Thermal Decomposition of Solid Hexaamminecobalt(III) Azide. A Model for the Cobalt Nitride Reaction

by Taylor B. Joyner

*Research Department, Naval Weapons Center, China Lake, California 93555* *(Received March 14, 1969)*

The induction periods typical of the isothermal decomposition of cobalt(III) ammine azides to CoN have been probed with hexaamminecobalt(III) azide. A model emphasizing topography proposes that the induction period involves a microscopic reaction growing a fixed distance (hypothesized as the depth of the first mosaic plane) with a subsequent rapid spreading through the intermosaic structure producing the final observable reaction. The microscopic growth may be accomplished by the CoN reaction in the absence of ammonia and by the cobalt(II) reaction when even minute amounts of ammonia are present. The model meets several tests.

## Introduction

Previous papers[1] have shown that the decompositions of cobalt(III) ammine azides to CoN are characterized by a marked induction period. To permit analysis of the rate data, a model was proposed and discussed briefly for azidopentaamminecobalt(III) azide. Subsequent work—with kinetic analyses based on the broad outlines of the hypothesis—established the generality of the reaction and gave insight into its chemistry.[1] Concurrent studies of the reaction

$$[Co(NH_3)_6](N_3)_3 \longrightarrow CoN + 6NH_3 + 4N_2 \quad (1)$$

have probed the induction period and found the model capable of explaining a variety of observations.

## Experimental Section

Preparation and procedure have been described.[1] Some earlier data will be reconsidered with regard to the model. Additional studies with "Crystals(B)"[1] attempted to provide a uniform environment during the induction period. Thus "7 Torr" runs commenced under 7 Torr of ammonia and allowed the products to accumulate; "0.4 Torr" runs started with 4 Torr of ammonia for 30% of the induction period (to provide ammonia during nucleation) after which the pressure was lowered and held at about 0.4 Torr by periodic ventings to a large volume; "0.1 Torr" runs were commenced as normal runs but the pressure was held at about 0.1 Torr by venting. Conditions were also altered during the induction period. Runs initiated under "normal"[1] or ammonia conditions were subsequently trapped. Conversely, initially trapped runs were altered to normal conditions.

## Results

Tables I and II give kinetic data (obtained as before[1]) for "Crystals(B)." Trapped and normal runs confirm previous findings. The ammonia runs have induction periods yielding apparent activation energies close to the 46 kcal/mol of the cobalt(II) reaction[2]

$$[Co(NH_3)_6](_3)_3N \longrightarrow Co(NH_3)_2(N_3)_2 + 4NH_3 + 1.5N_2 \quad (2)$$

The final CoN reactions have apparent activation energies that are rather lower than the expected 25 kcal/mol,[1] probably due to growth patterns imposed during an induction period dominated—as will be discussed—by the cobalt(II) rather than the CoN reaction.

The induction period is general for many crystal sizes. Table III summarizes trapped-normal runs for "Powder," "Crystals," and "Large-crystals."[1] The relationship of the induction period and the final reaction may be probed by making use of the duration, $D$, of the final reaction, defined as the time to cover the range $\alpha = 0.1$ to 0.95 where $\alpha$ is the fraction reacted. The upper limit includes the bulk of reaction but, hopefully, avoids prolongations caused by any abnormally large crystals. The lower limit marks the onset (usually rapid) of the final reaction and defines the duration of the induction period, $\tau$. (Alternate definitions from $0.05 < \alpha < 0.2$ would not damage the arguments.) Tables III and V use minutes to avoid unwieldy numbers in the discussions. The data from "Small-crystals"[1] are not included. These irregular curves are qualitatively understandable on the basis of the model and a distribution of particle sizes[1] but add nothing of quantitative value to this paper. Altered runs (Table V) will be discussed below.

In an effort at direct observation, a Large-crystal was decomposed to $\alpha = 0.5$, imbedded in paraffin, and cleaved. Microscopic examination showed a shrinking-volume pattern with an orange, apparently undisturbed inner region surrounded by black product.

## Discussion

A model should account for the following. The

(1) T. B. Joyner, *J. Phys. Chem.*, **74**, 1552 (1970), and references therein.

(2) T. B. Joyner, *ibid.*, **72**, 4386 (1968).

**Table I:** Induction Periods ($\tau$) and Rate Constants ($k_u$) for Crystals(B)

| Temp, °C | Conditions | $\tau$, sec | $k_u \times 10^4$, sec$^{-1}$ | Temp, °C | Conditions | $\tau$, sec | $k_u \times 10^4$, sec$^{-1}$ |
|---|---|---|---|---|---|---|---|
| 150 | Trapped[a] | 660 | | 150 | 0.4 Torr | 426 | 112 |
| 140 | Trapped | 1,116 | | 140 | 0.4 Torr | 1,512 | 47.7 |
| 130 | Trapped | 2,357 | | 140 | 0.4 Torr | 1,545 | 69.8 |
| 120 | Trapped | 5,267 | | 130 | 0.4 Torr | 5,670 | 36.0 |
| 120 | Trapped | 5,220 | | 130 | 0.4 Torr | 5,100 | 32.1 |
| 120 | Trapped | 4,860 | | 120 | 0.4 Torr | 26,010 | 22.3 |
| 110 | Trapped | 11,400 | | 120 | 0.4 Torr | 20,880 | 17.8 |
| 110 | Trapped | 10,800 | | 110 | 0.4 Torr | 90,000 | 11.0 |
| | | | | 110 | 0.4 Torr | 106,740 | 10.7 |
| 150 | Normal | 615 | 168 | | | | |
| 150 | Normal | 637 | 125 | 150 | 7 Torr | 540 | 121 |
| 140 | Normal | 1,668 | 88.3 | 140 | 7 Torr | 1,716 | 50.3 |
| 140 | Normal | 1,770 | 64.2 | 130 | 7 Torr | 7,320 | 36.7 |
| 130 | Normal | 7,384 | 40.9 | 120 | 7 Torr | 38,610 | 23.4 |
| 130 | Normal | 7,080 | 45.0 | | | | |
| 150 | 0.1 Torr | 566 | 143 | | | | |
| 140 | 0.1 Torr | 1,440 | 62.9 | | | | |
| 130 | 0.1 Torr | 5,310 | 36.7 | | | | |
| 120 | 0.1 Torr | 16,380 | 17.9 | | | | |
| 110 | 0.1 Torr | 49,800 | 11.4 | | | | |
| 100 | 0.1 Torr | 238,500 | 5.92 | | | | |

[a] Trapped throughout. Slow diffusion of ammonia to the trap prevents an accurate determination of $k_u$.

**Table II:** Apparent Activation Energies ($E_a$) and Preexponentials ($A$) for Crystals(B)

| Conditions | Treatment | $E_a$, kcal/mol | Log $A$, sec$^{-1}$ |
|---|---|---|---|
| Trapped | $\tau$ | 24.1 | 9.68 |
| Normal | $k_u$ | 20.6 | 8.80 |
| 0.1 Torr of $NH_3$ | $\tau$ | 38.2 | 17.03 |
| | $k_u$ | 19.5 | 8.14 |
| 0.4 Torr of $NH_3$ | $\tau$ | 43.9 | 20.06 |
| | $k_u$ | 18.2 | 7.40 |
| 7 Torr of $NH_3$ | $\tau$ | 50.3 | 23.39 |
| | $k_u$ | 17.3 | 6.94 |

induction period and final reactions can have similar apparent activation energies; the latter is independent of ammonia. Ammonia lengthens the induction period and alters its temperature dependence. Dusting with CoN can shorten the induction period and slow the final reaction without altering their temperature dependence. The decomposition maintains its essential character for particle sizes ranging over about four orders of magnitude. The last, illustrated by Figure 1, will be important to the discussion. For the present, it may be noted that a penetration of only a short distance (perhaps some tens of molecular layers) would consume a significant percentage of a Powder particle but constitute only a very preliminary feature of the decomposition of a Large-crystal.

The importance of defects in the decomposition of solids is generally recognized. As examples involving azides, Jach[3] has discussed the low-temperature reaction of lead azide, and Secco[4] has suggested a role for the mosaic structure in the decomposition of sodium azide. For present purposes, the inset of Figure 1 represents a crystal with an internal mosaic structure. In brief, the CoN and cobalt(II) reactions initiate on the surface and grow microscopically until reaching the first mosaic plane. The CoN reaction then spreads rapidly along the intermosaic structure, carving the crystal into decomposing blocklets and launching the final decomposition. The detailed analysis will be twofold. The general plausibility will be tested by runs with a near absence of ammonia during the induction period. (These yield the similar apparent activation energies for the induction period and final reaction.) Thereafter, the role of ammonia in the induction period will be examined.

*The Induction Period in the Absence of Ammonia.* Table III shows that $\tau$ varies by only a factor of 2 or 3 from Powder to Large-crystals while $D$ more nearly correlates with particle size. Qualitatively, this is reasonable. The depth of the mosaic plane need not vary greatly with crystal size, but the intermosaic reaction will take longer to traverse larger crystals. Assumption of a reasonably regular internal structure permits an approximate estimation of relative reaction rates in the blocklets and intermosaic regions and so tests the model for obvious inconsistencies.

The total time to reach $\alpha = 0.95$ will be the sum of $\tau$

(3) J. Jach, "Reactivity of Solids," G. M. Schwab, Ed., Elsevier Publishing Co., New York, N. Y., 1965, p 422.

(4) E. A. Secco, *J. Phys. Chem. Solids*, **24**, 469 (1963).

**Table III:** Observed Durations of the Induction Period and Final Reaction and Estimated Times for the Intermosaic and Blocklet Reactions

| Sample | $\tau$, min | $D$, min | $D_b$,[a] min | $D_i$,[b] min |
|---|---|---|---|---|
| | 150° | | | |
| Crystals[c] | 10.8 | 3.8 | 6.9 | .4 |
| Crystals (catalyzed) | 6.9 | 7.4 | 6.9 | 3.9 |
| Large-crystal[c] | 9.4 | 24.2 | 6.9 | 20.7 |
| Large-crystal | 9.4 | 22.0 | 6.9 | 18.5 |
| | 140° | | | |
| Powder[c] | 14.3 | Exploded | ... | ... |
| Crystals | 19.4 | 7.8 | 11.3 | 2.1 |
| Crystals (catalyzed) | 11.3 | 13.3 | 11.3 | 7.6 |
| Large-crystal | 19.9 | 40.3 | 11.3 | 34.6 |
| | 130° | | | |
| Powder | 21 | 4 | 8 | 0 |
| Crystals | 36 | 17 | 19 | 7.5 |
| Crystals (catalyzed) | 19 | 25 | 19 | 15.5 |
| Large-crystal | 37 | 76 | 19 | 67 |
| Large-crystal | 44 | 135 | 19 | 126 |
| | 120° | | | |
| Powder | 46 | 9 | 18 | 0 |
| Crystals | 86 | 44 | 36 | 26 |
| Crystals (catalyzed) | 36 | 62 | 36 | 44 |
| Large-crystal | 125 | 358 | 36 | 340 |
| | 110° | | | |
| Powder | 114 | 20 | 40 | 0 |
| Crystals | 217 | 87 | 67 | 53 |
| Crystals (catalyzed) | 67 | 137 | 67 | 103 |
| | 100° | | | |
| Powder | 287 | 62 | 124 | 0 |
| Crystals | 414 | 231 | 154 | 154 |
| Crystals (catalyzed) | 154 | 356 | 154 | 279 |
| | 95° | | | |
| Powder | 490 | 94 | 188 | 0 |
| Crystals | 1020 | 385 | 250 | 260 |
| Crystals (catalyzed) | 250 | 1100 | 250 | 975 |

[a] For Powder, $D_b = 2D$; for Crystals, $D_b$ is given by the $\tau$'s of catalyzed runs. Large-crystals are assumed to have $D_b$'s approximately equal to those of Crystals. [b] $D_i = D - (1/2)D_b$ for Crystals and Large-crystals; $D_i \simeq 0$ for Powder. [c] Powder has particle sizes in the range of $10^{-4}$ to $10^{-3}$ mm. Crystals are platelets with thin dimensions of 0.01 to 0.1 mm and faces up to 1 mm in length. Large-crystals have dimensions of 1 to 3 mm.

and $D$, where $D$ is composed of $D_i$ (the time for the intermosaic reaction to proceed from the first plane to the central blocklet) and $D_b/2$ with $D_b$ being the time for a reaction to pass through a blocklet. The $1/2$ accounts for attack of the central blocklet from two sides. The simplest analysis would equate $\tau$ with $D_b$;

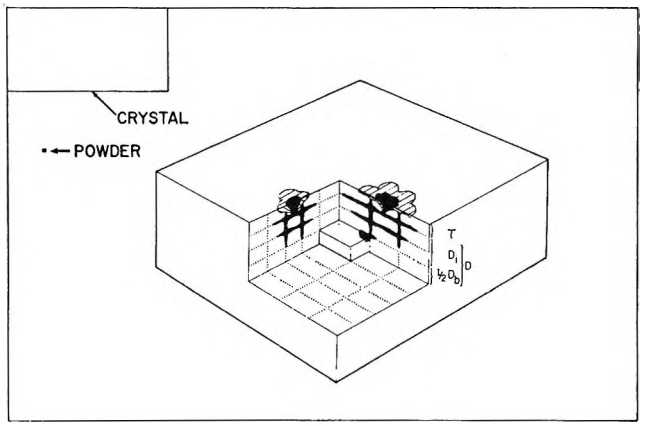


Figure 1. Approximate, relative cross sections of samples of $[Co(NH_3)_6](N_3)_3$ and the model of the CoN reaction. If the rectangle is taken as representing a 0.1 × 0.05 mm crystal, the dot is rather larger than a powder particle with a cross section of $10^{-6}$ mm² while the entire figure represents about 1/30 of the cross-sectional area of the larger single crystals (*ca.* 1 × 3 mm). The inset represents a crystal with the CoN reaction (black) and cobalt(II) reaction (cross-hatched) spreading from two surface nuclei. There is no attempt at scale. The regions of induction period growth, the final reaction, the intermosaic reaction, and the consumption of the last blocklets are indicated by $\tau$, $D$, $D_i$, and $D_b$, respectively.

however, it will be seen that an "effective nucleation" time, $D_n$, of uncertain origin is also necessary. To summarize

$$D_{0.95} = \tau + D = (D_n + D_b) + (D_i + D_b/2) \quad (3)$$

If $D_i$ were negligible—because of a very fast intermosaic reaction rate or a short distance of travel—the crystal would be quickly carved into decomposing blocklets with, therefore, $D_b = 2D$. If $\tau$ measured only growth through the first layer (no $D_n$), $\tau$ would equal $D_b$ and with $D_i$ negligible $\tau = D_b = 2D$. Although uncatalyzed runs with Crystals showed $\tau \simeq 2D$ to a remarkably misleading extent, Large-crystals have $\tau$'s from $0.3D$ to $0.5D$ suggesting an intermosaic reaction of significant duration. The quantity $D_n$ is required by both the Powder results and the CoN catalysis. Powder has $\tau \simeq 5D$ despite a probably negligible $D_i$ due to the small particle size and necessarily short intermosaic path. Additionally, the CoN catalysis shortens $\tau$ although dusting the surface would not alter the distance to the first plane. Thus $D_n$ was introduced and taken as zero for catalyzed runs.

For catalyzed Crystals runs, then, $D_b \simeq \tau$ and $D_i \simeq D - \tau/2$. For Powder, if $D_i$ is negligible, $D_b \simeq 2D$. These $D_b$'s (Table III) indicate a blocklet size in Crystals roughly twice that of Powder. The particle sizes, however, differ by between 10 and 100 (from some tenths of a micron for Powder to tens of microns for the thin dimension of Crystals). Thus Crystals have room for an intermosaic reaction path of considerable length.

This path will be even longer in Large-crystals. Although there is no direct evidence as to $D_n$, the similar induction periods suggest blocklet sizes roughly comparable to those of Crystals. Rather conservatively, then, Large-crystal blocklets may be taken as two to four times larger than those of Powder. (Even with $D_n = 0$ for Large-crystals, Table III would indicate a maximum blocklet size only seven times greater than Powder.) Considering the limits set by the small particle size of Powder, it seems evident that Large-crystals will have blocklet sizes of, at most, a few microns. Thus the events of the induction period will occur very close to the surface leaving hundreds of microns through which the intermosaic reaction must travel to reach the central blocklet. Table III indicates $D_i$'s 12 to 20 times those of Crystals. (The 150° data are in reasonable accord considering the rapidity of the Crystals run.) The $D_i$'s are thus approximately proportional, as they should be, to the macroscopic crystal size. It is worth emphasizing that the ability to account for the reaction over the entire range of particle sizes and consistently explain the varying ratios of $\tau$ and $D$ is a major test of the model.

The more sigmoidal curves and longer $D_i$'s of catalyzed runs may be understood on the basis of a less direct intermosaic reaction path. In uncatalyzed runs the initial nuclei may be numerous so that the microscopic CoN growths will penetrate the mosaic plane at many points. The intermosaic reactions will spread from these points, quickly link-up, and enter the crystal as an essentially shrinking-volume reaction preceding a region of blocklets in various stages of decomposition. Successful catalysis, on the other hand, may be rare so that only a few nuclei commence the immediate penetration that leads to the shortened induction period. The intermosaic reaction, in turn, must start from these few growths and spend time in an accelerative, branching growth (leaving behind decomposing blocklets) before establishing a continuous network. Thus the observed final reaction with an early, relatively slow start and an appreciable acceleratory period is understandable. The details will depend on the distribution of successful nucleations in the many crystals of the sample and thus may differ widely if uniform catalysis is hard to achieve (as seems likely). This is consistent with the observed irreproducibility of catalyzed runs.[1]

The "effective nucleation" period, $D_n$, remains a problem. Since the product is involved in the CoN reaction,[1] a possible explanation associates $D_n$ with the establishment of a CoN phase that catalysis provides directly. This requires, however, that the nucleation process in uncatalyzed runs also have an activation energy close to 25 kcal/mol so as to maintain the observed apparent activation energies. An alternative assumes rapid nucleation in all cases but ascribed $D_n$ to a difference in growth from a point (uncatalyzed reaction) and from a relatively large surface (provided by the catalyst). Bartlett, Tompkins, and Young[5] have suggested that micronuclei grow slowly owing to a greater entropy of activation. It is also conceivable, depending on reaction patterns, that the small nuclei will lose time in lateral growth while at least some of the growth from the large surface will penetrate directly toward the mosaic plane. Although the growth explanations are attractive in relation to altered runs (to be described), it is clear that more information is needed on the early reactions.

*The Induction Period in the Presence of Ammonia.* Ammonia adsorbed on the crystal and thus acting directly on the young reactions[1,2] can greatly prolong the induction period by promoting the cobalt(II) reaction. The model assumes that both reactions commence on the surface with the cobalt(II) reaction and its solid products restricting the spread of the CoN reaction and forcing it into primarily vertical growth. If ammonia is kept low, the CoN reaction prevails. However, ammonia favors the cobalt(II) reaction which may then isolate the tiny CoN phase. If the ammonia is not removed, the cobalt(II) reaction will ultimately reach the mosaic plane. There it will convert into the final CoN reaction.

If conversion is prompt, the $\tau$'s should yield an apparent activation energy appropriate for the cobalt(II) reaction.[2] Despite a great sensitivity to ammonia, this is apparently observed (Table II). The 0.4 Torr runs—probably most ideal with a uniform early environment and steady growth conditions that, hopefully, do not interfere with conversion into the final CoN reaction—give a good Arrhenius plot and an energy (44 kcal/mol) close to expectation. Normal

**Table IV:** Comparison of Crystals(B) Induction Periods with Extrapolated Times for the Complete Consumption of Powders by the 46-kcal/mol Cobalt(II) Reaction

| Temp, °C | —Time for complete consumption, sec— Preparation A[a] | Preparation B[a] | $\tau$, sec Crystals(B)[b] |
|---|---|---|---|
| 150 | 402 | 463 | 426 |
| 140 | 1,290 | 1,344 | 1,512 |
| 140 | 1,242 | | 1,545 |
| 140 | 1,284 | | |
| 130 | 6,000 | 6,120 | 5,670 |
| 130 | 5,988 | | 5,100 |
| 120 | 21,180 | 22,140 | 26,010 |
| 120 | | | 20,880 |
| 110 | 95,100 | 88,320 | 90,000 |
| | | | 106,740 |

[a] The powder samples are described in ref 2. [b] The $\tau$'s are those of the 0.4-Torr runs.

(5) B. E. Bartlett, F. C. Tompkins, and D. A. Young, *Nature*, **179**, 365 (1957).

**Table V:** Altered Runs with Crystals(B)

| Initial period[a] | | Final period[a] | | Initial CoN reaction,[b] % | Effective Co(II) reaction,[b,c] % | Final CoN reaction,[b] % | Total, % |
|---|---|---|---|---|---|---|---|
| Time, min | Conditions | Time, min | Conditions | | | | |
| 20 | Normal | 63 | Trapped | ... | ... | ... | ... |
| 45 | Normal | 53 | Trapped | 25 | 7 | 65 | 97 |
| 90 | Normal | 40 | Trapped | 25 | 20 | 49 | 94 |
| 182 | Normal | 16 | Trapped | 25 | 47 | 20 | 92 |
| 225 | Normal | 15 | Trapped | 25 | 59 | 19 | 103 |
| 10 | 7 Torr $NH_3$ | 71 | Trapped | ... | ... | ... | ... |
| 20 | 7 Torr $NH_3$ | 69 | Trapped | 12 | 3 | 85 | 100 |
| 90 | 7 Torr $NH_3$ | 51 | Trapped | 12 | 23 | 63 | 98 |
| 180 | 7 Torr $NH_3$ | 33 | Trapped | 12 | 49 | 41 | 102 |
| 25 | Trapped | 220 | Normal | 31 | 63 | ... | 94 |
| 50 | Trapped | 108 | Normal | 62 | 31 | ... | 93 |
| 50 | Trapped | 111 | Normal | 62 | 32 | ... | 94 |
| 65 | Trapped | 36 | Normal | 80 | 10 | ... | 90 |
| 20 / 80 | Trapped / Normal [d] | 36 | Trapped[d] | 25 | 23 | 44 | 92 |

[a] Columns 1 and 3 give the time spent under the conditions of columns 2 and 4, respectively. [b] Percentages are based on standard $\tau$'s of 81 and 348 min for trapped and ammoniacal conditions, respectively. [c] The effective Co(II) reaction is given by [(column 1) − 20] 100/348 for normal-trapped runs, [(column 1) − 10] 100/348 for 7-Torr-trapped runs and (column 3) 100/348 for initially trapped runs. [d] Doubly altered experiment: initially trapped for 20 min, normal for 80 min, and finally retrapped.

runs provide reasonable confirmation. The 7-Torr runs have longer induction periods. Probably conversion to the CoN reaction is delayed by the higher ammonia stabilizing somewhat the cobalt(II) complexes.[2] The 0.1-Torr runs give the shortest $\tau$'s; some CoN growth occurring after the ventings is suspected.

With Crystals and Large-crystals excess ammonia (*ca.* 100 Torr) greatly prolongs the induction period and permits the buildup of observable diazidodiamminecobalt(II). Anomalously fast final reactions, including partial explosions or pressure bursts, are attributed to rapid decomposition of the very sensitive cobalt(II) complexes accumulated in the internal structure during the long induction period.

Powder under even low ammonia yields cobalt(II). Since the particle size of powder is similar to estimated blocklet sizes (a few microns) for Crystals and Large-crystals, a rough agreement between the time needed for the cobalt(II) reaction to penetrate a Crystals blocklet or consume a Powder particle may be predicted. With Powder, the reaction of interest—the low-pressure, 46-kcal/mol reaction—either explodes or alters to a 32-kcal/mol reaction prior to completion.[2] Fortunately, the early decomposition is fairly linear—a shrinking-volume decomposition of thin plates has been hypothesized[2]—permitting extrapolation to the time needed for completion. Comparison (Table IV) with the $\tau$'s of the 0.4 Torr Crystals runs indicates accord with the model. (The very close agreement is, however, fortuitous.)

Altered runs also provide a test. If the induction period can involve growth by either of two reactions, conversion from one into the other should produce changes in $\tau$. Table V summarizes experiments at 120°. The lowest $\tau$'s for unaltered trapped and 0.4-Torr runs, 81 and 348 min, respectively, were taken as standards. (Longer $\tau$'s were attributed to delayed initiation of the final reaction.) A simple summation of the percentages of the trapped and 0.4-Torr induction periods represented by the two times of the altered runs was inadequate. The minor effect of 20 min under normal conditions on the total reaction time suggests an explanation.

If initiation occurs at moderately distant sites, some time may elapse before the CoN and cobalt(II) growths interfere. During this period—*ca.* 20 min for normal runs at 120°—the CoN reaction makes equal progress under trapped or normal conditions. Thereafter, barring removal of ammonia, the CoN phase will be isolated and later growth will be by the cobalt(II) reaction. Thus initially normal runs have an early CoN growth (Table V, column 5) accounting for about 25% of the induction period; a cobalt(II) growth (column 6, the time under normal conditions less the first 20 min when growth was by the CoN reaction); and the final CoN growth under trapped conditions (column 7). The totals (column 8) are close to 100%. The assumption that under 7 Torr of ammonia a favored cobalt(II) reaction can isolate the CoN growth in about 10 min also leads to satisfactory total percentages. Reverse experiments (initially trapped) and a doubly altered run also gave satisfactory results. The deviations from 100% are well within reason since conversions may not be instantaneous nor growth patterns match precisely.

It is uncertain how these runs relate to $D_n$. If a growth hypothesis for $D_n$ is accepted (and this seems

the simplest explanation), the cobalt(II) reaction would simply be interfering with the early special growth from the tiny nucleus. Interference—specifically, preemption of sites by the cobalt(II) reaction—may also prevent the CoN reaction from directly entering the crystal through the intersection of the mosaic structure and surface. Similarly, CoN growth in the internal structure during the induction period is probably inhibited by the difficulty in establishing the necessary product phase[1] in competition with the cobalt(II) reaction. The latter is favored by ammonia, and since escape of gas from the interior may be difficult, any early internal reaction will probably be to cobalt(II).

*Summary.* The model provides a simple and consistent explanation of a wide variety of results and makes it possible to account for the quite complex decomposition of hexaamminecobalt(III) azide on the basis of topography and the interplay of the CoN and cobalt(II) reactions. The following paper will discuss mechanisms in conjunction with the reactions of the substituted compounds.

# The Mechanisms of the Thermal Decompositions of Solid Cobalt(III) Ammine Azides

**by Taylor B. Joyner**

*Research Department, Naval Weapons Center, China Lake, California 93555* *(Received March 14, 1969)*

The kinetic parameters for the thermal decompositions of solid hexaamminecobalt(III) azide, azidopentaamminecobalt(III) azide, and *cis*- and *trans*-diazidotetraamminecobalt(III) azide have been reviewed and mechanisms for the production of CoN and cobalt(II) complexes have been proposed. The solid products are important in both reactions. The mechanisms include competitive steps which in conjunction with the distribution of microscopic accumulations of products can explain the interplay of the two systems leading to the induction period characteristic of the decomposition to CoN. The aggregation and crystallization of the cobalt(II) products are thought to be of importance in limiting the CoN reaction by removing both azide ions and cobalt(II) intermediates from the reaction front.

## Introduction

Studies of the thermal decompositions of solid hexaamminecobalt(III) azide, azidopentaamminecobalt(III) azide, and *cis*- and *trans*-diazidotetraamminecobalt(III) azide have yielded kinetic information on the reactions producing cobalt(II) complexes and CoN[1] and permitted formulation of a model for the latter.[2] With data available for the series, mechanisms may be considered in more detail than had seemed profitable for single compounds. Also, early questions[3] on the mechanistic consequences of variations in composition and the presence of two distinguishable types of azide may now be answered.

## Results

Experimental techniques and results have been presented.[1] Of interest now are the kinetic parameters for the reactions illustrated below (analogous equations hold for the substituted compounds)

$$[Co(NH_3)_6](N_3)_3 \longrightarrow CoN + 6NH_3 + 4N_2 \quad (1)$$

$$[Co(NH_3)_6](N_3)_3 \longrightarrow Co(NH_3)_2(N_3)_2 + 4NH_3 + 1.5N_2 \quad (2)$$

Both equations are idealized. The cobalt(II) reaction is complicated by the lability of the ammonia–cobalt(II) azide system and the existence of higher cobalt(II) ammines. Also, the residues of the CoN reaction may bear minor quantities of cobalt(0).

The CoN reaction has an induction period which can be prolonged by minute quantities of ammonia and shortened by dusting the crystals with CoN or freshly prepared cobalt. Table I summarizes the kinetic parameters obtained from both the final reactions and

(1) T. B. Joyner, *J. Phys. Chem.*, **74**, 1552 (1970), and references therein.

(2) T. B. Joyner, *ibid.*, **74**, 1558 (1970).

(3) T. B. Joyner and F. H. Verhoek, *J. Amer. Chem. Soc.*, **83**, 1069 (1961).

**Table I:** Apparent Activation Energies ($E_a$) and Preexponentials ($A$) for the Thermal Decomposition of Solid Cobalt(III) Ammine Azides

| Compound | Period | $E_a$, kcal/mol | $A$, sec$^{-1}$ |
|---|---|---|---|
| **The CoN Reaction** | | | |
| $[Co(NH_3)_6](N_3)_3$ | Induction | 25 ± 2[a] | 10 ± 2[a] |
| | Final | 25[b] | 10 |
| $[Co(NH_3)_6](N_3)_3$[c] | Induction | 21 | 8 |
| | Final | 25 | 11 |
| $[Co(NH_3)_5N_3](N_3)_2$ | Induction | 22 | 9 |
| | Final | 20 | 8 |
| *cis*-$[Co(NH_3)_4(N_3)_2]N_3$ | Induction | 23 | 10 |
| | Final | 24 | 11 |
| *trans*-$[Co(NH_3)_4(N_3)_2]N_3$ | Induction | 20 | 8 |
| | Final | 23 | 10 |

| Compound | Initial ammonia, Torr | $E_a$, kcal/mol | $A$, sec$^{-1}$ |
|---|---|---|---|
| **The Cobalt(II) Reaction** | | | |
| $[Co(NH_3)_6](N_3)_3$ | 0[d] | 46[e] ± 4[a] | 21 ± 3[a] |
| | 0 | 34[f] | 15 |
| | 50 | 33 | 15 |
| | 100 | 32 | 14 |
| | 200 | 32 | 14 |
| $[Co(NH_3)_5N_3](N_3)_2$ | 0 | 49 | 23 |
| | 50 | 46 | 21 |
| *cis*-$[Co(NH_3)_4(N_3)_2]N_3$ | 0 | (53)[g] | (26)[g] |
| | 50 | 59 | 30 |
| | 100 | 52 | 26 |
| *trans*-$[Co(NH_3)_4(N_3)_2]N_3$ | 0 | 54 | 25 |
| | 50 | 54 | 25 |
| | 100 | 55 | 26 |

[a] The uncertainties are discussed in the original papers. In general, the values are derived from several series of runs on various samples of the compound. While the uncertainty within a given series is usually small, the disagreement between the series is rather greater. This is particularly true of the cobalt(II) reaction which presents special problems. The listed limits apply throughout the respective sections and are rather generous estimates capable of including the great majority of the data. [b] A few lower values (20 kcal/mol) reflect, it is thought, variations in the reaction topographies. [c] Catalyzed runs. [d] Referred to as "normal" runs. [e] Derived from $\alpha < 0.5$ where $\alpha$ is the fraction reacted. [f] Derived from $\alpha > 0.5$. The self-generated ammonia influences the run. [g] The data are severely restricted. The 100-Torr runs are probably the best. The value for normal runs is a rough estimation based on a very narrow temperature range. The problem is discussed in the original paper.

the duration, $\tau$, of the induction periods. The CoN decomposition (induction period and final reaction) is characterized by apparent activation energies in the range of 20–26 kcal/mol for all four compounds. The only exceptions are the induction periods in the presence of ammonia (usually self-generated) which give values in the vicinity of 50 kcal/mol. The cobalt(II) reactions of the substituted compounds and of the hexaammine under low ammonia also have apparent activation energies of about 50 kcal/mol. The hexaammine under higher ammonia is unique in yielding a value of 32 kcal/mol for the cobalt(II) reaction. This brief summary indicates the most striking feature of the accumulated results, the great similarities in the reactions of four compounds. This is particularly remarkable since the compounds themselves differ in many important respects.

## Discussion

The rather unexpected similarities indicate mechanisms largely independent of the nature of the cation, the nature of the salt, and properties dependent on crystal structure. They also rule out several conceivable, and initially expected, mechanisms dependent on the presence of a coordinated azide ion and predicting a difference in the reactions of the hexaammine and the substituted compounds. These merit brief comment.

In simple metal azides the azide ion is symmetric. In covalent compounds it is asymmetric. The decomposition mechanisms differ. The former are thought to proceed by promotion of an electron to conduction or exciton bands, the latter by breakage of an N–N bond. (There have been several recent and excellent reviews of azide chemistry.[4-6]) Cobalt(III) ammines can have both asymmetric coordinated azides and symmetric lattice azides.[7] This being so, a difference might have been anticipated for the hexaammine (with only ionic azides) and the azidopentaammine with a possible cleavage reaction

$$(H_3N)_5CoN_3^{2+} \longrightarrow (H_3N)_5CoN^{2+} + N_2 \qquad (3)$$

Further differences could have been expected for the diazidotetraammines, particularly the *cis*, owing to the proximity of the two coordinated azides and the possibility that the initial cleavage would be followed by the rapid evolution of nitrogen and the release of considerable energy. Such differences were not observed.

A conceivable path would be a series of fast substitutions

$$[Co(NH_3)_6](N_3)_3 \longrightarrow [Co(NH_3)_5N_3](N_3)_2 + NH_3 \qquad (4)$$

$$[Co(NH_3)_5N_3](N_3)_2 \longrightarrow [Co(NH_3)_4(N_3)_2]N_3 + NH_3 \qquad (5)$$

and perhaps

$$[Co(NH_3)_4(N_3)_2]N_3 \longrightarrow Co(NH_3)_3(N_3)_3 + NH_3 \qquad (6)$$

to a common compound whose decomposition would be rate controlling. For several reasons this seems un-

(4) D. A. Young, "Decomposition of Solids," Pergamon Press, New York, N. Y., 1966, Chapter 5.

(5) A. D. Yoffe, "Developments in Inorganic Nitrogen Chemistry," C. B. Colburn, Ed., Elsevier Publishing Co., New York, N. Y., 1966, Chapter 2.

(6) P. Gray, *Quart. Rev.* (London), 17, 441 (1963).

(7) G. J. Palenik, *Acta Crystallogr.*, 17, 360 (1964).

likely. Optical and X-ray examination of partially decomposed crystals of the hexaammine and azidopentaammine have detected no evidence of a substitution reaction. Thus it would be restricted, if present at all, to the reaction zone. Inhibition by ammonia might be anticipated whereas, in fact, ammonia accelerates reaction 2 and has no direct effect on reaction 1. (An elaborate alternative involving a fast initial reduction, equilibration to $Co(NH_3)_4(N_3)_2$, and reoxidation to $[Co(NH_3)_4(N_3)_2]^+$ whose rate-controlling decomposition provides species for both the reduction of the next cobalt(III) ion and reoxidation of the intermediate seems unattractively complex.) Reaction 6 can compete with reaction 2 during the diazidotetraammine decompositions, but the observed survival of triazidotriamminecobalt(III) makes this compound an unlikely precursor. Finally, analogous chlorides and bromides, which in many ways resemble azides, require relatively high temperatures before undergoing rather complicated decompositions.[8] Searching specifically for substitution, Watt found that slow heating to 270° was necessary for conversion of hexaamminecobalt(III) chloride into the chloropentaammine.[9] Although the decompositions to cobalt(II) halides appear complex and viewpoints differ as to mechanisms,[8] the electron-transfer mechanism of Tanaka, *et al.*,[10] seems particularly relevant to the azides in that it does not require initial substitutions.

If substitution reactions are improbable precursors, it is apparent, particularly for the hexaammine, that electrons originating with the lattice azides will have to be transferred across the ligand sphere. Possible differences between the hexaammine and the substituted compounds were again anticipated by analogy to solution kinetics and the ability of unsaturated ligands to serve as bridges in oxidation–reduction reactions.[11] The failure to observe such differences is made less surprising by studies showing that reduction of the hexaamminecobalt(III) ion by the solvated electron is very fast, taking place on encounter.[12,13] While the nature and environment of electrons in solutions and solids are clearly enormously different, it is apparent that the ligand sphere need not inhibit rapid electron transfer.

A detailed discussion of the decompositions necessitates the recognition of two reaction systems under several quite different conditions. These are the CoN reaction in the presence of a widespread CoN phase, *i.e.*, the final CoN reaction; the cobalt(II) reaction (including the special case of the hexaammine under ammonia) in the presence of cobalt(II) products but without significant CoN; the induction period when tiny quantities of CoN and cobalt(II) are present in localized regions of the crystal; and the nucleation processes about which, unfortunately, little can be said.

*The CoN Reaction.* It has been proposed[1] that the rate-controlling reaction involves the solid product and the ionic, lattice azides. At present this reaction cannot be defined in detail. A rather general representation

$$N_3^- \longrightarrow N_3^0 + e^- \qquad (7)$$

resembles the mechanisms ascribed to simple azides.[4-6] As it stands it is a drastic oversimplification with no specification as to the nature or location of the electron (there are many possibilities involving reactant, product, or interfacial regions), the location of the reaction (the interface is important but possibly only as a recipient of electrons or radicals generated elsewhere), the nature of the solid products (whether they are aggregates of atoms or recognizable crystallized phases), or the nature and location of the azide radical.

Various schemes implying more specificity may be written. Two reactions suggest a direct reaction of the

$$CoN + N_3^- \longrightarrow Co + 2N_2 + e^- \qquad (8)$$

$$Co + N_3^- \longrightarrow CoN + N_2 + e^- \qquad (9)$$

azide with the products. (It will be recalled that minor quantities of cobalt(0) are observed in some residues and that freshly prepared cobalt can apparently shorten the induction period.[1]) These bear some similarity to early mechanisms proposed for barium azide, a compound which can also yield a nitride. Gunther, Andreew, and Ringbom[14] originally suggested

$$Ba + Ba(N_3)_2 \longrightarrow Ba_2N_2 + 2N_2 \qquad (10)$$

$$2Ba_2N_2 \longrightarrow Ba + Ba_3N_2 + N_2 \qquad (11)$$

In a remarkably detailed study, Torkar and Spath[15] have recently identified the activation energy for nucleus formation with the thermal excitation of excitons and written growth mechanisms involving $Ba^+$ ions, barium aggregates, and nitride formation by the reaction of the latter with active nitrogen

$$N_2^* + Ba_2 \longrightarrow Ba_2N_2 \qquad (12)$$

followed by eq 11. Unfortunately, in the case of the cobalt(III) ammine azides the detailed information necessary for a distinction between the various pos-

(8) W. W. Wendlandt and J. P. Smith, "The Thermal Properties of Transition Metal Ammine Complexes," Elsevier Publishing Co., New York, N. Y., 1967, Chapters 3, 4, and 5.

(9) G. W. Watt, *Inorg. Chem.*, **3**, 325 (1964).

(10) N. Tanaka, K. Nagase, and S. Nagakura, *Bull. Chem. Soc. Jap.*, **41**, 1143 (1968).

(11) F. Basolo and R. G. Pearson, "Mechanisms of Inorganic Reactions," John Wiley & Sons, Inc., New York, N. Y., 1967, p 470 ff.

(12) J. H. Baxendale, E. M. Fielden, and J. P. Keene, *Proc. Roy. Soc.*, **A266**, 320 (1965).

(13) J. F. Endicott and M. Z. Hoffman, *J. Phys. Chem.*, **70**, 3389 (1966).

(14) P. Gunther, K. Andreew, and A. Ringbom, *Z. Elektrochem.*, **36**, 211 (1930).

(15) K. Torkar and H. T. Spath, *Monatsh. Chem.*, **99**, 118 (1968).

sibilities is not yet on hand. This may, in any event, be difficult due to the complex nature of a reaction zone that may involve several species of cobalt compounds in various states of aggregation.

Whatever the details of the original reaction, the electron reduces the cobalt with the first step (again written for the hexaammine) given by

$$Co(NH_3)_6^{3+} + e^- \longrightarrow Co(NH_3)_6^{2+} \quad (13)$$

Ligand sphere rearrangements can occur

$$Co(NH_3)_6^{2+} + 2N_3^- \longrightarrow \{Co(NH_3)_2(N_3)_2\} + 4NH_3 \quad (14)$$

with the { } indicating that the initial product is an intermediate and not an organized solid phase. Such rearrangements, although relatively fast for solid cobalt(II) ammines, need not be immediate, thus affording additional opportunities for disruption in the reaction zone.[16]

Reception of a second electron will give cobalt(I)

$$Co(II) + e^- \longrightarrow Co(I) \quad (15)$$

More specific equations implying reduction before or after ligand rearrangement can be written but seem unjustified in the absence of certain knowledge of the structure of either the reacting species or cobalt(I). A third electron would give cobalt(0)

$$Co(I) + e^- \longrightarrow Co(0) \quad (16)$$

while the nitride could result from

$$Co + N_3^0 \longrightarrow CoN + N_2 \quad (17)$$

or mechanisms similar to those of Torkar and Spath.[15] Cobalt(I), however, is probably an energetic species with such conceivable alternatives as reaction with an azide ion

$$Co(I) + N_3^- \longrightarrow CoN + N_2 \quad (18)$$

A brief comment should be included as to the possible involvement of $N_2$ complexes and reactions of the type

$$cis\text{-}[Ru(en)_2(N_3)_2]PF_6 \longrightarrow cis\text{-}[Ru(en)_2N_2N_3]PF_6 \quad (19)$$

reported by Kane-Maguire, *et al.*[17,18] At present, it does not seem that the rate data permit the detection of such reactions although they could conceivably appear as competitors—particularly in the rather confused decomposition of *cis*-diazidotetraamminecobalt(III) azide[19]—or during the reactions of the various intermediates. They seem less likely as rate-controlling reactions due to the need for similar mechanisms for both the hexaammine and the substituted complexes and the absence of an attractive precursor reaction to a common compound.

*The Cobalt(II) Reaction.* Although the above scheme has cobalt(II) intermediates, production of a final cobalt(II) phase is a different problem. In particular, the cobalt(II) reaction propagates in the absence of CoN but in the presence of one or more cobalt(II) phases. The process is obviously complex with the high preexponentials (Table I) suggesting multiple rate constants. The complicating factors may be topographical or chemical. Continuing nucleation, the lability of the ammonia–cobalt(II) azide system, and kinetically significant rates of crystallization are examples of potential difficulties.

Despite the problems, analysis has permitted the suggestion of a rate-controlling step similar to eq 7 but associated with the cobalt(II) products (with the exceptional reaction of hexaammine under ammonia involving a transient hexaamminecobalt(II) azide phase).[16] The initial reduction and rearrangement, identical with eq 13 and 14, must be followed by an accretion process

$$\{Co(NH_3)_2(N_3)_2\} + [Co(NH_3)_2(N_3)_2]_x \longrightarrow [Co(NH_3)_2(N_3)_2]_{(x+1)} \quad (20)$$

adding the intermediate to the growing cobalt(II) phase.

The cobalt(II) product is clearly subject to further reduction. It may become particularly vulnerable late in the decomposition when the cobalt(III) available as a destination for the electrons is diminished. This reduction could lead to conversion into the CoN system. If this occurs late, the exothermic CoN reaction may initiate an explosion, frequently observed, of the accumulated, very sensitive cobalt(II) complexes.

*The Induction Period.* The very early interplay between the CoN and cobalt(II) reactions produces the growth patterns leading to the induction period and determines the subsequent course of the decomposition. The balance between the reactions may be particularly delicate due to the importance of the solid products. During the induction period the accumulations of products will be very small, but their location and shape may be critical.

Both mechanisms have possibilities for conversion into the alternate path. Particularly important competitive processes are provided by eq 15 and 20. The production of a cobalt(II) phase can interrupt the CoN reaction in two ways. It may remove the cobalt(II) intermediate from the CoN front prior to its reduction (eq 15) to cobalt(I). It may also remove azide ions by eq 14 and 20. If the azides in the cobalt(II) phase are comparatively immune to attack by CoN or cobalt(0) (eq 7–9), the CoN reaction will be hindered. Such a relative invulnerability might result from a simple

(16) T. B. Joyner, *J. Phys. Chem.*, 72, 4386 (1968).

(17) L. A. P. Kane-Maguire, P. S. Sheridan, F. Basolo, and R. G. Pearson, *J. Amer. Chem. Soc.*, 90, 5295 (1968).

(18) The author is indebted to Professor Hans B. Jonassen for raising these possibilities.

(19) T. B. Joyner, *J. Phys. Chem.*, 72, 703 (1968).

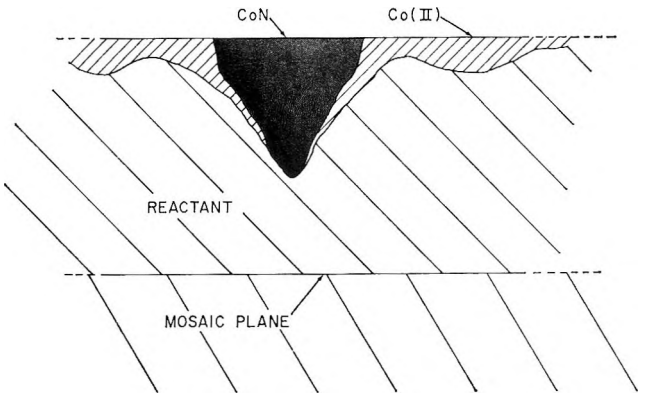


Figure 1. Hypothetical cross section of a crystal at a time early in the induction period. The location of the mosaic plane is arbitrarily drawn.

physical separation caused by crystallization of the product phases.

It is now necessary to consider how these competitive processes might operate during the induction period and, in particular, to explain why the early CoN reaction is so easily inhibited while the final CoN reaction dominates the decomposition and is independent of even large quantities of ammonia.[1,2] A plausible explanation is based on the differences in reactions propagating along a broad product front or dependent on a microscopic spike of product.

It is believed[2] that the cobalt(II) products restrict the early lateral growth of the CoN reaction and force it into primarily vertical growth with $\tau$ being the time to reach the first mosaic plane. Figure 1 illustrates a hypothetical cross section of a crystal at a time early in the induction period. Although the cobalt(II) reaction alone appears to be slower than the CoN reaction (as evidenced by the $\tau$'s[1,2]) competition for the intermediate (eq 20) may permit the phase to extend itself along the sides of the CoN spike. If the cobalt(II) phase—growing by its own mechanism[16] and competing for azide ions and the cobalt(II) intermediate (eq 14 and 20)—should outgrow and isolate the CoN spike, the induction period will be prolonged. Ammonia increases the chances of such an isolation by accelerating the cobalt(II) reaction.[16] Since ammonia adsorbed on the crystal can act directly on the young reaction sites, very tiny amounts may suffice to force induction period growth by the cobalt(II) reaction[2] or in the case of Powder convert the entire decomposition into the cobalt(II) path.

The situation during the final CoN reaction is very different. The CoN front is well established while an organized cobalt(II) phase is either nonexistent or present only in minor quantities too small to block CoN growth and themselves vulnerable to reduction by that now dominant reaction. Without a significant cobalt(II) phase to influence, ammonia will have no effect on the decomposition. Thus the quite different effects of ammonia during the induction period and final reaction are understandable on the basis of the proposed mechanisms and model.

*The Nucleation Period.* It is recognized that the above are propagation mechanisms dependent on the presence of products. Unfortunately, the data do not yet seem adequate for an understanding of the nucleation phenomena responsible for the generation of these materials. These initial events need study.

# Crystal Field–Spin Orbit Perturbation Calculations in $d^2$ and $d^8$ Trigonal Bipyramidal Complexes

by C. A. L. Becker,[1] Devon W. Meek,

*Department of Chemistry, The Ohio State University, Columbus, Ohio 43210*

and T. M. Dunn

*Department of Chemistry, The University of Michigan, Ann Arbor, Michigan 48104* *(Received March 17, 1969)*

The complete crystal field–spin orbit perturbation calculation for a $d^2$, $d^8$ configuration in $D_{3h}$ symmetry has been presented in both weak and strong crystalline field approximations. The weak-field basis functions are the Russell–Saunders $LS$-coupled $\{SLM_SM_L\}$ eigenfunctions of the free atom transformed to the $\{SLJM\}$ basis by use of the Clebsch–Gordon coefficients, and then symmetry adapted to the $D_{3h}$ crystalline field by means of the appropriate $D^j(\alpha,\beta,\gamma)(j = 1, 2, 3, 4)$ rotation matrices. Care is taken to preserve a consistent phase within the forty-five basis functions. The strong-field basis functions are taken as the $D_{3h}$ crystalline field (orbital-only) eigenfunctions, and constructed as linear combinations of the one-electron product-type component wavefunctions of the strong-field two-electron configurations. A correlation diagram to the weak-field approximation helps establish the requisite symmetries. The spin functions are then introduced explicitly and new linear combinations taken to establish the $D_{3h}$ (orbital and spin) symmetry eigenfunctions. The perturbation matrix elements are expressed in terms of the crystal field parameters $Dq$ and $Db$, the Slater–Condon–Shortley Coulombic parameters $F_2$ and $F_4$, and the one-electron spin–orbit coupling parameter $\lambda$. The simple (weak-field) crystal field calculations and $d^2$, $d^8$ correlation diagrams under $D_{3h}$ are partial results of the more extensive calculations, so they have also been illustrated and discussed. Calculations for $C_{3v}$ and other lower symmetries are basically similar to those for $D_{3h}$, except for the necessary modification of crystal field parameters. To illustrate the qualitative aspects of the complete calculations the perturbation matrices have been solved with approximated parametric values and the results discussed in reference to experimental absorption spectra of trigonal bipyramidal transition metal complexes.

## Introduction

Crystal field calculations, in both the simple and complete forms, have been performed for most $d^n$ configurations in cubic symmetry and have been found very useful in explaining the optical spectra of transition metal complexes.[2-5] The complete crystal field–spin orbit perturbation calculations for the regular trigonal bipyramid have not been extended beyond those of the $d^1$,$d^9$ configuration, however, although the simple crystal field calculations exist for many of the $d^n$ configurations.[6-8] Since trigonal bipyramidal coordination is now firmly established for many transition metals, especially for the $d^8$ configuration of Ni(II),[9] this work investigates the complete perturbation calculations for the $d^2$, $d^8$ configuration subjected to a regular $D_{3h}$ crystalline field.

The weak and strong crystalline field approximations used in the complete or exact perturbation calculations have been previously discussed.[3-5,10] The perturbation Hamiltonian consists of three terms

$$\mathcal{H}' = V_{CF}(r, \theta, \Phi) + \sum_{i>j}^{2} e^2/r_{ij} + \sum_{i=1}^{2} \xi(r_i)\, l_i s_i \quad (1)$$

the crystal field, Coulombic electron-electron repulsion, and spin–orbit perturbations, respectively, since the radial terms

$$\sum(-Ze^2/r_i - U(r_i))$$

become part of the zero-order Hamiltonian when one neglects configuration interaction. For the weak field basis functions we have assumed Russell–Saunders

(1) Department of Chemistry, The University of Texas, Austin, Texas 78712.

(2) Y. Tanabe and S. Sugano, *J. Phys. Soc. Jap.*, **9**, 753, 766 (1954); **11**, 864 (1956).

(3) A. D. Liehr, *J. Phys. Chem.*, **64**, 43 (1960).

(4) A. D. Liehr and C. J. Ballhausen, *Ann. Phys. (N. Y.)*, **6**, 134 (1959).

(5) A. D. Liehr, *J. Phys. Chem.*, **67**, 1314 (1963).

(6) M. Ciampolini, *Inorg. Chem.*, **5**, 35 (1966).

(7) M. J. Norgett, J. H. M. Thornley, and L. M. Venanzi, *J. Chem. Soc., A*, 540 (1967). See also the corrected extension of this work, M. J. Norgett and L. M. Venanzi, *Inorg. Chim. Acta*, **2**, 107 (1968).

(8) J. S. Wood, *Inorg. Chem.*, **7**, 852 (1968).

(9) The following references are but a few typical examples of the many recent papers on this subject: (a) L. M. Venanzi, *Angew. Chem.*, **76**, 621 (1964); (b) C. M. Harris, R. S. Nyholm, and D. J. Phillips, *J. Chem. Soc.*, 4379 (1960); (c) G. S. Benner, W. E. Hatfield, and D. W. Meek, *Inorg. Chem.*, **3**, 1544 (1964); (d) G. Dyer, J. G. Hartley, and L. M. Venanzi, *J. Chem. Soc.*, 1293, (1965); (e) G. Dyer and D. W. Meek, *Inorg. Chem.*, **4**, 1398 (1965); (f) L. Sacconi, M. Ciampolini, and G. P. Speroni, *J. Amer. Chem. Soc.*, **87**, 3102 (1965); (g) G. Dyer and D. W. Meek, *Inorg. Chem.*, **6**, 149 (1967); (h) G. S. Benner and D. W. Meek, *ibid.*, **6**, 1399 (1967); (i) M. Ciampolini and N. Nardi, *ibid.*, **5**, 41 (1966); (j) M. Ciampolini and G. P. Speroni, *ibid.*, **5**, 45 (1966).

(10) C. A. L. Becker, D. W. Meek, and T. M. Dunn, *J. Phys. Chem.*, **72**, 3588 (1968).

coupling, as is usually customary for transition metals of the first row.[11,12]

The many symmetry transformations required of the two-electron wavefunctions have been performed by use of the generalized $D^j(\alpha,\beta,\gamma)$ rotation matrices,[13] listed for convenience in the Appendix. Although our interest is directed at the complete crystal field–spin orbit perturbation calculations, we shall find the simple crystal field calculations for the $d^2$,$d^8$ configuration in trigonal bipyramidal environment very useful in that many matrix elements may be carried over directly into the more complete calculation. Also, interesting comparisons and contrasts may be observed, so the simple crystal field calculations must be our starting place.

## Crystal Field Calculations

An appropriate form of the simple crystal field calculations for a $d^2$ configuration of first row transition metal ions is within the "weak crystalline field" model.[14] In this approximation Russell–Saunders coupling splits the degenerate $d^2$ configuration into its $LS$ terms as a first-order perturbation (*i.e.*, $d^2 \rightarrow {}^3F, {}^1D, {}^3P, {}^1G, {}^1S$) and crystal field perturbation remains second order within these individual terms. Basis functions may now be taken in the $\{SL\,M_S\,M_L\}$ basis of the free atom. The correct linear combinations of one-electron product-type wavefunctions for the $d^2$ configuration are found as eigenfunctions of the square of the total (orbital) angular momentum operator ($M_{OP}^2$).[15] Wavefunctions for the $^3F$ and $^3P$ states have been given by Ballhausen,[16] so only the singlet-state (spin-paired) $d^2$ eigenfunctions are listed in Table I. For the simple crystal field calculations the one-electron spin functions may be omitted.

**Table I:** The $d^2$ Spin-Paired (Orbital) Eigenfunctions

$$\psi_G(4) = |\phi_2\phi_2| \qquad \psi_G(-4) = |\phi_{-2}\phi_{-2}|$$
$$\psi_G(3) = |\phi_2\phi_1| \qquad \psi_G(-3) = |\phi_{-1}\phi_{-2}|$$
$$\psi_G(2) = \sqrt{4/7}|\phi_1\phi_1| + \sqrt{3/7}|\phi_2\phi_0|$$
$$\psi_G(1) = \sqrt{1/7}|\phi_2\phi_{-1}| + \sqrt{3/7}|\phi_1\phi_0|$$
$$\psi_G(0) = \sqrt{1/35}|\phi_2\phi_{-2}| + \sqrt{16/35}|\phi_1\phi_{-1}| + \sqrt{18/35}|\phi_0\phi_0|$$
$$\psi_G(-1) = \sqrt{1/7}|\phi_1\phi_{-2}| + \sqrt{3/7}|\phi_0\phi_{-1}|$$
$$\psi_G(-2) = \sqrt{4/7}|\phi_{-1}\phi_{-1}| + \sqrt{3/7}|\phi_0\phi_{-2}|$$
$$\psi_D(2) = \sqrt{4/7}|\phi_2\phi_0| - \sqrt{3/7}|\phi_1\phi_1|$$
$$\psi_D(1) = \sqrt{1/7}|\phi_1\phi_0| - \sqrt{6/7}|\phi_2\phi_{-1}|$$
$$\psi_D(0) = \sqrt{4/7}|\phi_2\phi_{-2}| + \sqrt{1/7}|\phi_1\phi_{-1}| - \sqrt{2/7}|\phi_0\phi_0|$$
$$\psi_D(-1) = \sqrt{1/7}|\phi_0\phi_{-1}| - \sqrt{6/7}|\phi_1\phi_{-2}|$$
$$\psi_D(-2) = \sqrt{4/7}|\phi_0\phi_{-2}| - \sqrt{3/7}|\phi_{-1}\phi_{-1}|$$
$$\psi_S(0) = \sqrt{2/5}|\phi_2\phi_{-2}| - \sqrt{2/5}|\phi_1\phi_{-1}| - \sqrt{1/5}|\phi_0\phi_0|$$

There are a number of ways to determine the symmetries required of the crystalline field eigenfunctions. Let us calculate the symmetry properties of the real (trigonometric) atomic orbitals under a $D_{3h}$ crystalline field and use these results to draw analogy with the $d^2$ terms.[17] The trigonometric angular distributions transform as their Cartesian equivalents, so the rotation "characters" are readily observed from simple transformations of the Cartesian products. Symmetry properties of the (real) atomic orbitals are listed then in Table II.

**Table II:** Atomic Orbital Symmetry in $D_{3h}$ Crystal Field

| Atomic orbital | E | $C_3$ | $C_2$ | $\sigma_h$ | $D_{3h}$ | $m_l$ |
|---|---|---|---|---|---|---|
| s | 1 | 1 | 1 | 1 | $A_1'$ | 0 |
| $p_z$ | 1 | 1 | −1 | −1 | $A_2''$ | 0 |
| $p_x$, $p_y$ | 2 | −1 | 0 | 2 | E′ | ±1 |
| $d_{3z^2-r^2}$ | 1 | 1 | 1 | 1 | $A_1'$ | 0 |
| $d_{xy}$, $d_{x^2-y^2}$ | 2 | −1 | 0 | 2 | E′ | ±2 |
| $d_{xz}$, $d_{yz}$ | 2 | −1 | 0 | −2 | E″ | ±1 |
| $f_{z(5z^2-3r^2)}$ | 1 | 1 | −1 | −1 | $A_2''$ | 0 |
| $f_{x(x^2-3y^2)}$ | 1 | 1 | 1 | 1 | $A_1'$ | ±3 |
| $f_{y(3x^2-y^2)}$ | 1 | 1 | −1 | 1 | $A_2'$ | ±3 |
| $f_{x(5z^2-r^2)}$, $f_{y(5z^2-r^2)}$ | 2 | −1 | 0 | 2 | E′ | ±1 |
| $f_{(x^2-y^2)z}$, $f_{xyz}$ | 2 | −1 | 0 | −2 | E″ | ±2 |
| $g_{(35z^4-30z^2r^2+3r^4)}$ | 1 | 1 | 1 | 1 | $A_1'$ | 0 |
| $g_{xz(7z^2-3r^2)}$, $g_{yz(7z^2-3r^2)}$ | 2 | −1 | 0 | −2 | E″ | ±1 |
| $g2_{xy(7z^2-r^2)}$, $g_{(x^2-y^2)(7z^2-r^2)}$ | 2 | −1 | 0 | 2 | E′ | ±2 |
| $g_{xz(x^2-3y^2)}$ | 1 | 1 | −1 | −1 | $A_2''$ | ±3 |
| $g_{yz(3x^2-y^2)}$ | 1 | 1 | 1 | −1 | $A_1''$ | ±3 |
| $g_{(x^4-6x^2y^2+y^4)}$, $g4_{xy(x^2-y^2)}$ | 2 | −1 | 0 | 2 | E′ | ±4 |

Crystal field matrix elements are straightforwardly calculated in terms of the one-electron parameters for the quartic and quadratic radial dependencies, $Dq$ and $Db$, respectively, as previously defined.[10] The crystalline field perturbation of the $LS$ terms for the $d^2$ configuration is shown schematically in Figure 1, with the assumed approximation $Db = 1.72Dq$[18] so that a complete ordering of the levels may be suggested.[19] Even though this first-order secular determinant is

(11) These calculations are valid, then, to the limit in which Coulombic and spin–orbit perturbations are of comparable magnitudes,[12] but for spin–orbit perturbation significantly greater than Coulombic interaction, of course, the $j$–$j$ coupling to the $\{jjJM\}$ basis, rather than $LS$ coupling to the $\{SLJM\}$ basis, would be preferable.

(12) E. U. Condon and G. H. Shortley, "The Theory of Atomic Spectra," Cambridge Univ. Press, New York, N.Y., 1964, Chapter 11.

(13) M. Tinkham, "Group Theory and Quantum Mechanics," McGraw-Hill, New York, N. Y., 1964, Chapter 5.

(14) C. J. Ballhausen, "Introduction to Ligand Field Theory," McGraw-Hill, New York, N. Y., 1962, Chapter 4.

(15) H. Eyring, J. Walter, and G. E. Kimball, "Quantum Mechanics," John Wiley & Sons, New York, N. Y., 1964, Chapter 9.

(16) C. J. Ballhausen, *Kgl. Danske Videnskab. Selskab, Mat.-Fys. Medd.*, **29**, No. 8 (1955).

(17) In drawing an analogy between the symmetries of the one-electron wavefunctions and terms arising from several electrons, both functions with the same orbital angular momenta (*i.e.*, $l$ and $L$, respectively), due respect must be given to the parity of the atomic orbitals involved. The $\sigma_h$, $\sigma_v$, and $S_3$ operations of the $D_{3h}$ point group involve the inversion operation as well as a proper rotation, so the characters for the $^3F$ and $^3P$ wavefunctions (constructed from the gerade d-atomic orbitals) under these operations must differ by a $(-1)$ factor from those for the f and p atomic orbitals (ungerade; *i.e.*, $\chi(i) = -1$). This parity difference indicates that $\Gamma_i'$ representations for the one-electron orbitals must be $\Gamma_i''$ for the $d^2$ product-type wavefunctions and that $\Gamma_i''$ must become $\Gamma_i'$.

**Table III:** Symmetry Properties of the *LS* (Orbital) Eigenfunctions[a]

| | E | $C_3$ | $C_2$ | $\sigma_h$ | $S_3$ | $\sigma_v$ | $\Gamma_i$ |
|---|---|---|---|---|---|---|---|
| $\psi_F(3)$, $\psi_F(-3)$ | 2 | 2 | 0 | −2 | −2 | 0 | $\Gamma_7$ |
| $1/\sqrt{2}[\psi_F(3) + \psi_F(-3)]$ | 1 | 1 | −1 | −1 | −1 | 1 | $A_2''$ |
| $1/\sqrt{2}[\psi_F(3) - \psi_F(-3)]$ | 1 | 1 | 1 | −1 | −1 | −1 | $A_1''$ |
| $\psi_F(2)$, $\psi_F(-2)$ | 2 | −1 | 0 | 2 | −1 | 0 | E′ |
| $\psi_F(1)$, $\psi_F(-1)$ | 2 | −1 | 0 | −2 | 1 | 0 | E″ |
| $\psi_F(0)$ | 1 | 1 | −1 | 1 | 1 | −1 | $A_2'$ |
| $\psi_D(2)$, $\psi_D(-2)$ | 2 | −1 | 0 | 2 | −1 | 0 | E′ |
| $\psi_D(1)$, $\psi_D(-1)$ | 2 | −1 | 0 | −2 | 1 | 0 | E″ |
| $\psi_D(0)$ | 1 | 1 | 1 | 1 | 1 | 1 | $A_1'$ |
| $\psi_P(1)$, $\psi_P(-1)$ | 2 | −1 | 0 | −2 | 1 | 0 | E″ |
| $\psi_P(0)$ | 1 | 1 | −1 | 1 | 1 | −1 | $A_2'$ |
| $\psi_G(4)$, $\psi_G(-4)$ | 2 | −1 | 0 | 2 | −1 | 0 | E′ |
| $\psi_G(3)$, $\psi_G(-3)$ | 2 | 2 | 0 | −2 | −2 | 0 | $\Gamma_7$ |
| $1/\sqrt{2}[\psi_G(3) + \psi_G(-3)]$ | 1 | 1 | 1 | −1 | −1 | −1 | $A_1''$ |
| $1/\sqrt{2}[\psi_G(3) - \psi_G(-3)]$ | 1 | 1 | −1 | −1 | −1 | 1 | $A_2''$ |
| $\psi_G(2)$, $\psi_G(-2)$ | 2 | −1 | 0 | 2 | −1 | 0 | E′ |
| $\psi_G(1)$, $\psi_G(-1)$ | 2 | −1 | 0 | −2 | 1 | 0 | E″ |
| $\psi_G(0)$ | 1 | 1 | 1 | 1 | 1 | 1 | $A_1'$ |
| $\psi_S(0)$ | 1 | 1 | 1 | 1 | 1 | 1 | $A_1'$ |

[a] In actuality these are the $D_{3h}$ crystal field (orbital) symmetry eigenfunctions for the $d^2$ configuration.

entirely diagonal, the symmetry properties of the two-electron basis functions must nevertheless be investigated to establish the $D_{3h}$ crystalline field eigenfunctions. The symmetry transformations of the *LS*-coupled $d^2$ wavefunctions and of their required linear combinations (*ergo*, the $D_{3h}$ eigenfunctions), performed with use of the appropriate $D^2(\alpha,\beta,\gamma)$ rotation matrix, are listed in Table III.[20]

A second-order crystal field effect between first-order crystalline field levels of the same symmetries can now, of course, mix levels of different *LS* terms and of the same multiplicity. The second-order crystalline field interaction matrices are given below, where the term–term separation energies between *LS* terms of the same multiplicity are given by the Slater–Condon–Shortley parameters $F_2$ and $F_4$. The total Coulombic perturbation for these individual terms, as will be seen later, have of course different coefficients for the parameters. The $^1G(0)$ and $^1S(0)$ stabilization of the $^1A_1'[^1D(0)]$ level is seen to become increasingly important as the $Dq$ value approaches that for a strong field limit, in which $^1A_1'$ $[^1D(0)]$ must supplant $^3E'[^3F(\pm 2)]$ as the ground state for a $d^8$ configuration.

## The Weak-Field Approximation

In the Russell–Saunders *LS*-coupling approximation to the weak field basis functions the $\psi(SLM_SM_L)$ eigenfunctions are first calculated and then transformed to the $\{SLJM\}$ basis by means of the Clebsch–Gordon coefficients. As several independent methods of calculation for the *LS* eigenfunctions are available, let us first consider the method of (total) angular momentum lowering operators.[21] The forty-five two-electron $\{SLM_SM_L\}$ basis functions for the $d^2$ configuration as calculated by this method—which assures correct phase for all states within the same term but unfortunately not necessarily a consistent phase between the *LS* terms[22,23]—are listed in Table IV.

The *LS* eigenfunctions may also be constructed through use of vector-coupling formulas.[24] Here the individual *s*'s and *l*'s of the two equivalent electrons, $d^2$, are coupled to obtain the functions, $\psi(n_1l_1n_2l_2SLM_SM_L)$, which are just the product of coupled

(18) This very crude approximation has its origin in chapter 2 of F. Basolo and R. G. Pearson, "Mechanisms of Inorganic Reactions," John Wiley & Sons, New York, N. Y., 1958. The energy level diagram is, therefore, subject to experimental verification (or contradiction) as better relative magnitudes of $Dq$ and $Db$ are obtained from spectral data.

(19) The perturbation diagram for crystal field calculations in the method of symmetry operators[14] may be obtained from this diagram through the substitutions, $Db = -D\sigma$ and $Dq = -28/25\,D\tau$.

(20) This is basically the same set of crystal field symmetry eigenfunctions listed in Table I of ref 6. In ref 6, however, $^1G(3, \pm 2)$ should be $^1G(4, \pm 2)$, $^1E''(2)$ is really $^1E'(2)$, and $^1G(4, \pm 1)$ have been omitted. The missing $^1E''$ eigenfunctions arising from $^1G(4, \pm 1)$ have been included in ref 8.

(21) This method of calculation is that of N. M. Gray and L. A. Wills, *Phys. Rev.*, 38, 248 (1931), as exemplified in section 5[8] of ref 12.

(22) Because of their unique product-type component wavefunctions (*i.e.*, $(^1G, 0, 4) = |\Phi_2(\alpha)\Phi_2(\beta)|$ and $(^3F, 1, 3) = |\Phi_2(\alpha)\Phi_1(\alpha)|$), $\psi_G(0, 4)$ and $\psi_F(1, 3)$ can be directly identified in the conventional phase according to satisfaction of the phase criterion,[23] $\langle j_1j_2j_1(j_1 - J)|JJ\rangle$ real, $>0$, and then the remaining ($^1G$, $M_S$, $M_L$) and ($^3F$, $M_S$, $M_L$) states will be of this phase also, in satisfaction of the second phase criterion,[23] $J \pm |\ \tau JM\rangle = +\sqrt{J(J+1) - M(M \pm 1)}\ |\ \tau J, M \pm 1\rangle$. The ($^1D$, 0, 2) and ($^3P$, 1, 1) wavefunctions are simply orthonormalized to the ($^1G$, 0, 2) and ($^3F$, 1, 1) functions, respectively, however, so the phase is consistent therefore only within the $^1D$ and $^3P$ terms themselves, of course, and is arbitrary with respect to the other terms.

(23) A. Messiah, "Quantum Mechanics," Vol. II, Interscience Publ., New York, N.Y., 1962, Appendix C.

(24) This method of calculation is illustrated in section 6[8] of ref 12 and in article 27, chapter 13, of ref 23.

$$
\begin{array}{l|ll}
{}^3A_2'\,[{}^3F(0)] & -\frac{75}{14}\,Dq + \frac{2}{5}\,Db - E & -\frac{25}{7}\,Dq + \frac{6}{5}\,Db \\
{}^3A_2'\,[{}^3P(0)] & -\frac{25}{7}\,Dq + \frac{6}{5}\,Db & 15F_2 - 75F_4 - \frac{7}{5}\,Db - E
\end{array}
$$

$$
\begin{array}{l|ll}
{}^3E''[{}^3F(\pm1)] & -\frac{25}{28}\,Dq + \frac{3}{10}\,Db - E & \frac{25\sqrt{6}}{28}\,Dq + \frac{2\sqrt{6}}{5}\,Db \\
{}^3E''[{}^3P(\pm1)] & \frac{25\sqrt{6}}{28}\,Dq + \frac{2\sqrt{6}}{5}\,Db & 15F_2 - 75F_4 + \frac{7}{10}\,Db - E
\end{array}
\qquad (2)
$$

$${}^1A_1''[{}^1G(\pm3)] = {}^1A_2''[{}^1G(\pm3)] = -\frac{75}{28}\,Dq - \frac{1}{2}\,Db$$

$$
\begin{array}{l|ll}
{}^1E''[{}^1D(\pm1)] & -\frac{100}{49}\,Dq - \frac{3}{14}\,Db - E & \frac{125\sqrt{6}}{196}\,Dq + \frac{2\sqrt{6}}{7}\,Db \\
{}^1E''[{}^1G(\pm1)] & \frac{125\sqrt{6}}{196}\,Dq + \frac{2\sqrt{6}}{7}\,Db & \frac{225}{196}\,Dq + \frac{17}{14}\,Db + 7F_2 - 35F_4 - E
\end{array}
$$

$$
\begin{array}{l|lll}
{}^1E'\,[{}^1D(\pm2)] & \frac{25}{49}\,Dq + \frac{3}{7}\,Db - E & \frac{375\sqrt{3}}{98}\,Dq - \frac{2\sqrt{3}}{7}\,Db & 0 \\
{}^1E'\,[{}^1G(\pm2)] & \frac{375\sqrt{3}}{98}\,Dq - \frac{2\sqrt{3}}{7}\,Db & -\frac{275}{196}\,Dq + \frac{4}{7}\,Db + 7F_2 - 35F_4 - E & 0 \\
{}^1E'\,[{}^1G(\pm4)] & 0 & 0 & \frac{25}{14}\,Dq - 2Db + 7F_2 - 35F_4 - E
\end{array}
$$

$$
\begin{array}{l|lll}
{}^1A_1'\,[1D(0)] & \frac{150}{49}\,Dq - \frac{3}{7}\,Db - E & -\frac{125\sqrt{5}}{49}\,Dq - \frac{12\sqrt{5}}{35}\,Db & -(\sqrt{70}/5)\,Db \\
{}^1A_1'\,[{}^1G(0)] & -\frac{125\sqrt{5}}{49}\,Dq - \frac{12\sqrt{5}}{35}\,Db & \frac{225}{98}\,Dq + \frac{10}{7}\,Db + 7F_2 - 35F_4 - E & \frac{25\sqrt{14}}{14}\,Dq \\
{}^1A_1'\,[{}^1S(0)] & -(\sqrt{70}/5)\,Db & \frac{25\sqrt{14}}{14}\,Dq & 17F_2 + 90F_4 - E
\end{array}
$$

$${}^3E'\,[{}^3F(\pm2)] = \frac{25}{4}\,Dq$$

$${}^3A_1''\,[{}^3F(\pm3)] = {}^3A_2''[{}^3F(\pm3)] = -\frac{75}{28}\,Dq - \frac{1}{2}\,Db$$

orbital functions, $\psi(n_1l_1n_2l_2LM_L)$, with coupled spin functions, $\psi(s_1s_2SM_S)$.

The Clebsch–Gordon or Wigner coefficients[25] are used to construct the total spin and orbital angular momenta functions (*i.e.*, $j_1,j_2 = 1/2$, $J = S = 1,0$ and $j_1,j_2 = 2$, $J = 4,3,2,1,0$, respectively), and the angular momenta functions resulting from their products (*i.e.*, the $\{SLM_SM_L\}$ eigenfunctions) are identical with the wavefunctions in Table IV except that the $^3P$ functions are of different phase (*i.e.*, differ by a factor $[-1]$). The correct phase should always be preserved in this calculation, however, so the $^3P(M_S,M_L)$ functions in Table IV must therefore be multiplied by $(-1)$ for agreement with these $|l,m_l\rangle\,|l,m_s\rangle$ functions.

For $j_2 = 0$, the Wigner coefficient is,[26] $(j_10m_10|j_10jm) = \delta(j,j_1)\delta(m,m_1)$, so except for the phase change necessary to correlate $SLJ$ to $J_1J_2J$ (instead of the correlation of $LSJ$ to $J_1J_2J$ implied in the standard tables of Wigner coefficients), we have the $|JM\rangle$ transformation for the singlet states. The phase change is, however, $\{SLJM\} = (-1)^{L+S-J}\{LSJM\}$, so the weak field singlet-state basis functions (*i.e.*, the $\{SLJM\}$ eigenfunctions) have the same form as the $LS$ eigenfunctions, $|{}^1S,0,0,\rangle = ({}^1S,0,0)$, $|{}^1D,2,M\rangle = ({}^1D,0,M_L)$, and $|{}^1G,4,M\rangle = ({}^1G,0,M_L)$. The $\{LSJM\}$ basis of the triplet states is obtained as the linear combinations of the $\{LSM_LM_S\}$ basis prescribed by the Wigner coefficients (where $j_1 = L, j_2 = S$). After phase transformation to the $\{SLJM\}$ basis the $|{}^3F,J,M\rangle$ and $|{}^3P,J,M\rangle$ basis functions assume the forms given in Table V (in which $-({}^3P,M_S,M_L)$ has been used so that correct phase is present).

The symmetry levels into which the free-atom basis functions must separate under the perturbation of a

(25) Tabulations of the Clebsch–Gordon coefficients are readily available from such literature sources as ref 12, Tables 1–4;[3] ref 23, Appendix C; ref 13, section 5–10; J. M. Blatt and V. F. Weisskopf, "Theoretical Nuclear Physics," John Wiley & Sons, New York, N. Y., 1952, Appendix A; and E. P. Wigner, "Group Theory," trans. J. J. Griffin, Academic Press, New York, N. Y. 1959, Chapter 17.

(26) See eq 14[3] (6) of ref 12.

**Table IV:** The $[S,L,M_S,M_L]$ Basis Functions for $d^2$

| | | |
|---|---|---|
| | 4 | $\phi_2(\alpha)\phi_2(\beta)$ |
| | 3 | $\frac{1}{\sqrt{2}}[\phi_1(\alpha)\phi_2(\beta) + \phi_2(\alpha)\phi_1(\beta)]$ |
| | 2 | $\frac{2}{\sqrt{7}}\phi_1(\alpha)\phi_1(\beta) + \frac{\sqrt{3}}{\sqrt{14}}\phi_0(\alpha)\phi_2(\beta) + \frac{\sqrt{3}}{\sqrt{14}}\phi_2(\alpha)\phi_0(\beta)$ |
| | 1 | $\frac{\sqrt{3}}{\sqrt{7}}\phi_0(\alpha)\phi_1(\beta) + \frac{\sqrt{3}}{\sqrt{7}}\phi_1(\alpha)\phi_0(\beta) + \frac{1}{\sqrt{14}}\phi_{-1}(\alpha)\phi_2(\beta) + \frac{1}{\sqrt{14}}\phi_2(\alpha)\phi_{-1}(\beta)$ |
| $^1G$: | 0 | $\frac{4}{\sqrt{70}}\phi_1(\alpha)\phi_{-1}(\beta) + \frac{4}{\sqrt{70}}\phi_{-1}(\alpha)\phi_1(\beta) + \frac{6}{\sqrt{70}}\phi_0(\alpha)\phi_0(\beta) + \frac{1}{\sqrt{70}}\phi_2(\alpha)\phi_{-2}(\beta) + \frac{1}{\sqrt{70}}\phi_{-2}(\alpha)\phi_2(\beta)$ |
| | −1 | $\frac{\sqrt{3}}{\sqrt{7}}\phi_0(\alpha)\phi_{-1}(\beta) + \frac{\sqrt{3}}{\sqrt{7}}\phi_{-1}(\alpha)\phi_0(\beta) + \frac{1}{\sqrt{14}}\phi_1(\alpha)\phi_{-2}(\beta) + \frac{1}{\sqrt{14}}\phi_{-2}(\alpha)\phi_1(\beta)$ |
| | −2 | $\frac{2}{\sqrt{7}}\phi_{-1}(\alpha)\phi_{-1}(\beta) + \frac{\sqrt{3}}{\sqrt{14}}\phi_0(\alpha)\phi_{-2}(\beta) + \frac{\sqrt{3}}{\sqrt{14}}\phi_{-2}(\alpha)\phi_0(\beta)$ |
| | −3 | $\frac{1}{\sqrt{2}}[\phi_{-2}(\alpha)\phi_{-1}(\beta) + \phi_{-1}(\alpha)\phi_{-2}(\beta)]$ |
| | −4 | $\phi_{-2}(\alpha)\phi_{-2}(\beta)$ |
| | 3 | $\phi_2(\alpha)\phi_1(\alpha)$<br>$\frac{1}{\sqrt{2}}[\phi_2(\beta)\phi_1(\alpha) + \phi_2(\alpha)\phi_1(\beta)]$<br>$\phi_2(\beta)\phi_1(\beta)$ |
| | 2 | $\phi_2(\alpha)\phi_0(\alpha)$<br>$\frac{1}{\sqrt{2}}[\phi_2(\beta)\phi_0(\alpha) + \phi_2(\alpha)\phi_0(\beta)]$<br>$\phi_2(\beta)\phi_0(\beta)$ |
| | 1 | $\frac{\sqrt{2}}{\sqrt{5}}\phi_1(\alpha)\phi_0(\alpha) + \frac{\sqrt{3}}{\sqrt{5}}\phi_2(\alpha)\phi_{-1}(\alpha)$<br>$\frac{1}{\sqrt{5}}[\phi_1(\beta)\phi_0(\alpha) + \phi_1(\alpha)\phi_0(\beta)] + \frac{\sqrt{3}}{\sqrt{10}}[\phi_2(\beta)\phi_{-1}(\alpha) + \phi_2(\alpha)\phi_{-1}(\beta)]$<br>$\frac{\sqrt{2}}{\sqrt{5}}\phi_1(\beta)\phi_0(\beta) + \frac{\sqrt{3}}{\sqrt{5}}\phi_2(\beta)\phi_{-1}(\beta)$ |
| $^3F$: | 0 | $\frac{2}{\sqrt{5}}\phi_1(\alpha)\phi_{-1}(\alpha) + \frac{1}{\sqrt{5}}\phi_2(\alpha)\phi_{-2}(\alpha)$<br>$\frac{\sqrt{2}}{\sqrt{5}}[\phi_1(\beta)\phi_{-1}(\alpha) + \phi_1(\alpha)\phi_{-1}(\beta)] + \frac{1}{\sqrt{10}}[\phi_2(\beta)\phi_{-2}(\alpha) + \phi_2(\alpha)\phi_{-2}(\beta)]$<br>$\frac{2}{\sqrt{5}}\phi_1(\beta)\phi_{-1}(\beta) + \frac{1}{\sqrt{5}}\phi_2(\beta)\phi_{-2}(\beta)$ |
| | −1 | $\frac{\sqrt{2}}{\sqrt{5}}\phi_0(\alpha)\phi_{-1}(\alpha) + \frac{\sqrt{3}}{\sqrt{5}}\phi_1(\alpha)\phi_{-2}(\alpha)$<br>$\frac{1}{\sqrt{5}}[\phi_0(\beta)\phi_{-1}(\alpha) + \phi_0(\alpha)\phi_{-1}(\beta)] + \frac{\sqrt{3}}{\sqrt{10}}[\phi_1(\beta)\phi_{-2}(\alpha) + \phi_1(\alpha)\phi_{-2}(\beta)]$<br>$\frac{\sqrt{2}}{\sqrt{5}}\phi_0(\beta)\phi_{-1}(\beta) + \frac{\sqrt{3}}{\sqrt{5}}\phi_1(\beta)\phi_{-2}(\beta)$ |
| | −2 | $\phi_0(\alpha)\phi_{-2}(\alpha)$<br>$\frac{1}{\sqrt{2}}[\phi_0(\beta)\phi_{-2}(\alpha) + \phi_0(\alpha)\phi_{-2}(\beta)]$<br>$\phi_0(\beta)\phi_{-2}(\beta)$ |
| | −3 | $\phi_{-1}(\alpha)\phi_{-2}(\alpha)$<br>$\frac{1}{\sqrt{2}}[\phi_{-1}(\beta)\phi_{-2}(\alpha) + \phi_{-1}(\alpha)\phi_{-2}(\beta)]$<br>$\phi_{-1}(\beta)\phi_{-2}(\beta)$ |
| | 2 | $-\frac{\sqrt{3}}{\sqrt{7}}\phi_1(\alpha)\phi_1(\beta) + \frac{\sqrt{2}}{\sqrt{7}}\phi_0(\alpha)\phi_2(\beta) + \frac{\sqrt{2}}{\sqrt{7}}\phi_2(\alpha)\phi_0(\beta)$ |

**Table IV** (*Continued*)

| | | |
|---|---|---|
| | 1 | $\frac{\sqrt{3}}{\sqrt{7}}\phi_2(\alpha)\phi_{-1}(\beta) + \frac{\sqrt{3}}{\sqrt{7}}\phi_{-1}(\alpha)\phi_2(\beta) - \frac{1}{\sqrt{14}}\phi_1(\alpha)\phi_0(\beta) - \frac{1}{\sqrt{14}}\phi_0(\alpha)\phi_1(\beta)$ |
| $^1$D: | 0 | $\frac{1}{\sqrt{14}}\phi_1(\alpha)\phi_{-1}(\beta) + \frac{1}{\sqrt{14}}\phi_{-1}(\alpha)\phi_1(\beta) - \frac{\sqrt{2}}{\sqrt{7}}\phi_0(\alpha)\phi_0(\beta) + \frac{\sqrt{2}}{\sqrt{7}}\phi_{-2}(\alpha)\phi_{-2}(\beta) + \frac{\sqrt{2}}{\sqrt{7}}\phi_2(\alpha)\phi_{-2}(\beta)$ |
| | −1 | $-\frac{1}{\sqrt{14}}\phi_0(\alpha)\phi_{-1}(\beta) - \frac{1}{\sqrt{14}}\phi_{-1}(\alpha)\phi_0(\beta) + \frac{\sqrt{3}}{\sqrt{7}}\phi_1(\alpha)\phi_{-2}(\beta) + \frac{\sqrt{3}}{\sqrt{7}}\phi_{-2}(\alpha)\phi_1(\beta)$ |
| | −2 | $-\frac{\sqrt{3}}{\sqrt{7}}\phi_{-1}(\alpha)\phi_{-1}(\beta) + \frac{\sqrt{2}}{\sqrt{7}}\phi_0(\alpha)\phi_{-2}(\beta) + \frac{\sqrt{2}}{\sqrt{7}}\phi_{-2}(\alpha)\phi_0(\beta)$ |
| | 1 | $\frac{\sqrt{3}}{\sqrt{5}}\phi_1(\alpha)\phi_0(\alpha) - \frac{\sqrt{2}}{\sqrt{5}}\phi_2(\alpha)\phi_{-1}(\alpha)$<br>$\frac{\sqrt{3}}{\sqrt{10}}[\phi_1(\beta)\phi_0(\alpha) + \phi_1(\alpha)\phi_0(\beta)] - \frac{1}{\sqrt{5}}[\phi_2(\beta)\phi_{-1}(\alpha) + \phi_2(\alpha)\phi_{-1}(\beta)]$<br>$\frac{\sqrt{3}}{\sqrt{5}}\phi_1(\beta)\phi_0(\beta) - \frac{\sqrt{2}}{\sqrt{5}}\phi_2(\beta)\phi_{-1}(\beta)$ |
| $^3$P: | 0 | $\frac{1}{\sqrt{5}}\phi_1(\alpha)\phi_{-1}(\alpha) - \frac{\sqrt{4}}{\sqrt{5}}\phi_2(\alpha)\phi_{-2}(\alpha)$<br>$\frac{1}{\sqrt{10}}[\phi_1(\beta)\phi_{-1}(\alpha) + \phi_1(\alpha)\phi_{-1}(\beta)] - \frac{\sqrt{2}}{\sqrt{5}}[\phi_2(\beta)\phi_{-2}(\alpha) + \phi_2(\alpha)\phi_{-2}(\beta)]$<br>$\frac{1}{\sqrt{5}}\phi_1(\beta)\phi_{-1}(\beta) - \frac{\sqrt{4}}{\sqrt{5}}\phi_2(\beta)\phi_{-2}(\beta)$ |
| | −1 | $\frac{\sqrt{3}}{\sqrt{5}}\phi_0(\alpha)\phi_{-1}(\alpha) - \frac{\sqrt{2}}{\sqrt{5}}\phi_1(\alpha)\phi_{-2}(\alpha)$<br>$\frac{\sqrt{3}}{\sqrt{10}}[\phi_0(\beta)\phi_{-1}(\alpha) + \phi_0(\alpha)\phi_{-1}(\beta)] - \frac{1}{\sqrt{5}}[\phi_1(\beta)\phi_{-2}(\alpha) + \phi_1(\alpha)\phi_{-2}(\beta)]$<br>$\frac{\sqrt{3}}{\sqrt{5}}\phi_0(\beta)\phi_{-1}(\beta) - \frac{\sqrt{2}}{\sqrt{5}}\phi_1(\beta)\phi_{-2}(\beta)$ |
| $^1$S: | 0 | $-\frac{1}{\sqrt{5}}\phi_1(\alpha)\phi_{-1}(\beta) - \frac{1}{\sqrt{5}}\phi_{-1}(\alpha)\phi_1(\beta) + \frac{1}{\sqrt{5}}\phi_0(\alpha)\phi_0(\beta) + \frac{1}{\sqrt{5}}\phi_{-2}(\alpha)\phi_2(\beta) + \frac{1}{\sqrt{5}}\phi_2(\alpha)\phi_{-2}(\beta)$ |

regular trigonal bipyramidal crystalline field ($D_{3h}$) are readily shown to be[27,28]

$$
\begin{aligned}
|^1\mathrm{S}, 0, M\rangle &= {}^1\mathrm{S}_0 \longrightarrow \Gamma_1 \\
|^1\mathrm{G}, 4, M\rangle &= {}^1\mathrm{G}_4 \longrightarrow \Gamma_1 + 2\Gamma_3 + \Gamma_4 + \Gamma_5 + \Gamma_6 \\
|^1\mathrm{D}, 2, M\rangle &= {}^1\mathrm{D}_2 \longrightarrow \Gamma_1 + \Gamma_3 + \Gamma_6 \\
|^3\mathrm{P}, 2, M\rangle &= {}^3\mathrm{P}_2 \longrightarrow \Gamma_1 + \Gamma_3 + \Gamma_6 \\
|^3\mathrm{P}, 1, M\rangle &= {}^3\mathrm{P}_1 \longrightarrow \Gamma_2 + \Gamma_6 \qquad (3) \\
|^3\mathrm{P}, 0, M\rangle &= {}^3\mathrm{P}_0 \longrightarrow \Gamma_1 \\
|^3\mathrm{F}, 4, M\rangle &= {}^3\mathrm{F}_4 \longrightarrow \Gamma_1 + 2\Gamma_3 + \Gamma_4 + \Gamma_5 + \Gamma_6 \\
|^3\mathrm{F}, 3, M\rangle &= {}^3\mathrm{F}_3 \longrightarrow \Gamma_2 + \Gamma_3 + \Gamma_4 + \Gamma_5 + \Gamma_6 \\
|^3\mathrm{F}, 2, M\rangle &= {}^3\mathrm{F}_2 \longrightarrow \Gamma_1 + \Gamma_3 + \Gamma_5
\end{aligned}
$$

Transformation properties of the $|^{2S+1}L,J,M\rangle$ basis functions under the $D_{3h}$ symmetry operations can be observed with the use of the appropriate $D^j(\alpha,\beta,\gamma)$ rotation matrices.[29] From these rotation characters one readily sees that the symmetry requirements for $D_{3h}$ eigenfunctions are satisfied by the basis functions themselves, or by the elementary linear combinations of two basis functions (of the same absolute value $M$). By adopting the additional (arbitrary) symmetry requirement for distinguishing the "a" and "b" components of $\Gamma_3$ and $\Gamma_6$,[10,30] we easily identify the $D_{3h}$

$$C_3(z)\gamma_{3,6}^{(a,b)} = -e^{\pm\pi i/3}\gamma_{3,6}^{(a,b)} \qquad (4)$$

symmetry eigenfunctions listed in Table VI.

Since our basis functions are the standard $\{SLJM\}$ wavefunctions for the free-atom, the electrostatic term energies and the spin–orbit matrix elements are given in section 5[7] and Table I,[11] respectively, of ref 12. The crystal field perturbation is diagonal in $\Gamma_i$ and multiplicity, and straightforwardly calculated in terms of the one-electron integrals. The perturbation ma-

(27) Reducible representations for these eigenfunctions of total angular momentum are easily constructed by use of the standard equation for generalized rotational characters, as given, *e.g.*, in chapter 4 of ref 13 $\chi_J(\alpha) = \sin(J + 1/2)\alpha/\sin(\alpha/2)$.

(28) The order of the irreducible representations, $\Gamma_i$, of the $D_{3h}$ character table is that of F. A. Cotton, "Chemical Applications of Group Theory," Interscience Publishers, New York, 1963, Appendix II; *i.e.*, $A_1'$, $A_2'$, E′, $A_1''$, $A_2''$, E″, respectively.

(29) The $D_{3h}$ operations were performed through the following Eulerian rotations: $C_3(z)$, $\alpha = 2\pi/3$, $\beta,\gamma = 0$; $C_2(x)$, $\alpha = 0$, $\beta,\gamma = \pi$; $\sigma_v(xz) = C_2(y)$, $\alpha,\gamma = 0$, $\beta = \pi$; $\sigma_h(xy) = C_2(z)$, $\alpha = \pi,\beta,\gamma = 0$; and $S_3(z) = C_{6/5}(z)$, $\alpha = 5\pi/3,\beta,\gamma = 0$.

(30) See also ref 3 for the analogous $d^1$ calculations in cubic symmetry.

**Table V:** The $|^3F,J,M\rangle$ and $|^3P,J,M\rangle$ Basis Functions

$$|^3F, 4, 4\rangle = (^3F, 1, 3) = \phi_2(\alpha)\phi_1(\alpha)$$
$$|^3F, 4, 3\rangle = \sqrt{3/4}(^3F, 1, 2) + \sqrt{1/4}(^3F, 0, 3)$$
$$|^3F, 4, 2\rangle = \sqrt{15/28}(^3F, 1, 1) + \sqrt{3/7}(^3F, 0, 2) + \sqrt{1/28}(^3F, -1, 3)$$
$$|^3F, 4, 1\rangle = \sqrt{5/14}(^3F, 1, 0) + \sqrt{15/28}(^3F, 0, 1) + \sqrt{3/28}(^3F, -1, 2)$$
$$|^3F, 4, 0\rangle = \sqrt{3/14}(^3F, 1, -1) + \sqrt{4/7}(^3F, 0, 0) + \sqrt{3/14}(^3F, -1, 1)$$
$$|^3F, 4, -1\rangle = \sqrt{3/28}(^3F, 1, -2) + \sqrt{15/28}(^3F, 0, -1) + \sqrt{5/14}(^3F, -1, 0)$$
$$|^3F, 4, -2\rangle = \sqrt{1/28}(^3F, 1, -3) + \sqrt{3/7}(^3F, 0, -2) + \sqrt{15/28}(^3F, -1, -1)$$
$$|^3F, 4, -3\rangle = \sqrt{1/4}(^3F, 0, -3) + \sqrt{3/4}(^3F, -1, -2)$$
$$|^3F, 4, -4\rangle = (^3F, -1, -3) = \phi_{-1}(\beta)\phi_{-2}(\beta)$$
$$|^3F, 3, 3\rangle = \sqrt{1/4}(^3F, 1, 2) - \sqrt{3/4}(^3F, 0, 3)$$
$$|^3F, 3, 2\rangle = \sqrt{5/12}(^3F, 1, 1) - \sqrt{1/3}(^3F, 0, 2) - 1/2(^3F, -1, 3)$$
$$|^3F, 3, 1\rangle = \sqrt{1/2}(^3F, 1, 0) - \sqrt{1/12}(^3F, 0, 1) - \sqrt{5/12}(^3F, -1, 2)$$
$$|^3F, 3, 0\rangle = \sqrt{1/2}(^3F, 1, -1) - \sqrt{1/2}(^3F, -1, 1)$$
$$|^3F, 3, -1\rangle = \sqrt{5/12}(^3F, 1, -2) + \sqrt{1/12}(^3F, 0, -1) - \sqrt{1/2}(^3F, -1, 0)$$
$$|^3F, 3, -2\rangle = 1/2(^3F, 1, -3) + \sqrt{1/3}(^3F, 0, -2) - \sqrt{5/12}(^3F, -1, -1)$$
$$|^3F, 3, -3\rangle = \sqrt{3/4}(^3F, 0, -3) - \sqrt{1/4}(^3F, -1, -2)$$
$$|^3F, 2, 2\rangle = \sqrt{1/21}(^3F, 1, 1) - \sqrt{5/21}(^3F, 0, 2) + \sqrt{5/7}(^3F, -1, 3)$$
$$|^3F, 2, 1\rangle = \sqrt{1/7}(^3F, 1, 0) - \sqrt{8/21}(^3F, 0, 1) + \sqrt{10/21}(^3F, -1, 2)$$
$$|^3F, 2, 0\rangle = \sqrt{2/7}(^3F, 1, -1) - \sqrt{3/7}(^3F, 0, 0) + \sqrt{2/7}(^3F, -1, 1)$$
$$|^3F, 2, -1\rangle = \sqrt{10/21}(^3F, 1, -2) - \sqrt{8/21}(^3F, 0, -1) + \sqrt{1/7}(^3F, -1, 0)$$
$$|^3F, 2, -2\rangle = \sqrt{5/7}(^3F, 1, -3) - \sqrt{5/21}(^3F, 0, -2) + \sqrt{1/21}(^3F, -1, -1)$$
$$|^3P, 2, 2\rangle = -(^3P, 1, 1) = \sqrt{2/5}\phi_2(\alpha)\phi_{-1}(\alpha) - \sqrt{3/5}\phi_1(\alpha)\phi_0(\alpha)$$
$$|^3P, 2, 1\rangle = -\sqrt{1/2}(^3P, 1, 0) - \sqrt{1/2}(^3P, 0, 1)$$
$$|^3P, 2, 0\rangle = -\sqrt{1/6}(^3P, 1, -1) - \sqrt{2/3}(^3P, 0, 0) - \sqrt{1/6}(^3P, -1, 1)$$
$$|^3P, 2, -1\rangle = -\sqrt{1/2}(^3P, 0, -1) - \sqrt{1/2}(^3P, -1, 0)$$
$$|^3P, 2, -2\rangle = -(^3P, -1, -1)$$
$$|^3P, 1, 1\rangle = -\sqrt{1/2}(^3P, 1, 0) + \sqrt{1/2}(^3P, 0, 1)$$
$$|^3P, 1, 0\rangle = -\sqrt{1/2}(^3P, 1, -1) + \sqrt{1/2}(^3P, -1, 1)$$
$$|^3P, 1, -1\rangle = -\sqrt{1/2}(^3P, 0, -1) + \sqrt{1/2}(^3P, -1, 0)$$
$$|^3P, 0, 0\rangle = -\sqrt{1/3}(^3P, 1, -1) + \sqrt{1/3}(^3P, 0, 0) - \sqrt{1/3}(^3P, -1, 1)$$

trices for the "a" and "b" components of $\Gamma_3$ and $\Gamma_6$ are not identical, but differ by a $(-1)$ factor in several conjugate off-diagonal elements. As this phase-factor occurs to even powers in the cofactor expansion of the determinant, however, the perturbation energy levels of $\Gamma_{3a}$, $\Gamma_{3b}$ and of $\Gamma_{6a}$, $\Gamma_{6b}$ are indeed doubly degenerate.[31] The complete perturbation matrix for the $d^2$ configuration in a weak crystalline field approximation, then, is given below in its blocked form according to $\Gamma_i$.

**Table VI:** The $D_{3h}$ Weak-Field Symmetry Eigenfunctions for $d^2$

| | |
|---|---|
| $\Gamma_1(^1S_0) = \|^1S, 0, 0\rangle$ | $\Gamma_2(^3P_1) = \|^3P, 1, 0\rangle$ |
| $\Gamma_1(^3P_0) = \|^3P, 0, 0\rangle$ | $\Gamma_{6a}(^3P_1) = \|^3P, 1, 1\rangle$ |
| $\Gamma_{3a}(^3P_2) = \|^3P, 2, -2\rangle$ | $\Gamma_{6b}(^3P_1) = \|^3P, 1, -1\rangle$ |
| $\Gamma_{3b}(^3P_2) = \|^3P, 2, 2\rangle$ | $\Gamma_1(^1D_2) = \|^1D, 2, 0\rangle$ |
| $\Gamma_1(^3P_2) = \|^3P, 2, 0\rangle$ | $\Gamma_{3a}(^1D_2) = \|^1D, 2, -2\rangle$ |
| $\Gamma_{6a}(^3P_2) = \|^3P, 2, 1\rangle$ | $\Gamma_{3b}(^1D_2) = \|^1D, 2, 2\rangle$ |
| $\Gamma_{6b}(^3P_2) = \|^3P, 2, -1\rangle$ | $\Gamma_{6a}(^1D_2) = \|^1D, 2, 1\rangle$ |
| $\Gamma_1(^3F_2) = \|^3F, 2, 0\rangle$ | $\Gamma_{6b}(^1D_2) = \|^1D, 2, -1\rangle$ |
| $\Gamma_{3a}(^3F_2) = \|^3F, 2, -2\rangle$ | $\Gamma_{6a}(^3F_2) = \|^3F, 2, 1\rangle$ |
| $\Gamma_{3b}(^3F_2) = \|^3F, 2, 2\rangle$ | $\Gamma_{6b}(^3F_2) = \|^3F, 2, -1\rangle$ |
| $\Gamma_2(^3F_3) = \|^3F, 3, 0\rangle$ | |
| $\Gamma_{3a}(^3F_3) = \|^3F, 3, -2\rangle$ | $\Gamma_{3b}(^3F_3) = \|^3F, 3, 2\rangle$ |
| $\Gamma_{6a}(^3F_3) = \|^3F, 3, 1\rangle$ | $\Gamma_{6b}(^3F_2) = \|^3F, 3, -1\rangle$ |
| $\Gamma_4(^3F_3) = 1/\sqrt{2}\{\|^3F, 3, 3\rangle - \|^3F, 3, -3\rangle\}$ | |
| $\Gamma_5(^3F_3) = 1/\sqrt{2}\{\|^3F, 3, 3\rangle + \|^3F, 3, -3\rangle\}$ | |
| $\Gamma_{3a}'(^3F_4) = \|^3F, 4, 4\rangle$ | $\Gamma_{3a}''(^3F_4) = \|^3F, 4, -2\rangle$ |
| $\Gamma_{3b}'(^3F_4) = \|^3F, 4, -4\rangle$ | $\Gamma_{3b}''(^3F_4) = \|^3F, 4, 2\rangle$ |
| $\Gamma_{6a}(^3F_4) = \|^3F, 4, 1\rangle$ | $\Gamma_{6b}(^3F_4) = \|^3F, 4, -1\rangle$ |
| $\Gamma_1(^3F_4) = \|^3F, 4, 0\rangle$ | |
| $\Gamma_4(^3F_4) = 1/\sqrt{2}\{\|^3F, 4, 3\rangle + \|^3F, 4, -3\rangle\}$ | |
| $\Gamma_5(^3F_4) = 1/\sqrt{2}\{\|^3F, 4, 3\rangle - \|^3F, 4, -3\rangle\}$ | |
| $\Gamma_1(^1G_4) = \|^1G, 4, 0\rangle$ | |
| $\Gamma_{3a}'(^1G_4) = \|^1G, 4, 4\rangle$ | $\Gamma_{3a}''(^1G_4) = \|^1G, 4, -2\rangle$ |
| $\Gamma_{3b}'(^1G_4) = \|^1G, 4, -4\rangle$ | $\Gamma_{3b}''(^1G_4) = \|^1G, 4, 2\rangle$ |
| $\Gamma_{6a}(^1G_4) = \|^1G, 4, 1\rangle$ | $\Gamma_{6b}(^1G_4) = \|^1G, 4, -1\rangle$ |
| $\Gamma_4(^1G_4) = 1/\sqrt{2}\{\|^1G, 4, 3\rangle + \|^1G, 4, -3\rangle\}$ | |
| $\Gamma_5(^1G_4) = 1/\sqrt{2}\{\|^1G, 4, 3\rangle - \|^1G, 4, -3\rangle\}$ | |

## The Strong-Field Approximation

Like the weak-field approximation the strong crystalline field approximation is formulated in three steps: determination of the basis functions, construction of the symmetry eigenfunctions, and calculation of the perturbation matrices. The strong-field basis functions must be the $D_{3h}$ crystalline field (orbital) eigenfunctions. Two electrons occupy the one-electron d-atomic orbitals in the configurations of a strong trigonal bipyramidal crystalline field in order of increasing energy:[32] $(e'')^2$, $(e'')(e')$, $(e')^2$, $(e'')(a_1')$, $(e')(a_1')$, $(a_1')^2$. These direct products of one-electron symmetry states are reduced as, $A_1' + A_2' + E'$, $A_1'' + A_2'' + E''$, $A_1' + A_2' + E'$, $E''$, $E'$, and $A_1'$, respectively. By the correlation of these strong-field basis functions with the simple crystal field calculations in a weak-field ap-

(31) The $\Gamma_{3a}$, $\Gamma_{3b}$ and $\Gamma_{6a}$, $\Gamma_{6b}$ components also remain orthogonal in spin–orbit interaction, of course, as can be readily seen by inspection of their $J$ and $M$ values.

(32) Even in ordering the energy levels for the strong-field two-electron configuration, some proportionality between the intrinsically positive crystal field parameters $Dq$ and $Db$ must be assumed. As previously[18]—and for the same reasons and with the same restrictions—we have assumed the relationship, $Db = 1.72Dq$.

$\Gamma_1$

| | $^1S_0$ | $^3P_0$ | $^3P_2$ | $^1D_2$ | $^3F_2$ | $^3F_4$ | $^1G_4$ |
|---|---|---|---|---|---|---|---|
| $^1S_0$ | $14F_2 + 126F_4 - E$ | $-\sqrt{6}\lambda$ | 0 | $-\frac{\sqrt{14}}{75}Db$ | 0 | 0 | $\frac{25}{\sqrt{14}}Dq$ |
| $^3P_0$ | $-\sqrt{6}\lambda$ | $7F_2 - 84F_4 - \lambda - E$ | $\frac{7\sqrt{2}}{10}Db$ | 0 | $-2\sqrt{7}/5Db$ | $-\frac{25\sqrt{3}}{6\sqrt{7}}Dq$ | 0 |
| $^3P_2$ | 0 | $\frac{7\sqrt{2}}{10}Db$ | $7F_2 - 84F_4 + \frac{1}{2}\lambda - \frac{7}{10}Db - E$ | $\frac{\sqrt{21}}{\sqrt{10}}\lambda$ | $-\frac{75\sqrt{2}}{14\sqrt{7}}Dq + \frac{2\sqrt{2}}{5\sqrt{7}}Db$ | $\frac{125\sqrt{6}}{84\sqrt{7}}Dq - \frac{6\sqrt{6}}{5\sqrt{7}}Db$ | 0 |
| $^1D_2$ | $-\sqrt{14/15}Db$ | 0 | $\frac{\sqrt{21}}{\sqrt{10}}\lambda$ | $-3F_2 + 36F_4 + \frac{150}{49}Dq - \frac{3}{7}Db - E$ | $-2\sqrt{3}\lambda$ | 0 | $-\frac{625}{49\sqrt{5}}Dq - \frac{12\sqrt{5}}{35}Db$ |
| $^3F_2$ | 0 | $-\frac{2\sqrt{7}}{5}Db$ | $-\frac{75\sqrt{2}}{14\sqrt{7}}Dq + \frac{2\sqrt{2}}{5\sqrt{7}}Db$ | $-2\sqrt{3}\lambda$ | $-8F_2 - 9F_4 - 2\lambda - \frac{275}{98}Dq + \frac{12}{35}Db - E$ | $\frac{125\sqrt{3}}{98}Dq - \frac{\sqrt{3}}{35}Db$ | 0 |
| $^3F_4$ | 0 | $-\frac{25\sqrt{3}}{6\sqrt{7}}Dq$ | $\frac{125\sqrt{6}}{84\sqrt{7}}Dq - \frac{6\sqrt{6}}{5\sqrt{7}}Db$ | 0 | $\frac{125\sqrt{3}}{98}Dq - \frac{\sqrt{3}}{35}Db$ | $-8F_2 - 9F_4 + \frac{3}{2}\lambda - \frac{675}{196}Dq + \frac{6}{14}Db - E$ | $\lambda$ |
| $^1G_4$ | $\frac{25}{\sqrt{14}}Dq$ | 0 | 0 | $-\frac{625}{49\sqrt{5}}Dq - \frac{12}{7\sqrt{5}}Dt$ | 0 | $\lambda$ | $4F_2 + F_4 + \frac{225}{98}Dq + \frac{10}{7}Db - E$ |

$= 0$

$\Gamma_2$

| | $^3P_1$ | $^3F_3$ |
|---|---|---|
| $^3P_1$ | $7F_2 - 84F_4 - \frac{1}{2}\lambda + \frac{7}{10}Db - E$ | $-\frac{25\sqrt{6}}{28}Dq - \frac{2\sqrt{6}}{5}Db$ |
| $^3F_3$ | $-\frac{25\sqrt{6}}{28}Dq - \frac{2\sqrt{6}}{5}Db$ | $-8F_2 - 9F_4 - \frac{1}{2}\lambda - \frac{25}{28}Dq + \frac{3}{10}Db - E$ |

$= 0$

$\Gamma_4, \Gamma_5$

| | $^3P_3$ | $^3F_4$ | $^1G_4$ |
|---|---|---|---|
| $^3F_3$ | $-8F_2 - 9F_4 - \frac{1}{2}\lambda - \frac{25}{56}Dq - \frac{3}{8}Db - E$ | $\frac{125\sqrt{3}}{56}Dq + \frac{\sqrt{3}}{8}Db$ | 0 |
| $^3F_4$ | $\frac{125\sqrt{3}}{56}Dq + \frac{\sqrt{3}}{8}Db$ | $-8F_2 - 9F_4 + \frac{3}{2}\lambda - \frac{225}{56}Dq - \frac{1}{8}Db - E$ | $\lambda$ |
| $^1G_4$ | 0 | $\lambda$ | $4F_2 + F_4 - \frac{75}{28}Dq - \frac{1}{2}Db - E$ |

$= 0$

$\Gamma_3$

| | $^3P_2$ | $^3F_2$ | $^1D_2$ | $^3F_3$ | $^3F_4'$ | $^3F_4''$ | $^1G_4'$ | $^1G_4''$ |
|---|---|---|---|---|---|---|---|---|
| $^3P_2$ | $7F_2 - 84F_4 + \frac{1}{2}\lambda + \frac{7}{10}Db - E$ | $\frac{25\sqrt{2}}{28\sqrt{7}}Dq - \frac{2\sqrt{2}}{5\sqrt{7}}Db$ | $\sqrt{21/10}\lambda$ | $\pm\frac{125\sqrt{10}}{280}Dq \pm \frac{\sqrt{2}}{\sqrt{5}}Db$ | 0 | $-\frac{75\sqrt{10}}{392}Dq - \frac{3\sqrt{10}}{35}Db$ | 0 | 0 |
| $^3F_2$ | $\frac{25\sqrt{2}}{28\sqrt{7}}Dq - \frac{2\sqrt{2}}{5\sqrt{7}}Db$ | $-8F_2 - 9F_4 - 2\lambda - \frac{275}{588}Dq - \frac{12}{35}Db - E$ | $-2\sqrt{3/5}\lambda$ | $\mp\frac{275\sqrt{5}}{84\sqrt{7}}Dq \mp \frac{3\sqrt{5}}{10\sqrt{7}}Db$ | 0 | $-\frac{225\sqrt{5}}{196}Dq - \frac{\sqrt{5}}{70}Db$ | 0 | 0 |
| $^1D_2$ | $\sqrt{21/10}\lambda$ | $-2\sqrt{3/5}\lambda$ | $-3F_2 + 36F_4 + \frac{25}{49}Dq + \frac{1}{7}Db - E$ | 0 | 0 | 0 | 0 | $\frac{375\sqrt{3}}{98}Dq - \frac{2\sqrt{3}}{7}Db$ |
| $^3F_3$ | $\pm\frac{125\sqrt{10}}{280}Dq \pm \frac{\sqrt{2}}{\sqrt{5}}Db$ | $\mp\frac{275\sqrt{5}}{84\sqrt{7}}Dq \mp \frac{3\sqrt{5}}{10\sqrt{7}}Db$ | 0 | $-8F_2 - 9F_4 - \frac{1}{2}\lambda + \frac{175}{168}Dq - E$ | 0 | $\pm\frac{375\sqrt{7}}{392}Dq \mp \frac{\sqrt{7}}{14}Db$ | 0 | 0 |
| $^3F_4'$ | 0 | 0 | 0 | 0 | $-8F_2 - 9F_4 + \frac{3}{2}\lambda - \frac{75}{28}Dq - \frac{1}{2}Db - E$ | 0 | $\lambda$ | 0 |
| $^3F_4''$ | $-\frac{75\sqrt{10}}{392}Dq - \frac{3\sqrt{10}}{35}Db$ | $-\frac{225\sqrt{5}}{196}Dq - \frac{\sqrt{5}}{70}Db$ | 0 | $\pm\frac{375\sqrt{7}}{392}Dq \mp \frac{\sqrt{7}}{14}Db$ | 0 | $-8F_2 - 9F_4 + \frac{3}{2}\lambda + \frac{225}{392}Dq + \frac{1}{7}Db - E$ | 0 | $\lambda$ |
| $^1G_4'$ | 0 | 0 | 0 | 0 | $\lambda$ | 0 | $4F_2 + F_4 + \frac{25}{14}Dq - 2Db - E$ | 0 |
| $^1G_4''$ | 0 | 0 | $\frac{375\sqrt{2}}{98}Dq - \frac{2\sqrt{3}}{7}Db$ | 0 | 0 | $\lambda$ | 0 | $4F_2 + F_4 - \frac{275}{196}Dq + \frac{4}{7}Db - E$ |

$= 0$ (4)

$\Gamma_6$

| | $^3P_1$ | $^3P_2$ | $^1D_2$ | $^3P_2$ | $^3F_3$ | $^3F_4$ | $^1G_4$ |
|---|---|---|---|---|---|---|---|
| $^3P_1$ | $7F_2 - 84F_4 - \frac{1}{2}\lambda - \frac{7}{20}Db - E$ | $\mp\frac{21}{20}Db$ | 0 | $\mp\frac{\sqrt{14}}{5}Db$ | $\frac{75}{56}Dq - \frac{4}{5}Db$ | $\pm\frac{25\sqrt{35}}{56}Dq$ | 0 |
| $^3P_2$ | $\mp\frac{21}{20}Db$ | $7F_2 - 84F_4 + \frac{1}{2}\lambda - \frac{7}{20}Db - E$ | $\frac{\sqrt{21}}{\sqrt{10}}\lambda$ | $\frac{50\sqrt{14}}{98}Dq + \frac{\sqrt{14}}{35}Db$ | $\pm\frac{125}{56}Dq \mp \frac{2}{5}Db$ | $\frac{25\sqrt{35}}{392}Dq - \frac{6\sqrt{35}}{35}Db$ | 0 |
| $^1D_2$ | 0 | $\frac{\sqrt{21}}{\sqrt{10}}\lambda$ | $-3F_2 + 36F_4 - \frac{100}{49}Dq - \frac{3}{14}Db - E$ | $-2\sqrt{3}\lambda$ | 0 | 0 | $\frac{125\sqrt{6}}{196}Dq + \frac{2\sqrt{6}}{7}Db$ |
| $^3P_2$ | $\mp\frac{\sqrt{14}}{5}Db$ | $\frac{50\sqrt{14}}{98}Dq + \frac{\sqrt{14}}{35}Db$ | $-\frac{2\sqrt{3}}{\sqrt{5}}\lambda$ | $-8F_2 - 9F_4 - 2\lambda + \frac{275}{147}Dq + \frac{6}{35}Db - E$ | $\mp\frac{1375}{84\sqrt{14}}Db$ | $\frac{75\sqrt{10}}{392}Dq - \frac{\sqrt{10}}{70}Db$ | 0 |
| $^3F_3$ | $\frac{75}{56}Dq - \frac{4}{5}Db$ | $\pm\frac{125}{56}Dq \mp \frac{2}{5}Db$ | 0 | $\mp\frac{1375}{84\sqrt{14}}Db \pm \frac{3\sqrt{14}}{70}Db$ | $-8F_2 - 9F_4 - \frac{1}{2}\lambda - \frac{25}{168}Dq + \frac{9}{40}Db - E$ | $\mp\frac{225\sqrt{35}}{392}Dq \pm \frac{\sqrt{35}}{56}Db$ | 0 |
| $^3F_4$ | $\pm\frac{25\sqrt{35}}{56}Dq$ | $\frac{25\sqrt{35}}{392}Dq - \frac{6\sqrt{35}}{35}Db$ | 0 | $\frac{75\sqrt{10}}{392}Dq - \frac{\sqrt{10}}{70}Db$ | $\mp\frac{225\sqrt{35}}{392}Dq \pm \frac{\sqrt{35}}{56}Db$ | $-8F_2 - 9F_4 + \frac{3}{2}\lambda - \frac{675}{392}Dq + \frac{75}{56}Db - E$ | $\lambda$ |
| $^1G_4$ | 0 | 0 | $\frac{125\sqrt{6}}{196}Dq + \frac{2\sqrt{6}}{7}Db$ | 0 | 0 | $\lambda$ | $4F_2 + F_4 + \frac{225}{196}Dq + \frac{17}{14}Db - E$ |

$= 0$ (5)

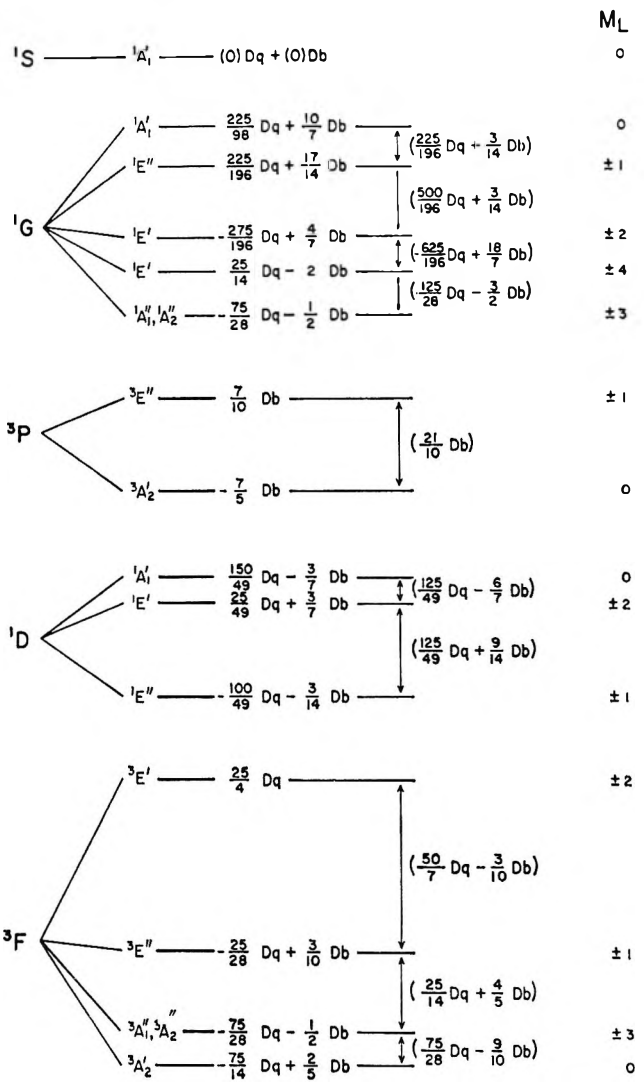


Figure 1. The schematic first-order weak crystalline field diagram for a $d^2$ configuration in a regular trigonal bipyramidal environment with $Db = 1.72Dq$.

proach,[33] we can assign the multiplicity of the states arising from each strong-field configuration

$$\begin{aligned}
(e'')^2 &\longrightarrow {}^1A_1' + {}^3A_2' + {}^1E' \\
(e'')(e') &\longrightarrow {}^1A_1'' + {}^3A_1'' + {}^1A_2'', {}^3A_2'' + {}^1E'' + {}^3E'' \\
(e')^2 &\longrightarrow {}^1A_1' + {}^3A_2' + {}^1E' \qquad (6) \\
(e'')(a_1') &\longrightarrow {}^1E'' + {}^3E'' \\
(e')(a_1') &\longrightarrow {}^1E' + {}^3E' \qquad (a_1')^2 \longrightarrow {}^1A_1'
\end{aligned}$$

The strong-field basis functions are simply the one-electron product-type orbital functions of the strong-field configurations, constructed to have the requisite symmetries of the correlation diagram. Spin functions must be (implicitly) included with these orbital functions, however, to distinguish the singlet and triplet spin states.[34] The transformation properties of the orbital components of these one-electron product wavefunctions are obtained through use of the appropriate $D^2(\alpha,\beta,\gamma)$ matrices, and from the rotation characters one can easily identify satisfactory eigenfunctions in terms of the component wavefunctions or their elementary linear combinations. The strong $D_{3h}$ crystalline field (orbital) eigenfunctions thus determined are shown in Table VII.

**Table VII:** The $D_{3h}$ Strong-Field Basis Functions for $d^2$

| | | |
|---|---|---|
| $(e'')^2$: | $^3A_2'$: | $\lvert\phi_1\phi_{-1}\rvert^{++}$, $1/\sqrt{2}[\lvert\phi_1\phi_{-1}\rvert^{+-} + \lvert\phi_1\phi_{-1}\rvert^{-+}]$, $\lvert\phi_1\phi_{-1}\rvert^{--}$ |
| | $^1A_1'$: | $1/\sqrt{2}[\lvert\phi_1\phi_{-1}\rvert^{+-} - \lvert\phi_1\phi_{-1}\rvert^{-+}]$ |
| | $^1E'$: | $\lvert\phi_1\phi_1\rvert^{+-}$, $\lvert\phi_{-1}\phi_{-1}\rvert^{+-}$ |
| $(e'')(e')$: | $^3A_2''$: | $1/\sqrt{2}\lvert\phi_2\phi_1\rvert^{++} + 1/\sqrt{2}\lvert\phi_{-1}\phi_{-2}\rvert^{++}$ |
| | | $1/2[\lvert\phi_2\phi_1\rvert^{+-} + \lvert\phi_2\phi_1\rvert^{-+} + \lvert\phi_{-1}\phi_{-2}\rvert^{+-} + \lvert\phi_{-1}\phi_{-2}\rvert^{-+}]$ |
| | | $1/\sqrt{2}\lvert\phi_2\phi_1\rvert^{--} + 1/\sqrt{2}\lvert\phi_{-1}\phi_{-2}\rvert^{--}$ |
| | $^3A_1''$: | $1/\sqrt{2}\lvert\phi_2\phi_1\rvert^{++} - 1/\sqrt{2}\lvert\phi_{-1}\phi_{-2}\rvert^{++}$ |
| | | $1/2[\lvert\phi_2\phi_1\rvert^{+-} + \lvert\phi_2\phi_1\rvert^{-+} - \lvert\phi_{-1}\phi_{-2}\rvert^{+-} - \lvert\phi_{-1}\phi_{-2}\rvert^{-+}]$ |
| | | $1/\sqrt{2}\lvert\phi_2\phi_1\rvert^{--} - 1/\sqrt{2}\lvert\phi_{-1}\phi_{-2}\rvert^{--}$ |
| | $^3E''$: | $\lvert\phi_2\phi_{-1}\rvert^{++}$, $1/\sqrt{2}[\lvert\phi_2\phi_{-1}\rvert^{+-} + \lvert\phi_2\phi_{-1}\rvert^{-+}]$, $\lvert\phi_2\phi_{-1}\rvert^{--}$ |
| | | $\lvert\phi_1\phi_{-2}\rvert^{++}$, $1/[\sqrt{2}\lvert\phi_1\phi_{-2}\rvert^{+-} + \lvert\phi_1\phi_{-2}\rvert^{-+}]$, $\lvert\phi_1\phi_{-2}\rvert^{--}$ |
| | $^1A_2''$: | $1/2[\lvert\phi_2\phi_1\rvert^{+-} - \lvert\phi_2\phi_1\rvert^{-+} + \lvert\phi_{-1}\phi_{-2}\rvert^{+-} - \lvert\phi_{-1}\phi_{-2}\rvert^{-+}]$ |
| | $^1A_1''$: | $1/2[\lvert\phi_2\phi_1\rvert^{+-} - \lvert\phi_2\phi_1\rvert^{-+} + \lvert\phi_{-1}\phi_{-2}\rvert^{+-} - \lvert\phi_{-1}\phi_{-2}\rvert^{-+}]$ |
| | $^1E''$: | $1/\sqrt{2}[\lvert\phi_2\phi_{-1}\rvert^{+-} - \lvert\phi_2\phi_{-1}\rvert^{-+}]$, $1/\sqrt{2}[\lvert\phi_1\phi_{-2}\rvert^{+-} - \lvert\phi_1\phi_{-2}\rvert^{-+}]$ |
| $(e')^2$: | $^3A_2'$: | $\lvert\phi_2\phi_{-2}\rvert^{++}$, $1/\sqrt{2}[\lvert\phi_2\phi_{-2}\rvert^{+-} + \lvert\phi_2\phi_{-2}\rvert^{-+}]$, $\lvert\phi_2\phi_{-2}\rvert^{--}$ |
| | $^1A_1'$: | $1/\sqrt{2}[\lvert\phi_2\phi_{-2}\rvert^{+-} - \lvert\phi_2\phi_{-2}\rvert^{-+}]$ |
| | $^1E'$: | $\lvert\phi_2\phi_2\rvert^{+-}$, $\lvert\phi_{-2}\phi_{-2}\rvert^{+-}$ |
| $(e'')(a_1')$: | $^3E''$: | $\lvert\phi_1\phi_0\rvert^{++}$, $1/\sqrt{2}[\lvert\phi_1\phi_0\rvert^{+-} + \lvert\phi_1\phi_0\rvert^{-+}]$, $\lvert\phi_1\phi_0\rvert^{--}$ |
| | | $\lvert\phi_0\phi_{-1}\rvert^{++}$, $1/\sqrt{2}[\lvert\phi_0\phi_{-1}\rvert^{+-} + \lvert\phi_0\phi_{-1}\rvert^{-+}]$, $\lvert\phi_0\phi_{-1}\rvert^{--}$ |
| | $^1E''$: | $1/\sqrt{2}[\lvert\phi_1\phi_0\rvert^{+-} - \lvert\phi_1\phi_0\rvert^{-+}]$, $1/\sqrt{2}[\lvert\phi_0\phi_{-1}\rvert^{+-} - \lvert\phi_0\phi_{-1}\rvert^{-+}]$ |
| $(e')(a_1')$: | $^3E'$: | $\lvert\phi_2\phi_0\rvert^{++}$, $1/\sqrt{2}[\lvert\phi_2\phi_0\rvert^{+-} + \lvert\phi_2\phi_0\rvert^{-+}]$, $\lvert\phi_2\phi_0\rvert^{--}$ |
| | | $\lvert\phi_0\phi_{-2}\rvert^{++}$, $1/\sqrt{2}[\lvert\phi_0\phi_{-2}\rvert^{+-} + \lvert\phi_0\phi_{-2}\rvert^{-+}]$, $\lvert\phi_0\phi_{-2}\rvert^{--}$ |
| | $^1E'$: | $1/\sqrt{2}[\lvert\phi_2\phi_0\rvert^{+-} - \lvert\phi_2\phi_0\rvert^{-+}]$, $1/\sqrt{2}[\lvert\phi_0\phi_{-2}\rvert^{+-} - \lvert\phi_0\phi_{-2}\rvert^{-+}]$ |
| $(a_1')^2$: | $^1A'$: | $\lvert\phi_0\phi_0\rvert^{+-}$ |

The strong-field basis functions are simply the one-electron product-type orbital functions of the strong-field configurations, constructed to have the requisite symmetries of the correlation diagram. Spin functions must be (implicitly) included with these orbital functions, however, to distinguish the singlet and triplet spin states.[34] The transformation properties of the orbital components of these one-electron product wavefunctions are obtained through use of the appropriate $D^2(\alpha,\beta,\gamma)$ matrices, and from the rotation

(33) For methods of constructing the correlation diagram between weak- and strong-field approximations see, for example, Chapters 8.4 and 4-h of ref 28 and 14, respectively.

(34) Ballhausen[14] well exemplifies this determination of symmetry properties for the two-electron orbital functions, where the rotation operators transform only the orbital functions and simply carry along the spin functions untransformed.

**Table VIII:** The $D_{3h}$ Strong-Field Symmetry Eigenfunctions for $d^2$

$$\Gamma_1(^1A_1'[(e'')^2]) = 1/\sqrt{2}[|\overset{+}{\phi_1}\overset{-}{\phi_{-1}}| - |\overset{-}{\phi_1}\overset{+}{\phi_{-1}}|]$$

$$\Gamma_1(^3_0A_1'[(e'')^2]) = 1/\sqrt{2}[|\overset{+}{\phi_1}\overset{-}{\phi_{-1}}| + |\overset{-}{\phi_1}\overset{+}{\phi_{-1}}|]$$

$$\Gamma_1(^3_\pm E''[(e'')(e')]) = 1/\sqrt{2}[|\overset{-}{\phi_2}\overset{+}{\phi_{-1}}| + |\overset{+}{\phi_1}\overset{-}{\phi_{-2}}|]$$

$$\Gamma_1(^1A_1'[(e')^2]) = 1/\sqrt{2}[|\overset{+}{\phi_2}\overset{-}{\phi_{-2}}| - |\overset{-}{\phi_2}\overset{+}{\phi_{-2}}|]$$

$$\Gamma_1(^3_0A_2'[(e')^2]) = 1/\sqrt{2}[|\overset{+}{\phi_2}\overset{-}{\phi_{-2}}| + |\overset{-}{\phi_2}\overset{+}{\phi_{-2}}|]$$

$$\Gamma_1(^3_\pm E''[(e'')(a_1')]) = 1/\sqrt{2}[|\overset{-}{\phi_1}\overset{-}{\phi_0}| + |\overset{+}{\phi_0}\overset{+}{\phi_{-1}}|]$$

$$\Gamma_1(^1A_1'[(a_1')^2]) = |\overset{+}{\phi_0}\overset{-}{\phi_0}|$$

$$\Gamma_2(^3_\pm E''[(e'')(e')]) = 1/\sqrt{2}[|\overset{-}{\phi_2}\overset{-}{\phi_{-1}}| - |\overset{+}{\phi_1}\overset{+}{\phi_{-2}}|]$$

$$\Gamma_2(^3_\pm E''[(e'')(a_1')]) = 1/\sqrt{2}[|\overset{-}{\phi_1}\overset{-}{\phi_0}| - |\overset{+}{\phi_0}\overset{+}{\phi_{-1}}|]$$

$$\Gamma_{3a}(^1E'[(e'')^2]) = |\overset{+}{\phi_{-1}}\overset{-}{\phi_{-1}}|$$

$$\Gamma_{3a}(^3_-E''[(e'')(e')]) = |\overset{-}{\phi_1}\overset{-}{\phi_{-2}}|$$

$$\Gamma_{3a}(^3_+A_1''[(e'')(e')]) = 1/\sqrt{2}[|\overset{+}{\phi_2}\overset{+}{\phi_1}| - |\overset{+}{\phi_{-1}}\overset{+}{\phi_{-2}}|]$$

$$\Gamma_{3a}(^3_+A_2''[(e'')(e')]) = 1/\sqrt{2}[|\overset{+}{\phi_2}\overset{+}{\phi_1}| + |\overset{+}{\phi_{-1}}\overset{+}{\phi_{-2}}|]$$

$$\Gamma_{3a}(^1E'[(e')^2]) = |\overset{+}{\phi_2}\overset{-}{\phi_2}|$$

$$\Gamma_{3a}(^3_-E''[(e'')(a_1')]) = |\overset{-}{\phi_0}\overset{-}{\phi_{-1}}|$$

$$\Gamma_{3a}(^1E'[(e')(a_1')]) = 1/\sqrt{2}[|\overset{+}{\phi_0}\overset{-}{\phi_{-2}}| - |\overset{-}{\phi_0}\overset{+}{\phi_{-2}}|]$$

$$\Gamma_{3a}(^3_0E'[(e')(a_1')]) = 1/\sqrt{2}[|\overset{+}{\phi_0}\overset{-}{\phi_{-2}}| + |\overset{-}{\phi_0}\overset{+}{\phi_{-2}}|]$$

$$\Gamma_{3b}(^1E'[(e'')^2]) = |\overset{+}{\phi_1}\overset{-}{\phi_1}|$$

$$\Gamma_{3b}(^3_+E''[(e'')(e')]) = |\overset{+}{\phi_2}\overset{-}{\phi_{-1}}|$$

$$\Gamma_{3b}(^3_-A_1''[(e'')(e')]) = 1/\sqrt{2}[|\overset{-}{\phi_2}\overset{-}{\phi_1}| - |\overset{-}{\phi_{-1}}\overset{-}{\phi_{-2}}|]$$

$$\Gamma_{3b}(^3_-A_2''[(e'')(e')]) = 1/\sqrt{2}[|\overset{-}{\phi_2}\overset{-}{\phi_1}| + |\overset{-}{\phi_{-1}}\overset{-}{\phi_{-2}}|]$$

$$\Gamma_{3b}(^1E'[(e')^2]) = |\overset{+}{\phi_{-2}}\overset{-}{\phi_{-2}}|$$

$$\Gamma_{3b}(^3_+E''[(e'')(a_1')]) = |\overset{+}{\phi_1}\overset{+}{\phi_0}|$$

$$\Gamma_{3b}(^1E'[(e')(a_1')]) = 1/\sqrt{2}[|\overset{+}{\phi_2}\overset{-}{\phi_0}| - |\overset{-}{\phi_2}\overset{+}{\phi_0}|]$$

$$\Gamma_{3b}(^3_0E'[(e')(a_1')]) = 1/\sqrt{2}[|\overset{+}{\phi_2}\overset{-}{\phi_0}| + |\overset{-}{\phi_2}\overset{+}{\phi_0}|]$$

$$\Gamma_4(^1A_1''[(e'')(e')]) = 1/2[|\overset{+}{\phi_2}\overset{-}{\phi_1}| - |\overset{-}{\phi_2}\overset{+}{\phi_1}| + |\overset{+}{\phi_{-1}}\overset{-}{\phi_{-2}}| - |\overset{-}{\phi_{-1}}\overset{+}{\phi_{-2}}|]$$

$$\Gamma_4(^3_0A_2''[(e'')(e')]) = 1/2[|\overset{+}{\phi_2}\overset{-}{\phi_1}| + |\overset{-}{\phi_2}\overset{+}{\phi_1}| + |\overset{+}{\phi_{-1}}\overset{-}{\phi_{-2}}| + |\overset{-}{\phi_{-1}}\overset{+}{\phi_{-2}}|]$$

$$\Gamma_4(^3_\pm E'[(e')(a_1')]) = 1/\sqrt{2}[|\overset{+}{\phi_2}\overset{+}{\phi_0}| + |\overset{-}{\phi_0}\overset{-}{\phi_{-2}}|]$$

$$\Gamma_5(^1A_2''[(e'')(e')]) = 1/2[|\overset{+}{\phi_2}\overset{-}{\phi_1}| - |\overset{-}{\phi_2}\overset{+}{\phi_1}| - |\overset{+}{\phi_{-1}}\overset{-}{\phi_{-2}}| + |\overset{-}{\phi_{-1}}\overset{+}{\phi_{-2}}|]$$

$$\Gamma_5(^3_3A_1''[(e'')(e')]) = 1/2[|\overset{+}{\phi_2}\overset{-}{\phi_1}| + |\overset{-}{\phi_2}\overset{+}{\phi_1}| - |\overset{+}{\phi_{-1}}\overset{-}{\phi_{-2}}| - |\overset{-}{\phi_{-1}}\overset{+}{\phi_{-2}}|]$$

$$\Gamma_5(^3_\pm E'[(e')(a_1')]) = 1/\sqrt{2}[|\overset{+}{\phi_2}\overset{+}{\phi_0}| - |\overset{-}{\phi_0}\overset{-}{\phi_{-2}}|]$$

$$\Gamma_{6a}(^3_+A_2'[(e'')^2]) = |\overset{+}{\phi_1}\overset{+}{\phi_{-1}}|$$

$$\Gamma_{6a}(^1E''[(e'')(e')]) = 1/\sqrt{2}[|\overset{+}{\phi_2}\overset{-}{\phi_{-1}}| - |\overset{-}{\phi_2}\overset{+}{\phi_{-1}}|]$$

$$\Gamma_{6a}(^3_0E''[(e'')(e')]) = 1/\sqrt{2}[|\overset{+}{\phi_2}\overset{-}{\phi_{-1}}| + |\overset{-}{\phi_2}\overset{+}{\phi_{-1}}|]$$

$$\Gamma_{6a}(^3_+A_2'[(e')^2]) = |\overset{+}{\phi_2}\overset{+}{\phi_{-2}}|$$

$$\Gamma_{6a}(^1E''[(e'')(a_1')]) = 1/\sqrt{2}[|\overset{+}{\phi_1}\overset{-}{\phi_0}| - |\overset{-}{\phi_1}\overset{+}{\phi_0}|]$$

$$\Gamma_{6a}(^3_0E''[(e'')(a_1')]) = 1/\sqrt{2}[|\overset{+}{\phi_1}\overset{-}{\phi_0}| + |\overset{-}{\phi_1}\overset{+}{\phi_0}|]$$

$$\Gamma_{6a}(^3_-E'[(e')(a_1')]) = |\overset{-}{\phi_2}\overset{-}{\phi_0}|$$

$$\Gamma_{6b}(^3_-A_2'[(e'')^2]) = |\overset{-}{\phi_1}\overset{-}{\phi_{-1}}|$$

$$\Gamma_{6b}(^1E''[(e'')(e')]) = 1/\sqrt{2}[|\overset{+}{\phi_1}\overset{-}{\phi_{-2}}| - |\overset{-}{\phi_1}\overset{+}{\phi_{-2}}|]$$

$$\Gamma_{6b}(^3_0E''[(e'')(e')]) = 1/\sqrt{2}[|\overset{+}{\phi_1}\overset{-}{\phi_{-2}}| + |\overset{-}{\phi_1}\overset{+}{\phi_{-2}}|]$$

$$\Gamma_{6b}(^3_-A_2'[(e')^2]) = |\overset{-}{\phi_2}\overset{-}{\phi_{-2}}|$$

$$\Gamma_{6b}(^1E''[(e'')(a_1')]) = 1/\sqrt{2}[|\overset{+}{\phi_0}\overset{-}{\phi_{-1}}| - |\overset{-}{\phi_0}\overset{+}{\phi_{-1}}|]$$

$$\Gamma_{6b}(^3_0E''[(e'')(a_1')]) = 1/\sqrt{2}[|\overset{+}{\phi_0}\overset{-}{\phi_{-1}}| + |\overset{-}{\phi_0}\overset{+}{\phi_{-1}}|]$$

$$\Gamma_{6b}(^3_+E'[(e')(a_1')]) = |\overset{+}{\phi_0}\overset{+}{\phi_{-2}}|$$

From the weak-field case we know that seven eigenfunctions of $\Gamma_1(A_1')$ symmetry, two of $\Gamma_2(A_2')$, eight of $\Gamma_3(E')$, three each of $\Gamma_4(A_1'')$ and $\Gamma_5(A_2'')$, and seven of $\Gamma_6(E'')$ are required for the $d^2$ configuration. The transformation properties of the basis functions (explicit spin) are easily obtained by successive application of the appropriate $D^2(\alpha,\beta,\gamma)$ matrices, and again this procedure identifies satisfactory symmetry eigenfunctions directly as the basis functions or their simple linear combinations. The strong $D_{3h}$ crystalline field symmetry eigenfunctions chosen in this work are listed in Table VIII. Here the rotation characters under $C_3(z)$ have again been used to distinguish the $\Gamma_3$ and $\Gamma_6$ components, and the preceding subscript of +, 0, or − on the symmetry designation of the basis functions has been appended to identify the spin state of the constituent triplet basis function or functions. It is observed that the only required linear combinations occur between components of a doubly degenerate crystalline field basis function, so the orbital character, but not the spin character, in these combinations has always been preserved in constructing the (total) symmetry eigenfunctions.

The matrix elements of Coulombic perturbation for the $D_{3h}$ strong-field symmetry eigenfunctions are calculated in terms of the Slater–Condon–Shortley parameters, $F_k$, by use of Tables $I^6$ and $II^6$ of ref 12.[35,36] The Coulombic perturbation is of course diagonal in $\Gamma_i$ and also in spin multiplicity. The matrix elements for the $\Gamma_{3a}$, $\Gamma_{3b}$ and for the $\Gamma_{6a}$, $\Gamma_{6b}$ components of the doubly degenerate eigenfunctions are identical, and so are the Coulombic terms for the $\Gamma_4$ and $\Gamma_5$ eigenfunctions so that these two 3 by 3 energy matrices can be degenerate

(35) Reference 12, Chapter 6.

(36) Reference 14, Chapter 2.

as they were in the weak-field approximation. Since the parameter $F_0$ appears identically in only the diagonal elements, it has been subtracted out of the secular determinant without altering the eigenvalues.

To calculate the spin–orbit perturbation on these two-electron wavefunctions, which are not of course total angular momentum eigenfunctions, we may use the generalized two-electron spin–orbit Hamiltonian expanded as the sum of one-electron operators, each operating only upon its designated electron[37]

$$\mathcal{H}' = \sum_{j=1}^{2} \xi(r_j)\{L_{zj}S_{zj} + {}^1/_2(L_{zj} + iL_{yj})(S_{zj} - iS_{yj}) + {}^1/_2(L_{zj} - iL_{yj})(S_{zj} + iS_{yj})\} \quad (7)$$

The one-electron components of the matrix elements then follow the general form,[37] and the spin–orbit

$$(\gamma s l m_s m_l|\ L\cdot S|\ \gamma' s l' m_s' m_l') = \hbar^2\delta(\gamma l m;\ \gamma' l' m') \times \{\delta(m_s,m_s')m_l m_s + {}^1/_2\delta(m_s',m_s \pm 1) \times \sqrt{(l - m + {}^1/_2)(l + m + {}^1/_2)}\} \quad (8)$$

perturbation matrices are easily computed. As in the weak field approximation the spin–orbit matrices for the $\Gamma_4$ and $\Gamma_5$ eigenfunctions are identical.

The strong crystalline field perturbation is of course completely diagonal, and the matrix elements are simply the sums of the one-electron crystal field (orbital) levels which are filled in that particular configuration. The total perturbation secular determinant for the $d^2$ configuration subjected to a strong trigonal bipyramidal crystalline field is given below, in a blocked form according to the $\Gamma_i$ symmetry of its basis functions. To be appropriate for a $d^8$ electronic system ($d^f$ positronic system) only the signs of the spin–orbit and crystal field parameters need be changed.

## $D_{3h}$ Correlation Diagrams

After computing the Coulombic perturbation we are now in a position to construct the strong-field portion of the $D_{3h}$ correlation diagram. Since both the crystalline field and Coulombic perturbations are expressed in two parameters, we adopt the following proportionalities for lack of experimental values[38]

$$Db = 1.72Dq \text{ and } F_2 = 14F_4$$

Tentative orderings of the crystal field levels within the $LS$ terms of the weak field eigenfunctions and of the Coulombic perturbation of the strong crystalline field (orbital) eigenfunctions are made, and a useful, if, nevertheless, still approximate, correlation diagram for the $d^2$ configuration in $D_{3h}$ crystalline field is obtained in Figure 2.

Since our interest is directed also at the $d^8$ configuration, we modify the correlation diagram so that it is appropriate to the $d^8$ configuration. A $d^2$ electronic and positronic configuration will be subjected to the same Coulombic perturbation (*i.e.*, $\sum_{i>j}^{2} e^2/r_{ij}$), so the ordering of the $LS$ terms in the weak-field case and the Coulombic perturbation levels within the strong field configurations are unchanged. The crystalline field perturbation, however, is a repulsion between the metal valence electrons and the substantially negative ligands, so its parameters must change signs for the positronic case. Thus the crystal field levels within the $LS$ terms of the weak-field case and the two-electron configurations of the strong field case are inverted in going from the $d^2$ to the $d^8$ configuration. This correlation diagram for a $d^8$ configuration in $D_{3h}$ symmetry, subject to the same approximations as was the $d^2$, is shown in Figure 3.

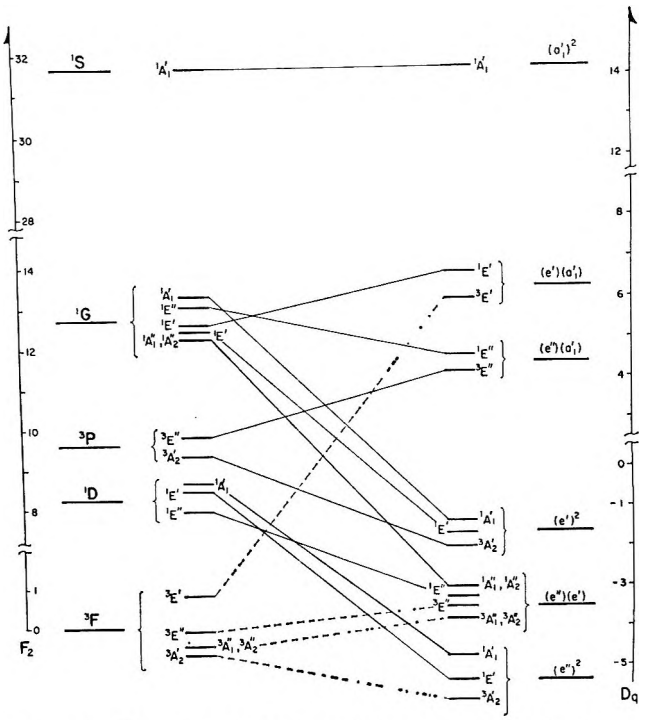


Figure 2. The approximated correlation diagram of the $d^2$ configuration in $D_{3h}$ environment with $Db = 1.72Dq$ and $F_2 = 14F_4$.

## Calculations for Lower Symmetry

As in the case of the $d^1$, $d^9$ calculations,[10] the crystal field and crystal field–spin orbit perturbation calculations for the $d^2$, $d^8$ configuration subjected to a distorted or pseudo-trigonal bipyramidal field[39,40] of $D_{3h}$,

(37) From equations $1^{11}$ (1) and $7^3$ (3) of ref 12.

(38) The approximate proportionality, $F_2/F_4 = 13.8$, results from evaluation of the specified integrals using the hydrogenic d-orbital radial functions.[36]

(39) Defined in the same manner as in ref 10, in that the distorted trigonal bipyramidal environment has unequal axial and equatorial bond lengths, or, equivalently, has nonidentical axial and equatorial ligands (*i.e.*, $MA_3B_2$), so that the resulting structure is still rigorously $D_{3h}$ in symmetry but has: $a$(equatorial)/$b$(axial) = c $\neq$ 1. A pseudo-trigonal bipyramidal environment may be considered that of $C_{3v}$, or lower, symmetry, in which the three equatorial ligands remain equivalent (*i.e.*, the $C_3$ axis is preserved) but the axial positions are no longer exchangeable. The crystal field potentials and/or parameters, in the ionic-model system of calculation,[40] will of course be different for these several examples.

| $\Gamma_1$ | $^3A_2'$ | $^1A_1'$ | $^3E''$ | $^3A_2'$ | $^1A_1'$ | $^3E''$ | $^1A_1'$ |
|---|---|---|---|---|---|---|---|
| $^3A_2'[(e'')^2]$ | $-5F_2 - 24F_4 - \frac{50}{7}Dq + Db - E$ | $\lambda$ | $\lambda$ | $-6F_2 + 30F_4$ | 0 | $\sqrt{3/2}\lambda$ | 0 |
| $^1A_1'[(e'')^2]$ | $\lambda$ | $7F_2 + 56F_4 - \frac{50}{7}Dq + Db - E$ | $\lambda$ | 0 | $-6F_2 - 40F_4$ | $-\sqrt{3/2}\lambda$ | $-\sqrt{2}F_2 - 30/2F_4$ |
| $^3E''[(e'')(e')]$ | $\lambda$ | $\lambda$ | $-2F_2 - 39F_4 - \frac{1}{2}\lambda - \frac{75}{28}Dq - \frac{1}{2}Db - E$ | $\lambda$ | $-\lambda$ | $-3\sqrt{6}F_2 + 15\sqrt{6}F_4$ | 0 |
| $^3A_2'[(e')^2]$ | $-6F_2 + 30F_4$ | 0 | $\lambda$ | $4F_2 - 69F_4 + \frac{25}{14}Dq - 2Db - E$ | $2\lambda$ | 0 | 0 |
| $^1A_1'[(e')^2]$ | 0 | $-6F_2 - 40F_4$ | $-\lambda$ | $2\lambda$ | $4F_2 + 71F_4 + \frac{25}{14}Dq - 2Db - E$ | 0 | $4\sqrt{2}F_2 + 15\sqrt{2}F_4$ |
| $^3E''[(e'')(a_1')]$ | $\sqrt{3/2}\lambda$ | $-\sqrt{3/2}\lambda$ | $-3\sqrt{6}F_2 + 15\sqrt{6}F_4$ | 0 | 0 | $F_2 - 54F_4 - \frac{1}{2}\lambda + \frac{25}{14}Dq + \frac{3}{2}Db - E$ | $\sqrt{3}\lambda$ |
| $^1A_1'[(a_1')^2]$ | 0 | $-\sqrt{2}F_2 - 30\sqrt{2}F_4$ | 0 | 0 | $4\sqrt{2}F_2 + 15\sqrt{2}F_4$ | $\sqrt{3}\lambda$ | $4F_2 + 36F_4 + \frac{75}{7}Dq + 2Db - E$ |

| $\Gamma_2$ | $^3E''$ | $^3E''$ |
|---|---|---|
| $^3E''[(e'')(e')]$ | $-2F_2 - 39F_4 - \frac{1}{2}\lambda - \frac{75}{28}Dq - \frac{1}{2}Db - E$ | $-3\sqrt{6}F_2 + 15\sqrt{6}F_4$ |
| $^3E''[(e'')(a_1')]$ | $-3\sqrt{6}F_2 + 15\sqrt{6}F_4$ | $F_2 - 54F_4 - \frac{1}{2}\lambda + \frac{25}{14}Dq + \frac{3}{2}Db - E$ |

$= 0$

| $\Gamma_4, \Gamma_5$ | $^3A_2'', ^3A_1''$ | $^1A_1'', ^1A_2''$ | $^3E'$ |
|---|---|---|---|
| $^3A_2'', ^3A_1''[(e'')(e')]$ | $-8F_2 - 9F_4 - \frac{75}{28}Dq - \frac{1}{2}Db - E$ | $1/2\lambda$ | $\sqrt{3/2}\lambda$ |
| $^1A_1'', ^1A_2''[(e'')(e')]$ | $1/2\lambda$ | $4F_2 + F_4 - \frac{75}{28}Dq - \frac{1}{2}Db - E$ | $\sqrt{3/2}\lambda$ |
| $^3E'[(e')(a_1')]$ | $\sqrt{3/2}\lambda$ | $\sqrt{3/2}\lambda$ | $-8F_2 - 9F_4 + \lambda + \frac{175}{28}Dq - E$ |

| $\Gamma_3$ | $^1E'$ | $^3A_1''$ | $^3E''$ | $^3A_2''$ | $^1E'$ | $^3E''$ | $^3E'$ | $^1E'$ |
|---|---|---|---|---|---|---|---|---|
| $^1E''[(e'')^2]$ | $F_2 + 16F_4 - \frac{50}{7}Dq + Db - E$ | $-\frac{\sqrt{2}}{2}\lambda$ | 0 | $\frac{\sqrt{2}}{2}\lambda$ | 0 | $\sqrt{6/4}\lambda$ | 0 | $2\sqrt{3}F_2 - 10\sqrt{3}F_4$ |
| $^3A_1''[(e'')(e')]$ | $-\frac{\sqrt{2}}{2}\lambda$ | $-8F_2 - 9F_4 - \frac{75}{28}Dq - \frac{1}{2}Db - E$ | 0 | $3/2\lambda$ | $\frac{\sqrt{2}}{2}\lambda$ | 0 | $-\frac{\sqrt{6}}{4}\lambda$ | $\sqrt{6/4}\lambda$ |
| $^3E''[(e'')(e')]$ | 0 | 0 | $-2F_2 - 39F_4 + \frac{1}{2}\lambda - \frac{75}{28}Dq - \frac{1}{2}Db - E$ | 0 | 0 | $-3\sqrt{6}F_2 + 15\sqrt{6}F_4$ | $\frac{\sqrt{3}}{2}\lambda$ | $\sqrt{3/2}\lambda$ |
| $^3A_2''[(e'')(e')]$ | $\frac{\sqrt{2}}{2}\lambda$ | $3/2\lambda$ | 0 | $-8F_2 - 9F_4 - \frac{75}{28}Dq - \frac{1}{2}Db - E$ | $\frac{\sqrt{2}}{2}\lambda$ | 0 | $\frac{\sqrt{6}}{4}\lambda$ | $-\sqrt{6/4}\lambda$ |
| $^1E'[(e')^2]$ | 0 | $\sqrt{2/2}\lambda$ | 0 | $\frac{\sqrt{2}}{2}\lambda$ | $4F_2 + F_4 + \frac{25}{14}Dq - 2Db - E$ | 0 | 0 | 0 |
| $^3E''[(e'')(a_1')]$ | $\frac{\sqrt{6}}{4}\lambda$ | 0 | $-3\sqrt{6}F_2 + 15\sqrt{6}F_4$ | 0 | 0 | $F_2 - 54F_4 + \frac{1}{2}\lambda + \frac{25}{14}Dq + \frac{3}{2}Db - E$ | $\frac{\sqrt{2}}{2}\lambda$ | $-\sqrt{2/2}\lambda$ |
| $^3E'[(e')(a_1')]$ | 0 | $-\sqrt{6/4}\lambda$ | $\sqrt{3/2}\lambda$ | $\sqrt{6/4}\lambda$ | 0 | $\frac{\sqrt{2}}{2}\lambda$ | $-8F_2 - 9F_4 + \frac{175}{28}Dq - E$ | $\lambda$ |
| $^1E'[(e')(a_1')]$ | $2\sqrt{3}F_2 - 10\sqrt{3}F_4$ | $\sqrt{6/4}\lambda$ | $\sqrt{3/2}\lambda$ | $-\sqrt{6/4}\lambda$ | 0 | $-\frac{\sqrt{2}}{2}\lambda$ | $\lambda$ | $21F_4 + \frac{175}{28}Dq - E$ |

$= 0$

| $\Gamma_6$ | $^3A_2'$ | $^3E''$ | $^1E''$ | $^3A_2'$ | $^3E''$ | $^1E''$ | $^3E'$ |
|---|---|---|---|---|---|---|---|
| $^3A_2'[(e'')^2]$ | $-5F_2 - 24F_4 - \frac{50}{7}Dq + Db - E$ | $\sqrt{2/2}\lambda$ | $-\sqrt{2/2}\lambda$ | $-6F_2 + 30F_4$ | $\sqrt{3/2}\lambda$ | $\sqrt{3/2}\lambda$ | 0 |
| $^3E''[(e'')(e')]$ | $\sqrt{2/2}\lambda$ | $-2F_2 - 39F_4 - \frac{75}{28}Dq - \frac{1}{2}Db - E$ | $3/2\lambda$ | $\sqrt{2/2}\lambda$ | $-3\sqrt{6}F_2 + 15\sqrt{6}F_4$ | 0 | $\sqrt{3/2}\lambda$ |
| $^1E''[(e'')(e')]$ | $-\sqrt{2/2}\lambda$ | $3/2\lambda$ | $-2F_2 + 31F_4 - \frac{75}{28}Dq - \frac{1}{2}Db - E$ | $\sqrt{2/2}\lambda$ | 0 | $\sqrt{6}F_2 - 5\sqrt{6}F_4$ | $-\sqrt{3/2}\lambda$ |
| $^3A_2'[(e')^2]$ | $-6F_2 + 30F_4$ | $\sqrt{2/2}\lambda$ | $\sqrt{2/2}\lambda$ | $4F_2 - 69F_4 + \frac{25}{14}Dq - 2Db - E$ | 0 | 0 | 0 |
| $^3E''[(e'')(a_1')]$ | $\sqrt{3/2}\lambda$ | $-3\sqrt{6}F_2 + 15\sqrt{6}F_4$ | 0 | 0 | $F_2 - 54F_4 + \frac{25}{14}Dq + \frac{3}{2}Db - E$ | $1/2\lambda$ | $\sqrt{2/2}\lambda$ |
| $^1E''[(e'')(a_1')]$ | $\sqrt{3/2}\lambda$ | 0 | $\sqrt{6}F_2 - 5\sqrt{6}F_4$ | 0 | $1/2\lambda$ | $3F_2 + 6F_4 + \frac{25}{14}Dq + \frac{3}{2}Db - E$ | $\sqrt{2/2}\lambda$ |
| $^3E'[(e')(a_1')]$ | 0 | $\sqrt{3/2}\lambda$ | $-\sqrt{3/2}\lambda$ | 0 | $\sqrt{2/2}\lambda$ | $\sqrt{2/2}\lambda$ | $-8F_2 - 9F_4 - \lambda + \frac{175}{28}Dq - E$ |

$= 0$ (9)

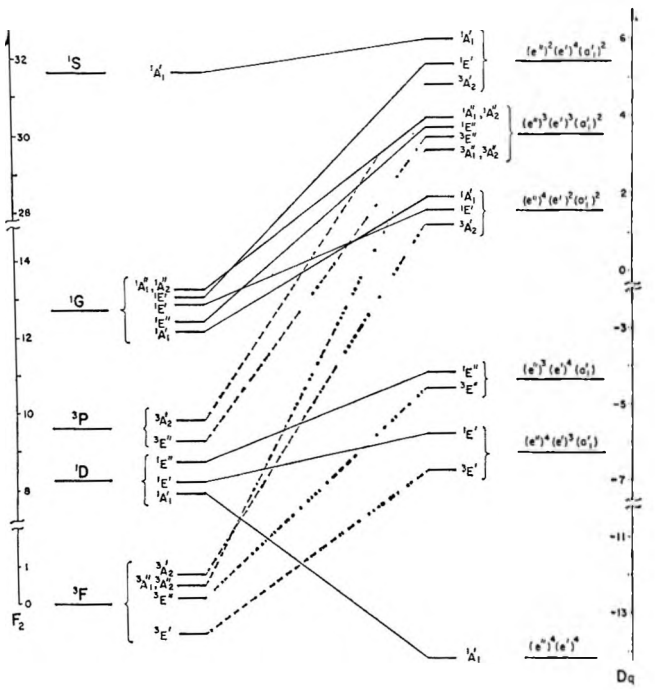

Figure 3. The approximated correlation diagram of the $d^8$ configuration in $D_{3h}$ environment with $Db = 1.72Dq$ and $F_2 = 14F_4$.

$C_{3v}$, $D_3$, or $C_3$ symmetry, are very analogous to those for the regular trigonal bipyramid. Although the lower symmetries remove the (formal) symmetry distinction between the E′ and E″ wavefunctions (*i.e.*, both become simply E), these eigenfunctions remain noninteracting under the (one-electron) crystal field perturbation; *i.e.*, the (one-electron) perturbation matrix is diagonal for $C_{3v}$ as well as for $D_{3h}$. This "accidental" noninteraction of eigenfunctions having the same symmetry carries over into the two-electron case in that the only nonzero off-diagonal crystal field matrix elements (in the weak field approximation) for $C_{3v}$ symmetry are those previously observed for $D_{3h}$. The additional off-diagonal elements "expected" for $C_{3v}$ symmetry; *i.e.*, crystal field interactions between $^3A_2[^3F(\pm3)] - {}^3A_2[^3P(0)]$; $^3E[^3F(\pm2)] - {}^3E[^3P(\pm1)]$; $^1E[^1D(\pm1)] - {}^1E[^1G(\pm2)]$, $^1E[^1G(\pm4)]$; $^1E[^1D(\pm2)] - {}^1E[^1G(\pm1)]$; and $^1A_1[^1G(\pm3)] - {}^1A_1[^1D(0)]$, $^1A_1[^1S(0)]$; all vanish because of the one-electron orbital relationships. Crystal field elements between $^1E'[^1G(\pm4)] - {}^1E'[^1G(\pm2)]$, $^1E'[^1D(\pm2)]$ could have been "expected" from symmetry arguments alone, already under $D_{3h}$ symmetry, but also vanish because of the diagonal nature of the one-electron perturbation. In the strong-field approximation the crystal field perturbation will remain entirely diagonal for $C_{3v}$, as it did under $D_{3h}$.

Although the calculations have not been performed, it should be safe to anticipate that the symmetry eigenfunctions under $C_{3v}$, $D_3$, and even $C_3$, while most probably not identical with those for $D_{3h}$, will nevertheless be only slightly different linear combinations of the same basis functions.[41] If this is true, the spin–orbit and Coulombic perturbations should be identical or at least equivalent, and the total perturbation matrices and resulting eigenvalues will be equivalent, after due adjustment has been made for the differing crystal field parameters. This similarity of the $D_{3h}$ and $C_{3v}$ perturbation has already been suggested by Norgett

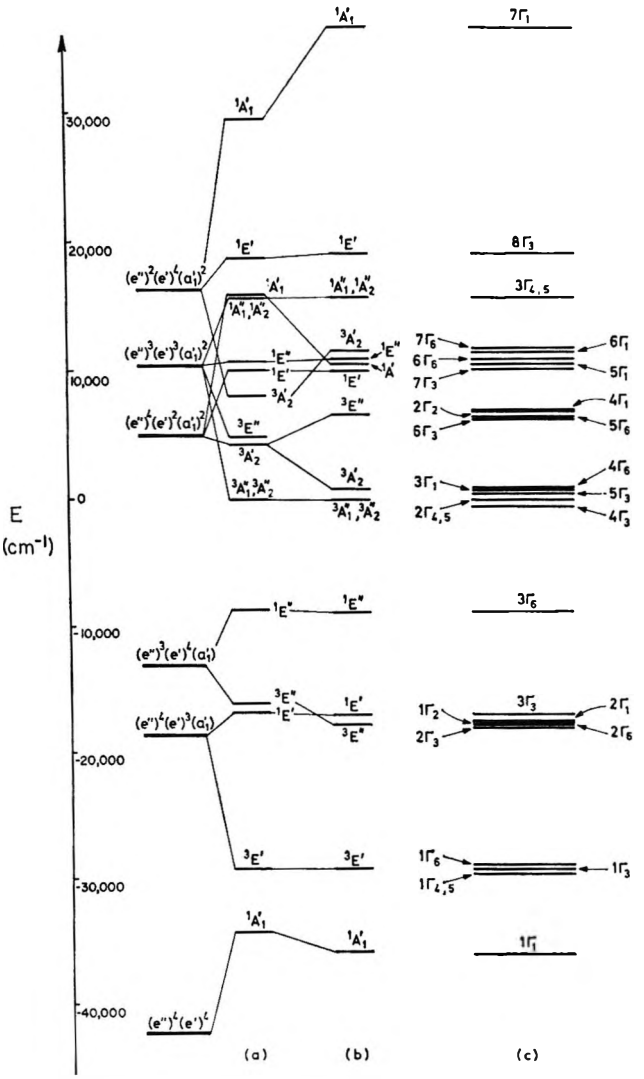

Figure 4. A perturbation energy diagram for trigonal bipyramidal Ni(II) using the approximated parametric values: $Dq = -3000$ cm$^{-1}$, $Db = 1.72Dq$, $F_2 = 1250$ cm$^{-1}$, $F_4 = 83$ cm$^{-1}$, and $\lambda = -335$ cm$^{-1}$.[52] a, strong crystal field limit; b, intermediate crystalline field perturbation; c, crystal field–spin orbit perturbation.

(40) T. M. Dunn, D. S. McClure, and R. G. Pearson, "Some Aspects of Crystal Field Theory," Harper and Row, New York, N. Y., 1965, Chapter 1.

(41) That is to say that while in $D_{3h}$, $\Gamma_{3a}$ $(^1D_2) = |^1D, 2, -2\rangle$, $\Gamma_{3b}$ $(^1D_2) = |^1D, 2, 2\rangle$ and $\Gamma_{5a}(^1D_2) = |^1D, 2, 1\rangle$, $\Gamma_{5b}$ $(^1D_2) = |^1D, 2, -1\rangle$, for example, under $C_{3v}$, say, $\Gamma_{3a,b}[1](^1D_2) = c_1|^1D, 2, -2\rangle + c_2|^1D, 2, 2\rangle$ and $\Gamma_{3a,b}[2](^1D_2) = c_1'|^1D, 2, -1\rangle + c_2'|^1D, 2, 1\rangle$, but the basis functions, $|^1D, 2, \pm2\rangle$,$|^1D, 2, \pm1\rangle$, not mixed under $D_{3h}$ because of symmetry considerations, will remain nonmixed under $C_{3h}$, even when mixing is now permitted by the symmetry. See ref 10 for a pertinent discussion of this problem in the $d^1$ case.

**Table IX:** Solution of the Weak-Field Matrices with Approximate Parametric Values[a] for $d^8$

| Simple crystal field | | | Crystal field–spin-orbit calculations | | |
|---|---|---|---|---|---|
| Weak crystal field limit | Intermediate crystal field | CF state | *LS* state | $\Gamma_i$ | Eigenvalue |
| −18,250 | −18,250 | $^3E'$ | $^3F_4$ | $1\Gamma_{4,5}$ | −18,650 |
| | | | $^3F_3$ | $1\Gamma_3$ | −18,350 |
| | | | $^3F_2$ | $1\Gamma_6$ | −18,300 |
| −10,300 | −12,050 | $^3E''$ | $^3F_4$ | $2\Gamma_3$ | −12,150 |
| | | | $^3F_4$ | $2\Gamma_6$ | −13,100 |
| | | | $^3F_3$ | $1\Gamma_2$ | −11,850 |
| | | | $^3F_4$ | $1\Gamma_1$ | −11,250 |
| −6,500 | −6,500 | $^3A_{1,2}''$ | $^3F_4$ | $3\Gamma_3$ | −7,100 |
| | | | $^3F_3$ | $2\Gamma_{4,5}$ | −6,500 |
| | | | $^3F_2$ | $4\Gamma_3$ | −5,750 |
| −5,150 | −5,500 | $^3A_2'$ | $^3F_3$ | $3\Gamma_6$ | −6,000 |
| | | | $^3F_2$ | $2\Gamma_1$ | −5,450 |
| −3,550 | −12,200 | $^1A_1'$ | $^1D_2$ | $3\Gamma_1$ | −12,450 |
| −2,250 | −6,300 | $^1E'$ | $^1D_2$ | $5\Gamma_3$ | −6,550 |
| 2,150 | 5,000 | $^1E''$ | $^1D_2$ | $4\Gamma_6$ | 5,400 |
| 350 | 2,100 | $^3E''$ | $^3P_2$ | $6\Gamma_3$ | 1,950 |
| | | | $^3P_2$ | $5\Gamma_6$ | 2,100 |
| | | | $^3P_0$ | $4\Gamma_1$ | 2,250 |
| | | | $^3P_1$ | $2\Gamma_2$ | 2,300 |
| 4,650 | 5,000 | $^3A_2'$ | $^3P_1$ | $6\Gamma_6$ | 4,700 |
| | | | $^3P_2$ | $5\Gamma_1$ | 4,900 |
| −600 | 5,900 | $^1A_1'$ | $^1G_4$ | $6\Gamma_1$ | 5,700 |
| 1,200 | −1,700 | $^1E''$ | $^1G_4$ | $7\Gamma_6$ | −1,700 |
| 5,600 | 9,650 | $^1E'$ | $^1G_4$ | $7\Gamma_3$ | 9,650 |
| 7,050 | 7,050 | $^1E'$ | $^1G_4$ | $8\Gamma_3$ | 7,050 |
| 9,350 | 9,350 | $^1A_{1,2}''$ | $^1G_4$ | $3\Gamma_{4,5}$ | 9,350 |
| 27,950 | 30,100 | $^1A_1'$ | $^1S_0$ | $7\Gamma_1$ | 30,150 |

[a] Using the parametric values $F_2 = 1250\ cm^{-1}$, $F_4 = 83\ cm^{-1}$, $Dq = -1200\ cm^{-1}$, $Db = 1.72Dq$, and $\lambda = -390\ cm^{-1}$.[52]

*et al.*[7] In this present work, however, application of these reduced-symmetry trigonal bipyramidal perturbation calculations seemed too limited to justify complete calculation.

## Conclusion

This concludes, then, the purpose of our work as stated at the outset—at least in theory. The qualitative aspects, as well as the possible application, of this work fail to emerge clearly, however, because of the unwieldy size of these perturbation matrices. Thus it becomes necessary to expand these matrices with specific values for the five parameters, $Dq$, $Db$, $F_2$, $F_4$, and $\lambda$—if only crude approximations—in order to observe their qualitative features, which will become quantitative upon use of correct parametric values. First we observe the weak-field approximation.

A value of $Dq = -1200\ cm^{-1}$ is assumed reasonable for the Ni(II) in trigonal bipyramidal complexes,[42-45] and the Slater–Condon–Shortley parameters are taken as $F_2 = 1250\ cm^{-1}$ and $F_4 = 83\ cm^{-1}$, being decreased 24% and 32%, respectively, from their free ion values.[45-47] The value of the spin–orbit parameter used is $\lambda = -390\ cm^{-1}$, which is 60% its free value,[48] and $Db$ has again been assumed $1.72Dq$. The results obtained from the weak-field perturbation matrices with these parameter values are summarized in Table IX, in which the energy levels obtained from the weak crystalline field limit of the $d^8$ correlation diagram (diagonal crystal field perturbation) and from an intermediate crystalline field perturbation matrix (crystal field–Coulombic perturbation) have also been included. One immediately observes the severe limitation of the weak crystal field limit—especially for the singlet levels and for $^2E''[^3F,^3P]$. These errors result, of course, because in the weak-field limit the off-diagonal crystal field matrix elements—which are quite significant in this example—have been ignored.[49]

(42) A somewhat smaller absolute value of $Dq$—say $-1000\ cm^{-1}$ which is closer to a median value within the range of known $Dq$ for octahedral coordination by polydentate N-coordinating ligands[43-45]—would give closer agreement with the observed spectra of trigonal bipyramidal high spin N:(II) complexes.[6] The $Dq$ value of $-1200\ cm^{-1}$ is roughly the largest observed value for octahedral (paramagnetic) Ni(II) complexes.[43-45]

(43) C. Klixbüll Jørgensen, *Acta Chem. Scand.*, **9**, 1362 (1955).

(44) C. Klixbüll Jørgensen, *ibid.*, **10**, 887 (1956).

(45) O. Bostrup and C. Klixbüll Jørgensen, *ibid.*, **11**, 1223 (1957).

(46) J. Hinze and H. H. Jaffe, *J. Chem. Phys.*, **38**, 1834 (1963).

(47) These values of $F_2$ and $F_4$, which are equivalent to $15B = 12{,}500\ cm^{-1}$ and $8B + 2C = 12{,}500\ cm^{-1}$ since $B = F_2 - 5F_4$ and $C = 35F_4$, are very appropriate for the nephelauxetic effect observed in octahedral complexes of Ni(II) with N-coordinating ligands.[45] These values of $F_k$ also exhibit, incidentally, an $F_2/F_4$ value of 15.

(48) J. S. Griffith, "The Theory of Transition-Metal Ions," Cambridge University Press, New York, N.Y., 1961, Appendix 6.

**Table X:** Solution of the Strong-Field Matrices with Approximate Parametric Values[a] for $d^8$

| Simple crystal field | | | Crystal field–spin orbit calculations | | |
|---|---|---|---|---|---|
| Strong crystal field limit | Intermediate crystal field | CF state | Orbital configuration | $\Gamma_i$ | Eigenvalue |
| −34,450 | −36,150 | $^1A_1'$ | $^1A_1'[(e'')^4(e')^4]$ | $1\Gamma_1$ | −36,200 |
| −29,450 | −29,500 | $^3E'$ | $^3E'[(e'')^4(e')^3(a_1')]$ | $1\Gamma_{4,5}$ | −29,850 |
| | | | | $1\Gamma_3$ | −29,500 |
| | | | | $1\Gamma_6$ | −29,200 |
| −17,000 | −17,250 | $^1E'$ | $^1E'[(e'')^4(e')^3(a_1')]$ | $3\Gamma_3$ | −17,200 |
| −16,300 | −18,000 | $^3E''$ | $^3E''[(e'')^3(e')^4(a_1')]$ | $2\Gamma_3$ | −18,200 |
| | | | | $2\Gamma_6$ | −18,000 |
| | | | | $1\Gamma_3$ | −17,800 |
| | | | | $2\Gamma_1$ | −17,800 |
| −8,850 | −9,050 | $^1E''$ | $^1E''[(e'')^3(e')^4(a_1')]$ | $3\Gamma_6$ | −9,050 |
| 4,250 | 775 | $^3A_2'$ | $^3A_2'[(e'')^4(e')^2(a_1')^2]$ | $3\Gamma_1$ | 700 |
| | | | | $4\Gamma_6$ | 750 |
| 10,050 | 10,050 | $^1E'$ | $^1E'[(e'')^4(e')^2(a_1')^2]$ | $7\Gamma_3$ | 10,050 |
| 15,850 | 10,500 | $^1A_1'$ | $^1A_1'[(e'')^4(e')^2(a_1')^2]$ | $5\Gamma_1$ | 10,500 |
| −150 | −150 | $^3A_{1,2}''$ | $^3A_{1,2}''[(e'')^3(e')^3(a_1')^2]$ | $4\Gamma_3$ | −650 |
| | | | | $2\Gamma_{4,5}$ | −150 |
| | | | | $5\Gamma_3$ | 400 |
| 4,900 | 6,550 | $^3E''$ | $^3E''[(e'')^3(e')^3(a_1')^2]$ | $6\Gamma_3$ | 6,350 |
| | | | | $5\Gamma_6$ | 6,500 |
| | | | | $2\Gamma_2$ | 6,700 |
| | | | | $4\Gamma_1$ | 6,700 |
| 10,700 | 10,900 | $^1E''$ | $^1E''[(e'')^3(e')^3(a_1')^2]$ | $6\Gamma_6$ | 10,800 |
| 15,700 | 15,700 | $^1A_{1,2}''$ | $^1A_{1,2}''[(e'')^3(e')^3(a_1')^2]$ | $3\Gamma_{4,5}$ | 15,700 |
| 8,000 | 11,500 | $^3A_2'$ | $^3A_2'[(e'')^2(e')^4(a_1')^2]$ | $6\Gamma_1$ | 11,500 |
| | | | | $7\Gamma_6$ | 11,650 |
| 18,850 | 19,100 | $^1E'$ | $^1E'[(e'')^2(e')^4(a_1')^2]$ | $8\Gamma_3$ | 19,100 |
| 29,650 | 36,700 | $^1A_1'$ | $^1A_1'[(e'')^2(e')^4(a_1')^2]$ | $7\Gamma_1$ | 36,750 |

[a] Using the parametric values $F_2 = 1250\ cm^{-1}$, $F_4 = 83\ cm^{-1}$, $Dq = -3000\ cm^{-1}$, $Db = 1.72Dq$, and $\lambda = -335\ cm^{-1}$.[52]

The spin-orbit coupling introduces, in general, only the refinement of a clustering of spin states about the crystalline field levels, since in this case the crystal field perturbation is dominant. Spin-orbit perturbation is significant, however, for levels such as $^3A_1''$, $^3A_2''$, where singlet–triplet mixing has become important. An optimum $Dq$ value was not selected, so close agreement cannot be expected, but it is apparent that a predicted spectrum for trigonal bipyramidal (paramagnetic) Ni(II) complexes from Table IX is in qualitative agreement with experiment and previous crystal field calculations.[6]

For an experimental application of the strong-field matrices one must turn to the diamagnetic complexes of Ni(II) with phosphines, arsines, and similar-type ligands, where the supposedly extensive $\pi$-type bonding of the ligand systems and consequent intense absorption spectra render these complexes very poor examples indeed for a crystal field model. Recognizing then from the outset the severe limitations of our theoretical model, we may begin by selecting reasonable approximated values for the parameters. Retaining the previous values for the $F_k$ parameters, $F_2 = 1250\ cm^{-1}$ and $F_4 = 83\ cm^{-1}$, *i.e.*, $15B = 8B + 2C = 12{,}500\ cm^{-1}$, and the relationship, $Db = 1.72Dq$, one sees from the crystal field calculations (diagonal) that a minimum value of $Dq = -2400\ cm^{-1}$ is needed to achieve spin-pairing.[50] Let us assume then a $Dq$ value of $-3000\ cm^{-1}$, say, and the spin–orbit parameter suggested by Moffitt and Ballhausen,[51] $\lambda(Ni^{2+}) = -335\ cm^{-1}$.[52]

The results from the strong crystal field and crystal field–spin orbit calculations are shown jointly in Table X and Figure 4. The strong crystal field limit is grossly in error for the $^3A_2'$ and $^1A_1'$ levels arising from the $(e'')^4(e')^2(a_1')^2$ and $(e'')^2(e')^4(a_1')^2$ strong field configurations. The spin–orbit perturbation of the $^3A_{1,2}''[(e'')^3(e')^3(a_1')^2]$ levels is most pronounced, but in general spin–orbit effects are slight compared to the large

(49) The weak crystal field limit cannot therefore even show the large stabilization of the $^1A_1'$ ($^1D$) state which allows it to cross the $^3E'$ ($^3F$) and become the ground state in the strong crystal field limit, and also gives a qualitatively incorrect overall crystal field splitting of the $^1D$ term as the strong field limit is approached. The E′ and E″ levels are more widely separated than are the $A_1'$ and E′ in the weak-field limit, but in the strong-field limit (in which the basis functions are selected diagonal to crystal field perturbation) the crystal field pattern of the one-electron configuration has been re-established: the $A_1'$ level widely separated from the more closely neighboring E′ and E″ levels.

(50) A greater nephelauxetic effect; *i.e.*, reduction of the free-ion $F_2$ and $F_4$ values—which is certainly feasible with these polydentate $\pi$-acceptor ligands—would of course allow spin-pairing with a smaller $Dq$ value.

(51) W. E. Moffitt and C. J. Ballhausen, *Ann. Rev. Phys. Chem.*, **7**, 107 (1956).

$$
D^{3}(\alpha,\beta,\gamma) =
\begin{bmatrix}
[\varepsilon_+^3]e^{-3i(\alpha+\gamma)} & -\sqrt{6}/2[\sin\beta][\varepsilon_+^2]e^{-i(3\alpha+2\gamma)} & \sqrt{15}[\varepsilon_+^2\varepsilon_-]e^{-i(3\alpha+\gamma)} & -\sqrt{5}/4[\sin^3\beta][e^{-3i\alpha}] \\
\sqrt{6}/2[\sin\beta][\varepsilon_+^2]e^{-i(2\alpha+3\gamma)} & \{\varepsilon_+^3 - 5\varepsilon_+^2\varepsilon_-\}e^{-2i(\alpha+\gamma)} & \sqrt{10}/4[\sin\beta](-2\varepsilon_+^2 + \sin^2\beta)e^{-i(2\alpha+\gamma)} & \sqrt{30}/4[\sin^2\beta\cos\beta][e^{-2i\alpha}] \\
\sqrt{15}[\varepsilon_+^2\varepsilon_-]e^{-i(\alpha+3\gamma)} & (\sqrt{10}/2[\sin\beta][\varepsilon_+^2] - \sqrt{10}/4[\sin^3\beta])e^{-i(\alpha+2\gamma)} & \{\varepsilon_+^3 - 8\varepsilon_+^2\varepsilon_- + 6\varepsilon_+\varepsilon_-^2\}e^{-i(\alpha+\gamma)} & \sqrt{3}\sin\beta\{-\varepsilon_+^2 + \tfrac{3}{4}\sin^2\beta - \varepsilon_-^2\}e^{-i\alpha} \\
\sqrt{5}/4[\sin^3\beta][e^{-3i\gamma}] & \sqrt{30}/4[\sin^2\beta\cos\beta][e^{-2i\gamma}] & \sqrt{3}[\sin\beta](\varepsilon_+^2 - \tfrac{3}{4}\sin^2\beta + \varepsilon_-^2)e^{-i\gamma} & \{\varepsilon_+^3 - 9\varepsilon_+^2\varepsilon_- + 9\varepsilon_+\varepsilon_-^2 - \varepsilon_-^3\} \\
\sqrt{15}/4[\sin^2\beta][\varepsilon_-]e^{i(\alpha-3\gamma)} & (\sqrt{10}/4[\sin^3\beta] - \sqrt{10}/2[\sin\beta][\varepsilon_-^2]\,e^{i(\alpha-2\gamma)} & \{\tfrac{3}{2}[\sin^2\beta][\varepsilon_+] - 2[\sin^2\beta][\varepsilon_-] + [\varepsilon_-^3]\}e^{i(\alpha-\gamma)} & \sqrt{3}\sin\beta\{\varepsilon_+^2 - \tfrac{3}{4}\sin^2\beta + \varepsilon_-^2\}e^{i\alpha} \\
\sqrt{6}/2[\sin\beta][\varepsilon_-^2]e^{i(2\alpha-3\gamma)} & \{5/4[\sin^2\beta][\varepsilon_-] - [\varepsilon_-^3]\}e^{2i(\alpha-\gamma)} & \sqrt{10}/4[\sin\beta](\sin^2\beta - 2\varepsilon_-^2)e^{i(2\alpha-\gamma)} & \sqrt{30}/4[\sin^2\beta\cos\beta][e^{2i\alpha}] \\
[\varepsilon_-^3]e^{3i(\alpha-\gamma)} & \sqrt{6}/2[\sin\beta][\varepsilon_-^2]e^{i(3\alpha-2\gamma)} & \sqrt{15}/4[\sin^2\beta][\varepsilon_-]e^{i(3\alpha-\gamma)} & \sqrt{5}/4[\sin^3\beta][e^{3i\alpha}]
\end{bmatrix}
$$

$$
\begin{bmatrix}
\sqrt{15}/4[\sin^2\beta][\varepsilon_-]e^{-i(3\alpha-\gamma)} & -\sqrt{6}/2[\sin\beta][\varepsilon_-^2]e^{-i(3\alpha-2\gamma)} & [\varepsilon_-^3]e^{-3i(\alpha-\gamma)} & \\
\sqrt{10}/4[\sin\beta](-\sin^2\beta + 2\varepsilon_-^2)e^{-i(2\alpha-\gamma)} & \{\tfrac{5}{4}[\sin^2\beta][\varepsilon_-] - [\varepsilon_-^3]\}e^{-2i(\alpha-\gamma)} & -\sqrt{6}/2[\sin\beta][\varepsilon_-^2]e^{-i(2\alpha-3\gamma)} & \\
\{\tfrac{3}{2}\sin^2\beta[\varepsilon_+] - 2\sin^2\beta[\varepsilon_-] + [\varepsilon_-^3]\}e^{-i(\alpha-\beta)} & \sqrt{10}/4[\sin\beta](-\sin^2\beta + 2\varepsilon_-^2)e^{-i(\alpha-2\gamma)} & \sqrt{15}/4[\sin^2\beta][\varepsilon_-]e^{-i(\alpha-3\gamma)} & \\
\sqrt{3}\sin\beta\{-\varepsilon_+^2 + \tfrac{3}{4}\sin^2\beta - \varepsilon_-^2\}e^{i\gamma} & \sqrt{30}/4[\sin^2\beta\cos\beta]e^{2i\gamma}] & -\sqrt{5}/4[\sin^3\beta][e^{3i\gamma}] & \\
\{\varepsilon_+^3 - 8\varepsilon_+^2\varepsilon_- + 6\varepsilon_+\varepsilon_-^2\}e^{i(\alpha+\gamma)} & \sqrt{10}/4[\sin\beta]\{-2\varepsilon_+^2 + \sin^2\beta\}e^{i(\alpha+2\gamma)} & \sqrt{15}[\varepsilon_+\varepsilon_-]e^{i(\alpha+3\gamma)} & \\
\sqrt{10}/4[\sin\beta]\{2\varepsilon_+^2 - \sin^2\beta\}e^{i(2\alpha+\gamma)} & \{\varepsilon_+^3 - 5\varepsilon_+\varepsilon_-^2\}e^{2i(\alpha+\gamma)} & -\sqrt{6}/2[\sin\beta][\varepsilon_+^2]e^{i(2\alpha+3\gamma)} & \\
\sqrt{15}[\varepsilon_+^2\varepsilon_-]e^{i(3\alpha+\gamma)} & \sqrt{6}/2[\sin\beta][\varepsilon_+^2]e^{i(3\alpha+2\gamma)} & [\varepsilon_+^3]e^{3i(\alpha+\gamma)} &
\end{bmatrix}
$$

$$
D^{4}(\alpha,\beta,\gamma) = \begin{bmatrix}
[\epsilon_+^4][e^{-4i(\alpha+\gamma)}] & -\sqrt{2}[\sin\beta][\epsilon_+^3][e^{-i(4\alpha+3\gamma)}] & \frac{\sqrt{7}}{2}[\sin^2\beta][\epsilon_+^2][e^{-i(4\alpha+2\gamma)}] & -\frac{\sqrt{7}}{\sqrt{8}}[\sin^3\beta][\epsilon_+][e^{-i(4\alpha+\gamma)}] \\
\sqrt{2}[\sin\beta][\epsilon_+^3][e^{-i(3\alpha+4\gamma)}] & \{\epsilon_+^4 - 7\epsilon_+^3\epsilon_-\}e^{-3i(\alpha+\gamma)} & \sqrt{14}\,[\sin\beta][\epsilon_+]\{-\tfrac{1}{2}\epsilon_+^2 + \tfrac{3}{8}\sin^2\beta\}e^{-i(3\alpha+2\gamma)} & \frac{\sqrt{7}}{16}\sin^2\beta\{12[\epsilon_+^2] - 5\sin^2\beta\}e^{-i(3\alpha+\gamma)} \\
\frac{\sqrt{7}}{2}[\sin^2\beta][\epsilon_+^2][e^{-i(2\alpha+4\gamma)}] & \{\frac{\sqrt{7}}{\sqrt{2}}[\sin\beta][\epsilon_+^3] - \frac{3\sqrt{14}}{3}[\sin^3\beta][\epsilon_+]\}e^{-i(2\alpha+3\gamma)} & \{[\epsilon_+^4] - 3[\sin^2\beta][\epsilon_+^2] + \tfrac{15}{16}\sin^4\beta\}e^{-2i(\alpha+\gamma)} & \sqrt{2}\,\sin\beta\{-\tfrac{3}{2}[\epsilon_+^3] + \tfrac{15}{8}[\sin^2\beta][\epsilon_+] - \tfrac{5}{4}[\sin^2\beta][\epsilon_-]\}e^{-i(2\alpha+\gamma)} \\
\frac{\sqrt{7}}{\sqrt{8}}[\sin^3\beta][\epsilon_+][e^{-i(\alpha+4\gamma)}] & \frac{\sqrt{7}}{16}[\sin^2\beta](12\epsilon_+^2 - 5\sin^2\beta)e^{-i(\alpha+3\gamma)} & \sqrt{2}\,\sin\beta\{\tfrac{3}{2}[\epsilon_+^3] - \tfrac{15}{8}[\sin^2\beta][\epsilon_+] + \tfrac{5}{4}[\sin^2\beta][\epsilon_-]\}e^{-i(\alpha+2\gamma)} & \{[\epsilon_+^4] - \tfrac{15}{4}[\sin^2\beta][\epsilon_+^2] + \tfrac{15}{8}\sin^4\beta - \tfrac{5}{2}[\sin^2\beta][\epsilon_-^2]\}e^{-i(\alpha+\gamma)} \\
\frac{\sqrt{70}}{16}[\sin^4\beta][e^{-4i\gamma}] & \frac{\sqrt{35}}{4}[\sin^3\beta\cos\beta][e^{-3i\gamma}] & \frac{\sqrt{10}}{8}[\sin^2\beta](7\cos^2\beta - 1)e^{-2i\gamma} & -\frac{\sqrt{5}}{4}[\sin\beta][\cos\beta](7\sin^2\beta - 4)e^{-i\gamma} \\
\frac{\sqrt{7}}{\sqrt{8}}[\sin^3\beta][\epsilon_-][e^{i(\alpha-4\gamma)}] & \frac{\sqrt{7}}{16}[\sin^2\beta](5\sin^2\beta - 12\epsilon_-^2)e^{i(\alpha-3\gamma)} & \sqrt{2}\,\sin\beta\{\frac{5}{4}[\sin^2\beta][\epsilon_+] - \frac{15}{8}[\sin^2\beta][\epsilon_-] + \frac{3}{2}[\epsilon_-^3]\}e^{i(\alpha-2\gamma)} & \{\frac{5}{2}[\sin^2\beta][\epsilon_+^2] - \frac{15}{8}\sin^4\beta + \frac{15}{4}[\sin^2\beta][\epsilon_-^2] - [\epsilon_-^4]\}e^{i(\alpha-\gamma)} \\
\frac{\sqrt{7}}{2}[\sin^2\beta][\epsilon_-^2][e^{i(2\alpha-4\gamma)}] & \sqrt{14}\,\sin\beta\{\tfrac{3}{8}[\sin^2\beta][\epsilon_-] - \tfrac{1}{2}[\epsilon_-^3]\}e^{i(2\alpha-3\gamma)} & \{\tfrac{15}{16}\sin^4\beta - 3[\sin^2\beta][\epsilon_-^2] + [\epsilon_-^4]\}e^{2i(\alpha-\gamma)} & \sqrt{2}\,\sin\beta\{\tfrac{5}{4}[\sin^2\beta][\epsilon_+] - \tfrac{15}{8}[\sin^2\beta][\epsilon_-] + \tfrac{3}{2}[\epsilon_-^3]\}e^{i(2\alpha-\gamma)} \\
\sqrt{2}[\sin\beta][\epsilon_-^3][e^{i(3\alpha-4\gamma)}] & \{7\epsilon_+\epsilon_-^3 - \epsilon_-^4\}e^{3i(\alpha-\gamma)} & \sqrt{14}\,\sin\beta\{\tfrac{3}{8}[\sin^2\beta][\epsilon_-] - \tfrac{1}{2}\epsilon_-^3\}e^{i(3\alpha-2\gamma)} & \frac{\sqrt{7}}{16}\sin^2\beta\{5\sin^2\beta - 12[\epsilon_-^2]\}e^{i(3\alpha-\gamma)} \\
[\epsilon_-^4][e^{4i(\alpha-\gamma)}] & \sqrt{2}\,[\sin\beta][\epsilon_-^3][e^{i(4\alpha-3\gamma)}] & \frac{\sqrt{7}}{2}[\sin^2\beta][\epsilon_-^2][e^{i(4\alpha-2\gamma)}] & \frac{\sqrt{7}}{\sqrt{8}}[\sin^3\beta][\epsilon_-][e^{i(4\alpha-\gamma)}]
\end{bmatrix}
$$

$$
\begin{bmatrix}
\frac{\sqrt{70}}{16}[\sin^4\beta][e^{-4i\alpha}] & -\frac{\sqrt{7}}{\sqrt{8}}[\sin^3\beta][\epsilon_-][e^{-i(4\alpha-\gamma)}] & \frac{\sqrt{7}}{2}[\sin^2\beta][\epsilon_-^2][e^{-i(4\alpha-2\gamma)}] & -\sqrt{2}\,[\sin\beta][\epsilon_-^3][e^{-i(4\alpha-3\gamma)}] & [\epsilon_-^4]e^{-4i(\alpha-\gamma)} \\
-\frac{\sqrt{35}}{4}[\sin^3\beta][\cos\beta][e^{-3i\alpha}] & \frac{\sqrt{7}}{16}[\sin^2\beta](5\sin^2\beta - 12\,\epsilon_-^2)e^{-i(3\alpha-\gamma)} & \sqrt{14}\,[\sin\beta][\epsilon_-](-\frac{3}{8}\sin^2\beta + \frac{1}{2}[\epsilon_-^2])e^{-i(3\alpha-2\gamma)} & \{7[\epsilon_+][\epsilon_-^3] - [\epsilon_-^4]\}e^{-3i(\alpha-\gamma)} & -\sqrt{2}\,[\sin\beta][\epsilon_-^3][e^{-i(3\alpha-4\gamma)}] \\
\frac{\sqrt{10}}{8}[\sin^2\beta](7\cos^2\beta - 1)e^{-2i\alpha} & \sqrt{2}\,\sin\beta[-\tfrac{5}{4}[\sin^2\beta][\epsilon_+] + \tfrac{15}{8}[\sin^2\beta][\epsilon_-] - \tfrac{3}{2}\epsilon_-^3]e^{-i(2\alpha-\gamma)} & \{\tfrac{15}{16}\sin^4\beta - 3[\sin^2\beta][\epsilon_-^2] + [\epsilon_-^4]\}e^{-2i(\alpha-\gamma)} & \sqrt{14}\,\sin\beta(-\tfrac{3}{8}[\sin^2\beta][\epsilon_-] + \tfrac{1}{2}[\epsilon_-^3])e^{-i(2\alpha-3\gamma)} & \frac{\sqrt{7}}{2}[\sin^2\beta][\epsilon_-^2][e^{-i(2\alpha-4\gamma)}] \\
\frac{\sqrt{5}}{4}[\sin\beta][\cos\beta](7\sin^2\beta - 4)e^{-i\alpha} & \{\tfrac{5}{2}[\sin^2\beta][\epsilon_+^2] - \tfrac{15}{8}\sin^4\beta + \tfrac{15}{4}[\sin^2\beta][\epsilon_-^2] - \epsilon_-^4\}e^{-i(\alpha-\gamma)} & \sqrt{2}\,\sin\beta(-\tfrac{5}{4}[\sin^2\beta][\epsilon_+] + \tfrac{15}{8}[\sin^2\beta][\epsilon_-] - \tfrac{3}{2}[\epsilon_-^3])e^{-i(\alpha-2\gamma)} & \frac{\sqrt{7}}{16}\sin^2\beta(5\sin^2\beta - 12[\epsilon_-^2])e^{-i(\alpha-3\gamma)} & -\frac{\sqrt{7}}{\sqrt{8}}[\sin^3\beta][\epsilon_-][e^{-i(\alpha-4\gamma)}] \\
\{\epsilon_+^4 - 4[\sin^2\beta][\epsilon_+^2] + \tfrac{9}{4}\sin^4\beta - 4[\sin^2\beta][\epsilon_-^2] + \epsilon_-^4\} & -\frac{\sqrt{5}}{4}[\sin\beta][\cos\beta](7\sin^2\beta - 4)e^{i\gamma} & \frac{\sqrt{10}}{8}[\sin^2\beta](7\cos^2\beta - 1)e^{2i\gamma} & -\frac{\sqrt{35}}{4}[\sin^3\beta][\cos\beta][e^{3i\gamma}] & \frac{\sqrt{70}}{16}[\sin^4\beta][e^{4i\gamma}] \\
-\frac{\sqrt{5}}{4}[\sin\beta][\cos\beta](7\sin^2\beta - 4)e^{i\alpha} & \{\epsilon_+^4 - \frac{15}{4}[\sin^2\beta][\epsilon_+^2] + \frac{15}{8}\sin^4\beta - \frac{5}{2}[\sin^2\beta][\epsilon_-^2]\}e^{i(\alpha+\gamma)} & \sqrt{2}\,\sin\beta(-\tfrac{3}{2}[\epsilon_+^3] + \tfrac{15}{8}[\sin^2\beta][\epsilon_+] - \tfrac{5}{4}[\sin^2\beta][\epsilon_-])e^{i(\alpha+2\gamma)} & \frac{\sqrt{7}}{16}\sin^2\beta(12[\epsilon_+^2] - 5\sin^2\beta)e^{i(\alpha+3\gamma)} & -\frac{\sqrt{7}}{\sqrt{8}}[\sin^3\beta][\epsilon_+][e^{i(\alpha+4\gamma)}] \\
\frac{\sqrt{10}}{8}[\sin^2\beta](7\cos^2\beta - 1)e^{2i\alpha} & \sqrt{2}\,\sin\beta\{\tfrac{3}{2}\epsilon_+^3] - \frac{15}{8}[\sin^2\beta][\epsilon_+] + \frac{5}{4}[\sin^2\beta][\epsilon_-]\}e^{i(2\alpha+\gamma)} & \{[\epsilon_+^4] - 3[\sin^2\beta][\epsilon_+^2] + \tfrac{15}{16}\sin^4\beta\}e^{2i(\alpha+\gamma)} & \sqrt{14}\,[\sin\beta][\epsilon_+](-\frac{1}{2}[\epsilon_+^2] + \frac{3}{8}\sin^2\beta)e^{i(2\alpha+3\gamma)} & \frac{\sqrt{7}}{2}[\sin^2\beta][\epsilon_+^2][e^{i(2\alpha+4\gamma)}] \\
\frac{\sqrt{35}}{4}[\sin^3\beta][\cos\beta][e^{3i\alpha}] & \frac{\sqrt{7}}{16}[\sin^2\beta](12[\epsilon_+^2] - 5\sin^2\beta)e^{i(3\alpha+\gamma)} & \sqrt{14}\,[\sin\beta][\epsilon_+](\frac{1}{2}[\epsilon_+^2] - \frac{3}{8}\sin^2\beta)e^{i(3\alpha+2\gamma)} & \{[\epsilon_+^4] - 7[\epsilon_+^3][\epsilon_-]\}e^{3i(\alpha+\gamma)} & -\sqrt{2}\,[\sin\beta][\epsilon_+^3][e^{i(3\alpha+4\gamma)}] \\
\frac{\sqrt{70}}{16}[\sin^4\beta][e^{4i\alpha}] & \frac{\sqrt{7}}{\sqrt{8}}[\sin^3\beta][\epsilon_+][e^{i(4\alpha+\gamma)}] & \frac{\sqrt{7}}{2}[\sin^2\beta][\epsilon_+^2][e^{i(4\alpha+2\gamma)}] & \sqrt{2}\,[\sin\beta][\epsilon_+^3][e^{i(4\alpha+3\gamma)}] & [\epsilon_+^4][e^{4i(\alpha+\gamma)}]
\end{bmatrix}
$$

values assigned the crystal field perturbation. Within this crystal field model then, the two lowest-energy (nominally) spin-allowed electronic transitions expected for diamagnetic Ni(II) in a trigonal bipyramidal environment; *i.e.*, $1\Gamma_1 \rightarrow 3\Gamma_3$ and $1\Gamma_1 \rightarrow 3\Gamma_6$, are predicted to occur at 19,000 $cm^{-1}$ and 27,150 $cm^{-1}$, respectively, in reasonable agreement with experiment and previous calculations.[7]

In final conclusion, then, the complete perturbation matrices for a $d^2$, $d^8$ configuration in $D_{3h}$ crystalline field and their method of calculation have been presented quantitatively in parametric form. Substitution of presumably qualitatively correct, but most probably quantitatively incorrect, parametric values has been made to suggest qualitative features. More and better experimental values can improve these parametric approximations and the speculations based upon them, but most of the observations made from these calculations should remain qualitatively correct.[52]

*Acknowledgment.* The authors wish to acknowledge gratefully the National Science Foundation for the financial support of this research and for a fellowship to C. A. L. B. during 1965–1967. The technical staff of Chemistry Laboratory IV (Department of Physical Chemistry) of the H. C. Ørsted Institute, Copenhagen, Denmark, is thanked for assistance in preparing the manuscript.

## Appendix

*Generalized Rotation Matrices.* The general transformation matrices for eigenfunctions of unspecified angular momenta, $D^j(\alpha,\beta,\gamma)$, used extensively in this work, are given by Tinkham[13] in the form of a generating function for the individual matrix element

$$D^j(\alpha,\beta,\gamma)_{m'm} = e^{-im'\alpha}\, e^{-im\gamma} \times \sum_k \frac{(-1)^k \sqrt{(j+m)!(j-m)!(j-m')!(j+m')!}}{k!\,(j+m-k)!(j-m'-k)!(k+m'-m)!}$$

$$(\cos\beta/2)^{2j-2k-m'+m}(-\sin\beta/2)^{2k+m'-m}$$

(The index $k$ assumes all integral values for which the denominator remains defined.) Completely generalized rotation matrices can now be constructed to as large a value of $j$ (total angular momentum) as necessary. The vector forms of the angular momentum eigenfunctions must be used with these $D^j(\alpha,\beta,\gamma)$ matrices, and the Condon and Shortley phase conventions[53] are appropriate.

The rotation matrices for $j = 0, 1, 2, 3, 4$ have been used in this work. The $D^0(\alpha,\beta,\gamma) = 1$, of course, implying an invariance to all rotation; $D^1(\alpha,\beta,\gamma)$ is given by Tinkham;[13] and $D^2(\alpha,\beta,\gamma)$ has been shown in a previous paper;[10] so only $D^3(\alpha,\beta,\gamma)$ and $D^4(\alpha,\beta,\gamma)$ are listed below—in which, for space and convenience only, $\epsilon_+ \equiv (\cos\beta/2)^2 = {}^1/_2\,(1 + \cos\beta)$ and $\epsilon_- \equiv (\sin\beta/2)^2 = {}^1/_2(1 - \sin\beta)$. We observe that the sines and cosines of half-angles, and consequently the double-valued property, present in the matrices of half-integral $j$ values,[10] have vanished in these $D^j(\alpha,\beta,\gamma)$ matrices, so there should be no sign ambiquity in the transformations performed.

(52) NOTE ADDED IN PROOF. Please note that throughout this paper $\lambda$ denotes the one-electron spin–orbit coupling parameter. However, the symbol $\zeta$ has often been used previously for this parameter, (see, *e.g.*, ref 12 and 48), and $\lambda$ has been reserved for the term spin–orbit coupling parameter, which for the $d^2$, $d^8$ configuration would be $|\lambda| = {}^1/_2\zeta$. Both the "weak" and "strong" crystal field calculations reported in this paper were performed for the one-electron parameter, and the choice of numerical value ($-390$ $cm^{-1}$) in the "weak-field" approximation was based on 60% of the appropriate free-ion value.[48] The "strong-field" value of $\lambda$ $-335$ $cm^{-1}$ corresponds to 52% of the appropriate free-ion value[48] and is not, therefore, the value used in ref 51, which in effect assumes a one-electron value of 670 $cm^{-1}$. Since the numerical values we assumed originally for $\lambda$ (*i.e.*, $\zeta_{3d}$) may be considered rather small, the weak- and strong-field matrices (Tables IX and X) were recalculated using $\lambda$ $-649$ $cm^{-1}$. Changes in the weak- and strong-field eigenvalues (last column in each table) are surprisingly small quantitatively and are completely insignificant in a qualitative sense; thus, we have not considered it necessary to include these new values at the proof stage of this paper. If the energy matrices are applied to specific experimental spectra, however, then of course it will be worthwhile to select more appropriate parametric values by attempting to fit the experimental data at hand.

(53) Reference 10, Chapter 3.

# An Electron Diffraction Investigation of Hexafluoroacetone, Hexafluoropropylimine, and Hexafluoroisobutene

by R. L. Hilderbrandt, A. L. Andreassen, and S. H. Bauer

*Department of Chemistry, Cornell University, Ithaca, New York 14850* *(Received September 9, 1969)*

The structures of $(CF_3)_2C{=}O$, $(CF_3)_2C{=}NH$, and $(CF_3)_2C{=}CH_2$ have been determined by gas-phase electron diffraction. Diffraction photographs for $(CH_3)_2C{=}O$, the structure of which is well known,[1,2] were analyzed concurrently to provide a check on the scale. It appears that replacement of $CH_3$ by $CF_3$ leads to a longer C—C bond (by 0.03–0.04 Å). Thus, C—C = 1.549 ± 0.008 Å in $(CF_3)_2C{=}O$, 1.533 ± 0.006 Å in $(CF_3)_2C{=}CH_2$, and 1.549 ± 0.007 Å in $(CF_3)_2C{=}NH$ in contrast to 1.507 Å in acetone and 1.505 Å in isobutene. This is accompanied by an appreciable lengthening of the C=X bond: C=O = 1.246 ± 0.014 Å and C=C = 1.373 ± 0.013 Å. The C—F bond distances obtained are in agreement with those found in previous studies: C–F = 1.335 ± 0.002 Å in $(CF_3)_2C{=}O$, 1.327 ± 0.002 Å in $(CF_3)_2C{=}CH_2$, and 1.324 ± 0.003 Å in $(CF_3)_2C{=}NH$. The C=N distance for $(CF_3)_2C{=}NH$ (1.294 ± 0.029 Å) appears to be the first estimation of this bond length. The structural parameters determined for $(CH_3)_2C{=}O$ are in excellent agreement with those obtained in recent microwave studies.[1,2]

## Introduction

Because of its high electronegativity and small size, fluorine when substituted into various compounds leads to significant structural changes. The effects of fluorine substitution into ethane, for instance, have been studied in depth, and the trends are well established.[3–5] In recently improved molecular orbital calculations,[6] fluorine substitution is used as a test of the theory, to check whether changes in molecular geometries are correctly predicted. It is therefore of interest to investigate structural trends in fluorine-substituted compounds in order to provide the needed experimental data for correlation with theory and with their well-known chemical behavior.

While the consequences of fluorine substitution on carbon–carbon single- and double-bond lengths have been the subject of numerous structural investigations,[3–5,7–10] little work has been done on compounds containing the system $F_3C{-}X{=}Y$. Schwendeman's[4] recent study of acetaldehyde and 1,1,1-trifluoroacetaldehyde suggested that $F_3C{-}X{=}Y$ may prove to be an unusual grouping. The present investigation revealed that upon fluorine substitution the C—C bond length increased, contrary to most previously observed trends.

## Experimental Section

The samples were obtained from the following sources: acetone, from Fisher Scientific (Certified ACS Spectroanalyzed); perfluoroacetone, from Pierce Chemical Co., Rockford, Ill.; hexafluoroacetonimine from the Hynes Chemical Research Corp., Durham, N. C. The sample of hexafluoroisobutene was graciously supplied by C. G. Krespan and W. J. Middleton of E. I. du Pont de Nemours and Co. Gas chromatographic analysis of these samples indicated better than 95% purity for all of them, and therefore no further purification was necessary.

Sectored diffraction photographs were taken with the dual-mode instrument,[11] in the convergent-beam mode. The sector was cut to level the background scattering produced by atomic carbon. Two sets of data were obtained for each compound, corresponding to the following conditions: 62 kV, at 253-mm nozzle-plate distance, covered the range from $q$ = 5 to 65 Å$^{-1}$, and 62 kV, at 124 mm, convered the range $q$ = 15 to 125 Å$^{-1}$. Exposures ranged from 30 to 120 sec, at a beam current of 0.3 μA, for sample inlet pressures of 5–10 Torr. Kodak Process plates were used. The fluorine-substituted samples, gaseous at room temperature, were introduced into the diffraction chamber through a double-needle valve regulator. The acetone sample was cooled to −35° with a Dry Ice–ethanol bath to provide an equilibrium pressure between 5 and 10 Torr. A magnesium oxide powder sample situated above the nozzle tip was introduced to establish the $q$ scale for the resulting patterns.

(1) R. Nelson and L. Pierce, *J. Mol. Spectrosc.*, **18**, 344 (1965).
(2) J. D. Swalen and C. C. Costain, *J. Chem. Phys.*, **31**, 1562 (1959).
(3) K. Kuchitsu, *ibid.*, **49**, 4456 (1968).
(4) R. Schwendeman, Thesis, University of Michigan, 1956.
(5) D. A. Swick and I. L. Karle, *J. Chem. Phys.*, **23**, 1499 (1955).
(6) M. S. Gordon and J. A. Pople, *ibid.*, **49**, 4643 (1968).
(7) B. Bak, D. Christensen, L. Hansen-Nygard, and J. Rastrup-Andersen, *Spectrochim. Acta*, **13**, 120 (1958).
(8) J. K. Tyler and J. Sheridan, *Trans. Faraday Soc.*, **79**, 2391 (1957).
(9) V. W. Laurie and D. T. Pence, *J. Chem. Phys.*, **38**, 2693 (1963).
(10) I. L. Karle and J. Karle, *ibid.*, **18**, 963 (1950).
(11) S. H. Bauer and K. Kimura, *J. Phys. Soc. Jap.*, **17**, 300 (1962).

For each operating condition pairs of light and dark plates were selected and microphotometered on the modified double-beam Jarrel Ash densitometer, which is equipped with a rotating stage driven at 600 rpm.[12] The analog signal from the densitometer was recorded on a Bristol strip chart recorder. The transmittances were read at 0.25-mm intervals, and the intensities were corrected for flatness and saturation,[13] in the usual manner. The experimental relative intensities, interpolated at integral $q$ [$\equiv(40/\lambda)$ sin $(\theta/2)$] values over the range 6–125, have been deposited with NAPS, as document NAPS-00777.

The data were analyzed in the conventional manner using the radial distribution functions and least-squares fitting of the intensity patterns. The elastic and inelastic form factors of Tavard, *et al.*,[14] were used in conjunction with the Ibers and Hoerni[15] phase-shift approximation. The radial distribution curves were used primarily for refinement of the pattern background in the manner described by the Karles,[16] while the final parameters and error estimates were obtained by the least-squares fitting of the experimental $sM(s)$ curve.

## Analysis

Since the parameters obtained from the analysis are subject to the constraints imposed upon the molecular geometry, it is necessary at the outset to make explicit the assumptions concerning the structures. In all cases, the three carbon atoms and the atom attached to the central carbon were assumed to lie in a plane. While this is consistent with the widely accepted condition for $sp^2$ hybridization, it must be viewed objectively as an imposed constraint. The hydrogens attached to the nitrogen of the imine and to the carbon in isobutene were also confined to the plane of the carbon atoms. The perfluoromethyl groups were required to maintain $C_{3v}$ symmetry about the C–C bond axis; *i.e.*, $F_2$ was obtained from $F_1$ by a 120° rotation about the C–C axis, and $F_3$ was obtained from $F_2$ by a further 120° rotation. This is equivalent to constraining the three C–C–F angles to be equal; similar conditions hold for the three F–C–F angles. Finally, the molecules were assumed to have overall $C_{2v}$ symmetry, with the exception of the hydrogen attached to nitrogen in the imine. Had it been found during the course of the analysis that these restricted models were inadequate to account for the recorded features of the intensity and radial distribution curves, some of these constraints might have been dropped. In light of the excellent agreement obtained under the above assumptions, this was not necessary.

Coordinates for the various models tested were calculated with a recently written algorithm for converting internal coordinates, such as bond distances, valence angles, and dihedral angles, into Cartesian coordinates.[17] This innovation greatly increased the speed and simplicity of the computations.

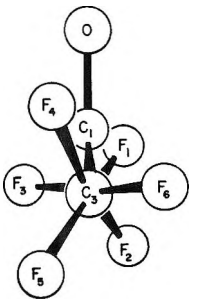


Figure 1. Minimum energy conformation for $(CF_3)_2CO$. View along $C_2$–$C_3$ line.

Subject to the above mentioned constraints, various models were tested for different combinations of the C–C–C angle and the rotational conformation of the methyl groups about the C–C axis. The model which was found to give a minimum in the residuals in the least-squares computation was one in which the fluorines were staggered ($\tau$ = 36°) when viewed along an axis drawn through the $C_2\cdots C_3$ atoms. This staggering is shown in Figure 1 for perfluoroacetone. Similar results were obtained for acetone although the angle was slightly smaller ($\tau$ = 33°), but the uncertainty was appreciably greater. Clearly the nonbonded repulsions play an important role in determining the equilibrium structure.

To justify the approximation in using models with no extensive interval rotations, it is necessary to estimate the barriers to rotation of the methyl groups. Berney[18] and Plaush and Pace[19] reported that the barrier height in hexafluoroacetone is 2800 and 1470 cal/mol, respectively. The case for acetone is not as convincing, however. Swalen and Costain[2] estimated the barrier height to be in the vicinity of 770 cal/mol. The rigid-molecule assumption is still justifiable in the latter case as long as it is qualified by including large mean-square amplitudes of motion for the various nonbonded distances.

The radial distribution curves show (Figure 2) that the dominant scattering contribution in the bonded region is due to the six C—F pairs. This outweighs the C=X contributions by a factor of 6, and the C—C contribution by a factor of 3. In addition, the near equality of the C—F and the C=X bond lengths

(12) S. H. Bauer, R. Jenkins, and R. L. Hilderbrandt, in preparation.
(13) J. L. Hencher and S. H. Bauer, *J. Amer. Chem. Soc.*, **89**, 5527 (1967).
(14) C. Tavard, D. Nicholas, and M. Rouault, *J. Chem. Phys.*, **64**, 540 (1967).
(15) J. A. Ibers and J. A. Hoerni, *Acta Cryst.*, **7**, 405 (1954).
(16) I. L. Karle and J. Karle, *J. Chem. Phys.*, **17**, 1052 (1949).
(17) R. L. Hilderbrandt, *ibid.*, **51**, 1654 (1969).
(18) C. V. Berney, *Spectrochim. Acta*, **21**, 1809 (1965).
(19) A. C. Plaush and E. L. Pace, *J. Chem. Phys.*, **47**, 44 (1967).

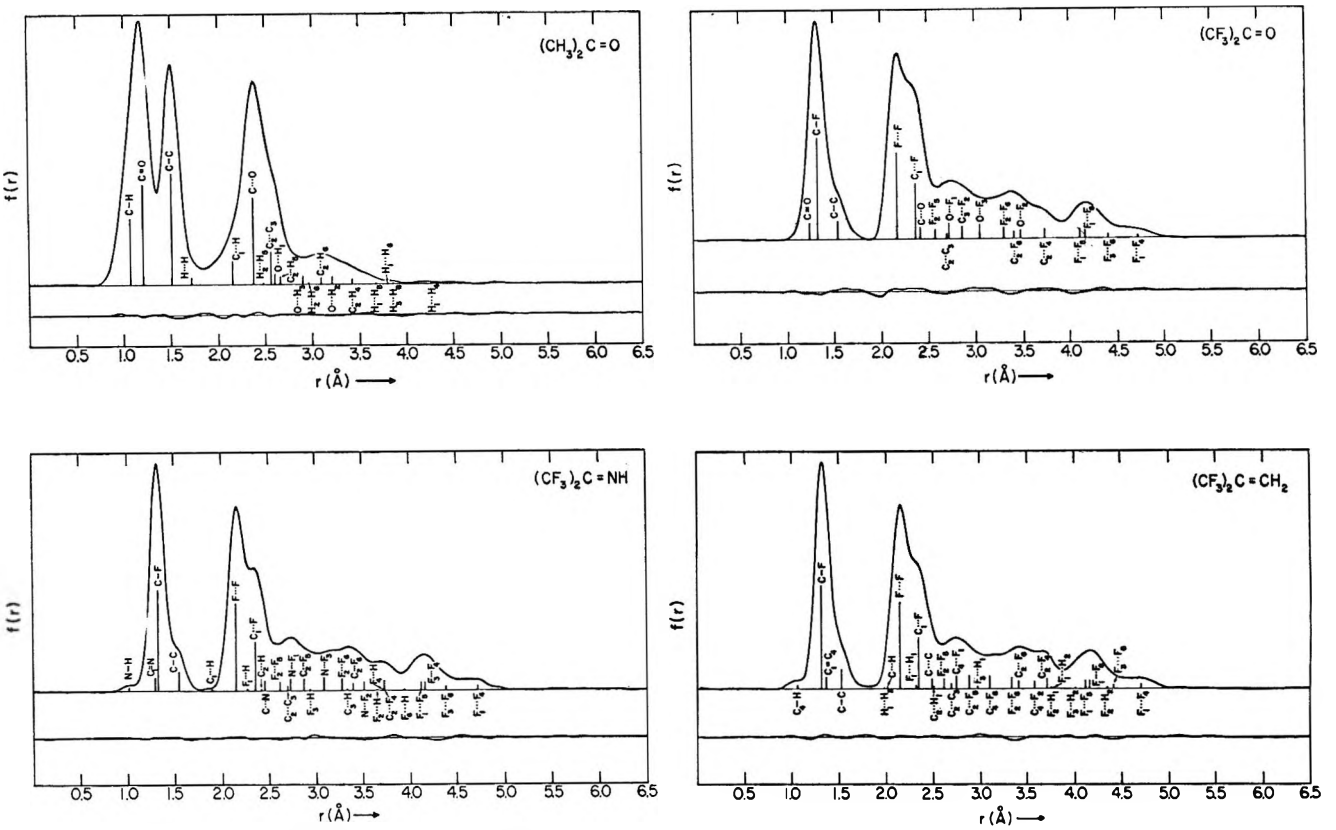


Figure 2. Refined radial distribution curves. In each case, the locations of the principal contributions are indicated by vertical lines, the lengths of which are proportional to $(n_{ij}Z_iZ_j/r_{ij})$. The magnitudes of the deviations between the experimental and calculated curves are indicated for each compound by the lower curve.

**Table I:** Least-Squares Values for $(F_3C)_2C{=}Y$

| | $(F_3C)_2C{=}O$ | $(F_3C)_2C{=}NH$ | $(F_3C)_2C{=}CH_2$ |
|---|---|---|---|
| F—C, Å | 1.335 ± 0.002 | 1.324 ± 0.003 | 1.327 ± 0.002 |
| C—C, Å | 1.549 ± 0.008 | 1.549 ± 0.007 | 1.533 ± 0.006 |
| C=Y, Å | 1.246 ± 0.014 | 1.294 ± 0.029 | 1.373 ± 0.013 |
| Y—H, Å | | 1.02 ± 0.05 | 1.07 ± 0.04 |
| FCC, deg | 110.3 ± 0.3 | 110.0 ± 0.4 | 110.5 ± 0.2 |
| CCC, deg | 121.4 ± 0.4 | 121.6 ± 0.4 | 123.6 ± 0.3 |
| CYH, deg | | 110.0 ± 9 | 111.0 ± 4 |
| Torsion, deg | 36.6 ± 1.1 | 35.1 ± 1.0 | 36.9 ± 0.7 |
| $l_{C-C}$, Å | 0.057 ± 0.013 | 0.051 ± 0.008 | 0.054 ± 0.007 |
| $l_{C-F}$, Å | 0.052 ± 0.003 | 0.052 ± 0.004 | 0.052 ± 0.005 |
| $l_{C-Y}$, Å | (0.049) assumed | 0.051 ± 0.024 | (0.049) assumed |
| $l_{Y-H}$, Å | | 0.050 ± 0.034 | 0.067 ± 0.034 |
| $l_{C\cdots F}$, Å | 0.058 ± 0.005 | 0.068 ± 0.005 | 0.066 ± 0.003 |
| $l_{,C\cdots F}$ Å | 0.062 ± 0.003 | 0.063 ± 0.004 | 0.062 ± 0.004 |
| $\sigma$ | 0.03278 | 0.02684 | 0.02116 |

leads to the rather large uncertainties obtained for the C=X distances (Table I). In the case of acetone, this complication does not arise and the C=O uncertainty is ±0.003 Å. However, in spite of these large uncertainties, the fact that the C—C and C=X bonds are longer in the fluorine- than in the hydrogen-substituted compounds is apparent. Initially the magnitude of this effect was suspected as arising from an unknown systematic error, and for this reason another set of data was obtained for each compound along with photographs for acetone. The latter data were taken under identical conditions and analyzed by the same procedures used for the other compounds. It is believed that any systematic errors such as scale factors and program errors in the analysis would thus have become apparent. For acetone, the parameters thus evaluated reproduced reasonably well those obtained in the microwave studies[1,2] (Table II). The

**Table I:** Comparison of Formulas 1, 2, and 7

| | $\pi M_n/cRT < 3$ | | | $\pi M_n/cRT > 3$ | | | All data | | |
|---|---|---|---|---|---|---|---|---|---|
| | Eq 1 | Eq 2 | Eq 7 | Eq 1 | Eq 2 | Eq 7 | Eq 1 | Eq 2 | Eq 7 |
| $M_n \times 10^{-5}$ | 3.4 | 3.4 | 3.4 | 5.7 | 2.9 | 3.5 | 3.89 | 3.06 | 3.41 |
| $\Gamma_2 \times 10^{-2}$ | 1.2 | 1.2 | 1.2 | 2.9 | 1.0 | 1.3 | 1.70 | 1.08 | 1.21 |
| $g$ | 0.26 | $a$ | 0.29 | 0.04 | $a$ | 0.28 | 0.098 | $a$ | 0.282 |

[a] $g$ fixed at $^1/_4$.

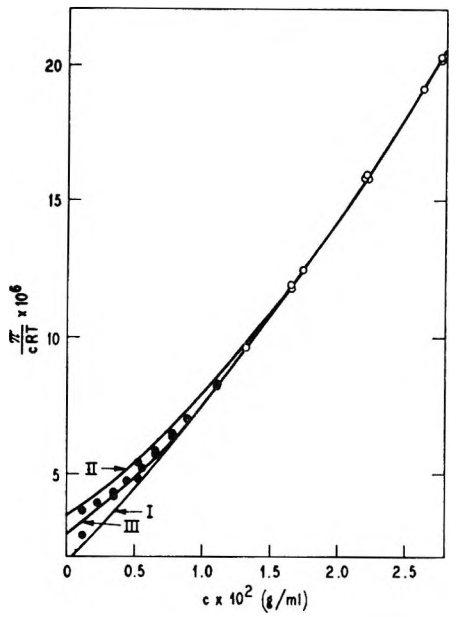


Figure 3. Data of Figure 1 for which $\pi M_n/cRT > 3$ fitted by three relations: I, eq 1; II, eq 2; III, eq 7. Filled circles not used in fitting.

with that calculated from (2) and from (1) when the series of (1) terminates with $\Gamma_3 c^2$. For this comparison we use the data of Figure 1, first using only those observations for which $\pi M_n/cRT < 3$. This restriction is that suggested by Flory[1] as being the region of validity for relations 1 and 2. The results of the three fittings for this case are shown in Figure 4 where the open circles indicate those observations used in the fitting, the filled circles those not used.

Within the region where data were used in fitting, the three relations result in nearly identical fitted curves having, within the precision of determination, the same values for the three parameters $M_n$, $\Gamma_2$, $g$; the first three columns of Table I list these values. Relations (1) and (2) extrapolate into the high concentration region with nearly the same curves while relation (7), with almost the same parameters, is constrained by its functional form to follow a different curve in extrapolation. As seen from Figure 2, this different curve comes much closer to the unused observations.

Major physical interest, however, centers at the low concentration end even if observations must be made at high concentrations. Accordingly, we test relation (7) when only the high concentration data of Figure 1 are used in fitting. Figure 3 shows the results of the test which includes relations (1) and (2) for comparison. Again the three relations fit equally well those data (open circles) used in the fitting but only relation (7) comes anywhere close to extrapolating through the center of scatter of the unused data (filled circles). This behavior of faithfully extrapolating through data not used in positioning or shaping the curve is most impressive and gives considerable confidence that extrapolations through regions devoid of data will yield the proper intercept at $c = 0$. The parameters determined by the high concentration fitting are shown in columns 4–6 of Table I. We call attention to the close agreement between the sets of parameters for the high and low concentration fittings provided only by using relation (7). Although relations (1) and (2) fit the data well outside their region of validity, the parameters of these relations determined by the same data are obviously incorrect.

The last three columns of Table I give the parameters determined by using all the data of Figure 1. Those determined by using relation (7) remain the same as for both the high and low concentration fittings (but with an increase in precision) while those from relations (1) and (2) take values intermediate between the high and low concentration values.

We show in Figures 4–8 five other polymer–solvent systems where the behavior of our relation (7) is tested by restricting the information supplied it to that of the high concentration measurements. The data in Figures 4, 5, and 6 are those reported by Browning and Ferry[2] for poly(vinyl acetate) in several solvents and temperatures. They show the same pronounced increase in curvature with decreasing concentration as our measurements on polystyrene (Figure 3). The long extrapolations forced on relation (7) come satisfactorily close to the data (filled circles) not used in fitting the parameters. In Figures 7 and 8 are two examples of systems for which the pronounced curvature at low concentrations is absent. They represent our data on two hydrogenated polybutadienes with differing ethyl branch content in 1-chloronaphthalene. In spite of the fact that the high concentration be-

(1) P. J. Flory, "Principles of Polymer Chemistry," Cornell University Press, Ithaca, N. Y., 1953, p 280.

(2) G. V. Browning and J. D. Ferry, *J. Chem. Phys.*, **17**, 1107 (1949).

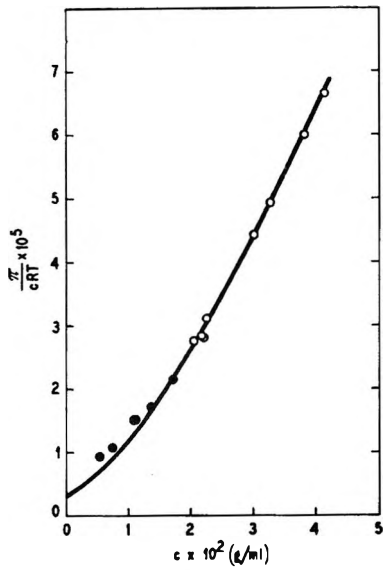


Figure 4. Poly(vinyl acetate) in 1,2,3-trichloropropane at 15°. Data from Browning and Ferry, ref 2. Filled circles not used in fitting.

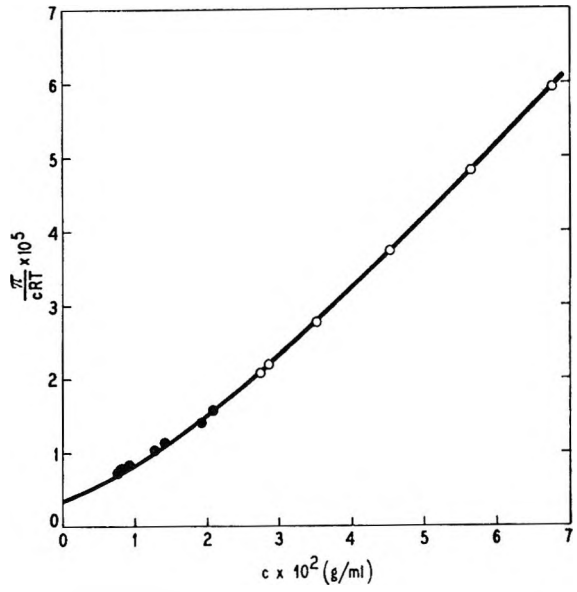


Figure 6. Poly(vinyl acetate) in butanone at 45°. Data from ref 2. Filled circles not used in fitting.

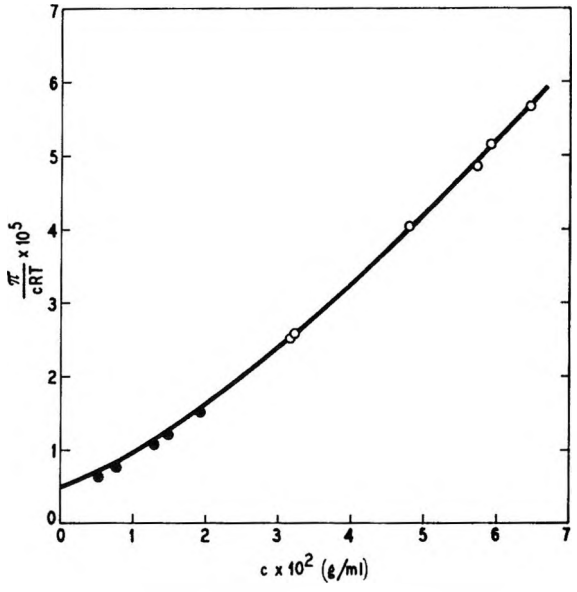


Figure 5. Poly(vinyl acetate) in butanone at 10°. Data from ref 2. Filled circles not used in fitting.

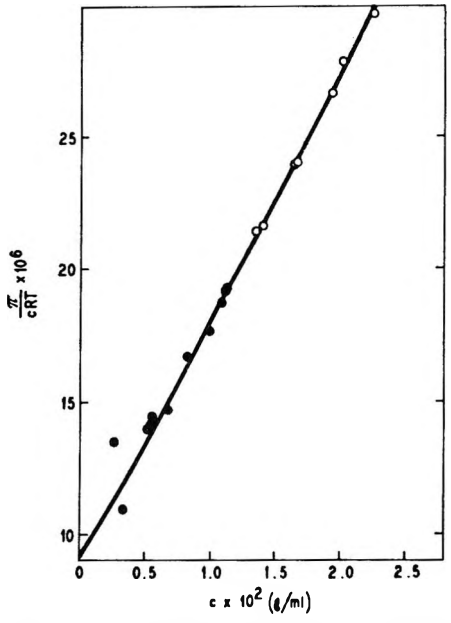


Figure 7. Hydrogenated polybutadiene in 1-chloronaphthalene at 130° (132 ethyls/1000 C). Filled circles not used in fitting.

havior for these systems visually appears to be the same (nearly linear) as that for Figures 3–6, the information extracted from the high concentrations allows a remarkably faithful extrapolation through the unused low concentration data.

Finally we show in Figures 9–11 data for six additional systems, taken from the literature, showing a greater variety of curve shapes. These are in pairs with the same polymer run in two different solvents. All data were used in curve fitting in these three figures and in addition the parameters were constrained to one molecular weight for each of the pairs. Figure 9 shows the successful fitting over the wide concentration range of Browning and Ferry's measurements[2] of a poly(vinyl acetate) in butanone and 1,2,3-trichloropropane. In Figure 10 we see Flory's data[3] on a polyisobutylene in both cyclohexane and benzene at 25°. Measurements at or near $\theta$ conditions, such as those in benzene, provide an excellent measure of $M_n$ since the variable of importance, $\Gamma c$, is small for all values of $c$ so that extrapolation to $\Gamma c = 0$ is very short. For the same reason, however, these data provide a very inadequate measure of $g$—there is not a sufficient range

(3) P. J. Flory, *J. Amer. Chem. Soc.*, 65, 372 (1943).

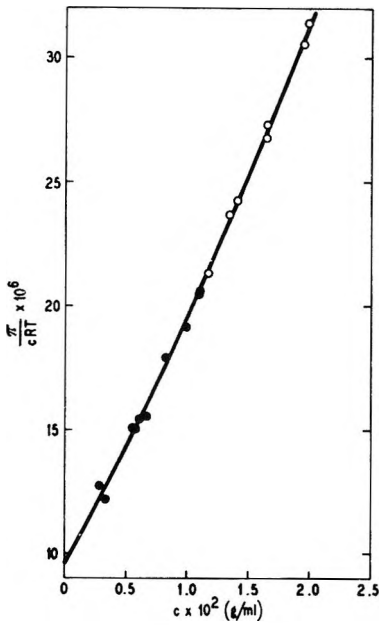


Figure 8. Hydrogenated polybutadiene in 1-chloronaphthalene at 130° (70 ethyls/1000 C). Filled circles not used in fitting.

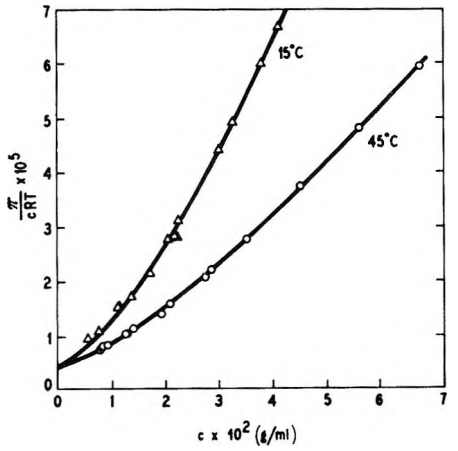


Figure 9. Poly(vinyl acetate) in butanone (O) and 1,2,3-trichloropropane (Δ). Data from ref 2.

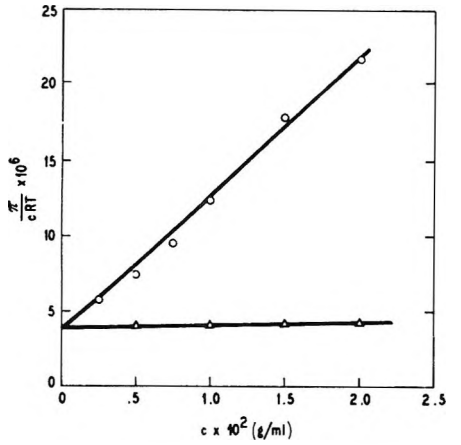


Figure 10. Polyisobutylene in cyclohexane (O) and benzene (Δ) at 25°. Data from ref 3.

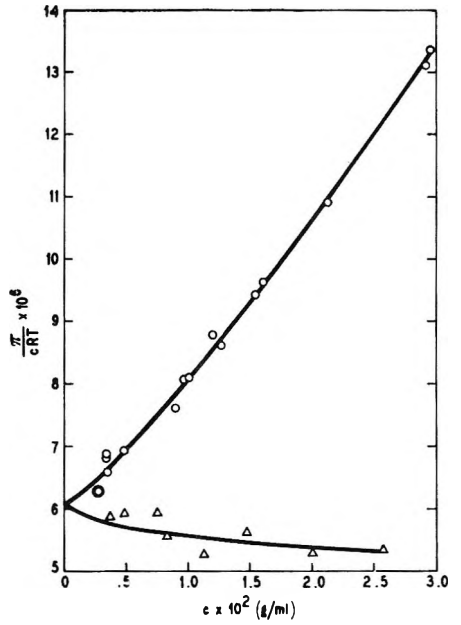


Figure 11. Poly(methyl methacrylate) in acetone (O) and acetonitrile (Δ) at 30.5°. Data from Fox, *et al.*, ref 4.

in values of $\Gamma c$. The last of these pairs are data reported by Fox, Kinsinger, Mason, and Schuele[4] for a poly(methyl methacrylate) in acetone and acetonitrile at 30.5°. The data and fitted curves are shown in Figure 11. The acetonitrile is such a poor solvent at the temperature of measurement that the second virial coefficient is negative for this system. The poor solvent may also be responsible (for practical reasons) for the increased scatter of data here.

Our function, relation (5), has the property that as $g'\Gamma c$ becomes large with respect to unity, the function approaches an asymptotic limit of $\exp(1/g')$. Numerically this limit may range from 7.4 to $\infty$ as $g$ varies from 0 to $1/2$. None of the data we have examined shows an inclination to reach a limit in $\pi/c$ within the range of $c$ available; however several sets of data appear to have an inflection in the $\pi/c$ *vs.* $c$ plot. According to (5) this inflection should occur at a concentration given by $4g/(1 - 2g)^2\Gamma$. At $g = 1/4$, for example, this inflection occurs at $\Gamma c = 4$ but might not be noticed from experimental measurements for the curve is nearly linear there. The function, relation (5), is plotted in Figure 12 against $\Gamma c$ for several values of $g$. It is at once apparent from the figure that (for sufficiently large values of $\Gamma c$) the function (5) is very sensitive to small changes in $g$. This means that with a suitable concentration range, the $g$ of this function will be well determined by the data. The function does not discriminate between $g$ values for $\Gamma c$ below about 0.5.

(4) T. G. Fox, J. B. Kinsinger, H. F. Mason, and E. M. Schuele, *Polymer*, 3, 71 (1962).

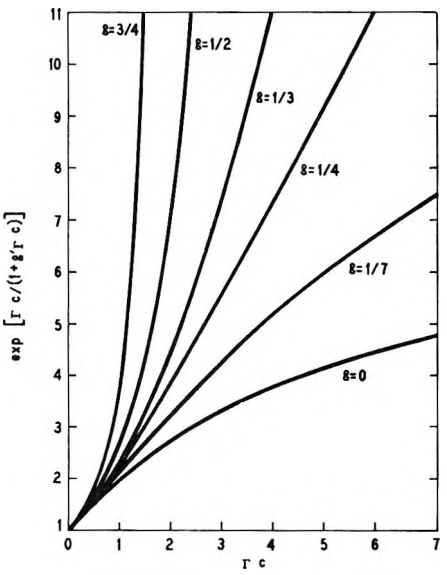


Figure 12. Behavior of concentration function, eq 5.

As a final comment on the nature of our function we point out a minor limitation. If (7) is to be considered logically valid for all values of $\Gamma c$ then $g$ must have an upper limit of $^1/_2$ otherwise the function has a discontinuity at $1 + g'\Gamma c = 0$. This upper limit of $g$ is less than the statistical-mechanical calculated value of $^5/_8$ (rigid sphere model) suggested by Stockmayer and Casassa[5] as a suitable upper limit.

This, if it indeed be a limitation, has not proved to be of any practical interest in our use of relation (7). In all cases we have examined for which there is an adequate measure of $g$ provided by the data, the value determined has been less than $^1/_2$. A curve for which $g = {}^3/_4$ has been included in Figure 12.

## IV. Recommended Data Handling

The present practice of treating osmotic measurements in order to extract information about the solute is to convert the original measurements to osmotic pressure by some relation such as (4). The derived values of osmotic pressure are then related, graphically or by some formula such as (2), to solute concentration. For apparatus like ours, this is logically objectionable for although each measurement of $h(c)$ with solute present is used just once, thus giving each its fair statistical weight, the value of $h(0)$ is used $n$ times for $n$ concentrations—unfairly assigning it a weight $n$ times that due. In the absence of a reliable extrapolation to zero concentration this is perhaps the soundest procedure in spite of the improper weighing.

However, in view of our experience with relation (7), we now feel that this formula will sufficiently properly extrapolate to zero concentration and that a more logical treatment of the measurements may be applied. The procedure we recommend is as follows: (a) Formulate the relation between primary observables and osmotic pressure for the instrument used such as relation (4) for our instrument. (b) Eliminate $\pi$ between this relation and eq 7. (c) In the resulting relation replace $h(0)$ by a parameter $h_0$. (d) Adjust the four parameters $h_0$, $M_n$, $\Gamma$, $g$ to give the best fit of $h(c)$ *vs.*/$c$ for all values of $c$ including $c = 0$.

When (b) and (c) are applied to (4) and (7) there results

$$h(c) = h_0 - (\rho'_{t_m} - \rho_{t_m})s/\rho_t + (cRT/M_nG\rho_t)\exp[\Gamma c/(1 + g'\Gamma c)] \quad (8)$$

The estimate of the parameter $h_0$, as a statistic determined by the data, has that weight incorrectly forced on $h(0)$ when (4) is used to calculate the variable, $\pi(c)$. The degrees of freedom remain the same for both (7) and (8), although (8) has one more parameter, it also has one more independent observation, $h(0)$. For display purposes the observed osmotic pressure, $\pi$, may be calculated from (4) with the single observation $h(0)$ replaced by the fitted parameter $h_0$; *i.e.*, from

$$G[\rho_t(h(c) - h_0) + (\rho'_{t_m} - \rho_{t_m})s] = \pi(c)$$

We explore now the benefits to be expected from using relation (8) over (7). These benefits arise from the extreme sensitivity of the estimates of the parameters of physical interest, $M_n$, $\Gamma$, and $g$, to $h(0)$; we have

$$1/M_n = (G\rho_t/RT)\lim_{c\to 0}(h(c) - h(0))/c = (G\rho_t/RT)(\mathrm{d}h/\mathrm{d}c)_{c=0}$$

$$\Gamma/M_n = (1/2!)(G\rho_t/RT)(\mathrm{d}^2h/\mathrm{d}c^2)_{c=0}$$

$$g\Gamma^2/M_n = (1/3!)(G\rho_t/RT)(\mathrm{d}^3h/\mathrm{d}c^3)_{c=0}$$

as general expressions displaying this emphasis on the value of the $c = 0$ measurement whether it be the statistic, $h_0$, or the observed $h(0)$. Therefore whatever arguments are marshalled in favor of the use of $h_0$ over $h(0)$ will have a direct bearing on $M_n$, $\Gamma$, and $g$. We shall speak more quantitatively of these parameters later.

As has been mentioned, all the observed quantities, $h(c)$, are subject to the same observational error. For example, the duplicate measurements of the data in Figure 1 provide an estimate for the standard deviation of $h$ as 0.034 cm. Deviations about the fitted line—some negative, others positive—have zero expectation for an adequate concentration function such as (5). The deviation of $h(0)$, however, is unique from the way $h(0)$ enters the working formula (4). Since $h(0)$ is used with every other observation, $h(c)$, the deviation of $h(0)$ will remain fixed and result in a constant bias for the set of measurements. This bias will carry over to the parameters $M_n$, $\Gamma$, and $g$. However in a single experiment to determine these parameters, there is no

(5) W. H. Stockmayer and E. F. Casassa, *J. Chem. Phys.*, **20**, 1560 (1952).

**Table II:** Parameters for Acetone

| | Nelson and Pierce[a] ($\mu$w,[c] 1965) | Swalen and Costain[b] ($\mu$w,[c] 1959) | This work (ED,[d] 1969) |
|---|---|---|---|
| H—C, Å | 1.085 ± 0.007 | 1.086 ± 0.010 | 1.076 ± 0.006 |
| C—C, Å | 1.507 ± 0.003 | 1.515 ± 0.005 | 1.507 ± 0.002 |
| C=O, Å | 1.222 ± 0.003 | 1.215 ± 0.005 (assumed) | 1.210 ± 0.003 |
| HCC, deg | 110.1 | 110.3 | 111.7 ± 1.5 |
| CCC, deg | 117.2 ± 0.3 | 116.1 | 116.7 ± 0.3 |
| $I_A$, amu Å$^2$ | 49.7296 | 49.7315 | 49.12 |
| $I_B$, amu Å$^2$ | 59.3698 | 59.3676 | 59.26 |
| $I_C$, amu Å$^2$ | 102.9559 | 102.9563 | 102.35 |
| Remarks | Axis of $CH_3$ group up 1.5° from C—C axis | Axis of $CH_3$ group up 1.5° from C—C axis | Torsion 33 ± 6° |

[a] R. Nelson and L. Pierce, *J. Mol. Spectrosc.*, **18**, 344 (1965). [b] J. D. Swalen and C. C. Costain, *J. Chem. Phys.*, **31**, 1562 (1959). [c] Microwave. [d] Electron diffraction.

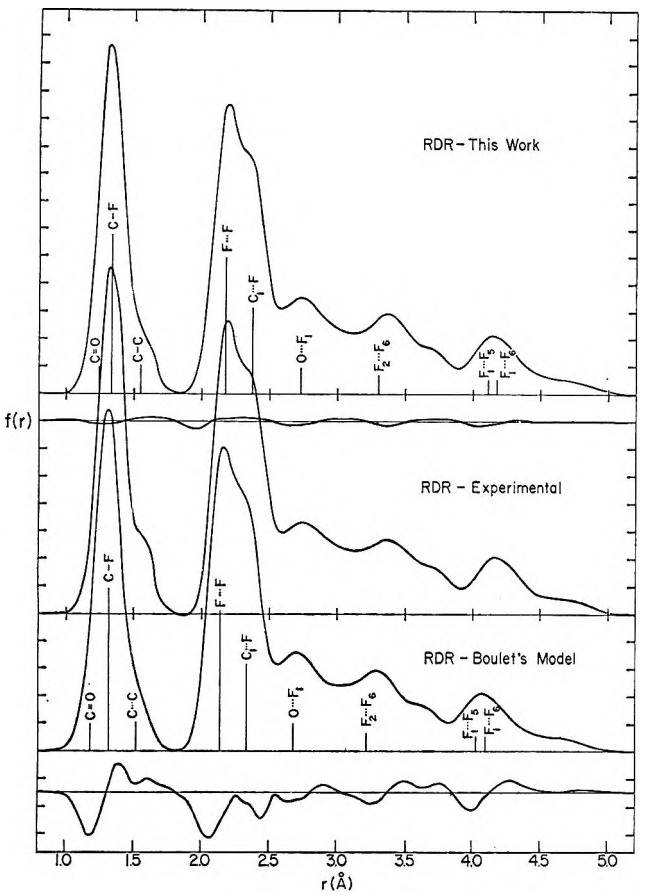


Figure 3. Comparison of the experimental radial distribution curve for $(CF_3)_2CO$ with those calculated for Boulet's model and for the structure deduced in this investigation.

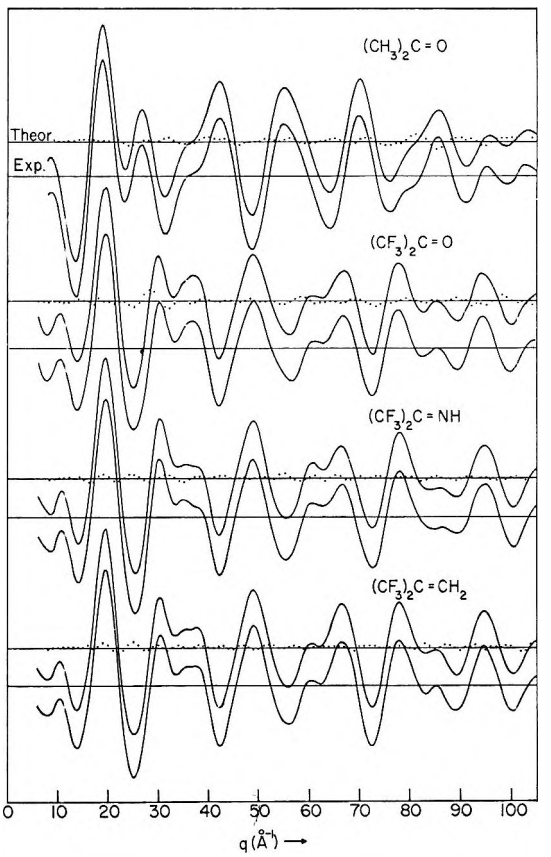


Figure 4. Comparisons of the experimental and calculated intensity curves. For each pair, the dotted curves show the differences between them.

largest discrepancies appear in the C=O and C—H distances. Perhaps if the C—H distance were corrected for anharmonicity this difference would be reduced. The moments of inertia listed in the last column of Table II were calculated for the electron diffraction model, assuming a rigid structure, while the entries in the other two columns were obtained from the observed rotational constants. The agreement is fairly good considering the unavoidable approximations. Supporting evidence for the observed parameters in these molecules is the fact that although the C=X and C—C distances appear to be appreciably longer than anticipated, the C—F bond lengths are in excellent agreement with all other previously reported investigations. The structure of perfluoroace-

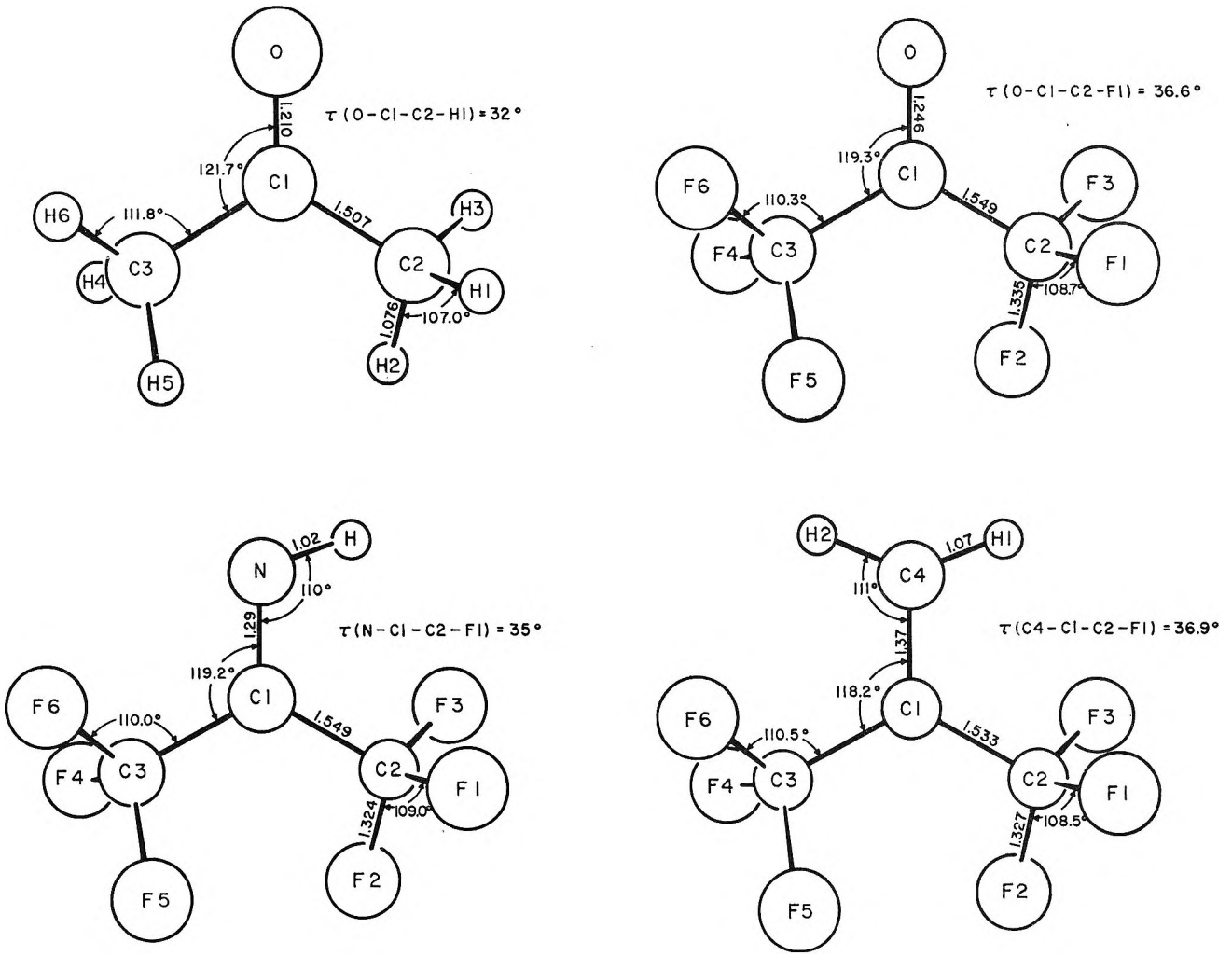


Figure 5. Minimum energy conformations and least-squares calculated parameters.

tone has previously been studied[20] by electron diffraction. The quoted bond lengths (C—F 1.321 Å, C=O 1.185 Å, and C—C 1.527 Å) are considerably shorter than those determined in this work, while the angular parameters agree quite well with those deduced in the present analysis. In Figure 3 the radial distribution curves calculated for our model and for Boulet's model are compared with the experimental radial distribution curve based on our data. While most of the observed features are reproduced by Boulet's model, there are noticeable discrepancies possibly arising from an error in the scale factor.

During the course of the analysis it was not possible to vary all of the mean-square amplitudes of vibration. The bonded $l_{ij}$'s were varied with the exception of C=O and C=C in perfluoroacetone and hexafluoroisobutene, respectively. Attempts to vary these parameters produced large correlations among the other parameters, particularly those distances under the bonded peak of the radial distribution curve. The $l_{ij}$'s used in these cases were estimated from corresponding unsubstituted species. The two nonbonded $l_{ij}$'s which could be varied were those for $C_1 \cdots F$ and $F \cdots F$ on the same carbon, both with rather low uncertainties. The remaining $l_{ij}$'s were either assumed or obtained by visual matching with the experimental radial distribution curve.

The final theoretical and experimental intensity curves for the best fitted least-squares models are shown in Figure 4. The errors quoted for the parameters listed in Table I are three times the standard deviations obtained in the least-squares calculations. As previously shown[21] this always places the quoted errors outside of the experimental errors estimated as due to calibrations and reading of the plates. The distances quoted are the $r_g(1)$ parameters defined by Bartell.[22] No attempt has been made to correct these values for anharmonicities or shrinkage. Also no attempt was made to take into account correlations

(20) G. A. Boulet, Thesis, University of Michigan, *Dissertation Abstr.*, **25**, 3283 (1964).

(21) R. L. Hilderbrandt and S. H. Bauer, *J. Mol. Struct.*, **3**, 325 (1969).

(22) L. S. Bartell, *J. Chem. Phys.*, **23**, 1269 (1955).

**Table III:** Dimensional Changes Due to F–H Substitution

| | X | C—X bond length, Å | Change in bond length, Å | Reported by |
|---|---|---|---|---|
| $H_3C—CH_3$ | | 1.5319 | Ref | Kuchitsu,[3] ED |
| $F_3C—CH_3$ | $-CH_3$ | 1.512 | −0.02 | Schwendeman,[4] ED |
| $F_3C—CF_3$ | $-CF_3$ | 1.56 | +0.02 | Swick and Karle,[5] ED |
| $H_2C=CH_2$ | | 1.334 | Ref | Bartell and Bonham,[a] ED |
| $F_2C=CH_2$ | $=CH_2$ | 1.315 | −0.019 | Laurie and Pence,[9] μw |
| $F_2C=CF_2$ | $=CF_2$ | 1.313 | −0.021 | Karle and Karle,[10] ED |
| HC≡CH | | 1.205 | Ref | Christensen, Eaton, Green, and Thompson,[b] ir |
| FC≡CH | ≡CH | 1.198 | −0.007 | Tyler and Sheridan,[8] μw |
| $H_3C—NH_2$ | | 1.465 | Ref | Higgenbotham and Bartell,[c] ED |
| $H_3C—NF_2$ | $-NF_2$ | 1.449 | −0.016 | Pierce, Hayes, and Bucher,[d] μw |
| $H_2CO$ | | 1.230 | Ref | Davidson, Stoicheff, and Berstein,[e] μw |
| FHCO | =O | 1.181 | −0.049 | Miller and Curl,[f] μw |
| $F_2CO$ | =O | 1.174 | −0.056 | Laurie and Pence,[9] μw |

[a] L. S. Bartell and R. H. Bonham, *J. Chem. Phys.*, **27**, 1414 (1957). [b] M. T. Christensen, *et al.*, *Proc. Roy. Soc.*, **A238**, 15 (1956). [c] H. K. Higgenbotham and L. S. Bartell, *J. Chem. Phys.*, **42**, 1131 (1965). [d] L. Pierce, R. G. Hayes, and J. F. Bucher, *ibid.*, **46**, 4352 (1967). [e] D. W. Davidson, B. P. Stoicheff, and H. J. Bernstein, *ibid.*, **22**, 289 (1959). [f] R. F. Miller and R. F. Curl, Jr., *ibid.*, **34**, 1847 (1961).

of adjacent data points; however, the $p/h$ parameter suggested by Morino, Kuchitsu, and Murata[23] was calculated and found to be approximately 0.30, indicating a relative off-diagonal weight of −0.30 would be appropriate. It is felt that multiplication of the standard deviations by a factor of 3 more than compensates for the neglect of the nondiagonal elements.

## Discussion

The results of this investigation (Figure 5) are consistent with the results reported by Schwendeman.[4] Three fluorine atoms substituted for hydrogens in a methyl group attached to a carbon which is in turn doubly bonded to a third species increase the length of the C—C bond by 0.03–0.04 Å. Further inspection of fluorine-substituted compounds for which structures have been determined revealed that, in general, two types of bonding exhibit two distinct trends.

Case 1 is schematically represented by $F_3C$–X, $F_2C$=X, or FC≡X, where X is N, C, O, or a halogen but is not double bonded to a third atom. In this case fluorine for hydrogen substitution decreases the CX bond length, with one notable exception: perfluoroethane.[5] Evidently, the nonbonded fluorine–fluorine repulsions in this molecule dominate and the C—C bond is lengthened to 1.56 Å.

Case 2 can be represented by $F_3C—X=Y$, where X is C or N, and Y is C, N, or O. In this case the observations indicate a lengthening of the CX bond. Table III and Table IV illustrate these two cases. The longer than anticipated C=X (X = N, C, O) separations found in the present investigation appear to be distinctive of this type of molecule. In 1,1,1-trifluoroacetaldehyde[3] the C=O distance is almost the same as in the parent compound, while in hexafluoroazomethane[24] the N=N distance is only 0.017 Å less than in the hydrogen analog. The longer C=X separations observed in these compounds might indeed be due to the presence of $CF_3$ groups but additional work is needed to substantiate this. In particular, the structures of $(CF_3)(CH_3)CO$ and $(CF_3)(CH_3)CCH_2$ may reveal C=X bond lengths intermediate between the unsubstituted and hexasubstituted species.

Although the INDO calculations by Gordon and Pople[6] are not sufficiently precise to check directly against the observed interatomic distances, one may have anticipated that their predicted *differences* due to H–F substitution on adjacent bond lengths would be of the correct sign and (hopefully) magnitude. In eight cases, three check fully, two show the indicated trend but the magnitudes are wrong, and for the remaining three cases, the directions of the increments are in error. Deviations are defined as $(F_{cpd} - H_{cpd})$. For the C—C bond length in $C_2H_6$ *vs.* $C_2F_6$, $\delta$(C—C) = +0.03 Å; for N—N in $N_2H_4$ *vs.* $N_2F_4$, $\delta$(N—N) = +0.03 Å; for C≡N in HCN *vs.* FCN, $\delta$(C≡N) = 0 (calculated values = observed values). For C—F, in the sequence $CH_nF_{4-n}$, they predicted $(C—F)_{n=0} - (C—F)_{n=3} = -0.01$ Å, while the observed magnitude is −0.06 Å; also $\delta(N—F)_{calcd} = 0$ for the pair $NHF_2$ *vs.* $NF_3$ while $\delta(N—F)_{obsd} = -0.03$ Å. Finally, for the pair $C_2H_4$ *vs.* $C_2F_4$ $\{(C=C)_F - (C=C)_H\}_{calcd} = +0.02$ Å, while $\delta_{obsd} = -0.02$ Å; for C=O in $H_2CO$ *vs.* $F_2CO$, $\delta_{calcd} = 0$ while $\delta_{obsd} = -0.06$ Å; for O—O in $H_2O_2$ *vs.* $F_2O_2$, $\delta_{calcd} = +0.01$ Å while $\delta_{obsd} = -0.27$ Å. Clearly some

(23) Y. Murata and Y. Morino, *Acta Cryst.*, **20**, 605 (1966).

(24) C. H. Chang, R. F. Porter, and S. H. Bauer, private communication.

**Table IV:** Dimensional Changes Due to F–H Substitution

| | Y | C—C or C—N bond lengths, Å | Change in bond lengths, Å | Reported by |
|---|---|---|---|---|
| $H_3CHC{=}O$ | $=O$ | 1.504 | Ref | Schwendeman,[4] ED |
| $F_3CHC{=}O$ | $=O$ | 1.540 | +0.036 | Ref 4 |
| $(H_3C)_2C{=}O$ | $=O$ | 1.507 | Ref | Nelson and Pierce,[1] $\mu$w |
| $(F_3C)_2C{=}O$ | $=O$ | 1.540 | +0.042 | This work, ED |
| $\{(H_3C)_2C{=}NH\}$ | $=NH$ | {1.51} | Ref | Estimated |
| $(F_3C)_2C{=}NH$ | $=NH$ | 1.549 | {+0.04} | This work, ED |
| $H_3CN{=}NCH_3$ (*trans*) | $=NCH_3$ | 1.474 | Ref | Chang, Porter, and Bauer,[24] ED |
| $F_3CN{=}NCH_3$ (*trans*) | $=NCH_3$ | 1.476 | +0.002 | Ref 24 |
| $F_3CN{=}NCF_3$ (*cis*) | $=NCF_3$ | 1.490 | +0.016 | Ref 24 |
| $H_3CC{\equiv}CH$ | $\equiv CH$ | 1.459 | Ref | Costain,[a] $\mu$w |
| $F_3CC{\equiv}CH$ | $\equiv CH$ | 1.464 | +0.005 | Shoolery, Shulman, Sheehan, Schomaker, and Yost,[b] ED and $\mu$w |
| $H_3CC{\equiv}CCH_3$ | $\equiv CCH_3$ | 1.467 | Ref | Chang and Bauer,[d] ED |
| $F_3CC{\equiv}CCH_3$ | $\equiv CCH_3$ | 1.464 | −0.003 | V. W. Laurie,[c] $\mu$w |
| $F_3CC{\equiv}CCF_3$ | $\equiv CCF_3$ | 1.475 | +0.008 | Chang and Bauer,[d] ED |
| $(H_3C)_2{=}CH_2$ | $=CH_2$ | 1.505 | Ref | Bartell and Bonham,[e] ED |
| $(F_3C)_2{=}CH_2$ | $=CH_2$ | 1.533 | +0.028 | This work, ED |

[a] C. C. Costain, *J. Chem. Phys.*, **29**, 864 (1958). [b] J. N. Shoolery, R. G. Shulman, W. F. Sheehan, V. Schomaker, and D. M. Yost, *ibid.*, **19**, 1364 (1951). [c] V. W. Laurie, *J. Chem. Phys.*, **30**, 1101 (1959). [d] Unpublished data. [e] L. S. Bartell and R. A. Bonham, *J. Chem. Phys.*, **32**, 824 (1960).

significant interactions were neglected in these calculations. It is interesting to note that their predictions of bond angles proved more successful than of bond lengths. The conformations of the $CF_3$ groups around the C—C bonds deduced in this investigation indicate that the minima in potential energy are not at the most symmetric positions. We believe this to be a real effect, and not merely an artifact of large amplitudes of torsional vibrations. Indeed, the helical twist in the C—C backbone of perfluoropolyethylene chains[25,26] is of a magnitude which checks closely with that expected for $\tau \approx 35°$.

*Acknowledgments.* The authors wish to thank the Material Science Center of Cornell University (MSC ARPA SD-68) for their financial support, and we also thank Drs. Krespan and Middleton for supplying us with a sample of hexafluoroisobutene.

(25) C. W. Bunn and E. R. Howells, *Nature*, **174**, 549 (1954).
(26) E. S. Clark and L. T. Muus, *Z. Kryst.*, **117**, 119 (1962).

# The Concentration Dependence of Osmotic Pressure

by Raymond L. Arnett and Robert Q. Gregg

*Phillips Petroleum Company, Bartlesville, Oklahoma 74003* *(Received April 7, 1969)*

The concentration function, $f(c) = \exp[\Gamma c/(1 + g'\Gamma c)]$, is shown to be eminently satisfactory for representing osmotic pressure data, $\pi = (cRT/M_n)f(c)$, from very dilute solutions to moderate concentrations. The data for testing the relation are drawn from macromolecular solutes. ($\Gamma$ is the second viral coefficient, $\Gamma_2$; $g'$ is written for $1/2 - g$ where $g$ is the ratio $\Gamma_3/\Gamma_2^2$; $c$ is concentration—mass/volume—of the solute whose number-average molecular weight is $M_n$; $R$ the gas constant; and $T$ the absolute temperature.) It is also shown that for data collected from a single osmometer, unbiased estimates of $M_n$, $\Gamma$, $g$ are obtained from the data only if the primary observed quantities, $h(c)$ (*e.g.*, manometric fluid height) from which $\pi$ is determined are used in the fitting and $h(0)$ is replaced by a parameter, $h_0$, also determined by the data.

## I. Introduction

Osmotic pressure is an important measurable quantity of solutions inasmuch as it yields useful thermodynamic information about the solute and its interaction with the solvent. When the solute is macromolecular, experience has shown the deviations from ideality to be so great that the osmotic coefficients of even dilute solutions differ widely from unity. For these solutions common practice is to use the virial form

$$\pi = (cRT/M_n)(1 + \Gamma_2 c + \Gamma_3 c^2 + \ldots)$$

or

$$\pi = (cRT/M_n)(1 + \Gamma_2 c + g\Gamma_2^2 c^2 + \ldots) \quad (1)$$

of the osmotic pressure, $\pi$, for its dependence on the concentration, $c$, of the solute whose number-average molecular weight is $M_n$. (Here $R$ is the molar gas constant, $T$ the absolute temperature of measurement, $\Gamma_j$ the $j$th virial coefficient, and $g \equiv \Gamma_3/\Gamma_2^2$.) However, the nature of things is such that the greater is $M_n$, the greater are the successive coefficients, $\Gamma_j$, but the smaller is the quantity measured. Thus to put himself into a measurable region, the experimenter is obliged to work with more concentrated solutions making necessary yet more terms of the virial expansion. (Alternatively, he may conduct a search for suitable conditions for which $\Gamma_{j+1}c^j$ are negligibly small; the search must be made for each polymer structure studied.)

Now it is a matter of common experience that unless there are many more data than parameters to be determined by them, the coefficients in a polynomial are not well determined by experimental data; they are very subject to the fluctuations of the data. Even when the resulting fitted curve may be satisfactory for interpolation, it is rarely satisfactory for extrapolation—a process always applied to polymer osmotic data.

In an attempt to circumvent some of these difficulties, it has become common practice to set $\Gamma_3 = \Gamma_2^2/4$ (*i.e.*, set $g = 1/4$) and to terminate the series with this term. The virial expansion actually used then becomes $(1 + \Gamma_2 c/2)^2$ so that

$$\pi = (cRT/M_n)(1 + \Gamma_2 c/2)^2 \quad (2)$$

The variable, $(\pi/c)^{1/2}$, is then fitted linearly to $c$.

We have had occasion to note the inadequacy of this treatment for some concentrations we were using and were led to explore the possibility of finding an explicit function, $f(c)$, containing no more than two adjustable parameters, such that

$$\pi = (cRT/M_n)f(c) \quad (3)$$

would satisfactorily fit the observations into the higher concentration region one must work with for high polymers. We report here the result of this search as well as other procedural aspects of the data handling we recommend in order to obtain better accuracy on the parameters.

## II. Experimental Section

The osmometer we used is a commercial one supplied by Mechrolab, Inc. (now supplied by Hewlett-Packard Co.). An analysis of the operation of this null instrument yields

$$G\{\rho_t[h(c) - h(0)] + (\rho'_T - \rho_T)s\} = \pi(c)$$
$$c = \omega\rho_{tm} \quad (4)$$

as the relations from which osmotic pressure and concentration are calculated from primary measured quantities. In (4), $G$ is the acceleration due to gravity, $\rho'_T$ is the solution density at the temperature of measurement, $T$, $h(c)$ is the height above a reference datum of the manometric fluid (the solvent) whose density is $\rho_t$ at the temperature, $t$, of the manometer and $\rho_T$ at $T$. The term involving $s$ is a correction occasioned by a vertical column (height $s$) of solution above the membrane; $\omega$ is the weight fraction of solute.

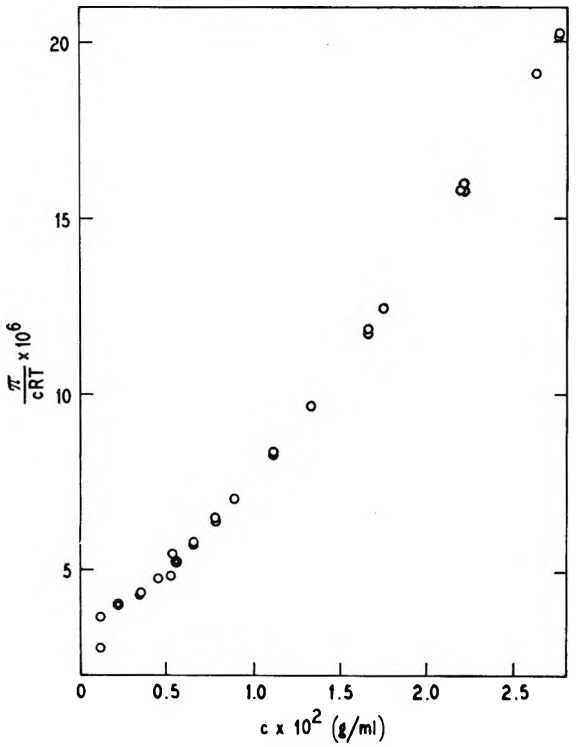


Figure 1. Data for a polystyrene in 1-chloronaphthalene at 130°.

We have determined, by means of (4), the osmotic pressure of a number of polymer solutions over a medium range of concentrations using gel cellophane membrane 450-D. As an example of these data we show in Figure 1, as a conventional plot, the results for a polystyrene in 1-chloronaphthalene solution at 130°. The supplier of the polymer reported its number-average molecular weight, determined osmotically, as $4.11 \times 10^5$. An examination of Figure 1 nicely reveals two facets of the data. The first concerns the stochastic nature of the measured estimates of the variable, $\pi/cRT$, and shows that the fluctuations of these estimates are greater at the low concentrations. Indeed if the error of observation of $h$ is a constant independent of the value of $h$, as it seems to be, and the error of $c$ is negligible compared to that of $h$, then the propagation of error formula predicts that the standard deviation of $\pi/cRT$ is inversely proportional to $c$. The second facet concerns the nature of $f(c)$ of relation (3)—the most curvature occurs at the low concentrations and diminishes as concentration increases. In this figure, at concentrations higher than 0.015 g/ml the data are almost linear.

Each of these behaviors of the data contrive to make a graphical determination of the intercept difficult and hence uncertain. On one hand the extrapolation demands continuing the curve through a region where the curvature is increasing making the position of the line uncertain while on the other recourse to measurements made at still lower concentrations is of little

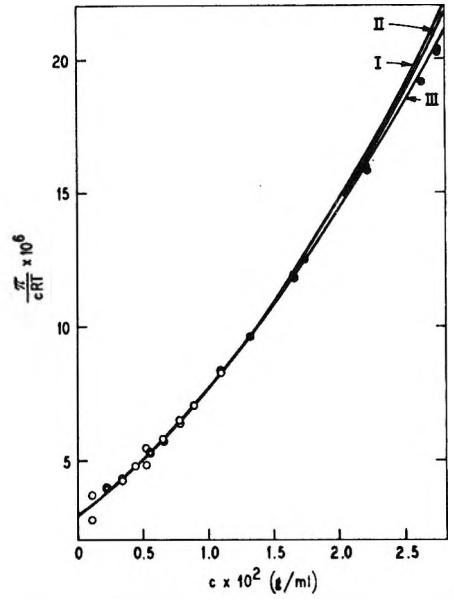


Figure 2. Data of Figure 1 for which $\pi M_n cRT < 3$ fitted by three relations: I, eq 1; II, eq 2; III, eq 7. Filled circles not used in fitting.

avail since the greater scatter in the data does not determine the true curve position well. Obviously, what thermodynamic information is to be learned, including solute molecular weight, must perforce come from that range of variables where the data exist. This means, for an analytic representation of the curve, that $M_n$ as well as the parameters in $f(c)$ are to be fixed by the data at $c > 0$ and that $f(c)$ be such that it not only faithfully follow the data through the range of $c$ for which data exist but also, if the parameters are to represent truth, must be constrained by its nature to extrapolate along a curve on which measurements would lie if they existed.

We have found a two-parameter function which comes very close to these ideal properties.

## III. Behavior of Concentration Function

We find that the function

$$f(c) = \exp[\Gamma c/(1 + g'\Gamma c)],\ g' = {}^1/_2 - g \qquad (5)$$

fits remarkably well all the data we have examined.

Expansion of (5) in a Maclaurin series yields

$$f(c) = 1 + \Gamma c + g\Gamma^2 c^2 + (g^2 - {}^1/_{12})\Gamma^3 c^3 + \ldots,\ (g'\Gamma c)^2 < 1 \qquad (6)$$

so that (5) may be put in the standard virial form for $(g'\Gamma c)^2 < 1$. In (6) the higher virial coefficients are written in terms of powers of $\Gamma$; *i.e.*

$$\Gamma_3 = g\Gamma^2,\ \Gamma_4 = (g^2 - {}^1/_{12})\Gamma^3, \ldots$$

In Figures 2 and 3 we compare the behavior of $\pi/cRT$ calculated from

$$\pi = (cRT/M_n) \exp[\Gamma c/(1 + g'\Gamma c)] \qquad (7)$$

measure of this bias provided by the data. Consider now using relation (8). Although the parameter $h_0$ is much influenced by the measurement $h(0)$, it is also influenced by all other measurements $h(c)$, $c \neq 0$. Therefore the resulting bias in $h_0$ (hence in $M_n$, $\Gamma$, $g$) may be expected to be smaller than that of a single measurement, $h(0)$. This expectation of a smaller bias in a single determination of $M_n$, $\Gamma$, and $g$ is the basis of the argument for introducing the parameter $h_0$.

The experimenter requires information as to the reliability of the determined parameters. The bias of a single determination becomes susceptible of measurement only on sufficient repetitions of the complete experiment to give reliable estimates for the standard deviations of the parameters. We have done this using 10 hypothetical experiments of 6 nonzero concentrations each. Values for each of the 4 parameters were selected and error-free values of $h(c)$ calculated for each concentration using relation (8). These error-free values were converted to 10 sets of "experimental" values by adding deviations chosen at random from a normal population of deviations having zero mean and a standard deviation of 0.034. Each of the 10 sets was then fitted both to relation (7) where $\pi$ was computed by (4) and to relation (8). The results of this are given in Table II.

**Table II:** Standard Deviations of Parameters from Relations (7) and (8)

True values $M_n = 338.7 \times 10^3$, $\Gamma = 121.2$, $g = 0.2783$

| | Std dev of | | |
|---|---|---|---|
| | $10^{-3}$ $M_n$ | $\Gamma$ | $g$ |
| Relation (7) | 40.3 | 16.9 | 0.0116 |
| Relation (8) | 32.3 | 13.8 | 0.0104 |

It is apparent from the table that each parameter is more reliably determined by a single experiment when relation (8) is used. In this connection it is important to note that the standard deviations listed are actually the root-mean-square deviations of the determined values from the true parameter values. This means that the data handling procedure we recommend gives improved accuracy not merely improved precision. The difference between squares of the standard deviations of (7)–(8) represents the variance introduced into each parameter, when (7) is used, by the bias in $h(0)$.

There is yet another facet in the comparison of the use of $h_0$ *vs.* $h(0)$ we wish to point out. This has to do with the measure of reliability of the parameter values provided by a least-squares fitting of the parameters in (8) *vs.* those in (7) to a set of measurements. The variance of each parameter determined by such a fitting using relation (8) is a measure of the true variance as given in Table II. For example the pooled estimate of the standard deviation of $M_n$ from the 10 fittings of relation (8) is $33.5 \times 10^3$ in agreement with the directly obtained value in Table II. Whereas this is true for (8), in using relation (7) there is an additional unmeasured variance arising from the bias in $h(0)$: witness the falsely flattering corresponding pooled estimate of $22.6 \times 10^3$ when in fact the actual value using (7) is nearly twice that figure. The pooled estimates referred to above are computed from sums of squares of deviations of observed points from the fitted line. Since, as we have just seen, these agree with the mean square deviations of observed minus true, it again follows that the fitted line of relation (8) is a good (unbiased) measure of the true behavior.

## V. Application to Cryoscopy and Ebullioscopy

From the equilibrium condition of solvent and solution separated by a membrane permeable only to the incompressible solvent we have

$$\mu_1(p,T,c) - \mu_1(p,t,0) = -v_1\pi \qquad (9)$$

expressing the chemical potential $\mu_1$ of the liquid solvent whose partial molal volume is $v_1$ in the solution where the solute concentration is $c$, to the chemical potential of the pure solvent at the same pressure and temperature, and to the osmotic pressure.

The equilibrium between the liquid solution of a solute that is insoluble in the crystalline solvent and the solvent crystal leads to

$$\mu_1(p,T,c) - \mu_1(p,T,0) = -\int_{T-\theta}^{T} S_F dt \qquad (10)$$

where $T$ is the melting point of the solvent crystal at pressure $p$ in the presence of pure liquid solvent, $T - \theta$ is the melting point in the presence of solution of concentration $c$, and $S_F$ is the partial molal entropy of fusion.

The corresponding expression for ebullioscopy where the pressure on the liquid is also the vapor pressure is

$$\mu_1(p,T,c) - \mu_1(p,T,0) = -\int_{T}^{T+\theta} S_v dt \qquad (11)$$

with $S_v$ the partial molal entropy of vaporization.

On eliminating the left member of each of (10) and (11) by means of (9) and in turn eliminating $\pi$ from these resulting expressions using (7) we have expressions for the concentration dependence of melting point lowering and boiling point elevation of solutions

$$\int_{T-\theta}^{T} S_F dt = (v_1 cRT/M_n) \exp[\Gamma_2 c/(1 + g'\Gamma_2 c)]$$
$$\int_{T}^{T+\theta} S_v dt = (v_1 cRT/M_n) \exp[\Gamma_2 c/(1 + g'\Gamma_2 c)] \qquad (12)$$

Evaluation of the integrals is made using appropriate

assumptions concerning the temperature dependence of the heats of transitions.

If, for example, the temperature interval, $\theta$, is so small that the transition entropies may be taken as constant within it—a likely situation for high polymers—then (12) and (13) become

$$\theta = (v_1 cRT^2/L_F M_n) \exp[\Gamma_2 c/(1 + g'\Gamma_2 c)] \quad (12a)$$

for the freezing point depression, $\theta$, and

$$\theta = (v_1 cRT^2/L_v M_n) \exp[\Gamma_2 c/(1 + g'\Gamma_2 c)] \quad (13a)$$

for the boiling point elevation, $\theta$. In these expressions, $L_F$ and $L_v$ are the latent heats per mole of fusion and vaporization, respectively, at the transition temperature, $T$.

*Acknowledgment.* The measurements reported on here from our laboratory were made by J. R. Donaldson.

# Hydrogen Bonding and Vapor Pressure Isotope Effect of Dimethylamine

**by H. Wolff and R. Würtz**

*Physikalisch-Chenisches Institut, Universität Heidelberg, 69 Heidelberg, Germany* *(Received August 6, 1969)*

The vapor pressure isotope effect of two isotopic compounds in solution is given by the ratio $p/p'$ of their partial pressures in the same solvent, where $p$ and $p'$ are the partial pressures of the heavy and of the light compound, respectively. The temperature and concentration dependence of this ratio has been determined for solutions in $n$-hexane of $(CH_3)_2NH$, $(CH_3)_2ND$, $(CD_3)_2NH$, and $(CD_3)_2ND$ between +20 and −50°. The ratio decreases with increasing temperature and is independent of concentration for pairs with equal amino groups but different methyl groups. These observations and the values indicate that the ratio is not influenced by association and depends primarily on the difference of the methyl group vibrations. However, for pairs with equal methyl groups but different amino groups the ratio increases with increasing temperature as well as with dilution, which shows that the ratio depends upon association and is determined by the intermolecular vibrations and the internal amino group vibrations. When methyl and amino groups both differ, the ratio is determined by the external and internal amino group vibrations as well as the internal methyl group vibrations. The values of the ratios and their temperature dependence differ from the results for methylamine, because in dimethylamine the number of methyl groups is increased and the association is decreased. Taking into account the association equilibrium, the ratio of partial pressures is given by a two-state function. From this function it has been calculated that the undiluted dimethylamine contains approximately 60–40% of free NH or ND groups in the temperature range of +20 to −20°. Similar results have been obtained from infrared measurements in the first harmonics.

## A. Introduction and Measurements

Methylamine is the only hydrogen-bonded molecule for which the temperature dependence as well as the recently detected concentration dependence[1-5] of the ratio $p/p'$ of vapor pressures ($p$ is the pressure of the heavy compound, $p'$ is the pressure of the light compound) have been investigated for the variously deuterated forms.[2] The results depended on whether the hydrogen-bonding group or another group of the molecule was deuterated. To extend these ideas and to study the effect of the second methyl group and of the weaker association, we measured the temperature and concentration dependence of $p/p'$ for the isotopic dimethylamines $(CH_3)_2NH$, $(CH_3)_2ND$, $(CD_3)_2NH$, and $(CD_3)_2ND$. The association constant $K_\nu^x = x_\nu/x_{\nu-1}x_1$ ($x_\nu$ is the mole fraction of the $\nu$-mer) has only half the value for dimethylamine in $n$-hexane than for methylamine in $n$-hexane.[6] As in the measurements of the methylamines we investigated solutions in $n$-hexane between +20 and −50°.

The ratios of the undiluted compounds were given directly by the measured pressures. The ratio of partial pressure at a mole fraction $x_1$ of dimethylamine were determined by eq 1 ($f_1$ and $f_1'$ are the activity coeffi-

$$\frac{p}{p'} = \frac{f_1 P}{f_1' P'} \quad (1)$$

(1) H. Wolff and A. Höpfner, *Ber. Bunsenges. Phys. Chem.*, **69**, 710 (1965).

(2) H. Wolff and A. Höpfner, *ibid.*, **71**, 461 (1967).

(3) H. Wolff and H.-E. Höppel, *ibid.*, **72**, 722 (1968).

(4) H. Wolff and A. Höpfner, *ibid.*, **73**, 480 (1969).

(5) H. Wolff and R. Würtz, *Z. Phys. Chem.* (Frankfurt am Main), **67**, 115 (1969).

(6) H. Wolff and H.-E. Höppel, *Ber. Bunsenges. Phys. Chem.*, **70**, 874 (1966).

**Table I:** Vapor Pressures of the System $(CH_3)_2NH$–*n*-Hexane in Torr[a]

| | Pressure | | | | | | | |
|---|---|---|---|---|---|---|---|---|
| $x_1$ | −50° | −40° | −30° | −20° | −10° | 0° | +10° | +20° |
| 0 | 2.2 | 3.8 | 7.7 | 14.3 | 26.7 | 45.5 | 75.6 | 121.3 |
| 0.0206 | 4.7 | 9.0 | 15.9 | 27.4 | 45.6 | 73.3 | 113.5 | 171.6 |
| 0.0706 | 10.4 | 19.1 | 33.4 | 55.2 | 87.5 | 133.5 | 198.2 | 285.9 |
| 0.1014 | 12.8 | 23.2 | 41.5 | 68.7 | 108.4 | 164.9 | 243.1 | 347.7 |
| 0.1508 | 15.3 | 29.1 | 51.8 | 86.1 | 136.1 | 206.5 | 303.5 | 428.8 |
| 0.2008 | 17.3 | 33.2 | 59.9 | 98.8 | 160.8 | 245.3 | 360.7 | 512.4 |
| 0.2707 | 19.6 | 37.6 | 68.6 | 116.5 | 187.7 | 289.1 | 428.3 | 612.0 |
| 0.2720 | 19.6 | 37.7 | 68.8 | 117.2 | 188.3 | 290.1 | 430.4 | 615.0 |
| 0.4031 | 21.9 | 43.2 | 79.6 | 137.7 | 224.9 | 350.4 | 522.7 | 750.0 |
| 0.6022 | 24.3 | 49.4 | 92.1 | 162.1 | 268.2 | 424.7 | 644.0 | 939.9 |
| 0.7157 | 25.7 | 52.4 | 98.8 | 174.2 | 289.4 | 461.5 | 704.0 | 1031.1 |
| 1.0 | 30.3 | 61.7 | 117.4 | 208.9 | 349.8 | 560.7 | 862.4 | 1276.9 |

[a] Our previous measurements[8] were repeated as they did not meet the high standard of precision which is essential for the determination of the ratio of partial vapor pressures when the mole fraction of amine approaches zero. However, only the pressures below $x_1 = 0.1014$ have to be taken from the above Table I. The previous values[6] can be used for pressures above $x_1 = 0.1014$. $x_1$ is the mole fraction of $(CH_3)_2NH$ in the liquid phase.

**Table II:** Vapor Pressures of the System $(CH_3)_2ND$–*n*-Hexane in Torr[a]

| | Pressure | | | | | | | |
|---|---|---|---|---|---|---|---|---|
| $x_1$ | −50° | −40° | −30° | −20° | −10° | 0° | +10° | +20° |
| 0 | 2.2 | 3.8 | 7.7 | 14.3 | 26.7 | 45.5 | 75.6 | 121.1 |
| 0.0048 | 2.5 | 5.0 | 9.4 | 17.3 | 30.8 | 52.4 | 85.2 | 133.4 |
| 0.0075 | 3.0 | 5.7 | 10.8 | 19.7 | 33.8 | 56.6 | 91.0 | 141.3 |
| 0.0207 | 4.9 | 9.0 | 15.3 | 27.9 | 45.3 | 74.1 | 114.8 | 173.2 |
| 0.0254 | 5.6 | 10.0 | 18.0 | 30.5 | 50.4 | 79.9 | 122.7 | 183.6 |
| 0.0484 | 8.2 | 15.2 | 26.6 | 44.3 | 70.6 | 108.9 | 163.2 | 238.6 |
| 0.0705 | 10.2 | 18.9 | 33.3 | 55.0 | 87.4 | 133.6 | 198.3 | 286.4 |
| 0.0922 | 11.8 | 22.5 | 39.1 | 64.7 | 102.3 | 156.3 | 231.1 | 331.8 |
| 0.1541 | 15.2 | 28.9 | 51.7 | 86.6 | 137.5 | 209.8 | 307.9 | 437.8 |
| 0.2535 | 18.3 | 35.7 | 64.9 | 111.3 | 178.2 | 276.6 | 409.5 | 584.6 |
| 0.3053 | 19.1 | 37.7 | 69.6 | 119.8 | 194.5 | 301.9 | 448.8 | 642.3 |
| 0.3526 | 20.1 | 40.1 | 73.9 | 128.3 | 209.5 | 327.1 | 484.9 | 706.3 |
| 0.4109 | 20.9 | 41.8 | 78.2 | 135.5 | 223.0 | 350.7 | 527.6 | 765.1 |
| 0.4494 | 21.5 | 43.2 | 80.2 | 140.4 | 231.1 | 364.3 | 549.6 | 798.5 |
| 0.5077 | 22.2 | 44.6 | 83.6 | 147.1 | 243.4 | 384.6 | 582.0 | 846.3 |
| 0.6055 | 23.1 | 47.3 | 88.8 | 157.3 | 262.1 | 417.3 | 635.5 | 932.2 |
| 0.6554 | 23.8 | 48.4 | 91.6 | 162.0 | 268.6 | 432.1 | 659.8 | 970.1 |
| 0.7038 | 24.6 | 49.7 | 94.0 | 167.3 | 279.5 | 447.4 | 685.0 | 1009.4 |
| 0.7538 | 25.0 | 50.9 | 96.7 | 172.2 | 288.2 | 461.5 | 708.6 | 1046.4 |
| 0.8037 | 25.7 | 52.5 | 100.5 | 177.3 | 297.6 | 477.2 | 734.1 | 1086.1 |
| 0.8545 | 26.6 | 54.2 | 102.4 | 182.6 | 307.2 | 493.1 | 759.0 | 1125.1 |
| 0.9021 | 27.3 | 55.6 | 105.7 | 188.3 | 316.8 | 509.3 | 784.9 | 1164.8 |
| 1 | 28.8 | 58.9 | 112.2 | 201.0 | 338.4 | 545.1 | 841.1 | 1249.2 |

[a] $x_1$ is the mole fraction of $(CH_3)_2ND$ in the liquid phase.

cients of heavy and light dimethylamine in hexane, $P$ and $P'$ are the pressures of the undiluted isotopic compounds). Equation 1 follows from the equations for the partial pressures

$$p = x_1 f_1 R P \tag{2a}$$

$$p' = x_1 f_1' R' P' \tag{2b}$$

($R$ and $R'$ are corrections for gas imperfection) when corrections for gas imperfections are taken to be equal.

The activity coefficients were obtained from measurements of the vapor pressure isotherms. These coefficients were calculated according to Barker[7] by means of the equations of Redlich and Kister[8]

$$\ln f_1 = Ax_2^2 - Bx_2^2(1 - 4x_1) + Cx_2^2(1 - 8x_1 + 12x_1^2) \tag{3a}$$

(7) J. A. Barker, *Aust. J. Chem.*, 6, 207 (1953).

(8) O. Redlich and A. T. Kister, *Ind. Eng. Chem.*, 21, 345 (1948).

**Table III:** Vapor Pressures of the System $(CD_3)_2NH$–*n*-Hexane in Torr[a]

| | Pressure | | | | | | | |
|---|---|---|---|---|---|---|---|---|
| $x_1$ | −50° | −40° | −30° | −20° | −10° | 0° | +10° | +20° |
| 0 | 2.2 | 3.8 | 7.7 | 14.3 | 26.7 | 45.5 | 75.6 | 121.1 |
| 0.0103 | 3.5 | 6.7 | 12.1 | 21.6 | 36.7 | 60.4 | 96.0 | 148.5 |
| 0.0254 | 5.8 | 10.5 | 18.6 | 31.4 | 51.2 | 81.9 | 124.7 | 185.9 |
| 0.0509 | 8.9 | 16.4 | 28.2 | 46.4 | 73.9 | 113.6 | 169.9 | 247.1 |
| 0.0763 | 11.5 | 20.9 | 36.4 | 59.8 | 94.4 | 143.9 | 212.1 | 304.1 |
| 0.1016 | 13.6 | 25.1 | 43.3 | 71.7 | 112.3 | 170.9 | 250.9 | 357.6 |
| 0.1504 | 16.2 | 30.6 | 54.0 | 90.3 | 141.8 | 214.7 | 312.9 | 442.5 |
| 0.2525 | 20.1 | 38.8 | 70.1 | 118.8 | 190.2 | 291.1 | 428.5 | 609.1 |
| 0.2685 | 20.3 | 39.8 | 72.2 | 122.0 | 195.3 | 299.3 | 441.2 | 626.0 |
| 0.2778 | 20.8 | 40.2 | 73.0 | 123.8 | 198.7 | 305.5 | 449.7 | 638.5 |
| 0.3539 | 22.6 | 44.1 | 80.7 | 138.5 | 223.8 | 347.5 | 516.1 | 739.9 |
| 0.4063 | 23.4 | 46.1 | 84.5 | 146.0 | 237.7 | 370.4 | 553.2 | 795.8 |
| 0.4258 | 23.7 | 46.8 | 86.5 | 149.4 | 243.9 | 380.2 | 569.3 | 819.9 |
| 0.5014 | 24.8 | 49.5 | 91.5 | 159.5 | 260.9 | 409.4 | 615.2 | 891.3 |
| 0.5529 | 25.4 | 50.9 | 94.8 | 167.3 | 272.1 | 428.2 | 646.3 | 938.3 |
| 0.6053 | 26.9 | 52.3 | 97.8 | 172.2 | 283.4 | 447.9 | 677.9 | 987.1 |
| 0.6531 | 27.0 | 53.9 | 100.9 | 177.1 | 292.8 | 463.9 | 703.8 | 1029.4 |
| 0.7044 | 28.5 | 55.3 | 103.8 | 182.5 | 303.3 | 480.9 | 732.0 | 1072.5 |
| 0.7546 | 28.6 | 56.9 | 106.8 | 188.1 | 312.9 | 497.9 | 759.1 | 1114.5 |
| 0.8024 | 29.3 | 58.2 | 109.7 | 193.9 | 322.7 | 514.4 | 785.0 | 1156.3 |
| 0.8529 | 29.9 | 60.1 | 113.1 | 200.1 | 333.5 | 531.8 | 813.5 | 1198.5 |
| 0.9218 | 31.2 | 63.0 | 118.4 | 209.2 | 349.8 | 558.7 | 855.0 | 1262.2 |
| 1 | 32.8 | 66.0 | 124.8 | 221.1 | 369.8 | 591.5 | 906.6 | 1339.4 |

[a] $x_1$ is the mole fraction of $(CD_3)_2NH$ in the liquid phase.

**Table IV:** Vapor Pressures of the System $(CD_3)_2ND$–*n*-Hexane in Torr[a]

| | Pressure | | | | | | | |
|---|---|---|---|---|---|---|---|---|
| $x_1$ | −50° | −40° | −30° | −20° | −10° | 0° | +10° | +20° |
| 0 | 2.2 | 3.8 | 7.7 | 14.3 | 26.7 | 45.5 | 75.6 | 121.1 |
| 0.0103 | 3.1 | 6.5 | 12.7 | 21.6 | 36.9 | 60.7 | 96.5 | 148.6 |
| 0.0256 | 5.9 | 10.4 | 18.7 | 31.8 | 51.9 | 82.1 | 125.7 | 187.6 |
| 0.0503 | 8.9 | 16.1 | 28.0 | 46.6 | 73.9 | 114.1 | 170.5 | 247.5 |
| 0.0761 | 11.6 | 21.1 | 36.2 | 60.0 | 94.6 | 144.3 | 212.7 | 305.8 |
| 0.1012 | 13.0 | 24.4 | 42.9 | 71.4 | 112.5 | 171.3 | 251.8 | 359.7 |
| 0.1516 | 15.9 | 30.4 | 53.9 | 90.3 | 142.9 | 218.0 | 320.3 | 456.3 |
| 0.2028 | 18.4 | 34.9 | 62.3 | 104.7 | 166.7 | 254.9 | 374.0 | 528.9 |
| 0.2538 | 19.8 | 37.9 | 68.7 | 117.0 | 187.6 | 288.6 | 426.0 | 605.5 |
| 0.3003 | 20.1 | 39.9 | 73.2 | 125.6 | 203.4 | 314.5 | 466.8 | 666.6 |
| 0.3512 | 21.4 | 42.2 | 77.8 | 133.7 | 218.0 | 339.6 | 506.8 | 727.3 |
| 0.4005 | 22.2 | 43.8 | 81.7 | 141.9 | 232.0 | 363.0 | 544.4 | 785.2 |
| 0.4504 | 22.9 | 45.7 | 84.8 | 148.1 | 242.9 | 381.6 | 572.8 | 827.7 |
| 0.5019 | 23.2 | 47.2 | 88.1 | 153.8 | 253.3 | 398.9 | 602.3 | 873.4 |
| 0.5485 | 24.1 | 48.5 | 91.1 | 159.8 | 264.6 | 418.1 | 633.7 | 924.4 |
| 0.6022 | 25.1 | 50.0 | 93.9 | 165.5 | 274.3 | 435.5 | 661.0 | 966.9 |
| 0.6533 | 25.5 | 51.2 | 96.8 | 171.3 | 284.9 | 453.2 | 690.7 | 1012.9 |
| 0.7011 | 26.0 | 52.8 | 99.6 | 176.0 | 293.4 | 468.0 | 714.2 | 1050.0 |
| 0.7533 | 26.8 | 54.3 | 102.5 | 181.7 | 303.6 | 484.9 | 741.7 | 1092.5 |
| 0.8003 | 27.4 | 55.6 | 105.5 | 186.7 | 312.5 | 499.7 | 766.3 | 1130.4 |
| 0.8519 | 28.7 | 57.6 | 108.6 | 192.8 | 323.2 | 517.9 | 795.7 | 1175.8 |
| 0.9012 | 29.4 | 59.3 | 112.0 | 199.0 | 333.4 | 535.5 | 823.0 | 1219.0 |
| 1 | 30.8 | 62.4 | 119.0 | 212.3 | 356.5 | 572.9 | 882.1 | 1309.7 |

[a] $x_1$ is the mole fraction of $(CD_3)_2ND$ in the liquid phase.

$$\ln f_2 = Ax_1^2 + Bx_1^2(1 - 4x_2) + Cx_1^2(1 - 8x_2 + 12x_2^2) \quad (3b)$$

where $A$, $B$, and $C$ are constants, using the mole volumes and the virial coefficients which were applied in a previous investigation of the $(CH_3)_2NH$–*n*-hexane system.[6] Measurements of the pressures and preparation of the compounds were performed as described for methylamine and other amines.[1,2] The vapor pressures of the first and last fraction of the compounds within the

**Table V:** Constants for the Calculation of the Activity Coefficients with Eq 3a and 3b

| Temp, °C | A | B | C | A | B | C |
|---|---|---|---|---|---|---|
| | (a) $(CH_3)_2NH$–*n*-Hexane | | | (b) $(CH_3)_2ND$–*n*-Hexane | | |
| +20 | 0.794 | +0.042 | 0.048 | 0.828 | +0.057 | 0.061 |
| +10 | 0.892 | +0.045 | 0.050 | 0.920 | +0.053 | 0.068 |
| 0 | 0.989 | +0.048 | 0.057 | 1.021 | +0.047 | 0.066 |
| −10 | 1.085 | +0.035 | 0.055 | 1.113 | +0.033 | 0.066 |
| −20 | 1.187 | +0.027 | 0.086 | 1.225 | +0.016 | 0.090 |
| −30 | 1.294 | +0.002 | 0.089 | 1.326 | +0.002 | 0.111 |
| −40 | 1.404 | +0.002 | 0.124 | 1.431 | −0.029 | 0.139 |
| −50 | 1.474 | −0.059 | 0.076 | 1.482 | −0.081 | 0.119 |
| | (c) $(CD_3)_2NH$–*n*-Hexane | | | (d) $(CD_3)_2ND$–*n*-Hexane | | |
| +20 | 0.792 | +0.063 | 0.049 | 0.824 | +0.046 | 0.063 |
| +10 | 0.888 | +0.061 | 0.049 | 0.925 | +0.050 | 0.067 |
| 0 | 0.984 | +0.054 | 0.054 | 1.023 | +0.045 | 0.073 |
| −10 | 1.078 | +0.047 | 0.056 | 1.117 | +0.038 | 0.077 |
| −20 | 1.189 | +0.033 | 0.076 | 1.228 | +0.021 | 0.097 |
| −30 | 1.287 | +0.014 | 0.086 | 1.328 | +0.006 | 0.109 |
| −40 | 1.396 | −0.010 | 0.121 | 1.441 | −0.016 | 0.151 |
| −50 | 1.452 | −0.029 | 0.168 | 1.495 | −0.078 | 0.137 |

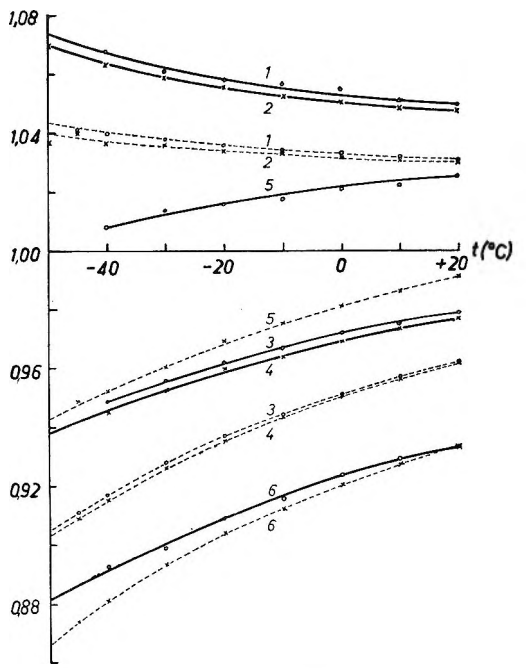


Figure 1. $p/p'$ values of undiluted isotopic dimethylamines (——) and methylamines (- - - - -), respectively, as a function of temperature. 1, $P_{(CD_3)_2NH}/P_{(CH_3)_2NH}$ and $P_{CD_3NH_2}/P_{CH_3NH_2}$; 2, $P_{(CD_3)_2ND}/P_{(CH_3)_2ND}$ and $P_{CD_3ND_2}/P_{CH_3ND_2}$; 3, $P_{(CH_3)_2ND}/P_{(CH_3)_2NH}$ and $P_{CH_3ND_2}/P_{CH_3NH_2}$; 4, $P_{(CD_3)_2ND}/P_{(CD_3)_2NH}$ and $P_{CD_3ND_2}/P_{CD_3NH_2}$; 5, $P_{(CD_3)_2ND}/P_{(CH_3)_2NH}$ and $P_{CD_3ND_2}/P_{CH_3NH_2}$; 6, $P_{(CH_3)_2ND}/P_{(CD_3)_2NH}$ and $P_{CH_3ND_2}/P_{CD_3NH_2}$). In ref 2 curves 1 and 2 as well as curves 3 and 4 should be interchanged. In the case of curve 6, $p$ is the pressure of the light and $p'$ the pressure of the heavy compound.

entire range of measurements had to be the same within ±0.2 Torr. $(CD_3)_2NH_2Cl$ (Merck, Darmstadt) was starting compound for the deuteriomethylated compounds. *n*-Hexane was research grade (Phillips Petroleum company, Bartlesville, Okla.).

## B. Results and Discussion

1. The measured pressures are given in Tables I–IV. The constants from which the activity coefficients are to be obtained with eq 3 are listed in Table V. Figure 1 shows the $p/p'$ values of the undiluted compounds (solid lines) and for comparison the $p/p'$ values of methylamine (dotted lines) as a function of temperature.

The $p/p'$ values of pairs with equal amino but different methyl groups (curves 1 and 2 in Figure 1) correspond to an inverse isotope effect on the vapor pressure ($p > p'$). The deviations from unity are 0.07–0.05, *i.e.*, 1.5–1.7 times the deviations in the case of methylamine. They decrease with increasing temperature, the amounts being approximately twice those of methylamine. For the interpretation we used the equation[9]

$$\frac{p}{p'} = \prod_{i=1}^{3N} q_i = \prod_{i=1}^{6} \left( \frac{\Theta'_{i\text{cond}}}{\Theta_{i\text{cond}}} \frac{\sinh \frac{\Theta_{i\text{cond}}}{2T}}{\sinh \frac{\Theta'_{i\text{cond}}}{2T}} \right) \times \prod_{i=7}^{3N} \left\{ \frac{\Theta'_{i\text{cond}}\Theta_{i\text{gas}}}{\Theta_{i\text{cond}}\Theta'_{i\text{gas}}} \frac{\sinh \frac{\Theta'_{i\text{gas}}}{2T} \sinh \frac{\Theta_{i\text{cond}}}{2T}}{\sinh \frac{\Theta_{i\text{gas}}}{2T} \sinh \frac{\Theta'_{i\text{cond}}}{2T}} \right\} \quad (4)$$

($\Theta_i$ is the characteristic temperature of vibrations, with $i$ ranging from 1 to 3 of the translations, with $i$ ranging from 4 to 6 of the librations, and with $i$ ranging from 7 to $3N$ of the intramolecular vibrations in the gaseous and in the condensed state; prime refers to the lighter isotopic compound) which gives $p/p'$ as a function of the difference between the inter- and the intramolecular

(9) J. Bigeleisen, *J. Chem. Phys.*, **34**, 1485 (1961).

vibrations of the compounds of a pair. As could be shown,[10,11] the factor of the intramolecular vibrations ($i = 7\text{–}3N$) generally decreases with increasing temperature, whereas the factor of the intermolecular vibrations ($i = 1\text{–}6$) increases. Obviously, the intermolecular vibrations of the amino groups cancel each other in eq 4, because the amino groups are the same. Thus the $p/p'$ values are determined primarily by the differences between the methyl group vibrations. The factor of these vibrations is contained twice in eq 4. Therefore the deviations of $p/p'$ values from unity as well as the decrease of these deviations with increase of temperature are crudely twice those of methylamine (taking into account that $(1 + y)^2 \approx 1 + 2y$ is valid for low values of $y$).

The $p/p'$ values of pairs with equal methyl groups but different amino groups (curves 3 and 4 in Figure 1) correspond to a normal isotope effect ($p < p'$). The difference between the $p/p'$ values of 0.94–0.98 and unity is, however, smaller than in the case of methylamine. The same is true for the increase of $p/p'$ with temperature. As the intermolecular vibrations are responsible for this increase, we have to assume that the methyl group vibrations cancel each other in eq 4 and that $p/p'$ is a function of the influence of the intermolecular vibrations which is reduced by the counteracting influence of the intramolecular amino group vibrations. Thus the smaller normal effect (compared with methylamine) and the somewhat weaker increase with temperature are explained by the weaker association of dimethylamine or by the lower frequency of the intermolecular vibrations and the smaller change of the intramolecular amino group vibrations generated by the weaker association.[10,11]

The $p/p'$ values of pairs with different amino groups and with different methyl groups represent combinations of the values already considered. Curve 5 in Figure 1, representing $p/p'$ when both groups of the same compound are deuterated, follows from multiplication of the values in curves 1 and 4. Both, curves 1 and 4, are higher than in the case of methylamine, therefore curve 5 for dimethylamine is also higher than that for methylamine. It lies in the region of the inverse effect, and its slope is less than that of curve 4. In contrast, curve 5 of methylamine lies completely in the region of the normal effect.

Curve 6 represents the $p/p'$ values for pairs in which the deuterated amino group is in one compound, and the deuteromethylated groups are in the other compound. Curve 6 follows from the division of the values of curve 3 by the values of curve 1. In this case, too, both 1 and 3 are higher than the corresponding curves for methylamine. The differences, however, cancel out in division. Therefore, curve 6 is nearly the same for dimethylamine and methylamine. Its slope is again less than the slope of curve 3, because of the decrease of curve 1.

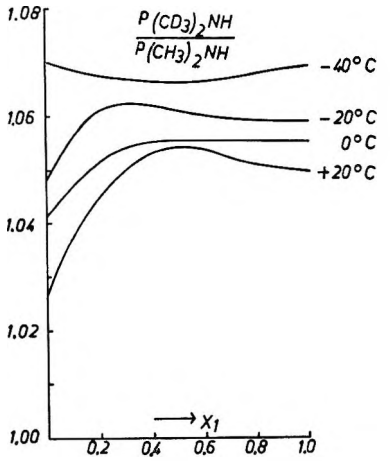


Figure 2. $p/p'$ values of $(CD_3)_2NH$ and $(CH_3)_2NH$ in solution with $n$-hexane between +20 and −40° as a function of mole fraction $x_1$ of dimethylamine.

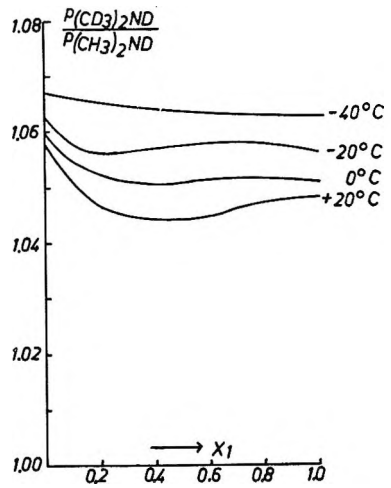


Figure 3. $p/p'$ values of $(CD_3)_2ND$ and $(CH_3)_2ND$ in solution with $n$-hexane between +20 and −40° as a function of mole fraction $x_1$ of dimethylamine.

2. Figures 2–7 represent the $p/p'$ values as a function of the mole fraction of dimethylamine for given temperatures. The approximate independence of the values on dilution (Figures 2 and 3) confirms the statement that the $p/p'$ values for pairs with equal amino groups and different methyl groups are nearly independent from association and are determined essentially by methyl group vibrations alone. (The deviations of the curves at low mole fractions from the horizontal may be due to errors.)

The $p/p'$ values depend heavily upon concentration for pairs with equal methyl groups but unequal amino groups (Figures 4 and 5). This observation corresponds to the expectation that the normal effect of the hydro-

(10) H. Wolff in "Physics of Ice," N. Riehl, B. Bullemer, and H. Engelhardt, Ed., Plenum Publishing Corp., New York, N. Y., 1969, p 305.

(11) H. Wolff and E. Wolff, *Ber. Bunsenges. Phys. Chem.*, **73**, 393 (1969).

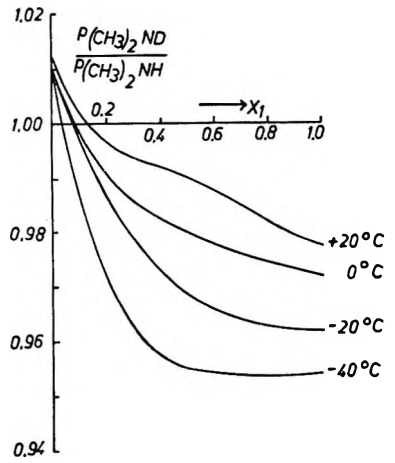


Figure 4. $p/p'$ values of $(CH_3)_2ND$ and $(CH_3)_2NH$ in solution with $n$-hexane between +20 and −40° as a function of mole fraction $x_1$ of dimethylamine.

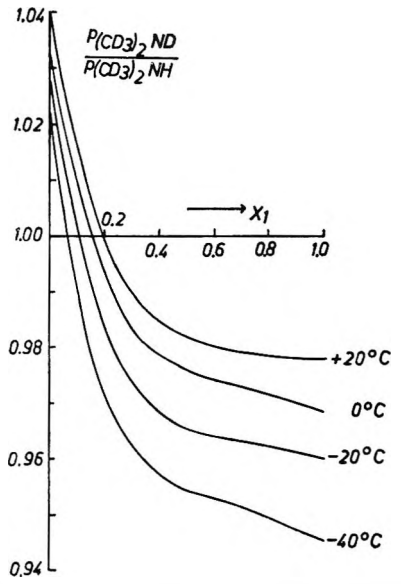


Figure 5. $p/p'$ values of $(CD_3)_2ND$ and $(CD_3)_2NH$ in solution with $n$-hexane between +20 and −40° as a function of mole fraction $x_1$ of dimethylamine.

gen-bonded molecules is replaced by the inverse effect of monomers. As could be shown,[3,12] this inverse effect results primarily from the solvent shift of intramolecular vibrations. The intermolecular vibrations of monomers are low in frequency or rotationlike and approximate the classical behavior of vibrations, therefore their factor in eq 4 being nearly 1.

The same explanation holds true for the concentration dependence of $p/p'$ for pairs with unequal groups (Figures 6 and 7). However, the effects of methyl and of amino group vibrations are to be multiplied in one case and divided in the other, as with curves 5 and 6 of Figure 1.

Equation 4 has to be replaced by the two-state function[11] (eq 5) if one takes into account the association

$$\frac{p}{p'} = \left(\prod_{i=1}^{3N} q_i\right)_{\text{bonded}}^{1-x} \left(\prod_{i=1}^{3N} q_i\right)_{\text{free}}^{x} \qquad (5)$$

equilibrium between dimethylamine molecules with free amino groups (mole fraction $x$) and molecules with hydrogen or deuterium bonded groups (mole fraction $1 - x$). Since $(\Pi q_i)_{\text{free}}{}^{x} > 1$ and $(\Pi q_i)_{\text{bonded}}{}^{1-x} > (\Pi q_i)_{\text{bonded}}$, it follows that $p/p'$ of the undiluted compounds, which are

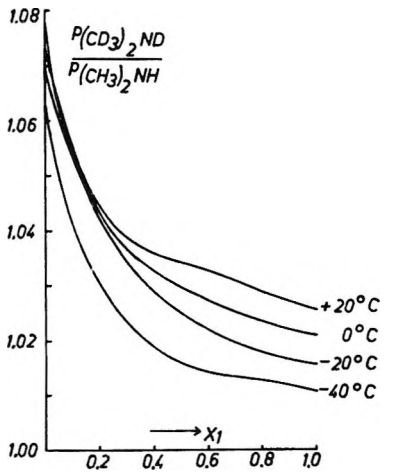


Figure 6. $p/p'$ values of $(CD_3)_2ND$ and $(CH_3)_2NH$ in solution with $n$-hexane between +20 and −40° as a function of mole fraction $x_1$ of dimethylamine.

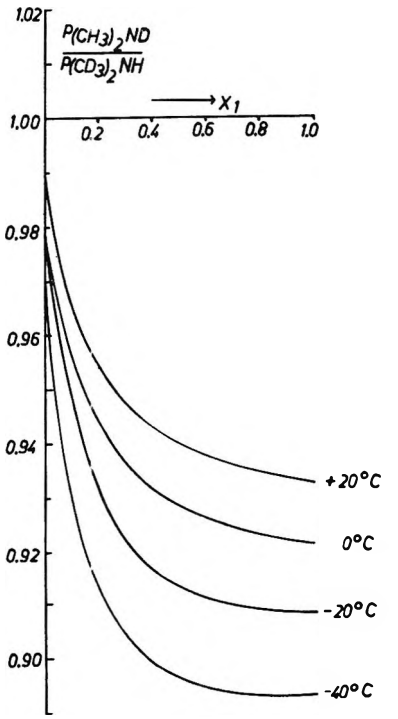


Figure 7. $p/p'$ values of $(CH_3)_2ND$ and $(CD_3)_2NH$ in solution with $n$-hexane between +20 and −40° as a function of mole fraction $x_1$ of dimethylamine. As in the case of curve 6 of Figure 1 $p$ is the pressure of the light and $p'$ the pressure of the heavy compound.

(12) H. Wolff, *Ber. Bunsenges. Phys. Chem.*, **73**, 399 (1969).

partly associated, is greater than $p/p'$ of the compounds associated perfectly. Furthermore it follows that $p/p'$ increases with temperature due to the temperature dependence according to eq 4 as well as due to the increase in the number of monomers.

Neglecting the presence of the solvent and the small difference of the association degree of corresponding NH and ND compounds, eq 5 may be assumed to be valid also for the dissolved molecules. (As has been shown for methylamine in ref 6 and as will be shown for dimethylamine in a forthcoming paper,[13] the ND compound is somewhat more associated.) The values of $(\Pi q_i)_{free}$ have then to be calculated from the frequencies of gaseous compounds and the solvent-shifted frequencies of monomers. Inserting the values of $p/p'$ and $x$ for two mole fractions results in two equations, the solution of which yields $(\Pi q_i)_{free}$ and $(\Pi q_i)_{bonded}$. Reinserting these values and inserting the value of the vapor pressure ratio of the pure compounds permits one to calculate the fraction $x$ of free groups in the undiluted state. Tentatively, the $p/p'$ values of $(CH_3)_2NH$– and $(CH_3)_2ND$–*n*-hexane at mole fractions of 0.1 and 0.2 (Figure 4) have been used for calculation. It could be assumed that these values are determined more exactly than those of $(CD_3)_2NH$– and $(CD_3)_2ND$–*n*-hexane, for they correspond to the expectation that the vapor pressure ratio of NH and ND compounds at the state of monomers amounts to 1.01–1.02. (The $p/p'$ values of monomers or values not influenced by association amount to 1.01–1.02 for $CH_3OH$–$CH_3OD$, 1.02–1.03 for $CH_3NH_2$–$CH_3ND_2$, and 1.04–1.06 for $CH_3NH_2$–$CD_3NH_2$.[12]) $x$ resulted from the fractions of monomers, dimers, trimers, and tetramers, determined as in ref 14, under the assumption that each of the different forms contains one free group (Table VI).

The values of 1.013 and 1.015 at +20 and −20° for $(\Pi q_i)_{free}$ resulting in this way are in reasonable agreement with those of 1.017, obtained from Figure 4 where $x_1$ approaches zero. Values of 0.92 are obtained for $(\Pi q_i)_{bonded}$. The value of 0.92 presumes that all molecules of dimethylamine are hydrogen bonded. If one inserts it in eq 5 and thereby relates it to the values of 0.978 or 0.962, measured at +20 and −20° for the undiluted compounds (Figure 4), one obtains the fractions 0.64 and 0.44, which are due to the free groups. Values of 0.59–0.33 in the same temperature range have been obtained from infrared measurements in the first harmonics.[15] Thus, even the simplified calculations with eq 5 give reasonable results.

**Table VI:** Fractions $x$ of Free Groups of $(CH_3)_2NH$ in *n*-Hexane Solution, Determined from Fraction $\beta_1$ of Monomers, $\beta_2$ of Dimers, $\beta_3$ of Trimers, and $\beta_4$ of Tetramers[a]

| Mole fraction $x_1$ of $(CH_3)_2NH$ in $C_6H_{14}$ soln | $\beta_1$ | $\beta_2$ | $\beta_3$ | $\beta_4$ | Fraction $x$ of free groups ($\beta_1 + 1/2\beta_2 + 1/3\beta_3 + 1/4\beta_4$) |
|---|---|---|---|---|---|
| | | +20° | | | |
| 0.1 | 0.841 | 0.065 | 0.008 | 0.002 | 0.916 |
| 0.2 | 0.717 | 0.096 | 0.021 | 0.007 | 0.841 |
| | | −20° | | | |
| 0.1 | 0.749 | 0.088 | 0.017 | 0.005 | 0.859 |
| 0.2 | 0.578 | 0.108 | 0.035 | 0.017 | 0.738 |

[a] The assumption is made that each of these forms contains one free group. $\beta_1$, $\beta_2$, $\beta_3$, and $\beta_4$ are calculated from the data of Table V as in ref 14, assuming validity of the theory of ideal associated solutions.

*Acknowledgment.* We gratefully acknowledge support of this work by the Fonds der Chemischen Industrie, Frankfurt, and by the Badische Anilin und Soda-Fabrik, Ludwigshafen.

(13) H. Wolff and R. Würtz, *Z. Phys. Chem.* (Frankfurt am Main), in press.

(14) H. Wolff and A. Höpfner, *Ber. Bunsenges. Phys. Chem.*, 66, 149 (1962).

(15) H. Wolff and G. Gamer, in preparation.

# Chemical Electrostatics. I. Electrostatic Description of the Markovnikov Rule[1]

by G. R. Haugen and S. W. Benson

*Department of Thermochemistry and Chemical Kinetics, Stanford Research Institute, Menlo Park, California 94025*
*(Received November 19, 1969)*

A critical evaluation of the applicability of electrostatic models in the intramolecular domain justifies the use of idealized electrostatic models, such as point dipoles and point aggregates of polarizable matter with field independent polarizabilities. The apparent inaccuracies in applying these idealized electrostatic models to explain molecular properties stems from the misapplication of these models in a region of enormously inhomogenous fields. The interaction between a point dipole and a dielectric sphere at molecular dimensions has been derived and suggests that under these conditions the electrostatic center and the geometric center do not coincide. In the case of the carbon–hydrogen bond, the interaction energy is corrected by about 30%, while the carbon–carbon bond requires a correction of 100% in the interaction energy. Starting with these corrected idealized electrostatic models, an electrostatic description of the Markovnikov rule has been developed, which utilizes the observed bond angles and distances, covalent radii of the atoms, macroscopic mean polarizabilities of the atoms, and molecular dielectric constant in the vicinity of the charged carbon atoms. The interactions of charged atoms with polarizable groups can be considered as idealized charge–dielectric sphere interactions. However, the polarizable matter in which the charge is embedded is treated as a continuous dielectric. The calculated stabilization energy of the positively charged carbon atom by a methyl group is 5.8 kcal/mol, while the negatively charged carbon atom is stabilized by 1.6 kcal/mol.

## I. Introduction

The Markovnikov rule[2] for addition to olefins can be stated as follows: the olefinic carbon atom that sustains a positive formal charge will be the one with the least number of attached hydrogen atoms. The enormous effect of $\alpha$-methyl substitution on kinetics of four-center gas-phase reactions is a manifestation of this rule. This kinetic orientation phenomenon is quantitatively exhibited as a decrease in activation energy of about 5–6 kcal/mol upon the substitution of a methyl for an $\alpha$ hydrogen and 1–2 kcal/mol upon substitution of a methyl for a $\beta$ hydrogen. In view of the fact that the kinetic data have been shown to be compatible with a very polar transition state, it is reasonable to idealize this transition state as a semiion quadrupole.[2]

It is the purpose of this article to develop a quantitative electrostatic description of this idealized transition state that is capable of predicting these orientation effects from other molecular properties. A prerequisite is the critical evaluation of the applicability of idealized electrostatic models (*i.e.*, point dipoles, point aggregates of polarizable matter, and concept of continuous polarizable matter) in the intramolecular domain.

## II. Electrostatic Fields in Molecules

Hitherto, the apparent failure of intramolecular electrostatic models has been attributed to one or more of the following objections.

1. Incapability of representing the electric field of a finite intramolecular dipole by the point dipole approximation. The potential of a dipole ($\mu$) of finite length ($l$) can be represented as a converging series of ascending power of $l/r$, where $r$ is the distance from its dipole center. The first, second, and third terms are[3]

$$\phi = \phi_0\{1 + \delta + \Delta + \ldots\} \qquad (1)$$

where $\phi_0$, $\delta$, and $\Delta$ represent the potential of a point dipole $(\mu \cos\theta)/(r^2)$, $\{(5\cos^2\theta - 3)/(8)\}((l)/(r))^2$, and $\{(63\cos^4\theta - 70\cos^2\theta + 15)/(128)\}((l)/(r))^4$, respectively. The second and third terms in the expansion represent, at most, a 32% correction at distances comparable with the size of the dipole; the higher order terms will always be negligible (see Table I). The correction terms will enhance the ideal dipole potential in some configurations and reduce it in others. If the potentials of a finite dipole and a point dipole are integrated over all possible positions on a surface of a sphere, the enhancement of the total potential of a nonideal dipole over that of the ideal dipole at a distance comparable to the length of the dipole is only 6%.

2. Saturation effects at submolecular distances, the failure of the linear relationship between the induced dipole ($\vec{\mu}_{ind}$) and the local electric field ($F$). The normal linear relationship requires the polarizability tensor to be

(1) This work was supported by Grant No. 1 RO 1 AP00698-01, Public Health Service, Department of Health, Education, and Welfare.

(2) (a) G. K. Ingold, "Structure and Mechanism in Organic Chemistry," Cornell University Press, Ithaca, N. Y., 1953; (b) S. W. Benson and A. N. Bose, *J. Chem. Phys.*, **39**, 3463 (1963).

(3) C. J. F. Bottcher, "Theory of Electric Polarization," Elsevier Publishing Co., New York, N. Y., 1952.

**Table I:** Correction Factor for the Potential of a Finite Dipole (see eq 1)

| | cos θ = 0 | | cos θ = 1 | |
|---|---|---|---|---|
| l/r | δ | Δ | δ | Δ |
| 0 | 0 | 0 | 0 | 0 |
| 0.1 | −0.004 | +0.000 | +0.003 | +0.000 |
| 0.2 | −0.015 | +0.000 | +0.010 | +0.000 |
| 0.3 | −0.034 | +0.001 | +0.023 | +0.001 |
| 0.4 | −0.060 | +0.003 | +0.040 | +0.002 |
| 0.5 | −0.094 | +0.007 | +0.063 | +0.004 |
| 0.6 | −0.135 | +0.015 | +0.090 | +0.008 |
| 0.7 | −0.184 | +0.028 | +0.123 | +0.015 |
| 0.8 | −0.240 | +0.048 | +0.160 | +0.026 |
| 0.9 | −0.304 | +0.081 | +0.203 | +0.041 |
| 1.0 | −0.375 | +0.117 | +0.250 | +0.063 |

independent of the local field ($\vec{\mu}_{ind} = \alpha\vec{F}$). Accordingly, the saturation effects demand a field dependent polarizability tensor ($\vec{\mu}_{ind} = [\alpha - \beta|\vec{F}|]\vec{F}$). Let us pursue the implications of a field dependent polarizability tensor. The electronic polarization has the following form

$$P_E = \frac{4\pi N}{3} \sum \frac{e^2}{f} \tag{2}$$

where $f$ represents the restoring force constant of the electrons. ($P_E$ the electronic polarization is calculated from the refractive index.) Then the change in dipole ($\Delta\mu$) induced by a change in the electric field intensity ($\Delta F$) is given by

$$\Delta\mu = -\frac{e^2}{f}\Delta F \tag{3}$$

This equation is a combination of the two well known relations

$$e\Delta F = -f\Delta X \tag{4}$$

$$\Delta\mu = e\Delta X \tag{5}$$

Note that this is the typical linear expression between induced dipole and the electrostatic field strength. Now, suppose that the relationship between displacement and electrostatic field strength is not linear, *i.e.*

$$-e\Delta F_{local} = +f_1\Delta X_{local} - f_2(\Delta X_{local})^2 \tag{6}$$

$$\Delta X_{local} \cong \frac{e\Delta F_{local}}{f_1} + \frac{f_2}{f_1^3} e^2(\Delta F_{local})^2 \tag{7}$$

$$= -\frac{e\Delta F_{local}}{f_1}\left(1 - \frac{f_2}{f_1^2} e\Delta F_{local}\right) \tag{8}$$

Let us perturb the local field by a small external electrostatic field ($\delta F$). This is actually what occurs when the polarizability of a molecule is measured. Hence

$$\Delta X_{external + local} = -\frac{e(\Delta F_{local} + \delta F)}{f_1}\left(1 - \frac{f_2}{f_1^2} e(\Delta F_{local} + \delta F)\right) \tag{9}$$

and

$$\delta X = \Delta X_{external + local} - \Delta X_{local} \cong -\frac{e\delta F}{f_1}\left(1 - \frac{2ef_2}{f_1^2}\Delta F_{local}\right) \tag{10}$$

Accordingly, the dipole induced by the external field is

$$\delta\mu = e\delta X = -\frac{e^2\delta F}{f_1}\left(1 - \frac{2ef_2}{f_1^2}\Delta F_{local}\right) \tag{11}$$

and the true polarizability is diminished by local saturation effects. Local fields vary considerably from compound to compound, as attested to by the enormous variation in molecular polarity. Consequently, bond polarizabilities should be strongly dependent on environment. However, this is contrary to observation; molar bond refraction is an additive property.[4]

3. Impossibility of representing the negative charge or polarizable matter by point aggregates. The center of positive charge aggregates is unequivocally located at the nuclei. Thus, the critical suppositions are the location of the center of negative charge aggregates and the center of aggregates of polarizable matter. Inasmuch as the polarizable matter is the electron, both the negative charge center and the center of polarizability should coincide. The problem is one of representing the electron distribution in the molecule. An acknowledged example of this in electrostatics is the spherical body.[3] The electrostatic field of a charge and/or polarized spherical body is equivalent to a simple finite array of point charges. Two theorems of electrostatics that emphasize the one to one correspondence between spatial charge distribution and idealized array of point charges are stated here to stress the interchange ability of these models. "The average reaction field of an arbitrary system of fixed charges in a spherical cavity in a dielectric can be represented by an ideal dipole moment of the system of charges relative to the center of the cavity" and "A spherical surface with a surface charge density, $\sigma$, represented by ((constant)/$(4\pi))(2l + 1)/(d^{l+2})[P_l(\cos\theta)]$, where $d$ is the radius of the sphere and $P_l(\cos\vartheta)$ represents the Legendre functions, has a potential, $\phi$, given by

$$\sum_{l=0}^{\infty}\left(A_l r^l + \frac{B_l}{r^{l+1}}\right) P_l(\cos\theta)$$

Examples: 1. If $l = 0$, then $\sigma$ is given by $e/4\pi a^2$. The charge $e$ is evenly distributed over a spherical surface. The potential inside the spherical surface is a constant, whereas, outside the sphere, the potential is that of a point charge located at the center of the sphere. 2. If $l = 1$, then $\sigma$ is given by $[(3m)/(4\pi a^3)]\cos\theta$, where $m$ represents the dipole moment of the system.

(4) K. G. Denbigh, *Trans. Faraday Soc.*, **36**, 936 (1950); S. N. Wang, *J. Chem. Phys.*, **7**, 1012 (1939); K. S. Pitzer, *Advan. Chem. Phys.*, **2**, 59 (1959); J. W. LeFevre, *Advan. Phys. Org. Chem.*, **3**, 1 (1965).

Again this charge distribution gives a uniform field inside the sphere and the potential outside the sphere is that of an ideal dipole, located at the center of the sphere. 3. If $l = 2$, then $\sigma$ is given by $[(5Q)/(4\pi a^4)]\cdot(3\cos^2\theta - 1)$ where $Q$ is an axial quadrupole moment of the surface charge distribution. The field inside the sphere is a linear function of the coordinates, while the potential outside the sphere is that of an ideal axial quadrupole located at the center of the sphere and directed along the $Z$ axis."

In view of the fact that the electron is a negatively charged particle whose motion is entirely determined by external and local fields, the spatial distribution of the electron determines the center of charge density which is also the representative center of polarizable matter.

The difficulty of using the concepts and relationships that hold for molecular electrostatics at intramolecular dimensions does not stem from a failure of these basic concepts described herein above, but from the nonuniformity of the electric field at these dimensions. A feel for the enormous field gradients that exists and the problems associated with integrating their effects over a finite volume can be achieved by two simple calculations (see Figures 1 and 2). Note that as the distance between a point dipole and a finite region of space approaches the dimension of that region (radius), the electric field strength in the quadrants closest to the dipole increase sharply over the value in the distant quadrants (see Figures 1a and 1b). The integration of the effects of this inhomogeneous electric field over the finite region of space may not coalesce to a representative point. Even if there happens to be a representative point, it cannot coincide with the geometrical center of the region.

The calculations depicted in Figure 2 compare the electric field strengths at the point $p$, generated by a point dipole ($\vec{m}$) and its induced partner ($\vec{m}'$). Observe that, as the point $p$ approaches the induced dipole ($\vec{m}'$), the electric field strength due to the original dipole ($\vec{m}$) becomes insignificant, even if the quantity $\alpha\sqrt{7}/S^3$ is less than one. Consequently, if the polarizability ($\alpha$) and distances ($S$ and $S \pm \lambda$) have a particular correspondence, the electric field effects of the original dipole ($\vec{m}$) can be propagated by an inductive mechanism rather than directly across the intervening space.[5,6]

These inhomogeneous electrostatic effects necessitate the reevaluation of the interaction energy between spherical particles and electric fields emanating from point charges or point dipoles.

(*a*) *Conducting Sphere.* The method of images in electrostatic theory allows the calculation of the interaction of a charged or uncharged metallic sphere and a simple distribution of point charges. The simple, well-known relations are obeyed at distances approaching the radius of the sphere, irrespective of the size of this sphere.[7] That is, the interaction of the induced charge distribution in a metallic sphere with a point charge or dipole is exact at all dimensions, the only restriction being that the point charge or dipole is located outside the metallic sphere.

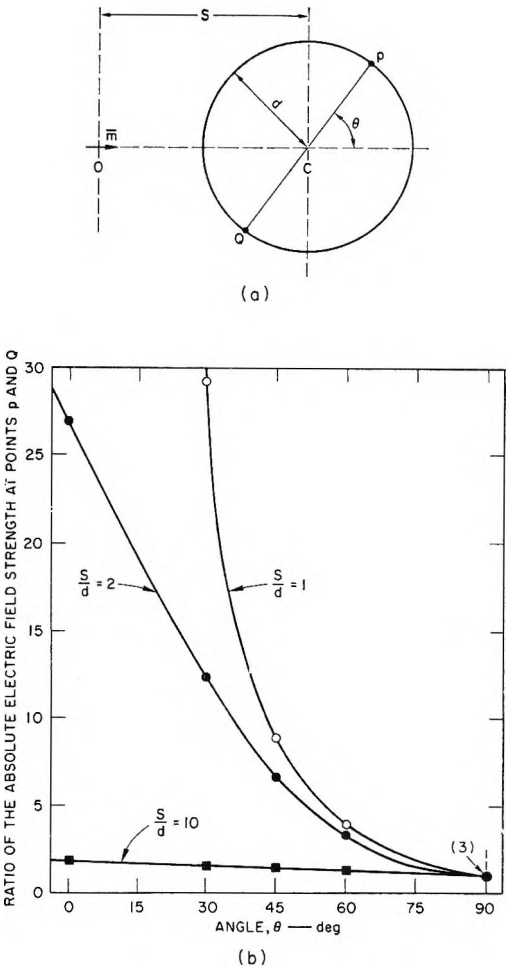


Figure 1. The ratio of electric field strength, $|\vec{F}_Q|/|\vec{F}_p|$ due to a point dipole ($\vec{m}$) is shown as a function of its angle, $\theta$, and the ratio of dimensions, $S/d$.

$$|\vec{F}_Q|/|\vec{F}_p| = \left(\frac{1 + (S/d)^2 + 2(S/d)\cos\theta}{1 + (S/d)^2 - 2(S/d)\cos\theta}\right)^{3/2} \times \left(\frac{4 - \dfrac{3\sin^2\theta}{(1 + (S/d)^2 - 2(S/d)\cos\theta)}}{4 - \dfrac{3\sin^2\theta}{(1 + (S/d)^2 + 2(S/d)\cos\theta)}}\right)^{1/2}$$

(*b*) *Dielectric Spheres.* Consider a point charge $e$ located at a distance $S$ from the center of a dielectric sphere of radius $a$. The distance $S$ must always be larger than the radius of the sphere. Using the properties of the Legendre functions, the work of polarization $w$ has the exact form[3]

(5) This concept of an alternative inductive mechanism for propagation of electrostatic effects has been proposed previously.[6]

(6) See C. K. Ingold, *Chem. Rev.*, 15, 225 (1934); A. E. Remick, *J. Chem. Phys.*, 9, 653 (1941).

(7) E. S. Rittner, *ibid.*, 19, 1030 (1951).

$$w = -\frac{1}{2}\frac{e^2\alpha}{S^4}\sum_{l=0}^{\infty}\frac{l(\epsilon+2)}{l(\epsilon+1)+1}\left(\frac{a}{S}\right)^{2l-2} \qquad (12)$$

where $\epsilon$ represents the dielectric constant of the homogeneous dielectric sphere, and $\alpha$ represents the polarizability of the dielectric sphere, $\alpha = [(\epsilon-1)/(\epsilon+2)]a^3$. The first term, $-{}^1/_2(e^2\alpha)/(S^4)$, depicts the ideal work of polarization and the second term

$$\sum_{l=0}^{\infty}\frac{l(\epsilon+2)}{l(\epsilon+1)+1}\left(\frac{a}{S}\right)^{2l-2}$$

is the correction factor which converges toward one as the ratio $a/S$ tends toward zero. In Table II, the values of the correction factor for some arbitrary values of $\epsilon$ and for some typical ratios of $a/S$ found in intramolecular dimensions are tabulated.

In the case where the radius is 67% of the separation between the point charge and the center of the dielectric sphere, the actual energy is about 100% larger than the value calculated for the limit of $a/S$ approaching zero. The correction factor is essentially independent of the dielectric constant of the sphere.

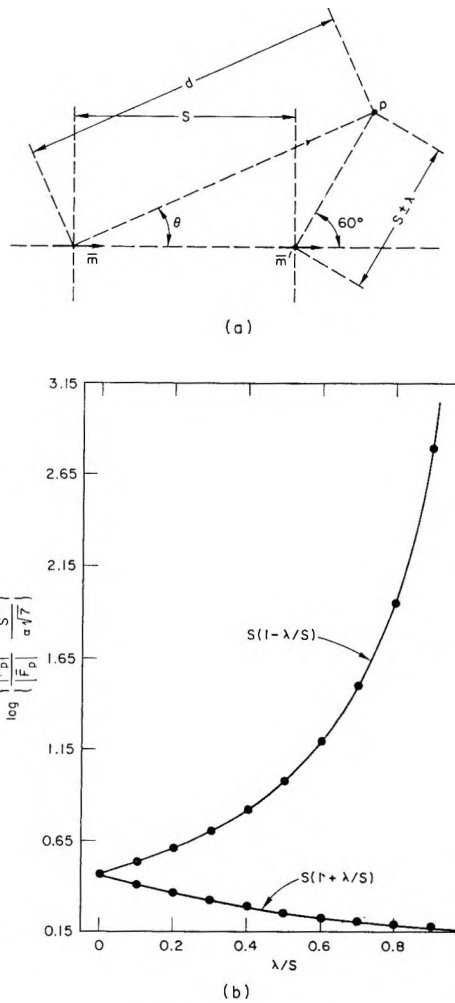


Figure 2. The quantity $|\vec{F}'_p|/|\vec{F}_p|(S^3/\alpha\sqrt{7})$ is represented as a function of the distance between the induced dipole, $\vec{m}'$ and the point $p$. The absolute field strength at point $p$ due to the original dipole, $\vec{m}$, and the induced dipole, $\vec{m}'$, are represented by $|\vec{F}'_p|$ and $|\vec{F}_p|$, respectively: $\{|\vec{F}'_p|/|\vec{F}_p|\}(S^3/\alpha\sqrt{7}) = [d^3/S^3(1 \pm (\lambda/S))^3]\sqrt{3\cos^2\theta + 1}$.

**Table II:** Correction Factor, $\sum_{0=l}^{\infty}\frac{l(\epsilon+2)}{l(\epsilon+1)+1}\left(\frac{a}{S}\right)^{2l-2}$

| $a/S$ | $\epsilon = 2$ | $\epsilon = 4$ | $\epsilon = 6$ |
|---|---|---|---|
| $^2/_3$ | 1.94 | 1.88 | 1.86 |
| $^1/_2$ | 1.38 | 1.36 | 1.36 |
| $^1/_3$ | 1.14 | 1.14 | 1.13 |
| $^1/_4$ | 1.07 | 1.07 | 1.07 |
| $^1/_{10}$ | 1.01 | 1.01 | 1.01 |

In Appendix A, we have outlined the derivation of the exact formula for the work of polarization of a dielectric sphere with dielectric constant, $\epsilon$, by a point dipole. The relations encountered can be simplified by choosing the case with the highest symmetry, *i.e.*, the point dipole situated on the $Z$ axis at a distance $S$ from the center of the dielectric sphere and pointing toward this center. The work of polarization, $w$, of the dielectric sphere of radius, $a$, by a point dipole, $m$, is denoted by the equation

$$w = -\frac{2m^2\alpha}{S^6}\sum_{l=0}^{\infty}\frac{l(\epsilon+2)(l+1)^2}{4[l(\epsilon+1)+1]}\left(\frac{a}{S}\right)^{2l-2} \qquad (13)$$

where $\alpha$ represents the polarizability of the dielectric sphere, $\alpha = [(\epsilon-1)/(\epsilon+2)]a^3$. Again, the first term, $(-2m^2\alpha)/(S^6)$, depicts the ideal work of polarization and the second term, $\Sigma_{l=0}^{\infty} l(\epsilon+2)(l+1)^2/4[l(\epsilon+1)+1]\,(a/S)^{2l-2}$, a correction factor which converges toward one as the ratio $a/S$ tends toward zero. In Table III, the values of this correction factor for some arbitrary values of $\epsilon$ and for some typical ratios of $a/S$ are tabulated. The correction factor for the interaction of a dielectric sphere with a point dipole is greater than that for a point charge. In the case where the radius is 67% of the separation between the point dipole and the center of the dielectric sphere, the actual energy is over 300% larger than the ideal value. Again, the correction factor is essentially independent of the dielectric constant.

**Table III:** Correction Factor, $\sum_{l=0}^{\infty}\frac{l(\epsilon+2)(l+1)^2}{4[l(\epsilon+1)+1]}\left(\frac{a}{S}\right)^{2l-2}$

| $a/S$ | $\epsilon = 2$ | $\epsilon = 4$ | $\epsilon = 6$ |
|---|---|---|---|
| $^2/_3$ | 4.36 | 4.51 | 4.37 |
| $^1/_2$ | 1.99 | 2.05 | 2.02 |
| $^1/_3$ | 1.33 | 1.34 | 1.32 |
| $^1/_4$ | 1.17 | 1.17 | 1.17 |
| $^1/_{10}$ | 1.03 | 1.02 | 1.02 |

## III. Electrostatic Model for the Markovnikov Rule

Herein, is set forth a simple electrostatic model of the transition state that resolves the Markovnikov orientation rule as an enhanced stabilization of the positive olefinic carbon atom over the negative olefinic carbon atom by the attached polarizable groups, whose observed mean polarizabilities are tabulated in Table IV.

**Table IV:** Polarizability of Bonds and Atoms

| Bond | $\alpha_l$,[a] Å$^3$ | $\alpha_t$,[a] Å$^3$ | $\alpha$,[a] Å$^3$ | Ref |
|---|---|---|---|---|
| C=C | 2.80 | 0.75 | 1.43 | *b* |
| C—H | 0.64 | 0.64 | 0.64 | *b* |
| C—C | 0.99 | 0.27 | 0.51 | *b* |
| C—($CH_3$) | 2.91 | 2.19 | 2.43 | *c* |
| C— | | | 0.26 | *d* |
| H— | | | 0.38 | *d* |
| H— | | | 0.40 | *d*, *e* |
| ($CH_3$)— | | | 2.17 | *d* |
| ($CH_3$)— | | | 2.24 | *e* |
| $CH_4$ | 2.60 | 2.60 | 2.60 | *f* |
| C | | | 1.04 | *f* |

[a] $\alpha_l$ represents the longitudinal polarizability, $\alpha_t$ represents the transverse polarizability, and $\alpha$ represents the mean polarizability of the particular bond, $^1/_3(\alpha_l + 2\alpha_t)$. [b] Bond polarizabilities are the values reported by R. J. W. LeFevre, *Advan. Phys. Org. Chem.*, **3** (1965). [c] $\alpha_l$(C–$CH_3$) = $\alpha_l$(C–C) + $^1/_3\alpha_l$(C–H) + $^8/_3\alpha_t$(C–H); $\alpha_t$(C–$CH_3$) = $\alpha_t$(C–C) + $^1/_3\alpha_l$(C–H) + $^5/_3\alpha_t$(C–H) using LeFevre values for bond polarizabilities (note *b*), these relations reduce to $\alpha_l$(C–$CH_3$) = $\alpha_l$(C–C) + 3$\alpha_l$(C–H) = 2.91 Å$^3$; $\alpha_t$(C–$CH_3$) = $\alpha_t$(C–C) + 3$\alpha_t$(C–H) = 2.19 Å$^3$. [d] We have assumed that the mean polarizability of the bond is an additive property of the bonded atoms: $\alpha$(A–B) = $\alpha$(A–) + $\alpha$(B–). Accordingly, $\alpha$(C–) = $^1/_2\alpha$(C–C), $\alpha$(H–) = $\alpha$(C–H) − $^1/_2\alpha$(C–C), $\alpha$($CH_3$–) = $\alpha$(C–$CH_3$) − $^1/_2\alpha$(C–C). [e] A comparison is possible by deriving the mean polarizability of the bonded hydrogen atom from the mean polarizability of the hydrogen molecule and the bonded methyl group from the mean polarizability of ethane: $\alpha$(H–) = $^1/_2\alpha$($H_2$) = 0.40 Å$^3$ and $\alpha$($CH_3$–) = $^1/_2\alpha$($C_2H_6$) = 2.24 Å$^3$ where the values for the mean polarizability of the hydrogen and ethane molecules are taken from "Landolt-Börnstein Zahlenwerte and Funktionen. I. Bond Atom und Molekular-Physik," 3. Teil Molekeln II. [f] Polarizability of $CH_4$ is taken from "Landolt Börnstein Zahlenwerte und Funktionen. I. Bond Atom und Molekular-Physik," 3. Teil Molekeln II. A total mean polarizability of a bonded carbon atom in $sp^3$ hydridization is $\alpha$(C) = $\alpha$($CH_4$) − 4$\alpha$(H–), $\alpha$(C) = 2.60 Å$^3$ − 4(0.39 Å) = 1.04 Å. This value can also be derived from the relation $\alpha$(C) = 4$\alpha$(C–) = 4(0.26) = 1.04 Å.

It should be emphasized that this description is considering only the olefinic portion of the transition state. Actually, the transition state is a semiionic pair[2,8] which is formed concertedly when the olefin and the additive cooccupy a region in phase space. The olefin bond is depicted as having two positive centers located at the olefinic carbon nuclei. An electron distribution is portrayed by a family of surfaces of revolution (equipotential surfaces) with two focal points representing the effective centers of negative charge. In the ground state, the representative centers of negative charge and positive charge are conjectured to concur, inasmuch as the observed molecular dipole moments for olefins are very small. However, the polarized state of the olefinic bond existing in the transition state has the aspect of a formal charge separation; one olefinic carbon atom having a formal negative charge of half an electronic charge, and the other a formal positive charge of half an electronic charge.[8] The positive charge centers are one of the terminals of the induced dipoles. Consequently, there are two of these dipoles with their positive ends located at the nuclei of the olefinic carbon atoms as positioned in the transition state. We have assumed that they are point dipoles and that the total field energy necessary to polarize the double bond is given by[8] $^1/_2[(332.0)d^2q^2/\alpha]$ kcal/mol where $d$ is the distance between the nuclei in ångströms, $q$ the formal charge located at the nuclei in units of electronic charge, and $\alpha$ the longitudal polarizability of the double bond. The point dipoles situated on each of the olefinic carbon atoms interact with the polarizable matter associated with that olefinic carbon atom and with the polarizable groups and/or atoms attached to that specific olefinic carbon. The next-near-neighbor polarization effects are insignificant. This is a consequence of the attenuation of the field effects by the continuous polarizable electron cloud in which the point dipoles are embedded and the rapid reduction in field strength with increasing distance. If this electrostatic system is to be treated in terms of point dipole–point particle interactions, the polarizable matter must be separated into two distinct domains. The interaction of the point dipole situated on the olefinic carbon atom with a bonded atom or group is considered to be closely approximated by the electrostatic interaction of a point dipole with a dielectric sphere. The radius of this sphere is assigned the covalent radius of the bonding atom, its mean polarizability derived from macroscopic mean polarizabilities (see Table IV), and the distance between the point dipole center and the center of the dielectric sphere is equated to the internuclear bond distance. The ideal interaction energy must be corrected for the inhomogeneous field effects that have been discussed before. On the other hand, it is necessary to treat the polarizable matter centered around the olefinic carbon atom as a continuous dielectric, since the simple point dipole–point particle model is inadequate in the instance of spatial overlap of the point dipole and polarizable matter.

The polarization of the olefin bond is pictured as a shift of its bonding electron resulting in a formal charge separation. The resultant point dipole is embedded in both the core and bonding electrons of the carbon atom. A decreased screening effect will occur for the carbon atom sustaining the positive formal charge which sug-

(8) S. W. Benson and G. R. Haugen, *J. Amer. Chem. Soc.*, **87**, 4036 (1965).

gests that the electron in this domain experiences an increase in potential. On the other hand, the carbon atoms with the formal negative charge realize an increase in the screening effect and, accordingly, a decrease in potential acting on the electron in this region. The virial theorem (relating time average kinetic energy and potential) and conservation of angular momenta (relating time average kinetic energy and radius) suggest that the time average volume occupied by the electrons in the vicinity of the carbon atom with negative formal charge will be increased while a decrease will occur for the atom with the positive formal charge. In conjunction with these spatial modifications, the reciprocal dependence of dielectric constant and force constant compels an increase in dielectric constant in the region of the carbon atom with negative formal charge and concurrently a decrease in the dielectric constant for the vicinity of the positive formal charge. The energy of polarization will be considered in separate parts in order to elucidate the effects of each aggregate of polarizable matter on the stabilization.

*A. Energy Necessary to Polarize the Double Bond.* The classical electrostatic derivation of the energy of an induced dipole in a polarizing field[3] is used to evaluate this term

$$w_1 = \frac{1}{2}\frac{(332.0)(1.40)^2(1/2)^2}{2.80} \text{ kcal/mol}$$
$$= 29.05 \text{ kcal/mol}$$

where the logitudinal polarizability (2.80 Å$^3$), the olefinic carbon atom transition state internuclear distance (1.40 Å), and the formal charge residing on the olefinic carbon atoms in the transition state ($\pm 1/2$ electron) are substituted for $\alpha$, $d$, and $q$, respectively. This is the work necessary to generate the formal charge separation in the polarizable matter surrounding the olefinic carbon atoms.

*B. Energy of Interaction of Olefinic Carbon Point Dipole with a Polarizable Hydrogen Atom Attached to This Carbon Atom.* The bonded hydrogen atom is depicted as a dielectric sphere with a radius equal to its covalent radius. The ratio of the radius of the dielectric sphere to the separation between the point dipole and the center of the sphere is 0.29, since the carbon–hydrogen bond length and the hydrogen atom covalent radius are 1.09 Å and 0.32 Å, respectively. Therefore, the correction factor, $\sum_{l=0}^{\infty} \frac{l(\epsilon+2)(l+1)^2}{4[l(\epsilon+1)+1]}\left(\frac{a}{S}\right)^{2l-2}$, in eq 13 is 1.29. An evaluation of the stabilization energy of this hydrogen atom on the point dipole situated on the olefinic carbon atom can be obtained by a slight modification of this equation[9]

$$w_2(H) = -\frac{(332.0)(1.29)(0.38)(1.40)^2(1/2)^2}{(1.09)^6(4)} \times (3/2\cos^2 60 + 1/2)f_{\pm} \text{ kcal/mol}$$
$$= -\{10.39 \text{ kcal/mol per H atom}\}f_{\pm} \quad (14)$$

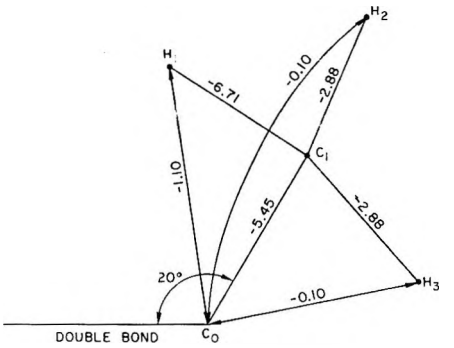


Figure. 3. The pairwise interaction of a methyl group attached to a carbon atom sustaining a point dipole. Note: Pairwise stabilization energy is in units of kcal/mol. Notation: $C_0$, $C_1$, $H_j$ represent the olefinic carbon atom sustaining a point dipole, the "methyl group" carbon atom, the "methyl group" hydrogen atom j, respectively. The selected bond lengths are from the "Table of Interatomic Distances and Configurations in Molecules and Ions," Special Publication No. 11, The Chemical Society, Burlington House, W. 1, London, 1958. Carbon–carbon bond, 1.541 Å and carbon–hydrogen bond, 1.090 Å. If the methyl group is rotated, the total stabilization energy of the three hydrogen bonds remains the same.

where the factor ($3/2\cos^2 60 + 1/2$) represents the angular dependence of the polarization energy with respect to the direction of the dipole and the line of centers. The factor $f_{\pm}$ expresses the diminution of the point dipole field due to the continuous dielectric surrounding the dipole; the positive and negative signs refer to the vicinity of the olefinic carbon atoms sustaining the positive and negative formal charges, respectively. It will be instructive, as for now, to treat this factor as a parameter and later relate it to other molecular properties.

*C. Energy of Interaction of Olefinic Carbon Point Dipole with an Attached Polarizable Methyl or Ethyl Group.* Next the energy of polarization of a methyl group by a dipole situated on the olefinic carbon atom will be considered, but before this calculation can be attempted, a polarizability of the dielectric sphere representing the methyl group must be estimated. Inasmuch as the methyl group is composed of a set of dielectric spheres representing the carbon atom and three attached hydrogen atoms which are asymmetrically located around the carbon atom, a weighted averaging must be utilized.

*1. The Effective Polarizability of a Dielectric Sphere Representing the Methyl Group.* The total interaction energy of a point dipole positioned on the carbon atom $C_0$ (see Figure 3) with an assemblage of dielectric spheres depicting the various atoms of the methyl group can

(9) Values substituted into eq 13. Factor converting the units, 332.0 Å kcal/mol/charge$^2$; mean polarizability of the bonded hydrogen atom, 0.38 Å$^3$; olefinic carbon dipole, $1/2(1.40)(1/2)$ Å-charge; distance between dipole and center of dielectric sphere, 1.09 Å; angle between direction of dipole and line of centers, 60°.

be analyzed in terms of two particle interactions (see Appendix B). In particular, the total energy of interaction is a composite of the following terms.

(*a*) *The Primary Dipole–Dielectric Sphere Interaction.* The energy of interaction of the unpolarizable point dipole located on the olefinic carbon atom with each of the polarizable dielectric spheres can be evaluated by utilizing eq 13, if the angular dependence of the polarization energy is taken into account. The four possible interactions of this type are $W_a(C_0,C_1) = -5.45$ kcal/mol and $W_a(C_0,H_1) = W_a(C_0,H_2) = W_a(C_0,H_3) = -0.078$ kcal/mol. It is seen that this direct interaction of the dipole with the polarizable matter of the methyl group diminishes rapidly with increasing distance in such a way that the immediately adjacent atom (*i.e.*, carbon atom $C_1$) contributes the majority of the stabilization.

(*b*) *The Secondary Dipole–Dielectric Sphere Interaction.* Again, the basic eq 13 can be used, along with a factor representing the angular dependence of the polarization energy and a correction for the back polarization of the carbon atom by the induced dipoles in the hydrogen atoms, to determine the energy of interaction of the point dipole induced in carbon atom $C_1$ by the primary dipole on $C_0$ with the three dielectric spheres substituted for the hydrogen atoms. The values found for these three interactions are $W_b(C_1,H_1) = -6.71$ kcal/mol and $W_b(C_1,H_2) = W_b(C_1,H_3) = -2.88$ kcal/mol. Observe that the field effects of the dipole on the olefinic carbon are transmitted along the carbon–carbon bond, rather than a direct spatial effect. This must bear upon the relationship between the carbon–carbon bond length and its polarizability.

(*c*) *The Primary Dipole–Induced Dipole Interaction.* This is an examination of the energy of interaction of the primary dipole situated on $C_0$ with the induced dipole in each of the hydrogen atoms resulting from the primary dipole by way of the carbon atom $C_1$. That is, the primary dipole on $C_0$ induces a dipole onto carbon atom $C_1$, which in turn produces a dipole on the hydrogen atom by induction. It is the energy of interaction between these hydrogen atom dipoles and the primary dipole that is under consideration in this section, their values are $W_c(C_0,H_1) = -1.10$ kcal/mol and $W_c(C_0,H_2) = W_c(C_0,H_3) = -0.10$ kcal/mol. It is interesting to note that once more the field effects transmitted along the carbon–carbon bond outweighs the direct spatial propagation.

(*d*) *The Tri-Wise Interaction of the Hydrogen Atom Dipoles.* In Appendix D the total energy of interaction of the three induced hydrogen atom dipoles is evaluated by resolving the system into pairwise interactions. This energy is less than 1% of the total initial induced energy, $\Sigma_{i=1}^{3} W_b(C_1,H_i)$, and accordingly has been disregarded.

It will be prudent at this point to represent the methyl group as a dielectric sphere centered on the carbon atom with a radius equal to the covalent radius of the carbon atom and assign a weighted average for the polarizability. Handling the methyl group in this fashion restates the electrostatic model in terms of point dipoles and point aggregates of polarizable matter. The assignment of an average polarizability for the methyl group can be accomplished by determining the polarizability of a spherical dielectric that is equivalent in energy to the methyl group stabilization energy (see Appendix B)

$$\frac{-(1/2)\alpha(\mathrm{wt})\,\mathrm{corr}\left\{\frac{a(x)}{S}\right\}\mu^2}{S^6} G(C_0,x) = W_a(C_0,C_1) + \sum_{i=1}^{3}\{W_a(C_0,H_i) + W_b(C_1,H_i) + W_c(C_0,H_i)\} \quad (15)^{10}$$

and upon substitution

$$\frac{-(1/2)(332.0)\alpha(\mathrm{wt})(2.00)(1.40)^2(1/2)^2}{(1.541)^6(4)}\frac{7}{4} =$$

$$-19.46 \text{ kcal/mol}^{11}$$

Thus, we obtain $\alpha(\mathrm{wt}) = 3.72$ Å$^3$. Note that the apparent polarizability of a methyl group in a nonuniform field (3.72 Å$^3$) is nearly 72% larger than the polarizability in a uniform field (2.17 Å$^3$, see Table IV).

*2. The Effective Polarizability of a Dielectric Sphere Representing the Ethyl Group.* In a manner similar to that already discussed, the enhancement in the stabilization energy upon replacement of a methyl group hydrogen atom with another methyl group can be computed (see Appendix B). In particular, the stabilization energy of the original methyl group hydrogen atom is forfeited and supplanted with the stabilization of the subordinate methyl group (see Figure 4). The interaction energies, $W_a(C_0,H_3)$ (−0.078 kcal/mol), $W_c(C_0,H_3)$ (−0.10 kcal/mol), and $W_b(C_1,H_3)$ (−2.88 kcal/mol), are replaced with the series of interactions $W_b(C_1,C_2)$ (−1.08 kcal/mol), $W_b(C_2,H_3)$ (−1.57 kcal/mol), $W_b(C_2,H_4)$ (−0.64 kcal/mol), $W_b(C_2,H_5)$ (−0.64 kcal/mol), and $W_c(C_0,C_2)$ (−0.06 kcal/mol). Thus, the total stabilization energy of an ethyl group is −20.40 kcal/mol; less than 1 kcal/mol of extra stability is contributed by the subordinate methyl group. A restatement of the electrostatic polarization of the ethyl group, in terms of a dielectric sphere centered on the carbon atom $C_1$ and having a radius equal to the covalent radius of the carbon atom, assigns a weighted

(10) corr $\{a(x)/S\}$ denotes the correction factor $\Sigma_{l=0}^{\infty}[l(\epsilon+2)(l+1)^2/4(l(\epsilon+1)+1)][a(x)/S]^{2l-2}$.

(11) The same stabilization energy is obtained by allowing the hydrogen atoms to occupy all positions accessible by rotation of the methyl group.

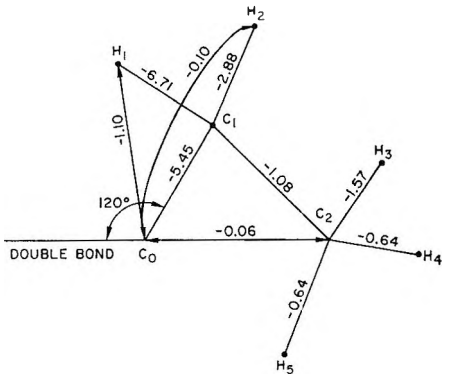


Figure 4. The pairwise interaction of an ethyl group attached to a carbon atom sustaining a point dipole. Note: Pairwise stabilization energy is in units of kcal/mol. Notation $C_0$, $C_1$, $H_j$ represent the olefinic carbon atom sustaining a point dipole, the methyl group carbon atom 1, its methyl group hydrogen atom j, respectively. The carbon atom $C_2$ projects out of the plane defined by the double bond and $C_0$–$C_1$ bond. This configuration is preferred over the one with the carbon atom $C_2$ in the plane, where the hydrogen atoms attached to carbon $C_2$ would sterically interfere with the hydrogens bonded to the olefinic carbons.

where the factor $(^3/_2 \cos^2 60 + {}^1/_2)$ represents the angular dependence of the polarization energy with respect to the direction of the dipole and the line of centers, the correction factor, $\sum_{l=0}^{\infty} \frac{l(\epsilon+2)(l+1)^2}{4[l(\epsilon+1)+1]}\left(\frac{a}{s}\right)^{2l-2}$, for the carbon–carbon bond is 2.00, and the term $f_\pm$ has been defined in a previous section.

*D. Repulsive Energy between Induced Dipoles in Adjacent Groups Bonded to the Same Olefinic Carbon Atom.* Böttcher's[3] equations for an idealized model of a pair of interacting point dipoles can be utilized to evaluate the repulsion work encountered in bringing the resultant induced dipoles in each group from infinite separation to their adjacent bonding position. The relationship between this repulsive energy and the electrostatic parameters is easily ascertained, if we consider only the interaction between the dipoles induced in the central atom of the groups, that is, the atom directly linked to a common olefinic carbon atom. This is a reasonable presumption in light of the rapid attenuation of the nonuniform fields inducing the dipoles. Direct substitution leads to relation 18. There are three conceivable types of adjacent group interactions, *i.e.*, $W_3\{H,H\}$, $W_3\{H,C\}$, and $W_3\{C,C\}$; the repulsive energy for each one is computed as shown

$$W_3\{x,y\} = \frac{\alpha\{x\}\,\alpha\{y\}\left(\mathrm{corr}\left\{\frac{a\{x\}}{s\{C_0,x\}}\right\}\right)^{1/2}\left(\mathrm{corr}\left\{\frac{a\{y\}}{s\{C_0,y\}}\right\}\right)^{1/2}\mu^2 G(C_0,x,y)}{(S\{C_0,x\})^3(S\{C_0,y\})^3(S\{x,y\})^3} f_\pm{}^{14} \quad (18)$$

average polarizability of 3.86 Å$^3$. This apparent polarizability of an ethyl group in a nonuniform field is only slightly less than the polarizability in a uniform field (4.09 Å$^3$).[12] In a uniform field, the total aggregate of polarizable matter of this group contributes equally to the polarization energy, while in a nonuniform field the leading carbon atoms and surrounding bonds contribute 96% of the stabilization.

The bonded methyl or ethyl group is depicted as a dielectric sphere with a radius equal to the covalent radius of the carbon atom (0.77 Å), having a weighted average polarizability of 3.72 Å$^3$ and 3.86 Å$^3$, respectively. Analogous to the evaluation of the stabilization energy of a hydrogen atom (eq 14), the methyl and ethyl groups have, respectively, the enhanced stabilization energy

$$W_2(\mathrm{Me}) = \frac{-(332.0)(2.00)(3.72)(1.40)^2(^1/_2)^2}{(1.541)^6(4)} \times (^3/_2 \cos^2 60 + {}^1/_2) f_\pm \text{ kcal/mol}^{13}$$

$$= -\{19.46 \text{ kcal/mol per Me group}\} f_\pm \quad (16)$$

and

$$W_2(\mathrm{Et}) = \frac{-(332.0)(2.00)(3.86)(1.40)^2(^1/_2)^2}{(1.541)^6(4)} \times (^3/_2 \cos^2 60 + {}^1/_2) f_\pm \text{ kcal/mol}^{13}$$

$$= -\{20.40 \text{ kcal/mol per Et group}\} f_\pm \quad (17)$$

$$W_3\{H,H\} = \frac{(0.38 \text{ Å}^3)^2(1.29)(1.40\text{Å})^2(^1/_2)^2 \times (3.435)(332.0 \text{ Å kcal/mol})}{(1.09 \text{ Å})^6(1.890 \text{ Å})^3(4)} f_\pm$$

$$= (+2.30 \text{ kcal/mol per pair of adjacent H, H}\} f_\pm$$

$$W_3\{H,C\} = \frac{(0.38 \text{ Å}^3)(1.04 \text{ Å}^3)(1.29)^{1/2}(2.00)^{1/2} \times (1.40 \text{ Å})^2(^1/_2)^2(3.375)(332.0 \text{ Å kcal/mol})}{(1.09 \text{ Å})^3(1.541 \text{ Å})^3(2.290 \text{ Å})^3(4)} f_\pm$$

$$= (+1.53 \text{ kcal/mol per pair of adjacent H, C}\} f_\pm$$

$$W_3\{C,C\} = \frac{(1.04 \text{ Å}^3)^2(2.00)(1.40 \text{ Å})^2(^1/_2)^2(3.435) \times (332.0 \text{ Å kcal/mol}) f_\pm}{(1.541 \text{ Å})^6(2.670 \text{ Å})^3(4)}$$

$$= \{+1.19 \text{ kcal/mol per pair of adjacent C, C}\} f_\pm$$

The magnitude of this primary interaction justifies the omission of the secondary repulsions.

(12) The mean polarizability of ethane, $C_2H_6$, is 4.47 Å$^3$. See Table IV. The mean poarizability of the ethyl group, $C_2H_5$, is $\alpha(C_2H_6) - \alpha(H) = 4.47 - 0.38 = 4.09$ Å$^3$.

**Table V:** Activation Energy of Generation of a Semiion Pair in an Olefinic Bond

| Olefins: Pos center | Olefins: Neg center | Preferred activation energy[a] | Activation energy calcd from electrostatic model: $f_+ = 0.65, f_- = 0.14$ $E_{act}$ energy | Δ | $f_+ = 0.60$ $f_- = 0.16$ $E_{act}$ energy | Δ | $f_+ = 0.58, f_- = 0.17$ $E_{act}$ energy | Δ |
|---|---|---|---|---|---|---|---|---|
| $CH_2$=$CH_2$ | | +14.50 | +14.60 | −0.1 | +15.01 | −0.5 | +15.19 | −0.7 |
| CHMe=$CH_2$ | | +9.90 | +8.05 | +1.9 | +9.10 | +0.8 | +9.48 | +0.4 |
| $CH_2$=CHMe | | +14.90 | +13.07 | +1.8 | +13.43 | +1.5 | +13.52 | +1.4 |
| $CMe_2$=$CH_2$ | | +2.46 | +1.94 | +0.5 | +3.45 | +1.0 | +4.02 | +1.6 |
| $CH_2$=$CMe_2$ | | +12.46 | +11.76 | +0.7 | +11.92 | +0.5 | +11.92 | +0.5 |
| CHMe=CHMe | | +7.46 | +6.68 | +0.8 | +7.53 | −0.1 | +7.81 | −0.3 |
| $CMe_2$=CHMe | | +1.40 | +0.56 | +0.8 | +1.88 | −0.5 | +2.35 | −1.0 |
| CHMe=$CMe_2$ | | +6.40 | +5.36 | +1.0 | +6.02 | +0.4 | +6.21 | −0.2 |
| CHEt=$CH_2$ | | +9.03 | +7.44 | +1.6 | +8.54 | +0.5 | +8.94 | +0.1 |
| $CH_2$=CHEt | | +14.03 | +12.94 | +1.1 | +13.28 | +0.8 | +13.36 | +0.7 |
| CMeEt=$CH_2$ | | +1.95 | +1.33 | +0.6 | +2.89 | −0.9 | +3.48 | −1.5 |
| $CH_2$=CMeEt | | +11.95 | +11.62 | +0.3 | +11.77 | +0.2 | +11.76 | +0.2 |
| Av dev | | | | 0.9 | | 0.6 | | 0.7 |

*E. The Total Enery of Generation of a Semiion Pair in an Olefinic Bond.* The work required to sustain 0.5 of a formal charge differential between the olefinic carbon atoms is comprised of the polarization energy of the olefinic bond, the stabilization energy of the polarizable matter bonded to the olefinic carbon atoms, and the dipole repulsion between the adjacent polarizable matter; or formulated in terms of a quantitative relationship

$$W_{\text{total}} = W_1 + (h_+)W_2\{\text{H}\} + (h_-)W_2\{\text{H}\} + (m_+)W_2\{\text{Me}\} + (m_-)W_2\{\text{Me}\} + (2 - m_+ - h_+)W_2\{\text{Et}\} + (2 - m_- - h_-)W_2\{\text{Et}\} + \left[\frac{(h_+ - 1)}{2} h_+f_+ + \frac{(h_- - 1)}{2} h_-f_-\right]W_3\{\text{H,H}\} + \left[\frac{(h_+ - 2)(h_+ - 1)}{2} f_+ + \frac{(h_- - 2)(h_- - 1)}{2} f_-\right] \times W_3\{\text{C,C}\} + [(2 - h_+)h_+f_+ + (2 - h_-)h_-f_-]W_3\{\text{C,H}\}$$

or

$$W_{\text{total}} = +29.05 + (-10.39)(h_+f_+ + h_-f_-) + (-19.46)(m_+f_+ + m_-f_-) + (-20.40)[(2 - m_+ - h_+)f_+ + (2 - m_- - h_-)f_-] + \left[\frac{(h_+ - 1)}{2} h_+f_+ + \frac{(h_- - 1)}{2} h_-f_-\right](2.30) + \left[\frac{(h_+ - 2)(h_+ - 1)}{2} f_+ + \frac{(h_- - 2)(h_- - 1)}{2} f_-\right] \times (1.19) + [(2 - h_+)h_+f_+ + (2 - h_-)h_-f_-] (1.53) \quad (19)$$

where $h_\pm$ and $m_\pm$ represent the number of hydrogen atoms and methyl groups attached to the positive and negative olefinic carbon atoms, respectively. In Table V, the work calculated from eq 19 is compared with the activation energy of formation of an olefinic semiion pair estimated from an empirical electrostatic approach. This permits an estimate of the parameters $f_+$ and $f_-$.

Recapitulating, work is necessary to polarize the $\pi$ electrons of the olefinic bond and to overcome the repulsive forces acting between the dipoles induced in the polarizable groups bonded to each olefinic carbon atom. The stabilization energy of the polarizable groups reduces this work. The contribution of each group to the total stabilization energy is moderated by the continuous dielectric surrounding the olefinic carbon atoms and the parameter $f_\pm$ is an evaluation of this moderation. These parameters $f_+$ and $f_-$ are a measure of the effective dielectric constant in the vicinity of the positively and negatively charged olefinic carbon atoms, respectively. This variation of the effective dielectric constant along the polarized olefinic bond is the explanation for the difference in the stabilization energy of a methyl group in the vicinity of the positive and negative charged olefinic carbon atom (see Tables V and VI).

## IV. The Molecular Dielectric Constant for the Vicinity of a Polarized Olefin Bond

Let us develop the relationship between the parameter $f_\pm$ and the pseudo-molecular dielectric constant associated with each end of the polarized olefinic bond. The solution of this problem necessitates the choice of a manageable model for the effects of a continuous dielectric. At this phase in the calculation, we have disregarded the polarizable matter in the vicinitv of

(13) Values substituted into eq 12. Factor converting the units, 332.0 Å kcal/mol/charge²; mean polarizability of the bonded methyl or ethyl group, 3.72 Å³ or 3.86 Å³, respectively; olefinic carbon dipole, ½(1.40) (½) Å-charge; distance between dipole and center of dielectric sphere, 1.541 Å; angle between direction of dipole and line of centers, 60°.

(14) See Appendixes for definition of terms. In particular, $G(C_0, x, y)$ represents the geometric factor relating the position of the induced dipoles with respect to each other and corr$\{a(x)/S\}$, the correction factor described in an earlier section.

**Table VI**

| Olefins compared | Stabilization energy, kcal/mol, calculated from electrostatic model $f_+ = 0.65, f_- = 0.14$ | $f_+ = 0.60, f_- = 0.16$ | $f_+ = 0.58, f_- = 0.17$ | $= 0.51, f_- = 0.17$[a] |
|---|---|---|---|---|
| (a) Methyl Group Stabilization of Positive Charged Olefinic Carbon Atom | | | | |
| $CH_2{=}CH_2$, $CHMe{=}CH_2$ | 6.6 | 5.9 | 5.7 | |
| $CHMe{=}CH_2$, $CMe_2{=}CH_2$ | 6.1 | 5.7 | 5.5 | |
| $CH_2{=}CHMe$, $CHMe{=}CHMe$ | 6.4 | 5.9 | 5.7 | |
| $CHMe{=}CHMe$, $CMe_2{=}CHMe$ | 6.1 | 5.7 | 5.5 | |
| | Av 6.3 | Av 5.8 | Av 5.6 | Av 5.0 |
| (b) Methyl Group Stabilization of Negative Charged Olefinic Carbon Atom | | | | |
| $CH_2{=}CH_2$, $CH_2{=}CHMe$ | 1.5 | 1.6 | 1.7 | |
| $CH_2{=}CHMe$, $CH_2{=}CMe_2$ | 1.3 | 1.5 | 1.6 | |
| $CHMe{=}CHMe$, $CHMe{=}CMe_2$ | 1.3 | 1.5 | 1.6 | |
| $CHMe{=}CH_2$, $CHMe{=}CHMe$ | 1.4 | 1.6 | 1.7 | |
| | Av 1.4 | Av 1.6 | Av 1.7 | Av 1.7 |
| (c) Ethyl Group Stabilization of Positive Charged Olefinic Carbon Atom | | | | |
| $CH_2{=}CH_2$, $CHEt{=}CH_2$ | 7.2 | 6.5 | 6.3 | |
| $CHMe{=}CH_2$, $CMeEt{=}CH_2$ | 6.7 | 6.2 | 6.0 | |
| | Av 7.0 | Av 6.3 | Av 6.2 | |
| (d) Ethyl Group Stabilization of Negative Charged Olefinic Carbon Atom | | | | |
| $CH_2{=}CH_2$, $CH_2{=}CHEt$ | 1.7 | 1.7 | 1.8 | |
| $CH_2{=}CMeH$, $CH_2{=}CMeEt$ | 1.5 | 1.7 | 1.8 | |
| | Av 1.6 | Av 1.7 | Av 1.8 | |

[a] Derived from isoelectronic dielectric constants of Neon (see Table VIII).

**Table VII:** The Estimated Molecular Dielectric Constant of the Polarized Olefinic Bond

| $f_+$ | $\epsilon_+$ | $f_-$ | $\epsilon_-$ | $\epsilon_-/\epsilon_+$ | $\epsilon_-/\epsilon_{Ne}$[a] | $\epsilon_+/\epsilon_{Ne}$[a] | $\epsilon_-/\epsilon_0$[c] | $\epsilon_+/\epsilon_0$[c] |
|---|---|---|---|---|---|---|---|---|
| 0.65 | 1.36 | 0.14 | 3.52 | 2.58 | 1.61 | 0.62 | 1.89 | 0.73 |
| 0.60 | 1.44 | 0.16 | 3.25 | 2.26 | 1.49 | 0.66 | 1.75 | 0.78 |
| 0.58 | 1.47 | 0.17 | 3.15 | 2.14 | 1.44 | 0.68 | 1.69 | 0.79 |
| (0.51)[b] | (1.6)[b] | (0.17)[b] | (3.1)[b] | (1.94)[b] | (1.42)[b] | (0.74) | ... | ... |

[a] $\epsilon_{Ne}$ represents the molecular dielectric constant of the neon atom, see Table III. [b] Values in parentheses derived from isoelectronic dielectric constant of the neon atom, see Table VIII. [c] $\epsilon_0$ represents the molecular dielectric constant of an aromatic bonded carbon atom, $\overline{\underline{C}}$ (see Table IX).

**Table VIII:** Dielectric Constant of an Isoelectronic Series of Atoms

| $X^+$ | Radius,[c] Å | Polarizability,[b] Å³ | $\epsilon_+$[a] | $X^0$ | Radius,[c] Å | Polarizability,[b] Å³ | $\epsilon_0$[a] | $X^-$ | Radius,[c] Å | Polarizability,[b] Å³ | $\epsilon_-$[a] | $\epsilon_-/\epsilon_+$ | $\epsilon_-/\epsilon_0$ | $\epsilon_+/\epsilon_0$ |
|---|---|---|---|---|---|---|---|---|---|---|---|---|---|---|
| $Li^+$ | 0.60 | 0.03 | 1.48 | He | 0.93 | 0.211 | 2.06 | | | | | | | 0.72 |
| $Na^+$ | 0.95 | 0.196 | 1.89 | Ne | 1.12 | 0.398 | 2.18 | $F^-$ | 1.36 | 1.04 | 3.12 | 1.65 | 1.43 | 0.87 |
| $K^+$ | 1.33 | 0.88 | 2.79 | Ar | 1.54 | 1.63 | 3.42 | $Cl^-$ | 1.81 | 3.53 | 5.43 | 1.94 | 1.59 | 0.82 |
| $Rb^+$ | 1.48 | 1.56 | 3.79 | Kr | 1.69 | 2.48 | 4.18 | $Br^-$ | 1.95 | 4.97 | 7.14 | 1.88 | 1.71 | 0.91 |
| $Cs^+$ | 1.69 | 2.56 | 4.38 | Xe | 1.90 | 4.01 | 5.24 | $I^-$ | 2.16 | 7.55 | 10.0 | 2.28 | 1.91 | 0.84 |

[a] Dielectric constant, $\epsilon$, calculated from the equation, $\alpha = [(\epsilon - 1)/(\epsilon + 2)]r^3$, where $\alpha$ and $r$ represent the polarizability in Å³ and radius in Å, respectively. [b] "Landolt-Börnstein, Zahlenwerte und Funktionen. I. Band Atom und Molekular-Physik," 3. Teil Molekeln II. Molekular-repaktion und Elektrische Polarisierbarkeit. [c] L. Pauling, "The Nature of the Chemical Bond," Cornell University Press, Ithaca, N. Y., 1948.

the olefinic dipole. We have used a local external field to initially generate this dipole. Then we assumed that this unpolarizable dipole existed under vacuum and examined its interaction with a dielectric sphere representing an atom or group.

The immersion of the point dipole into a small spherical hole in an infinite medium of dielectric constant $\epsilon$ will modify the external potential by $3/(2\epsilon + 1)$.[15] Therefore, the desired relationship between the parameter $f_{\pm}$ and the molecular dielectric constant is

$$(f_{\pm})^{1/2} = \frac{3}{2\epsilon_{\pm} + 1} \qquad (20)$$

The molecular dielectric constants derived from this equation are tabulated in Table VII. A proper analysis demands the justification of these values. However, it is difficult to evaluate these quantities and we must be content with a qualitative comparison. The dielectric constants for an isoelectronic series of atoms are shown in Table VIII. Considering the approximations involved in evaluating the molecular dielectric constants; the ratios $\epsilon_-/\epsilon_0$, $\epsilon_+/\epsilon_0$, and $\epsilon_-/\epsilon_+$ for the olefinic carbon atoms are in satisfactory agreement with those for the isoelectronic series. The dielectric constant for carbon–carbon bonds in different states of hybridization can be evaluated by squaring the bond refractivities; see Table IX.

**Table IX:** Dielectric Constants of Carbon-Carbon Bonds

| Bond | $n$ (D line, 20°)[a] | $\epsilon_{bond}$ |
|---|---|---|
| C—C | 1.296 | 1.68 |
| $C\underset{0}{-}C$ | 2.73 | 7.45 |
| C=C | 4.15 | 17.2 |
| C≡C | 5.87 | 34.4 |
| —C | 0.648 | 0.42 |
| $\underset{0}{-}C$ | 1.365 | 1.86 |
| =C | 2.075 | 4.30 |
| ≡C | 2.935 | 8.61 |

[a] A. I. Vogel, W. T. Cresswell, G. H. Jeffery, and J. Leicester, *J. Chem. Soc.*, 514 (1952).

A comparison between $\epsilon_{\pm}$ and $\epsilon_{bond}$ (see Tables VII and IX) indicates that the environment in the vicinity of the positively charged carbon atom is interjacent to a single bonded carbon atom and an aromatic bonded carbon atom, while the environment of the negatively charged carbon atom is interjacent to an aromatic bonded carbon atom and an olefinic bonded carbon atom. Thus, the polarization of the olefinic bond increases the effective screening at one carbon atom while decreasing it at the other carbon atom. This results in a negative and positive effective nuclear charge at the respective carbon atoms, which enhances and decreases the dielectric constant in the vicinity of these atoms, respectively.

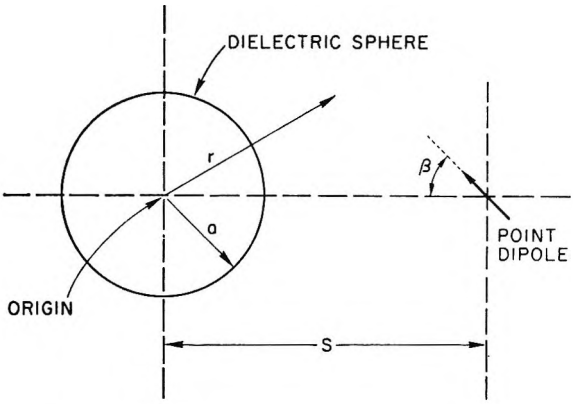


Figure 5.

## Appendix A. Work of Polarization of a Dielectric Sphere by a Point Dipole

The center of the dielectric sphere is chosen as the origin of the coordinate system, see Figure 5. In the absence of the dielectric sphere, the potential is represented by $\Phi_0$. When the distance $r$ is smaller than the distance of any charge to the origin, $\Phi_0$ can be expressed as

$$\Phi_0 = \sum_{l=0}^{\infty} \sum_{m=-l}^{l} a_l^{(m)} r^l P_l^{(m)}(\cos\theta) e^{jm\psi}\ ^{16} \qquad (1)$$

In the presence of the dielectric sphere, the potentials in the dielectric and outside the dielectric are represented by $\Phi_2$ and $\Phi_1$, respectively. These are expressed as[16]

$$\Phi_2 = \sum_{l=0}^{\infty} \sum_{m=-l}^{l} [A_l^{(m)} r^l + B_l^{(m)} r^{-l-1}] P_l^{(m)}(\cos\theta) e^{jm\psi} \qquad (2)$$

$$\Phi_1 = \Phi_0 + \Phi_1' \qquad (3)$$

$$\Phi_1' = \sum_{l=0}^{\infty} \sum_{m=-l}^{l} [C_l^{(m)} r^l + D_l^{(m)} r^{-l-1}] P_l^{(m)}(\cos\theta) e^{jm\psi} \qquad (4)$$

Equation 4 holds for all values of $r$ greater than $a$, but less than $s$. The boundary conditions are the following[16] at infinite $(\Phi_1')_{r\to\infty} = 0$ and at the origin $(\Phi_2)_{r=0}$ is finite. These conditions require the constants $C_l^{(m)}$ and $B_l^{(m)}$ to equal zero for all values of $m$ and $l$. The boundary conditions at the surface of the sphere are[16] $(\Phi_2)_{r=a} = (\Phi_1)_{r=a}$ and $\epsilon(\partial\Phi_2/\partial r)_{r=a} = (\partial\Phi_1/\partial r)_{r=a}$. These conditions permit the determination of the constants $A_l^{(m)}$ and $D_l^{(m)}$, and substitution into eq 2, 3, and 4 gives the following expressions

$$\Phi_2 = \sum_{l=0}^{\infty} \sum_{m=-l}^{l} \frac{2l+1}{(\epsilon+1)l+1} \times a_l^{(m)} r^l P_l^{(m)}(\cos\theta) e^{jm\psi} \qquad (5a)$$

(15) S. Flugge, "Handbuch der Physik," Band XVII, Dielektrika, Springer-Verlag, Berlin, 1956.

(16) C. J. F. Böttcher, "Theory of Electric Polarization," Elsevier Publishing Co., Amsterdam, 1952, p 102.

and

$$\Phi_1 = \sum_{l=0}^{\infty} \sum_{m=-l}^{l} \left[ a_l^{(m)} r^l - \frac{(\epsilon - 1)l}{(\epsilon + 1)l + 1} a^{2l+1} \times a_l^{(m)} r^{-l-1} \right] P_l^{(m)}(\cos\theta) e^{jm\psi} \quad (6a)$$

The problem is reduced to the derivation of the potential of an ideal dipole under vacuum, expressed as a function of the distance to an arbitrary origin (see Figure 6).

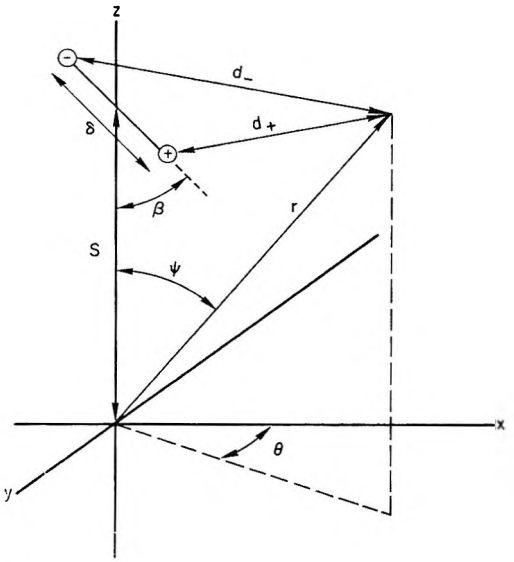


Figure 6.

It can be shown that for the point dipole approximation, $\lim \delta/s \to 0$

$$\Phi_0 = (+\mu \cos\beta) \sum_{l=0}^{\infty} l \frac{s^{l-1}}{r^{l+1}} P_l(\cos\theta) \text{ for } r > s$$

and $\lim \delta/s \to 0$

$$\Phi_0 = (-\mu \cos\beta) \sum_{l=0}^{\infty} (l+1) \frac{r^l}{s^{l+2}} P_l(\cos\theta) \text{ for } r < s$$

Consequently, $a_l^{(m)} = 0$ for $m \neq 0$ and all values of $l$. This simplifies eq 5a and 6a

$$\Phi_2 = \sum_{l=0}^{\infty} \frac{2l+1}{(\epsilon+1)l+1} a_l r^l P_l(\cos\theta) \quad (5b)$$

$$\Phi_1 = \sum_{l=0}^{\infty} \left[ a_l r^l - \frac{(\epsilon-1)l}{(\epsilon+1)l+1} \times r^{-l-1} a^{2l+1} a_l \right] P_l(\cos\theta) \quad (6b)$$

The potential of a point dipole under vacuum can be represented by a converging series:[17] for the domain $r > s$

$$\Phi_0 = \mu \cos\beta \sum_{l=0}^{\infty} l \frac{s^{l-1}}{r^{l+1}} P_l(\cos\theta) \quad (7)$$

Consequently, $a_l = -\{[\mu \cos\beta(l+1)]/s^{l+2}\}$ and for domain $r < s$

$$\Phi_0 = -\mu \cos\beta \sum_{l=0}^{\infty} (l+1) \frac{r^l}{s^{l+2}} P_l(\cos\theta) \quad (8)$$

Consequently, $r^l a_l = -\{[\mu \cos\beta(l+1)r^l]/s^{l+2}\}$. Equations 5b and 6b can be reduced to the following expressions for the case of complete symmetry about the $z$ axis ($\cos\beta = 1$)

$$\Phi_2 = -\mu \sum_{l=0}^{\infty} \left[ \frac{(2l+1)l+1}{(\epsilon+1)l+1} \right] \frac{r^l}{s^{l+2}} P_l(\cos\theta) \quad (6)$$

$$\Phi_1 = -\mu \sum_{l=0}^{\infty} \left[ \frac{(l+1)r^l}{s^{l+2}} - \frac{(\epsilon-1)l(l+1)}{(\epsilon+1)l+1} \frac{a^{2l+1} r^{-l-1}}{s^{l+2}} \right] P_l(\cos\theta) \quad (10)$$

The components $(E_2)_r$ and $(E_2)_\theta$ of the electric field in the dielectric are given by

$$(E_2)_r = -\frac{\partial \Phi_2}{\partial r} = + \mu \sum_{l=0}^{\infty} \frac{(l+1)(2l+1)}{(\epsilon+1)l+1} \frac{l r^{l-1}}{s^{l+2}} P_l(\cos\theta) \quad (11)$$

and

$$(E_2)_\theta = -\frac{1}{r} \frac{\partial \Phi_2}{\partial \theta} = + \mu \sum_{l=0}^{\infty} \frac{(l+1)(2l+1)}{(\epsilon+1)l+1} \frac{r^{l-1}}{s^{l+2}} \sin\theta \frac{dP_l(\cos\theta)}{d(\cos\theta)} \quad (12)$$

In the absence of a dielectric, the components of the electric field become the following

$$(E_0)_r = -\frac{\partial \Phi_0}{\partial r} = \mu \sum_{l=0}^{\infty} \frac{(l+1)l r^{l-1}}{s^{l+2}} P_l(\cos\theta)$$

and

$$(E_0)_\theta = -\frac{1}{r} \frac{\partial \Phi_0}{\partial \theta} = \mu \sum_{l=0}^{\infty} \frac{(l+1) r^{l-1}}{s^{l+2}} \sin\theta \frac{dP_l(\cos\theta)}{d(\cos\theta)}$$

The work of polarization of a dielectric is calculatable from the relation[18]

$$w = -\frac{1}{8\pi} \int \bar{E}_0 \cdot \bar{E}_2 (\epsilon - 1) dv \quad (13)$$

or

(17) See ref 16, p 22.

(18) See ref 16, p 136.

$$w = -\frac{1}{8\pi}\int_a^\infty \int_0^\pi \{(E_0)_r(E_2)_r + (E_0)_\theta(E_2)_\theta\}(\epsilon - 1)2\pi r^2 \sin\theta \, dr d\theta \quad (14)$$

Substitution of the components of $\bar{E}_0$ and $\bar{E}_2$ into eq 14 gives

$$w = -\frac{(\epsilon-1)\mu^2}{4}\sum_{l=0}^{\infty}\sum_{k=0}^{\infty}\left[\frac{(l+1)(2l+1)(k+1)}{\{(\epsilon+1)l+1\}s^{l+k+4}}\right]\times \int_0^a (r^{l+k})dr \cdot \int_{-1}^{+1}\left\{lkP_l(\tau)P_l(\tau) + (1-\tau^2)\frac{dP_l(\tau)}{d(\tau)}\frac{dP_k(\tau)}{d(\tau)}\right\}d\tau \quad (15)$$

where $\tau$ represents $\cos\theta$. The legendre functions have the following properties[19]

$$\int_{-1}^{+1}(1-\tau^2)\frac{dP_l(\tau)}{d\tau}\frac{dP_k(\tau)}{d\tau}d\tau = \int_{-1}^{+1}P_k(\tau)l(l+1)P_l(\tau)d\tau$$

and the orthogonal relation

$$\int_{-1}^{+1}P_l(\tau)P_k(\tau)d\tau = \frac{2}{2l+1}\delta_{kl}, \begin{cases} k = l, \delta_{kl} = 1 \\ k \neq l, \delta_{kl} = 0 \end{cases}$$

which can be used to reduce eq 15. The simplification of eq 15 results in the relation

$$w = -\frac{2\mu^2\alpha}{s^6}\sum_{l=0}^{\infty}\frac{(\epsilon+2)l(l+1)^2}{4[(\epsilon+1)l+1]}\left(\frac{a}{s}\right)^{2l-2}$$

where $\alpha = ((\epsilon-1)/(\epsilon+2))a^3$.

## Appendix B. The Polarization of the Methyl and Ethyl Groups in Terms of Pairwise Interactions

*Methyl Group.* Böttcher[20] has derived the electrostatic interaction energy of two particle systems for the idealized model of point charges and point dipoles, situated at the centers of the particles. The inaccuracies in these models, when the distance between the particles is of the same order of magnitude as their radii, have been alleviated by the application of the correction derived in Appendix A. This correction factor is only dependent on the ratio of the covalent radius of atom y, $a(y)$, to the distance between centers of the atom y and the point dipole. The definitions of the notation used are depicted in the following list: $W(z,y)$ = interaction energy between particles z and y; $\alpha(y)$ = mean polarizability of atom y, units Å$^3$; $a(y)$ = covalent radius of atom y, units Å; $S(z,y)$ = distance between the centers of atoms z and y, units Å; corr$(a(y)/s(z,y))$ = denotes the correction factor[21]

$$\sum_{l=0}^{\infty}\frac{l(\epsilon+2)(l+1)^2}{4[l(\epsilon+1)+1]}\left[\frac{a(y)}{s(z,y)}\right]^{2l-2}$$

$\mu$ = formal dipole located on atom $C_0$, $^1/_2$(1.40 Å) ($^1/_2$ formal charge).

*(a) The Primary Dipole–Dielectric Sphere Interaction.* Energy of interaction of the original unpolarizable point dipole and a polarizable dielectric sphere

$$W_a(C_0,x) = -\frac{1}{2}\left\{\left(\alpha(x)\ \text{corr}\left(\frac{a(x)}{s(C_0,x)}\right)\mu^2\right)\Big/[s(C_0,x)]^6\right\}G(C_0,x)$$

The function $G(C_0,x)$[22] represents the angular dependence of the polarization energy upon the direction of the dipole at $C_0$ and the line of centers between $C_0$ and $x$.

The four possible interactions of this type are calculated below

$$W_a(C_0,C_1) = -\frac{1}{2}\frac{(1.04\ \text{Å}^3)(2.00)(1.40\ \text{Å})^2(^1/_2)^2}{(1.541\ \text{Å})^6(4)}\times \frac{7}{4}(332.0\ \text{Å kcal/mol}) = -5.45\ \text{kcal/mol}$$

and

$$W_a(C_0,H_1) = W_a(C_0,H_2) = W_a(C_0,H_3) = -\frac{1}{2}\frac{(0.38\ \text{Å}^3)(1.05)(1.40\ \text{Å})^2(^1/_2)^2}{(2.170\ \text{Å})^6(4)}(1.002)\times(332.0\ \text{Å kcal/mol}) = -0.078\ \text{kcal/mol}$$

*(b) The Secondary Dipole–Dielectric Sphere Interaction.* Energy of interaction of the induced point dipole situated on carbon $C_1$ and a polarizable dielectric sphere. (The back polarization of the carbon atom $C_1$ by the induced dipoles in the hydrogen atoms will be discussed in Appendix C; as for now, this effect is neglected.)

$$W_b(C_1,x) = -\frac{1}{2}\frac{\alpha(x)[\alpha(C_1)]^2\ \text{corr}\left[\frac{a(x)}{s(C_1,x)}\right]\times \text{corr}\left[\frac{a(C_1)}{s(C_0,C_1)}\right]\mu^2 G(C_0,C_1)G(C_1,x)}{[s(C_1,x)]^6[s(C_0,C_1)]^6}$$

where the functions $G(C_0,C_1)$ and $G(C_1,x)$[23] represent

(19) See ref 16, p 460

(20) See ref 16, pp 139–149.

(21) The interaction energy of a point dipole and a dielectric sphere (radius $a$) is equal to $W = -(2\alpha m^2/s^6)\text{corr}(a/s)$ (see Appendix A). This interaction could be reconsidered as the energy of an induced point dipole in a polarizing field ($\vec{E}$), $W = (1/2)\alpha\vec{E}\cdot\vec{E}$. Since the electric field of a point dipole pointing along the line of centers toward the dielectric sphere is $\vec{E} = (2\vec{m}/S^3)$ the energy of interaction becomes $W = -(2\alpha m^2/s^6)$. A comparison indicates that the correction factor inside the dielectric sphere for the electric field radiating from the point dipole is the square root of corr$(a/s)$.

(22) $G(C_0,C_1)$ and $G(C_0,H_i)$ represent the angular functions $(3\cos^2 60 + 1)$ and $(3[\cos^2 88.2][1 - 0.252(1 - \cos\gamma_i)]^2 + 1)$, respectively. $\cos\gamma_i = 1, -^1/_2$, and $-^1/_2$ for $i = 1, 2$, and 3.

(23) $G(C_0, C_1)$ and $G(C_1, x)$ represents the angular functions $(3\cos^2 60 + 1)^{1/2}$ and $(3.03\cos^2\gamma_i + 1.324)$, respectively. $\cos\gamma_i = 1, -^1/_2$, and $-^1/_2$ for $i = 1, 2$, and 3.

the angular dependence of the polarization energy upon the direction of the original and induced dipoles and the line of centers between the respective atoms. The evaluation of the interaction energy for each of the three hydrogens is portrayed below

$$W_b(C_1,H_1) = -\frac{1}{2}\frac{(0.38\ \text{Å}^3)(1.04\ \text{Å}^3)^2(1.29)\times(2.00)(1.40\ \text{Å})^2(1/2)^2}{(1.09\ \text{Å})^6(1.541\ \text{Å})^6(4)}\times\frac{\sqrt{7}}{2}(4.35)(332.0\ \text{Å kcal/mol})$$

$$= -5.44\ \text{kcal/mol}$$

(−6.71 kcal/mol corrected for back polarization, see Appendix C)

$$W_b(C_1,H_2) = W_b(C_1,H_3) = -\frac{1}{2}\frac{(0.38\ \text{Å}^3)(1.04\ \text{Å}^3)^2(1.29)(2.00)(1.40\ \text{Å})^2(1/2)^2}{(1.09\ \text{Å})^6(1.541\ \text{Å})^6(4)}\times\frac{\sqrt{7}}{2}(2.08)(332.0\ \text{Å kcal/mol}) = -2.60\ \text{kcal/mol}$$

(−2.88 kcal/mol corrected for back polarization, see Appendix C).

(c) *The Primary Dipole–Induced Dipole Interactions.* The energy of interactions of the original unpolarizable point dipole with the induced dipoles in the hydrogen atoms

$$W_c(C_0,x) = -\frac{1}{2}\frac{\alpha(x)\alpha(C_1)\left(\text{corr}\left[\frac{a(x)}{s(C_1,x)}\right]\right)^{1/2}\times\left(\text{corr}\left[\frac{a(C_1)}{s(C_0,C_1)}\right]\right)^{1/2}\mu^2}{[s(C_1,x)]^3[s(C_0,C_1)]^3[s(C_0,x)]^3}G(C_0,C_1,x)$$

where the function $G(C_0,C_1,x)$[24] represents the angular dependence of the magnitude and direction of the induced dipole in hydrogen atom $x$ with respect to the position of the original dipole on carbon atom $C_0$. Substituting the appropriate values, the three possible interaction energies become

$$W_c(C_0,H_1) = -\frac{1}{2}\frac{(0.38\ \text{Å}^3)(1.04\ \text{Å}^3)(1.29)^{1/2}\times(2.00)^{1/2}(1.40\ \text{Å})^2(1/2)^2}{(1.09\ \text{Å})^3(1.541\ \text{Å})^3(2.170\ \text{Å})^3(4)}\times(4.218)(332.0\ \text{Å kcal/mol}) = -1.10\ \text{kcal/mol}$$

and

$$W_c(C_0,H_2) = W_c(C_0,H_3) = -\frac{1}{2}\frac{(0.38\ \text{Å}^3)(1.04\ \text{Å}^3)(1.29)^{1/2}\times(2.00)^{1/2}(1.40\ \text{Å})^2(1/2)^2(0.376)}{(1.09\ \text{Å})^3(1.541\ \text{Å})^3(2.170\ \text{Å})^3(4)}\times(332.0\ \text{Å kcal/mol}) = -0.098\ \text{kcal/mol}$$

*Ethyl Group.* The pairwise interaction energies of a subordinate methyl group have been calculated by a method similar to that described herein above. Tabulated below are the relevant equations

$$W_b(C_1,C_2) = -\frac{1}{2}\frac{\alpha(C_2)[\alpha(C_1)]^2\text{corr}\left[\frac{a(C_2)}{s(C_1,C_2)}\right]\times\text{corr}\left[\frac{a(C_1)}{s(C_0,C_1)}\right]\mu^2G(C_0,C_1)G(C_1,C_2)}{[s(C_1,C_2)]^6[s(C_0,C_1)]^6}$$

$$= -\frac{1}{2}\frac{(1.04\ \text{Å}^3)^3(2.00)^2(1.40\ \text{Å})^2(1/2)^2}{(1.541\ \text{Å})^{12}(4)}\times\frac{7}{(4)}(1.178)(332.0\ \text{Å kcal/mol})$$

$$= -1.04\ \text{kcal/mol}$$

$$W_b(C_2,H_t) = -\frac{1}{2}\frac{\alpha(H_i)[\alpha(C)]^4\,\text{corr}\left[\frac{a(H_i)}{s(C_2,H_i)}\right]\times\left(\text{corr}\left[\frac{a(c)}{s(C,C)}\right]\right)^2\mu^2G(C_0,C_1)\times G(C_1,C_2)G(C_2,H_i)}{[s(C_2,H_t)]^6[s(C,C)]^{12}}$$

$$W_b(C_2,H_3) = -\frac{1}{2}\frac{(0.38\ \text{Å}^3)(1.04\ \text{Å}^3)^4(1.29)\times(2.00)^2(1.40\ \text{Å})^2(1/2)^2}{(1.09\ \text{Å})^6(1.541\ \text{Å})^{12}(4)}\times\frac{7}{(4)}(1.178)(3.990)(332.0\ \text{Å kcal/mol})$$

$$= -1.26\ \text{kcal/mol}$$

$$W_b(C_2,H_4) = W_b(C_2,H_5) = -\frac{1}{2}\frac{(0.38\ \text{Å}^3)(1.04\ \text{Å}^3)^4(1.29)(2.00)^2(1.40\ \text{Å})^2(1/2)}{(1.09\ \text{Å})^6(1.541\ \text{Å})^{12}(4)}\times\frac{7}{(4)}(1.178)(1.748)(332.0\ \text{Å kcal/mol})$$

$$= -0.55\ \text{kcal/mol}$$

$$W_c(C_0,C_2) = -\frac{1}{2}\frac{\alpha(C_c)\alpha(C_1)\left(\text{corr}\left[\frac{a(C_2)}{s(C_1,C_2)}\right]\right)^{1/2}\times\left(\text{corr}\left[\frac{a(C_1)}{s(C_0,C_1)}\right]\right)^{1/2}\mu^2G(C_0,C_1,C_2)}{[s(C_1,C_2)]^3[s(C_0,C_1)]^3[s(C_0,C_2)]^3}$$

$$= -\frac{1}{2}\frac{(1.04\ \text{Å}^3)^2(2.00)(1.40\ \text{Å})^2(1/2)^2}{(1.541\ \text{Å})^6(2.675\ \text{Å})^3(4)}\times\frac{\sqrt{7}}{(2)}(0.126)(332.0\ \text{Å kcal/mol})$$

$$= -0.06\ \text{kcal/mol}$$

(24) $G(C_0, C_1, x)$ has the value of +4.218 for hydrogen $H_1$ and + 0.376 for the hydrogens $H_2$ and $H_3$.

Correcting for back polarization enhances the following interaction energies (see Appendix C): $W_b(C_1,C_2) = -1.08$ kcal/mol; $W_b(C_2,H_3) = -1.57$ kcal/mol; $W_b(C_2,H_4) = W_b(C_2,H_5) = -0.64$ kcal/mol.

A comparison of the distribution of the electrostatic stabilization energy in the methyl group and ethyl group is portrayed below in Table X.

**Table X:**

| Pairwise interaction energy | Methyl group, energy | Ethyl group, energy |
|---|---|---|
| $W_a(C_0, C_1)$ | −5.45 kcal/mol | −5.45 kcal/mol |
| $W_a(C_0, H_1)$ | −0.08 kcal/mol | −0.08 kcal/mol |
| $W_a(C_0, H_2)$ | −0.08 kcal/mol | −0.08 kcal/mol |
| $W_a(C_0, H_3)$ | −0.08 kcal/mol | [c] |
| $W_b(C_1, H_1)$ | −6.71 kcal/mol[a] | −6.71 kcal/mol[a] |
| $W_b(C_1, H_2)$ | −2.88 kcal/mol[a] | −2.88 kcal/mol[a] |
| $W_b(C_1, H_3)$ | −2.88 kcal/mol[a] | [c] |
| $W_b(C_1, C_2)$ | [c] | −1.08 kcal/mol[a] |
| $W_b(C_2, H_3)$ | [c] | −1.57 kcal/mol[a] |
| $W_b(C_2, H_4)$ | [c] | −0.64 kcal/mol[a] |
| $W_b(C_2, H_5)$ | [c] | −0.64 kcal/mol[a] |
| $W_c(C_0, H_1)$ | −1.10 kcal/mol | −1.10 kcal/mol |
| $W_c(C_0, H_2)$ | −0.10 kcal/mol | −0.10 kcal/mol |
| $W_c(C_0, H_3)$ | −0.10 kcal/mol | [c] |
| $W_c(C_0, C_2)$ | [c] | −0.06 kcal/mol |
| $W_d(H_1, H_2)$ | [b] | [b] |
| $W_d(H_1, H_3)$ | [b] | [b] |
| $W_d(H_2, H_3)$ | [b] | [b] |
| $W_d(H_3, H_4)$ | [b] | [b] |
| $W_d(H_3, H_5)$ | [b] | [b] |
| $W_d(H_4, H_5)$ | [b] | [b] |
| Total stabilization energy | −19.46 kcal/mol | −20.40 kcal/mol |

[a] These interaction energies have been corrected for back polarization, see Appendix C. [b] These interaction energies have been assumed to be negligible (see Appendix D). [c] In this group the interaction is missing.

## Appendix C. The Back Polarization of the Carbon Atom $C_1$ by the Induced Dipoles in the Hydrogen Atoms Attached to This Atom

Böttcher (see Appendix B, ref 20) idealized models of two particle electrostatic interactions allows for the occurrence of back polarization. The idealized interaction energy between a dipole, $\vec{m}$, with a polarizability, $\beta$, and a dielectric sphere of polarizability, $\alpha$, separated by a distance, $s$, is

$$W = -\frac{3\alpha m^2 \cos^2\theta \cos^2\gamma}{2s^6}\Gamma_A - \frac{1}{2}\frac{\alpha m^2}{s^6}\Gamma_B$$

where $\cos^2\gamma$ has the values 1, $^1/_4$, and $^1/_4$, depending on the position of the hydrogen atoms around the methyl group axis, *i.e.*, $H_1$, $H_2$, and $H_3$, and $\theta$ represents the angle between the dipole, $\vec{m}$, and the direction of centers, $\vec{s}(C_1, H_1)$. The back polarization terms $\Gamma_A$ and $\Gamma_B$ are explicitly

$$\Gamma_A = \left(\frac{1}{1-\frac{4\alpha\beta}{s^6}}\right)\left[\left(\frac{1}{1-\frac{\alpha\beta}{s^6}}\right) - \frac{\left(\frac{4\alpha\beta}{s^6}\right)^2}{\left(1-\frac{4\alpha\beta}{s^6}\right)\left(1+\frac{\alpha\beta}{s^6}\right)}\right]$$

and $\Gamma_B = 1/[1 - \alpha\beta/s^6]$. In the case of negligible back polarization, the interaction energy reduces to the familiar form

$$\lim_{\beta\to 0} W = (1/2)(\alpha m^2/s^6)(3\cos^2\theta\cos^2\gamma + 1)$$

Attention must be drawn to the appropriate polarizabilities to be substituted in the back polarization terms. $\alpha$ refers to the mean polarizability of the hydrogen atom and a value of 0.38 Å$^3$ has been utilized in this article. However, the concept of pairwise interaction dictates that the back polarization of the carbon atom be considered separately for each carbon–hydrogen bond, *i.e.*, the polarizability of the carbon atom associated with each carbon–hydrogen bond is 0.26 Å$^3$, see Table IV. On substitution, the magnitudes of the back polarization terms are found to be $\Gamma_A = 1.31$ and $\Gamma_B = 1.06$. These factors enhance the interaction energies, $W_b(C_1,x)$ derived in Appendix B, as evidenced here; $W_b(C_1,H_1) = -6.71$ kcal/mol, an increase of 23%, and $W_b(C_1,H_2) = W_b(C_1,H_3) = -2.88$ kcal/mol, an increase of 11%.

## Appendix D. The Interaction Energy of the Hydrogen Atom Dipoles in the Methyl Group

Böttcher (see Appendix B, ref 20) idealized models of two particle interaction allow the determination of the dipole–dipole interaction of the hydrogen atoms taken in pairs

$$W(H_1,H_2) = W(H_1,H_3) = -\frac{1}{3^{3/2}}\frac{\alpha^2 m^2}{s^9}\left[\frac{15}{4}\cos^2\theta - 1\right]$$

and

$$W(H_2,H_3) = -\frac{1}{3^{3/2}}\frac{\alpha^2 m^2}{s^9}\left[-\frac{30}{8}\cos^2\theta - 1\right]$$

where $\theta$ represents the angle between the dipole, $\vec{m}$, located on carbon atom, $C_1$, and the direction between centers, $\vec{s}(C_1,H_1)$. Now let us compare the total energies

$$\frac{1}{2}\sum_{\substack{i=1\\ i\neq j}}^{3}\sum_{j=1}^{3} W(H_i,H_j) \text{ and } \sum_{i=1}^{3} W_b(C_1,H_1)$$

It is obvious that

$$\frac{1}{2}\sum_{\substack{i=1\\ i\neq j}}^{3}\sum_{j=1}^{3} W(H_i,H_j) = -\frac{\alpha^2 m^2}{s^9}\frac{1}{\sqrt{3}}\left[\frac{10}{8}\cos^2\theta - 1\right]$$

and

$$\sum_{i=1}^{3} W_b(C_1,H_i) = -\frac{\alpha m^2}{s^6} 3\left[\frac{3}{2}\cos^2\theta + 1\right]$$

consequently

$$\frac{1}{2}\sum_{\substack{i=1\\ i\neq j}}^{3}\sum_{j=1}^{3} W(H_i,H_j) = \frac{\alpha[{}^{10}/_{8}\cos^2\theta - 1]}{3^{3/2}s^3({}^{3}/_{2}\cos^2\theta + 1)}\sum_{i=1}^{3} W_b(C_1,H_i) =$$

$$\frac{(0.38\ \text{Å}^3)({}^{10}/_{8}\cos^2 41 - 1)}{3^{3/2}(1.09\ \text{Å})^3({}^{3}/_{2}\cos^2 41 + 1)}\sum_{i=1}^{3} W_b(C_1,H_i)$$

$$= -0.0087\sum_{i=1}^{3} W_b(C_1,H_i)$$

The total interaction energy involved in the hydrogen atom induced dipoles is less than 1% of the total interaction energy between the carbon atom $C_1$ dipole and the three hydrogen atoms.

# Effects of Dissolved Oxygen on the Electron Spin Resonance Signal Intensities of Trapped Hydrogen Atoms and Some of Their Reactions in Acidic Ice Matrices

by D. E. Holmes,[1] N. B. Nazhat, and J. J. Weiss

*Laboratory of Radiation Chemistry, School of Chemistry, The University, Newcastle upon Tyne, England*
*(Received January 6, 1969)*

Electron spin resonance spectra of irradiated acidic ices saturated with oxygen and nitrogen show that the formation and the yields of trapped hydrogen atoms at 77°K are practically independent of dissolved oxygen while their esr signal intensities are dependent, under certain conditions, on the oxygen content and the applied microwave power. During annealing of irradiated ices containing thymine and oxygen at 100°K, hydrogen atoms react to form thymine hydrogen atom adduct radicals and hydroperoxide radicals. Upon annealing to 175°K, oxygen reacts with the thymine hydrogen atom adduct radicals to form 5,6-dihydrothymyl peroxide radicals. These reactions of hydrogen atoms and oxygen, in irradiated ices at 77–195°K, are discussed in relation to similar reactions in the liquid phase.

## Introduction

Hydrogen atoms are formed and trapped in γ-irradiated, frozen, acidic solutions (ices).[2-4] The hydrogen atom yields reportedly are not affected by dissolved oxygen.[2,3a,5] Upon annealing and release of the hydrogen atoms from their traps, the atoms can add to the 5,6 double bond of dissolved thymine to form 5,6-dihydrothymyl-5-yl radicals (thH·).[6-8] This communication describes the increase in the "apparent" yield of trapped hydrogen atoms ($H_t$) and the decrease in the yield of dihydrothymyl radicals when nitrogen-saturated acidic ices containing thymine are saturated with oxygen before freezing and irradiation.

## Methods

Reagent grade $H_2SO_4$, $O_2$, $N_2$, and thymine (th) were used with triply distilled water to make the solutions. The samples were 1 *M* in $H_2SO_4$ and were bubbled with the appropriate gas for 15 min before freezing into small ice cylinders as previously described.[9] These cylinders were then irradiated in sealed, nitrogen-flushed, Pyrex tubes at 77°K with $^{60}Co$ γ rays to a total dose of approximately 3 Mrads at a dose rate of 0.15 Mrad/hr. After irradiation, the samples were transferred, without allowing to warm up, into a standard electron spin reso-

(1) Fellow in Radiological Research of the James Picker Foundation, 1966–1968. Present address: Department of Biochemistry & Biophysics, University of Hawaii, Honolulu, Hawaii 96822.

(2) H. Zeldes and R. Livingston, *Phys. Rev.*, **96**, 1702 (1954).

(3) (a) L. Kevan, P. N. Moorthy, and J. J. Weiss, *Nature*, **199**, 689 (1963); (b) J. Zimbrick and L. Kevan, *J. Chem. Phys.*, **47**, 5000 (1967).

(4) P. N. Moorthy and J. J. Weiss in "Solvated Electron," Advances in Chemistry Series, No. 50, American Chemical Society, Washington, D. C., 1965, p 180.

(5) R. Livingston and A. J. Weinberger, *J. Chem. Phys.*, **33**, 499 (1960).

(6) C. Elston, Ph.D. Dissertation, The University, Newcastle upon Tyne, 1967.

(7) D. E. Holmes and J. J. Weiss, *Int. J. Radiat. Biol.*, **14**, 187 (1968).

(8) D. E. Holmes, B. N. Nazhat, and J. J. Weiss, *Radiat. Res.*, **35**, 510 (1968).

(9) L. Kevan, P. N. Moorthy, and J. J. Weiss, *J. Amer. Chem. Soc.*, **86**, 771 (1964).

nance (esr) dewar with a thin-walled quartz tip which fitted into the esr cavity. Annealing was usually accomplished by transferring the irradiated samples to a container immersed in Dry Ice at 195°K. However, in some cases the samples were annealed by removing the liquid nitrogen from the dewar for predetermined lengths of time which allowed the samples to warm to thermocouple-calibrated temperatures. Esr spectra were recorded with the samples at 77°K. Most esr measurements were made with a Varian E-3 spectrometer. Microwave power values were taken directly from a calibrated dial inherent with the spectrometer. A Varian V-4502-13 esr spectrometer in the low-power configuration was used for the $H_t$ measurements below 1-mW rf power. The low-power values were calibrated using an HP 431B power meter. The magnetic field sweep and $g$-factor calibrations utilized peroxylamine disulfonate and diphenylpicrylhydrazyl (DPPH), respectively. However, for more accurate measurements of $g$ factors, the klystron frequency of the V-4502 spectrometer was monitored by HP 5253B and HP 2590B frequency converters coupled to an HP 5245L electronic counter while the magnetic field was calibrated using a proton resonance gauss meter coupled to the electronic counter.

## Results and Discussion

Figure 1a shows the first-derivative esr spectrum of nitrogen-saturated, acidic ice ($N_2$–ice) after irradiation. Figure 1b shows a similar spectrum after oxygen saturation ($O_2$–ice) and irradiation. A comparison of Figure 1a with b shows almost no differences in the central regions of the spectra which result from hydroxyl-free radicals as well as $SO_4^-$ radical ions.[4] The lines of the $H_t$ doublet are separated by approximately 505 G and have satellite lines as previously reported.[10] When thymine ($10^{-2}$ $M$) is included in the ices (th–ices), esr spectra, $H_t$ ratios, and $H_t$ line widths are observed which are similar to those obtained from samples containing no thymine. Table I gives the relative intensities and line widths of the main $H_t$ line, downfield, at 1-mW rf power which were observed in each sample under conditions of partial power saturation. The observed $H_t$ signals differ in that the intensities in the $O_2$–ices are larger than in the $N_2$–ices. This is unusual, since oxygen might be expected to scavenge radiation-released electrons by reaction 1, which are responsible for hydrogen atom formation[4] according to reaction 2

$$e^- + O_2 \longrightarrow O_2^- \xrightarrow{H^+} HO_2\cdot \qquad (1)$$

$$e^- + HSO_4^- \longrightarrow H_t + SO_4^{2-} \qquad (2)$$

$$e^- + H^+ \longrightarrow H \longrightarrow H_t\cdot \qquad (3)$$

The concentrations of $O_2$ and $HSO_4^-$ are approximately $10^{-3}$ and 1 $M$, respectively. Although the rate constants of these reactions in ice at 77°K are not known,

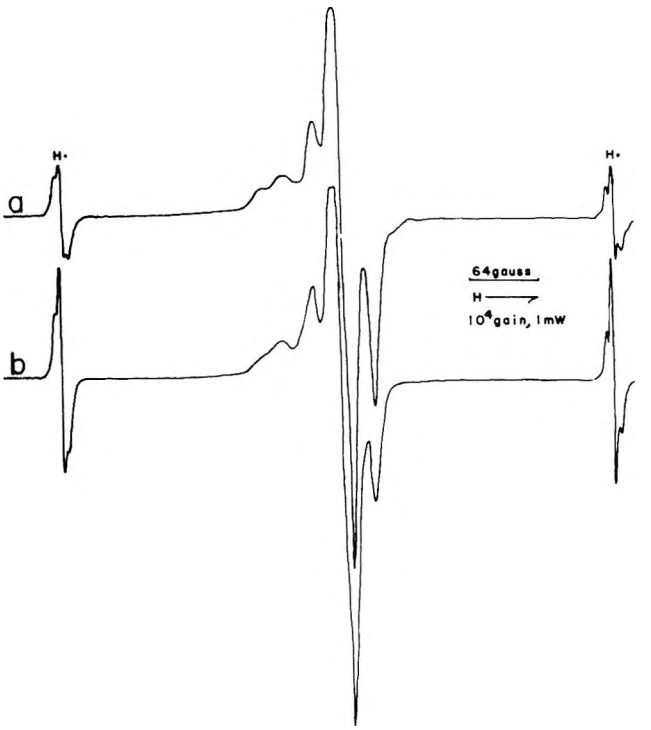


Figure 1. First-derivative esr spectra of irradiated acidic (a) $N_2$–ice and (b) $O_2$–ice at 77°K and 1-mW microwave power.

**Table I:** Relative $H_t$ Signal Intensities in Irradiated Ices under Partial Power Saturation

| Sample | Relative intensity of $H_t$ | Relative line width |
|---|---|---|
| $N_2$–ice | 4.5 | 3.4 |
| $O_2$–ice | 7.9 | 3.3 |
| th–$N_2$–ice | 3.7 | 3.5 |
| th–$O_2$–ice | 7.0 | 3.4 |

it has been shown that the *ratios* of many of the rate constants in frozen aqueous systems are quantitatively parallel to those in aqueous solutions at room temperature.[9,11] Thus, consideration of the relevant rate constants in water at 20° ($k_1 = 1.9 \times 10^{10}$ $M^{-1}$ sec$^{-1}$, ref 12; $k_2 \approx 10^7$ $M^{-1}$ sec$^{-1}$, as estimated from the reaction of $e^-$ with $H_2PO_4^-$ in ref 13; $k_3 = 3 \times 10^{10}$ $M^{-1}$ sec$^{-1}$, ref 14) would suggest that if reaction 3 is important, $O_2$ would not be able to capture any appreciable part of the electrons and the $H_t$ intensities should be the same in the presence of oxygen. The failure to observe the esr signal of $O_2^-$ ($g_{||} = 2.175$, ref 15) or of $HO_2\cdot$

(10) W. Kohnlein and J. H. Venable, Jr., *Nature*, 215, 618 (1967).

(11) L. Kevan, *J. Amer. Chem. Soc.*, 89, 4238 (1967).

(12) E. J. Hart and E. M. Fielden in "Solvated Electron," Advances in Chemistry Series, No. 50, American Chemical Society, Washington, D. C., 1965, p 253.

(13) M. Halmann and I. Platzner, *J. Phys. Chem.*, 70, 2281 (1966).

(14) S. Gordon, E. J. Hart, M. S. Matheson, J. Rabani, and J. K. Thomas, *J. Amer. Chem. Soc.*, 85, 1375 (1963).

(15) J. E. Bennett, D. J. E. Ingram, M. C. R. Symons, P. George, and J. S. Griffith, *Phil. Mag.*, 46, 443 (1955).

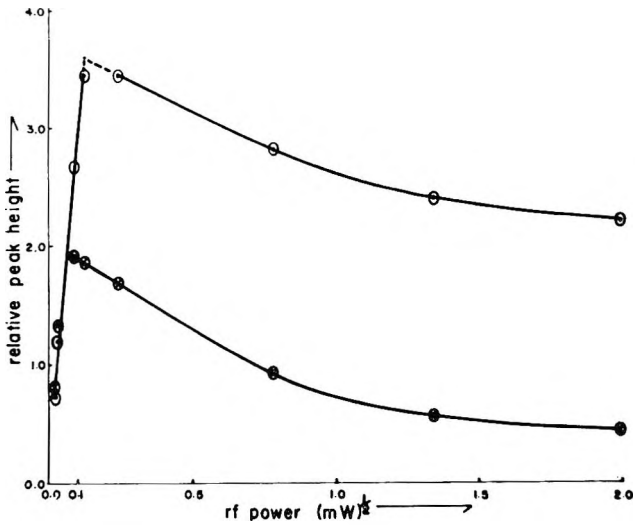


Figure 2. Relationship between applied microwave power and esr spectral intensity of the downfield, main $H_t$ line in irradiated acidic $O_2$-saturated (⊙) and $N_2$-saturated (⊗) ice at 77°K.

($g_{||}$ = 2.035, ref 16) from reaction 1 before annealing the irradiated $O_2$–ice and the observation of $H_t$ intensities converging at low rf powers in $N_2$– and $O_2$–ices as discussed later suggest that under the present conditions, reactions 2 and 3 do predominate over reaction 1. The slight lowering of the $H_t$ intensity upon the inclusion of thymine (Table I) and the observation of a small yield of thymine hydrogen atom addition radicals before annealing indicate that thymine competes with $HSO_4^-$ for radiation-produced electrons which yields thH· or reacts with radiation-induced hydrogen atoms at 77°K.

Microwave power saturation studies at 77°K from 0.4 μW to 8 mW indicate that oxygen provides a mechanism of relaxation[17] for the trapped hydrogen atoms above about 5 μW and increases the "apparent" $H_t$ yield in $O_2$–ice relative to $N_2$–ice. Figure 2 shows the power saturation curve for the main line of the downfield $H_t$ signal in nitrogen-saturated and oxygen-saturated ices. At powers below about 5 μW, the trapped hydrogen atoms in $N_2$– and $O_2$–ices have spin–lattice relaxation times ($T_1$) such that the spins can easily dispose of their energy and the $H_t$ signal intensities are the same. As the power is increased to greater than 5 μW, the spin–lattice relaxation in the $N_2$–ice can no longer adequately dispose of the energy, and the $H_t$ intensity saturates. However, in $O_2$–ice, where $T_1$ is larger, which adequately disposes of energies up to 20 μW, this allows the $H_t$ signal intensity to increase. Therefore, in $O_2$–ice, the trapped hydrogen atoms evidently relax through a nearby oxygen molecule which in turn is able to transfer the microwave energy to the surrounding environment. Above 20 μW, the spin–lattice relaxation time cannot dispose of the energy, the $H_t$ signal intensity power saturates, and the signal decreases. When the irradiated ices are examined at a power above the $H_t$ convergence value, the $H_t$ intensity from $O_2$–ice is larger than the $H_t$ intensity obtained from the $N_2$–ice, although both samples contain approximately the same number of trapped hydrogen atoms. Table I shows that there is very little change in the line width of the $H_t$ main line when nitrogen is replaced by oxygen in the irradiated ices. This indicates that the shape of the line remains constant and inhomogeneous saturation broadening occurs.[17] Thus, the line width of the $H_t$ main resonance is apparently governed by hyperfine interactions with protons of the environment.

Livingston and Weinberger[5] found no effect of dissolved oxygen on $H_t$ or hydrogen yields in γ-irradiated, frozen $H_2SO_4$ glasses (0.129 mole fraction). The $H_t$ yields in $H_2SO_4$ glasses are quite large compared to polycrystalline ices, and the oxygen effect may be masked in comparison to that effect obtained in the ices used in the present experiments. Since other authors[3] have not observed oxygen effects on $H_t$ signal intensities in irradiated polycrystalline acidic ices, the explanation most probably is that rf powers below the $H_t$ saturation level were previously used with the oxygenated samples and thus no oxygen effect would be observed on $H_t$. Power saturation of $H_t$ in acidic glasses[3a,5] and ices[3a] has been generally observed.

Ingalls and Pearson[18] observed that the esr peak height from a sample of irradiated terphenyl was dependent on the dissolved oxygen content and the microwave power. They found that small changes in the quantity of dissolved oxygen alter the slope of the power curve in some specific range of power, while the power curve was independent of oxygen content at sufficiently low powers. Esr spectra from petroleum oils show similar oxygen effects with microwave power.[19] These effects have been interpreted as due to oxygen decreasing the relaxation time and thereby reducing power saturation.

The scavenging of some hydrogen atoms by oxygen during annealing can be seen by comparing the yields of 5,6-dihydrothymyl-5-yl radicals (thH·) in the irradiated acidic ices containing $10^{-2}$ *M* thymine and dissolved oxygen where the following reactions might take place

$$H\cdot + th \longrightarrow thH\cdot \quad (4)$$

$$H\cdot + O_2 \longrightarrow HO_2\cdot \quad (5)$$

Upon annealing the th–$N_2$–ice to 100°K, the trapped hydrogen atoms are released and add to position 6 of the dissolved thymine to yield thH· radicals (Figure 3a) according to reaction 4. The large central signal is

(16) S. J. Wyard and R. C. Smith, Sixth International Symposium on Free Radicals, Cambridge, 1963.

(17) D. J. E. Ingram, "Free Radicals as Studied by ESR," Butterworth and Co. Ltd., London, 1958.

(18) R. B. Ingalls and G. A. Pearson, *Anal. Chim. Acta*, **25**, 566 (1961).

(19) A. J. Saraceno and D. D. Coggeshall, *J. Chem. Phys.*, **34**, 260 (1961).

**Table II:** $g$ Tensors

| Sample | $g_1$ | $g_2$ | $g_3$ | $g_{\|\|}$ | $g_\perp$ |
|---|---|---|---|---|---|
| $N_2$–ice (Figure 3a) | 2.019 | 2.013 | 2.0060 | 2.019 | 2.0095 |
| $SO_4\cdot^-$ (ref 4) | 2.0189 | 2.0130 | 2.0053 | 2.0189 | 2.0092 |
| Peak DP (Figure 3b) | 2.036 | | | 2.036 | |
| th–$O_2$–ice (Figure 4b) | 2.040 | 2.0059 | 2.0019 | 2.040 | 2.0039 |
| $O_2$–ice (Figure 5) | 2.036 | 2.0059 | 2.0046 | 2.036 | |
| | | | 2.0019 | | |
| th–$O_2$–ice (Figure 6) | 2.040 | 2.018 | 2.0019 | 2.040 | |
| $O_2^-$ (ref 15) | 2.175 | | | 2.175 | 2.002 |
| $H_2O_2$–ice ($HO_2$, ref 16) | 2.035 | 2.0065 | 2.0023 | 2.035 | 2.0044 |
| $H_2O_2$–ice ($HO_3$, ref 16) | 2.061 | | | 2.061 | 2.0045 |
| Polypropylene–$O_2$ (ref 20) | 2.035 | 2.0059 | 2.0019 | 2.035 | 2.0039 |

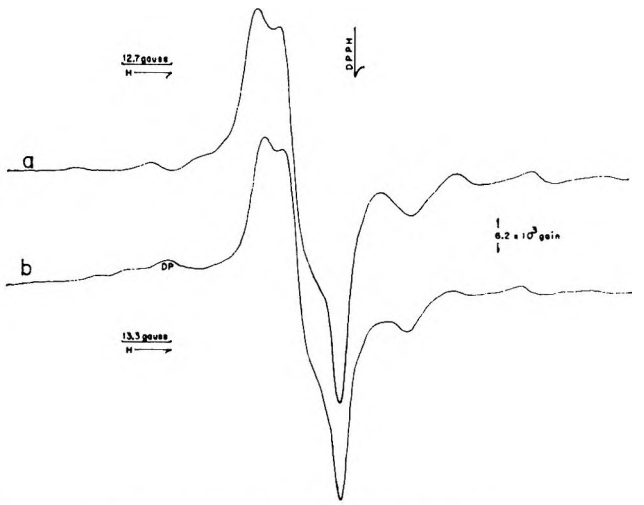


Figure 3. First-derivative esr spectra of irradiated acidic (a) thymine–$N_2$–ice and (b) thymine–$O_2$–ice at 77°K after annealing to 100°K.

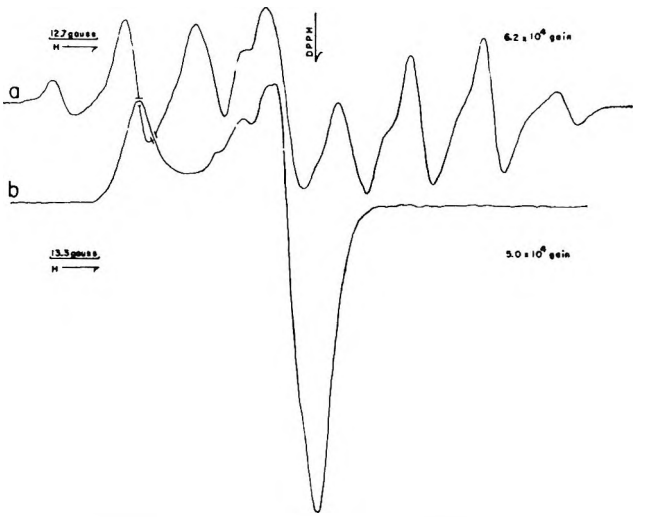


Figure 4. First-derivative esr spectra of irradiated acidic (a) thymine–$N_2$–ice and (b) thymine–$O_2$–ice at 77°K after annealing to 175°K.

almost identical with the radical identified as $SO_4\cdot^-$ by Moorthy and Weiss[4] (Table II). When irradiated $O_2$–ice containing thymine is annealed to 100°K, hydrogen atoms are released, thH· radicals are formed, and a small downfield peak (DP) is observed (Figure 3b). The large signal from $SO_4\cdot^-$ in the spectral center prevents any positive identification of peak DP as due to $HO_2$ radicals. However, a comparison of the $g$ factor of peak DP with $g_1$ from $HO_2\cdot$ in Table II suggests that $HO_2\cdot$ radicals may be formed in $O_2$–ices. The $g$ tensors for the radicals in irradiated ices after various annealings and $g$ tensors for related radicals are listed in Table II. Since most of the experimental spectra appear to result from fully anisotropic $g$ tensors, $g_1$, and $g_3$ are taken at low- and high-field shoulders, respectively, while $g_2$ is taken at the cross-over point near the center of the spectrum.[21] The $g$ tensor $g_1$ is approximately equivalent to $g_{||}$ while the average of $g_2$ and $g_3$ is approximately equivalent to $g_\perp$.

The thH intensity in the th–$O_2$–ice annealed to 100°K is decreased by about 40% from that in the th–$N_2$–ice. In contrast to the effect of oxygen on the $H_t$ intensity (Figure 2), the thH intensity is not affected by dissolved oxygen from 1 to 8 mW. If the ices are annealed to 175°K, the $SO_4\cdot^-$ radical almost completely disappears leaving the thH radical in the $N_2$–ice (Figure 4a) and an asymmetric doublet in the $O_2$–ice (Figure 4b). The thH signal seen in Figure 3b from partially annealed th–$O_2$–ice has now disappeared while the downfield peak DP has become part of the asymmetric doublet in Figure 4b. The change in the signal intensity of peak DP during annealing from 100°K (Figure 3b) to 175°K (Figure 4b) cannot be estimated, since the peak DP rides on the tail of a background signal which decays before 156°K. However, during annealing of the th–$O_2$–ice from 156 to 175°K, the signal height of peak DP increases by approximately 17%. A comparison of the respective concentrations ($O_2$, $10^{-3}$ $M$; thymine, $10^{-2}$ $M$) and the rates of reaction 4 ($k_4 \approx 10^9$ $M^{-1}$ sec$^{-1}$, estimated from H· + uracil in ref 22) and reaction 5 ($k_5 = 1.9 \times 10^{10}$ $M^{-1}$ sec$^{-1}$, ref

(20) M. Iwasaki and Y. Sakai, *J. Polym. Sci., Part A-2*, 6, 265 (1968).

(21) P. W. Atkins and M. C. R. Symons, "The Structure of Inorganic Radicals," Elsevier Publishing Co., Amsterdam, 1967, Appendix 5A.3.

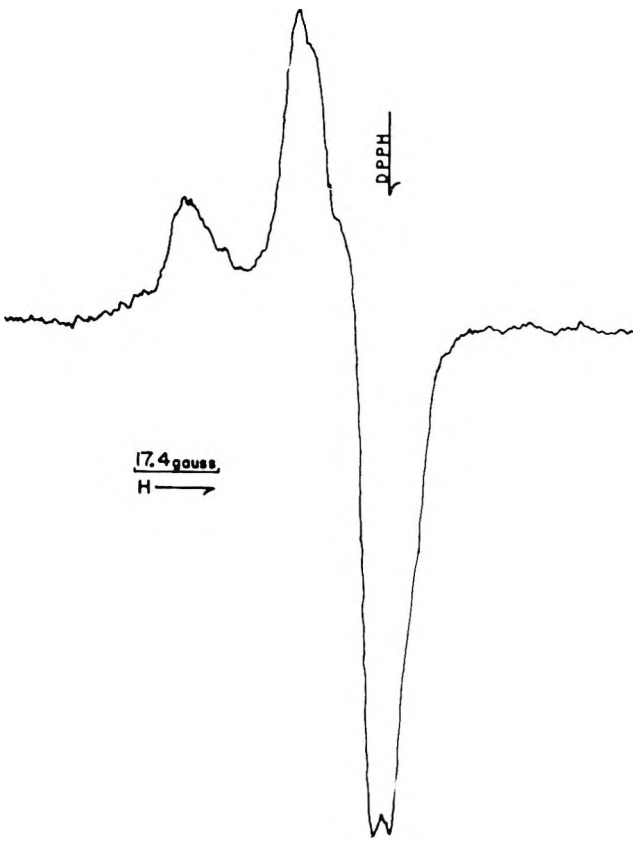


Figure 5. First-derivative esr spectrum of irradiated acidic $O_2$–ice at 77°K after annealing to 175°K.

23) indicates that oxygen and thymine compete approximately equally for hydrogen atoms. Therefore, a composite spectrum of $HO_2$ and thH radicals should result in Figure 3b. Table II shows that the $g_1$ factor of Figure 4b is larger than the $g$ factor of peak DP in Figure 3b. Thus, upon annealing th–$O_2$–ice to 175°K, the disappearance of the thH· signal from the ice while thH· is stable in the th–$N_2$–ice and the formation of an asymmetric signal with a $g_1$ factor different from that $g$ factor of peak DP (assumed to be $HO_2$·) suggest that dihydrothymyl peroxide radicals (thH–$O_2$·) have been formed as in

$$\text{thH}\cdot + O_2 \longrightarrow \text{thH–}O_2\cdot \qquad (6)$$

The formation of thH–$O_2$ radicals has been observed by Holmes[24] where thH radicals formed by exposure of polycrystalline thymine to gaseous hydrogen atoms react with oxygen in a gas-flow system. Although the esr spectrum of thH–$O_2$ appeared to be a singlet, an unambiguous spectrum could not be obtained. Thus, as observed, the doublet in Figure 4b should contain a contribution from the dihydrothymyl peroxide radical.

Figure 5 shows the radical left in $O_2$–ice without thymine after annealing to 175°K. Although this spectrum may contain some contributions from the

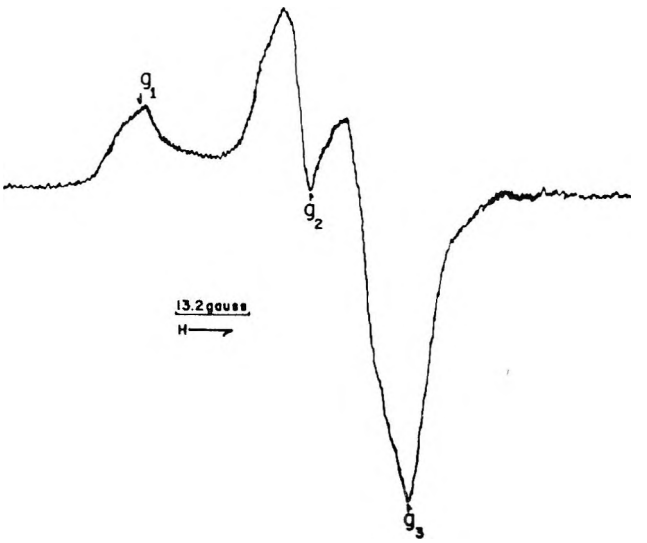


Figure 6. First derivative esr spectrum of irradiated acidic thymine–$O_2$–ice at 77°K after annealing to 195°K.

$SO_4\cdot^-$ radical, the $g$-tensor values (Table II) indicate that Figure 5 probably results from $HO_2$ radicals formed in reaction 5. Annealing the thymine-containing $O_2$–ice from 175 to 195°K (Figure 6) results in a further change in the asymmetric doublet of Figure 4b. Since the change appears to be due to the loss of a radical with a line at a $g$ factor of about 2.018, the $SO_4\cdot^-$ radical is assumed to decay at approximately 195°K. All esr signals disappear from the ices during annealing to 215°K.

These scavenging data may explain why Holmes and Weiss[7] could not observe low yields of $H_t$ or hydrogen atom adduct radicals in irradiated deoxyribonucleic acid ices and gels unless air was removed before freezing and irradiation. When the irradiated deoxyribonucleic acid samples containing dissolved air were annealed to 195°K and examined at 77°K in the esr spectrometer, an asymmetric signal was found[25] similar to those in Figures 4b and 6.

The results reported in this paper indicate that the applied microwave power and the concentration of dissolved oxygen are important parameters to be considered when comparing esr signals in irradiated, frozen solutions.

*Acknowledgment.* We wish to thank Mr. W. J. Terry for his assistance in measuring the microwave powers and the $g$ tensors.

(22) G. Scholes and M. J. Simic, *J. Phys. Chem.*, **68**, 1738 (1964).
(23) J. P. Sweet and J. K. Thomas, *ibid.*, **68**, 1363 (1964).
(24) D. E. Holmes, Ph.D. Dissertation, University of California, Los Angeles, Calif., 1966.
(25) D. E. Holmes and J. J. Weiss, unpublished results, 1967.

# The Effect of Water as a Proton Donor on the Decay of Anthracene and Naphthalene Anion Radicals in Aqueous Mixtures of Acetonitrile, Dimethylformamide, and Dimethyl Sulfoxide

by John R. Jezorek and Harry B. Mark, Jr.

*Department of Chemistry, The University of Michigan, Ann Arbor, Michigan 48104* *(Received October 13, 1969)*

The polarographic reduction of naphthalene and anthracene is reported in acetonitrile (MeCN), dimethylformamide (DMF), and dimethyl sulfoxide (DMSO) using water as proton donor. The results in MeCN are similar to those obtained in earlier studies with phenol and resorcinol donors. In DMF and DMSO, however, a dramatic difference is obtained. The reduction waves do not double as expected, and much larger concentrations of water are necessary to achieve a maximum $n$(app) value, even though DMF is isodielectric with MeCN. These results are interpreted in terms of the interaction of water with the nonaqueous component, resulting in a viscosity increase and reduced water availability for protonation. Coulometric confirmation that $n$(app) maximum values correspond to a two-electron change is reported. Methyl alcohol used as a proton donor in DMF gives more "normal" protonation behavior and adds credence to the hypothesis that the varying results with water are due to its unique interaction with the nonaqueous component. Aqueous protonation rates are found to be several orders of magnitude smaller than those with phenol or resorcinol donors, and about ten times slower in DMF and DMSO than in MeCN. Water is also found to affect the correlation of half-wave potentials with Hückel molecular orbital parameters.

## Introduction

There has been a great deal of interest in recent years in the electrochemistry of aromatic hydrocarbons in nonaqueous solvents.[1-8] In solvents such as dimethylformamide (DMF) and acetonitrile (MeCN) aromatic anion radicals are relatively stable. Recent studies have shown that when an electroinert proton donor such as phenol or resorcinol is present the radical ions decay *via* an ECE mechanism to the dihydro derivative of the hydrocarbon.[4,8] The usual result is an increase in the limiting current of the first polarographic wave of the hydrocarbon and an anodic shift of the half-wave potential ($E_{1/2}$). When total protonation of the radical anion is achieved for relatively high proton-donor concentrations, the limiting current is double its original value in aprotic media.[1-8]

Of considerable interest is the effect of water as a proton donor on the rate of decay of the aromatic radical anions in aprotic solvents such as DMF, DMSO (dimethyl sulfoxide), and MeCN; these nonaqueous solvents are the most frequently used in electrochemical investigations. This is a logical step from a theoretical point of view as well as a practical one. It is important to know how much water can be tolerated in a solvent system which is being used to study the $R|R\cdot^-$ and/or $R\cdot^-|R^{2-}$ couples. For example, one would like to be certain that only the mono- or dianions are formed in a polarographic reduction and that no protonation of either of these species occurs, as this would affect both the measured diffusion current and half-wave potential. Some comments concerning the effect of water on the reduction of aromatic hydrocarbons have been published, but no systematic investigation has been carried out.[1,9,10] The effect of water is of special interest with respect to a quantitative understanding of solvent purity on electrochemical studies of organic systems and theoretical correlations of electrochemical experiments and molecular orbital parameters.[7,8]

Accordingly the polarograms of naphthalene and anthracene were studied in the above solvents with known amounts of water present. Also, coulometric determinations of the number of electrons transferred, $n$, during electrolysis in DMF and DMSO were obtained. Methanol was also employed as a proton donor in the DMF–naphthalene system and its effect as a

(1) G. J. Hoijtink, J. van Schooten, E. DeBoer, and W. I. J. Aalbersberg, *Rec. Trav. Chim. Pays-Bas*, **73**, 355 (1954).

(2) (a) D. E. G. Austen, P. H. Given, D. J. E. Ingram, and M. E. Peover, *Nature*, **182**, 1784 (1958); (b) P. H. Given and M. E. Peover, *J. Chem. Soc.*, **1960**, 385.

(3) A. C. Aten, C. Buthker, and G. J. Hoijtink, *Trans. Faraday Soc.*, **55**, 325 (1959).

(4) (a) N. H. Velthorst and G. J. Hoijtink, *J. Amer. Chem. Soc.*, **87**, 4529 (1965); (b) *ibid.*, **89**, 209 (1967).

(5) K. S. V. Santhanam and A. J. Bard, *ibid.*, **88**, 2669 (1966).

(6) J. Janata, J. Gendell, R. C. Lawton, and H. B. Mark, Jr., *ibid.*, **90**, 5226 (1968).

(7) J. Janata and H. B. Mark, Jr., *J. Phys. Chem.*, **72**, 3616 (1968).

(8) H. B. Mark, Jr., *Rec. Chem. Progr.*, **29**, 217 (1968).

(9) P. H. Given, *J. Chem. Soc.*, 2684 (1958).

(10) S. Wawzonek, E. W. Blaha, R. Berkey, and M. E. Runner, *J. Electrochem. Soc.*, **102**, 235 (1955).

proton donor compared and contrasted with that of water. Approximate rate constants are reported for the aqueous–nonaqueous systems and compared with those obtained using organic proton donors such as resorcinol and phenol.[6,7] The effect of the ECE electrode reaction mechanism on MO correlation values is examined quantitatively.

## Experimental Section

*Instrumentation.* Polarograms were obtained using a three-electrode system based on the operational amplifier circuits of DeFord[11] and were recorded on an Electro Instruments Model 500 X–Y recorder without damping. All current values are reported as the maximum current at the end of drop life. The dropping mercury electrodes had flow rates of 1.24–1.30 mg/sec under open circuit conditions in 0.1 *M* tetrabutylammonium perchlorate (TBAP) solutions. Drop times varied from solution to solution and were measured at the half-wave potentials.

The reference electrode used for all measurements was a silver wire immersed in a 0.01 *M* $Ag^+ClO_4^-$–0.1 *M* TBAP anhydrous solution of the solvent being studied. The reference cell consisted of an approximately 4–6-cm length of about 2-mm diameter polyethylene tubing, into one end of which was tightly fitted one-half of a 2-cm length of Corning Glass Works porous cane (also known as "thirsty glass"). The remaining half of this "thirsty glass" was then tightly fitted into one end of a salt bridge, an approximately 6-cm length of the same diameter polyethylene tubing. The latter section of polyethylene was filled with a 0.1 *M* TBAP solution of the anhydrous solvent being studied. A second 2-cm piece of "thirsty glass" was tightly fitted into the open end, care being taken to exclude any air bubbles from the salt bridge chamber. With MeCN, a very volatile solvent, epoxy resin was used to seal off the open end of the reference electrode compartment.[12]

The constant-potential coulometry experiments were carried out in a flow cell which allowed the macroscopic electrolysis at a mercury pool electrode to continue while the instantaneous polarographic diffusion current was measured at a dropping mercury electrode. This cell system has been described previously.[13] Electrolyses were carried out at a constant potential on the diffusion plateau of the first polarographic wave. The $Ag|Ag^+ClO_4^-$ reference electrode was used here also. The apparatus and procedure for deoxygenating the solutions have been described in a previous paper.[7] All polarograms were run at 25.0 ± 0.05°.

Relative diffusion coefficient comparison measurements were performed using the procedure of Macero and Rulfs.[14] A small sample cell was constructed from 3 cm of 8-mm glass tubing. The cylinder was closed at one end and ground flat at the open end. The volume was 0.796 ml. The sample used was 0.01 *M* anthracene. An attached glass rod permitted the cell to be lowered and raised in the polarographic cell containing 7.0 ml of solvent which was 0.1 *M* in supporting electrolyte. The sample cell was carefully lowered below the surface of the solvent in the polarographic cell, and diffusion was allowed to proceed. It was then removed after a time and the anthracene current measured polarographically. This procedure was performed several times over a period of 5 hr.

*Chemicals and Solutions.* All solvents were Matheson Coleman and Bell Spectroquality grade. The DMSO and MeCN were used as received, since polarographic scans with only supporting electrolyte present exhibited no Faradaic current until the expected breakdown potential was reached.

The purification procedure for DMF previously described was followed in this investigation.[6] Naphthalene (Eastman, reagent grade) was recrystallized from 95% ethanol. Anthracene was MC and B, blue-violet, Fluorescence grade, and was used as received. Tetrabutylammonium perchlorate (TBAP) supporting electrolyte, polarographic grade (Southwestern Analytical Chemicals, Inc., Austin, Texas), was stored in a desiccator over silica gel before use as were hydrocarbon samples. Solvents were stored over Linde Type 4A molecular sieves. All solutions were 0.1 *M* in TBAP. Under these conditions only non-Faradaic currents were observed in the aprotic solvents until background breakdown. All binary solvent systems (aqueous–nonaqueous or methanol–nonaqueous) were prepared by weight to a known volume. The methanol (MeOH) was Eastman reagent grade, and the water was triply distilled.[15]

Half-wave potentials, diffusion currents ($i_d$), and drop times ($t$) of the first polarographic waves ($R|R\cdot^-$) for millimolar naphthalene and anthracene solutions in the three solvents employed under anhydrous, aprotic

(11) (a) D. D. DeFord, Analytical Division, 133rd National Meeting of the American Chemical Society, San Francisco, Calif., 1958; (b) W. M. Schwarz and I. Shain, *Anal. Chem.*, **35**, 1770 (1963).

(12) The reference electrode–salt bridge system was stored in the dark when not in use to prevent photolytic reduction of the silver ion. When this was done, the reference electrode potential was quite stable and it could be used for several days before the solutions required changing. On initial preparation of the "thirsty glass" reference system, about 1 day of "aging" was necessary before stable voltage readings were obtained. After this the reference electrode–salt bridge was stored in a closed tube of the appropriate solvent to prevent the glass from drying out. This was especially necessary with MeCN, as it is extremely volatile. When these precautions were exercised, the reference electrode could be used immediately; this was true even if the reference and salt bridge solutions had just been changed, as long as the porous glass was not permitted to become dry.

(13) J. Janata and H. B. Mark, Jr., *Anal. Chem.*, **39**, 1896 (1967).

(14) D. J. Macero and C. L. Rulfs, *J. Electroanal. Chem.*, **7**, 328 (1964).

(15) The middle distillation was from basic potassium permanganate.

**Table I:** Half-Wave Potentials, Diffusion Current, and Drop Time for Hydrocarbons in MeCN, DMF, and DMSO

| Solvent | | $E_{1/2}$, V *vs.* Ag\|AgClO$_4$ | $i_d$, μA | $t$, sec at $E_{1/2}$ |
|---|---|---|---|---|
| MeCN | (a) Naphthalene | −2.856 | 5.83 | 1.40 |
| | (b) Anthracene | −2.276 | 4.72 | 2.67 |
| DMF | (a) Naphthalene | −2.917 | 4.67 | 1.67 |
| | (b) Anthracene | −2.405 | 3.45 | 2.62 |
| DMSO | (a) Naphthalene | −2.763 | 2.54 | 1.60 |
| | (b) Anthracene | −2.155 | 2.43 | 2.88 |

conditions are given in Table I. Uncertainty in $E_{1/2}$ is ±10 mV; in $i_d$, ±0.05 μA; and in $t$, ±0.05 sec.

## Results

Both the first (R|R·⁻) and second (R·⁻|R²⁻) polarographic waves of anthracene are accessible in all solvent systems while the second naphthalene wave (R·⁻|R²⁻) lies beyond background breakdown. Naphthalene, which possesses the smaller molecular orbital system,[16] would be expected to be reduced more difficultly than anthracene, and indeed its $E_{1/2}$ is about 0.5–0.6 V negative to anthracene in all solvents studied.

It immediately became apparent in this study that protonation of the radical anion of both hydrocarbons by water was much slower than by the organic proton donors previously investigated[6,7] and also depended significantly on the nature of the nonaqueous component in which it was dissolved. With donors such as phenol or resorcinol, concentrations of the same order of magnitude as the hydrocarbon result in complete protonation of R·⁻ in the time scan of polarographic measurement; *i.e.*, the first wave doubles in height.[6,7] With water at least a three order of magnitude concentration excess was necessary to achieve total protonation of R·⁻.

Of the three solvents studied, protonation proceeded fastest in MeCN (dielectric constant, ε, 36.7). The value of $n$(app)[17] reaches a maximum for millimolar naphthalene, 1.89, at a water concentration about 1.25 *M*, or about 6 mol %, as shown in Figure 1. The maximum for anthracene, 1.90, is attained at a water concentration near 3.6 *M*, about 17 mol %. In all cases studied, $n$(app) maximum was attained at a lower water concentration for naphthalene than anthracene, as expected.[16] Aside from the much larger proton donor concentration necessary to reach $n$(app) maximum these data for MeCN are similar to those obtained in the earlier studies where more acidic donors were used.[6,7]

However, in DMF (ε 36.7) a dramatic difference from the results in MeCN was noted for both hydrocarbons. The maximum $n$(app) is not reached until about 35 mol % for naphthalene and 50 mol % for anthracene. In addition, $n$(app) maximum is far removed from the theoretical value of 2.0, being only about 1.3 for naphthalene and 1.2 for anthracene as shown in Figure 2. At the solvent composition corresponding to $n$(app) maximum, the second anthracene wave had completely disappeared. Moreover, it was found that $n$(app) is less than 1.0 at low water concentrations, and after the maximum is reached, it begins to decrease again. This latter trend continues as far as solubility and water interference limitations allow data to be taken, near 70% water.[18]

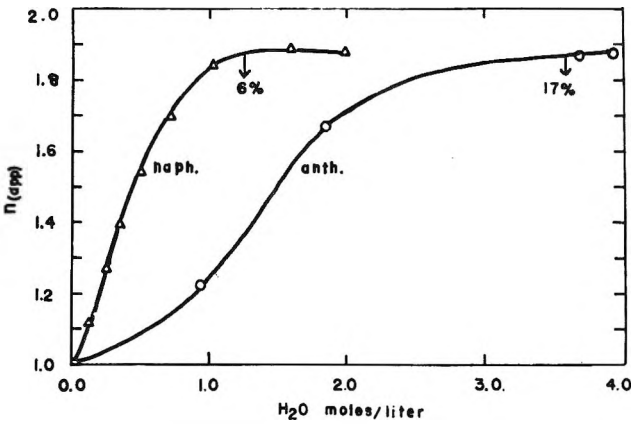


Figure 1. A plot of $n$(apparent), the ratio of the limiting current of the first polarographic reduction wave in the solvent mixture to that in the aprotic solvent, as a function of added $H_2O$ in the MeCN–$H_2O$–0.1 *M* TBAP solvent system. The hydrocarbons are $10^{-3}$ *M* naphthalene and anthracene.

A similar deviation of $n$(app) from theory was obtained with water in DMSO (ε 46.6). The maximum $n$(app) was not attained until 45–50 mol % water for naphthalene and about 60 mol % for anthracene; $n$(app) maximum was about 1.6 for naphthalene and about 1.1 for anthracene, as seen in Figure 3. Again the second anthracene wave was completely removed at $n$(app) maximum.

In order to verify that the maximum current was diffusion limited under aprotic conditions and corresponded to an $n$ value of 1.0 and to determine the true value of $n$(app) maximum, a series of constant potential coulometry experiments was performed. The electronically integrated current, $Q$, during the constant-potential electrolysis was plotted *vs.* the instantaneous

(16) A. Streitwieser, Jr., "Molecular Orbital Theory for Organic Chemistry," John Wiley & Sons, New York, N. Y., 1969, p 178.

(17) $n$(app) = $i/i_d$, where $i$ is the polarographic limiting current in the water–MeCN mixture, and $i_d$ is the diffusion current in the aprotic solvent.

(18) It was found that the water–DMF solvent, 0.1 *M* TBAP, had a rather significant background current, starting around −2.6 V *vs.* Ag|Ag⁺ClO$_4$⁻ in DMF and growing larger until final breakdown near −3.2 V. This phenomenon is apparently a result of slow proton discharge or a Faradaic process which results from some product of a water-impurity or water–DMF reaction. A set of correction curves was constructed and the current contribution from this "solvent breakdown" was subtracted from the total current value obtained with hydrocarbon sample present. Neither the DMSO- or MeCN–water systems were found to exhibit such a complicating factor.

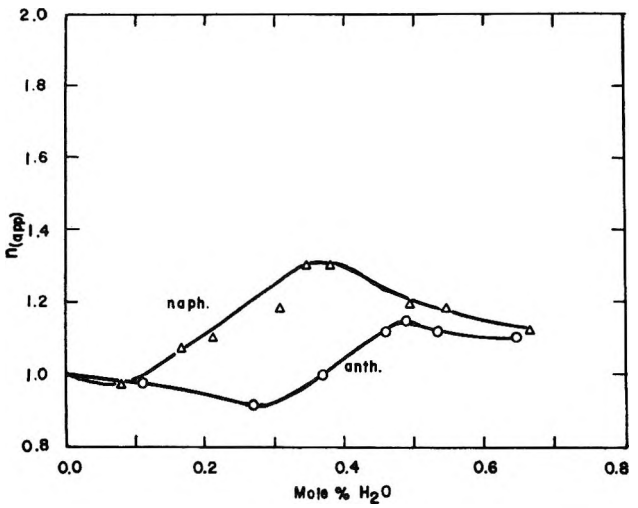


Figure 2. A plot of $n$(apparent) for the first reduction wave of $10^{-3}$ $M$ naphthalene and anthracene as a function of added $H_2O$ in the DMF–$H_2O$–0.1 $M$ TBAP solvent system.

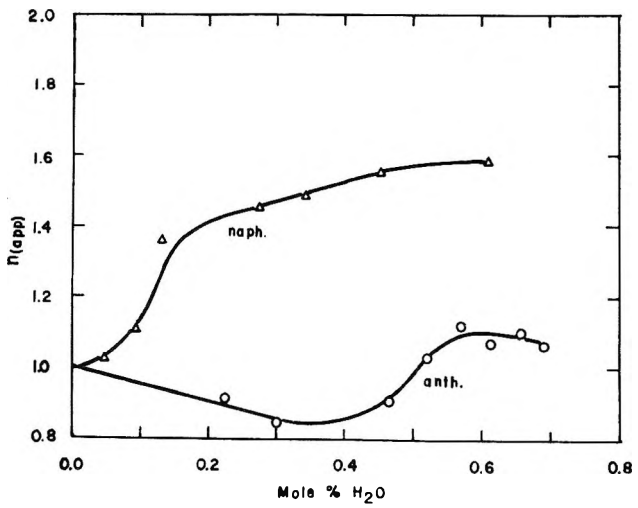


Figure 3. A plot of $n$(apparent) for the first reduction wave of millimolar naphthalene and anthracene as a function of added $H_2O$ in the DMSO–$H_2O$–0.1 $M$ TBAP solvent system.

polarographic limiting current of the solution according to the modified Faraday expression.[6] The slope of $i_d$ *vs.* $Q$ is inversely dependent on $n$, the number of electrons transferred in the overall reaction.[6]

Both anthracene and naphthalene were investigated in DMSO and DMSO–water solutions. The slope of $i_d$ *vs.* $Q$ for both hydrocarbons corresponded, under anhydrous conditions, to the expected theoretical slope for $n = 1$. For naphthalene at 52 mol % water and for anthracene at 66% water the experimental slope was essentially the same as the theoretical for $n = 2$. Naphthalene was also electrolyzed in DMF and DMF–water solutions. The experimental value of $n$ was very close to 1 in anhydrous solution and very close to 2 at 40 mol % water, the point of $n$(app) maximum.[19]

## Discussion

An investigation of the enthalpy of mixing of water and MeCN by Vierk revealed only a small attraction of one solvent for the other.[20] The enthalpy ($\Delta H$) is endothermic over nearly the whole composition range; the minimum of the plot, about 200 cal/mol, occurs between 30 and 40 mol % water. These results indicate that the main reaction on mixing water with MeCN, at least in the regions of low water concentration, is breaking of water–water hydrogen bonds, so that essentially "free" water is present in mixtures of these species.[21]

Unlike that of the water–MeCN system, the enthalpy of mixing of DMSO and water reported by Tommila is quite exothermic.[22] Maximum heat release, over 700 cal/mol, occurs near 65 mol % water. Cowie and Toporowski reported similar enthalpy data for the DMSO–water system and also reported the viscosity change of the system as a function of the amount of added water.[23] The viscosity rises from 2.0 cP for pure DMSO to a value of 3.8 cP for 65% water. These data indicate very strong interaction between the two components and a greatly increased structure in the higher water concentration regions.

Extensive interaction also exists in the DMF–water system. The viscosity of an approximately 70 mol % water solution is nearly four times that of pure DMF, as shown by Hale and Parsons.[24] This very marked increase in viscosity implies significant interaction of water with DMF and formation of a rather rigid structure. Indeed, when large amounts of water are added to DMF or DMSO the container becomes too hot to hold. It is most likely the unshared electron pairs on the oxygen atoms of the amide and sulfoxide moieties in DMF and DMSO which facilitate this very strong hydrogen bonding interact with water.

Ting, *et al.*, suggested that two DMF or DMSO molecules are hydrogen bonded to one water molecule and reported large entropy losses for these interactions.[25]

(19) The slopes of $i_d$ *vs.* $Q$ reported for the anhydrous solutions of DMSO and DMF were taken from the first 20–25% of the electrolysis reaction. It was observed that anthracene (but not naphthalene) solutions which were open to the light exhibited changing polarograms (large background currents) and abnormally large $n$ values (pink solutions). This was true for both anhydrous and water–nonaqueous mixtures (orange on electrolysis). Thus, all measurements were made in the dark. These photochemical reactions of anthracene with water are under investigation.

(20) A. Vierk, *Z. Anorg. Chem.*, **261**, 285 (1950).

(21) F. Franks and D. J. G. Ives, *Quart. Rev.*, **20**, 1 (1966).

(22) E. Tommila and M. Murto, *Acta Chem. Scand.*, **17**, 1947 (1963).

(23) J. M. G. Cowie and P. M. Toporowski, *Can. J. Chem.*, **39**, 2240 (1961).

(24) J. M. Hale and R. Parsons in "Advances in Polarography," Vol. III, I. S. Longmuir, Ed., Pergamon Press, New York, N. Y., 1960, p 829.

(25) S. F. Ting, S. M. Wang, and N. C. Li, *Can. J. Chem.*, **45**, 425 (1967).

They also indicated the possibility of three DMF molecules interacting with one water molecule

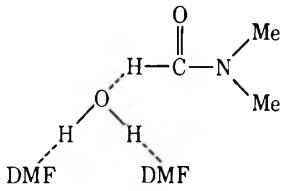


Such an arrangement is likewise possible for DMSO and would lead to branched polymeric chains. Two-dimensional polymers such as these are probably the cause of the viscosity increases at lower water concentrations. Franks reported that DMF and DMSO are practically unassociated in the pure liquid form.[26] At higher water concentrations three-dimensional, tetrahedral water–water interaction begins to occur in addition to the water–nonaqueous interaction discussed above. According to the theories of solute–water interaction developed by Frank and others over the last 20 years, large bulky molecules (like DMF and DMSO), possessing uncharged hydrocarbon groups, can cause this water structure to be reinforced or tightened compared to pure water.[27,28] This effect, as well as that of DMF– or DMSO–water hydrogen-bond formation accounts for the large viscosity increase, heat release, and structure maximum in the higher water concentration regions.

Because the nitrile group of MeCN is not very reactive toward water and comparatively little structure increase or "deactivation" of the water molecules occurs, protonation of the aromatic radical anions appears to proceed relatively easily in this solvent system. That $n$(app) does not attain a value of 2 (with resorcinol this value *was* obtained in all three solvents) is the result of a slight increase (10–20%) in the viscosity of the water–MeCN solvent compared to pure MeCN.[20] The diffusion coefficient, $D$, exists in a 1:1 inverse relationship with viscosity, while the diffusion current is directly dependent on the square root of $D$, according to the Ilkovic equation.[24] This slight increase in viscosity is probably due to the beginnings of water–water bond formation in the 10–20% water solution, where $n$(app) maximum is found. MeCN is practically unassociated in the liquid state, as are DMF and DMSO.[26]

In the DMF– and DMSO–water mixtures, however, the water is less able to interact with the radical anions, as it is firmly fixed in the polymeric network. Hence, much larger concentrations than in MeCN are necessary to effect complete protonation. This more rigid network, resulting in the increased viscosity, causes $n$(app) to be considerably lower than in the MeCN system. The experimental value of $n$(app) at the 60–70 mol % water–DMF composition (Figure 2) for both hydrocarbons is only slightly greater than 1.0, about half of the theoretical value. This correlates

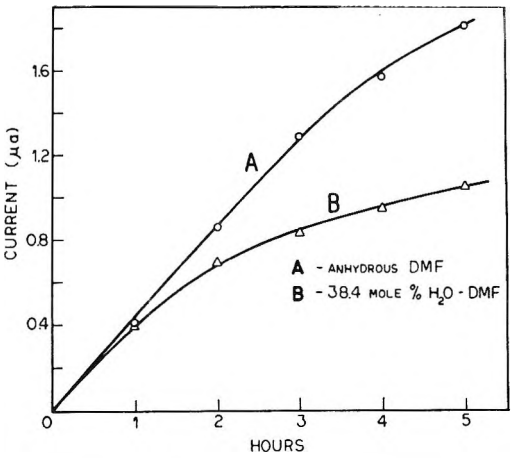


Figure 4. Polarographic diffusion current of the first anthracene reduction wave as a function of time of diffusion: A, anhydrous DMF—0.1 $M$ TBAP; B, 38.4 mol % $H_2O$–DMF–0.1 $M$ TBAP.

rather well with the fourfold viscosity increase at this solvent composition reported by Hale and Parsons.[24] These authors also reported the diffusion current of cadmium(II), lead(II), and thallium(I) over the whole water–DMF composition range.[24] Each of these ions exhibits a current minimum at 70 mol % water which is about half of the value in either of the pure solvents (which have nearly equal viscosities).

In this study a series of comparative diffusion experiments using anthracene in pure DMF and a 38.4 mol % water–DMF mixture has been carried out. The results are interpreted in terms of a smaller diffusion coefficient in the solvent mixture than in the pure solvent. The $n$(app) measurements reported above (Figure 2) indicate that anthracene has the same limiting current at these two solvent compositions ($n$(app) $\approx$ 1). Therefore, equal concentrations of anthracene should result in equal polarographic currents. It was found, however, that the currents obtained after equal periods of diffusion from the small cell into the polarographic cell were not equal for the two solvents. That of the aqueous solution was much lower than that of the anhydrous solution, as shown in Figure 4. After 4–5 hr of diffusion the aqueous solution current was about 60% of the anhydrous value. The viscosity data of Hale and Parsons indicate that this fraction should be about 70%.[24] The experimental value is certainly in the right range, however, considering the "roughness" of the experiment. The closeness of the currents after only 1 hr of diffusion is probably due to the initial "washing" of the sample out of the cylinder and into the polarographic cell,

(26) F. Franks in "Physico-Chemical Processes in Mixed Aqueous Solvents," F. Franks, Ed., Elsevier Publishing Co., New York, N. Y., 1967, p 50.

(27) H. S. Frank and W.-Y. Wen, *Discussions Faraday Soc.*, **24**, 133 (1957).

(28) H. S. Frank and M. Evans, *J. Chem. Phys.*, **13**, 507 (1945).

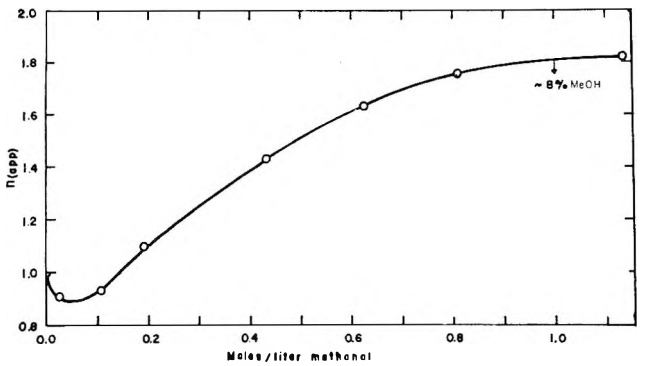


Figure 5. Plot of $n$(apparent) for the first reduction wave of $10^{-3}$ $M$ naphthalene as a function of added MeOH in the MeOH–DMF–0.1 $M$ TBAP solvent system.

masking any small difference. While this simple experiment is admittedly semiquantitative, it still leads to the same conclusion as the ionic data of Hale and Parsons,[24] namely, that the diffusion coefficient does indeed become significantly smaller in aqueous DMF.

The data of Cowie and Toporowski[23] on the DMSO–water system indicate a doubling of the viscosity from pure DMSO to about 65% water. Thus, $n$(app) should be about 1.5 rather than 2.0 at 65% water by the inverse square root relationship of current to viscosity. Our data for naphthalene are in fairly good agreement. However, $n$(app) for anthracene is well below the value suggested by the viscosity data at 65% water. The reason for this discrepancy is not apparent at this time.

Two effects are working in opposition here, then. As water is added to the DMF or DMSO solution, protonation tends to cause a current increase, while increased viscosity tends to cause a current decrease. The increased viscosity also explains the fact that $n$(app) for both hydrocarbons falls below 1.0 in DMF and DMSO, before the current increase due to protonation begins to have much effect.

The viscosity of the DMF- and the DMSO–water system begins to decrease after about 75% water and the diffusion currents of cadmium(II), lead(II), and thallium(I) begin to increasse toward the pure water value.[23,24] Therefore $n$(app) ought to begin to increase again after 75 mol % water. However, hydrocarbon solubility limitations and gross interference with the hydrocarbon polarographic waves due to proton discharge in these solvent regions prevented this expectation from being substantiated experimentally.

*Methanol Proton Donor.* Since MeOH only has one proton capable of hydrogen bonding, it is not able to form the rigid three-dimensional solvent network like that of water. Even at low concentrations in DMF, where water is involved only in two-dimensional structures, MeOH should not form as substantial a

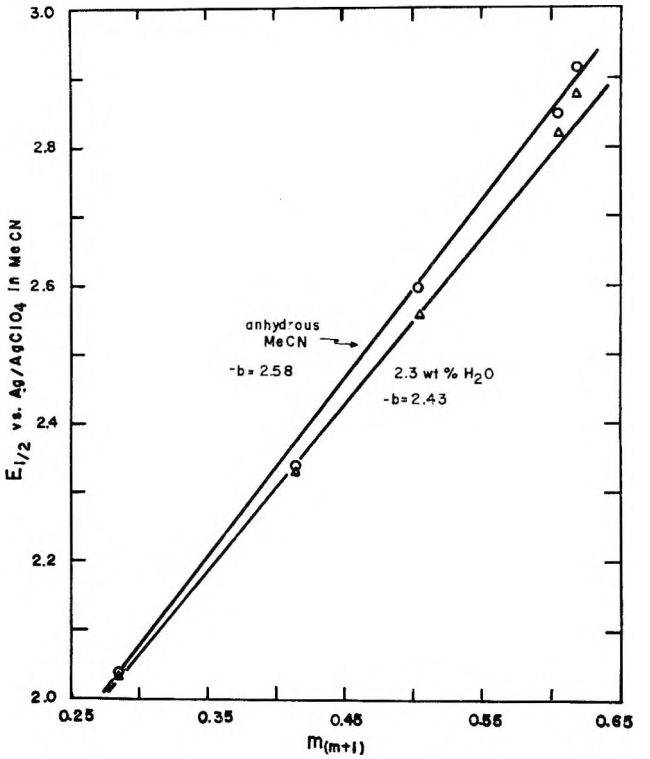


Figure 6. Plot of $E_{1/2}$ *vs.* Ag|AgClO$_4$ (0.01 $M$) as a function of the coefficient of the energy of the lowest vacant molecular orbital of the hydrocarbons (pairs from top to bottom) naphthalene, phenanthrene, *trans*-stilbene, anthracene, and acenpahthalene. Top line is in anhydrous MeCN–0.1 $M$ TBAP; bottom line is in a 2.3 wt % (5.1 mol %) $H_2O$–MeCN–0.1 $M$ solvent system.

polymeric network. Therefore $n$(app) maximum should approach more closely the theoretical value of 2. It was of interest, then, to compare this proton donor with water. All things being equal, the MeOH would be expected to be a weaker acid than water due to the inductive effect of the methyl group; since it has only one donatable proton compared to two for water, more of it should have to be added to reach $n$(app) maximum. In fact, quite the opposite was found. Whereas $n$(app) maximum for naphthalene in DMF–water solutions occurs at about 35 mol % water, with a value of 1.3, $n$(app) maximum in DMF–MeOH occurred at about 8 mol % MeOH, and had a value of 1.8 (Figure 5). Therefore the much weaker interaction of MeOH with the nonaqueous component not only resulted in an $n$(app) value much closer to the theoretical, as expected, but also in a significantly faster reaction with the radical anions. These results tend to substantiate the conclusions that the extremely strong and unique interaction of water with DMF and DMSO results in its lessened availability for protonation. In addition the viscosity increase leads to a current smaller than theoretical.

Values of the rate constants, $k$, of the reaction of the aromatic anion radicals with water were estimated from

a computer-calculated plot of the polarographic $n$(app) *vs.* $k't$ as calculated by Nicholson, *et al.*;[29] $k'$ is $k$[HX], [HX] is the proton donor concentration, and $t$ is the drop time. Values of the order of 5 l. mol$^{-1}$ sec$^{-1}$ were obtained for naphthalene in MeCN, while $k$ dropped to around 0.5 in DMF and DMSO. These values are from two to three orders of magnitude smaller than those obtained with phenol or resorcinol as proton donor.[6,7]

*Molecular Orbital Correlation Considerations.* Theoretical calculations show that there should be a linear correlation between the half-wave potential of unsaturated hydrocarbons and the Hückel molecular orbital energy of the lowest vacant molecular orbital, MO, of the hydrocarbon.[30] The relation between the reversible thermodynamic half-wave potential and the effective value of the bond integral of the system, $-b$, is $E_{1/2} = -bm_{(m+1)} + c$ where $m_{(m+1)}$ is the coefficient of the energy of the lowest vacant MO of the hydrocarbon, and $c$ is a constant. Several workers have shown that this linear relationship is valid experimentally.[8,31,32] However, in view of the fact that these studies of the protonation of aromatic anion radicals exhibit different protonation rate constants for the hydrocarbons naphthalene and anthracene and that many previous correlation studies were done in aqueous–nonaqueous mixtures or hydroxylic solvents,[16,33,34] it was of interest to investigate the effect of water as proton donor on the correlations. Therefore the half-wave potential of several hydrocarbons of approximately millimolar concentration was measured in anhydrous MeCN and in a 2.3 wt % water–MeCN solution (5.12 mol %) and plotted *vs.* $m_{(m+1)}$ (Figure 6).

For the anhydrous system $-b$ was found to be 2.58 and for the aqueous mixture 2.43, a 6% difference. It might be noted that previous values reported are 2.37 in 75% aqueous dioxane and 2.41 in 2-methoxyethanol,[16] both lower than the aprotic value found in these measurements. The change in the slope, $-b$, occurs because the hydrocarbons with lower values of $m_{(m+1)}$ are also expected to have lower protonation rate constants than those with larger $m_{(m+1)}$ values, and, consequently, the $E_{1/2}$ values are shifted in the anodic direction a smaller amount. Fry and Reed have obtained similar results concerning $E_{1/2}$ correlations of imines with MO parameters.[34b] Thus, a valid $E_{1/2}$ *vs.* $m_{(m+1)}$ correlation cannot be obtained unless a totally aprotic solvent system is employed.

## Conclusion

It is seen that water does have an effect on the stability of the aromatic radical anions electrochemically produced in aprotic solvents but that the effect is measurable only at relatively high water concentrations; this is true even in MeCN where the water is relatively "free" from hydrogen bonding. Therefore, extremely scrupulous drying of solvents should not be necessary for routine polarographic studies, and ordinary precautions (molecular sieves) to keep water out of the solvent should be sufficient.

It should also be noted here that while MeCN and DMF are isodielectric ($\epsilon$ = 36 at 25°) and while their aqueous mixtures are nearly so over the entire composition range,[35] the behavior of water with respect to the decay of the anion radicals in these solvents is dramatically different. The dielectric constant has been used for a long tine, as *per* the Born equation, to attempt explanations of what are usually described vaguely as solvent effects. This parameter, however, is a macroscopic property of the fluid, while the electrostatic situation in the vicinity of any particular solvent molecule or "cluster" may be quite different than this average value. What must be considered, therefore, are microscopic properties of the fluid such as solvent molecule shape, size, type of functional groups attached, dipole moment, and the like; in the case of a mixture, one must consider the possibilities of interaction between the components, the possibility of enhanced or decreased structure, the resulting orientation of reacting species due to interaction with the other solvent component, and so forth. This investigation is just one of many recent ones which indicate that more than simple electrostatics is involved in solute–solvent interaction.[26,36]

*Acknowledgments.* The research reported herein has been supported in part by National Science Foundation Grant No. GP-9307 and in part by the American Chemical Society, Petroleum Research Fund, Grant No. 2880-A3,5.

(29) R. S. Nicholson, J. M. Wilson, and M. L. Olmstead, *Anal. Chem.*, **38**, 542 (1966).

(30) A. Maccoll, *Nature*, **163**, 178 (1949).

(31) G. J. Hoijtink and J. vanSchooten, *Rec. Trav. Chim. Pays-Bas*, **71**, 1089 (1952).

(32) A. Pullman, B. Pullman, and G. Berthier, *Bull. Soc. Chim. Fr*, **17**, 591 (1950).

(33) G. J. Hoijtink, *Rec. Trav. Chim. Pays-Bas*, **74**, 1525 (1955).

(34) (a) I. Bergman, *Trans. Faraday Soc.*, **50**, 829 (1954); (b) A. J. Fry and R. G. Reed, *J. Amer. Chem. Soc.*, **91**, 6448 (1969).

(35) G. Douheret and M. Morenas, *Compt. Rend.*, **264**, 729 (1967).

(36) A. D'Aprano and R. M. Fuoss, *J. Phys. Chem.*, **73**, 400 (1969).

# Sedimentation Coefficients for Multicomponent Systems in the Ultracentrifuge

by C. R. Phillips and T. N. Smith

*The University of Adelaide, Adelaide, South Australia* *(Received April 1, 1969)*

Conclusions from a hydrodynamic treatment of differential sedimentation are applied to the settling of macromolecules in the ultracentrifuge. For the correlation of sedimentation coefficients in multicomponent systems dominated by the effects of weight and viscosity, an equation involving the individual sedimentation coefficients at infinite dilution and concentration-dependent geometric factors is proposed.

## Introduction

Differences between the sedimentation coefficients of the various components permit the analysis and fractionation of mixtures of macromolecular species in the ultracentrifuge.

For any one species settling alone through a liquid, it is a simple matter to determine experimentally the sedimentation coefficient as a function of concentration. Satisfactory description of this concentration dependence is usually possible, at least over a limited range, with the simple, linear equation

$$s = s_0(1 - kc) \tag{1}$$

where $s$ is the sedimentation coefficient at volume fraction $c$, $s_0$ is the sedimentation coefficient at infinite dilution, and $k$ is an experimental constant. The value of $s_0$ is a property of the effective size and density of the particular species while the value of $k$ shows some generality from species to species but does, as indicated by Creeth and Knight,[1] depend upon the shape of the macromolecule.

While the settling properties of the component species of a mixture can be defined individually, this information is not directly applicable to the mixture itself since, as remarked by Johnston and Ogston,[2] there is a hydrodynamic interaction between the various species during the settling of the mixture.

Various forms of relationships have been proposed for this interaction between sedimentation coefficients. While recognizing that a better understanding of the settling process would be required before proper account of the interaction effect could be taken, Johnston and Ogston[2] have proposed an allowance based on total volume fraction of the species present in the mixture such that

$$s_1 = s_{10}[1 - k(c_1 + c_2)] \tag{2}$$

Schachman[3] reviewed a considerable body of experimental evidence on the settling of two solute species and suggests a somewhat more general form of relationship

$$s = s_{10}[1 - k_1c_1 - k_{21}c_2] \tag{3}$$

which includes a coefficient, $k_{21}$, expressing the effec of species 2 on the sedimentation of species 1.

Although these equations permit correlation of data over a limited range, they enjoy no substantial basis in hydrodynamic theory. However, some understanding of the differential sedimentation process has come from work in the gravitational settling of macroscopic particles in recent years. This can be applied to the ultracentrifuge where the effects of weight and viscosity dominate so that the settling process is purely hydrodynamic.

It is the purpose of this paper to present conclusions from the theoretical work on macroscopic systems and to suggest bases for the correlation of sedimentation coefficients in mixed systems in the ultracentrifuge.

## Hydrodynamic Theory

The problem of the slow settling of a single, solid sphere through an infinite body of fluid has long been solved by Stokes[4] to yield for settling velocity the result

$$U_S = \frac{2}{9}\frac{a^2(\rho_s - \rho)\omega^2 r}{\eta} \tag{4}$$

where $a$ is the radius of the sphere, $\rho_s$ is the density of the sphere, $\rho$ is the density of the fluid, $\eta$ is the viscosity of the fluid, and $\omega^2 r$ is the field acceleration. For systems with appreciable solid fractions where particles are in close proximity, the flow fields associated with each particle interact and the solution of the flow equations is vastly complicated. Attempts to circumvent the difficulties involved in finding solutions for such systems have been made by utilizing modified fluid densities and viscosities to represent the effects of the rest of the system on any one particle. This has not been a fruitful approach and it presents serious inconsistencies when any generalization to

(1) J. M. Creeth and C. G. Knight, *Biochim. Biophys. Acta*, 102, 549 (1965).

(2) J. P. Johnston and A. G. Ogston, *Trans. Faraday Soc.*, 42, 789 (1946).

(3) H. K. Schachman, "Ultracentrifugation in Biochemistry," Academic Press, Inc., New York, N. Y., 1959.

(4) G. G. Stokes, *Trans. Cambridge Phil. Soc.*, 9, 8 (1851).

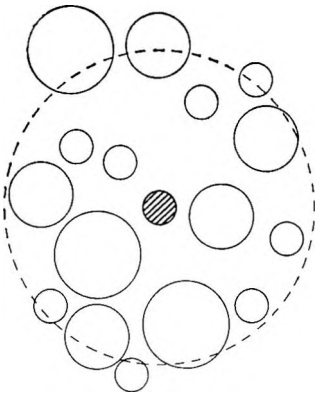

Figure 1. The basis of the hydrodynamic model—an object particle and particles interacting with it within the sample space.

multispecies systems is made.[5] The interactions between particles arise from dynamic effects in the interstitial fluid and can be evaluated only by solution of the proper hydrodynamic equations. The treatise by Happel and Brenner[6] gives a thorough exposition of the formulation of and of methods for the solution of these equations.

Special difficulties arise, unfortunately, in the treatment of systems where the particles are not regularly distributed in fluid space or where the particles are not uniform. This problem, the particular problem of multispecies systems and differential sedimentation, is posed by Phillips and Smith[7] and a simplified solution is developed.

Briefly, the model used in the simplified solution consists of an object particle in the center of a spherical sample volume of the particle–fluid space as illustrated in Figure 1. Flow continuity is satisfied within this volume. That is, there is return flow of fluid for motion of the object particle. With the provision that all particles of the one species move with the same velocity, the interactions of the object particle with all other particles randomly distributed within the sample block are considered and an approximate solution to the hydrodynamic equations is obtained. The hydrodynamic drag on the spherical object particle is found to be a linear function of the settling velocities of all species. Thus

$$F_i = 4\pi a_i \eta \sum_{j=1}^{M} \alpha_{ij} U_j \tag{5}$$

where $F_i$ is the drag on a sphere of species $i$, $a_i$ is its radius, $\eta$ is the fluid viscosity, $U_j$ is the velocity of species $j$, and $\alpha_{ij}$ is a constant dependent only on the geometry of the system. Equating this drag to the net weight of the sphere in pure fluid, the relationship

$$U_{Si} = \frac{2}{3} \sum_{j=1}^{M} \alpha_{ij} U_j \tag{6}$$

where $U_{Si}$ is the Stokes settling velocity is obtained.

Equation 6 expresses the settling velocities of all $M$ species in a set of linear equations involving the settling velocities of the individual species at infinite dilution. It is easy to form the determinant of the coefficients $\alpha_{ij}$ in this equation to obtain the explicit relationship

$$U_i = \sum_{j=1}^{M} \beta_{ij} U_{Sj} \tag{7}$$

where the $\beta_{ij}$ involve products of the $\alpha_{ij}$ and are, consequently, geometric factors.

The total geometry of a settling system is defined by the size ratios and the volume fractions of the various species. Local, instantaneous geometries do, of course, vary within the scope of random allocation of the particles in space. Values of the geometric coefficients for any one system should, therefore, be based on computations over the range of local, random configurations of particles. Phillips[5] has computed values of $\alpha_{ij}$ for binary systems of spherical particles over a range of size ratios and volume fractions. To illustrate the pattern of these results, Figure 2 shows the effect of volume fraction on the sedimentation velocities in two different mixtures of two solid species. In Figure 2(a) the sizes of the species are the same but their effective densities differ, while in Figure 2(b) the sizes are different but the effective densities are the same. In both systems the concentrations of each species are in the ratio 1:1.

**Application to the Ultracentrifuge**

Under conditions of the predominance of weight and hydrodynamic forces in the ultracentrifuge, eq 7 may be used as a basis for the correlation of sedimentation coefficients in mixed-species systems.

While molecular species are not spherical in shape, they do have determinable settling velocities at infinite dilution. These velocities, corresponding to the $U_{Sj}$ of eq 7, imply effective values of particle radius and density. For a system containing specified components, therefore, the geometry depends only upon the concentrations of the various species. Thus for a binary system the settling velocities are given by

$$\begin{aligned} U_1 &= \beta_{11} U_{S1} + \beta_{12} U_{S2} \\ U_2 &= \beta_{21} U_{S1} + \beta_{22} U_{S2} \end{aligned} \tag{8}$$

where the $\beta_{ij}$ are functions of the volume fractions of the two species.

There are evident similarities between the hydrodynamic eq 8 and the empirical eq 3 for the settling of two solid species. Equation 3 can be written as

$$s_1 = (1 - k_1 c_1) s_{10} + (-k_{21} c_2 (s_{10}/s_{20})) s_{20} \tag{9}$$

(5) C. R. Phillips, Ph.D. Thesis, University of Adelaide, 1967.

(6) J. Happel and H. Brenner, "Low Reynolds Number Hydrodynamics," Prentice-Hall, Inc., Englewood Cliffs, N. J., 1965.

(7) C. R. Phillips and T. N. Smith, *Chem. Eng. Sci.*, **24**, 1321 (1969).

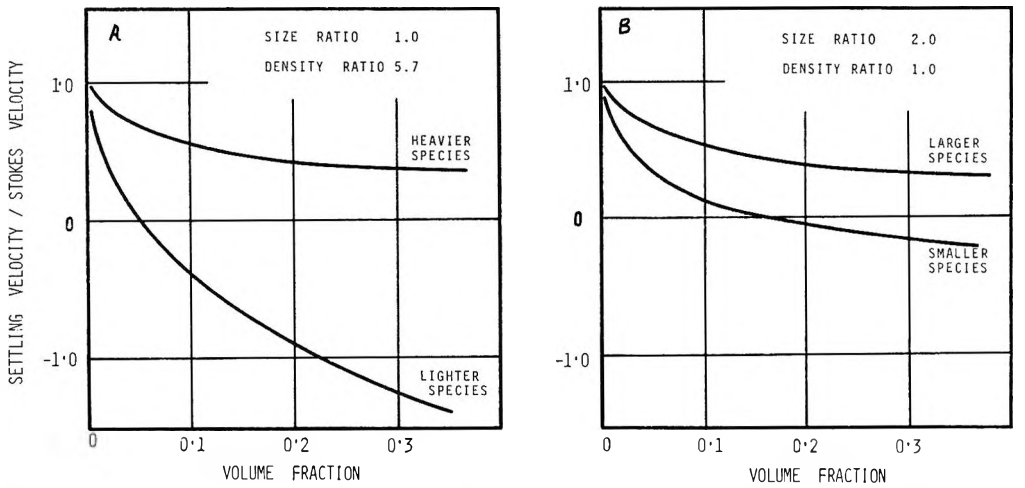


Figure 2. The effect of volume fraction on the settling velocities of (a) mixed-density and (b) mixed-size species. In both systems the volume fractions of each species are in the ratio 1:1.

which is an especially simple form of eq 8 since $k_1$ and $k_{21}$ have constant values. As is evident from the computations on the hydrodynamic model as shown in Figure 2, this linear relationship may be quite satisfactory over a limited range of low concentrations but it is certainly not adequate as a general form of correlation for two-species settling. The appropriate form would make both $k_1$ and $k_{21}$ functions of both concentrations, $c_1$ and $c_2$.

Equation 8, expressed in sedimentation coefficients rather than velocities, gives the appropriate form as

$$\begin{aligned} s_1 &= k_{11}s_{10} + k_{12}s_{20} \\ s_2 &= k_{21}s_{10} + k_{22}s_{20} \end{aligned} \tag{10}$$

The principal conclusion of this paper is that the coefficients $k_{ij}$ in eq 10, which is based on a hydrodynamic treatment of mixed-species settling, are concentration dependent. While the theoretical results of Phillips[5] for the settling of rigid spheres in a range of geometries are available, it cannot be suggested that these results be applied directly to assign definite values to the $k_{ij}$ since the hydrodynamic behavior of macromolecules of various shapes with, perhaps, intermolecular forces strong enough to promote some degree of spatial ordering must differ substantially from that of rigid spheres. However, some generality of the $k_{ij}$ from system to system is to be expected where the effective size ratios of the settling species correspond.

## Formulation of Phenomenological Equations

The hydrodynamic treatment of sedimentation takes no account of diffusion effects or interparticle forces. While the viscous forces may well predominate in the settling of macromolecules, the other effects become relatively more significant with decreasing molecular size. Flow in the ultracentrifuge when viscous forces can be neglected is usually described by means of the "phenomenological" equations of irreversible thermodynamics. In this approach the mass flux of any settling species is linearly dependent on "forces" associated with all species in the system. Thus

$$J_i = \sum_{k=1}^{M} L_{ik}X_k \tag{11}$$

for the components $i = 1, 2, \ldots, M$ where $J_i$ is the mass flux, $X_k$ is the force associated with species $k$, and $L_{ik}$ is the coefficient giving the effect of this force on the flux of component $i$.

In the interests of generality, it is possible to formulate a viscous term for inclusion in the phenomenological equations so that they may be applied to the settling of large molecules. The viscous drag on a spherical particle is given by eq 5. Expressed as a viscous force per unit mass this becomes

$$\begin{aligned} X_{\eta i} &= F_i/(4/3)\pi a_i^3\rho_i \\ &= \frac{3\eta}{\rho_i a_i^2}\sum_{j=1}^{M}\alpha_{ij}U_j \end{aligned} \tag{12}$$

which, with substitution for the settling velocities in terms of mass fluxes, gives

$$X_{\eta i} = \frac{3\eta}{\rho_i a_i^2}\sum_{j=1}^{M}\alpha_{ij}\frac{J_j}{\rho_j c_j} \tag{13}$$

While this term describes the viscous force effectively, its introduction complicates the phenomenological equations very considerably since they are no longer explicit with regard to the mass flux of any species.

# NOTES

## γ-Irradiation Effects on the Thermal Stability and Decomposition of Ammonium Perchlorate

by Scott Fogler

*Division of Chemical Engineering, University of Michigan, Ann Arbor, Michigan 48104*

and David Lawson

*Jet Propulsion Laboratories, California Institute of Technology, Pasadena, California 91103* *(Received March 26, 1969)*

Studies were conducted on the decomposition of γ-irradiated and unirradiated ammonium perchlorate at temperatures around 135°, whereas most similar investigations have been undertaken at substantially higher temperatures. One technique of observing the decomposition of ammonium perchlorate (AP) is to measure its weight loss as a function of time. Large variations in the amount of weight losses have been observed between different lots of ammonium perchlorate.[1] Some lots of ammonium perchlorate lost no weight after being stored at 135° for 600 hr, while other lots lost a very large percentage of their initial weight. The lot used in this study (lot 253 manufactured by the American Potash and Chemical Co.) was typical of those lots which lost substantial amounts of weight.

The decomposition of ammonium perchlorate can be considered to take place in three periods: the induction period, the acceleration period, and the decay period. The induction period is that time during which the ammonium perchlorate has decomposed a negligible amount so as to be almost undetectable in terms of per cent weight loss (*i.e.*, approximately 0.5% weight loss). Bircumshaw and Newman studied the decomposition of ammonium perchlorate in the temperature range of 200–300° and found the induction period to be of the order of 10–40 min.[2] However, in the studies reported in the present work at 135°, the induction period is the order of 300–400 hr.

The effects of γ irradiation on the decomposition process were studied in experiments by Herley and Levy[3] and Freeman and Anderson.[4,5] However, these irradiation decomposition studies were undertaken at high temperatures in which there was essentially very little or no induction period. In Herley's study, it was found that at high temperatures, induction period was totally eliminated with γ radiation. However, in the study reported here it was found that at lower temperatures the induction period was not completely eliminated even with very long irradiation times.

### I. Experimental Apparatus and Procedure

The experiments conducted in this study were divided into three segments: a qualitative analysis of the product gases given off by the ammonium perchlorate (AP) at various times during the decomposition, the effect of γ irradiation on the decomposition of unground AP at low temperatures, and the effect of γ radiation on ground AP at low temperatures.

In the first phase of this study, a mass spectrometer was used in the qualitative analysis of the gaseous decomposition products. In these tests approximately 2.0 g of AP were placed in a 0.75-in. test tube which had two stopcock outlets at the top of the tube. The tube containing the AP was immersed in a Haillikaner Instrument Thermotrol silicone oil constant-temperature bath which maintained the temperature of the AP sample at 135 ± 0.01°. The AP sample tube was removed from the bath at approximately 24-hr intervals, and the gas above the AP was analyzed in a mass spectrometer.

In the second segment of this study a sample of the AP was irradiated with γ rays for different lengths of time. The $^{60}Co$ source emitted approximately 1.1 Mrads of γ rays into $H_2O$/hr. After irradiation the AP samples were weighed and then placed in a constant-temperature air oven maintained at 135 ± 1°. Control samples which had not been irradiated were also placed in the constant-temperature bath. The samples were removed at various times and weighed. The weight loss of the samples at various times was obtained and recorded as per cent weight loss.

In the third series of experiments samples of lot 253 were ground up with an LNP Micropulverizer. The average particle size was determined by utilizing stainless steel ASTM sieves. The ground AP particle size was about 15 μ, while the unground AP had an average particle size of about 200 μ.

### II. Discussion and Results

In the first series of experiments it was observed that

(1) D. Udlock, Jet Propulsion Laboratory, private communication, 1968.

(2) L. L. Bircumshaw and B. H. Newman, *Proc. Roy. Soc.* **A227**, 115 (1954).

(3) P. J. Herley and P. W. Levy, *Nature*, **221**, 128 (1966).

(4) E. S. Freeman and D. A. Anderson, *J. Phys. Chem.*, **65**, 1662 (1961).

(5) E. S. Freeman and D. A. Anderson, ASTM Special Publication, No. 359, 1963, p 58.

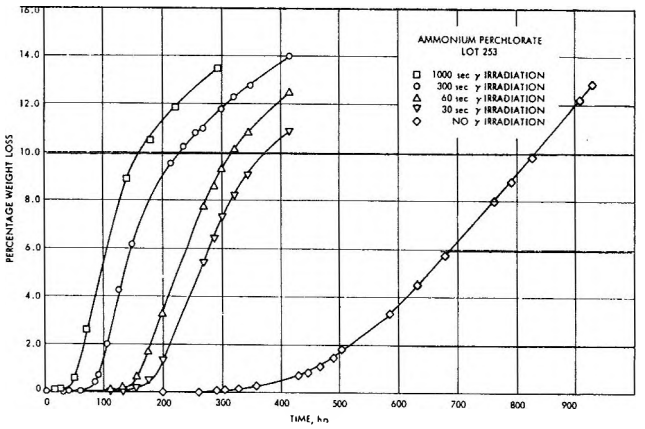


Figure 1. Decomposition curves for unground ammonium perchlorate maintained at 135°.

essentially no gaseous products could be detected in the sample tubes during the first 280 hr they were in the 135° temperature bath. At the end of 280 hr, however, a small peak on the mass spectrometer output was observed, corresponding to a trace of NO. This was the only gas that appeared above the sample in addition to air, which had appeared in the previous analyses. For the sample which was not exposed to $\gamma$ radiation, it is observed from Figure 1 that at the end of 280 hr the first measurable weight loss was observed. By the time the sample had been in the 135° bath for 360 hr the NO peak had become significant, and a trace amount of HCl could be observed from the analysis. After being immersed in the bath 400 hr, very large peaks (*i.e.*, $m/e$) of $H_2O$, $N_2$, NO, $O_2$, HCl, and Cl appeared in the analysis of the gas phase above the ammonium perchlorate sample. At the end of 500 hr, the following additional $m/e$ peaks were observed on the output from the mass spectrometer: 97, 81, 60, 55, 45, 41, and 38. It is plausible that these $m/e$ ratios could represent combinations of N, O, and Cl (*e.g.*, $NClO_2$, nitryl chloride). Residual peaks above the background of nearly all other mass to charge ratios of 25 to 95 were also observed in the 500-hr gas analysis.

The nitric oxide and hydrochloric acid were also the first and second detectable compounds to be observed in the decomposition of the samples exposed to $\gamma$ irradiation.

Since it was observed that the first gas to be liberated was nitric oxide and since some of the products are thought to be nitrosyl chlorides, it was believed that possibly nitric oxide was one of the gases which was autocatalytically attacking the solid phase. To determine if AP would react with nitric oxide, it was placed in a sample tube which was first flushed with helium, after which nitric oxide was passed through the system replacing the helium and the tube was closed. At the end of 3 hr the contents in the gas phase above the AP were analyzed in a mass spectrometer. Various products were given off, which included water, $ClO_2$, with several other compounds being present in small amounts. These results indicate that NO did indeed react with AP and that once NO is liberated, it could autocatalytically attack the remaining AP.

In Figure 1 the per cent weight loss is plotted as a function of time (in hours) for unground AP samples undergoing 1000, 300, 60, and 30 sec of $\gamma$ irradiation and a sample undergoing no irradiation. Samples were also irradiated for 1500 and 2000 sec, and the weight loss curves for these tests were found to coincide with the weight loss curve for the 1000-sec irradiation. In other words, irradiating a sample for more than 1000 sec did not appear to produce any further changes in decomposition rate or induction time. The rates of decomposition given in Table I are expressed in terms of per cent weight loss per hour.

**Table I:** Acceleratory Period Decomposition Rates of Ammonium Perchlorate

| Type AP | $\gamma$-Irradiation time, sec | Rate, %/hr |
|---|---|---|
| Unground | None | 0.0275 |
| Unground | 30 | 0.0650 |
| Unground | 60 | 0.0680 |
| Unground | 300 | 0.0950 |
| Unground | 1000 | 0.0950 |
| Ground | None | 0.0013 |
| Ground | 60 | 0.0023 |
| Ground | 300 | 0.0024 |

By observing the decomposition rate below a weight loss of 1%, it appears that the transition time in going from induction to the acceleratory period increases with decreasing irradiation time. This transition period can particularly be seen in the case of the sample that was not irradiated, as it required approximately 150 hr between the time at which the induction period ends and the time at which the acceleratory period is reached. After irradiating the sample with $\gamma$ radiation, one observes that the rates during the acceleratory period only differ by approximately 50%. Consequently, the main difference in exposure times to $\gamma$ radiation is manifested in the length of time of the induction period. As previously mentioned, one could take the induction time as that time required to reach 0.5% weight loss or 0.5% decomposition. An alternate way of expressing the induction time would be to extrapolate the acceleratory rate period down to 0% weight loss and then take this intercept as being the induction time. Utilizing this latter method, a plot of log of the irradiation time *vs.* induction period is shown in Figure 2.

The third phase of this study is concerned with the decomposition of ground AP. The per cent weight loss–time curves with and without $\gamma$ radiation for

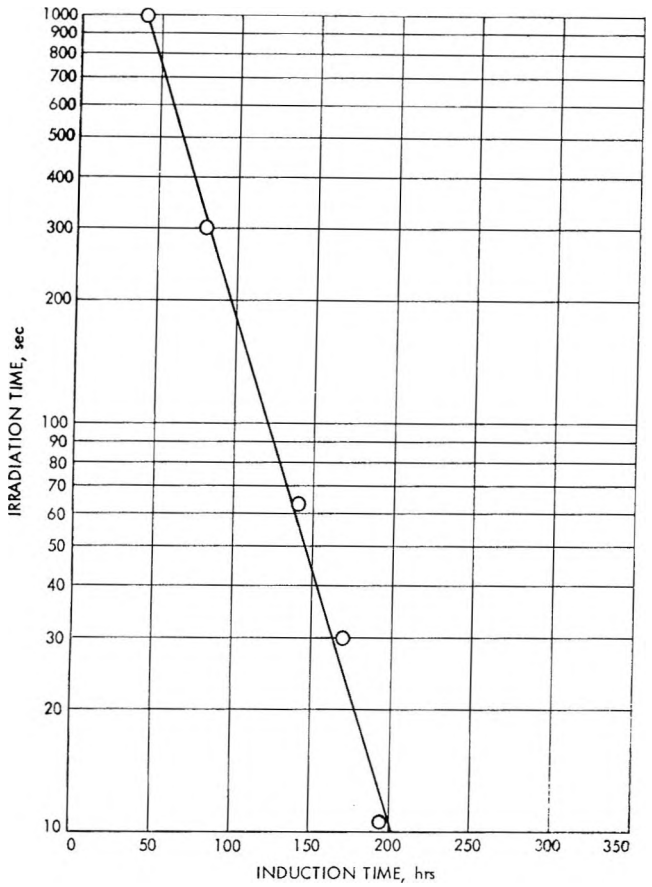


Figure 2. Induction time as a function of irradiation time for unground ammonium perchlorate maintained at 135°.

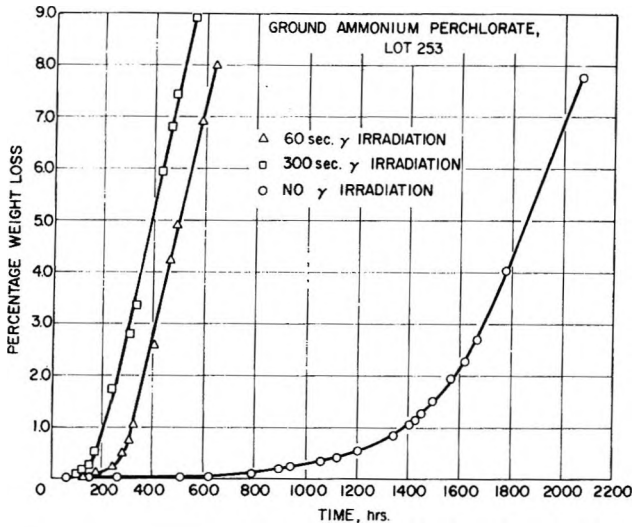


Figure 3. Decomposition curves for ground ammonium perchlorate maintained at 135°.

ground AP are shown in Figure 3. A comparison of Figures 1 and 3 reveals that the ground ammonium perchlorate takes a substantially longer time to decompose. Although the mechanism which produces these differences in stability is unknown at this time, these results were consistent and quite reproducible in a variety of tests conducted at the Jet Propulsion Laboratory. The induction time of ground AP was roughly 600 hr longer than that of unground AP. The decomposition rate during the acceleratory period of ground AP (Table I) is approximately $^1/_{20}$ the rate of unground AP during this same period.

## III. Summary

In this study, one of the first gases detected in the decomposition of ammonium perchlorate at 135° was nitric oxide. It was also found that nitric oxide reacted rapidly with ammonium perchlorate when it was injected in a test tube above the ammonium perchlorate. Some of the gases detected in the long-term decomposition, other than nitric oxide, were HCl, water, and certain nitrosyl chlorides. When samples of ammonium perchlorate were exposed to $\gamma$ radiation, it was found that the induction time decreased with increasing irradiation time up to an irradiation time of 1000 sec. The induction time was found to be directly proportional to the log of the irradiation time for samples which were irradiated less than 1000 sec. When the ammonium perchlorate was ground, it took a substantially longer time to decompose than the unground ammonium perchlorate.

*Acknowledgments.* This paper presents the results of one phase of research carried out at the Jet Propulsion Laboratory, California Institute of Technology, under Contract No. NAS 7-100, sponsored by the National Aeronautics and Space Administration.

# A Note on Optimum Parameters for the Generalized Lennard-Jones Intermolecular Potential

by Robert C. Ahlert, Gabriel Biguria, and John W. Gaston, Jr.

*Rutgers, The State University, New Brunswick, New Jersey 08903* *(Received April 28, 1969)*

In ref 1, the use of equilibrium and nonequilibrium data in the development of optimum potential function parameters was discussed. Emphasis was placed on use of data in the range of temperatures below $T_{6-12}^* = 2$, as recommended by Klein and Hanley.[2,3] An objective function defined on low-pressure transport properties yielded numerous local minimum points for both argon and methane. An objective function based

(1) W. F. Vogl and R. C. Ahlert, *J. Phys. Chem.*, **73**, 2304 (1969).

(2) M. Klein, *J. Res. Nat. Bur. Stand.*, **70A**, 259 (1966).

(3) H. J. M. Hanley and M. Klein, National Bureau of Standards Technical Note 360, U. S. Government Printing Office, Washington, D. C., 1967.

upon thermodynamic properties over ranges of both temperature and pressure, the latter to as high as 200 atm, generated a universal minimum and unique potential parameters. This was true for both argon and methane, with either compressibility or the Joule–Thomson coefficient as the state variable of the objective function.

The objective is to generate a useful potential energy model for molecular interactions from a minimum amount of experimental data. A relatively high degree of flexibility in the potential model is desired also. The work of ref 1 led the authors to a conclusion that thermodynamic data were a suitable basis for development of potential functions. However, the inclusion of thermodynamic data at elevated pressures requires the inclusion of at least the third term in the virial equation of state. Numerical evaluation of the third virial coefficient involves the assumption of pairwise additivity. This approach is acknowledged to be unrealistic,[4] while the numerical evaluation of third virial coefficients is quite time consuming, even with a large computer.

Present work employed equilibrium data at low (zero) pressure. The immediate objective was to question the applicability of Klein's criterion for temperature range. In addition, the choice of thermodynamic properties and the breadth of the temperature range required to ensure a unique potential function were examined. Because of an extensive literature, as well as the experience of earlier analyses, methane was chosen as the vehicle for this investigation.

**The Curse of Multimodality**

A generalized Lennard-Jones potential in the form

$$\phi(r) = -\frac{c}{r^6} + \frac{d}{r^\delta} \qquad (1)$$

was chosen, leaving the theoretically acceptable attractive exponent of 6 invariant. Convergent series solutions for the cluster integral, representing the second virial coefficient, are found in the literature.[5-7] Equivalent convergent series can be written for the temperature derivative of the second virial coefficient.

Three objective functions were examined. The first was based on the second virial coefficient, while the second employed the product of temperature and the derivative of the second virial coefficient. The temperature-derivative product was chosen to maintain dimensional consistency. The third objective function consisted of an unweighted, linear combination of the first two. Experimental second virial data were required in the first case. Experimental or derived Joule–Thomson coefficients, second virial data, and heat capacities, at zero pressure, were required in the second and third instances.

Din's compilation[8] was chosen as the initial source of data. Zero-pressure heat capacities were based upon the experimental data of Rossini,[9] as reduced to polynomial representation by Din.[8] $T^*$ is defined as the temperature divided by depth of the potential well for the Lennard-Jones model, reduced by the Boltzmann constant, *i.e.*, $T/\epsilon/k$. An acceptable value of the 6–12 Lennard-Jones well depth for methane is approximately 145°K.[1] Thus, $T_{6-12}^* = 2$ corresponds to a temperature of about 290°K. This study was initiated with 6 data points at 20° intervals over a range from 200 to 300°K, *i.e.*, a range of 100° located for the most part below the limit of $T_{6-12}^* = 2$.

Complete analyses were carried out at repulsive exponents of 15 and 48. These represented extremes of interest, supplementing earlier work at $\delta = 12$.[1,10] The derivative objective function exhibited unique minima for the case of 6 data points. The virial objective function was bimodal at $\delta = 15$ and unimodal at $\delta = 48$. The combined objective function exhibited this same *bimodal–unimodal* behavior, as a function of the repulsive exponent.

To test the effect of the number of data points chosen as reference, this analysis was expanded to include the same temperature range by intervals of 10° leading to manipulation of 11 data points. In all three cases, the effect of increased data over the common temperature range was relatively insignificant. The only effect was an increase in absolute magnitude of the objective functions. The location and number of minima were not influenced.

Comparable calculations were made with data from the same source at 20° intervals over a temperature range corresponding to approximately $2 < T_{6-12}^* < 3$, *i.e.*, 300–460°K. The combined range, involving temperatures between 200 and 460°K, was investigated, also. The virial objective function displayed unimodality in both the high-temperature and combined temperature ranges. The derivative objective function continued to display only unimodality, but the high-temperature data group produced an objective function that lacked a clearly defined minimum. In all cases the combined objective function paralleled the virial objective function. Inconsistencies developed with this single source of data were the most significant result of the initial analysis.

(4) J. S. Rowlinson, *Discuss. Faraday Soc.*, **40**, 19 (1965).

(5) J. O. Hirschfelder, C. F. Curtiss, and R. C. Bird, "Molecular Theory of Gases and Liquids," John Wiley and Sons, New York, N. Y., 1954.

(6) T. Kihara, *Rev. Mod. Phys.*, **25**, 39 (1952).

(7) R. C. Ahlert, G. Biguria, and J. Gaston, Jr., *A.I.Ch.E. J.*, **14**, 5, 816 (1968).

(8) F. Din, "Thermodynamic Functions of Gases," Vol. I and II, 1st ed, Butterworth and Co. Ltd., London, 1961.

(9) F. Rossini, "Selected Values of Properties of Hydrocarbons," American Petroleum Institute, Project 44, Carnegie Press, Pittsburgh, Pa., 1952.

(10) R. C. Ahlert and W. F. Vogl, *A.I.Ch.E. J.*, **12**, 1025 (1966).

### Evaluation of Source Data

To define the role of choice of experimental data, values of the virial coefficient and the zero-pressure Joule–Thomson coefficient from several sources were compared.[8,11–17] Analysis of the virial data indicated a high degree of agreement between the several sources. Hanley and Klein pointed out that some error can be tolerated in experimental data without destroying the capacity of the data to define a potential function. For the virial coefficient, this error is given by $0.04 \cdot [B(T)]$ at $T_{6-12}^* = 2$ or about 2.4 cc/mol for methane and is not a function of temperature. Virial data from the several sources generally meet this specification.

Joule–Thomson data were quite the opposite; it was highly scattered and exhibited variations between sources of as much as 25% of the average value at a particular temperature. It was demonstrated that the variation of Joule–Thomson coefficients in the literature produced large variations in the location of the optimum attractive coefficient. These observations were in agreement with requirements on Joule–Thomson data according to Hanley and Klein. They claimed errors greater than 1% make it impossible to distinguish between members of a family of potentials. Because of this problem, the literature Joule–Thomson coefficient data for methane were discarded as a source of information on the intermolecular potential.

### Final Treatment of Second Virial Data

A polynomial expression for all of the virial data was used to generate an 18-point data set with the following distribution: 120–180°K, 4 points; 200–300°K, 11 points; >300°K, 3 points. Low-temperature and high-temperature points (the high-temperature points each at 500 and 600°K) were used to broaden the range substantially. At the upper end, the range extended to a $T_{6-12}^*$ of approximately 4 and at the lower end to a $T_{6-12}^*$ of about 0.8.

The initial part of the investigation led to several instances of multimodality or lack of uniqueness in the objective function of the second virial coefficient, even when the Hanley and Klein criteria were satisfied. To test whether this lack of uniqueness resulted from using too small a temperature range, it was decided to use the extended range from $T_{6-12}^* \cong 0.8$ to $T_{6-12}^* \cong 4$. As shown by the distribution given, the interval lower than $T_{6-12}^* = 2$ was more heavily weighed to satisfy the Hanley and Klein criteria.

Figure 1 shows clearly that the set of virial data selected led to unique minima at all repulsive exponents. Each curve of constant repulsive exponent ($\delta$) differs significantly from the others as well. The locus of "constant $\delta$" optimum ($c$, $d$) pairs exhibits a "global" minimum at $\delta \simeq 21$. This set of parameters gave the best overall fit. Model constants associated with this point are: $c/K = 1.04 \times 10^6$ °K, Å$^6$ and $d/K = 2.01 \times 10^{14}$ °K, Å$^{21}$. These constants are within ±10% of the true minimum.

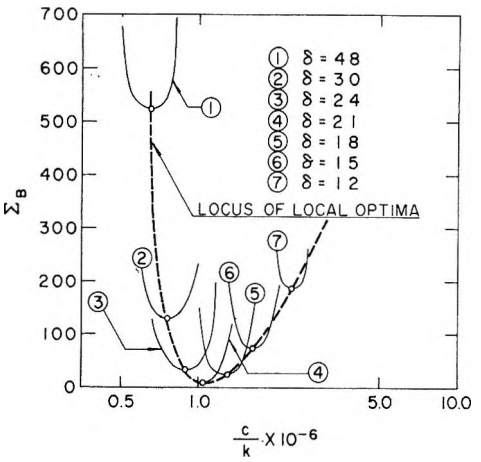


Figure 1. Local optimum potential function parameters for methane.

The dispersion coefficient, $c_6/k$, can be calculated theoretically. The value of $c_6/k$ obtained by Dalgarno[18] is: $c_6/k = 1.04 \times 10^6$ °K, Å$^6$, which is identical with the value predicted by the optimization on virial data. This extraordinary agreement is somewhat deceiving. Dalgarno suggested that the theoretical dispersion coefficient is probably accurate to better than ±10%. Thus, theoretical calculation of the dispersion coefficient predicted a value consistent with that obtained from the search scheme and within the limits of uncertainty on both results.

### Discussion

The optimum set ($\delta = 21$) and two suboptimum sets ($\delta = 12$, $\delta = 48$) of potential parameters obtained from the virial optimization were employed to predict theoretical values of $\mu^0$ at temperatures between 150 and 350°K. Figure 2 shows the results of these calculations with respect to the uncertainty of experimental data. All three sets of parameters yield curves that fall within the spread of the latter. Thus, no distinction can be drawn on the basis of this data population.

The pattern of the $\sigma$ and $\epsilon/K$ for various local optimum $\delta$'s parallels closely the result Hanley and Klein

(11) G. Thomaes and R. Van Steenwinkel, *Nature*, **187**, 230 (1960).

(12) D. Douslin, "Progress in International Research on Thermodynamics and Transport Properties," Princeton University, 1962, p 135.

(13) M. R. Jones, M. A. Byrne, and L. A. K. Staveley, *Trans. Faraday Soc.*, **64**, 1747 (1968).

(14) M. L. Jones, Jr., D. T. Mage, R. C. Faulkner, Jr., and D. L. Katz, *Chem. Eng. Progr. Symp. Ser.*, **44**, 52 (1963).

(15) C. S. Mathews and C. O. Hurd, *Trans. Amer. Inst. Chem. Eng.*, **42**, 55 (1946).

(16) B. A. Budenholzer, B. H. Sage, and W. N. Lacey, *Ind. Eng. Chem.*, **31**, 369 (1939).

(17) R. C. Ahlert, "Joule-Thomson Coefficients and Equations of State for Mixtures," Lehigh University, Bethlehem, Pa., 1964.

(18) A. Dalgarno, "Intermolecular Forces," J. O. Hirschfelder, Ed., John Wiley and Sons, New York, N. Y., 1967.

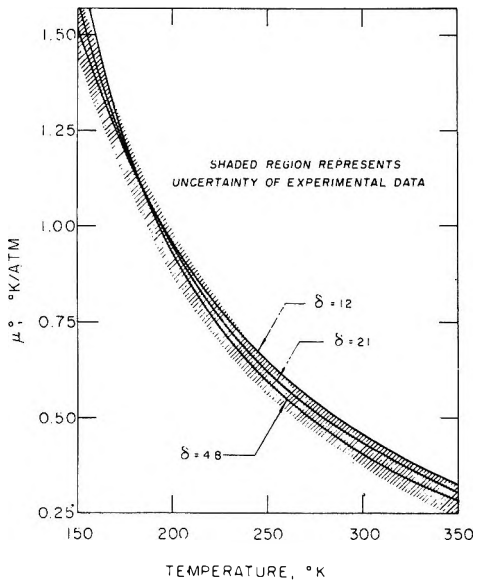


Figure 2. Comparison of selected Joule–Thomson coefficient predictions with the results of experiment.

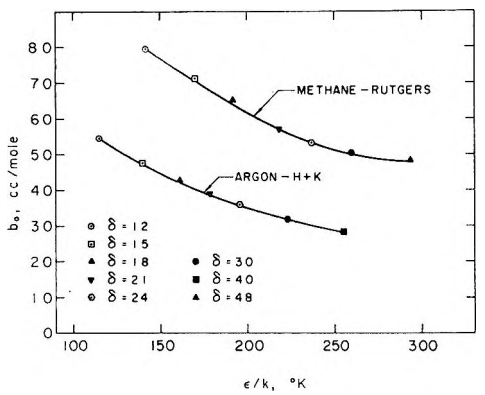


Figure 3. Comparison of well depths and residual volumes for local optimum parameters.

obtained for argon. As $\delta \rightarrow 48$, the potential well depth becomes greater and the repulsive wall becomes steeper (harder). For $\delta \rightarrow 12$, well depth decreases and the repulsive wall becomes softer. The optimum condition, $\delta = 21$, occurs at an intermediate condition. These results are described in Figure 3. At present, there is no method that can be used to determine directly the dimerization energy and thus, the well depth, independently and without *a priori* selection of a potential energy model. The well depth resulting from the optimum parameters is $\epsilon/k_{6-21} = 218°K$.

Multimodality in the virial objective function only disappeared when the temperature range was increased. The final set of data selected was heavily weighed toward the potentially sensitive temperature region according to the Hanley and Klein criteria. It appears that it is necessary, but not sufficient, to use data in the temperature-sensitive region specified by the Hanley–Klein criteria in order to obtain the best set of parameters for the generalized Lennard-Jones potential. Using data in this region does not guarantee uniqueness in the intermolecular potential parameters. A necessary condition for uniqueness appears to be the use of experimental data over a broad temperature range. The authors found that for the virial objective function, a temperature range of $0.8 < T_{6-12}^* < 4$ was satisfactory. The range between 200 and 300°K was inadequate for specification of the virial objective function, although this region was within the temperature limits of the Hanley and Klein criteria.

## Hydrogen-Bond Effect in the Radiation Resistance of Chloral Hydrate to γ Rays

by F. K. Milia and E. K. Hadjoudis

*Nuclear Research Center, "Democritos," Athens, Greece*
*(Received June 11, 1969)*

In a previous work, using γ rays, we[1] investigated the influence of the crystal structure on the radioresistance of *p*-dichlorobenzene by irradiating two different crystalline modifications of this compound, and we found that the height of the nuclear quadrupole resonance line corresponding to the α form decreased to half that of the β form for the same dose of irradiation. This difference was attributed to differences in the crystal structures of the two forms. In the light of the above work, we wish to examine the influence of additional factors, such as the hydrogen bond, on the radioresistance. For this purpose we chose chloral hydrate, $CCl_3CH(OH)_2$, which is known to present a triplet structure in its quadrupole spectrum,[2] with components located at 37.513, 38.699, and 38.784 Mcps at 23°. Thus the two lines are separated by about 80 kc while the third is almost 1.25 Mc lower than the other pair. It is known that small splittings are attributed to crystallographically nonequivalent atoms[3] while splittings of greater than 0.5 Mc must be attributed to a different type of chemical bonding to the chlorine atoms. The original crystal structure of chloral hydrate[4] shows three different C–Cl distances, 1.79, 1.78, and 1.72 Å, and it was suggested[5] that the two chlorines at longer distances are hydrogen bonded through the hydroxyl groups of adjacent molecules. Such an interpretation is consistent with the quadrupole resonance spectrum if the lowest frequency line is attributed to the nonhydrogen-bonded chlorine, while the two higher frequencies and slightly split lines are

(1) F. Milia and E. K. Hadjoudis, *J. Phys. Chem.*, **72**, 4707 (1968).
(2) H. C. Allen, Jr., *J. Amer. Chem. Soc.*, **74**, 6074 (1952).
(3) H. G. Dehmelt, *Z. Phys.*, **130**, 356 (1951).
(4) S. Kondo and I. Nitta, *X-Sen*, **6**, 53 (1950).
(5) H. C. Allen, Jr., *J. Phys. Chem.*, **57**, 501 (1953).

attributed to chlorines involved in hydrogen bonds. This is in disagreement with theoretical considerations which indicate that the hydrogen-bonded chlorines should have a lower frequency.[5] However, it was later found by Ogawa[6] that the structure of Kondo and Nitta was in error; he redetermined the structure of chloral hydrate and showed that the three C–Cl distances were 1.86, 1.87, and 1.72 Å, while the nature of the hydrogen bonds was revealed unambiguously.

In view of these circumstances and on the radioresistance results reported below, we looked more critically at the correct structure and derived some conclusions.

## Experimental Section

The spectrophotometer used in this work has been described previously.[1] The irradiation facility used was a $^{60}Co$ source whose dose rate was $2 \times 10^5$ R/hr. The frequencies were measured with a Beckman frequency meter, Model 7175 H, and are accurate to ±5 kc. Resistance to $\gamma$ rays was measured, using the intensity of each component of the triplet at 23°. During the irradiation the samples were held at 23° by circulating water from a thermostat since this compound is transformed[6] on heating into a high-temperature form at 52.6°. The practice was to measure the height of the nuclear quadrupole resonance lines of the powdered compound before and after the irradiation with different doses. To avoid instrumental variations, the height of the line of each sample under study was always compared to that of a standard sample measured afterward. In this region no variation in the line width was detectable. All the powdered crystalline samples measured were of the same grain size, 0.104 mm, since we observed[7] that this quantity has an effect in the radiation damage with $\gamma$ rays. The intensity of the three lines of chloral hydrate, in contrast to the usual situation, recovers in a few days to almost the value it had before the irradiation. However, this recovery cannot affect the values measured for the radioresistance since the highest doses used have been delivered in 3 hr, whereas recovery becomes significant after a few days.

## Results and Discussion

The results of these measurements are shown in Figure 1. Two of the three curves thus obtained are practically identical while the third lies lower. This means that the damage in chloral hydrate is larger when we measure at 37.513 Mcps than at 38.699 or 38.784 Mcps, the last two showing the same damage. This difference is attributed to the different type of chemical bonding to the chlorine atoms. The crystal structure of chloral hydrate shows that there is only one hydrogen-bonded chlorine atom, chlorine number (1) in Ogawa's[6] notation. If we attribute the lower frequency to this chlorine atom, then a consistent

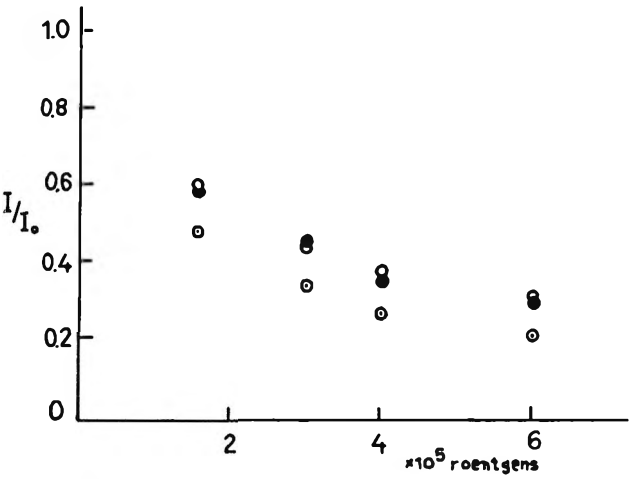


Figure 1. Radiation resistance of chloral hydrate to $\gamma$ rays: ● = $\nu_3$, 38.699 Mcps; ○ = $\nu_3$, 38.784 Mcps; ⊙ = $\nu_1$, 37.513 Mcps.

picture emerges from the theory[5] which required lower frequency for hydrogen-bonded chlorines and from the radioresistance results since hydrogen bonding results in longer and hence weaker C–Cl bond.[8] Thus, we feel that too much reliance should not be put on the figures quoted by Ogawa[4] for the length of the C–Cl bonds (the hydrogen-bonded chlorine should have a higher value than the two other nonhydrogen-bonded chlorines), since, in fact, as is pointed out by Ogawa himself, for several reasons, he could not obtain sufficiently accurate intensity data; especially the position of the carbon atom bonded with the chlorine atoms was less accurately determined because of the overlapping in the three projected planes seen in Figures 1, 2, and 3 of his paper.

*Acknowledgments.* We wish to thank Mr. M. Voudouris for technical assistance.

(6) F. Ogawa, *Bull. Chem. Soc. Jap.*, **36**, 610 (1963).

(7) F. K. Milia and E. K. Hadjoudis, unpublished observations.

(8) L. Pauling, "The Nature of the Chemical Bond," Cornell University Press, Ithaca, N. Y., 1967, p 107.

# Internal Rotation in Solid Glycine from Low-Temperature Heat Capacity Data

by Robert Chun-Jen Li and Neil S. Berman

*School of Engineering, Arizona State University, Tempe, Arizona 85281* *(Received July 30, 1969)*

Glycine has received considerable attention recently for its biological interest and because some of its compounds are ferroelectric. Nuclear magnetic resonance[1]

(1) V. Saraswati and R. Vijayaraghavan, *J. Phys. Soc. Jap.*, **23**, 590 (1967).

and electron spin resonance[2] studies show internal motion of the $NH_3^+$ group changing from a rigid structure at temperatures below 100°K to a rotation at temperatures above 200°K. A similar result along with other information on the molecule can be obtained from low-temperature heat capacity data. Extensive data are available for the calculation of the heat capacity from infrared spectra and comparisons can be made with the experimentally measured heat capacities of Hutchens, *et al.*,[3] for the solid. Only the skeletal bending motions and the barriers to internal rotation are in doubt, and these parameters can be selected to give the best agreement with experiment. The results are valuable in interpreting the behavior of solid glycine as a function of temperature.

Calculations of the heat capacity of a solid from molecular parameters have been illustrated by Simpson and Beynon[4] based on the earlier work of Wulff.[5] In this work the lattice expansion contribution to the heat capacity, $C_p - C_v$, was determined by including a term due to internal rotation as suggested by Simpson and Beynon. The other contributions are from the lattice vibrations, $C_v^L$, the internal vibrations $C_v^I$, and internal rotation, $C_v^{IR}$. These were all calculated in the standard manner given by Wulff or Simpson and Beynon.

Table I gives the vibrational assignment for glycine

**Table I:** Assignments of the Vibrational Frequencies of Glycine

| Assignment | Freq, $cm^{-1}$ |
|---|---|
| $NH_3^+$ antisym str | 3180 |
| $CH_2$ antisym str | 2915 |
| $CH_2$ sym str | 2830 |
| $NH_3^+$ sym str | 2620 |
| $COO^-$ antisym str | 1604 |
| $NH_3^+$ deg def | 1585 |
| sym $NH_3^+$ def | 1527 |
| sym $NH_3^+$ def | 1514 |
| sym $NH_3^+$ def | 1502 |
| $CH_2$ scissor | 1443 |
| $COO^-$ sym str | 1413 |
| $CH_2$ wag with C–C str | 1334 |
| $CH_2$ twist | 1314 |
| $NH_3^+$ rock | 1133 |
| $NH_3^+$ rock | 1114 |
| C–N str | 1035 |
| $CH_2$ rock | 912 |
| $COO^-$ scissor | 894 |
| $COO^-$ bend | 700 |
| $COO^-$ wag | 608 |
| $COO^-$ rock | 420 |
| C–C–N bend | 360 |

which was selected along with a Debye temperature of 245°K for six degrees of freedom to fit the data best. The frequencies in Table I were taken from the infrared studies of Suzuki and Shimanouchi,[6] Laulicht, *et al.*,[7] and Tsuboi, *et al.*[8]

The two groups which can rotate internally in glycine were found to have reduced moments of inertia of $3.295 \times 10^{-40}$ g/cm² for $NH_3^+$ group and $3.02 \times 10^{-39}$ g/cm² for the $COO^-$ group. Using a threefold cosine type barrier the heights of the barriers for internal rotation were 3.45 ± 0.2 kcal/mol for the $NH_3^+$ and 61 ± 3 kcal/mol for the $COO^-$ group. Intermolecular angles and lengths from Albrecht and Corey[9] and Marsh[10,11] were used to obtain the reduced moments of inertia.

Table II shows the results of the calculations using the above parameters and the following expression for the lattice expansion

$$C_p - C_v = 0.0125C_v^L + 0.000043[C_v^I + C_v^{IR}]^2T$$

The deviations between the calculated and observed heat capacities are less than 0.33% above 40°K and the maximum absolute error was 0.08 cal/mol deg. The agreement is better than for other studies of low-temperature heat capacities.[4,5]

The internal rotation barriers indicate that the $COO^-$ group may be treated as an ordinary vibration with a frequency of 421 $cm^{-1}$. There is no rotation of this group in agreement with the solid structure of double layers of molecules held together by hydrogen bonds. The $NH_3^+$ group provides most of the contribution to the $C_v^{IR}$ shown in Table II at temperatures below 200°K. The tables of Pitzer and Gwinn[12] were used to calculate the heat capacity contribution of the $NH_3^+$ rotation. A curve of heat capacity contribution from internal rotation from 70°K to higher temperatures would have an inflection in the same temperature range as the curves obtained for the second moment *vs.* temperature from proton magnetic resonance.

The close agreement of the calculated results to the experimental for the ionic organic crystal indicates that the method can be applied to other structures and salts of this type. In other molecules $NH_2$ groups have been found to have barriers to internal rotation of 3.3 kcal/mol for hydrazine and 3.7 kcal/mol for methyl hydra-

(2) H. Reitboeck, *Biophysik*, 4, 15 (1967).

(3) J. O. Hutchens, A. G. Cole, and J. W. Stout, *J. Amer. Chem. Soc.*, **82**, 4813 (1960).

(4) K. O. Simpson and E. T. Beynon, *J. Phys. Chem.*, **71**, 2796 (1967).

(5) C. A. Wulff, *J. Chem. Phys.*, **39**, 1227 (1963).

(6) S. Suzuki and T. Shimanouchi, *Spectrochim. Acta*, **19**, 1195 (1963).

(7) I. Laulicht, S. Pinchas, D. Samuel, and I. Wasserman, *J. Phys. Chem.*, **70**, 2719 (1966).

(8) M. Tsuboi, T. Onishi, I. Nakagawa, T. Shimanouchi, and S. Mizushima, *Spectrochim. Acta*, **12**, 253 (1958).

(9) G. Albrecht and R. B. Corey, *J. Amer. Chem. Soc.*, **61**, 1087 (1939).

(10) R. E. Marsh, *Acta Crystallogr.*, **10**, 814 (1957).

(11) R. E. Marsh, *ibid.*, **11**, 654 (1958).

(12) K. S. Pitzer and W. D. Gwinn, *J. Chem. Phys.*, **10**, 428 (1942).

**Table II:** Heat Capacity of Glycine (cal/mol deg)

| Temp, °K | $C_v^L$ | $C_v^I$ | $C_p - C_v$ | $C_v^{IR}$ | $C_p$, calcd | $C_p$[3] | $C_p - C_p$, calcd |
|---|---|---|---|---|---|---|---|
| 20 | 0.51 | 0.00 | 0.01 | 0.00 | 0.52 | 0.57 | 0.05 |
| 40 | 3.04 | 0.00 | 0.04 | 0.00 | 3.08 | 3.10 | 0.02 |
| 60 | 5.85 | 0.03 | 0.07 | 0.08 | 6.03 | 6.01 | −0.02 |
| 80 | 7.78 | 0.20 | 0.10 | 0.31 | 8.39 | 8.42 | 0.03 |
| 100 | 8.99 | 0.52 | 0.12 | 0.67 | 10.30 | 10.34 | 0.04 |
| 120 | 9.77 | 0.96 | 0.14 | 1.06 | 11.93 | 11.95 | 0.02 |
| 140 | 10.28 | 1.49 | 0.18 | 1.44 | 13.39 | 13.40 | 0.01 |
| 160 | 10.63 | 2.09 | 0.24 | 1.78 | 14.74 | 14.74 | 0.00 |
| 180 | 10.89 | 2.74 | 0.31 | 2.08 | 16.02 | 16.02 | 0.00 |
| 200 | 11.07 | 3.44 | 0.43 | 2.33 | 17.27 | 17.28 | 0.01 |
| 220 | 11.22 | 4.18 | 0.57 | 2.54 | 18.51 | 18.52 | 0.01 |
| 240 | 11.33 | 4.98 | 0.75 | 2.72 | 19.78 | 19.80 | 0.02 |
| 260 | 11.41 | 5.80 | 0.99 | 2.87 | 21.07 | 21.14 | 0.07 |
| 280 | 11.48 | 6.67 | 1.27 | 3.00 | 22.42 | 22.48 | 0.06 |
| 300 | 11.54 | 7.57 | 1.61 | 3.10 | 23.82 | 23.84 | 0.02 |

zine as listed by Miller.[13] The addition of another hydrogen to the $NH_2$ group and removal of it from the oxygen has led to correct results in the rigid solid. In contrast to other work on low-temperature heat capacities, the results found here for glycine cannot be extrapolated to the gas phase.

(13) S. I. Miller, *J. Chem. Educ.*, 41, 421 (1964).

## A Nuclear Magnetic Resonance Study of the Effect of Charge on Solvent Orientation of a Series of Chromium(III) Complexes. II

by Lawrence S. Frankel[1]

*Department of Chemistry, University of Massachusetts, Amherst, Massachusetts 01002* *(Received August 25, 1969)*

An nmr technique for studying the average orientation of neutral molecules in the solvation shell (second coordination sphere) of Cr(III) complexes was recently reported.[2,3] Basically the experiment compares the spin–spin relaxation times ($T_2$) of two or more nonequivalent protons of the same molecule in the presence of a nonlabile paramagnetic Cr(III) complex. It is reasonable to expect that these results should be appliable to Co(III) compounds with the same ligands. Ideally one might hope that substitution reactions that involve the entering neutral ligand as a stoichiometric component of the transition state might be rationalized on this basis.

Previously the average orientation of N,N-dimethylformamide, N,N-dimethylacetamide, and methanol was reported for a series of Cr(III) compounds of varying charge and ligand.[2] For ±3 charged solutes the solvation shell was strongly oriented along the ligand dipole moment vector. For lesser charged solutes the orientation is more random in nature.

In the present investigation we restrict attention to ±3 charged complexes. The complexes used were $Cr(H_2O)_6(ClO_4)_3$, $Cr(en)_3(ClO_4)_3 \cdot 2H_2O$ (en = ethylenediamine), and $K_3Cr(NCS)_6$. Data for a variety of pyridine, phosphoryl, acetate, carbonyl, and nitrile solvents are reported. The choice of solute is restricted by solubility. The solvent must have two or more resonances which are not unduly complicated by spin–spin interactions. Our primary objective is to test further in a qualitative manner an ion dipole model and try to learn the factors that determine solvent orientation effects.

The equipment, source of Cr(III) complexes, experimental errors, theoretical considerations, and chemical limitations are not significantly different from those previously reported.[2] All solvents employed are readily available from commercial sources and were used without further purification. With the exception of trace amounts of water, no other proton signals were observed in a pure solution of the solvents.

The line width at half-height ($\Delta\nu$) is related to the spin–spin relaxation rate by $\pi\Delta\nu = 1/T_2$. If the relaxation times of two nuclei of the same molecule are compared

$$\Delta\nu_1/\Delta\nu_2 = r_2^{-6}/r_1^{-6} \quad (1)$$

where $r$ is the distance from the paramagnetic metal to the proton under consideration. The data are summarized in Table I.

(1) Rohm and Haas Co., Research Laboratory 13, Philadelphia, Pa. 19137

(2) L. S. Frankel, *J. Phys. Chem.*, 73, 3897 (1969).

(3) Other related work: B. M. Fung, *J. Amer. Chem. Soc.*, 89, 5788 (1969); D. R. Eaton, *Can J. Chem.*, 47, 2645 (1969).

**Table I:** Summary of Preferential Solvation Results

| Solvent | Solute[a] | Proton probes | Relative line widths of proton probes |
|---|---|---|---|
| 2,3-Lutidine | en | $CH_3(3)/CH_3(2)$ | 0.48 |
| | NCS | $CH_3(3)/CH_2(2)$ | 1.90 |
| 3,5-Lutidine | en | $CH_3(3,5)/H(2)$ | ≈3.0 |
| | NCS | $CH_3(3,5)/H(2)$ | ≈0.6 |
| $(H)P(O)(OCH_3)_2$ | $H_2O$ | $H/OCH_3$ | 1.65 |
| | en | $H/OCH_3$ | 1.50 |
| | NCS | $H/OCH_3$ | 0.65 |
| $(CH_3)P(O)(OCH_3)_2$ | $H_2O$ | $CH_3/OCH_3$ | 1.10 |
| | en | $CH_3/OCH_3$ | 1.15 |
| | NCS | $CH_3/OCH_3$ | 0.93 |
| *m*-Tolyl acetate | NCS | $COCH_3/CH_3$ | 3.6 |
| *p*-Tolyl acetate | NCS | $COCH_3/CH_3$ | 3.3 |
| | NCS | $COCH_3/HC_6H_5$ | 2.8 |
| Benzyl acetate | NCS | $COCH_3/CH_2$ | 1.23 |
| | NCS | $COCH_3/HC_6H_5$ | 2.4 |
| *p*-Tolualdehyde | NCS | $OCH/CH_3$ | 2.2 |
| *p*-Methylacetophenone | NCS | $OCCH_3/CH_3$ | 2.6 |
| *o*-Methylbenzyl cyanide | NCS | $CH_2/CH_3$ | 1.80 |
| *m*-Methylbenzyl cyanide | NCS | $CH_2/CH_3$ | 4.5 |
| *p*-Methylbenzyl cyanide | NCS | $CH_2/CH_3$ | 5.6 |

[a] $Cr(en)_3^{3+}$ = en, $Cr(H_2O)_6^{3+}$ = $H_2O$, $Cr(NCS)_6^{3-}$ = NCS.

The following pyridine derivatives were employed 2,3-lutidine and 3,5-lutidine. Based on chemical shift and intensity comparisons with β-picoline and 2,4,6-trimethylpyridine the methyl group in the 2 position is at low field relative to a methyl group in the 3 position. The dipole moment of pyridine points toward the nitrogen atom (negative end).[4] Under the influence of an anion $\Delta\nu(3) > \Delta\nu(2)$ while a cation reverses the inequality in agreement with an ion dipole model. The data for 3,5-lutidine is only approximate because the proton in the 2 position shows long-range coupling with the 4 position. 2,3-Lutidine is a sufficiently rigid molecule so that the distance dependence of eq 1 may be tested. The calculations were made as previously described.[2] The complex ion radii employed were 3.6 Å for $Cr(en)_3^{3+}$ and 4.9 Å for $Cr(NCS)_6^{3-}$. The following solvent bond distances were employed: N=C, 1.35 Å; C=C, 1.40 Å; C—C, 1.53 Å; C—H, 1.09 Å.[5] All ring angles were assumed to be 60°. Evaluation of the sixth-power dependence gives $\Delta\nu(3)/\Delta\nu(2) = 0.37$ for $Cr(en)_3^{3+}$ and $\Delta\nu(3)/\Delta\nu(2) = 2.0$ for $Cr(NCS)_6^{3-}$ in reasonable agreement with the experimental values 0.48, 1.90.

The rate of substitution of the first $SCN^-$ from $Cr(NCS)_6^{3-}$ by methanol ($3.47 \times 10^{-5}$ $sec^{-1}$) and pyridine ($1.89 \times 10^{-5}$ $sec^{-1}$) are comparable.[6] Previously it has been shown that the hydroxy group of methanol is preferentially oriented relative to the methyl group[2] and is therefore in a relatively favorable position to react. However the donor site in pyridine has an extremely unfavorable orientation in the solvation shell. Apparently the relative orientation of the donor site in the solvation shell does not have a particularly striking effect.

The following phosphoryl solvents were employed dimethyl hydrogen phosphite (DMHP) = $(H)P(O)(OCH_3)_2$ and dimethyl methylphosphonate (DMMP) = $(CH_3)P(O)(OCH_3)_2$. All proton resonances are doublets due to spin–spin coupling with the phosphorus nucleus. The line widths were obtained from the components of the doublets. Since we are observing a second-sphere relaxation time, complications due to phosphorus chemical exchange spin decoupling will not occur.[7] The dipole moments should be dominated by the phosphoryl group which contains a large resonance contribution from the $P^+—O^-$ structure. The line width data are summarized in Table I. Under the influence of a cation, the proton nearest the phosphoryl group is broadened greatest in agreement with an ion dipole model. Although an anion shows a line width reversal, the direction of the positive end of the net dipole moment and its relative distance to the protons is not obvious. The relative line widths are larger for DMHP than for DMMP because the P—H proton is closer to the phosphoryl group. The flexibility of the methoxy group makes direct calculations difficult. The line width ratio for $P—H:P—CH_3$ in $Cr(en)_3^{3+}$ is 1.30 (obtained by combining DMMP and DMHP data). The net dipole moment is assumed to be collinear with the phosphoryl group. The following bond distances were employed: P=O, 1.48 Å;[8] P—H, 1.42 Å;[4] P–C, 1.87 Å;[4] and C–H, 1.09 Å.[4] The OPH, OPC, and PCH angles were assumed to be 109°. Evaluation of eq 1 for $Cr(en)_3^{3+}$ gives 1.4 in good agreement with the experimental value.

The following acetate solvents were employed: *m*- and *p*-tolyl acetate and benzyl acetate. The directions of the net dipole moments are dominated by the acetate group. The acetate methyl group is nearer the positive and negative end of the net dipole moment than is the phenyl methyl group. Under the influence of an anion the methyl acetate group is observed to be preferentially oriented. The changes in the relative line widths of the *p*- and *m*-methyl groups and the methylene protons are as anticipated from the geometry of the solvent. A deceptively simple (one major peak) phenyl proton spectra is obtained for *p*-tolyl acetate and ben-

(4) C. K. Ingold, "Structure and Mechanism in Organic Chemistry," Cornell University Press, Ithaca, N. Y., 1953, p 102.

(5) "Handbook of Chemistry and Physics," 46th ed, The Chemical Rubber Publishing Co., Cleveland, Ohio, 1962, pp F118, F120.

(6) S. Behrendt, C. H. Langford, and L. S. Frankel, *J. Amer. Chem. Soc.*, **91**, 2236 (1969).

(7) L. S. Frankel, *J. Chem. Phys.*, **50**, 943 (1969); *J. Mol. Spectrosc.*, **29**, 273 (1969); *Inorg. Chem.*, **8**, 1784 (1969).

(8) H. K. Wang, *Acta Chem. Scand.*, **19**, 879 (1965).

zyl acetate. The line width ratios of acetate methyl to phenyl are also consistent with proposed geometry of the solvation shell.

The directions of the net dipole moments of *p*-tolualdehyde and *p*-methylacetophenone are dominated by the carbonyl group. As with the acetate derivatives, the proton nearest the carbonyl group is preferentially oriented under the influence of an anion.

The following nitrile solvents were employed: *ortho*-, *meta*-, and *para*-substituted methylbenzyl cyanide. Under the influence of an anion, the methylene protons are preferentially oriented. The relative values observed for *ortho*, *meta*, and *para* substitution vary in a systematic fashion.

These results clearly show that neutral molecules in the solvation shell of $\pm 3$ charged solutes show well-defined intramolecular orientation effects. Although an ion dipole model does a good job in accounting for the experimental results, other interactions can selectively explain some of the results.[2] For example, hydrogen bonding between the ligand hydrogens of $Cr(H_2O)_6^{3+}$ and the phosphoryl oxygen produces an orientation which is comparable to an ion dipole interaction.

*Acknowledgment.* We gratefully acknowledge the support of the Directorate of Chemical Science, Air Force Office of Scientific Research, under Grant AFOSR 212-65.

## The Quenching of Mercury ($^3P_1$) Resonance Radiation by Aromatic Molecules

by Gilbert J. Mains[1a] and Mendel Trachtman[1b]

*Department of Physical Sciences,*
*Philadelphia College of Textiles and Science,*
*Philadelphia, Pennsylvania 19144* *(Received September 16, 1969)*

The mechanisms by which molecules quench the $^3P_1$ excited electronic state of atomic mercury have fascinated and, to a certain extent, eluded photochemists ever since Stuart's original study in 1925.[2] Darwent[3] first suggested that quenching diameters of contributing groups are additive; a suggestion which has been confirmed (within limits) by careful studies of Gunning and coworkers and Cvetanovic and coworkers in recent years. Reviews by these two investigators[4,5] represent the best compilations of quenching cross sections currently available. It is noteworthy that while extensive studies have been made of the quenching efficiencies of saturated and unsaturated hydrocarbons, the only quenching cross section for an aromatic hydrocarbon, benzene, was reported over 30 years ago. Since a complete understanding of the quenching mechanisms requires knowledge of the effects of structure on the quenching efficiencies of aromatic as well as saturated hydrocarbon systems, we have undertaken the measurements reported herein. We have measured the quenching cross section for benzene, benzene-$d_6$, and eight substituted benzene compounds.

The apparatus used was essentially that described by Yang.[6] A collimated beam of 2537-Å resonance radiation from a low-pressure mercury lamp [Oriel Optics Corp., mercury–argon lamp] was introduced into a quartz sample cell through an Infrasil window. The intensity of mercury fluorescence was measured using an 1P28 photomultiplier tube located 90° from the exciting beam in the horizontal plane. The mercury reservoir, a quartz tube sealed immediately below the sample cell, was maintained at 0° using an ice slush bath. Fluorescence measurements, which constituted the determination of the photocurrent, $Q$, in arbitrary units, were made randomly at high and low pressures of quenching gas, M, to avoid systematic errors. All chemicals used in this work were either spectrographic or research grade as specified by the supplier. Purity was confirmed by gas chromatographic analysis. The isotopic $C_6D_6$ was obtained from Stohler Chemical Co. and certified by them as 99.5% isotopically pure. It was used as received.

The data were found to be consistent with the modified Stern–Volmer formula developed by Yang.[6] Typical plots are shown in Figure 1 for $C_6H_6$ and $C_6D_6$, and in Figure 2 for the three isomers of xylene. The straight lines were drawn according to a least-squares fit of the data to the modified Stern–Volmer formula, *i.e.*

$$[1 - Q/Q_0]^{-1} = \alpha + \beta[\mathrm{M}]^{-1} \qquad (1)$$

where $Q$ is the fluorescent photocurrent in the presence of [M] mol/l. of quenching gas, M, and $Q_0$ is the fluorescent photocurrent in the absence of quenching gas. $\alpha$ and $\beta$ are constants related to the quenching rate constant, $k_Q$, and the mean lifetime of $^3P_1$ Hg atoms in the sample cell, $t$, by the equation $\beta = k_Q t\alpha$. Thus, the ratio of the slope to the intercept in Figure 1 and Figure 2 gives values for $k_Q t$. $t$ may be calculated from the equation derived by Yang for a similar geometry, *i.e.*

$$t = t_0(1 + 0.25 \times 10^4 pr) \qquad (2)$$

(1) (a) Department of Chemistry, University of Detroit, Detroit, Mich. 48221; (b) author to whom reprint requests and correspondence should be directed.

(2) H. A. Stuart, *Z. Physik*, **32**, 262 (1925).

(3) B. deB. Darwent, *J. Chem. Phys.*, **18**, 1532 (1950).

(4) H. E. Gunning and C. P. Strausz, *Advan. Photochem.*, **1**, 209 (1963).

(5) R. J. Cvetanovic, *Progr. React. Kinet.*, **2**, 39 (1964).

(6) K. Yang, *J. Amer. Chem. Soc.*, **88**, 4575 (1966).

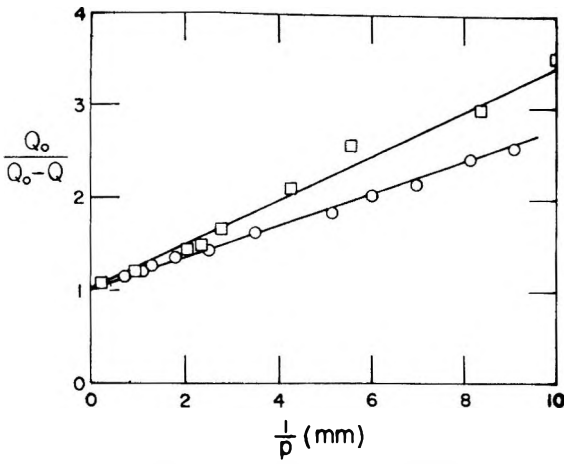


Figure 1. Quenching data of $C_6H_6$ (□) and $C_6D_6$ (○).

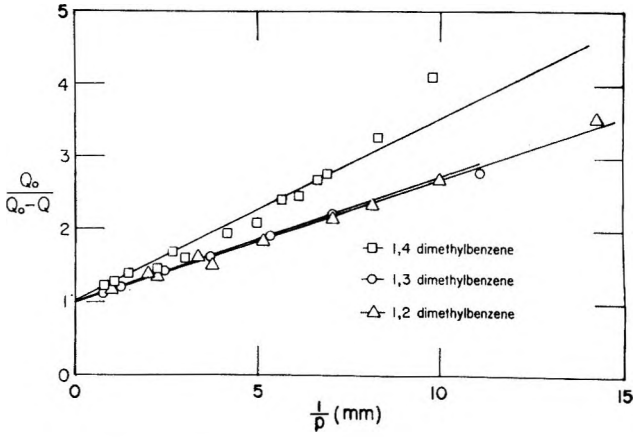


Figure 2. Quenching data of the various xylenes.

where $t_0$ is the mean radiative lifetime of an isolated $^3P_1$ Hg atom [$1.08 \times 10^{-7}$ sec], $p$ is the pressure of mercury vapor [$1.85 \times 10^{-4}$ mm], and $r$ is the distance from the irradiated slab of Hg vapor to the emerging surface of the cell [3.55 cm in this study]. Hence, $t$ was taken as $2.85 \times 10^{-7}$ sec for all the experiments reported here. The quenching cross section, $\sigma_Q^2$, is readily calculated from $k_Q$ using the familiar equation from elementary collision theory.[6]

In Table I we report $k_Qt$, $k_Q$, and $\sigma_Q^2$ for the ten aromatic compounds studied. Also reported in Table I for comparison are values for $\sigma_V^2$, the Hg–M collision cross section calculated by assuming the diameter of Hg to be 2.38 Å and estimating the diameter of M from the "$b$" constant in van der Waals' equation of state. Except for benzene and $p$-xylene, the quenching cross sections are all considerably larger than the collision cross section estimated from van der Waals radii; in many instances, the quenching cross sections are more than 50% larger than the estimates based on van der Waals radii. It would appear that the energy-transfer processes involved in physical quenching of $^3P_1$ Hg atoms occur over rather long internuclear distances, say 10 Å, and

**Table I:** $tk_Q$ and $\sigma^2$ Values in the Quenching of Hg($^3P_1$) Atoms by Various Aromatic Molecules at 25°

| Compd | $tk_Q$ | $10^{-10}k_Q$[a] | $\sigma_Q^2$, Å$^2$ | $\sigma_V^2$, Å$^2$ |
|---|---|---|---|---|
| Benzene $C_6H_6$ | 3.83 | 24.9 | 39.4 | 36.3 |
| Toluene | 5.41 | 35.3 | 59.1 | 41.4 |
| $p$-Xylene | 3.62 | 23.6 | 41.5 | 45.5 |
| $m$-Xylene | 5.34 | 34.8 | 61.2 | 45.1 |
| $o$-Xylene | 5.74 | 37.9 | 65.7 | 44.9 |
| Chlorobenzene | 6.08 | 39.6 | 71.0 | 41.2 |
| Fluorobenzene | 5.67 | 37.0 | 62.8 | 39.0 |
| Bromobenzene | 4.41 | 28.8 | 56.9 | 42.3 |
| Ethylbenzene | 5.96 | 38.9 | 68.3 | 43.9 |
| Benzene $C_6D_6$ | 6.18 | 40.4 | 65.4 | (36.3) |

[a] Units: l. mol$^{-1}$ sec$^{-1}$.

that Gunning's suggestion[7] that $^3P_1$ Hg atoms exhibit electrophilic character and interact with $\pi$-electron systems preferentially is supported by these observations. Note should also be taken that the quenching cross section for benzene, 39.4 Å$^2$, while low in comparison with the quenching cross section of the other aromatic compounds, is in excellent agreement with the value reported by Bates.[8] This agreement supports the quenching cross section measurements reported here and suggests that a better understanding of the quenching act could be obtained if we understood why benzene and $p$-xylene exhibit such relatively *small* quenching cross sections. Neglecting, for the moment, benzene and $p$-xylene it should be noted that no simple correlation exists for the trends in quenching rate constants for the other aromatic molecules reported in Table I. Attempts by us to explain substituent effects in terms of dipole moments, or polarizabilities, or even Hammett $\sigma$–$\rho$ correlations have not been successful. This is not particularly surprising in view of our fragmented knowledge of energy-transfer processes,[9] although Mettee[10] has reported some success in correlation of polarizabilities with quenching probabilities for $SO_2$. However, in view of the very large isotope effect observed in this study for the $C_6H_6$–$C_6D_6$ system, such a correlation must be ruled out for the quenching of $^3P_1$ Hg atoms by aromatic compounds.

The remarkable effect of deuteration on the quenching cross section of benzene suggests that vibronic factors may be rate determining in the quenching mechanism. The marked effect of deuteration on singlet–triplet intersystem crossing probabilities seems well

(7) Y. Rousseau, O. P. Strausz, and H. E. Gunning, *J. Chem. Phys.*, **39**, 962 (1963).

(8) J. R. Bates, *J. Amer. Chem. Soc.*, **54**, 569 (1932).

(9) A. B. Callear, "Photochemistry and Reaction Kinetics," P. G. Ashmore, F. S. Dainton, and T. M. Sugden, Ed., Cambridge University Press, Cambridge, 1967, p 133.

(10) H. D. Mettee, *J. Phys. Chem.*, **73**, 1071 (1969).

established. Thus, a mechanism involving such a crossing may be postulated as

| | Rate |
|---|---|
| $Hg + h\nu = Hg^*$ | $I_a$ |
| $Hg^* = Hg + h\nu$ | $k_f[Hg^*]$ |
| $Hg^* + Ar = (Hg^*\text{–}Ar)$ | $k_c[Hg^*][Ar]$ |
| $(Hg^*\text{–}Ar) = (Hg\text{–}Ar^*)$ | $k_i[Hg^*\text{–}Ar]$ |
| $(Hg^*\text{–}Ar) = Hg^* + Ar$ | $k_d[Hg^*\text{–}Ar]$ |
| $(Hg\text{–}Ar^*) = Hg + Ar^*$ | $k_t[Hg\text{–}Ar^*]$ |
| $Ar^* = Ar$ | $k_r[Ar^*]$ |

This mechanism is similar in some respects to that suggested by Yang[11] and, by application of the usual steady-state approximations, leads to the following relationship between $k_Q$ and the rate constants defined above

$$k_Q = k_c[k_i/(k_i + k_d)] \quad (3)$$

If one assumes a loose complex, we might place an upper limit of, say, $50 \times 10^{10} < k_c < 75 \times 10^{10}$ l. mol$^{-1}$ sec$^{-1}$ for formation of the complex. Variations in $k_Q$ could then be attributed to the relative magnitudes of the rates of intersystem crossing, $k_i$, and decomposition of the complex without energy transfer, $k_d$.

It is also possible that the increase in quenching cross section upon deuteration is the result of more efficient quenching to the Hg $^3P_0$ state by $C_6D_6$ than $C_6H_6$. Such an effect has been observed in saturated hydrocarbon systems.[12] Inclusion of such a step in the mechanism, *i.e.*, $(Hg^*\text{–}Ar) = Hg'(^3P_0) + Ar'$ (vibrated, rotated, excited), rate $= K_i'(Hg^*\text{–}Ar)$, results in the addition of $K_i'$ to the numerator and denominator of the bracket term in eq 3 and requires $k_i'$ to be much larger for $C_6D_6$ than for $C_6H_6$.

Since the number of compounds studied is limited to those reported in Table I, it would not be prudent to attempt further justification of the proposed mechanism or to discuss in detail the factors which determine the magnitudes of $k_i$ and $k_i'$. Additional work is in progress involving partial deuteration and the effects of multiple substituents on the quenching cross section. It is hoped that these further studies will yield insight necessary for a more general interpretation.

*Acknowledgment.* C. Shelhaimer and W. Hufford participated in some of the experiments reported here. We acknowledge their help with thanks.

(11) K. Yang, *J. Amer. Chem. Soc.*, **87**, 5294 (1965).

(12) S. Penzes, A. J. Yarwood, O. P. Stransz, and H. E. Gunning, *J. Chem. Phys.*, **43**, 4534 (1965).

# COMMUNICATIONS TO THE EDITOR

## Electron Spin Resonance of Radicals Formed in the Reaction of Nitrogen Dioxide with Olefins

*Sir:* Recently, Bielski and Gebicki published an esr study on the interaction of $NO_2$ and olefinic solvents in which they attributed the esr spectra to the existence of $NO_2$ olefin $\pi$ complexes.[1]

We have been studying this subject for some time, too. Since our results do not give any evidence for the existence of these $\pi$ complexes we feel urged to give a preliminary account of our investigations. We particularly investigated the interaction of $NO_2$ with various styrenes, since the esr spectra obtained with these compounds reveal the interaction of the unpaired electron with several nuclei rather than with a single nitrogen nucleus as observed with most aliphatic olefins.

When a small quantity of $NO_2$ reacts with styrene below 0° we obtain the same spectrum as Bielski and Gebicki (Figure 1A of ref 1). This spectrum consists mainly of a superposition of two spectra, each of these showing the interaction of an unpaired electron with one nitrogen nucleus and two magnetically equivalent protons. The species from which these two spectra result and the spectra themselves will be referred to as A and B in the following.

The hyperfine parameters of A and B can be found in Table I. Figure 1 gives the total spectrum together with the line reconstructions for A and B, based on the parameters given in Table I. The individual lines are broad (1.5 G) and those of A show a partially resolved further hfs (see Figure 1).

**Table I:** Hfs Constants of the Radicals Formed in the Reaction of $NO_2$ with Styrene

| Radical | $a_N$ | $a_H$ (2 protons) |
|---|---|---|
| A | 14.9 | 11.4 |
| B | 14.5 | 6.6 |

Using pentadeuteriostyrene, where only the ring protons are replaced by deuterium, we found essentially the same spectrum where now, however, the nine individual lines of A and B show a further splitting, as is shown in Figure 2. Apparently, the ring hydrogens contribute to a large extent to the hyperfine width. Deuterium substitution gives narrowing since $\mu_D = 0.15\mu_H$. We analyzed this substructure of the spectra with the aid of computer simulation. To increase clarity, the substructures of the lowest field lines for both A and B are given separately in Figure 3, together with their computer simulations. The parameters used in the simulations were: substructure of A: 2 protons with $a_H = 0.50$ G, 2 protons with $a_H = 0.21$ G and a line width of 0.25 G. Substructure of B: four protons with $a_H = 0.44$ G and a line width of 0.27 G.

Exactly the same spectra A and B as in Figure 1 were obtained when $\alpha,\alpha'$-diphenyl-$\beta,\beta'$-dinitrodiethylamine (prepared according to ref 2) was oxidized with *p*-nitroperbenzoic acid (PBZ), while spectra A and B of Figure 2 were obtained when $\alpha,\alpha'$-di(pentadeuteriophenyl)-$\beta,\beta'$-dinitrodiethylamine was oxidized with PBZ. The relative intensity of A and B depends on the temperature at which the oxidation takes place and on the purity of the amine. When very pure amine was used (4 times recrystallized from ethyl alcohol) and when the oxidation was performed below 40°, only A was observed; when impure amine (*i.e.*, contaminated with some $\beta$-nitrostyrene) was used or when the oxidation was performed above 60°, B was also observed. From the above it seems that A must be attributed to

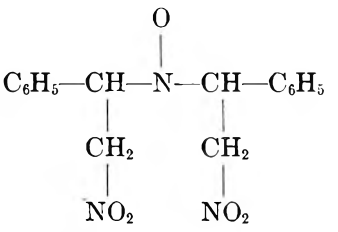

and in the deuterated species to

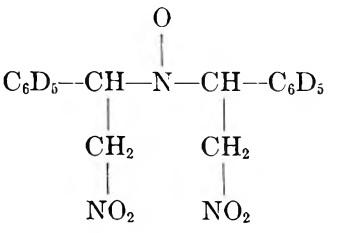

(1) B. H. J. Bielski and J. M. Gebicki, *J. Phys. Chem.*, **73**, 1402 (1969).

(2) D. E. Worrall, *J. Amer. Chem. Soc.*, **60**, 2841 (1938).

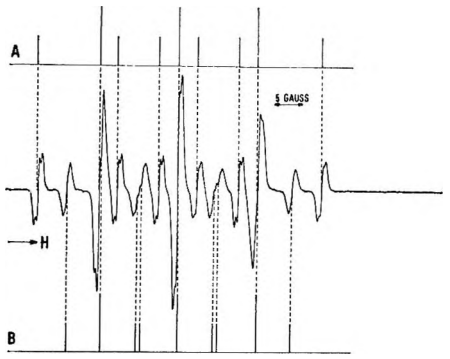


Figure 1. Spectrum of styrene with $NO_2$, together with line reconstructions for A and B.

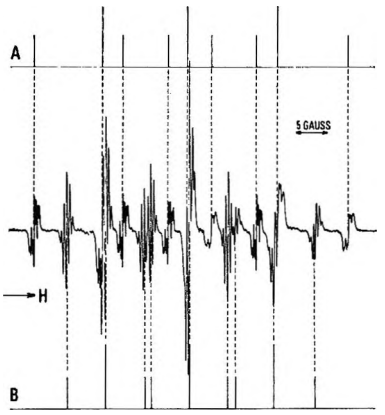


Figure 2. Spectrum of pentadeuteriostyrene with $NO_2$, together with line reconstructions for A and B. Interactions with $\gamma$ protons are not included in the line reconstructions.

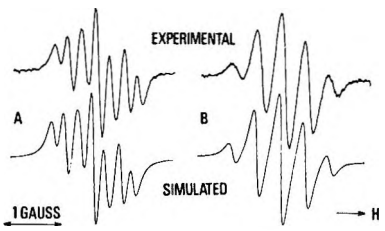


Figure 3. Experimental and computer-simulated substructures of the lowest-field lines of A and B.

steric hindrance accounting for the inequivalence of the $\gamma$ $CH_2$ protons. For B we suggest

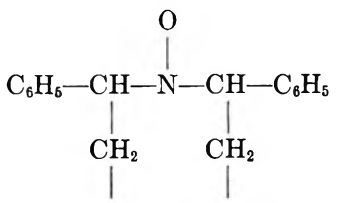

and in the deuterated species

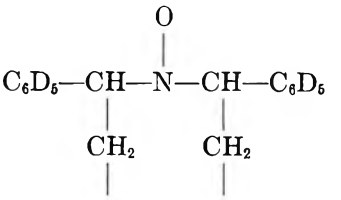

in which it is not clear what the missing $\gamma$ substituents are. From these assignments it follows that the substructures in Figures 2 and 3 must be attributed to the four aliphatic $\gamma$ protons of A and B. This was confirmed by the use of heptadeuteriostyrene, in which only the styrene $\alpha$ proton is not replaced by deuterium. Here we find no substructures; all nine lines of both A and B are single Lorentians with a width of ~0.1 G.

For A, no interaction with the nitrogens of the $\gamma$ $NO_2$ group is observed. This is not surprising, since the magnetic moment of $^{14}N$ is much smaller than the magnetic moment of the proton. Surprisingly, Bielski and Gebicki state not to have observed radical A and they only report a sextet with $a_N$ = 12.9 G and $a_H$ = 3.1 G. We find that this sextet is not present in the reaction mixture when a *small* quantity of $NO_2$ is used at low temperatures. It is only formed by the introduction of more $NO_2$ at higher temperatures. In this case the spectrum is initially a superposition of A, B, and the sextet. When one keeps the mixture for some time at room temperature, A and B disappear and the sextet remains. We find this process to be independent of the presence of solid particles. Bielski and Gebicki report these solid particles to consist of polystyrene. We find however, that they mainly consist of the dimer of the $\alpha$-nitroso-$\beta$-nitro addition product of styrene: $C_6H_5CHNOCH_2NO_2$. We conclude that the sextet must be attributed to a nitroxide and not, as Bielski and Gebicki state, to a $\pi$ complex of $NO_2$ and styrene. One would expect such a $\pi$ complex, if it exists, to be observable immediately after the introduction of $NO_2$ at low temperatures and not to see it appear at higher temperatures after a substantial amount of other reaction products have already been formed. As to the structure of the nitroxide leading to the sextet, we cannot make any definite assignment. It may be, however, that it is something like

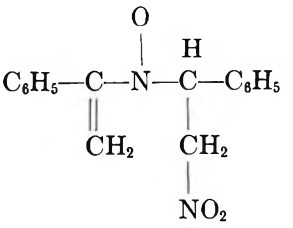

which has only one $\beta$ proton. ($\alpha$, $\beta$, and $\gamma$ refer only to the nitroxide here, *i.e.*, $\alpha$ is bonded directly to N, $\beta$ to the next C, etc.) The low value of $a_N$ for the

sextet (12.9 G) seems to be in agreement with the presence of the double bond adjacent to the nitroxide group in this structure. We used pentadeuteriostyrene in an attempt to resolve any $\gamma$-proton interactions in the sextet. Some substructure was observed, but unfortunately the resolution was insufficient for estimating the number of $\gamma$ protons involved. When using heptadeuteriostyrene, the sextet was also obtained. This proves only that the interaction with the $\alpha$ proton of styrene is observed in the sextet spectrum, which does not contradict the suggested structure.

In the reaction of $NO_2$ with $\alpha$-methylstyrene we observe the same spectrum as Bielski and Gebicki. No large interactions with $\alpha$ protons of the styrene are observed, since these are not present. The three lines of the spectrum show a badly resolved structure. This must be due to weak interactions with the phenyl hydrogens, the $\alpha$ (here $\alpha$ and $\beta$ refer to the styrene, *i.e.*, $\alpha$ is bonded to the $\alpha$ carbon of styrene, $\beta$ to the $\beta$ carbon) methyl hydrogens, and the $\beta$ hydrogens. When the solution containing the radical is cooled to 77°K the spectrum in Figure 4 is observed. From this we derived the following hyperfine and $g$ parameters: $a_{||}^N = 34.6$ G, $a_\perp^N = 4.8$ G, $g_{||} = 2.0023$, $g_\perp = 2.0077$. The assignments of $a_{||}$ and $g_{||}$ are shown in Figure 4. $a_\perp$ and $g_\perp$ were calculated from: $a_{iso} = {}^1/_3(a_{||} + 2a_\perp)$ and $g_{iso} = {}^1/_3(g_{||} + 2g_\perp)$. These values are characteristic for nitroxides.[3,4] We therefore assign this spectrum to the same type of nitroxide as found in the case of styrene. Spectra of the above kind we obtained with all of some twenty substituted styrenes investigated. We hope to publish a detailed account of this work in the near future.

We also investigated the spectra in the reaction of $NO_2$ with a large number of aliphatic olefins at temperatures from −60 up to 20° and with varying amounts of $NO_2$. In all cases a superposition of several spectra was observed, of which a triplet with $a_N = 12.5$–$15.0$ G and $g_{iso} = 2.0054$–$65$ was the most stable and by far the most intense species. The intensity of this spectrum was always much enhanced (up to 20 times) when we used a mixture of NO and $NO_2$ instead of pure $NO_2$. When $NO_2$-free NO was used together with carefully deoxygenated styrenes, no paramagnetism was found. Bielski and Gebicki assign these spectra to $\pi$ complexes of $NO_2$ and olefins. We fail to see any evidence for this assignment. The remarkable increase in intensity when a mixture of NO and $NO_2$ is used instead of pure $NO_2$ is not expected for a $\pi$ complex. Furthermore, a solvent dependence for $a_N$ would be expected but could not be found. The only observation of solvent dependence is reported by Schaafsma and Kommandeur for $NO_2$ with limonene,[5] but this could not be reproduced and must have been due to the use of impure limonene. Finally, when the solutions containing the radical were cooled down to 77°K we found spectra similar to those of Figure 4. From these spectra we always found for $a_{||}$, $a_\perp$, $g_{||}$, and $g_\perp$ values which were characteristic for dialkyl nitroxides.

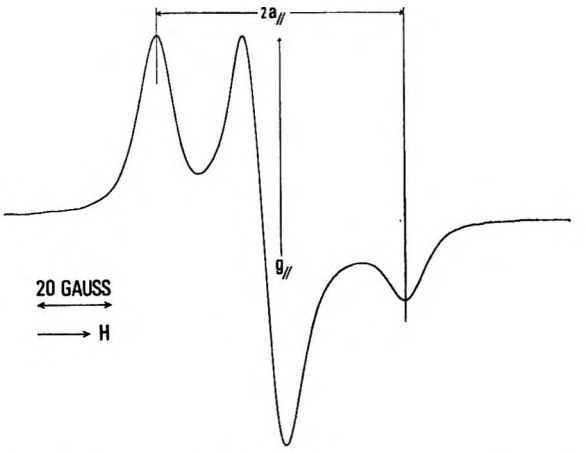


Figure 4. The spectrum of $\alpha$-methylstyrene with $NO_2$ at 77°K

Bielski and Gebicki argue that $\pi$ complexes would account for the *cis–trans* isomerization of olefins in the reaction with $NO_2$. Such isomerization can, however, also take place in the generally accepted[6] nitro-radical intermediate, by rotation along the C–C bond. Bielski and Gebicki object to the proposal of this nitro-radical intermediate because it is not observed in esr. However, it is quite possible that it is too short-lived for observation.

From these data we conclude that the spectra are due to nitroxides. Since unfortunately in almost all cases only the nitrogen hfs is observed, assignments concerning the exact structure of the nitroxides are much more difficult to make than in the case of the styrenes. Perhaps the use of partially deuterated olefins would be helpful in making such assignments.

Styrene, $\alpha$-methylstyrene, and all olefins used were of the highest available commercial grades and were vacuum distilled twice before use. The deuterated styrenes were prepared according to well-established procedures and were vacuum distilled twice before use. In the case of styrene we checked out that it made no difference whether the stabilizer was present or not.

(3) N. Edelstein, A. Kwok, and A. H. Maki, *J. Chem. Phys.*, **41**, 179 (1964).

(4) J. A. McRae and M. C. R. Symons, *Nature*, **210**, 1259 (1966).

(5) T. J. Schaafsma and J. Kommandeur, *J. Chem. Phys.*, **42**, 438 (1965).

(6) H. Shechter, *Rec. Chem. Progr.*, **25**, 55 (1964).

LABORATORY OF PHYSICAL CHEMISTRY
UNIVERSITY OF GRONINGEN, BLOEMSINGEL 10,
GRONINGEN, THE NETHERLANDS

L. JONKMAN
H. MULLER
C. KIERS
J. KOMMANDEUR

RECEIVED AUGUST 4, 1969

## Logarithmic Term in Conductivity Equation for Dilute Solutions of Strong Electrolytes

*Sir:* The well-known Fuoss–Onsager equation[1,2] for extrapolation of conductivities of (1:1) electrolytes to infinite dilution is

$$\Lambda = \Lambda_0 - S\sqrt{c} + Ec \log c + Jc$$

in which $S$ gives the limiting law. The $Ec \log c$ term makes a small but significant contribution in the accurate extrapolation to $\Lambda_0$, when a plot of $(\Lambda + S\sqrt{c} - Ec \log c)$ *vs.* $c$ is applied, using an approximate value for $\Lambda_0$. The form of $E$ is $(E_1\Lambda_0 - E_2)$, in which both $E_1$ and $E_2$ depend only upon solvent properties and temperature. Recently, Fernández-Prini and Prue,[3] in a comparison of equations derived by Fuoss and by Pitts,[4] state that both give the same value of $E$. This is certainly true for $E_1$, the dominant term, which is not surprising, since a common model is treated by closely similar mathematical methods. It is also true that $E_2$ is the same in both cases, but it has in fact a completely different origin in the two theories.

Both derivations are based upon the Onsager continuity equation, for which the terminology of Fuoss and Accascina[2] will be used. For conductance, with a static applied field, $E$, and the solution at rest, the continuity equation can be written

$$\nabla_2 f_{ji}(\mathbf{r}) v_{ji}(\mathbf{r}_1,\mathbf{r}) + \nabla_1 f_{ij}(-\mathbf{r}) v_{ij}(\mathbf{r}_2,-\mathbf{r}) = 0$$

which, as $\nabla_2 = -\nabla_1 = \nabla$ and $f_{ji}(\mathbf{r}) = f_{ij}(-\mathbf{r})$, reduces to

$$\nabla f_{ji}(\mathbf{r})\{\mathbf{v}_{ji}(\mathbf{r}_1,\mathbf{r}) - \mathbf{v}_{ij}(\mathbf{r}_2,-\mathbf{r})\} = 0$$

In this, $\mathbf{v}_{ji}$ is the velocity of an i ion, situated at distance $\mathbf{r}_2$ from an arbitrary origin, in the vicinity of j ion, situated at $\mathbf{r}_1$, $\mathbf{v}_{ji}$, $\mathbf{r}_1$, and $\mathbf{r}_2$ all being vector quantities. As indicated, $\mathbf{v}_{ji}$ depends upon the position of the j ion at $\mathbf{r}_1$ and the distance of the i ion from the j ion, $\mathbf{r} = \mathbf{r}_2 - \mathbf{r}_1$. Correspondingly, $\mathbf{v}_{ij}$ is the velocity of a j ion in the vicinity of an i ion. The dominant part of $\mathbf{v}_{ji}$ is the velocity obtained from the product of its mobility, $\omega_i$, and the total local force acting upon the i ion. The first approximation to this part alone is used in calculating the first approximation to the asymmetric potential, $\psi_j'$, about a j ion. The calculations involved are fully presented by Fuoss and Accascina[2] and by Pitts[4] for their respective theories and are not relevant to the present note. By using a second approximation to this part of $\mathbf{v}_{ji}$, both theories introduce a complex group of exponential integrals into the second approximation to $\psi_j'$; and, when these have been expanded and reduced for use at small concentrations, both theories lead to the same logarithmic term, $E_1\Lambda_0 c \log c$, for $\Lambda$.

In the second approximation, however, it is necessary also to introduce an additional term into $\mathbf{v}_{ji}$, namely, $\mathbf{v}_i(\mathbf{r}_2)$, the velocity of the fluid medium at the site of the i ion. Since the i ion has a finite size, this is really a fiction, and is taken as the fluid velocity which would exist at the center of the i ion if it were a point. In the Fuoss theory, this is assumed to be determined by the velocity field in the fluid which is created by motion of the j ion. If the fluid velocity at a distance $\mathbf{r}$ from this ion is denoted by $\mathbf{v}_j(\mathbf{r})$, then this can be evaluated and is put equal to $\mathbf{v}_i(\mathbf{r}_2)$. Solving for the effect of $\mathbf{v}_j(\mathbf{r})$ upon $\psi_j'$, we find that further exponential integrals are introduced and expansion of these leads to the logarithmic term $-E_2 c \log c$ in $\Lambda$.

Pitts[4] placed a completely different interpretation upon $\mathbf{v}_i(\mathbf{r}_2)$ in that he has put it equal to the electrophoretic velocity produced at the site of the i ion by the action of the external field upon the whole ionic atmosphere about the i ion. The introduction of such a term is open to question, but, in any case, if it is used, it should be additional to the $\mathbf{v}_j(\mathbf{r})$ term used by Fuoss, and, most important for the present note, it does not lead to any exponential integrals and thus gives rise to no term in $c \log c$.

On the other hand, in assessing the second approximation as it affects $\Lambda$, Pitts solved the hydrodynamic equation for the effect of the first approximation to the asymmetric distribution in the ionic atmosphere of the j ion upon its velocity. This introduces a term containing exponential integrals and, as pointed out by Fernández-Prini and Prue,[3] these lead to the same contribution $-E_2 c \log c$ upon expansion. To clarify the difference in approach, if the relaxation correction to be applied field $E$ is denoted by $\Delta E/E$, and the electrophoretic correction to $\Lambda$ for the unperturbed ionic atmosphere is $\Lambda_5$, the Fuoss expression for $\Lambda$ is

$$\Lambda = (\Lambda_0 - \Lambda_e)(1 + \Delta E/E)$$

while the Pitts expression is

$$\Lambda = \Lambda_0(1 + \Delta E/E) - \Lambda_e - \Lambda_e'$$

Here, $\Lambda_e'$ is the additional electrophoretic effect due to asymmetry and replaces $\Lambda_e \times \Delta E/E$.

In applying the Onsager continuity equation, the evaluation of $\mathbf{v}_i(\mathbf{r}_2)$ by Fuoss as equal to $\mathbf{v}_j(\mathbf{r})$ is more correct than that of Pitts, while the calculation of $\Lambda_e'$ is more rigorous than $\Lambda_e \times \Delta E/E$. On this basis, if the value of $E_2$ is left unchanged, $E$ should really be given by $(E_1\Lambda_0 - 2E_2)$.

As an example, for a (1:1) electrolyte in water at 25°, $E_1 = 0.5276$ and $E_2 = 20.33$, whence, for $\Lambda_0 = 150$, $E = 38.48$ instead of 58.81. The proportionate change in $E$ varies considerably for other cases, *e.g.*,

(1) R. M. Fuoss, *J. Amer. Chem. Soc.*, **81**, 2659 (1959).

(2) R. M. Fuoss and F. Accascina, "Electrolytic Conductance," Interscience Publishers, New York, N. Y., 1959.

(3) R. Fernández-Prini and J. E. Prue, *Z. Physik. Chem.* (Leipzig), **228**, 373 (1965).

(4) E. Pitts, *Proc. Roy. Soc.*, **A217**, 43 (1953).

it would be greater for lithium halides in water, due to the smaller values of $\Lambda_0$ and much less for halogen acids in water, due to the very high values of $\Lambda_0$. Since the $Ec \log c$ term is small, the effect of the extrapolation of $(\Lambda + S\sqrt{c} - Ec \log c)$ *vs.* $c$ upon $\Lambda_0$ is not serious; but the gradient of the line obtained, giving $J$, can be seriously affected. Since $J$ depends upon the distance of closest approach between ions, $a$, and is used to calculate $a$, the significance of such calculations becomes open to question. Actually, the true relationship between $J$ and $a$ presents a difficult problem. As pointed out by Fernández-Prini and Prue,[3] the Fuoss theory and the Pitts theory give different expressions, since they employ different terms in the continuity equation, as just discussed, different mathematical methods of approximation, and different boundary conditions. A further discussion of these differences appears in a recent paper by Pitts, *et al.*[5] Still other expressions arise if a synthesis of the Fuoss and Pitts theories is attempted, along the lines presented for the $Ec \log c$ term, but a discussion of this requires a lengthy analysis which lies beyond the scope of this note.

The sole point it is desired to make here is that the Fuoss and Pitt theories need not be mutually exclusive, since they are based upon the same model. The fact that, as they stand, both yield the same values of $E$ is accidental. On theoretical grounds, the contributions of both to $E$ seem to be sound and, if this is accepted, the correct value of $E$ is $(E_1\Lambda_0 - 2E_2)$ instead of $(E_1\Lambda_0 - E_2)$.

(5) E. Pitts, B. E. Tabor, and J. Daly, *Trans. Faraday Soc.*, **65**, 849 (1969).

NATIONAL CHEMICAL RESEARCH LABORATORY P. C. CARMAN
SOUTH AFRICAN COUNCIL FOR SCIENTIFIC
AND INDUSTRIAL RESEARCH
PRETORIA, SOUTH AFRICA

RECEIVED NOVEMBER 13, 1969